

Special Issue Reprint

---

# Intelligent Safety Monitoring and Prevention Process in Coal Mines

---

Edited by  
Feng Du, Aitao Zhou and Bo Li

[mdpi.com/journal/processes](https://mdpi.com/journal/processes)

# **Intelligent Safety Monitoring and Prevention Process in Coal Mines**



# Intelligent Safety Monitoring and Prevention Process in Coal Mines

Guest Editors

**Feng Du**

**Aitao Zhou**

**Bo Li**



Basel • Beijing • Wuhan • Barcelona • Belgrade • Novi Sad • Cluj • Manchester

*Guest Editors*

Feng Du

China University of Mining  
and Technology

Beijing

China

Aitao Zhou

China University of Mining  
and Technology

Beijing

China

Bo Li

Henan Polytechnic  
University

Jiaozuo

China

*Editorial Office*

MDPI AG

Grosspeteranlage 5

4052 Basel, Switzerland

This is a reprint of the Special Issue, published open access by the journal *Processes* (ISSN 2227-9717), freely accessible at: [https://www.mdpi.com/journal/processes/special\\_issues/Z946B2SJ92](https://www.mdpi.com/journal/processes/special_issues/Z946B2SJ92).

For citation purposes, cite each article independently as indicated on the article page online and as indicated below:

Lastname, A.A.; Lastname, B.B. Article Title. <i>Journal Name</i> <b>Year</b> , <i>Volume Number</i> , Page Range.
--

**ISBN 978-3-7258-3135-7 (Hbk)**

**ISBN 978-3-7258-3136-4 (PDF)**

**<https://doi.org/10.3390/books978-3-7258-3136-4>**

© 2025 by the authors. Articles in this book are Open Access and distributed under the Creative Commons Attribution (CC BY) license. The book as a whole is distributed by MDPI under the terms and conditions of the Creative Commons Attribution-NonCommercial-NoDerivs (CC BY-NC-ND) license (<https://creativecommons.org/licenses/by-nc-nd/4.0/>).

# Contents

<b>Feng Du, Aitao Zhou and Bo Li</b> Special Issue “Intelligent Safety Monitoring and Prevention Process in Coal Mines” Reprinted from: <i>Processes</i> <b>2025</b> , <i>13</i> , 85, <a href="https://doi.org/10.3390/pr13010085">https://doi.org/10.3390/pr13010085</a> . . . . .	<b>1</b>
<b>Zebin Zhu, Jian Feng, Yuguo Kang, Biao Zhang and Xue Ling</b> Simulation Research and Practical Application of Cutting Teeth for Drill Bits in Life-Support Holes Reprinted from: <i>Processes</i> <b>2024</b> , <i>12</i> , 2130, <a href="https://doi.org/10.3390/pr12102130">https://doi.org/10.3390/pr12102130</a> . . . . .	<b>6</b>
<b>Chunguang Zhao, Peng Gao, Jinlin Ruan, Yang Pu, Yuan Sun, Xiaoyang Cheng and Yu Sun</b> Research on Hotspots and Evolutionary Trends in Coal Mine Gas Prevention Reprinted from: <i>Processes</i> <b>2024</b> , <i>12</i> , 1993, <a href="https://doi.org/10.3390/pr12091993">https://doi.org/10.3390/pr12091993</a> . . . . .	<b>22</b>
<b>Wenbin Wu, Zhen Wang, Zhuangzhuang Yao, Jianyun Qin and Xinglan Yu</b> Study on Permeability Enhancement of Seepage–Damage Coupling Model of Gas-Bearing Coal by Water Injection Reprinted from: <i>Processes</i> <b>2024</b> , <i>12</i> , 1899, <a href="https://doi.org/10.3390/pr12091899">https://doi.org/10.3390/pr12091899</a> . . . . .	<b>43</b>
<b>Yongming Yin, Dacang Wang, Quanjie Zhu, Guangyu Yang, Xuexi Chen, Xiaohui Liu and Yongfeng Liu</b> Research on Intelligent Design and Visualization of Gas Extraction Drilling Based on PSO–LSTM Reprinted from: <i>Processes</i> <b>2024</b> , <i>12</i> , 1691, <a href="https://doi.org/10.3390/pr12081691">https://doi.org/10.3390/pr12081691</a> . . . . .	<b>62</b>
<b>Yunfei Zuo, Jianyu Zhang, Lidong Yang, Feiran Wang and Zhengang Wang</b> A Study on the Effect of Different Charge Structures on the Permeability Enhancement of Coal Seam Blasting Reprinted from: <i>Processes</i> <b>2024</b> , <i>12</i> , 1645, <a href="https://doi.org/10.3390/pr12081645">https://doi.org/10.3390/pr12081645</a> . . . . .	<b>83</b>
<b>Huijie Zhang, Maoliang Shen, Zhonggang Huo, Yibin Zhang, Longyong Shu and Yang Li</b> Research on Gas Drainage Pipeline Leakage Detection and Localization Based on the Pressure Gradient Method Reprinted from: <i>Processes</i> <b>2024</b> , <i>12</i> , 1590, <a href="https://doi.org/10.3390/pr12081590">https://doi.org/10.3390/pr12081590</a> . . . . .	<b>96</b>
<b>Xiaoyu Cheng, Cheng Cheng, Lu Xiao and Xingying Ma</b> Response Surface Analysis on Multiple Parameter Effects on Borehole Gas Extraction Efficiency Reprinted from: <i>Processes</i> <b>2024</b> , <i>12</i> , 1587, <a href="https://doi.org/10.3390/pr12081587">https://doi.org/10.3390/pr12081587</a> . . . . .	<b>116</b>
<b>Cheng Cheng, Xiao-Yu Cheng, Long Chen and Xing-Ying Ma</b> Research on Gas Control Technology in Goaf Based on the Influence of Mining Speed Reprinted from: <i>Processes</i> <b>2024</b> , <i>12</i> , 1528, <a href="https://doi.org/10.3390/pr12071528">https://doi.org/10.3390/pr12071528</a> . . . . .	<b>130</b>
<b>Yu Zhang, Kongyi Fang and Zhengjia Guo</b> Distriformer: Research on a Distributed Training Rockburst Prediction Method Reprinted from: <i>Processes</i> <b>2024</b> , <i>12</i> , 1205, <a href="https://doi.org/10.3390/pr12061205">https://doi.org/10.3390/pr12061205</a> . . . . .	<b>145</b>
<b>Muhammad Kamran, Waseem Chaudhry, Blessing Olamide Taiwo, Shahab Hosseini and Hafeezur Rehman</b> Decision Intelligence-Based Predictive Modelling of Hard Rock Pillar Stability Using K-Nearest Neighbour Coupled with Grey Wolf Optimization Algorithm Reprinted from: <i>Processes</i> <b>2024</b> , <i>12</i> , 783, <a href="https://doi.org/10.3390/pr12040783">https://doi.org/10.3390/pr12040783</a> . . . . .	<b>158</b>

<b>Suihan Yang, Xiangzhi Wei, Linlin Chen, Zhiliu Wang and Wen Wang</b> Analysis of Rock Burst Mechanism in Extra-Thick Coal Seam Controlled by Thrust Fault under Mining Disturbance Reprinted from: <i>Processes</i> <b>2024</b> , <i>12</i> , 320, <a href="https://doi.org/10.3390/pr12020320">https://doi.org/10.3390/pr12020320</a> . . . . .	<b>180</b>
<b>Yu Hao, Huanhuan Yang, Lijun Zhang and Chaolun Sun</b> Study on the Effectiveness of the Integral Emergency Response System for Coal Mine Water Hazard Accidents Based on Combination Weighting Reprinted from: <i>Processes</i> <b>2024</b> , <i>12</i> , 235, <a href="https://doi.org/10.3390/pr12010235">https://doi.org/10.3390/pr12010235</a> . . . . .	<b>200</b>
<b>Ji Ma, Jiashuo Li, Shuai Zhang, Shengtao Yang, Xiaohang Dong and Dongsheng Liu</b> Numerical Simulation Analysis of Acoustic Emission Characteristics during the Drilling Pressure Relief Process in Coal Seams under Different Influencing Factors Reprinted from: <i>Processes</i> <b>2023</b> , <i>11</i> , 3277, <a href="https://doi.org/10.3390/pr11123277">https://doi.org/10.3390/pr11123277</a> . . . . .	<b>218</b>
<b>Zhigang Zhang, Linchao Dai, Haitao Sun, Yanbao Liu, Huiming Yang, Rifu Li and Yi Zhang</b> Study on the Spatiotemporal Dynamic Evolution Law of a Deep Thick Hard Roof and Coal Seam Reprinted from: <i>Processes</i> <b>2023</b> , <i>11</i> , 3173, <a href="https://doi.org/10.3390/pr11113173">https://doi.org/10.3390/pr11113173</a> . . . . .	<b>241</b>
<b>Yaochuang Wang, Pengkun Chen and Shen Wang</b> Study of Overlying Rock Structure and Intensive Pressure Control Technology of Island Longwall Panel in Extra-Thick Coal Seams Reprinted from: <i>Processes</i> <b>2023</b> , <i>11</i> , 3083, <a href="https://doi.org/10.3390/pr11113083">https://doi.org/10.3390/pr11113083</a> . . . . .	<b>256</b>
<b>Xiaoping Li, Guoping Han, Yong Wang, Jie Xu, Jie Du, Bo Yang, et al.</b> Study on Performance Optimization of Water-Rich Grouting Materials Based on Response Surface Methodology Reprinted from: <i>Processes</i> <b>2023</b> , <i>11</i> , 2789, <a href="https://doi.org/10.3390/pr11092789">https://doi.org/10.3390/pr11092789</a> . . . . .	<b>281</b>
<b>Haiyan Ma, Hongkai Zhang, Kunlin Yang, Yingjie Hu, Zeyu Yang and Nianjie Ma</b> Research on the Positioning Accuracy of the Cutting Head of a Tunneling Machine Based on Ultra-Wideband Positioning Technology Reprinted from: <i>Processes</i> <b>2023</b> , <i>11</i> , 2534, <a href="https://doi.org/10.3390/pr11092534">https://doi.org/10.3390/pr11092534</a> . . . . .	<b>295</b>
<b>Gang Cheng, Haiyan Wang, Bo Tan and Shuhui Fu</b> Carbon Dioxide Prevents Oxygen Adsorption at Low-Temperature Oxidation Stage of Low-Rank Coal: Laboratory Study and Molecular Simulation Reprinted from: <i>Processes</i> <b>2023</b> , <i>11</i> , 2504, <a href="https://doi.org/10.3390/pr11082504">https://doi.org/10.3390/pr11082504</a> . . . . .	<b>310</b>
<b>Chaolun Sun, Yu Hao, Jianping Wei and Lijun Zhang</b> Research on the Evaluation of Emergency Management Synergy Capability of Coal Mines Based on the Entropy Weight Matter-Element Extension Model Reprinted from: <i>Processes</i> <b>2023</b> , <i>11</i> , 2492, <a href="https://doi.org/10.3390/pr11082492">https://doi.org/10.3390/pr11082492</a> . . . . .	<b>332</b>
<b>Feiran Wang, Zhansuo Ji, Haiyan Wang, Yue Chen, Tao Wang, Ruoyi Tao, et al.</b> Analysis of the Current Status and Hot Technologies of Coal Spontaneous Combustion Warning Reprinted from: <i>Processes</i> <b>2023</b> , <i>11</i> , 2480, <a href="https://doi.org/10.3390/pr11082480">https://doi.org/10.3390/pr11082480</a> . . . . .	<b>346</b>
<b>Li Li, Xiao Zhang, Bin Hu and Shun Lei</b> Preliminary Exploration of the Technology of Coal Reshaping and Replacement Mining of Abandoned Coal in Goafs Reprinted from: <i>Processes</i> <b>2023</b> , <i>11</i> , 2474, <a href="https://doi.org/10.3390/pr11082474">https://doi.org/10.3390/pr11082474</a> . . . . .	<b>363</b>

<b>Han Gao, Feng Du, Xiaoyu Cheng, Jinjie Zhang and Aitao Zhou</b> Study on the Influence Mechanism of Air Leakage on Gas Extraction Effect—A Numerical Case Study of the Coal Mine Site in Anhui Reprinted from: <i>Processes</i> <b>2023</b> , <i>11</i> , 2161, <a href="https://doi.org/10.3390/pr11072161">https://doi.org/10.3390/pr11072161</a> . . . . .	<b>381</b>
<b>Zuo Sun, Yingjie Liu, Qingjie Qi, Jiamei Chai and Beifang Gu</b> The Influence of High-Pressure Water Jet Cutting Parameters on the Relief of Pressure around the Coal Slot Reprinted from: <i>Processes</i> <b>2023</b> , <i>11</i> , 2071, <a href="https://doi.org/10.3390/pr11072071">https://doi.org/10.3390/pr11072071</a> . . . . .	<b>399</b>
<b>Zhuangzhuang Yao, Zhigang Zhang and Linchao Dai</b> Research on Hydraulic Thruster-Enhanced Permeability Technology of Soft Coal Drilling through Strata Based on Packer Sealing Method Reprinted from: <i>Processes</i> <b>2023</b> , <i>11</i> , 1959, <a href="https://doi.org/10.3390/pr11071959">https://doi.org/10.3390/pr11071959</a> . . . . .	<b>413</b>
<b>Dandan Han, Guchen Niu, Hongqing Zhu, Tianyao Chang, Bing Liu, Yongbo Ren, et al.</b> Exploration and Frontier of Coal Spontaneous Combustion Fire Prevention Materials Reprinted from: <i>Processes</i> <b>2024</b> , <i>12</i> , 1155, <a href="https://doi.org/10.3390/pr12061155">https://doi.org/10.3390/pr12061155</a> . . . . .	<b>429</b>





Editorial

# Special Issue “Intelligent Safety Monitoring and Prevention Process in Coal Mines”

Feng Du <sup>1,\*</sup>, Aitao Zhou <sup>1</sup> and Bo Li <sup>2</sup>

<sup>1</sup> School of Emergency Management and Safety Engineering, China University of Mining and Technology-Beijing, Beijing 100083, China; cumtbzat@126.com

<sup>2</sup> State Key Laboratory Cultivation Base for Gas Geology and Gas Control, Henan Polytechnic University, Jiaozuo 454000, China; anquanlibo@163.com

\* Correspondence: fdu@cumtb.edu.cn

Coal mine safety has always been the top priority of the coal industry. Despite the rapid development of renewable energy, coal is still the main source of energy in many countries. With the continuous progress in the development of coal mining technology, the depth and scale of mines continue to expand, the operating environment is more complex, and the safety risk is significantly increased [1–3]. In order to ensure the life safety of miners and the continuity of production, intelligent monitoring and prevention have become important means of coal mine safety management. The advanced intelligent sensing and prevention technology of coal mine disasters is one of the key technologies to be broken through in the intelligent management of coal mine safety.

In the aspect of the intelligent early warning and monitoring prevention of coal mine disasters, Miao et al. [4] constructed a gas safety situation prediction model based on the risk of a coal mine gas explosion. Coal and gas outbursts are powerful natural disasters in underground coal mine production, which seriously threaten the safety of coal mine production. Liu et al. [5–8] constructed an intelligent prediction model for intelligent monitoring and early warning of coal and gas outbursts. Liu et al. [9] summarized the early warning methods and prevention and control technologies of coal spontaneous combustion monitoring and early research progress. Mine fire is a serious threat to the safety of workers. Shen et al. [10–13] have carried out a lot of research on the theory and practice of the intelligent monitoring and early warning of mine fires. Rock bursts often threaten the lives of construction workers. Li et al. [14–17] improved different intelligent prediction methods, which are of great value for the accurate prediction and prevention of rock bursts. In addition, in view of the complex stress situation of coal mines and the different situation of underground production, the intelligent prediction and early warning method proposed by Li et al. [18–23] is of great significance to the safety of coal mine production.

This Special Issue of the journal *Processes* titled “Intelligent Safety Monitoring and Prevention Process in Coal Mines” collects research papers on the progress of intelligent safety monitoring and prevention in coal mines in a forum. The content covers the safety technology research of coal mine disaster mechanisms and risk identification, coal mine disaster multi-information intelligent early warning, coal mine disaster prevention mechanisms, and intelligent prevention and control. Many studies are interdisciplinary in nature, but the ultimate theme of different studies is coal mine production safety. It involves gas extraction, fire and explosion prevention, prediction and early warning, complex force analysis, and so on.

To comprehensively understand the research status and hotspots of coal mine gas management at home and abroad, Zhao et al. [24] analyzed the data from 2000 to 2023

Received: 15 October 2024

Accepted: 2 December 2024

Published: 2 January 2025

**Citation:** Du, F.; Zhou, A.; Li, B. Special Issue “Intelligent Safety Monitoring and Prevention Process in Coal Mines”. *Processes* **2025**, *13*, 85. <https://doi.org/10.3390/pr13010085>

**Copyright:** © 2025 by the authors. Licensee MDPI, Basel, Switzerland. This article is an open access article distributed under the terms and conditions of the Creative Commons Attribution (CC BY) license (<https://creativecommons.org/licenses/by/4.0/>).

to provide references for relevant researchers' research and literature search. In terms of coal mine gas extraction prevention and control, Yin et al. [25] proposed an intelligent optimization method for gas extraction parameters, quickly generated a three-dimensional model of gas extraction drilling, and improved the intelligent level of gas extraction drilling. Zhang et al. [26] proposed a leak detection and location method of gas drainage pipeline based on the pressure gradient method, which laid a foundation for fault diagnosis and location of the coal mine gas drainage pipe network. Cheng et al. [27] analyzed the interaction between different factors and their influence on effective gas extraction radius. Cheng et al. [28] analyzed the efficiency of gas extraction in goaf under different mining rates, which provided a theoretical basis for identifying the gas enrichment areas in the overburden caused by mining and improved the efficiency of gas extraction at the working face. Li et al. [29] prepared a new type of water-rich grouting material (RW) using a composite coagulant and other additives, which is conducive to improving the grouting quality and sealing effect of extraction boreholes. Gao et al. [30] studied the effects of extraction time, extraction negative pressure, and air leakage on gas extraction and revealed the mechanism of gas leakage around the gas extraction borehole.

In the process of coal seam mining, the mine will encounter a variety of complex stress conditions, which mainly come from the geological structure, mining methods, support measures, and other aspects. Yang et al. [31] studied the rock burst mechanism in extremely thick coal seams controlled by thrust faults under mining disturbance and fault action. Ma et al. [32] studied the acoustic emission characteristics in the process of coal seam drilling pressure relief under different influencing factors and analyzed the influence of deep hard roof cracks on the safe mining of thick coal seams. Zhang et al. [33] studied the dynamic evolution of the stress field, displacement field, energy field, and plastic zone during mining of coal seams and overlying strata. Wang et al. [34] analyzed the mining characteristics of island longwall roofs in extremely thick coal seams and obtained the mechanical characteristics of isolated working faces under special conditions. Sun et al. [35] discussed the influence of the cutting parameters of high-pressure water jets on the pressure relief around coal grooves, which provided valuable theoretical guidance for the grooving of high-pressure water jets.

Coal spontaneous combustion disaster is one of the most serious mine accidents in China, which poses a great threat to underground personal safety and coal production. In order to prevent and control the hazards of coal spontaneous combustion and build an efficient coal spontaneous combustion early warning system, Wang et al. [36] analyzed the research hotspots in the field of coal spontaneous combustion early warning. Cheng et al. [37] conducted a laboratory study and molecular simulation on the oxygen adsorption of low-rank coal prevented by carbon dioxide at the low-temperature oxidation stage, which has certain guiding significance for the study of carbon dioxide prevention and control of coal spontaneous combustion. Han et al. [38] investigated the current situation of coal spontaneous combustion (CSC) fire prevention and reviewed and prospected the existing fire prevention materials from three aspects: physical, chemical, and physicochemical suppression.

In terms of coal seam permeability increase, Wu et al. [39] explored the mechanism and influencing factors of water injection and permeability increase and introduced a mechanical model for calculating ground stress changes, which can help evaluate the impact of water injection and permeability increase. Zuo et al. [40] studied the effect of different fused coil structures on coal seam blasting in order to increase the permeability of coal seams. Yao et al. [41] studied soft coal hydraulic fracturing punching technology with the packer tool column sealing method in view of the characteristics of "three soft" outburst coal seams in Henan province with large gas content, poor permeability, and great mining

difficulty, providing new ideas and technical support for hydraulic increased permeability technology in this field.

In terms of coal mine safety management and evaluation, Hao et al. [42] constructed the effectiveness measurement index system of the emergency response system, which provided a new idea for how to improve the comprehensive emergency response ability of coal mine flood accidents and also provided support for the decision-making of improving the emergency response ability of coal mines. Sun et al. [43] built a hierarchical evaluation index system based on the emergency management process to provide decision support for the construction of the emergency management coordination capacity of coal mining enterprises.

In terms of intelligent prediction, Zhang et al. [44] proposed a distributed training rockburst prediction method named Distriformer, which improves the accuracy of rockburst prediction. Kamran et al. [45] used the K-Nearest Neighbor and Gray Wolf optimization algorithm (KNN-GWO) to develop the application of decision intelligence-based stability prediction modeling of hard rock columns in underground engineering structures, which provides an excellent benchmark for accurate prediction of the stability of hard rock columns.

In other aspects related to coal mine safety, Ma et al. [46] studied the positioning accuracy of tunnel boring machine cutting heads based on UWB positioning technology. Li et al. [47] discussed the interaction between the strength of filling materials and the size of loose coal in the CRRM process, analyzed the scientific problems faced in each link in the process of filling and replacing waste coal in goaf, and proposed further improvement methods. The technical system of abandoned coal filling and replacement was improved.

The above studies have been discussed and studied in many aspects, such as theory, experiment, and numerical simulation for coal mine safety production, intelligent monitoring, and prevention processes, and solved many problems in coal mine safety from multiple perspectives across multiple disciplines. In the face of the many challenges faced by coal mine safety production, there is still a lot to be explored in the future, and it is worth exploring. The journal will continue to solicit high-quality contributions in these domains.

We thank all contributors and editors for their enthusiastic support of the Special Issue, as well as the editorial staff of the journal *Processes* for their efforts.

**Funding:** This research received no external funding.

**Conflicts of Interest:** The authors declare no conflicts of interest.

## References

1. Yuan, L.; Wang, E.; Ma, Y.; Liu, Y.; Li, X. Research progress of coal and rock dynamic disasters and scientific and technological problems in China. *J. China Coal Soc.* **2023**, *48*, 1825–1845. (In Chinese) [CrossRef]
2. Wang, K.; Du, F. Coal-gas compound dynamic disasters in China: A review. *Process Saf. Environ. Prot.* **2020**, *133*, 1–17. [CrossRef]
3. Dai, L. Safety classification and application of coal-rock gas compound dynamic disaster in coal mine. *IOP Conf. Ser. Earth Environ. Sci.* **2021**, *651*, 032036. [CrossRef]
4. Miao, D.; Lv, Y.; Yu, K.; Liu, L.; Jiang, J. Research on coal mine hidden danger analysis and risk early warning technology based on data mining in China. *Process Saf. Environ. Prot.* **2023**, *171*, 1–17. [CrossRef]
5. Liu, X.; Du, Z.; Wang, E.; Jiang, A.; Tian, H.; Wang, K.; Xiong, Y.; Wang, H. Intelligent recognition of coal and gas outburst precursor and potential hazards using YOLOv8 neural network. *Geomech. Geophys. Geo-Energy Geo-Resour.* **2024**, *10*, 117. [CrossRef]
6. Du, Z.; Liu, X.; Wang, J.; Jiang, G.; Meng, Z.; Jia, H.; Xie, H.; Zhou, X. Response Characteristics of Gas Concentration Level in Mining Process and Intelligent Recognition Method Based on BI-LSTM. *Min. Metall. Explor.* **2023**, *40*, 807–818. [CrossRef]
7. Yuan, H.; Ji, S.; Liu, G.; Xiong, L.; Li, H.; Cao, Z.; Xia, Z. Investigation on Intelligent Early Warning of Rock Burst Disasters Using the PCA-PSO-ELM Model. *Appl. Sci.* **2023**, *13*, 8796. [CrossRef]

8. Lan, T.; Zhang, Z.; Sun, J.; Zhao, W.; Zhang, M.; Jia, W.; Liu, M.; Guo, X. Regional prediction and prevention analysis of rockburst hazard based on the Gaussian process for binary classification. *Front. Earth Sci.* **2022**, *10*, 959232. [CrossRef]
9. Liu, Y.; Wen, H.; Chen, C.; Guo, J.; Jin, Y.; Zheng, X.; Cheng, X.; Li, D. Research Status and Development Trend of Coal Spontaneous Combustion Fire and Prevention Technology in China: A Review. *ACS Omega* **2024**, *9*, 21727–21750. [CrossRef]
10. Shen, Y.; Li, Y.; Li, Z. Application of Intelligent Inspection Robot in Coal Mine Industrial Heritage Landscape: Taking Wangshiwa Coal Mine as an Example. *Front. Neurobotics* **2022**, *16*, 865146. [CrossRef]
11. Wang, W.; Liu, H.; Yang, B.; Zhang, D.; Lyu, H.; Song, X.; Shu, C. Pyrolysis characteristics and dynamics analysis of a coal mine roadway conveyor belt. *J. Therm. Anal. Calorim.* **2022**, *148*, 4823–4832. [CrossRef]
12. Gong, W.; Hu, J.; Wang, Z.; Wei, Y.; Li, Y.; Zhang, T.; Zhang, Q.; Liu, T.; Ning, Y.; Zhang, W.; et al. Recent advances in laser gas sensors for applications to safety monitoring in intelligent coal mines. *Front. Phys.* **2022**, *10*, 1058475. [CrossRef]
13. Li, D.; Liu, Z.; Armaghani, D.; Xiao, P.; Zhou, J. Novel Ensemble Tree Solution for Rockburst Prediction Using Deep Forest. *Mathematics* **2022**, *10*, 787. [CrossRef]
14. Li, M.; Li, K.; Qin, Q. A rockburst prediction model based on extreme learning machine with improved Harris Hawks optimization and its application. *Tunn. Undergr. Space Technol.* **2023**, *134*, 104978. [CrossRef]
15. Basnet, P.; Mahtab, S.; Jin, A. A comprehensive review of intelligent machine learning based predicting methods in long-term and short-term rock burst prediction. *Tunn. Undergr. Space Technol.* **2023**, *142*, 105434. [CrossRef]
16. Di, Y.; Wang, E.; Li, Z.; Liu, X.; Huang, T.; Yao, J. Comprehensive early warning method of microseismic, acoustic emission, and electromagnetic radiation signals of rock burst based on deep learning. *Int. J. Rock Mech. Min. Sci.* **2023**, *170*, 105519. [CrossRef]
17. Chen, J.; Zhu, C.; Du, J.; Pu, Y.; Pan, P.; Bai, J.; Qi, Q. A quantitative pre-warning for coal burst hazardous zones in a deep coal mine based on the spatio-temporal forecast of microseismic events. *Process Saf. Environ. Prot.* **2022**, *159*, 1105–1112. [CrossRef]
18. Li, Z.; Fan, J.; Feng, G.; Qi, C.; Zhang, J. A New Method for Identifying Coal Pillar Instability Based on Energy and Stress Correlation Characteristics and Its Engineering Application. *Minerals* **2023**, *13*, 1507. [CrossRef]
19. Li, A.; Cui, G.; Wang, P.; Wang, X.; Hong, Z.; Kong, J.; Kan, J. Deformation and Failure Laws of Surrounding Rocks of Coal Roadways under High Dynamic Load and Intelligent Prediction. *Sustainability* **2023**, *15*, 1313. [CrossRef]
20. Dai, J.; Shan, P.; Zhou, Q. Study on Intelligent Identification Method of Coal Pillar Stability in Fully Mechanized Caving Face of Thick Coal Seam. *Energies* **2020**, *13*, 305. [CrossRef]
21. Mitra, S.; Kumar, D.; Chaulya, S.; Kumar, C. Prediction of Strata Monitoring System in Underground Coal Mines Using IoT. *J. Geol. Soc. India* **2022**, *98*, 232–236. [CrossRef]
22. Li, F.; Kong, D.; Li, Q.; Shang, Y.; Cheng, Z.; He, L. Failure analysis and prediction of roof instability in end face under repeated mining using early warning system. *Sci. Rep.* **2023**, *13*, 8764. [CrossRef] [PubMed]
23. Chen, Y.; Liu, C.; Liu, J.; Yang, P.; Wu, F.; Liu, S.; Liu, H.; Yu, X. Intelligent prediction for support resistance in working faces of coal mine: A research based on deep spatiotemporal sequence models. *Expert Syst. Appl.* **2024**, *238*, 122020. [CrossRef]
24. Zhao, C.; Gao, P.; Ruan, J.; Pu, Y.; Sun, Y.; Cheng, X.; Sun, Y. Research on Hotspots and Evolutionary Trends in Coal Mine Gas Prevention. *Processes* **2024**, *12*, 1993. [CrossRef]
25. Yin, Y.; Wang, D.; Zhu, Q.; Yang, G.; Chen, X.; Liu, X.; Liu, Y. Research on Intelligent Design and Visualization of Gas Extraction Drilling Based on PSO–LSTM. *Processes* **2024**, *12*, 1691. [CrossRef]
26. Zhang, H.; Shen, M.; Huo, Z.; Zhang, Y.; Shu, L.; Li, Y. Research on Gas Drainage Pipeline Leakage Detection and Localization Based on the Pressure Gradient Method. *Processes* **2024**, *12*, 1590. [CrossRef]
27. Cheng, X.; Cheng, C.; Xiao, L.; Ma, X. Response Surface Analysis on Multiple Parameter Effects on Borehole Gas Extraction Efficiency. *Processes* **2024**, *12*, 1587. [CrossRef]
28. Cheng, C.; Cheng, X.-Y.; Chen, L.; Ma, X.-Y. Research on Gas Control Technology in Goaf Based on the Influence of Mining Speed. *Processes* **2024**, *12*, 1528. [CrossRef]
29. Li, X.; Han, G.; Wang, Y.; Xu, J.; Du, J.; Yang, B.; Zhang, M.; Li, T.; Li, B. Study on Performance Optimization of Water-Rich Grouting Materials Based on Response Surface Methodology. *Processes* **2023**, *11*, 2789. [CrossRef]
30. Gao, H.; Du, F.; Cheng, X.; Zhang, J.; Zhou, A. Study on the Influence Mechanism of Air Leakage on Gas Extraction Effect—A Numerical Case Study of the Coal Mine Site in Anhui. *Processes* **2023**, *11*, 2161. [CrossRef]
31. Yang, S.; Wei, X.; Chen, L.; Wang, Z.; Wang, W. Analysis of Rock Burst Mechanism in Extra-Thick Coal Seam Controlled by Thrust Fault under Mining Disturbance. *Processes* **2024**, *12*, 320. [CrossRef]
32. Ma, J.; Li, J.; Zhang, S.; Yang, S.; Dong, X.; Liu, D. Numerical Simulation Analysis of Acoustic Emission Characteristics during the Drilling Pressure Relief Process in Coal Seams under Different Influencing Factors. *Processes* **2023**, *11*, 3277. [CrossRef]
33. Wang, Y.; Chen, P.; Wang, S. Study of Overlying Rock Structure and Intensive Pressure Control Technology of Island Longwall Panel in Extra-Thick Coal Seams. *Processes* **2023**, *11*, 3083. [CrossRef]
34. Zhang, Z.; Dai, L.; Sun, H.; Liu, Y.; Yang, H.; Li, R.; Zhang, Y. Study on the Spatiotemporal Dynamic Evolution Law of a Deep Thick Hard Roof and Coal Seam. *Processes* **2023**, *11*, 3173. [CrossRef]

35. Sun, Z.; Liu, Y.; Qi, Q.; Chai, J.; Gu, B. The Influence of High-Pressure Water Jet Cutting Parameters on the Relief of Pressure around the Coal Slot. *Processes* **2023**, *11*, 2071. [CrossRef]
36. Wang, F.; Ji, Z.; Wang, H.; Chen, Y.; Wang, T.; Tao, R.; Su, C.; Niu, G. Analysis of the Current Status and Hot Technologies of Coal Spontaneous Combustion Warning. *Processes* **2023**, *11*, 2480. [CrossRef]
37. Cheng, G.; Wang, H.; Tan, B.; Fu, S. Carbon Dioxide Prevents Oxygen Adsorption at Low-Temperature Oxidation Stage of Low-Rank Coal: Laboratory Study and Molecular Simulation. *Processes* **2023**, *11*, 2504. [CrossRef]
38. Han, D.; Niu, G.; Zhu, H.; Chang, T.; Liu, B.; Ren, Y.; Wang, Y.; Song, B. Exploration and Frontier of Coal Spontaneous Combustion Fire Prevention Materials. *Processes* **2024**, *12*, 1155. [CrossRef]
39. Wu, W.; Wang, Z.; Yao, Z.; Qin, J.; Yu, X. Study on Permeability Enhancement of Seepage–Damage Coupling Model of Gas-Bearing Coal by Water Injection. *Processes* **2024**, *12*, 1899. [CrossRef]
40. Zuo, Y.; Zhang, J.; Yang, L.; Wang, F.; Wang, Z. A Study on the Effect of Different Charge Structures on the Permeability Enhancement of Coal Seam Blasting. *Processes* **2024**, *12*, 1645. [CrossRef]
41. Yao, Z.; Zhang, Z.; Dai, L. Research on Hydraulic Thruster-Enhanced Permeability Technology of Soft Coal Drilling through Strata Based on Packer Sealing Method. *Processes* **2023**, *11*, 1959. [CrossRef]
42. Hao, Y.; Yang, H.; Zhang, L.; Sun, C. Study on the Effectiveness of the Integral Emergency Response System for Coal Mine Water Hazard Accidents Based on Combination Weighting. *Processes* **2024**, *12*, 235. [CrossRef]
43. Sun, C.; Hao, Y.; Wei, J.; Zhang, L. Research on the Evaluation of Emergency Management Synergy Capability of Coal Mines Based on the Entropy Weight Matter-Element Extension Model. *Processes* **2023**, *11*, 2492. [CrossRef]
44. Zhang, Y.; Fang, K.; Guo, Z. Distriformer: Research on a Distributed Training Rockburst Prediction Method. *Processes* **2024**, *12*, 1205. [CrossRef]
45. Kamran, M.; Chaudhry, W.; Taiwo, B.O.; Hosseini, S.; Rehman, H. Decision Intelligence-Based Predictive Modelling of Hard Rock Pillar Stability Using K-Nearest Neighbour Coupled with Grey Wolf Optimization Algorithm. *Processes* **2024**, *12*, 783. [CrossRef]
46. Ma, H.; Zhang, H.; Yang, K.; Hu, Y.; Yang, Z.; Ma, N. Research on the Positioning Accuracy of the Cutting Head of a Tunneling Machine Based on Ultra-Wideband Positioning Technology. *Processes* **2023**, *11*, 2534. [CrossRef]
47. Li, L.; Zhang, X.; Hu, B.; Lei, S. Preliminary Exploration of the Technology of Coal Reshaping and Replacement Mining of Abandoned Coal in Goafs. *Processes* **2023**, *11*, 2474. [CrossRef]

**Disclaimer/Publisher’s Note:** The statements, opinions and data contained in all publications are solely those of the individual author(s) and contributor(s) and not of MDPI and/or the editor(s). MDPI and/or the editor(s) disclaim responsibility for any injury to people or property resulting from any ideas, methods, instructions or products referred to in the content.

Article

# Simulation Research and Practical Application of Cutting Teeth for Drill Bits in Life-Support Holes

Zebin Zhu <sup>1,2,3</sup>, Jian Feng <sup>1,2</sup>, Yuguo Kang <sup>1,2,\*</sup>, Biao Zhang <sup>1,2</sup> and Xue Ling <sup>4</sup>

<sup>1</sup> Beijing Dadi Hi Tech Geological Exploration Co., Ltd., Beijing 100040, China; zhuzebin110@163.com (Z.Z.); fengjianhpu@163.com (J.F.); zb556@163.com (B.Z.)

<sup>2</sup> National Mine Emergency Rescue Daditekan Team, Beijing 100043, China

<sup>3</sup> School of Emergency Management and Safety Engineering, China University of Mining & Technology, Beijing 100083, China

<sup>4</sup> School of Engineering and Technology, China University of Geosciences (Beijing), Beijing 100083, China; lingxue@cugb.edu.cn

\* Correspondence: kangyuguo2007@163.com

**Abstract:** This study aims to achieve rapid drilling of life-support holes, regarding the optimization design of drill bits as the key, among which the simulation analysis of drill bit cutting teeth is an important technical means. Firstly, based on the rock mechanics test results in the study area combined with the corresponding logging information, the analysis and evaluation of the geological conditions in the study area were completed, a complete rock mechanics characteristic profile was established, and the drillability of the rock was calculated to be relatively good. Then, a numerical simulation of parallel cutting of rock with conical teeth was established by experimentally testing rock mechanics parameters and using the discrete element method (PFC2D). The simulation study of the drill bit cutting teeth was completed by parameter calibration, analysis of rock cutting morphology, analysis of the number of rock cutting cracks, and analysis of the specific work of rock cutting and breaking. It was determined that the optimal rock-entering angle of the drill bit cutting teeth in the Shouyang mining area is 14°. Finally, verified by field practice, the optimized drill bit has stable performance, strong cutting ability, and good wear resistance; the maximum instantaneous mechanical drilling speed reaches 58.14 m/h, and it shows a slightly worn state after continuously drilling 582 m in the stratum, meeting the requirements of one-trip drilling and hole formation for life-support holes. This research provides a scientific basis and practical techniques for the construction of life-support holes in the Shouyang mining area and under similar geological conditions. It can provide more effective emergency plans and rescue strategies for possible mine disasters in the future, which is crucial for improving the technical system of emergency rescue for mine accidents and enhancing the emergency rescue capability of surface drilling.

**Citation:** Zhu, Z.; Feng, J.; Kang, Y.; Zhang, B.; Ling, X. Simulation Research and Practical Application of Cutting Teeth for Drill Bits in Life-Support Holes. *Processes* **2024**, *12*, 2130. <https://doi.org/10.3390/pr12102130>

Academic Editor: Carlos Sierra Fernández

Received: 28 August 2024

Revised: 16 September 2024

Accepted: 21 September 2024

Published: 30 September 2024



**Copyright:** © 2024 by the authors. Licensee MDPI, Basel, Switzerland. This article is an open access article distributed under the terms and conditions of the Creative Commons Attribution (CC BY) license (<https://creativecommons.org/licenses/by/4.0/>).

**Keywords:** life-support hole; emergency rescue; PDC cutter; numerical simulation

## 1. Introduction

The life-support hole is an indispensable part of mine rescue. It not only provides the hope of survival for trapped miners but also provides effective rescue means for the rescuers [1,2]. Fast drilling is one of the core requirements of life-guarantee hole drilling. Specifically, the hole is formed within 72 h of gold rescue time at a depth of 600 m—that is, within 72 h, it is necessary to complete the drilling and hole fixing of the first surface soil section, the drilling and hole fixing of the second bedrock section, and the construction of the third open hole section depends on the disaster site [3]. At present, the concern for the safe and rapid drilling and trajectory control of life-support holes is mostly reflected in the application aspect [4–6]. Coupled with the sudden occurrence of rescue events, conventional drilling methods are often copied for operations [7,8]. There is a lack of systematic and sufficient research on the basic geological conditions in disaster areas and

the adaptability of drilling techniques, resulting in slow on-site rescue operations [9,10]. Shanxi Province is one of the main coal-producing areas in China, with a relatively high risk of mine accidents [11,12]. The loose and medium–soft strata commonly existing in the region bring unique challenges to the construction of life-support holes during rescue. Given the lack of rescue experience under such special geological conditions, it is extremely important to conduct targeted preliminary research. Through these studies, more effective emergency plans and rescue strategies can be provided for possible mine disasters in the future, which can not only better protect the lives and safety of miners, but also improve the efficiency and success rate of rescue operations.

The performance of the cutting teeth of the bit directly affects the drilling efficiency of the bit [13,14]. Through simulation analysis, the design and parameters of the cutting teeth can be optimized, and the cutting speed and drilling ability of the drill bit can be improved, so as to speed up the construction progress of the life-support hole [15–19]. Compared with physical experiments, simulation has many advantages, such as saving time and cost, reducing material consumption, and easily adjusting various parameters in the simulation process to observe the cutting effect under different conditions [20–22]. In addition, simulation also allows researchers to predict and verify the performance of drill design without actually manufacturing the drill, which is particularly useful for iterative optimization of drill design [23–25]. At present, with the improvement in computing power and the progress of simulation technology, many research institutions and enterprises at home and abroad are using PDC bit simulation technology to obtain more accurate predictions of the rock-breaking process [26–31]. Its main research and development direction can be divided into the following two parts: The first is research on the personalized drill bit [32]; taking into account the differences in the formation, there will be personalized drills for different regions in the future to complete local optimization. The second is the improvement in simulation accuracy. With the development of computer technology, more advanced finite element models and constitutive models can be applied to construct more refined grids to complete the simulation of drill bits.

Therefore, this study selected Shouyang mining area with a relatively high risk of mine accidents as the research object. Based on the analysis and evaluation of the geological conditions in the study area, the simulation analysis of the cutting teeth of the drill bit is completed. The optimization of the rock entry angle of the drill bit is carried out in order to improve the cutting ability of the PDC bit, optimize the overall performance of the bit, and achieve the purpose of rapid rock-breaking drilling.

## 2. Overview of the Study Area

As shown in Figure 1, Shouyang mining area is located in the central part of Shanxi, at the northern end of Qinshui basin. It is mainly a monoclinic structure with an east–west trend and southward tilt, accompanied by a secondary wide and gentle fold. The dip angle of the stratum is gentle, and the middle part is steeper. The faults and collapse columns are more developed. The test area develops multiple strata, among which the Liujiagou Formation and Shiqianfeng Formation are locally developed, and the actual drilling probability is low, as shown in Table 1. Ordovician strata are usually not drilled. The main drilled strata include the Upper Shihezi Formation, which is mainly fine-grained sandstone and mudstone, while the Lower Shihezi strata are mostly feldspar quartz sandstone and mudstone interbeds, with aluminum mudstone on top. The Shanxi Formation is dominated by sandstone, mudstone, and coal seams. The Taiyuan Formation is dominated by quartz sandstone, mudstone, coal seams, and limestone.



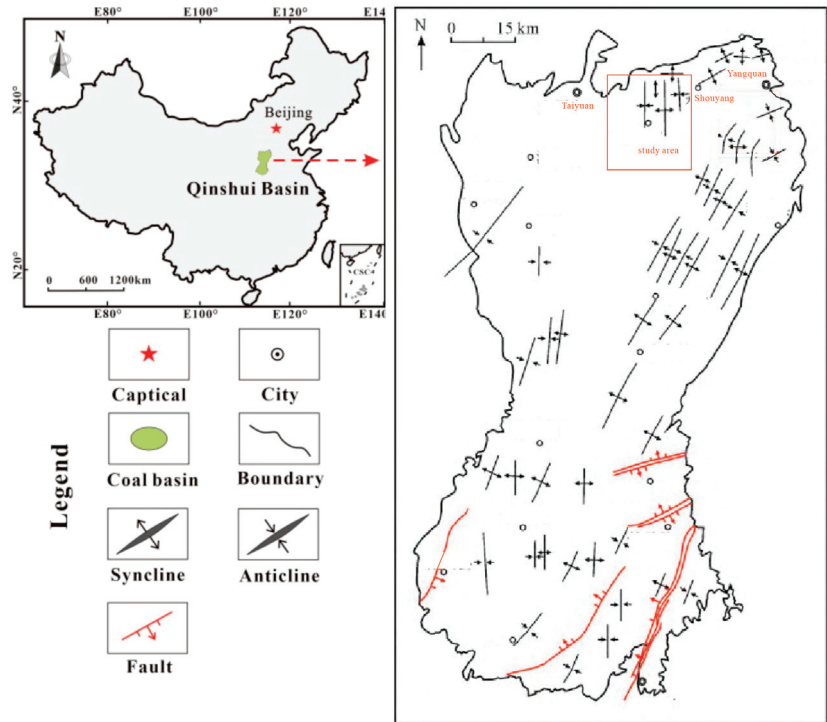


Figure 1. Regional location map.

Table 1. Geological stratification of Shouyang mining area.

Stratification					Lithological Description	
Erathem	System	Series	Formation	Designation		
Cenozoic erathem	Quaternary system	Pleistocene series		Q	Modern alluvial, diluvium, sand, gravel, clay, etc.	
Mesozoic erathem	Triassic system	Lower series	Liujiagou formation	T <sub>1</sub> l	It is mainly composed of fine-grained feldspar sandstone, sandy mudstone, and siltstone.	
			Shiqianfeng formation	P <sub>2</sub> sh	Sandstone, sandy mudstone, and mudstone.	
		Upper series	Upper stone box formation	P <sub>2</sub> s	P <sub>2</sub> s <sup>2+3</sup> : fine-grained sandstone and sandy mudstone composition. P <sub>2</sub> s <sup>1</sup> : fine-grained sandstone, mudstone, and sandy mudstone.	
		Paleozoic erathem	Permian system	Lower stone box formation	P <sub>1</sub> x	P <sub>1</sub> x <sup>2</sup> : it is composed of medium- and coarse-grained feldspar quartz sandstone and sandy mudstone, with 1–3 layers of aluminum mudstone at the top. P <sub>1</sub> x <sup>1</sup> : sandy mudstone, mudstone, and medium- and fine-grained feldspar quartz sandstone.
				Lower series	Shanxi formation	P <sub>1</sub> s

Table 1. Cont.

Erathem	System	Stratification			Lithological Description
		Series	Formation	Designation	
Paleozoic erathem	Carboniferous system	Upper series	Taiyuan formation	C <sub>3t</sub>	C <sub>3t</sub> <sup>3</sup> : medium-grained to siltstone, sandy mudstone, mudstone, and coal seams. C <sub>3t</sub> <sup>1</sup> : quartz sandstone, sandy mudstone, mudstone, and coal seam. C <sub>3t</sub> <sup>2</sup> : limestone, coal seam, sandstone, mudstone, etc.
		Middle series	Benxi formation	C <sub>2b</sub>	Sandy mudstone with sandstone, limestone, and coal line.

### 3. Rock Mechanics Characteristics of Strata

The mechanical characteristics of formation rock are necessary for the simulation study of drill cutting teeth [33]. It can provide the basis of real physical environment simulation so that the simulation is more in line with the actual working conditions. It is helpful to optimize the design and material selection of cutting teeth so that the cutting teeth can adapt to different rock conditions. The wear and failure modes of the cutting teeth can be predicted and improved in advance. It can also improve drilling efficiency and reduce costs, such as avoiding bit replacement and waste of drilling time. In short, it is an important factor to improve the performance of the drill bit and optimize the drilling process.

Obtaining accurate rock mechanics parameters is the basis for studying the mechanical characteristics of strata. In this study, based on the surface drilling project in the mining area, the borehole core was obtained and the specimen was reprocessed in the laboratory. The TAR-1500 hydraulic servo test system was used to carry out the whole process test of triaxial stress and strain. As shown in Table 2, it is the triaxial compression test results of the X-65 hole in Shouyang mining area. Based on the test results and the logging methods such as acoustic wave and density, the dynamic rock mechanics parameters are obtained and the complete rock mechanics characteristic profile is established. The rock drillability is calculated based on the acoustic logging method, as shown in Figure 2. All types of data extracted in the figure strictly comply with the technical standards in the “Coalbed Methane Logging Operation Regulations” (Q/CUCBM 0401—2002) issued by China United Coalbed Methane Corporation Limited. It can be seen from the figure that the Shouyang mining area is dominated by medium–fine sandstone plus mudstone and siltstone. The formation hardness is medium–soft, and the local formation is hard. The compressive strength of the bedrock formation is between 5.87 and 73.17 MPa, with an average of 33.25 MPa. The drillability grade is between 2.8 and 6.6, with an average of 5.1, and the comprehensive evaluation of drillability is good.

Table 2. Results of triaxial compression test.

Hole Segment (m)	Rock Name	Compressive Strength (MPa)	Tensile Strength (MPa)	Shear Strength (MPa)	Angle of Internal Friction $\varphi$ (°)	Cohesion C	Elastic Modulus (10 <sup>5</sup> MPa)	Poisson Ratio
570.2 ~571.90	Silty mudstone	35.4	4.83	17.13	37.83	3.76	0.20	0.24
572.33 ~577.95	Siltstone	36.6	4.36	21.25	38.91	4.03	0.22	0.20
580.1 ~581.7	Fine sandstone	79.6	4.81	31.54	38.19	7.46	0.33	0.20

Table 2. Cont.

Hole Segment (m)	Rock Name	Compressive Strength (MPa)	Tensile Strength (MPa)	Shear Strength (MPa)	Angle of Internal Friction $\varphi$ (°)	Cohesion C	Elastic Modulus ( $10^5$ MPa)	Poisson Ratio
582.7 ~582.96	Grit stone	25.5	2.07	9.48	33.45	3.64	0.11	0.24
583.6 ~585.17	Fine-medium sandstone	73.2	4.53	16.97	30.93	7.04	0.16	0.25
589.15 ~590.30	Mudstone	43.7	2.80	11.22	34.91	3.34	0.12	0.22

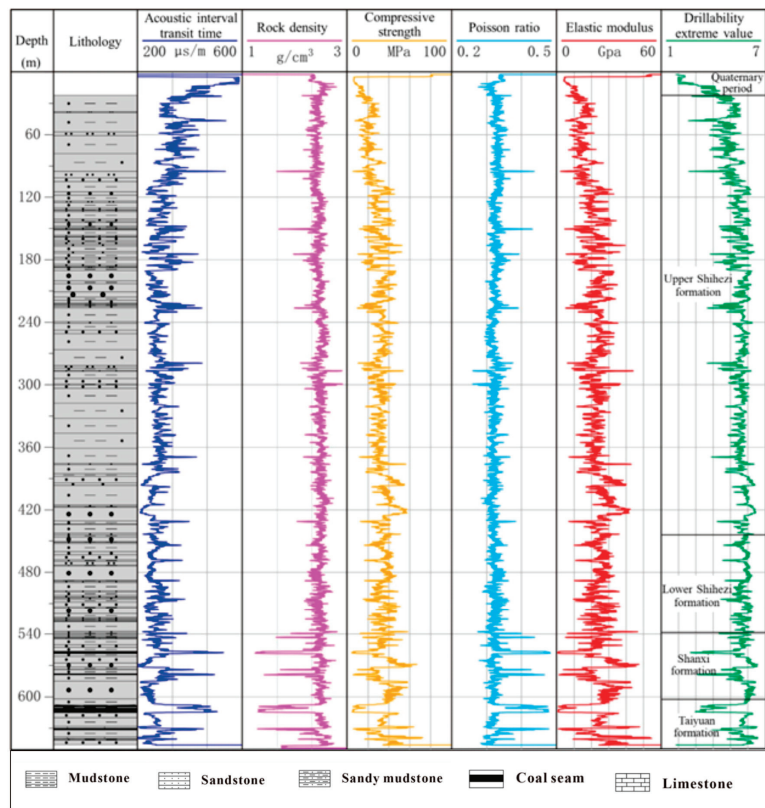


Figure 2. Rock mechanical characteristics profile of X-65 hole formation.

#### 4. Simulation Analysis of Drill Cutting Teeth

Engineering practice shows that PDC bits have become the preferred bit type for rescue in most areas of China due to their common advantageous characteristics and wide applicability. Their cutting teeth are the basic cutting units, and their performance directly determines the drilling effect. This paper selects the fine sandstone stratum with the highest strength in the bedrock stratum and uses PFC software 9.1 (Particle Flow Code) analysis combined with the indoor experiment method to optimize the rock-entering angle of the drill bit teeth, aiming to improve the cutting ability, optimize the overall performance, and achieve rapid rock-breaking drilling [34]. As a representative software based on discontinuous medium mechanics, PFC can not only simulate the macroscopic

and mesoscopic mechanical characteristics of rock materials but also reveal the dynamic mechanical characteristics at the mesoscopic level, which can provide a reliable theoretical basis for drill bit design optimization, performance improvement, and service life extension as well as help the research and development in related fields [35,36]. In the relevant research on rock cutting, most of them focus on the essence of plastic–brittle failure and the mechanism of plastic–brittle transformation during the rock failure process, while there are relatively few studies on the form of crack propagation and the mesoscopic mechanism of rock chip spalling [37,38]. Based on the previous achievements, this paper establishes a numerical simulation of parallel cutting of rock with conical teeth by experimentally testing rock mechanics parameters and using the discrete element method (PFC2D) to study the cutting morphology, the number of cutting cracks, and the specific work of rock breaking at different cutting angles. Moreover, choosing PFC2D for simulation can better represent the process of crack initiation and propagation, providing theoretical guidance for improving the drilling speed in rock drilling engineering.

#### 4.1. Parameter Calibration

Firstly, based on the macroscopic mechanical properties of fine sandstone measured by laboratory experiments, PFC2 D software 5.0 was used to calibrate the microscopic particle parameters. Since PFC2D uses granular materials to simulate strong materials, cementing is required. Therefore, the calibration process involves not only the microscopic parameters of the particles themselves but also the parameters of the bond. Through the simulation of uniaxial compression test, the elastic modulus, compressive strength, and Poisson’s ratio of the model were calibrated. Subsequently, the parameters of PFC2D were calibrated according to the macroscopic mechanical parameters of fine sandstone in the rock mechanics sample test of X-65 hole, and a set of mesoscopic particle parameters that can accurately simulate the required rock properties was obtained after fine tuning, as shown in Table 3.

**Table 3.** Model particle properties.

Particle Parameters	Particle Modulus (Gpa)	Stiffness Ratio	Friction Axis Factor	Density (g/cm <sup>3</sup> )	Maximum Particle Size (mm)	Minimum Particle Size (mm)
	15	1.5	0.5	2.64	0.3	0.2
Parallel bond key parameters	Bond modulus (Gpa)	Bond stiffness ratio	Angle of friction (°)	Bonding cohesion (MPa)	Tensile bond strength (MPa)	Bonding generates gap (mm)
	15	1.5	40	32	64	0.04

#### 4.2. Analysis of Rock Cutting Morphology

The rock cutting numerical simulation is carried out by using the particle parameters obtained by parameter calibration. The rock sample is designed as a 50 mm × 100 mm 2D granular particle and a parallel bond bonding sample. The rock cutting simulation experiment uses two cutting methods and carries out continuous loading. The design of cutting scheme is shown in Figure 3. The number of sample particles is 22,606, and the tool is cut to the left at a loading speed of 1 m/s. Four groups of rock cutting tests under different cutting angles ( $\theta_1$ – $\theta_4$  groups) were carried out, which were 8°, 10°, 12°, and 14°, respectively. The results are shown in Figure 2.

According to the simulation results (Figures 4–7), when the cutting teeth contact with the rock, the cutting teeth will produce cutting force on the rock surface, causing elastic deformation and plastic deformation of the rock. As the cutting progresses, the stress field inside the rock changes, resulting in microscopic cracks inside the rock. These micro cracks will continue to expand with the movement of the cutting teeth and gradually develop from micro cracks to macro cracks, forming the cutting area of the cutting teeth. In the cutting area, with the increase in the number and width of cracks, more rock fragments are separated from the rock mass, forming a broken area of cutting teeth. When the crack

develops to a certain extent, the cutting teeth will have a large relative displacement with the rock such that a large number of rock blocks are separated from the rock mass, forming a peeling area of the cutting teeth. These different regions correspond to different rock-breaking mechanisms of the cutting teeth, namely, cutting, compaction, shearing, and crushing, which cause different degrees of damage to the rock mass.

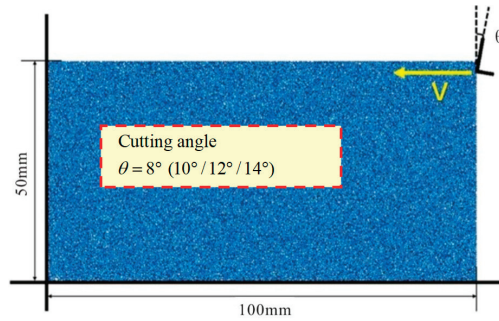


Figure 3. Schematic diagram of rock cutting model.

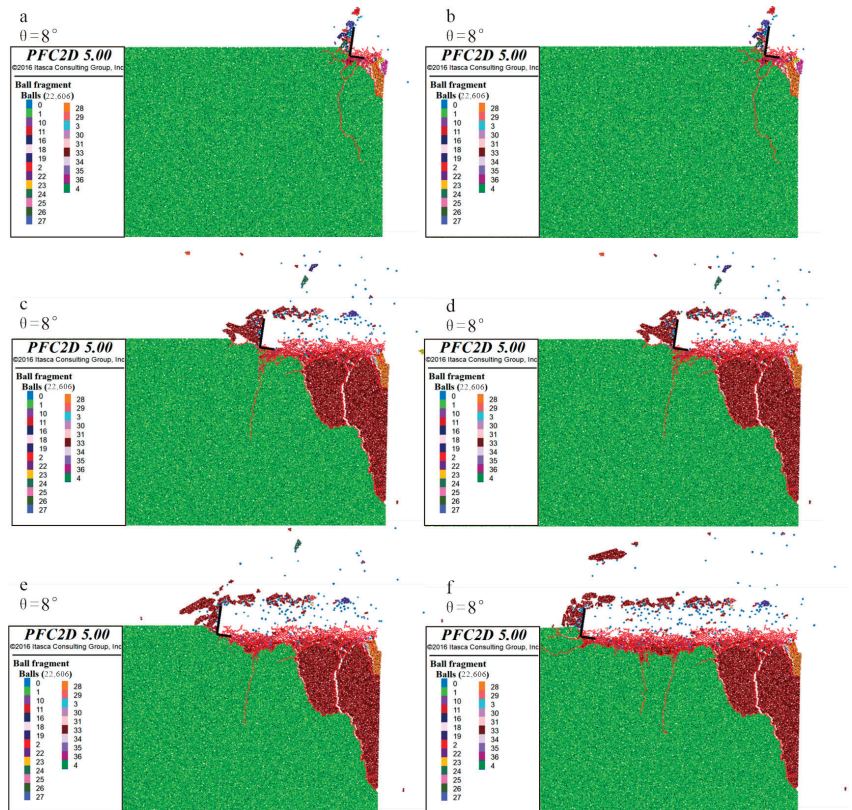
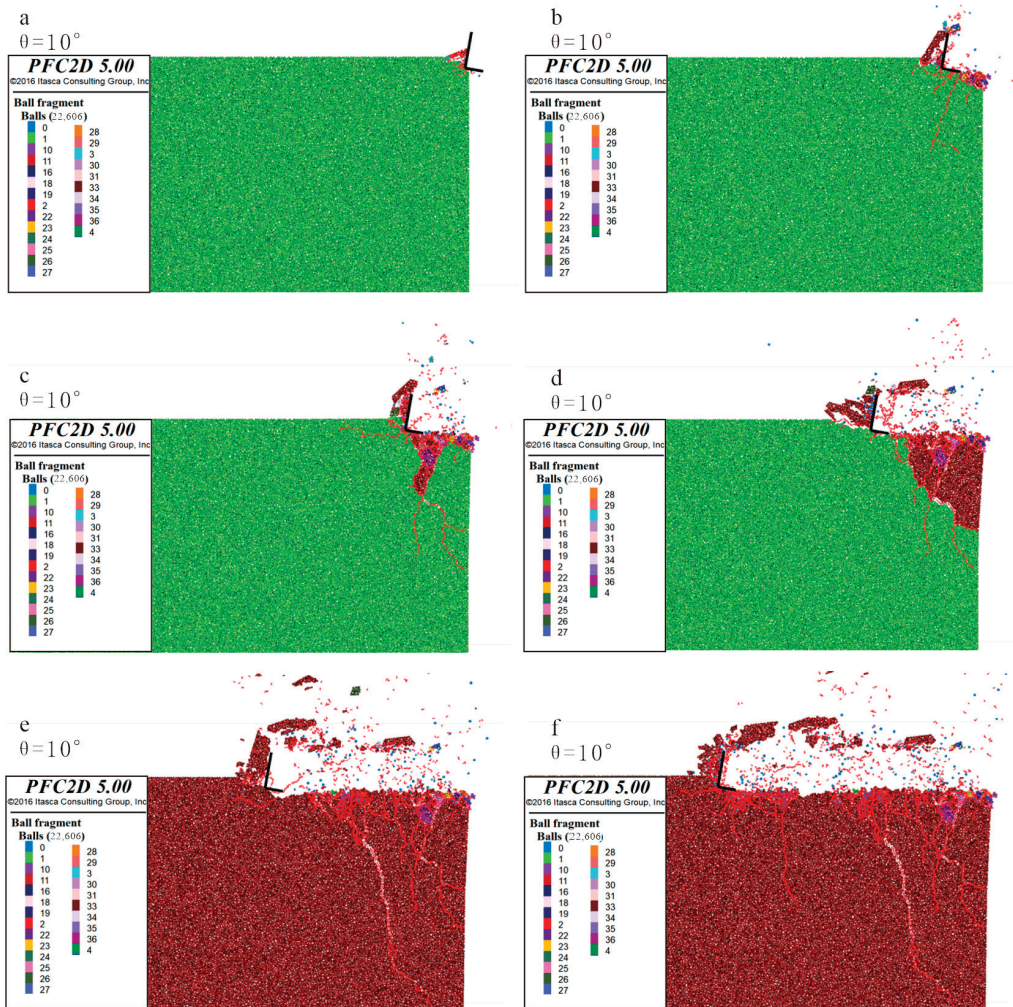
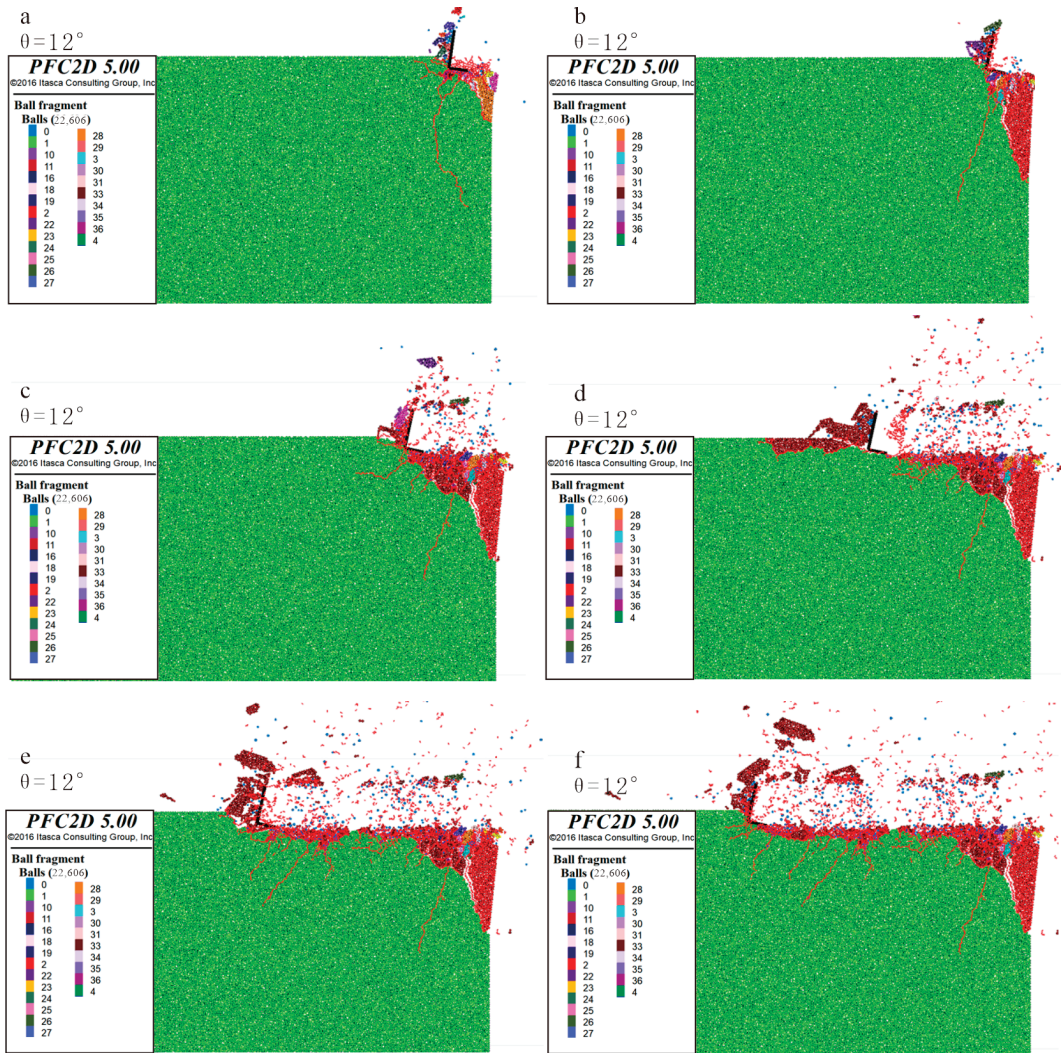


Figure 4. Experimental group 01. Cutting debris morphology and crack propagation diagram. Figures (a–f) are diagrams showing the morphology of cutting chips and crack propagation at different time stages during the cutting process.

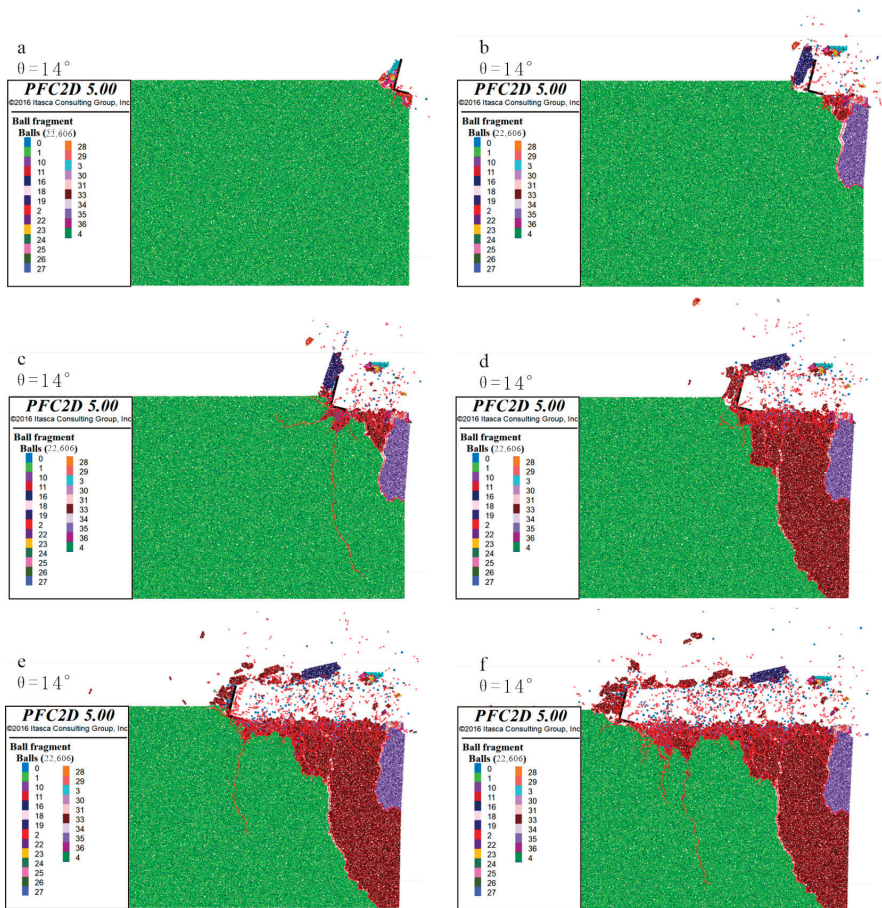


**Figure 5.** Experimental group 02. Cutting debris morphology and crack propagation diagram. Figures (a–f) are diagrams showing the morphology of cutting chips and crack propagation at different time stages during the cutting process.

When the cutting angle  $\theta$  is  $10^\circ$ , compared with the process diagram of the cutting angle  $\theta$  of  $8^\circ$ , it can be found that when the cutting angle  $\theta$  is  $10^\circ$  the crack development speed and the rock fragments separated from the rock sample are greater than the crack development speed and the fragment size of the cutting angle  $\theta$  of  $8^\circ$ —that is, a larger size of cutting is produced. Similarly, the comparison between  $12^\circ$  and  $14^\circ$  is the same. That is to say, as the cutting angle increases, the crack growth rate increases, and the rock fragments separated from the rock sample also increase.



**Figure 6.** Experimental group  $\theta 3$ . Cutting debris morphology and crack propagation diagram. Figures (a–f) are diagrams showing the morphology of cutting chips and crack propagation at different time stages during the cutting process.

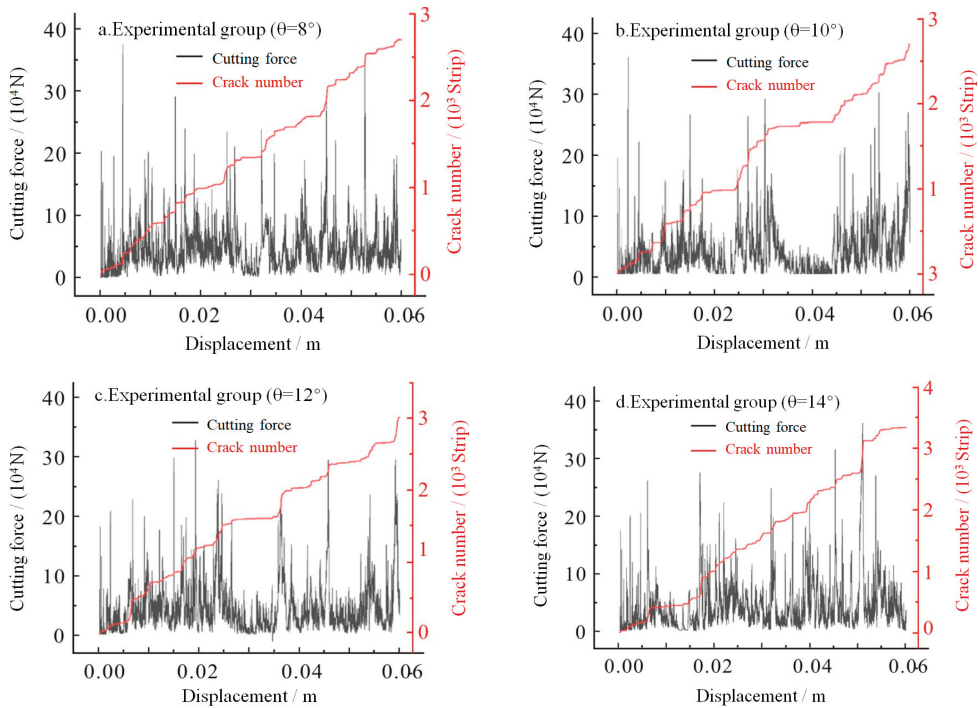


**Figure 7.** Experimental group  $\theta_4$ . Cutting debris morphology and crack propagation diagram. Figures (a–f) are diagrams showing the morphology of cutting chips and crack propagation at different time stages during the cutting process.

#### 4.3. Analysis of Rock Cutting Crack Number

The real-time cutting force  $F$  and the number of cracks  $N$  of the four groups of cutting experiments are plotted with the change in the cutting distance  $X$  of the drilling teeth in Figure 8. From the four sets of data in Figure 8, it can be seen that the peak of the cutting force basically corresponds to the sharp increase in the number of cracks. It shows that there is a great correlation between the increase in crack number and the peak value of cutting force, which shows a periodic law. It can also be observed that there is almost no change in the number of cracks in the area where the cutting force is small and the fluctuation is slow. Combined with the morphology of the previous cutting process, it can be known that there will be large-sized cuttings at the time when the peak cutting force and the number of cracks increase sharply, and the chips are generated by large chips accompanied by small chips during the entire cutting process.





**Figure 8.** Summary of four groups of cutting forces and crack numbers.

By deriving the relationship between the number of cracks and the displacement, it can be found that the number of cracks increases with the increase in the cutting angle  $\theta$ . There are two ways of crack growth in the process of cutting: large step growth and small amplitude growth, which correspond to the large-sized cuttings produced by brittle failure and the small-sized cuttings produced by plastic failure, respectively. Comparing Figure 8a with Figure 8b, it can be found that the larger size of rock debris produced when the  $\theta$  angle increases from  $8^\circ$  to  $10^\circ$  corresponds to the large crack step in the crack diagram. Comparing the experimental group  $\theta_2$  ( $\theta = 10^\circ$ ) with the experimental group  $\theta_3$  ( $\theta = 12^\circ$ ), it can be found that the large crack step in Figure 8c is smaller than that in Figure 8d, which is consistent with the phenomenon that less large-sized cuttings are produced when the  $\theta$  angle is  $12^\circ$  in the cutting topography.

#### 4.4. Rock Cutting Rock Breaking Specific Work

The rock cutting process simulated by PFC2D is different from the actual situation. In the simulation, to calculate the energy consumption generated by the loading tool, only the force load generated by the tool in contact with the rock is integrated along the loading path. For parallel cutting, since the y-direction displacement is 0, it means that there is no energy consumption in the y direction. Therefore, only the energy consumption in the x direction needs to be calculated. In this way, the energy consumption of parallel cutting can be obtained by calculating the energy consumption in the x direction (Equation (1)).

$$\varepsilon_x = \int F_x dx \quad (1)$$

where  $\varepsilon_x$  is the energy consumed by the system in the process of rock cutting, J, and  $F_x$  is the cutting force in the horizontal direction of the tool, N.

In PFC, with the help of the Fish language programming function, the change in contact force between particles can be tracked and monitored in real time. Once the contact force is reduced to 0, it is determined that the rock particles have peeled off from the rock matrix. These exfoliated particles were then counted to determine the total number of exfoliated particles. As shown in Figure 9, the color of the exfoliated particles is different from that of the rock matrix, and the exfoliated particles can be clearly identified and distinguished. Finally, the total volume of rock breaking  $V$  (Equation (2)) can be calculated by multiplying the total number of exfoliated particles by the volume of a single particle.

$$V = N \frac{\pi D^2}{4} \quad (2)$$

where  $N$  is the number of rock debris particles, dimensionless, and  $D$  is the average particle size, m.

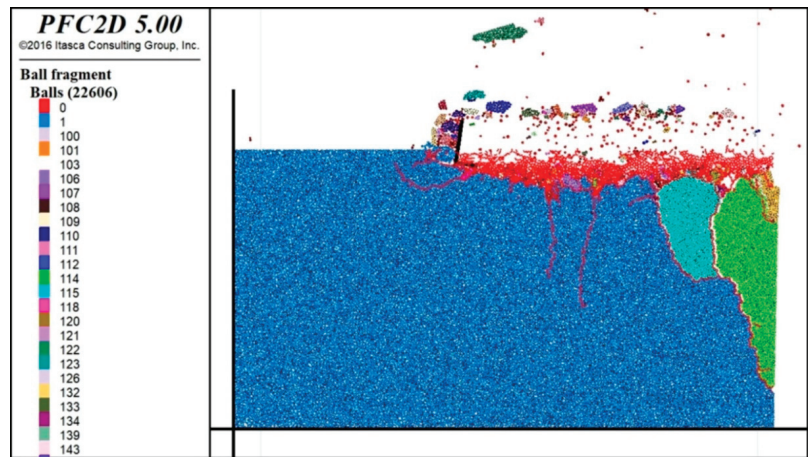


Figure 9. Viewing the number of peeled particles.

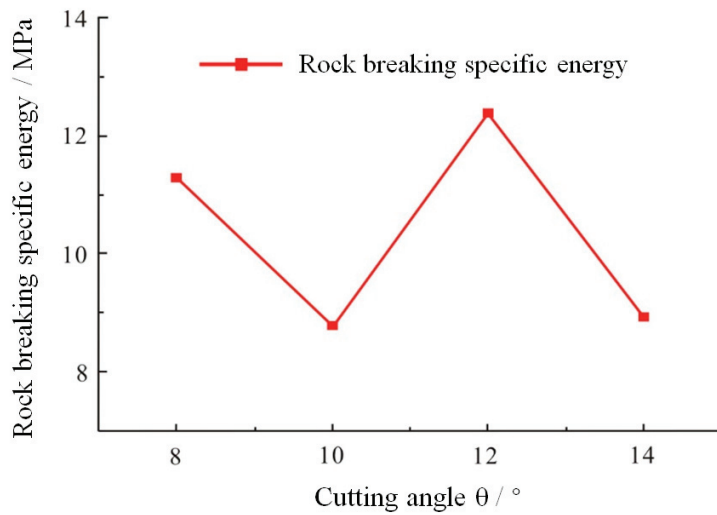
According to the above Equation (2), the rock cutting rock breaking volume of four groups of different cutting angles is calculated as follows:  $2.486 \times 10^{-4} \text{ m}^2$ ,  $3.595 \times 10^{-4} \text{ m}^2$ ,  $2.187 \times 10^{-4} \text{ m}^2$ , and  $3.770 \times 10^{-4} \text{ m}^2$ .

The method of calculating the specific work of rock breaking in PFC2D is to ratio the energy of rock breaking to the volume of consumption:

$$MSE_{2D} = \frac{\text{Rock - breaking energy}}{\text{Rock breaking volume}} = \frac{\epsilon_{x-2D}}{V} \quad (3)$$

where  $MSE_{2D}$  is the specific work of rock breaking under 2D condition,  $V$  is the volume of rock debris, and  $\epsilon_x$  is the energy consumed by parallel cutting.

According to Equation (3), the specific work of rock cutting under four different cutting angles is calculated as follows: 11.282 MPa, 8.783 MPa, 12.386 MPa, and 8.931 MPa. It can be found from the comparison of the cutting topography that the rock-breaking specific work of the experimental group 02 and the experimental group 04 producing larger chips is smaller, and the rock-breaking specific work of the experimental group 03 producing smaller chips is larger. It can be found that the larger-sized cuttings produced by brittle failure have larger rock-breaking volume and smaller rock-breaking specific work, which means that when the cutting angle  $\theta$  is  $10^\circ$  and  $14^\circ$ , more cuttings can be produced and the energy required is smaller—that is, the rock-breaking efficiency is higher. When the cutting angle  $\theta$  is  $12^\circ$ , less cuttings are produced and the efficiency is lower, as shown in Figure 10.



**Figure 10.** Comparison chart of rock-breaking specific work for four groups.

In conclusion, the strata in this area are normally deposited coal measures strata, and the lithology of the strata is mainly the alternation of sandstone and mudstone without special hard rocks. Therefore, on the basis of ensuring high rock-breaking efficiency,  $14^\circ$  is selected as the rock-entry angle of drill bit cutting teeth suitable for the Shouyang mining area for bit arrangement optimization and the rock-breaking effect is the most ideal. The main reasons to be considered are two parts: on the one hand, in relatively soft geological layers, a larger cutting angle can enable the drill bit to cut into the stratum more quickly and improve the drilling efficiency; on the other hand, a larger cutting angle usually forms a larger chip removal space, which is conducive to discharging the broken rock cuttings. To a certain extent, this can reduce the risk of drill bit jamming or damage caused by chip blockage.

### 5. Engineering Practice

In the drilling operation of the X-154 hole of ground gas control hole in Shouyang mining area, based on the simulation analysis results of bit cutting teeth, the PDC bit was made and tested by selecting the bit cutting teeth into the rock angle of  $14^\circ$ . The drill assembly is a personalized PDC bit + single-bend screw drill. The drilling flushing fluid and drilling parameters are consistent with the gas control hole project completed in advance. The field verification shows that the optimized drill bit has stable performance, strong cutting ability, and good wear resistance. The maximum instantaneous penetration rate reaches 58.14 m/h and shows a slight wear state after 582 m continuous drilling in the formation, as shown in Figure 11, which is conducive to the control of hole deviation and azimuth and meets the needs of one-time drilling of life-support holes.



(a) The drill before use (PDC,  $\varnothing 215.9$  mm)      (b) The drill after use (PDC,  $\varnothing 215.9$  mm)

**Figure 11.** Wear situation of personalized drill bits during on-site testing.

## 6. Conclusions

- (1) The Shouyang mining area is dominated by medium–fine sandstone plus mudstone and siltstone. The formation hardness is medium–soft, and the local formation is hard. The compressive strength of the bedrock formation is between 5.87 and 73.17 MPa, with an average of 33.25 MPa. The drillability grade is between 2.8 and 6.6, with an average of 5.1, and the comprehensive evaluation of drillability is good.
- (2) A numerical simulation of parallel cutting of rock with conical teeth was established by experimentally testing rock mechanics parameters and using the discrete element method (PFC2D). The cutting morphology, number of cutting cracks, and specific work of rock breaking at different cutting angles during the rock cutting process were studied, and it was determined that the rock-entering angles of the drill bit cutting teeth suitable for the Shouyang mining area is  $14^\circ$ .
- (3) Based on the simulation analysis results of the cutting teeth of the drill bit, the PDC bit was made with the cutting teeth of the drill bit entering the rock at an angle of  $14^\circ$ , and the practical application was carried out. The optimized bit has stable performance, strong cutting ability, and good wear resistance. The maximum instantaneous mechanical drilling speed reaches 58.14 m/h, and it is slightly worn after continuous drilling in the formation for 582 m, which can meet the construction requirements of the life-guarantee hole.

**Author Contributions:** Writing—original draft preparation, Z.Z. and J.F.; methodology, Y.K.; validation, Y.K. and B.Z.; formal analysis, Z.Z., Y.K. and J.F.; investigation, B.Z. and X.L.; conceptualization, Z.Z., J.F., Y.K., B.Z. and X.L.; supervision, Y.K. All authors have read and agreed to the published version of the manuscript.

**Funding:** This work was supported by the National Key Research and Development Program of China under 2023YFC3010900.

**Data Availability Statement:** Data are contained within the article.

**Acknowledgments:** We also would like to thank the anonymous reviewers for their valuable comments and suggestions that led to a substantially improved manuscript.

**Conflicts of Interest:** Author Zhu Zebin, Feng Jian, Kang Yuguo and Zhang Biao were employed by Beijing Dadi Hi Tech Geological Exploration Co., Ltd. Author Ling Xue was employed by School of Engineering and Technology, China University of Geosciences (Beijing). The authors declare no conflicts of interest.

## References

- Zhang, B.; Kang, Y.G.; Huang, Y.; Zhang, M.; Zhou, G.; Ren, Y.; Liu, J.; Gao, K.; Zhao, Y. Key technologies of surface efficient life support hole forming for mine rescue. *Coal Geol. Explor.* **2022**, *50*, 14–23. [CrossRef]
- Kang, Y.G.; Zhang, B.; Zhang, M. Key technology and application of surface life support hole demonstration project in Meihuajing Mine. *Saf. Coal Mines* **2022**, *53*, 113–120.
- Tian, H.L.; Zou, Z.J.; Hao, S.J.; Cao, M.; Zhou, G.; Huang, Y.; Gu, H.; Wang, L. Key technologies and equipment of quickly and safely building life support and rescue channel in mine disastery. *Coal Geol. Explor.* **2022**, *50*, 2. [CrossRef]
- Zare-Reisabadi, M.R.; Kaffash, A.; Shadizadeh, S.R. Determination of optimal well trajectory during drilling and production based on borehole stability. *Int. J. Rock Mech. Min. Sci.* **2012**, *56*, 77–87. [CrossRef]
- Boukredera, F.S.; Hadjadj, A.; Youcefi, M.R. Drilling vibrations diagnostic through drilling data analyses and visualization in real time application. *Earth Sci. Inform.* **2021**, *14*, 1919–1936. [CrossRef]
- Bout, G.; Brito, D.; Gómez, R.; Carvajal, G.; Ramírez, G. Physics-Based Observers for Measurement-While-Drilling System in Down-the-Hole Drills. *Mathematics* **2023**, *10*, 4814. [CrossRef]
- He, J.-F.; Zhao, Z.-Q.; Yin, Q.-L.; Luo, Y.-J.; Gan, X. Design and optimisation on rapid rescue well-drilling technology with large-diameter pneumatic hammers. *Int. J. Min. Reclam. Environ.* **2019**, *34*, 19–33. [CrossRef]
- Dehnert, J.; Stopp, J.; Windisch, P.; Schönherr, B. Quick-Erect Stopping System for radiation protection and mine rescue in small-scale mining. *Minning Metall. Explor.* **2020**, *37*, 1807–1817.
- Zheng, X.; Wang, H.; Guo, J.; Zhang, D. Method for multi-information drilling detection after mining disasters. *Comput. Electr. Eng.* **2020**, *86*, 106726. [CrossRef]
- Liu, L.; Zhou, J.; Kong, L.; Wang, Y.; Li, J. Analysis of the dynamic response and impact parameters of pneumatic down-the-hole hammer drilling rescue holes. *Geoenergy Sci. Eng.* **2023**, *228*, 211935. [CrossRef]
- Zhao, J.Z.; Shi, B.H. Division of coalbed methane-enriched units in the Qinshui Basin. *Chin. Sci. Bull.* **2005**, *50*, 140–145. [CrossRef]
- Wang, B.; Zhang, Q.; Qu, Z.; Zhang, Y. South Anze Structure and Its Control on Coalbed Methane Aggregation in the Qinshui Basin and the Mechanism of Syncline Gas Enrichment in the Qinshui Basin. *Energies* **2023**, *16*, 4521. [CrossRef]
- Han, X.M.; Xue, L.B.; Xu, J. Influence mechanism of polycrystalline diamond compact bit temperature rise based on thermo-fluid-solid coupling. *Sci. Prog.* **2023**, *106*, 00368504231214704. [CrossRef]
- Zhang, Z.; Zhao, D.; Zhao, Y.; Zhou, Y.; Tang, Q.; Han, J. Simulation and experimental study on temperature and stress field of full-sized PDC bits in rock breaking process. *J. Pet. Sci. Eng.* **2019**, *186*, 106679. [CrossRef]
- Gao, K.; Xu, X.; Jiao, S.; Li, Z. Modeling and experimental research on temperature field of full-sized PDC bits in rock drilling and coring. *Energy Rep.* **2022**, *8*, 8928–8938. [CrossRef]
- Wang, X.R.; Zhang, H.; Zhang, K.S. Rock breaking simulation and optimization design of multi-ridged PDC cutters. *J. China Univ. Pet.* **2022**, *46*, 63–71.
- Li, Y.C. Research status on rock-breaking mechanism and performance testing methods of PDC bit cutters. *Diam. Abras. Eng.* **2023**, *43*, 553–567. [CrossRef]
- Pang, Z.Y.; Xing, X.S.; Wu, Z.Q.; Ma, M.Y.; Mao, L.J. Experimental study on rock breaking by full-size PDC bit in heterogeneous layer. *Exp. Technol. Manag.* **2023**, *40*, 44–51. [CrossRef]
- Zhu, X.H.; Dan, Z.W. Numerical simulation of rock breaking by PDC cutters in hot dry rocks. *Nat. Gas Ind.* **2019**, *39*, 125–134.
- Cai, C.; Tan, Z.B.; Xuan, L.C.; Yang, Y.X.; Ren, H.T.; Pu, Z.C.; Zhang, P.; Xie, S. A study on drilling breakage and rock breaking mechanism by using separated impact-scraping and cutting compound bit. *J. Vib. Shock* **2022**, *41*, 232–241.
- Bazaluk, O.; Velychkovych, A.; Ropyak, L.; Pashechko, M.; Pryhorovska, T.; Lozynskyi, V. Influence of Heavy Weight Drill Pipe Material and Drill Bit Manufacturing Errors on Stress State of Steel Blades. *Energies* **2021**, *14*, 4198. [CrossRef]
- Yang, Y.; Yang, Y.X.; Ren, H.T.; Qi, Q.L.; Huang, Z.Q.; Zhou, C.X. Experimental study on motion and mechanical characteristics of the vertical wheel in the rock-breaking process. *Pet. Sci.* **2023**, *20*, 495–506. [CrossRef]
- Yu, J.P.; Zou, D.Y.; Liu, X.A.; Zhang, Y. Simulation and Experimental Study on Hybrid Bit with Different Cutters. *Int. J. Simul. Model.* **2021**, *20*, 87–98. [CrossRef]
- Niu, S.; Li, Y.; Xie, B.; Yang, Y.; Li, G.; Huang, K. Unit experimental and numerical simulation study on rock breaking mechanism of disc-like hybrid bit. *Geoenergy Sci. Eng.* **2023**, *228*, 212006. [CrossRef]
- Huang, K.L.; Ai, Z.J.; Yang, Y.X. Working characteristics research on the impacting–cutting hybrid bit. *Adv. Mech. Eng.* **2019**, *11*, 168781401985094. [CrossRef]
- Ayop, A.Z.; Bahruddin, A.Z.; Maulianda, B.; Prakasan, A.; Dovletov, S.; Atdayev, E.; Rani, A.M.A.; Elraies, K.A.; Ganat, T.A.-A.; Barati, R.; et al. Numerical modeling on drilling fluid and cutter design effect on drilling bit cutter thermal wear and breakdown. *J. Pet. Explor. Prod. Technol.* **2020**, *10*, 959–968. [CrossRef]
- Sun, R.J.; Ju, P.; Shi, Z.J. Simulation study of new directional drilling PDC bit used in coal mine. *Geosyst. Eng.* **2017**, *20*, 142–148. [CrossRef]
- Zhang, X.; Li, X.; Gao, K.D.; Zeng, Q.L. Analysis of Different Positional Relationships of Adjacent Double Picks on Cutting Force. *Int. J. Simul. Model.* **2022**, *21*, 651–662. [CrossRef]
- Wu, Z.B.; Yuan, Y.F.; Zhang, W.X.; Huang, J.J. Numerical simulation of rock breaking with intelligent bionic PDC Bit. *Sci. Technol. Eng.* **2023**, *23*, 6870–6880.

30. Kuang, Y.C.; Zhang, M.M.; Feng, M.; Guo, C.; Zhang, Y. Simulation Model of PDC Tooth Cutting Rock and Experimental Research on the Bit. *Chin. J. Undergr. Space Eng.* **2018**, *14*, 1218–1225.
31. Peng, Q.; Zhou, Y.C.; Zhou, B.; Liu, C.; Liu, Y. Development and Field Test of a Non-Planar Cutter PDC Bit with Convex Ridges. *Pet. Drill. Tech.* **2020**, *48*, 49–55.
32. Tian, H.; Ren, H.; Song, D.; Yang, Y. Research on cutting track and working load of directional drilling PDC bit. *J. Pet. Sci. Eng.* **2021**, *208*, 109480. [CrossRef]
33. Chen, L.; Li, D.; He, J.; Meng, L.; Chi, Q.; Li, G.; Chen, W.; Zhao, Y.; Yi, X.; Xia, C. Study on the mechanism of multidimensional cutting teeth and the influencing factors of rock breaking efficiency. *PLoS ONE* **2024**, *19*, e0297176. [CrossRef] [PubMed]
34. Wang, M.; Cao, P. Calibrating the Micromechanical Parameters of the PFC2D(3D) Models Using the Improved Simulated Annealing Algorithm. *Math. Probl. Eng.* **2017**, *2017*, 6401835. [CrossRef]
35. Yuan, L.-W.; Li, S.-M.; Peng, B.; Chen, Y.-M. Study on Failure Process of Tailing Dams Based on Particle Flow Theories. *Int. J. Simul. Model.* **2015**, *14*, 658–668. [CrossRef]
36. Haeri, H.; Sarfarazi, V.; Marji, M.F. Static and Dynamic Response of Rock Engineering Models. *Iran. J. Sci. Technol. Trans. Civ. Eng.* **2021**, *46*, 327–341. [CrossRef]
37. Yilmaz, N.G.; Yurdakul, M.; Goktan, R. Prediction of radial bit cutting force in high-strength rocks using multiple linear regression analysis. *Int. J. Rock Mech. Min. Sci.* **2007**, *44*, 962–970. [CrossRef]
38. Liu, H.J.; Ling, X.; Ma, J.T. Analysis of rock breaking process of single tooth straight cutting based on PFC2D. *Drill. Eng.* **2023**, *50*, 156–162.

**Disclaimer/Publisher's Note:** The statements, opinions and data contained in all publications are solely those of the individual author(s) and contributor(s) and not of MDPI and/or the editor(s). MDPI and/or the editor(s) disclaim responsibility for any injury to people or property resulting from any ideas, methods, instructions or products referred to in the content.

## Article

# Research on Hotspots and Evolutionary Trends in Coal Mine Gas Prevention

Chunguang Zhao <sup>1</sup>, Peng Gao <sup>1</sup>, Jinlin Ruan <sup>1</sup>, Yang Pu <sup>2,3</sup>, Yuan Sun <sup>1</sup>, Xiaoyang Cheng <sup>2,3,\*</sup> and Yu Sun <sup>1</sup>

- <sup>1</sup> Baode Coal Mine of Guoneng Shendong Coal Group Co., Ltd., Xinzhou 036600, China; 10015093@chnenergy.com.cn (C.Z.); gaopeng\_xauat@163.com (P.G.); ruanjinlin2024@163.com (J.R.); sunyuan202008@163.com (Y.S.); sunyu\_568790586@sina.cn (Y.S.)
- <sup>2</sup> China Coal Technology Engineering Group, Chongqing Research Institute, Chongqing 400039, China; puyang\_0429@126.com
- <sup>3</sup> State Key Laboratory of Coal Mine Disaster Prevention and Control, Chongqing 400037, China
- \* Correspondence: chengxiaoyang2020@163.com

**Abstract:** Mine gas accidents have received widespread attention at home and abroad, because mine gas accidents often cause casualties and property losses once they occur. This study was conducted in order to have a more comprehensive understanding of the research status of and research hotspots in coal mine gas management at home and abroad, and to provide references for relevant researchers' studies and literature searches. Using the Web of Science (WOS) core database as the data source, this paper analyzed the data from the period of 2000–2023 under the headings of “gas governance”, “Gas Control Technology”, “Pre-mining gas methods in coal mines”, “Methods of Gas Mining in Coal Mines”, “Post-mining gas”, and “Post-mining gas methods in coal mines”. “Methods in Coal Mines”, “Methods of Gas Mining in Coal Mines”, and “Post-mining Gas Methods in Coal Mines” were searched, and the CiteSpace tool was utilized to provide a multi-dimensional visual presentation of the literature, including authors, the number of journals issued, countries of issue, keywords, etc., in order to explore the research hotspots in this field. The analysis results show the following: the development process in the field of gas prevention and control is mainly divided into the three stages of initial exploration, steady development, and explosive surge; China, Australia, and the United States are the top three countries in terms of the number of articles published, and they have a greater influence in the field, but there is a closer connection between the regions in Europe; a certain group size has been formed by the researchers and research institutes in this field, the China University of Mining and Technology is more active in this field, ranking as the first in terms of the number of articles issued, and it has a cooperative relationship with many universities; Kai Wang and Enyuan Wang are the core authors in this field, while C. Ozgen Karacan also has a large body of research in the field, and his research results are widely recognized; the main journals issued in this field are *Fuel* and *Energy Policy*, while other journals have been frequently cited, and these journals have an important role in the field. In these journals, “Coal mine methane: A review of capture and utilization practices with benefits to mining safety and to greenhouse gas reduction” is one of the most important articles in the field. Thin coal seams, coal mining workings, and coal and gas protrusion are current research hotspots.

**Keywords:** CiteSpace; coal mine gas prevention; knowledge mapping; visualization

**Citation:** Zhao, C.; Gao, P.; Ruan, J.; Pu, Y.; Sun, Y.; Cheng, X.; Sun, Y. Research on Hotspots and Evolutionary Trends in Coal Mine Gas Prevention. *Processes* **2024**, *12*, 1993. <https://doi.org/10.3390/pr12091993>

Academic Editor: Ye Huang

Received: 2 August 2024

Revised: 12 September 2024

Accepted: 13 September 2024

Published: 15 September 2024



**Copyright:** © 2024 by the authors. Licensee MDPI, Basel, Switzerland. This article is an open access article distributed under the terms and conditions of the Creative Commons Attribution (CC BY) license (<https://creativecommons.org/licenses/by/4.0/>).

## 1. Introduction

Coal is an important basic energy source, which plays an important role in the economic development of each country [1–3], and in the future, coal mines will still serve several industries, such as power plants, chemical enterprises, iron and steel mills, etc. In the process of coal mining, accidents involving gas, roofs, fire, etc., may occur, and they can cause a large number of casualties, as shown in Table 1. with gas accidents causing the largest number of casualties. Moreover, as the depth of coal mining increases year by

year, coal production gradually enters the deep mining stage, and at present, China's coal mines are deepening at a rate of 10–25 m per year. With the increase in mining depth, the gas pressure in the coal seam rises, the ground stress in the coal seam increases, and, due to the low permeability of the deep coal seam, gas extraction is difficult, which makes gas management difficult in turn, and the risk of coal and gas protrusion increases [4–6], which is a serious threat to the production safety of mines.

**Table 1.** China's coal mine accidents by type, 2016–2022.

Accident Type	Number of Accidents/Incidents	Number of Deaths/People
Gas	119	618
Roof plate	329	538
Transport	265	296
Electromechanics	106	118
Flood damage	45	167
Fire	5	55
Other	157	198

Due to varying geological conditions across different mines, it is challenging to establish a standardized treatment plan. Consequently, scientists worldwide have conducted various studies on gas control to prevent coal mine gas disasters. The primary research areas include methods for determining gas emissions, reducing gas pressure, and gas extraction (including the extraction rate and efficiency) [7,8]. The main methods for managing mine gas include ventilation and gas extraction. However, due to the complexity of on-site conditions, a single method, whether ventilation or gas extraction, often cannot meet actual needs. Therefore, new technologies and techniques for gas control have been developed [9–11]. The advancement of these novel technologies not only augments and enriches the body of knowledge pertaining to gas prevention [12,13], but also guarantees the secure production of mines.

In recent years, researchers at home and abroad have carried out a significant amount of research on gas prevention and control technology, and achieved many research results. Liu Hanwen [14] and others effectively blocked outflow channels by equalizing pressure and plugging leakage. Cheng Lei [15] effectively resisted the abnormal outflow of gas caused by changes in atmospheric parameters by adopting such technical measures as gas extraction from the hollow area, equalizing pressure ventilation in the working face, and spraying and plugging the leakage wind in the roadway. Zhang Liangliang [16] utilized a combination of dampers and regulating windows to suppress gas outflow from the confined wall of an old empty tunnel. Wang Jiren [17] and others implemented equal-pressure ventilation to suppress gas outflow from the confined wall of an old empty area. Sun Guangjian [18] proposed shallow-source and high-level drilling with the insertion of pipe extraction technology. Lu Haiguan [19] proposed the riser extraction of an empty zone and the joint extraction of extraction wells in view of the layered mining process in a synthesized mining face. Cai Minbo [20] proposed to effectively reduce the amount of gas gushing out from the bottom plate fissure by increasing the air supply to the working face, sealing the bottom plate fissure, extracting gas from the bottom plate by unloading the pressure, and extracting gas from the bottom plate by blocking the bottom plate fissure.

To date, scholars and experts from both domestic and international research communities have conducted comprehensive and detailed research on the prevention and control of gas in coal mines. However, there has been relatively little effort in consolidating the existing findings. Current review articles often have limitations in exploring the relationships and evolutionary processes between different knowledge systems in gas prevention. They fall short in clearly presenting the scholarly exploration of various knowledge connections, the intrinsic links between research themes, key research and journals pivotal to the research process, and the indicators of future research trends. To accurately display this knowledge, it is essential to utilize certain bibliometric analysis



tools and techniques. These tools help isolate various useful relationships from a large volume of research, enabling deep insights and scientific understanding of coal mine gas prevention. Commonly used tools for visualization analysis in academia include CiteSpace, SPSS, Ucinet, and VOSviewer [21–25].

CiteSpace is a powerful software tool for constructing visual knowledge structures, offering strong capabilities for literature organization and summarization. Currently, many scholars utilize CiteSpace to summarize various research topics in mining. For example, in a study conducted by Wang et al. [26], CiteSpace was employed as a scientific knowledge mapping tool to deeply explore and organize the important topic of mine fires. By systematically collating, visualizing, and interpreting a large volume of relevant academic research, the study successfully identified the core focus and development trends in mine fire research over recent years. Similarly, in order to investigate the current status and development trends in the study of coal porosity, Shao et al. employed two visualization analytical tools, namely, VOSviewer and CiteSpace [27]. Their findings highlighted the main knowledge structures in coal porosity research, revealing a significant paradigm shift in this field. The shift is from traditional macro-level descriptions and analyses to more detailed micro-level investigations. Furthermore, the analysis identified several current focal points in coal porosity research, including the application of molecular simulation techniques, the characterization of pore structures, the investigation of methane storage, and the analysis of methane adsorption behavior.

Dong et al. [28], based on mine water disaster incidents from 2000 to 2019, used CiteSpace software to organize and analyze 1612 documents. Their study analyzed and summarized the research hotspots and directions in this field. They identified three major unresolved issues in mine water prevention and control: the detection of concealed water sources, the quantitative measurement of water sources, and the rapid identification of dangerous water inrush sources.

Xu et al. [29] analyzed the evolution patterns of hydraulic fracturing in coal seams. Using CiteSpace software, they conducted a visualization analysis of recently published studies. The research team identified several key areas of focus within the field of hydraulic fracturing in coal seams. These included an investigation of the impact of hydraulic fracturing on coal seam permeability, an exploration of the potential applications of numerical simulation techniques, and a study of related seepage models. The study successfully summarized trends in the field concerning the timeline, institutions, and keywords associated with the publications.

In their study on gas outbursts, Xu et al. [30] employed Web of Science (WOS) as the data source and utilized CiteSpace software to analyze and mine research from 2000 to 2021 in the field of gas outbursts. By conducting a comprehensive and systematic analysis of various factors, including the number of publications, publication years, countries, institutions, and keywords, the researchers were able to successfully identify and elucidate the evolutionary patterns of keywords in the coal and gas outburst field over time. Additionally, they introduced new clustering labels for gas control methods, providing scientific references for gas prevention strategies.

In this paper, we visualize and analyze coal mine gas governance through a CiteSpace knowledge graph, examine the current research status and major issues in the field through the knowledge graph analysis of the number of publications, countries, issuing institutions, and authors, as well as keywords, determine the changing characteristics of the research content, and anticipate the direction of the development of future research through the division of the different research phases and the in-depth interpretation of key studies, aiming at providing research inspiration for subsequent researchers.

## 2. Data and Methods

### 2.1. Data Source

WOS is an influential professional and comprehensive scientific information service platform in the research community. Therefore, this paper takes the core dataset of WOS as

the source data. According to the current actual situation of gas governance, searches were conducted for the following topics: “gas governance”, “Gas Control Technology”, “Pre-mining gas methods in coal mines”, “Methods of Gas Mining in Coal Mines”, and “Post-mining gas methods in coal mines”. The search cutoff date was set for 31 December 2023. Irrelevant documents were removed one by one, resulting in a total of 1156 articles. After applying the de-duplication and filtering functions in CiteSpace, 1121 relevant references were obtained.

## 2.2. Methods

Professor C.M. Chen is the developer of CiteSpace, a form of knowledge mapping and analysis software, which he introduced to China. The software includes a number of core features, including but not limited to keyword clustering, keyword co-occurrence analysis, author collaboration exploration, institutional distribution discovery, and research integration, as well as a variety of visualization techniques. Its distinguishing feature is its ability to translate the vast amount of data contained in the WOS database into a variety of knowledge maps with precision and fidelity. Through visualization, it reveals the deep structural features and connections within scientific research fields. Compared with other software types, such as VOSviewer, CiteSpace provides rich visualization effects, including changes in node size, color, shape, etc., as well as dynamic displays of network structures. It also provides a variety of visualization tools and interpretation methods, such as cluster analysis, path analysis, strategic point analysis, etc., to help researchers dig deeper into the intrinsic connections between and laws of the data. To process and analyze the data collected in this study, we used an advanced visualization and bibliometric tool, CiteSpace (version 6.3.R1), which was developed by Dr. ChaomMeiChen of the School of Information Science and Technology at Drexel University (Philadelphia, USA).

## 3. Results and Discussion

### 3.1. Annual Publication Trends

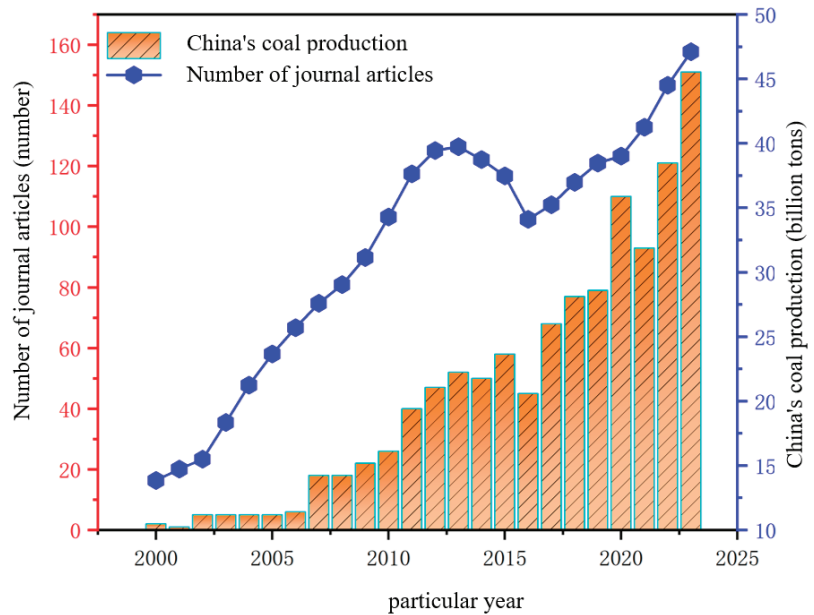
The quantity of research can be used as a quantitative indicator to ascertain the level of academic activity and the trajectory of development within a given field. It intuitively reflects the accumulation of research achievements and the dynamic state of knowledge innovation in related disciplines. The publication volume in the field of coal mine methane prevention from 2000 to 2023 is shown in Figure 1.

**Initial exploration stage (2000–2006):** During this period, the average number of publications on coal mine gas prevention was only four per year. Research in this stage was limited, and the topic was in its nascent phase. The mines at this time were relatively shallow, with favorable geological conditions and fewer gas disasters, leading to minimal research on gas prevention. The objective of the research team was to investigate novel technologies and methodologies for the control and prevention of mine gas accidents. Additionally, the limited number of publication channels and the early stage of internet development restricted the dissemination of research, resulting in lower publication volumes.

**Steady development stage (2007–2019):** This period, spanning 13 years, marked significant growth in the field of mine gas prevention. The number of publications increased at a steady rate, with an average of 46 academic papers published per year. This increase reflects the growing exposure of gas problems as mining depths increased. Researchers began exploring and studying gas prevention from various angles. The steady rise in publications indicates a period of expanding research activity and growing interest in addressing gas issues.

**Explosive growth stage (2020–2023):** In this stage, the average number of publications per year surged to 119. This dramatic increase is attributed to the deepening research into mine gas prevention and the enhanced understanding of gas control mechanisms. The surge indicates that the field has attracted significant attention and is entering a new development phase. Researchers are now attempting to explain gas prevention from a mechanistic

perspective, reflecting a deeper and more advanced understanding of the subject. The exponential growth indicates a significant shift in the field's developmental trajectory.



**Figure 1.** Number of papers published on gas management.

Regression analysis of the year and the number of journal publications yielded the following model equation:  $\text{publications} = 1.283 * \text{year} - 2550.133$ . The model R-squared value was 0.879. Therefore, the predicted number of journal publications on coal mine gas management in 2050 was approximately 80.

### 3.2. National Publication Volume and Collaboration Analysis

To examine the primary countries/regions involved in coal mine gas prevention and their collaborative relationships, CiteSpace was used to create a knowledge map of international collaborations. The knowledge map is shown in Figure 2.

According to the CiteSpace knowledge map analysis, a total of 42 countries have contributed significantly to research on gas prevention. The top three countries by publication volume are China, with 534 papers (38.58%); the United States, with 154 papers (11.12%); and Australia, with 96 papers (6.94%). The map depicts the geographical distribution of countries, with the size of each node proportional to the number of publications originating from that country. The connections between the nodes visually represent collaborative relationships between different geographic regions.

It is important to note that the presence and characteristics of connections, particularly their thickness, provide rich information on the closeness and intensity of collaborations between countries and regions. Darker colors at the centers of the circles indicate that research in the field began earlier in those countries.

The analysis reveals that collaborations between countries such as the Netherlands, Switzerland, Germany, and Scotland are notably closer compared to those between other countries. China and Poland also show relatively strong collaboration, while Russia has fewer publications. As can be seen from the figure, there is closer cooperation on mine gas management in the European region, and there are fewer links with countries other than Europe, especially China, the United States, and Australia, which have larger outputs. Coal mine production by region is shown in Figure 3. The situation of coal mine gas is different

from one country to another. For example, most of the coal seams in the Chico Lomã coalfield in the Paraná Basin, in Brazil, have high contents of minerals and inerts, which directly affects the production and storage of gas in the seams. Therefore, it is necessary to intensify cooperation and communication between countries.

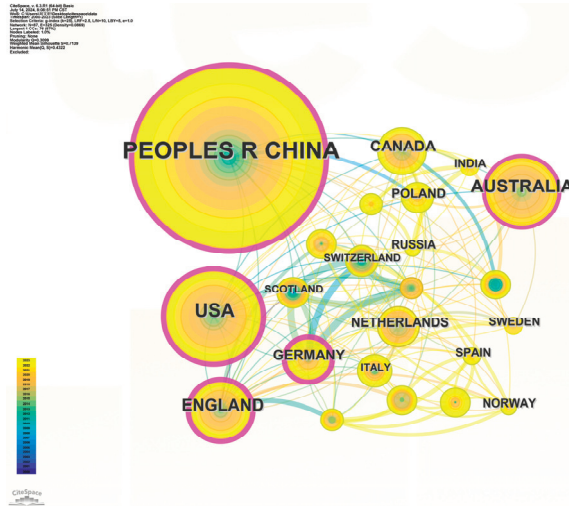


Figure 2. Knowledge map of cooperation between countries and regions.

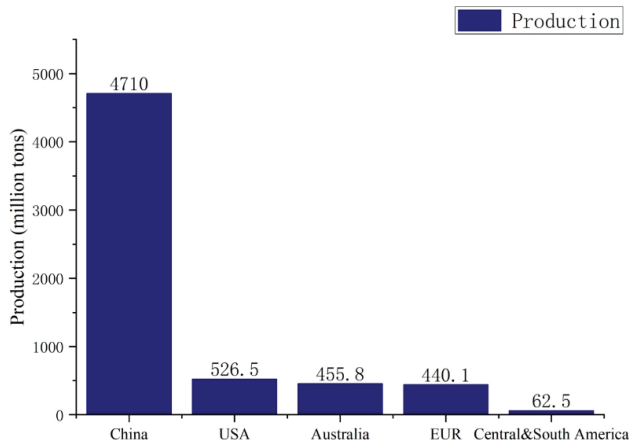
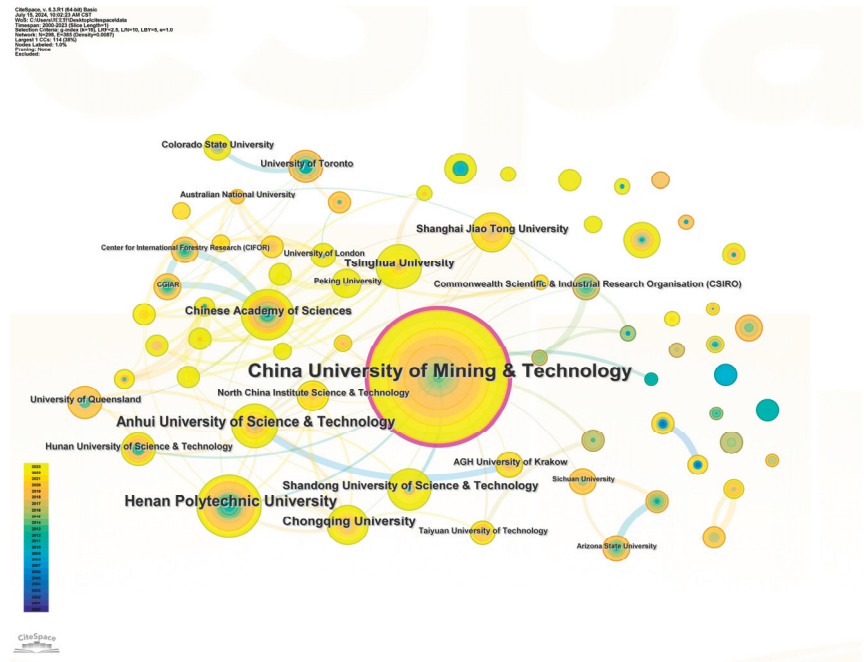


Figure 3. Map of coal mine production by region.

### 3.3. Research Institutions and Collaboration Analysis

In order to ascertain the most productive institutions in the field of coal mine gas prevention and analyze their collaborations, we examined research institutions and their collaborative relationships [31]. CiteSpace was used to generate a collaboration network map featuring 208 nodes and 276 connections, as shown in Figure 4. The visual representation of the research output level of each institution is determined by the size of the nodes, while the connections between nodes illustrate the degree of collaboration between institutions.



**Figure 4.** Knowledge map of research institution collaboration.

As illustrated in Figure 4, the leading institutions in the field of coal mine gas prevention include China University of Mining and Technology, Henan Polytechnic University, Anhui University of Science and Technology, Chongqing University, the Chinese Academy of Sciences, and Tsinghua University. These institutions are notable for their significant research output, ranking among the top six in publication volume. China University of Mining and Technology, in particular, has established close collaborative relationships with over 20 research institutions, such as Shandong University of Science and Technology, Henan Polytechnic University, the Chinese Academy of Sciences, Taiyuan University of Technology, the Commonwealth Scientific & Industrial Research Organisation (CSIRO), and AGH University of Science and Technology.

The map reveals a clear regional pattern in coal mine gas prevention research, where collaborations between academic institutions are often influenced by geographic proximity. Institutions located closer to each other tend to have more intensive collaborations, while the degree of collaboration generally decreases with increasing geographic distance. Compared to domestic collaborations, international cooperation is relatively limited, which may constrain the development of coal mine gas prevention technologies. This regional disparity is often due to national policies and logistical challenges in resource exchange. However, this does not mean that international or intercontinental research collaborations are unfeasible; they are not yet mainstream in the current research collaboration model and require further promotion and development.

### 3.4. Author Analysis

#### 3.4.1. Publication Volume and Collaboration Analysis

Price's Law, as proposed by the British physicist and science historian, Derek J. de Solla Price [27], represents a significant theoretical framework for understanding the growth patterns of scientific research output. The precise formula is as follows:

$$M = 0.794 \times \sqrt{N_{\max}} \quad (1)$$

In the context of Price’s Law, the term  $N_{\max}$  denotes the maximum number of papers that can be published by a single author within a given field.  $M$  represents the minimum number of highly active, influential, and significantly contributing authors in a particular research area.

A systematic analysis and comprehensive examination of bibliographic data affords the opportunity to obtain a substantial body of information regarding pertinent authors. This encompasses, but is not limited to, the following: the research output, the average number of citations per paper, the distribution of the journal impact factor of published papers, the coverage and depth of research topics, and the structure and stability of collaboration networks. The comprehensive nature of these data enables an objective assessment of an author’s academic output efficiency and influence, which is of paramount importance for identifying their position and role within the academic community. When conducting extensive analyses of the author group, it is of particular interest to focus on high-output authors and core authors, given their distinctive status and noteworthy contributions.

Table 1 presents a list of the eight most prolific authors, accompanied by a summary of their publication output and related information. As indicated in Table 1,  $N_{\max}$  is 16, which means that  $M$  is 3.18. Thus, in the field of coal mine gas prevention, core authors need to have published at least four papers.

From Table 2, it can be observed that most of the top eight authors by publication volume are affiliated with China University of Mining and Technology, followed by China University of Mining and Technology (Beijing), Anhui University of Science and Technology, and North China University of Science and Technology. The author with the highest publication volume is Wang Enyuan [32–47], from China University of Mining and Technology, who has published 16 papers. The second highest is Wang Kai [29,30,48–59], from China University of Mining and Technology (Beijing). Notably, all of the top eight authors are from China, indicating that gas prevention in China is a major research topic, leading to a higher number of publications.

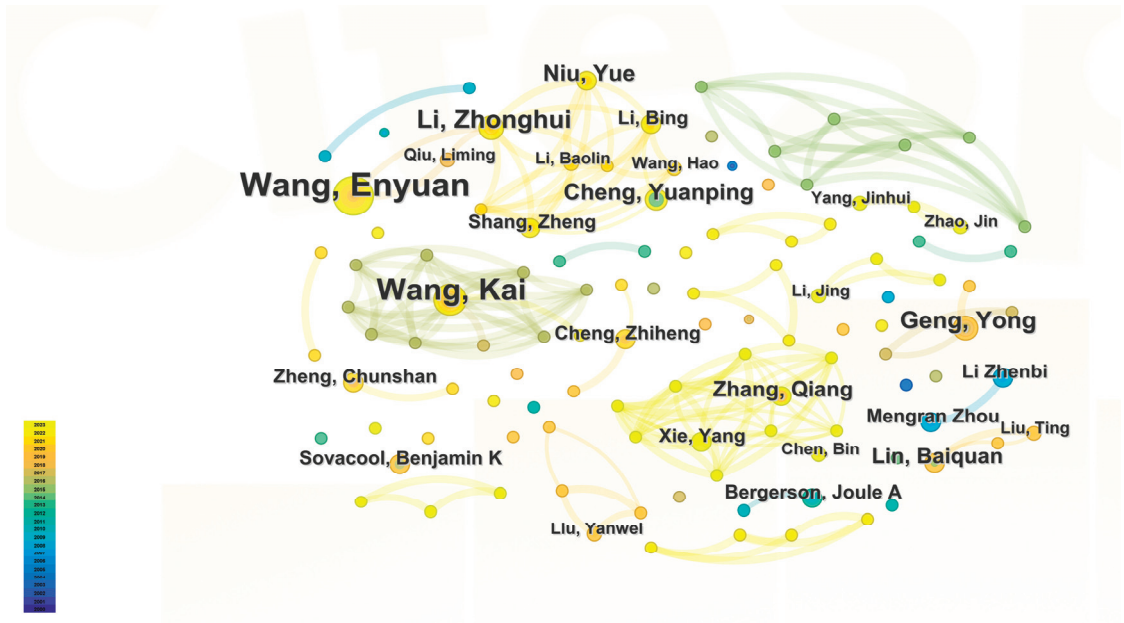
**Table 2.** Institutions to which the main authors belong, the number of publications, and their percentage share of the total number of publications.

Rank	Author	Organization	Volume of Publication	Proportions
1	Wang Enyuan	China University of Mining and Technology	16	3.6%
2	Wang Kai	China University of Mining and Technology (Beijing)	13	3.8%
3	Li Zhonghui	China University of Mining and Technology	8	1.8%
4	Cheng Yuanping	China University of Mining and Technology	6	1.4%
5	Niu Yue	China University of Mining and Technology	6	1.4%
6	Lin Boquan	China University of Mining and Technology	5	1.2%
7	Chunshan Zheng	Anhui University of Science and Technology	4	0.9%
8	Cheng Zhiheng	North China Institute of Science and Technology	4	0.9%

Subsequently, the WOS dataset was imported into the CiteSpace analytical platform for further examination. The research period was defined as extending from 2000 to 2023, with time intervals defined as biannual. In the course of the “node type” analysis, the “authors” category was the primary focus. The frequency of keyword occurrences was analyzed in depth using the “Pathfinder” path algorithm, along with the “Pruning Networks” and “Pruning the Merge Network” techniques. This process generated a map showcasing the author collaboration patterns.

From Figure 5, it can be observed that in the field of gas prevention, there is a close network of collaboration among authors, forming an interconnected web of relationships. The network in the top-left corner includes Wang Enyuan, Li Zhonghui, and Niu Yue, all of whom are affiliated with China University of Mining and Technology. Wang Enyuan is the central figure in this network, focusing on research related to gas prevention warning tools, coal and gas outburst mechanisms, and related studies. Below this network, Wang Kai leads another collaborative network. It is evident that those who closely collaborate with

Wang Kai are affiliated with China University of Mining and Technology (Beijing). This network primarily deals with the distribution patterns of gas fractures and permeability changes under different conditions. The network led by Zhang Qiang and Xie Yang is situated in the middle.



**Figure 5.** Knowledge map of collaborative author analysis.

The author collaboration map indicates that the majority of researchers engaged in the field of coal mine gas prevention are affiliated with the China University of Mining and Technology, Xi'an University of Science and Technology, Henan Polytechnic University, Shandong University of Science and Technology, and China University of Mining and Technology (Beijing).

Furthermore, the institutions are geographically close, and the collaboration is notably intensive within the same research institutions. When different research institutions are involved, collaboration between researchers tends to decrease. This phenomenon indicates that while there is a substantial corpus of research on gas prevention, there is a paucity of evidence of large-scale, structured collaborative research and interdisciplinary knowledge exchange between scholars.

This regional and fragmented nature of collaboration suggests that extensive, organized collaborative research and knowledge sharing across different regions are lacking. In the advancement of gas prevention, it is imperative that scholars engaged in its development engage in profound academic discourse and collaboration, as this will facilitate the growth of the discipline. It is thus also imperative that researchers in the field of gas prevention engage in more rigorous and frequent collaboration and communication in order to facilitate the integration of resources and the sharing of knowledge.

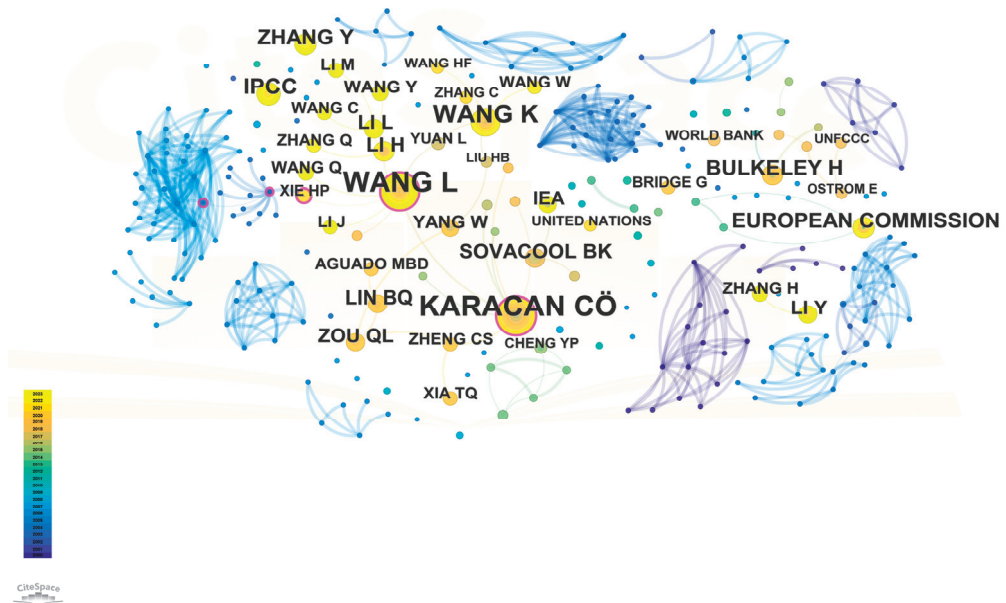
### 3.4.2. Author Co-Citation Analysis

The examination of author co-citations constitutes a fundamental methodological approach within the domain of scientific inquiry. This analytical technique facilitates a deeper understanding of the mechanisms through which scientific knowledge is disseminated and the interactions within and between academic disciplines. The fundamental premise

of this methodology is the comprehensive monitoring and examination of a particular phenomenon: the co-citation of two or more authors' independent works in the same context as cited in the research papers of other scholars. This phenomenon is defined as "co-citation".

The concept of co-citation not only serves as a direct reflection of the extent of academic influence, but is also an important indicator of potential connections and tendencies toward collaborative work between authors and the academic disciplines to which they contribute. The analysis of co-citation patterns allows for the acquisition of insights into inter-scholar relationships, the identification of influential works and authors, and the comprehension of the underlying structure of knowledge exchange within a field of study.

Figure 6 reveals a group of highly cited authors in the field, including C. Ozgen Karacan, Wang Kai, and Wang Enyuan. In this visualization, the size of the circles represents the academic influence and activity level within this research area. C. Ozgen Karacan, despite having fewer publications compared to other prominent domestic scholars, is highly recognized in the field due to the high quality of his academic articles, which are widely cited and respected. Wang Kai and Wang Enyuan are acknowledged for their contributions to the micro-theories of gas and gas seepage in coal, receiving substantial recognition for and citations of their research. Additionally, several other authors have published high-quality papers that have been recognized and cited by peers, contributing to the field's knowledge base.



**Figure 6.** Knowledge map of co-cited authors.

### 3.5. Journal Analysis

#### 3.5.1. Major Journals Analysis

Academic journals play an irreplaceable and central role in the process of scientific research communication and results diffusion. Based on the detailed data provided by the WOS database, we conducted an in-depth investigation on the publication situation in the field of gas management and selected the top journals, as shown in Table 3. Among them, the *Fuel* journal ranked first, with 63 papers, followed by *Advanced Materials Research*, with 41 papers, and *Energies*, with 36 papers. The impact factor is a kind of index that is used to assess the influence of academic journals by calculating the average number of



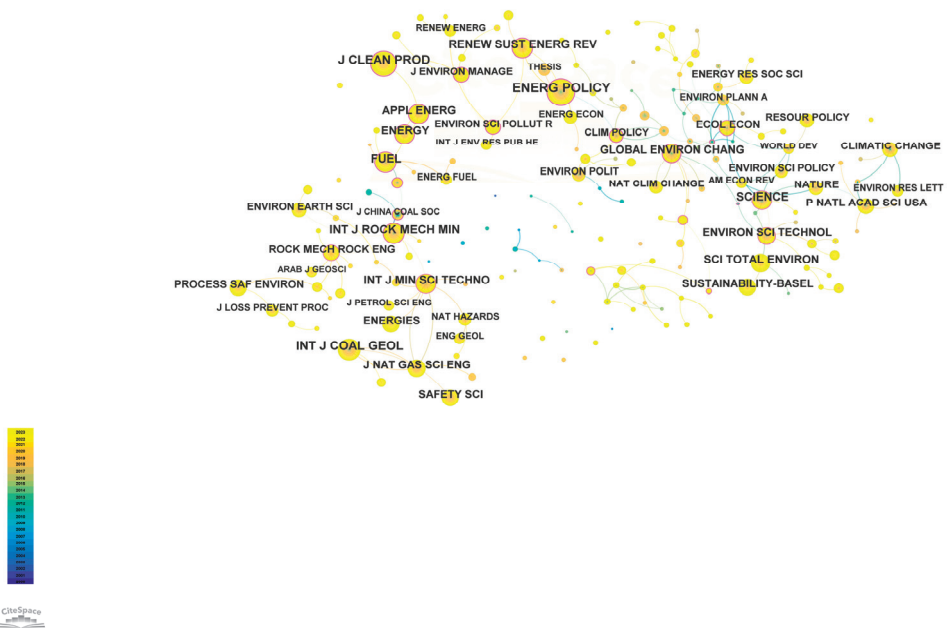
citations of journals. Usually, the higher the impact factor of a journal, the more frequently the articles in the journal are cited by other scholars, and the greater its influence. From the table, we can see that *Advanced Materials Research* has the largest impact factor, of 27.4, which indicates that it is more influential in this field, while *Shock and Vibration* has the smallest impact factor in this table, which indicates that it is less influential among these top ten journals.

**Table 3.** Main published journals in the field of gas management.

Rank	Journal Name	Volume of Publications	Proportions	Impact Factor	Citation Index
1	<i>Fuel</i>	63	5.62%	8.035	SCI
2	<i>Advanced Materials Research</i>	41	3.66%	27.4	SCI
3	<i>Energies</i>	36	3.21%	2.262	SCI
4	<i>Geofluids</i>	30	2.68%	7.231	SCI
5	<i>Journal of Natural Gas Science and Engineering</i>	27	2.41%	5.285	SCI
6	<i>IOP Conference Series: Earth and Environmental Science</i>	25	2.23%	5.80	SCI
7	<i>Applied Mechanics and Materials Sustainability</i>	24	2.14%	2.866	SCI
8		21	1.87%	3.30	SCI
9	<i>Advances in Civil Engineering</i>	20	1.78%	1.924	SCI
10	<i>Shock and Vibration</i>	17	1.52%	1.60	SCI

### 3.5.2. Journal Co-Citation Analysis

In conducting an analysis of the co-citation networks of academic journals, nodes were designated as “Cited Journal” and the Pathfinder algorithm was employed for the pathfinding process. This resulted in the generation of a journal co-citation map, as illustrated in Figure 7. Table 4 provides a detailed overview of the ten most highly cited academic journals.



**Figure 7.** Knowledge map of journals’ co-citation cues.

**Table 4.** Top ten highly cited journals.

Rank	Journal Name	Co-Citation
1	<i>Energy Policy</i>	268
2	<i>Journal of Cleaner Production</i>	212
3	<i>International Journal of Coal Geology</i>	208
4	<i>International Journal of Rock Mechanics and Mining Sciences</i>	172
5	<i>Fuel</i>	151
6	<i>Science</i>	149
7	<i>Renewable and Sustainable Energy Reviews</i>	141
8	<i>Applied Energy</i>	135
9	<i>International Journal of Mining Science and Technology</i>	135
10	<i>Energy</i>	132

In the journal co-citation analysis, the following journals were frequently cited: *Energy Policy*, *Journal of Cleaner Production*, *International Journal of Rock Mechanics and Mining Sciences*, *International Journal of Coal Geology*, *Fuel*, *Science*, *Renewable and Sustainable Energy Reviews*, *Applied Energy*, *International Journal of Mining Science and Technology*, and *Energy*.

It is notable that among these journals, *Energy Policy*, *Journal of Cleaner Production*, and *International Journal of Coal Geology* occupy a pivotal position with regard to both average citations and co-citation metrics. As a general rule, the ten journals listed in the table are regarded as esteemed academic outlets with considerable visibility and influence within the global research community. They are particularly significant in the field of gas prevention research, with journals like *Energy Policy*, *Journal of Cleaner Production*, *Fuel*, *International Journal of Coal Geology*, and *International Journal of Rock Mechanics and Mining Sciences* being central to the study of gas prevention.

### 3.6. Core Research Citation Analysis

To conduct an exhaustive examination of the literature with the greatest impact on the field of gas prevention, we selected the ten most frequently cited papers [60–69] as the focus of our analysis. The set comprises nine specialized papers and one review article. As illustrated in Table 5, a review of the distribution of publication times for these highly cited documents reveals the following: The top ten most frequently cited papers were all published after 2010, indicating that research in this field became active only after 2010. The most frequently cited article, published in 2011, represents early research explorations in the field. Another highly cited article, from 2013, signifies a period of steady development in the field. Most of the subsequent high-citation papers were published after 2015, reflecting new insights gained from earlier academic work, leading to a surge in academic publications.

The development trajectory of gas prevention can be summarized in several stages, as follows:

- (1) Early stage: this phase mainly involved introducing mine gas and discussing the relationship between mine gas emissions and environmental protection.
- (2) Steady development stage: the focus shifted to exploring new technologies for gas prevention, with a particular emphasis on techniques like protective layers in mining.
- (3) Mechanistic stage: later papers concentrated on the mechanistic aspects of mine gas prevention.
- (4) Review stage: after years of accumulation and development, the field saw comprehensive and systematic reviews of current gas prevention technologies, marking a new high point in integrating theoretical research and practical experience.

These stages illustrate the field's progression from initial explorations to a sophisticated understanding and systematic evaluation of gas prevention technologies.

Table 5. Top ten highly cited studies.

Rank	Title	Typology	Journal Name	Author	Year of Publication	Citation
1	Coal mine methane: A review of capture and utilization practices with benefits to mining safety and to greenhouse gas reduction	Review	<i>International Journal of Coal Geology</i>	C. Ozgen Karacan [62]	2011	12
2	Control of coal and gas outbursts in Huainan mines in China: A review	Article	<i>Journal of Rock Mechanics and Geotechnical Engineering</i>	Liang Yuan [68]	2016	9
3	The elimination of coal and gas outburst disasters by long distance lower protective seam mining combined with stress-relief gas extraction in the Huaibei coal mine area	Article	<i>Journal of Natural Gas Science and Engineering</i>	Liu Haibo [63]	2015	9
4	Novel integrated techniques of drilling-slotting-separation-sealing for enhanced coal bed methane recovery in underground coal mines	Article	<i>Journal of Natural Gas Science and Engineering</i>	Zou Quanle [67]	2015	8
5	Safe strategy for coal and gas outburst prevention in deep-and-thick coal seams using a soft rock protective layer mining	Article	<i>Safety Science</i>	Wang Liang [65]	2020	8
6	Gas outburst disasters and the mining technology of key protective seam in coal seam group in the Huainan coalfield	Article	<i>Natural Hazards</i>	Wang Haifeng [64]	2013	8
7	Review of coal and gas outburst in Australian underground coal mines	Review	<i>International Journal of Mining Science and Technology</i>	Dennis J. Black [69]	2019	8
8	Evaluation of the remote lower protective seam mining for coal mine gas control: A typical case study from the Zhuxianzhuang Coal Mine, Huaibei Coalfield, China	Article	<i>Journal of Natural Gas Science and Engineering</i>	Kan Jin [61]	2016	8
9	Environmental impact of coal mine methane emissions and responding strategies in China	Article	<i>International Journal of Greenhouse Gas Control</i>	Cheng Yuan Ping [60]	2011	7
10	Fatal gas explosion accidents on Chinese coal mines and the characteristics of unsafe behaviors: 2000–2014	Review	<i>Safety Science</i>	Yin Wentao [66]	2017	7

### 3.7. Hotspots and Frontiers in Mine Gas Prevention Research

#### 3.7.1. Keyword Co-Occurrence Analysis

The use of keywords is an indispensable component of academic papers at both the content level and the structural level. Essentially, keywords are concise and precise distillations of the core themes and ideas of papers, serving as “tags” that succinctly convey the central topics and research directions. Analyzing keywords is a systematic process of examining and interpreting the focal points of research papers.

The WOS data were transformed into a format suitable for analysis using CiteSpace. This process encompassed the period between 2000 and 2023 and involved dividing this timespan into two-year intervals. The keyword was designated as the node type for the analysis. The resulting keyword co-occurrence network is illustrated in Figure 8.

As illustrated in Figure 8, each keyword is represented as a node, with connecting lines indicating the association law between the keywords. In the event that a pair of keywords was identified as occurring together within the same body of research, it was necessary to establish a line of connection between them. In network diagrams, the size of a node is directly proportional to the frequency of the occurrence of the keyword it represents in



### 3.7.2. Keyword Clustering

A total of 33 clusters were obtained from the keyword extraction analyzed above, and the clusters with fewer than 10 keywords were filtered by CiteSpace's built-in filtering function. Figure 9 shows the main clusters in this paper, based on # 0, # 1... # 7 sorting. From the figure, it can be seen that coal mining faces, gas protrusion, and thin coal seams are the areas of focus of research in this field. Through the analysis, the following was established:

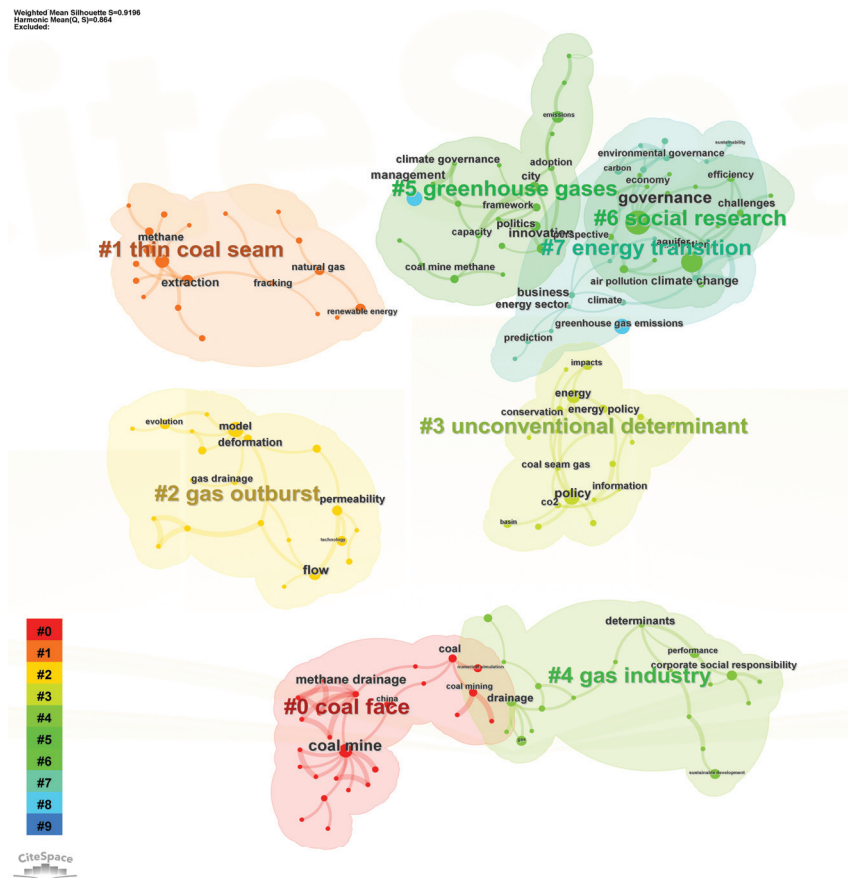


Figure 9. Knowledge map of keyword clustering.

① The coal mining face is a special environment, mostly located in deep underground, which not only has narrow space, high temperatures and humidity, and poor lighting and visual conditions, but also has a variety of potential safety hazards and hazardous factors, including coal mine gas, which may cause extremely serious consequences. Therefore, it is of great practical significance to carry out research on coal mining face gas in order to improve the effectiveness of gas management.

As a large number of joints and fissures will be produced during the mining process, the mining fissure field will be the main channel for gas transportation, and it is beneficial for field work to put forward targeted and efficient measures to prevent and control gas by clarifying the law of gas transportation under mining conditions. The “O” circle theory of gas extraction established by Qian Minggao has been widely used in field practice, and the field practice shows that the “O” circle theory can effectively improve the efficiency of gas extraction and has great applicability. Liang Bing et al. [70] used COMSOL Multiphysics to

study the gas outflow law of the lower seam and the inner part of the filling body during the application of the seam filling method, and found that the gas in the lower seam would inflow to the working face through the medium of the filling body; in the process of mining, the gas pressure of the working face gradually decreased with the mining time. Kuroiwa T. et al. [71] simulated coal–gas protrusion under different gas pressures using profiled coal. Alekseev A.D. et al. [72] innovatively carried out simulation experiments of coal and gas herniation under triaxial stress loading.

Currently, of the main extraction technologies of cross, grid, and parallel extraction, in actual work, grid extraction is more widely used. Its overall economy is higher, the overall effect on gas control is better, and it can also help with calibration. For high-gas mines, due to the very high gas content underground, the use of intensive coal seam extraction technology for gas control should be considered first. There are also gas control technologies, such as high-level drilling extraction technology, integrated drilling and cutting penetration-enhancing and pressure-removing extraction technology, etc.

② In the process of coal mine gas disaster prevention and control, the coal and gas protrusion model is crucial to the study of coal and gas protrusion mechanisms, since it can maximize the simulation of the evolution processes and disaster-causing mechanisms of gas disasters in the process of mining so as to reveal the mechanism of coal and gas protrusion, and the model is of great theoretical and practical significance for coal-mining enterprises to take targeted gas prevention and control measures.

In terms of the mechanism of coal and gas outburst, before the middle of the 20th century, the research on the mechanism of coal and gas outburst was dominated by foreign scholars, and there were mainly four types of hypotheses, the gas-dominant hypothesis, the geostress hypothesis, the chemical nature of the role hypothesis, and the comprehensive role hypothesis. In recent years, there have been some new developments in the research on the mechanism of coal and gas herniation at home and abroad. Dennis J. Black [69] analyzed 878 herniations in 22 coal mines in Australia, and most of the herniations were related to the abnormal geological conditions; however, in the absence of abnormal geological formations, coal mining in the areas where the gas content is greater than the currently accepted threshold level will not significantly increase the risk of herniation. B.B. Beamish and P.J. Crosdale [73] believe that coal and gas protrusion easily occurs near faults, which is directly caused by the reduction in the length of the pressure-relief zone in front of the workings, and the abnormally high gas pressure and stress gradient. Our scholars have made various attempts to hypothesize the mechanism of protrusion. Jiang Chenglin and Yu Qixiang, by simulating the presence of spherical cap-shaped coal pieces in the residual coal samples of pressed-out holes under the condition of Shimen uncovering, confirmed that the destruction of the coal body in the process of coal and gas protrusion was carried out in the form of spherical shell destabilization, and put forward the hypothesis of spherical shell destabilization. Paterson [74] believed that protrusion is caused by the structural instability of the coal rock body and that the change in the gas pressure gradient led to the structural instability of the coal rock body, and established a mathematical model for the theoretical analysis of protrusion. Ectors P. et al. [75] believed that protrusion mainly occurs due to the result of the joint action of the elastic potential energy of the coal rock body and the internal energy of the gas, and put forward, for the first time, an energy equation for the protrusion process. Sato et al. [76] analyzed from an external point of view, and through the analysis of the seismic wave of a protrusion, they concluded that earthquakes can induce coal and gas protrusion accidents. Hanes et al. [77] analyzed and researched the coal and gas protrusion phenomenon in Australian coal mines, and concluded that both gas and stress play an important role in the protrusion process, but that in protrusion, one of these factors is predominant.

In terms of coal and gas protrusion modeling, in the 1950s, the Soviet Union, Germany, and other countries began to make different experimental devices to simulate the individual aspects of protrusion or the entire protrusion process. Khodot, through a large number of experiments and data analysis, for the first time, put forward the energy equation for coal

and gas protrusion, in which the deformation potential of the coal body and the internal energy of the gas combine to trigger coal and gas protrusion. Zhou Shining and Sun Sucheng believed that the flow of coal seam gas conforms to Darcy's permeability law, and that the basic parameters affecting gas flow are gas pressure, permeability coefficient and content coefficient. According to the theory of gas seepage in porous media, the flow of coal seam gas is divided into unidirectional, radial, and spherical flow. According to the law of mass conservation, the change in gas content in the coal body is equal to the change in the specific flow rates of inflow and outflow, and the differential equations are used to calculate the average and gas flow processes in non-homogeneous coal seams.

③ Research shows that about 80% of protrusion accidents occur in areas of geological tectonic activity, and the distribution and risk of protrusion and geological tectonic correlation show strong regularity. Shepherd et al. investigated the causes of protrusion accidents in several coal-producing countries and found that the majority of protrusions occur in backslope axes, folding hubs, faults, and other strong deformation zones, that protrusion is closely related to geological tectonics, and that the stress states of different tectonic deformation control zones will have a significant effect on the distribution and gas content of coal seams [78]. The stress state, tectonic coal distribution, and coal seam gas contents in different tectonic deformation control zones all have obvious impacts on the protrusion. Gray counted 105 cases of protrusion in major coal-producing countries in the world, among which 87 cases, or 83%, had clear geological tectonic zones near the protrusion point. Wold et al. [79] concluded that the protrusion disasters in Australian coal mines are related to the existence of geological structures in the coal seams or the surrounding rocks, and that the spatial sizes of these structures can range from 0.5 to 0.5 m. The spatial dimensions of these formations can range from a few millimeters to several meters. In addition, Frodsham et al. [80] clearly proved this point and studied the tectonic deformation characteristics and their influence on coal and gas protrusion with respect to specific tectonic deformation patterns, such as dorsal slopes, syncline, thrust faults, normal faults, and layer-slip faults. In China, Lei Dongji et al. [81] concluded that the West Yu mining area experienced strong tectonic extrusion and shear in the Early–Middle Indo–Chinese and Yanshan phases, that the shear effect of the late slip tectonics caused further damage to the coal seam structure, making the Class IV and Class V coals in the 21 coal seams thicker, and that the protruding accidents occurring in the coal mines in the region were significantly controlled by tectonics.

④ Compared with the mining of medium-thickness coal seams and thick coal seams, thin coal seam mining has the following characteristics: ① the mining space is narrow, with limited space for equipment operations and small personnel activity areas, and it is easily affected by geological conditions; ② thin coal seams are mostly used as the first mining protection layer to liberate the neighboring high-gas coal seams, the geological conditions are unclear, and the detection requirements are high; ③ the working faces of thin coal seams advance at a high speed, the half-coalite back to the mining roadway is slow, and the mining and mining succession is tense; ④ the working environment of thin coal seams is poor, and remote monitoring and inspection are difficult. Therefore, it is necessary to research and develop supporting intelligent mining technology to increase the degree of automation of thin coal seam mining, reduce mining costs, and increase mining efficiency. At present, there are four commonly used mechanized mining methods for thin coal seams: integrated mining by drum miners, integrated mining by coal planers, continuous mining by coal miners, and auger mining by coal miners, among which integrated mining by drum miners is the mainstream mechanized mining method (with a proportion of 85%).

⑤ In recent years, China's coal industry has undergone profound structural adjustment and innovation in response to environmental protection needs and improved resource utilization, gradually abandoning inefficient production capacity and actively transforming to high efficiency and intelligence. In this process, coal mines pay special attention to updating safety equipment, especially investment in gas prevention technology and equipment. As coal mines move toward deeper development, there is a growing demand for

deep-hole drilling and the measurement of coal seam gas concentration. This technology can accurately obtain real-time information on the gas concentration and pressure in coal seams, thus significantly reducing the possibility of gas explosions and playing a key role in strengthening coal mine safety control. In addition, hydraulic seepage enhancement technology is undergoing a transformation from refinement and regionalization to intelligence, which not only strengthens control accuracy and penetration enhancement, but also realizes the accurate prediction of mining time, providing strong technical support for durable and stable mine operation. Gas explosion prevention technology upgrades, especially intelligent, remote, online, and centralized monitoring and control systems, are crucial. With the help of these advanced technologies, coal mines can implement instant gas concentration detection and risk warning at off-site locations, and respond quickly to ensure the safety of mine operations.

#### 4. Conclusions

In this study, a total of 1121 documents related to gas management in the WOS core database were systematically counted and deeply analyzed, and the knowledge map of this field was constructed with the help of CiteSpace software technology to visualize its knowledge structure and research lineage. The conclusions are as follows:

- (1) The research on coal mine gas management has developed through three stages: the initial exploration stage (2000–2006), the steady development stage (2007–2019), and the explosive surge stage (2020–2023). This evolution is positively correlated with China's coal mine production.
- (2) The top three countries in terms of the number of articles issued are China, the United States, and Australia. However, the cooperative relationship between European countries is closer compared to that between other countries. The research institutions are China University of Mining and Technology, Henan University of Science and Technology, Anhui University of Science and Technology, etc., and Enyuan Wang and Kai Wang are the core authors.
- (3) *Fuel*, *Advanced Materials Research*, and *Energies* are the top three journals, and *Energy Policy*, *Journal of Cleaner Production*, and *International Journal of Coal Geology* play a key role in both average citation and co-citation. Co-citations play an important role. The research paper entitled "Coal mine methane: A review of capture and utilization practices with benefits to mining safety and to greenhouse gas reduction" was cited in the top three journals. It also topped the list in terms of citations.
- (4) The current research on coal mine methane prevention and control mainly focuses on coal mining faces, gas protrusion, and thin coal seams, specifically on permeability, coal seam deformation, etc. In the future, coal mine methane prevention and control will be developed through new equipment, new technologies, and intelligence.

**Author Contributions:** Writing—original draft, X.C.; writing—review and editing, C.Z., P.G., J.R., Y.P., Y.S. (Yuan Sun) and Y.S. (Yu Sun). All authors have read and agreed to the published version of the manuscript.

**Funding:** This research received no external funding.

**Data Availability Statement:** The original contributions presented in the study are included in the article, further inquiries can be directed to the corresponding author.

**Conflicts of Interest:** Authors Chunguang Zhao, Peng Gao, Jinlin Ruan, Yuan Sun and Yu Sun were employed by the company Baode Coal Mine of Guoneng Shendong Coal Group Co., Ltd. The remaining authors declare that the research was conducted in the absence of any commercial or financial relationships that could be construed as a potential conflict of interest.



## References

- Chen, J.; Lv, Y.Q.; Fan, T.Z. Research on the evolution and driving factors of digitalization of energy in China-A new perspective based on coupling coordination. *Heliyon* **2023**, *9*, 21. [CrossRef] [PubMed]
- Rong, F.; Victor, D.G. Coal liquefaction policy in China: Explaining the policy reversal since 2006. *Energy Policy* **2011**, *39*, 8175–8184. [CrossRef]
- Yan, D.; Su, F.; Wang, Z.W.; Chen, Z.Z.; Lei, Y.; Ye, B. Achieving high-quality development in China's coal-based cities: How heterogeneities green innovation promote carbon emission performance? *Environ. Dev. Sustain.* **2024**, *26*, 13921–13941. [CrossRef]
- Li, L.L.; Tang, J.P.; Sun, S.J.; Ding, J.H. Experimental study of the influence of water content on energy conversion of coal and gas outburst. *Nat. Hazards* **2019**, *97*, 1083–1097. [CrossRef]
- Xin, M.; Fukun, X.; Guangyi, S. Catastrophe analysis of coal and gas outburst process. In Proceedings of the International Conference on Mine Hazards Prevention and Control, Qingdao, China, 17 October 2007; pp. 159–162.
- Zhang, Y.G.; Cao, S.L.; Yan, J.W.; Zhang, Z.M. Mechanism of coal-gas outburst based on deformed coal. In Proceedings of the International Symposium on Mining Science and Safety Technology, Jiaozuo, China, 16–19 April 2007; pp. 1382–1386.
- Zhao, Y.Q.; Xu, H.T. Experimental of Gas Drainage in Low Permeability Coal Seam. In Proceedings of the International Forum on Porous Flow and Applications, Wuhan, China, 24–26 April 2009; pp. 27–31.
- Zhao, Z.M.; Wang, G. The research of gas drainage technology in Daning coal mine. In Proceedings of the 4th International Conference on Civil Engineering, Architecture and Building Materials (CEABM), Haikou, China, 24–25 May 2014; pp. 2558–2563.
- Cui, Q.Q.; Ning, J.; Yin, X.H. Network Control Technology applied in Remote Mine Ventilation Control System. In Proceedings of the 31st Chinese Control And Decision Conference (CCDC), Nanchang, China, 3–5 June 2019; pp. 4528–4532.
- Gao, H.A.; Gao, Y.B.; Qi, J.C.; Fu, Q.; Zhang, X.Y. Study on surrounding rock deformation and gas control of entry automatically formed by roof cutting in high-gas coal seam. *Energy Explor. Exploit.* **2023**, *41*, 1559–1575. [CrossRef]
- He, L.W.; Dai, Y.C.; Xue, S.; Zheng, C.S.; Han, B.Q.; Guo, X. Study on Gas Control Methods Optimization for Mining Safety. *Adv. Civ. Eng.* **2021**, *2021*, 13. [CrossRef]
- Li, C.Y.; Zhang, L.L. Study on the occurrence law of gas in Fukang mining area. In Proceedings of the 6th International Conference on Advances in Energy Resources and Environment Engineering (ICAEESE), Chongqing, China, 20–22 November 2020.
- Zhang, J.F.; Shi, S.L.; Lu, Y.; You, B.; Wu, F.H.; Zhang, L.Z.; Xie, Y.D.; Zhang, J.J.; Miao, Z.Q. Coal Mine Gas Abnormal Emission Inducing Factors, Manifestation Emission Mechanism. *Fresenius Environ. Bull.* **2022**, *31*, 6569–6575.
- Li, L.H.-w.Y. Analysis and Control of Harmful Gas Over Limit during Gateway Driving Along Goaf. *Coal Sci. Technol.* **2011**, *39*, 69–71. [CrossRef]
- Lei, C. The Influencing Factors of Gas Emission in Closed Goaf and the Prevention and Control Measures. *Manag. Technol. SM* **2018**, *31*, 194–196. [CrossRef]
- Zhang, L.L. Research on Monitoring and Early Warning Technology of Coal and Gas Outburst Hazard. *Shandong Coal Sci. Technol.* **2018**, *12*, 196–198, 201, 204. [CrossRef]
- Ren, W.J.; Ying, Z.; Ge, H.; Yu, H.C.; Hua, Z.C. Numerical simulation on reasonable balance between different gasdrainage methods and spontaneous combustion in gob area. *J. Saf. Sci. Technol.* **2015**, *11*, 26–32.
- Guangjian, S.; Yang, Z.; Zhe, L.; Fangtian, W. Gas Prevention in Upper Corner by Shallow Source High-level Drilling and Intubation Drainage. *Coal Technol.* **2022**, *41*, 112–117. [CrossRef]
- Haiguang, L. Study on Gas Control Technology of Slicing Mining Technology in Fully Mechanized Face of Yuecheng Coal Mine. *Coal Technol.* **2022**, *41*, 163–165. [CrossRef]
- Bo, C.M.; Shuai, L. Study on technology of pressure relief gas control in mining of protective layers in close coal seam groups. *Coal Sci. Technol. Mag.* **2023**, *44*, 162–166. [CrossRef]
- Ding, X.; Yang, Z. Knowledge mapping of platform research: A visual analysis using VOSviewer and CiteSpace. *Electron. Commer. Res.* **2022**, *22*, 787–809. [CrossRef]
- Liu, H.; Hong, R.; Xiang, C.L.; Lv, C.; Li, H.H. Visualization and analysis of mapping knowledge domains for spontaneous combustion studies. *Fuel* **2020**, *262*, 13. [CrossRef]
- Qiu, H.H.; Liu, L.G. A Study on the Evolution of Carbon Capture and Storage Technology Based on Knowledge Mapping. *Energies* **2018**, *11*, 25. [CrossRef]
- van Eck, N.J.; Waltman, L. Software survey: VOSviewer, a computer program for bibliometric mapping. *Scientometrics* **2010**, *84*, 523–538. [CrossRef]
- Yue, T.; Liu, H.W.; Long, R.Y.; Chen, H.; Gan, X.; Liu, J.L. Research trends and hotspots related to global carbon footprint based on bibliometric analysis: 2007–2018. *Environ. Sci. Pollut. Res.* **2020**, *27*, 17671–17691. [CrossRef]
- Wang, F.R.; Tan, B.; Chen, Y.; Fang, X.Y.; Jia, G.W.; Wang, H.Y.; Cheng, G.; Shao, Z.Z. A visual knowledge map analysis of mine fire research based on CiteSpace. *Environ. Sci. Pollut. Res.* **2022**, *29*, 77609–77624. [CrossRef]
- Shao, X.H.; Zhang, X.R.; Wang, W.C. Comparison of density functional theory and molecular simulation methods for pore size distribution of mesoporous materials. *Acta Phys.-Chim. Sin.* **2003**, *19*, 538–542. [CrossRef]
- Dong, S.N.; Zheng, L.W.; Tang, S.L.; Shi, P.Z. A Scientometric Analysis of Trends in Coal Mine Water Inrush Prevention and Control for the Period 2000–2019. *Mine Water Environ.* **2020**, *39*, 3–12. [CrossRef]

29. Xu, C.; Yang, T.; Wang, K.; Ma, S.H.; Su, M.Q.; Zhou, A.T. Research on the evolution law of hot spots in the field of coal seam hydraulic fracturing based on bibliometric analysis: Review from a new scientific perspective. *Environ. Sci. Pollut. Res.* **2023**, *30*, 86618–86631. [CrossRef]
30. Xu, C.; Yang, T.; Wang, K.; Guo, L.; Li, X.M. Knowledge domain and hotspot trends in coal and gas outburst: A scientometric review based on CiteSpace analysis. *Environ. Sci. Pollut. Res.* **2023**, *30*, 29086–29099. [CrossRef]
31. Zhao, Y.X.; Liu, S.M.; Elsworth, D.; Jiang, Y.D.; Zhu, J. Pore Structure Characterization of Coal by Synchrotron Small-Angle X-ray Scattering and Transmission Electron Microscopy. *Energy Fuels* **2014**, *28*, 3704–3711. [CrossRef]
32. Di, Y.Y.; Wang, E.Y.; Huang, T. Identification method for microseismic, acoustic emission and electromagnetic radiation interference signals of rock burst based on deep neural networks. *Int. J. Rock Mech. Min. Sci.* **2023**, *170*, 17. [CrossRef]
33. Hu, S.B.; Wang, X.F.; Wang, E.Y. Experimental study of true triaxial high pressure subcritical water impact fracturing. *Sci. Rep.* **2024**, *14*, 15. [CrossRef]
34. Li, Z.H.; Shan, T.C.; Wang, E.Y.; Niu, Y.; Wang, X.R.; Zhang, X.; Jia, H.S.; Chen, D.; Yin, S.; Sun, W.C. Experimental study on response and precursor of pressure stimulated currents of combined coal-rock under cycling stress. *Int. J. Rock Mech. Min. Sci.* **2024**, *177*, 16. [CrossRef]
35. Liu, H.; Wang, E.Y. Influence of functional groups on the microporous development and CO<sub>2</sub>-CH<sub>4</sub> adsorption: A molecular simulation investigation. *Energy Explor. Exploit.* **2024**, *42*, 1344–1358. [CrossRef]
36. Liu, Q.L.; Li, Z.H.; Wang, E.Y.; Feng, X.J.; Kong, X.G.; Wang, D.M. Synchronous Inversion of Coal Seam Gas Pressure and Permeability Based on a Dual Porosity/Dual Permeability Model and Surrogate Optimization Algorithm. *Nat. Resour. Res.* **2023**, *32*, 2115–2136. [CrossRef]
37. Liu, Q.L.; Li, Z.H.; Wang, E.Y.; Kong, X.G.; Feng, X.J.; Liu, Y.B.; Wang, D.M.; Zhang, C.L. A New Method for Determining Coal Seam Permeability based on a Gas-Solid Coupling Model and PSO plus LM Hybrid Optimization Algorithm. *Nat. Resour. Res.* **2023**, *32*, 1265–1282. [CrossRef]
38. Liu, Y.B.; Wang, E.Y.; Jiang, C.B.; Zhang, D.M.; Li, M.H.; Yu, B.C.; Zhao, D. True Triaxial Experimental Study of Anisotropic Mechanical Behavior and Permeability Evolution of Initially Fractured Coal. *Nat. Resour. Res.* **2023**, *32*, 567–585. [CrossRef]
39. Liu, Y.B.; Wang, E.Y.; Li, M.H.; Song, Z.L.; Zhang, L.; Zhao, D. Mechanical response and gas flow characteristics of pre-drilled coal subjected to true triaxial stresses. *Gas Sci. Eng.* **2023**, *111*, 12. [CrossRef]
40. Niu, Y.; Wang, E.Y.; Li, Z.H.; Gao, F.; Zhang, Z.Z.; Li, B.L.; Zhang, X. Identification of Coal and Gas Outburst-Hazardous Zones by Electric Potential Inversion During Mining Process in Deep Coal Seam. *Rock Mech. Rock Eng.* **2022**, *55*, 3439–3450. [CrossRef]
41. Ou, J.C.; Wang, E.Y.; Li, Z.H.; Li, N.; Liu, H.; Wang, X.Y. Study on the Evolutionary Characteristics of Acoustic-Magnetic-Electric Signals in the Entire Process of Coal and Gas Outburst. *Sustainability* **2023**, *15*, 16. [CrossRef]
42. Wang, X.F.; Hu, S.B.; Wang, E.Y. Experimental Research and Fractal Analysis of Supercritical CO<sub>2</sub> Pneumatic Fracturing under True Triaxial Stress. *Energy Fuels* **2023**, *37*, 12113–12122. [CrossRef]
43. Zhang, C.; Wang, P.; Wang, E.; Chen, D.; Li, C. Characteristics of coal resources in China and statistical analysis and preventive measures for coal mine accidents. *Int. J. Coal Sci. Technol.* **2023**, *10*, 22. [CrossRef]
44. Zhang, C.L.; Wang, Y.B.; Wang, E.Y.; Zhou, X.F.; Wang, P.Z.; Zeng, W. Influence of coal seam gas pressure on the propagation mechanism of outburst two-phase flow in visual roadway. *Fuel* **2022**, *322*, 11. [CrossRef]
45. Zhang, G.R.; Wang, E.Y. Risk identification for coal and gas outburst in underground coal mines: A critical review and future directions. *Gas Sci. Eng.* **2023**, *118*, 19. [CrossRef]
46. Zhang, G.R.; Wang, E.Y.; Ou, J.C.; Li, Z.H. Regional Prediction of Coal and Gas Outburst Under Uncertain Conditions Based on the Spatial Distribution of Risk Index. *Nat. Resour. Res.* **2022**, *31*, 3319–3339. [CrossRef]
47. Zhao, E.L.; Wang, E.Y.; Chen, H.P. Experiments on the Coal Measures Sandstone's Dynamic Mechanical Parameter Characteristics under the Combined Action of Temperature and Dynamic Load. *Appl. Sci.* **2023**, *13*, 21. [CrossRef]
48. Du, F.; Wang, K.; Guo, Y.Y.; Wang, G.D.; Wang, L.; Wang, Y.H. The mechanism of rockburst-outburst coupling disaster considering the coal-rock combination: An experiment study. *Geomech. Eng.* **2020**, *22*, 255–264. [CrossRef]
49. Guo, H.J.; Tang, H.L.; Wu, Y.C.; Wang, K.; Xu, C. Gas seepage in underground coal seams: Application of the equivalent scale of coal matrix-fracture structures in coal permeability measurements. *Fuel* **2021**, *288*, 9. [CrossRef]
50. Guo, H.J.; Wang, K.; Cheng, Y.P.; Yuan, L.; Xu, C. Model development and analysis of coal permeability based on the equivalent characteristics of dual-porosity structure. *J. Geophys. Eng.* **2020**, *17*, 313–327. [CrossRef]
51. Pan, J.N.; Wang, H.C.; Wang, K.; Niu, Q.H. Relationship of fractures in coal with lithotype and thickness of coal lithotype. *Geomech. Eng.* **2014**, *6*, 613–624. [CrossRef]
52. Sun, X.Y.; Liu, K.; Jin, T.X.; Wang, K.; Lin, S.R.; Pang, J.W.; Xie, J.L. Dynamic mechanical response and failure characteristics of coal and rock under saltwater immersion conditions. *Sci. Rep.* **2024**, *14*, 24. [CrossRef]
53. Wang, K.; Du, F.; Zhang, X.; Wang, L.; Xin, C.P. Mechanical properties and permeability evolution in gas-bearing coal-rock combination body under triaxial conditions. *Environ. Earth Sci.* **2017**, *76*, 19. [CrossRef]
54. Wang, K.; Fu, Q.; Xu, C.; Zhao, C.Y.; Zhao, W.; Yang, T. Influence of Coal Pillars on the Stress and Permeability of Mining-Disturbed Coal Seams for CBM Drainage. *Min. Metall. Explor.* **2022**, *39*, 2449–2459. [CrossRef]
55. Wang, K.; Zhou, A.T.; Zhang, J.F.; Zhang, P. Real-time numerical simulations and experimental research for the propagation characteristics of shock waves and gas flow during coal and gas outburst. *Saf. Sci.* **2012**, *50*, 835–841. [CrossRef]

56. Xu, C.; Yang, G.; Wang, K.; Fu, Q. Uneven stress and permeability variation of mining-disturbed coal seam for targeted CBM drainage: A case study in Baode coal mine, eastern Ordos Basin, China. *Fuel* **2021**, *289*, 10. [CrossRef]
57. Yan, Z.M.; Wang, K.; Zang, J.; Wang, C.; Liu, A. Anisotropic coal permeability and its stress sensitivity. *Int. J. Min. Sci. Technol.* **2019**, *29*, 507–511. [CrossRef]
58. Zhao, W.; Zhao, D.; Wang, K.; Fan, L.; Zhao, Z.H.; Dong, H.Z.; Shu, L.Y. Will greenhouse gas emissions increase with mining depth in coal mines? An analysis of gas occurrence under varying in-situ stress conditions. *Sci. Total Environ.* **2024**, *945*, 11. [CrossRef] [PubMed]
59. Zhou, A.T.; Wang, K.; Fan, L.P.; Tao, B. Propagation characteristics of pulverized coal and gas two-phase flow during an outburst. *PLoS ONE* **2017**, *12*, 13. [CrossRef] [PubMed]
60. Cheng, Y.P.; Wang, L.; Zhang, X.L. Environmental impact of coal mine methane emissions and responding strategies in China. *Int. J. Greenh. Gas Control* **2011**, *5*, 157–166. [CrossRef]
61. Jin, K.; Cheng, Y.P.; Wang, W.; Liu, H.B.; Liu, Z.D.; Zhang, H. Evaluation of the remote lower protective seam mining for coal mine gas control: A typical case study from the Zhuxianzhuang Coal Mine, Huaibei Coalfield, China. *J. Nat. Gas Sci. Eng.* **2016**, *33*, 44–55. [CrossRef]
62. Karacan, C.; Ruiz, F.A.; Cotè, M.; Phipps, S. Coal mine methane: A review of capture and utilization practices with benefits to mining safety and to greenhouse gas reduction. *Int. J. Coal Geol.* **2011**, *86*, 121–156. [CrossRef]
63. Liu, H.B.; Cheng, Y.P. The elimination of coal and gas outburst disasters by long distance lower protective seam mining combined with stress-relief gas extraction in the Huaibei coal mine area. *J. Nat. Gas Sci. Eng.* **2015**, *27*, 346–353. [CrossRef]
64. Wang, H.F.; Cheng, Y.P.; Yuan, L. Gas outburst disasters and the mining technology of key protective seam in coal seam group in the Huainan coalfield. *Nat. Hazards* **2013**, *67*, 763–782. [CrossRef]
65. Wang, L.; Lu, Z.; Chen, D.P.; Liu, Q.Q.; Chu, P.; Shu, L.Y.; Ullah, B.; Wen, Z.J. Safe strategy for coal and gas outburst prevention in deep-and-thick coal seams using a soft rock protective layer mining. *Saf. Sci.* **2020**, *129*, 12. [CrossRef]
66. Yin, W.T.; Fu, G.; Yang, C.; Jiang, Z.G.; Zhu, K.; Gao, Y. Fatal gas explosion accidents on Chinese coal mines and the characteristics of unsafe behaviors: 2000–2014. *Saf. Sci.* **2017**, *92*, 173–179. [CrossRef]
67. Zou, Q.L.; Lin, B.Q.; Zheng, C.S.; Hao, Z.Y.; Zhai, C.; Liu, T.; Liang, J.Y.; Yan, F.Z.; Yang, W.; Zhu, C.J. Novel integrated techniques of drilling-slotting-separation-sealing for enhanced coal bed methane recovery in underground coal mines. *J. Nat. Gas Sci. Eng.* **2015**, *26*, 960–973. [CrossRef]
68. Yuan, L. Control of coal and gas outbursts in Huainan mines in China: A review. *J. Rock Mech Geotech* **2016**, *8*, 559–567. [CrossRef]
69. Black, D.J. Review of coal and gas outburst in Australian underground coal mines. *Int. J. Min. Sci. Technol.* **2019**, *29*, 815–824. [CrossRef]
70. Bing, L.; Peng, Y.X.; Wei, S. Seepage coupling model of in-seam gas extraction and its applications. *J. China Univ. Min. Technol.* **2014**, *43*, 208–213. [CrossRef]
71. Kuroiwa, T.; Tashiro, T. Experimental Study on Coal Pulverization and Gas Emission in a Moment of Outbursts of Gas and Coal. *J. Min. Metall. Inst. Jpn.* **1960**, *76*, 227–232.
72. Alekseev, A.D.; Nedodayev, N.V.; Starikov, G.P. Destruction of coal saturated with gas under triaxial stress field on destressing: Modeling of outbursts of coal and gas. *Inst. Probl. Mekhaniki AN USSR (Preprint)* **1980**, *139*, 30.
73. Beamish, B.; Crosdale, P.J. Instantaneous outbursts in underground coal mines: An overview and association with coal type. *Int. J. Coal Geol.* **1998**, *35*, 27–55. [CrossRef]
74. Paterson, L. A model for outbursts in coal. *Int. J. Rock Mech. Min. Sci. Geomech. Abstr.* **2008**, *23*, 327–332. [CrossRef]
75. Ectors, P.; Zahn, D. Sudden outbursts of coal and gas: Vibrations wave processes in the strata (in Russian): Osipov, S N Ugol Ukrainy, V21, N9, Sept 1977, P37–40. *Int. J. Rock Mech. Min. Sci. Geomech. Abstr.* **2013**, *15*, 9219–9222.
76. Sato, K.; Fujii, Y. Source mechanism of a large scale gas outburst at Sunagawa Coal Mine in Japan. *Pageoph* **1988**, *129*, 325–343. [CrossRef]
77. Hanes, J.; Lama, R.D.; Shepherd, J. Research Into The Phenomenon Of Outbursts Of Coal And Gas In Some Australian Collieries. In Proceedings of the 5th ISRM Congress, Melbourne, Australia, 10–15 April 1983.
78. Shepherd, J.; Rixon, L.K.; Griffiths, L. Outbursts and geological structures in coal mines: A review. *Int. J. Rock Mech. Min. Sci. Geomech. Abstr.* **1981**, *18*, 267–283. [CrossRef]
79. Wold, M.B.; Connell, L.D.; Choi, S.K. The Role of Spatial Variability in Coal Seam Parameters on Gas Outburst Behaviour During Coal Mining. *Int. J. Coal Geol.* **2008**, *75*, 1–14. [CrossRef]
80. Frodsham, K.; Gayer, R.A. The impact of tectonic deformation upon coal seams in the South Wales coalfield, UK. *Int. J. Coal Geol.* **1999**, *38*, 297–332. [CrossRef]
81. Lei, D.; Li, C.; Zhang, Z.; Zhang, Y. Coal and gas outburst mechanism of the “Three Soft” coal seam in western Henan. *Min. Sci. Technol.* **2010**, *20*, 712–717. [CrossRef]

**Disclaimer/Publisher’s Note:** The statements, opinions and data contained in all publications are solely those of the individual author(s) and contributor(s) and not of MDPI and/or the editor(s). MDPI and/or the editor(s) disclaim responsibility for any injury to people or property resulting from any ideas, methods, instructions or products referred to in the content.

## Article

# Study on Permeability Enhancement of Seepage–Damage Coupling Model of Gas-Bearing Coal by Water Injection

Wenbin Wu <sup>1,2</sup>, Zhen Wang <sup>2,\*</sup>, Zhuangzhuang Yao <sup>2,3,\*</sup>, Jianyun Qin <sup>4</sup> and Xinglan Yu <sup>1</sup>

<sup>1</sup> College of Energy and Mining Engineering, Shandong University of Science and Technology, Qingdao 266590, China; cqwenbinwu@163.com (W.W.); 202182010061@sdust.edu.cn (X.Y.)

<sup>2</sup> China Coal Technology Engineering Group, Chongqing Research Institute, Chongqing 400037, China

<sup>3</sup> China Coal Technology Engineering Group, Chinese Institute of Coal Science, Beijing 100013, China

<sup>4</sup> Kuche Yushuling Coal Mine Co., Ltd., Kuche 842099, China; qzzin@163.com

\* Correspondence: cumtwangzhen@126.com (Z.W.); 17300238664@163.com (Z.Y.)

**Abstract:** The use of high-pressure water injection technology in gas-bearing coal seams is an important method for effectively addressing coalbed methane issues. To explore the mechanisms and influencing factors of water injection and permeability enhancement, a model was established based on the theories of unstable seepage and elastic damage in coal and rock mass. Additionally, a mechanical model of elastic damage-based beams was established, taking into account rheological damage, and the mechanical property variation of the surrounding rock in the working face was analyzed. The study included numerical simulations and verification with practical examples. The results suggested that high-pressure water injection could cause damage to the coal body and deformation of the roof, resulting in changes in ground stress, which was a significant contributor to the increase in coal seam permeability. The study showed positive correlations between rheological effects, injection time, injection flow rate, coal seam depth, and the influence range of water injection. Case studies indicated that the long-term influence range of water injection was approximately 60 m, which aligned with field results. The paper introduces a mechanical model for calculating variations in ground stress. This model can help assess the impact of water injection and permeability enhancement, providing valuable insights for related engineering projects.

**Keywords:** water injection; elastic foundation beam; time-variant damage; coupled damage model; coal seam permeability

**Citation:** Wu, W.; Wang, Z.; Yao, Z.; Qin, J.; Yu, X. Study on Permeability Enhancement of Seepage–Damage Coupling Model of Gas-Bearing Coal by Water Injection. *Processes* **2024**, *12*, 1899. <https://doi.org/10.3390/pr12091899>

Academic Editor: Carlos Sierra Fernández

Received: 17 July 2024

Revised: 25 August 2024

Accepted: 3 September 2024

Published: 4 September 2024



**Copyright:** © 2024 by the authors. Licensee MDPI, Basel, Switzerland. This article is an open access article distributed under the terms and conditions of the Creative Commons Attribution (CC BY) license (<https://creativecommons.org/licenses/by/4.0/>).

## 1. Introduction

The geological conditions of coal seams in some regions of China are very complex, characterized by soft structures, high gas content, and low permeability [1,2]. Less than 30% of coal seams have a permeability greater than  $1.0 \times 10^{-3} \mu\text{m}^2$ , and in high-gas mines, 95% of the coal seams are classified as having low permeability [3]. In recent years, due to the increase in mining depth, the occurrence conditions of coal seams have also changed, such as increased gas content, elevated gas pressure, and decreased permeability of surrounding rock. Gas disasters have gradually become one of the main factors restricting the safe and efficient mining of high-gas outburst mines. It is crucial to enhance traditional gas extraction methods to improve efficiency [4,5]. Improving the permeability of coal seams is a key measure in boosting gas extraction efficiency [6]. Therefore, to enhance the permeability of coal seams, their structure must be reformed. High-pressure water injection into coal seams is an effective way to increase the permeability of coal rock mass and to facilitate regional gas control [7–9]. In recent years, many scholars have conducted in-depth research on the seepage of coal seam water injection through theoretical calculations, experimental research, numerical simulations, and other means, achieving numerous results [10–14].

Hydraulic fracturing technology originated from the development methods for enhancing low-permeability oil and gas reservoirs. Since oil and gas reservoirs consist mainly

of sandstone and other hard rock formations, hydraulic fracturing technology has led to a relatively advanced understanding of crack initiation mechanisms, crack propagation processes, and related technologies. Zhen [15] employed a radial seepage experiment system to measure the permeability of raw coal samples and subsequently numerically simulated the stress–seepage evolution patterns within the coal matrix surrounding water injection boreholes. Fu et al. [16], using a self-developed numerical program specifically designed to model the coupling between rock fracture processes and fluid flow, captured the evolution of rock cracks during seepage-induced damage. Based on the Drucker–Prager criterion, statistical strength theory, and continuous damage medium theory, Wang [17] derived the rock damage evolution equation and developed a numerical simulation program for seepage in damaged rock, utilizing the finite element software COMSOL (latest v. 6.2) and MATLAB for computational analysis. Chen et al. [18] conducted a thorough permeability test to study the evolution of damage and permeability characteristics of rock under confining pressure. They employed continuum damage mechanics theory, coupled with plastic damage evolution and seepage effects. Researchers have analyzed damage evolution and permeability, but their analyses were not based on multi-level coupled damage, and there is relatively little research about water injection scenarios. Jia et al. [19] explored the damage evolution and seepage behavior of surrounding rock during tunnel excavation, considering the combined influence of pore water pressure and damage. Wang et al. [20] used the finite difference method and discrete element method, and constructed a fluid–solid coupling model to analyze the deformation and failure patterns of coal around boreholes as well as the seepage behavior during coal seam water injection under varying lateral pressure coefficients. They used the fluid–solid coupling model to analyze seepage behavior. However, factors such as permeability and initial and rheological damage in the coal seam can all affect the results, so a comprehensive analysis is necessary.

Compared with hard oil and gas reservoirs, the mechanisms and corresponding technology of high-pressure water injection and permeability increase in coal seams, especially soft-permeability coal seams, are different [21]. Liang proposed a nonlinear pore elastic damage model considering anisotropic characteristics [22]. The fully coupled finite element method was utilized to calculate and analyze the multi-phase coupling effect of gas, liquid, and solid during the coal seam water injection process, yielding favorable results. Zhou et al. [23], combined with fractal theory, studied the pore characteristics and seepage evolution process of coal in the process of water injection by nuclear magnetic resonance, and analyzed the influence of pore connectivity and water injection pressure change on the effect of coal seam water injection. Liu et al. [24] conducted a simulation to study the impact of coal seam water injection on pressure relief and permeability enhancement on the actual working face. The study was based on porous media seepage theory and its influencing factors.

When studying the issue of water injection in coal seams and increased permeability, scholars did not consider the effects of rheological damage, as well as the deformation of the coal seam and overlying strata, on the permeability of the coal seam. In light of this, this paper establishes a mechanical model of the foundation beam to analyze the influence of roof deformation on coal permeability. By establishing coupled damage evolution equations, a comprehensive analysis is conducted on the effects of initial damage, seepage damage, and rheological damage during the water injection process. The mechanism and external influencing factors of high-pressure water injection on coal permeability are studied, and the model and calculation results are verified through practical engineering applications.

## 2. Establishment of a Theoretical Model of Coal Seam Water Injection

### 2.1. Establishment of Coupled Damage Constitutive Model

It was assumed that the strength of rock micro-elements obeys Weibull distribution [25]; as such, the expression of foundation damage variable  $D_0$  can be obtained:

$$D_0 = 1 - e^{-\frac{1}{m} \left( \frac{\epsilon_0}{\epsilon_c} \right)^m} \quad (1)$$

where  $m$  and  $a$  are Weibull distribution parameters, and  $\epsilon_0$  is the strain of the basic damage state.

Xu H. [26] conducted a uniaxial compression creep test on soft rock, and obtained the relationship between the rheological damage variable  $D_1$  of rock with time:

$$D_1 = \frac{E_0 - E_\infty}{E_0} (1 - e^{-\alpha_1 t_0}) \tag{2}$$

where  $E_\infty$  is the final elastic modulus of rock mass, MPa;  $\alpha_1$  is the elastic modulus attenuation parameter,  $d^{-1}$ ; and  $t_0$  is the rheological time, d.

Considering the rheological damage under the premise of basic damage of rock, according to the strain equivalent hypothesis of Lemaitre [27] and the principle of continuous damage mechanics, the coupled damage constitutive model of rock can be obtained:

$$\sigma = E\epsilon(1 - D_0)(1 - D_1) = E\epsilon(1 - D) \tag{3}$$

where  $\sigma$  is the stress in the coupled damage state MPa;  $E$  is the elastic modulus of rock material before damage, MPa; and  $\epsilon$  is the strain in the coupled damage state.

Then, the coupling damage variable is expressed as

$$D = D_0 + D_1 - D_0D_1 \tag{4}$$

After the failure of the loaded rock, its strength does not immediately change to 0, but there is residual strength generated by friction. In the Lemaitre strain equivalence hypothesis, the residual strength is considered to modify Equation (3) [28] and the damage threshold of rock material [29]. The constitutive model of rock damage considering the damage threshold and residual strength can be obtained as follows:

$$\sigma = \begin{cases} E\epsilon & \epsilon - \epsilon_a \leq 0 \\ E\epsilon(1 - D) + \sigma_r D & \epsilon - \epsilon_a > 0 \end{cases} \tag{5}$$

where  $\sigma_r$  is the residual strength, MPa, and  $\epsilon_a$  is the damage strain threshold.

### 2.2. Establishment of Mechanical Model of Elastic Damage Foundation Beam

During the process of water injection, the coal seam surrounding the borehole undergoes damage, leading to a redistribution of the surrounding stress. For the sake of research convenience, based on the theory of elastic foundation beams, the basic roof is considered as a rock beam of unit width, while the coal seam and the immediate roof are regarded as the foundation. Subsequently, the mechanical model of the foundation beam is established. As shown in Figure 1, the model uses a single width of the main roof and coal seam. The main roof has a vertical downward uniform load  $q$ ;  $q$  is taken as the weight of the overlying strata, and  $p(x)$  is the basic reaction force. The foundation beam model is symmetrical around the borehole water injection hole, so half of it is taken as the research object for analysis.

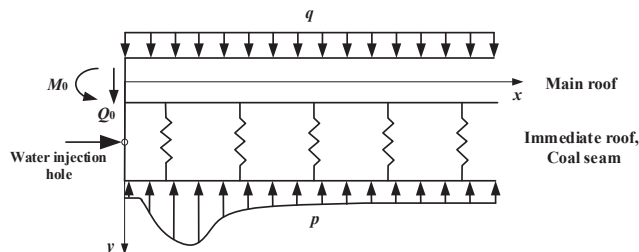


Figure 1. Schematic diagram of the mechanical model of the elastic foundation beam.

Based on the theory of beams, the differential equation of the deflection curve of the beam on any foundation is

$$E_r I \frac{d^4 y}{dx^4} = q - p \quad (6)$$

where  $E_r$  is the elastic modulus under plane strain conditions, MPa;  $E_r = E'_r / (1 - \nu_r^2)$ ,  $E'_r$  is the elastic modulus of the main roof, MPa;  $\nu_r$  is the Poisson's ratio of the main roof;  $I$  is a moment of inertia,  $m^4$ ;  $y$  is the deflection of the main roof, m;  $p(x)$  is the foundation reaction force, MPa;  $q$  is the uniformly distributed overlying strata load acting on the rocking beam,  $q = \gamma H$ , MPa;  $\gamma$  is the average volume force of the overlying strata,  $kN/m^3$ ; and  $H$  is the buried depth of the coal seam, m.

Taking into account the damage sustained by the coal mass, the foundation reaction force will undergo changes. Consequently, the foundation beam ceases to satisfy the original equation, necessitating the establishment of a new differential equation for the deflection curve for pertinent analysis. It is assumed that the deformation of the coal seam along the  $y$ -axis direction is uniform, that is,  $\varepsilon_y = y/m_0$ , where  $m_0$  denotes the thickness of the coal seam, and the foundation support reaction force  $p$  on the coal seam surface is approximately regarded as the vertical stress in the  $y$ -axis direction of the coal. The damage constitutive equation is shown in Formula (5). Combined with Formula (6), the differential equation of the deflection curve of the elastic damaged foundation beam considering the threshold and residual strength can be deduced as follows:

$$\frac{d^4 y}{dx^4} + \frac{k_1}{E_r I} y = \frac{\gamma H}{E_r I}, \quad y - y_a \leq 0 \quad (7)$$

$$\frac{d^4 y}{dx^4} + \frac{k_1}{E_r I} y(1 - D) + \frac{\sigma_r}{E_r I} D = \frac{\gamma H}{E_r I}, \quad y - y_a > 0 \quad (8)$$

where  $k_1 = E_b / m_0$ , with  $E_b$  representing the elastic modulus under plane strain condition, MPa;  $E_b = E'_b / (1 - \nu_b^2)$ , with  $E'_b$  representing the elastic modulus of the foundation, MPa; and  $\nu_b$  is the Poisson's ratio of the foundation.

### 2.3. Establishment of Seepage–Damage Model of Coal Seam Water Injection

Due to the limitation of upper and lower coal rock, models are usually simplified as a plane strain problem in the process of solving the stress field formed by seepage around the borehole [30]. Therefore, at the end of coal seam water injection, the solution process of the stress field formed by the unstable seepage around the borehole is simplified as a plane strain problem.

#### (1) Theoretical analysis of unstable seepage

Percolation differential equation:

$$\frac{\partial^2 P}{\partial r^2} + \frac{1}{r} \cdot \frac{\partial P}{\partial r} = \frac{\phi \mu C_t}{K} \cdot \frac{\partial P}{\partial t} \quad (9)$$

Initial condition, when  $t = 0$ :

$$P(r, 0) = P_0 \quad (10)$$

The boundary (inner boundary) condition at  $r = a$ :

$$r \frac{\partial P}{\partial r} \Big|_{r=a} = \frac{Q \mu}{2 \pi K h} \quad (11)$$

Boundary (outer boundary) conditions at infinitely large strata:

$$\lim_{r \rightarrow \infty} P(r, t) = P_0 \quad (12)$$

where ( $r$ ) is the distance from the center of the borehole, m; ( $t$ ) is seepage time, h; ( $P$ ) is pore water pressure, MPa; ( $P_0$ ) is the initial pore water pressure, MPa; ( $Q$ ) is flow rate,  $\text{m}^3/\text{h}$ ; ( $K$ ) is coal seam permeability,  $\mu\text{m}^2$ ; ( $h$ ) is the thickness of coal seam, m; ( $\mu$ ) is fluid viscosity, Pa·s; ( $a$ ) is the borehole radius, m; ( $C_t$ ) is the compression coefficient,  $\text{MPa}^{-1}$ ; and ( $\phi$ ) is the porosity of coal seam.

Effective stress field distribution and stress boundary conditions formed by seepage action:

$$\frac{d\sigma'_r}{dr} + \frac{\sigma'_r - \sigma'_\theta}{r} + \alpha \frac{dP}{dr} = 0 \quad (13)$$

$$\begin{cases} \sigma'_r = P_w - \alpha P_w & r = a \\ \sigma'_r = P_0 - \alpha P_0 & r = c \end{cases} \quad (14)$$

where  $\sigma'_r$  is the effective radial stress, MPa;  $\sigma'_\theta$  is the effective circumferential stress, MPa;  $c$  is the outer radius, m;  $\theta$  is the angle; and  $P_w$  is the inner boundary water pressure of the borehole, MPa.

## (2) The influence of stress on seepage

Based on Biot's effective stress, in the elastic stage, the larger the effective stress, the smaller the porosity of the rock [31]. The permeability changes with the porosity and has a cubic relationship with the porosity [32]. The relationship is

$$\bar{\sigma}_v = (\sigma'_r + \sigma'_\theta + \sigma'_z) - \alpha P \quad (15)$$

$$\phi = (\phi_0 - \phi_r) \cdot e^{-\alpha_\phi \bar{\sigma}_v} + \phi_r \quad (16)$$

$$K = K_0(\phi/\phi_0)^3 \quad (17)$$

where  $\bar{\sigma}_v$  is the average effective stress, MPa;  $\phi_0$  and  $\phi_r$  are the initial porosity under a 0 stress state and the ultimate porosity under a high-pressure state, respectively;  $\alpha_\phi$  is the sensitivity coefficient of porosity to stress,  $\text{Pa}^{-1}$ , which, here, is  $5.0 \times 10^{-8} \text{ Pa}^{-1}$ ; and  $K_0$  represents the initial permeability of the medium under a 0 stress state,  $\mu\text{m}^2$ .

## (3) Effect of damage on permeability

The permeability model is a constitutive equation that describes the flow of water through a rock mass. The model includes a damage variable, which accounts for changes in rock permeability when the rock is damaged by fluid intrusion. The relationship can be expressed as

$$K_D = K_0(\phi/\phi_0)^3 \cdot e^{\alpha_k D_2} \quad (18)$$

where  $K_D$  is the permeability after damage,  $\mu\text{m}^2$ ;  $D_2$  is the seepage damage variable caused by seepage; and  $\alpha_k$  is the influence coefficient of damage on permeability, which, here, is 5.0.

From the initial damage variable expression (1), the expression of the seepage damage variable is

$$D_2 = 1 - e^{-\frac{1}{m} \left( \frac{\bar{\varepsilon}_2}{\varepsilon_c} \right)^m} \quad (19)$$

where  $\bar{\varepsilon}_2$  is the equivalent strain.

For in-plane strain problems,

$$\bar{\varepsilon}_2 = \frac{\sqrt{2}}{3} \sqrt{(\varepsilon_r - \varepsilon_\theta)^2 + \varepsilon_r^2 + \varepsilon_\theta^2} \quad (20)$$



### 3. Analysis of Initial Damage and Influencing Factors of Surrounding Rock of Coal Seam Water Injection Hole

During the initial stage of injecting water into the coal seam, drilling boreholes and injecting high-pressure water causes changes in the stress of the surrounding rock which in turn affects the permeability of the rock. The stress and seepage fields are both important in the mechanical environment of the surrounding rock of water injection boreholes, and they influence each other. As a result of this process, coal and rock inevitably undergo damage, leading to a damaged area with reduced mechanical properties. Therefore, it is vital to analyze the evolution of damage and stress distribution in the surrounding rock after drilling and seepage to assess rock stability.

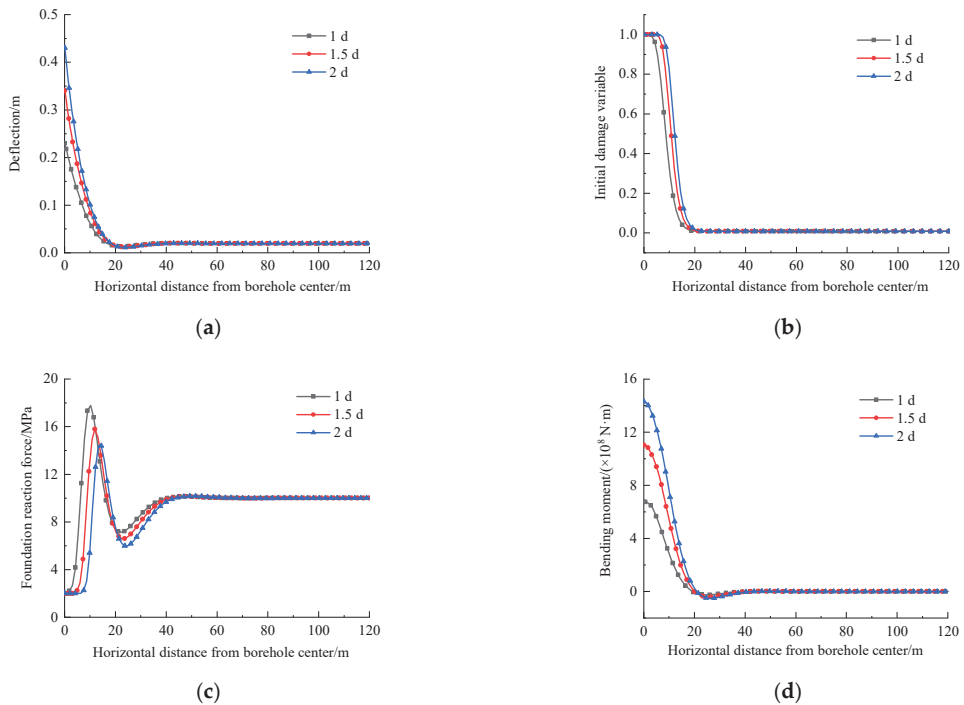
The basic mechanical parameters required for calculation are shown in Table 1. The data in Table 1 are from the technical service report of Hemei No.6 Coal Mine. The data in Table 1 are substituted into the mechanical model of an elastic damage foundation beam, considering the foundation damage and seepage damage generated in the process of coal seam water injection, and the total damage variable formed by the combination of the two is defined as the initial damage. The deflection curve of the coal seam roof is numerically calculated using Matlab to solve the differential equation. On this basis, the coal seam reaction force and the initial damage are further obtained to reveal the variation law of the permeability of the coal seam, as well as the variation law of the bending moment of the roof, and the influence of the roof deformation on the permeability enhancement effect of the coal seam water injection is studied. The influence of water injection time, water injection flow rate, and buried depth of coal seam on the deflection, initial damage, foundation reaction force, and bending moment curve of the foundation beam is analyzed under the condition that other parameters remain unchanged.

**Table 1.** Basic mechanical parameters.

Parameter Name	Unit	Numerical Value
Initial pore water pressure ( $P_0$ )	MPa	2
Gas pressure ( $P_s$ )	MPa	1
Flow rate ( $Q$ )	m <sup>3</sup> /h	8
Water injection time ( $t$ )	d	2
Initial permeability ( $K_0$ )	μm <sup>2</sup>	$3.7 \times 10^{-5}$
Thickness of stratum ( $h$ )	m	10
Fluid viscosity ( $\mu$ )	Pa·s	$1 \times 10^{-3}$
Coefficient of compressibility ( $C_t$ )	MPa <sup>-1</sup>	0.06
Original porosity ( $\phi_0$ )		0.039
Ultimate porosity ( $\phi_r$ )		0.009
Radius of drill hole ( $a$ )	m	0.05
Poisson ratio ( $\nu$ )		0.5
Average volume force of overlying strata ( $\gamma$ )	kN/m <sup>3</sup>	25
Burial depth of coal seam ( $H$ )	m	400
Rock beam stiffness ( $E_r I$ )	N·m <sup>2</sup>	0.5
Coal seam thickness ( $m_0$ )	m	3
Plane strain elastic modulus of coal seam ( $E_b$ )	GPa	1.5
Peak stress ( $\sigma_c$ )	MPa	20.91
Peak strain ( $\epsilon_c$ )		0.207
Residual strength ( $\sigma_r$ )	MPa	2

#### 3.1. The Influence of Different Water Injection Time

In the case of other parameters being unchanged, the influence of the change in water injection time on the deflection, initial damage, foundation reaction force, and bending moment of the foundation beam is shown in Figure 2.



**Figure 2.** Effect of different water injection time on damaged foundation beam. (a) Deflection. (b) Initial damage variable. (c) Foundation reaction force. (d) Bending moment.

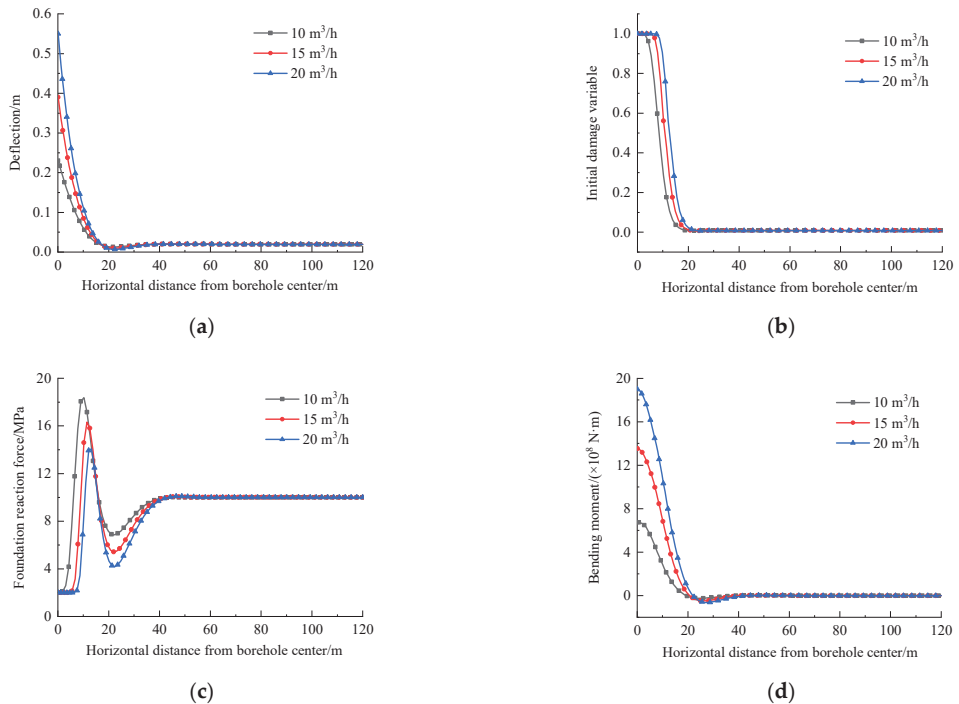
From Figure 2, it is evident that the deflection and bending moments of the basic roof reach their maximum values at the top of the borehole. As the water injection time increases, both the deflection and bending moments of the basic roof exhibit an increase within a specific horizontal distance from the borehole center. Furthermore, with prolonged water injection, the extent of damage expands under the same degree of damage, and the initial damage intensifies at the same horizontal distance from the borehole center. At water injection times of 1 day, 1.5 days, and 2 days, the peak values of the basic reaction force are, respectively, 17.78 MPa, 15.78 MPa, and 14.43 MPa, with peak positions at 10.3 m, 12 m, and 13.3 m. Notably, as the time for water injection increases, the maximum value of the basic reaction force decreases, and the position of this maximum gradually shifts away from the borehole. The influence ranges of the foundation reaction force are 34 m, 36 m, and 39 m, respectively, indicating an expansion of the influence range with increased water injection time. This suggests that continuous water injection enables water to reach positions further away from the injection hole, thereby enhancing the influence range of water injection and permeability.

### 3.2. The Influence of Different Water Injection Flow

Under the condition that other parameters remain unchanged, the influence of the change in water injection flow on the deflection, initial damage, foundation reaction force, and bending moment of the foundation beam is shown in Figure 3.

It is evident from Figure 3 that the maximum deflection and bending moments of the main roof occur at the top of the borehole. As the water injection flow increases, there is a corresponding increase in the deflection and bending moments of the main roof within a specific range of horizontal distance from the borehole center. Additionally, the range of damage and initial damage also increase proportionally with the distance from the borehole center. When the water injection flow rates are  $10 \text{ m}^3/\text{h}$ ,  $15 \text{ m}^3/\text{h}$ , and  $20 \text{ m}^3/\text{h}$ , the peak

values of the basic reaction force are 18.36 MPa, 16.33 MPa, and 14.08 MPa, respectively, with peak positions at 10.3 m, 11.4 m, and 13.3 m. As the water injection flow rate increases, the maximum value of the basic reaction force decreases, and the maximum position gradually moves away from the borehole. The influence range of the foundation reaction force is 35 m, 37 m, and 38.5 m, respectively, and is also increasing. It is evident that the influence range of water injection also increases with the water injection flow rate.



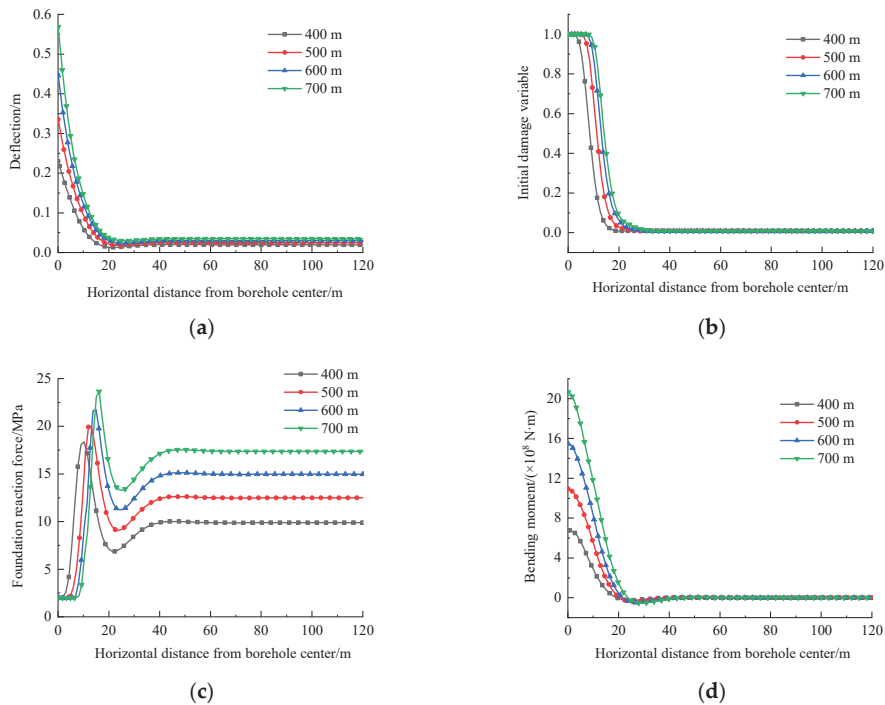
**Figure 3.** Effect of different water injection flow on damaged foundation beam. (a) Deflection. (b) Initial damage variable. (c) Foundation reaction force. (d) Bending moment.

### 3.3. The Influence of Different Coal Seam Buried Depth

Under the condition that all other parameters remain constant, Figure 4 illustrates how changes in coal seam depth affect the deflection, initial damage, foundation reaction force, and bending moment of the foundation beam.

As seen in Figure 4, the deflection and bending moments of the primary roof are greatest at the top of the borehole. The greater the burial depth is, the larger the maximum bending moment is. The deflection of the beam at the borehole and away from the center of the borehole also increases. That is to say, when the burial depth of the coal seam increases, the relative deformation also increases, which is relatively close to the engineering practice. When the burial depths are 400 m, 500 m, 600 m, and 700 m, the peak values of the foundation reaction force are 18.36 MPa, 19.9 MPa, 21.74 MPa, and 23.64 MPa, and the peak positions are 10.3 m, 12 m, 15 m, and 16.2 m, respectively. As the buried depth increases, the maximum value of the foundation reaction force also increases, and the position of this maximum value moves farther away from the borehole. It is important to remember that before reaching the maximum value of the foundation reaction force, a greater depth of burial results in a smaller force. The range of influence of the foundation reaction force is 35 m, 36 m, 36.8 m, and 38 m, respectively. With an increase in buried depth, the influence range of the foundation reaction force also expands. It is clear that as the depth of the buried

coal seam increases, the area of influence of water injection and permeability enhancement also expands.



**Figure 4.** The influence of different buried depth of coal seam on damaged foundation beam. (a) Deflection. (b) Initial damage variable. (c) Foundation reaction force. (d) Bending moment.

#### 4. Study on the Influence Scope of Water Injection for Enhancing Permeability in Coal Seams

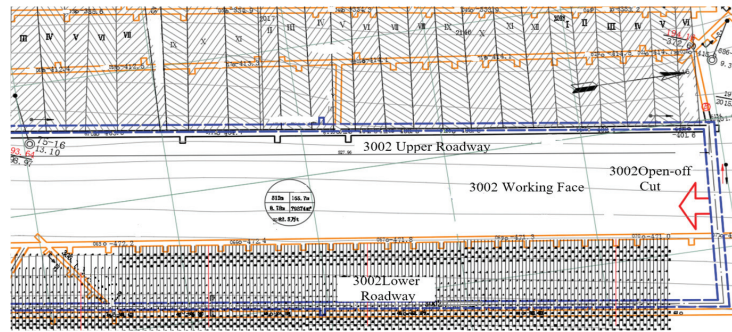
Improving the permeability of a coal seam is essential for enhancing the efficiency of gas extraction. However, this water injection process can lead to initial damage near the borehole and subsequent rheological damage over time. These types of damage can alter the stress and permeability of the coal. For example, in December 2011, Hemei No. 6 Coal Mine carried out multiple water injections to increase the permeability of the 3002 lower heading face of the II1 coal seam, leading to a coal and gas outburst in June 2021. However, the mine did not investigate the extent of its influence. Therefore, it is necessary to determine the range and degree of initial and rheological damage of the coal based on relevant theories.

##### 4.1. Project

To enhance the permeability of the II1 coal seam in Hemei No.6 Coal Mine, water injection was performed in the lower section of the mine, specifically targeting the 3002 working face. This working face is situated within the 30 mining area of the third level of the mine. It is bordered by 585 North Lane and an unmined area to the east, the goaf of the 2146 working face to the west, solid coal to the south, and the three-level boundary return air lane (north) and another unmined area to the north. The coal seam in the working face is stable and the structure is simple. The buried depth of the coal seam is 130~950 m, the average thickness of the coal seam is 7.48 m, the dip angle of the coal seam is 10~30°, and the average dip angle is 20°. The pseudo-roof of II1 coal is not developed, and the immediate roof is grayish-brown sandy mudstone, mainly quartz feldspar, with an average

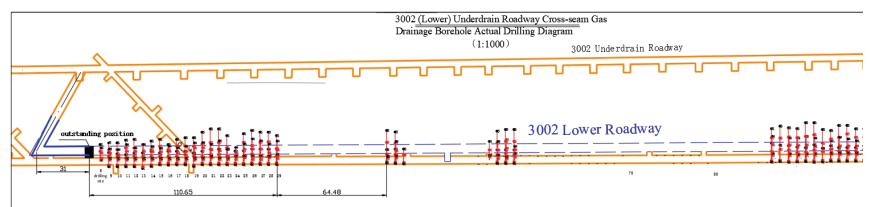
thickness of 3.90 m. The main roof consists of grayish-brown medium-grained sandstone, primarily composed of quartz feldspar. It has a thickness ranging from 4.80 m to 13.3 m, with an average thickness of 6.95 m.

The drilling parameters are designed according to the geological conditions. The borehole diameter is 94 mm, the sealing length is 12–20 m, and the drilling is based on a 0.5 m coal seam. Among them, 3002 bottom pumping lane 1~30 # drilling field drilling is designed, 31~37 # drilling field drilling is designed, 58~80 # drilling field drilling is designed, and 81~110 # drilling field drilling is designed; the drilling hole of 8~36 # drilling field in 3002 bottom drainage roadway is designed, the drilling hole of 37~59 # drilling field is designed, and the drilling hole of 60~89 # drilling field is designed. The specific layout is shown in Figure 5.



**Figure 5.** General map of regional outburst prevention measures in 3002 working face.

To further improve the extraction effect, two rounds of crosslayer boreholes were designed for the 3002 lower crossheading in No.6 Coal Mine of Hemei Coal Industry Co., Ltd., Weinan, Shannxi, and hydraulic punching and anti-reflection measures were taken in each round of construction. The first round of supplementary drilling is shown in Figure 6. A total of 101 groups of drilling fields are designed for the construction of a 3002 bottom drainage roadway. The spacing of the drilling fields is 5 m. There are 5 boreholes in each drilling field, with a total of 505 boreholes, and the boreholes penetrate the coal seam to reach 0.5 m. The construction of this round of boreholes commenced in March 2021. By 3 June 2021, a total of 203 boreholes with a sealing length of 12–20 m were completed.



**Figure 6.** Construction plan of the first round of supplementary drilling.

For the construction of the second round of supplementary drilling for the lower bottom drainage roadway, 101 drilling fields were designed with a spacing of 5 m. Each drilling field consisted of 3 boreholes, totaling 303 boreholes. The boreholes penetrated the coal seam to a depth of 0.5 m from the top, and the sealing length ranged from 12 to 20 m.

#### 4.2. Long-Term Influence Scope of Water Injection for Enhancing Permeability

(1) The influence range of water injection in the initial stage of increasing permeability

The basic mechanical parameters of the 3002 working face in Hemei No.6 Coal Mine are shown in Table 2.

**Table 2.** Basic mechanical parameters of 3002 working face.

Parameter Name	Unit	Numerical Value
Initial pore water pressure ( $P_0$ )	MPa	2
Gas pressure ( $P_g$ )	MPa	1.2
Flow rate ( $Q$ )	m <sup>3</sup> /h	12
Water injection time ( $t$ )	d	2
Initial permeability ( $K_0$ )	μm <sup>2</sup>	$3.7 \times 10^{-5}$
Thickness of stratum ( $h$ )	m	10
Fluid viscosity ( $\mu$ )	Pa·s	$1 \times 10^{-3}$
Coefficient of compressibility ( $C_t$ )	MPa <sup>-1</sup>	0.06
Original porosity ( $\phi_0$ )		0.039
Ultimate porosity ( $\phi_r$ )		0.009
Radius of drill hole ( $a$ )	m	0.047
Poisson ratio ( $\nu$ )		0.5
Average volume force of overlying strata ( $\gamma$ )	kN/m <sup>3</sup>	25
Burial depth of coal seam ( $H$ )	m	700
Rock beam stiffness ( $E_r I$ )	N·m <sup>2</sup>	0.5
Coal seam thickness ( $m_0$ )	m	10
Plane strain elastic modulus of coal seam ( $E_b$ )	GPa	1.5
Peak stress ( $\sigma_c$ )	MPa	20.91
Peak strain ( $\epsilon_c$ )		0.207
Residual strength ( $\sigma_r$ )	MPa	2
Elastic modulus attenuation parameter ( $\alpha_1$ )		0.1

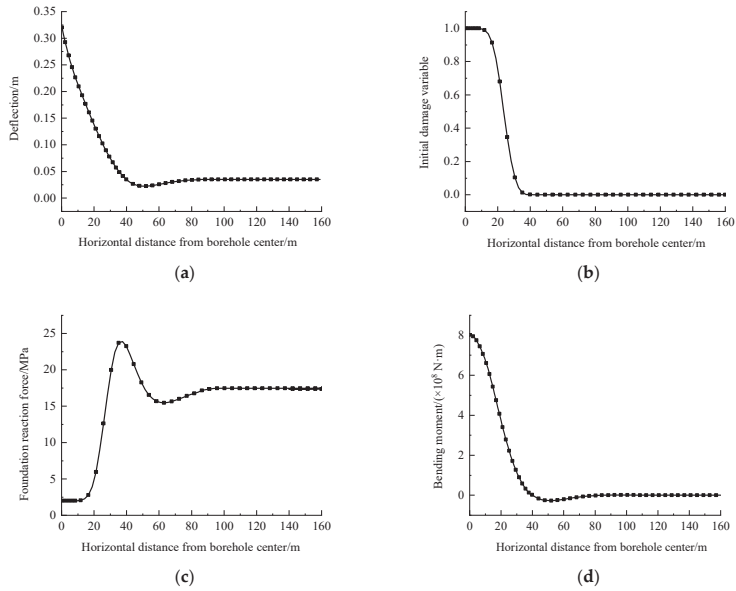
The data from Table 2 are substituted into the established mechanical model of the elastic damage foundation beam. Together with the initial damage evolution equation derived after coal seam water injection, the differential equation of the deflection curve is numerically solved using Matlab, and the theoretical curve is plotted, as depicted in Figure 7. To investigate the impact of the initial damage induced by water injection on the deflection, foundation reaction force, and bending moment curve of the foundation beam under coal elasticity conditions, the initial influence range of water injection is determined.

Figure 7 reveals that when considering foundation damage caused by drilling excavation during water injection and seepage damage resulting from unstable seepage post-high-pressure water injection—collectively termed as the initial damage during water injection and infiltration—the application of the elastic damage foundation beam model reveals a complete damage zone proximate to the water injection hole, characterized by a damage variable of 1. In this area, the foundation reaction force remains constant despite any increase in deformation, indicating residual strength. This reaction force peaks within the damage zone. As the horizontal distance from the borehole center increases, the deflection and bending moments gradually decrease. In horizontal directions further from the borehole center, beam deflection stabilizes, indicating that coal deformation tends towards stability at low values, not reaching the deformation threshold for damage. In this state, the coal remains elastic, with a damage value of 0, and the foundation reaction force numerically equates to the overburden load. The damage influence range extends approximately 45 m from the center of the borehole horizontally, and there is minimal variation in these parameters beyond 45 m in the deep section. It can be seen that after considering the initial damage, the influence range of 3002 working faces in the initial stage of water injection is about 45 m.

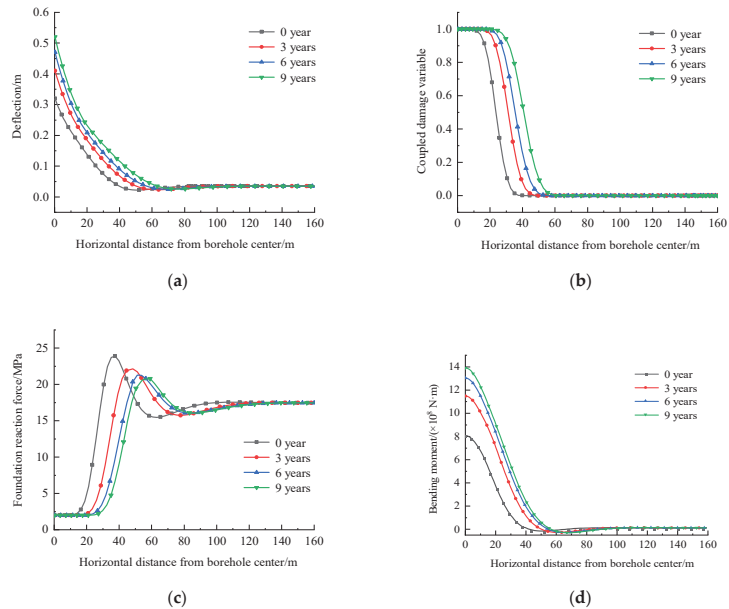
## (2) Long-term influence range of water injection for increasing permeability

The data in Table 2 are substituted into the established mechanical model of elastic damage foundation beam. The differential equation for the deflection curve is calculated using Matlab, taking into account the evolution equation of the total damage variable, including initial damage and rheological damage. The theoretical curve is then plotted as shown in Figure 8. This study investigates the impact of water injection on the deflection, foundation reaction force, and bending moment curve of the foundation beam over 9 years,

focusing on the influence of initial damage and later rheological damage caused by water injection to determine the long-term effects.



**Figure 7.** The influence of initial damage on the foundation beam at the initial stage of water injection and permeability enhancement. (a) Deflection. (b) Initial damage variable. (c) Foundation reaction force. (d) Bending moment.



**Figure 8.** Influence of long-term coupling damage of water injection and permeability enhancement on foundation beam. (a) Deflection. (b) Damage variable. (c) Foundation reaction force. (d) Bending moment.

Taking into account the initial damage to the coal seam caused by water injection and permeability enhancement, and considering the subsequent rheological damage, it can be inferred from Figure 8 that as rheological time increases, the deflection and bending moments of the foundation beam gradually escalates, particularly in the vicinity of the borehole. The basic reaction force exhibits significant variation, with its maximum position shifting deeper into the coal over time, and its influence range is expanding. With the prolongation of creep time, both the failure zone and the damage zone expand. Within the damage zone, at a constant horizontal distance from the borehole center, the severity of coal damage intensifies with the prolongation of creep time. In the engineering example presented in this paper, it is evident that after 9 years, the horizontal influence range of damage extends approximately 60 m from the borehole center, while the variations in these variables beyond the 60 m depth are minimal. This indicates that, after accounting for the coupling of initial and rheological damage, the long-term influence range of water injection and permeability enhancement in the 3002 working face is approximately 60 m.

#### 4.3. Mechanism Analysis of Coal Seam Water Injection Permeability Increasing

In the oil and gas industry, the main purpose of hydraulic fracturing technology is to produce penetrating cracks in relatively hard reservoirs, while in the coal industry, high-pressure water injection into soft low-permeability coal seams will lead to changes in the original equilibrium state of the coal within a certain range, resulting in damage and deformation of the coal seam roof, thereby changing the permeability of the coal seam. The drainage measures are adjusted based on the permeability of the coal seam and the gas occurrence. This includes drilling for further bottom drainage. It can be seen that when analyzing and studying the mechanism of coal seam water injection and permeability increase, the coupling effect of solid deformation of coal and roof and fluid flow must be considered to make the results conform to the engineering practice.

The coal damage caused by water injection in coal seam is composed of three parts. The first part is mainly seepage damage. In the process of water injection and pressure holding, the pore pressure changes, which causes the effective stress change in gas-bearing coal, and the erosion of the coal skeleton, resulting in the occurrence and development of pores and fissures, and the seepage damage of coal. The second part is the basic damage. After the drainage process at the end of the drainage, the stress state of the coal and rock mass changes again, and the roof of the coal seam sinks, resulting in the basic damage of the coal, and the permeability changes again. The third part is the rheological damage. For the coal seam that has not been mined for a long time after the drainage, the coal will be further damaged due to the rheology, resulting in the deformation of the coal seam and the roof. The closure and opening degree of pores and cracks in the coal seam also change, and the permeability of the coal seam further changes.

In the process of injecting water into coal seams to increase permeability, the area near the borehole where permeability increases can be called the effective range of permeability increase. The permeability of the area far away from the borehole remains unchanged. Between these two areas, due to roof subsidence and increased vertical stress on the coal seam, there is a transition area where permeability does not change much or may even decrease.

To prevent gas disasters and control gas occurrences, the spacing between boreholes should be arranged reasonably based on the coal seam's permeability and the state of gas occurrences. This is important when implementing drainage measures such as drilling further bottom drainage roadways in coal seams with water injection and permeability increase.

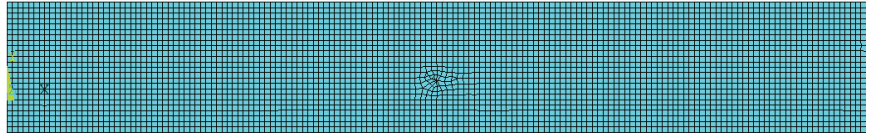
#### 4.4. Numerical Simulation of Influence Range of Water Injection Increasing Permeability

##### (1) Finite element model

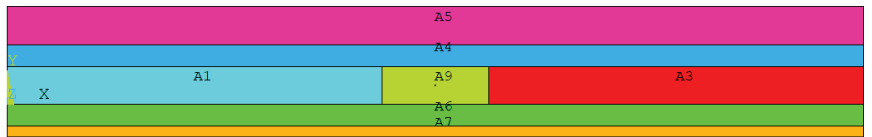
Considering the initial damage and rheological damage of the coal near the water injection hole in the III coal seam of Hemei No.6 Coal Mine, based on the basic mechanical parameters of the 3002 working face in Table 1, ANSYS software (latest v. R2) is used



to carry out numerical simulation, and the finite element model of the surrounding rock near the water injection hole in the gas-bearing coal seam is established, as shown in Figures 9 and 10. In Figure 10, A1, A3, and A9 are coal seams, A1 and A3 are elastic zones at the end of water injection, A9 is the damage zone at the end of water injection, A4 is the direct roof, A5 is the old roof, A6 is the direct bottom, and A7 is the old bottom.



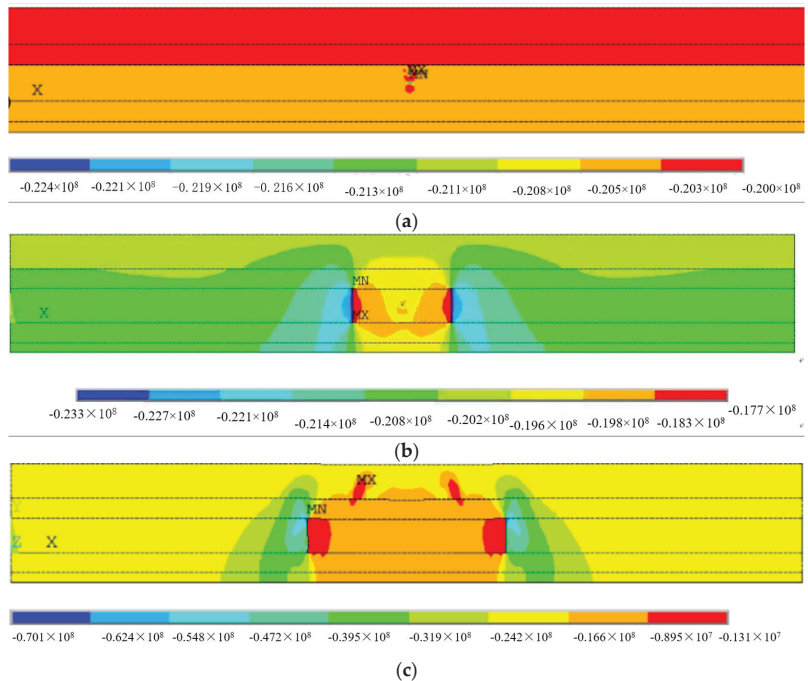
**Figure 9.** Mesh division of two-dimensional geometric model of initial and rheological damage of coal rock water injection and permeability increase.



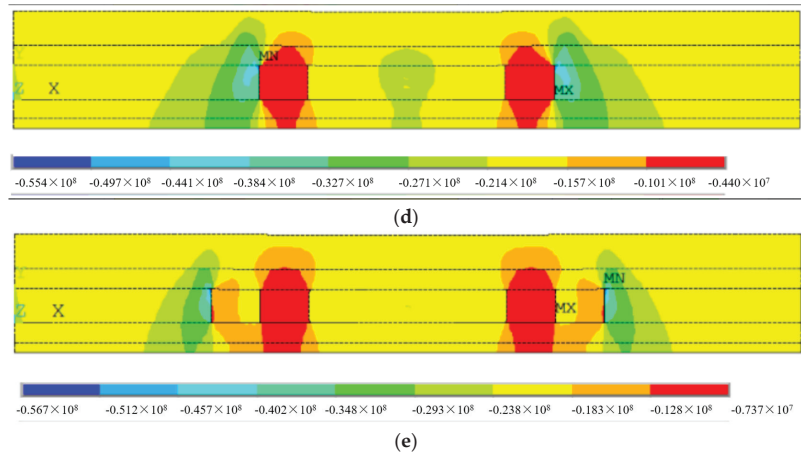
**Figure 10.** Two-dimensional geometric model of coal rock water injection permeability damage.

(2) Result analysis

The above finite element model is simulated and analyzed. The variation law of vertical stress in gas-bearing coal seams after considering initial damage and rheological damage is studied within 9 years, and the results are compared with those obtained by numerical calculation. The vertical stress program obtained by numerical simulation is shown in Figure 11.



**Figure 11.** Cont.



**Figure 11.** Model vertical stress cloud diagram. (a) Original rock stress state. (b) Under the action of initial damage. (c) Under the action of initial damage and rheological damage after 3 years. (d) Under the action of initial damage and rheological damage after 6 years. (e) Under the action of initial damage and rheological damage after 9 years.

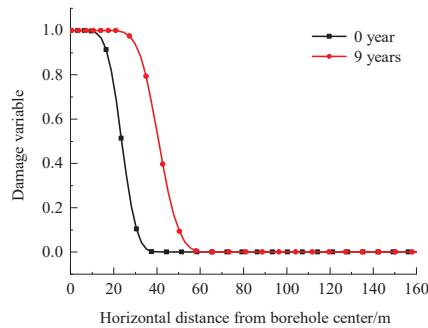
Examining the calculation results presented in Figure 11, it is evident that the vertical stress change area of the coal expands as rheological time progresses. Figure 11a illustrates that, before coal seam construction, the coal remains in its original rock stress state, with no alteration in vertical stress. Conversely, Figure 11b reveals that, following water injection, the vertical stress of the coal undergoes changes due to the coupling effect of seepage and damage. Even in the failure zone of the borehole's rock, residual strength still exists after failure. In the damage zone of the borehole surrounding rock, the vertical stress reaches the maximum near the borehole due to the influence of stress concentration. With the increase in distance from the center of the borehole, the vertical stress gradually decreases. In the elastic zone of the surrounding rock of the borehole, the vertical stress gradually decreases to the original rock stress with the increase in the distance from the center of the borehole. It can be seen from Figure 11c–e that after considering the rheological damage, the overall change trend in the vertical stress is the same as that when only the initial damage is considered, and it finally tends to the original ground stress. With the extension of time, the distance between the peak position of vertical stress and the drilling hole increases, and the influence range increases.

From the analysis above, we observe that injecting water into the coal seam causes seepage, leading to changes in the mechanical state and properties of the coal rock. At the same time, the seepage–damage coupling effect changes the vertical stress distribution. After considering the rheological damage, with the continuation of time, the stress concentration area shifts to the deep part of the coal seam, and the influence range of water injection and permeability increase gradually increases. It can be seen that the vertical stress variation law obtained by numerical simulation under the coupling action of initial and rheological damage of coal and rock water injection is consistent with the variation law of basic reaction force obtained by numerical calculation under the coupling action of initial and rheological damage of coal and rock water injection. The numerical calculation and numerical simulation results are compared and verified with each other.

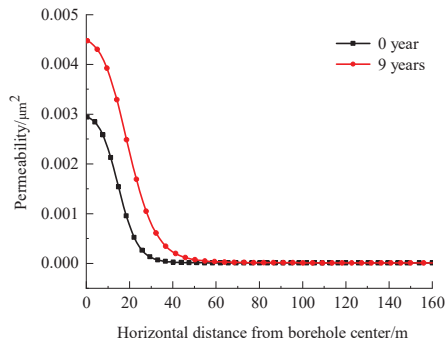
#### 4.5. The Gas Parameter Test and Effect Analysis of the III Coal Seam in the Affected Area of Water Injection and Permeability Increase

Based on the above research results, according to Equation (18), Matlab software (2017) is used for numerical calculation, and the coal seam damage distribution map and permeability distribution map of the 3002 working face of Hemei No.6 Coal Mine at the

initial stage of water injection and the 9th year of rheology are obtained, as shown in Figures 12 and 13.



**Figure 12.** The damage distribution map of a coal seam in the initial stage and the ninth year of rheology.



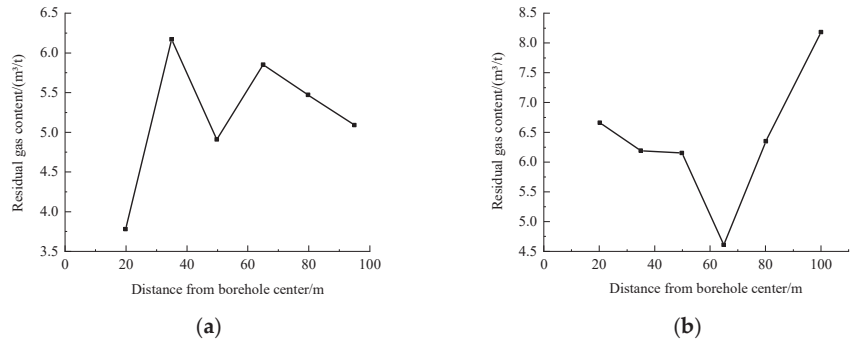
**Figure 13.** Initial and rheological ninth-year coal seam permeability distribution map.

It is evident from Figures 12 and 13 that the permeability of coal gradually increases with the rise in the damage variable. Additionally, the extent of permeability increase also grows gradually with increasing rheological time. Combined with Figures 7c and 8c, it can be found that in the process of coal seam water injection and permeability increase, the stress in the damaged area around the borehole is small and the permeability is large. Far away from the borehole, the coal seam is in an elastic state, the original rock stress state does not change, and the coal permeability is small; it can also be seen from the distribution law of permeability that the initial influence range of water injection and permeability increase in the 3002 working face is about 45 m, and the long-term influence range is about 60 m.

The gas parameters of the No.21 coal seam in the affected area of water injection and permeability increase in the 3002 working face were tested on site. Based on the relationship between coal permeability and damage, the effect of gas extraction was analyzed to verify the accuracy of the long-term influence range of coal seam water injection and permeability increase obtained by the above coupling damage foundation beam mechanical model. The gas parameter test of the III1 coal seam in the affected area of water injection and permeability increase in the 3002 working face is shown in Figure 14.

Meng [33] conducted an analysis of how coal permeability changes before and after water injection by examining the relationship between confining pressure, axial pressure, and permeability. However, the study did not take into account the impact of rheological damage. Figures 12 and 13 compare scenarios with and without rheological damage, demonstrating that coal seam damage expands over time, leading to changes in permeability. The study suggests that coal permeability during water injection is significantly

influenced by vertical stress. The established coupled damage evolution equation and foundation beam model enable a more accurate analysis of vertical stress in the surrounding rock, considering rheological effects. Figure 14 illustrates that the coal seam near the water injection borehole has high permeability, low residual gas content, and efficient gas extraction, while the original state area far from the borehole maintains low coal permeability and high gas content. The numerical simulation and calculation results align with the trend in residual gas content changes observed in field tests. These observations indicate that the stressed zone after water injection of the coal seam should be less than 65 m. The test conclusion supports the numerical calculation conclusion.



**Figure 14.** Gas parameter test. (a) Upper side of the water injection hole. (b) Lower side of the water injection hole.

## 5. Conclusions

- (1) The complexity of enhancing coal seam permeability through water injection involves intricate interactions between coal and the roof, as well as fluid flow. The coupling between rheological damage and permeation damage is evident in the fact that fluid permeation may accelerate the rheological process of the rock mass, increase the effective stress state within the rock mass, and subsequently affect its rheological properties. Additionally, the coupling between rheological damage and fracture damage is evident as micro-cracks within the rock mass gradually expand and connect during long-term rheological processes, providing more favorable conditions for external fracturing. Simultaneously, external fracturing may also accelerate the rheological damage process of the rock mass. To establish a connection between theoretical analysis and engineering practice, we thoroughly consider coal seepage damage, foundation damage, and rheological damage. By establishing a mechanical model of an elastic damage foundation beam that accounts for the deformation of both the coal seam and the roof, a theoretical foundation is provided for studying the effects of coal seam water injection and permeability enhancement.
- (2) Injecting high-pressure water into a coal seam causes varying degrees of deformation in the coal and the roof near the borehole, which in turn changes the permeability in those areas of the coal seam. The affected areas can be classified into three zones: the effective infiltration zone, the transition zone, and the original state zone. Research has given us insights into how the time of water injection, flow rate, and depth of the coal seam affect the deformation patterns of the roof rock and the effectiveness of water injection. When the water injection time, flow rate, and coal seam depth increase, the deflection and bending moments of the basic roof also increase within a certain horizontal distance from the borehole center. This causes the damage range within the coal seam to expand and the influence range of water injection and permeability to enlarge. Studies have shown that the model created in this paper can quantitatively analyze the deformation of the coal seam roof and the progression of coal seam damage

based on water injection time, flow rate, and coal seam depth, thereby determining the influence range of permeability in the coal seam.

To summarize, by calculating the variation patterns of mechanical properties of the coal seam and surrounding rock using the mechanical model established in this paper, the influence range of external factors on permeability can be determined, providing a theoretical basis for underground engineering.

- (3) Numerical simulation software was utilized to validate the results of numerical calculations. This provided the vertical stress distribution, taking into account initial damage and rheological damage in the coal near the water injection borehole. The variation pattern of vertical stress obtained from numerical simulation aligns with the variation pattern of basic reaction force derived from numerical calculations.
- (4) The long-term influence range of water injection and permeability increase in the 3002 working face of Hemei No.6 Coal Mine is 60 m. The conclusion of the field test of gas parameters of the III coal seam in the affected area is consistent with the conclusion of numerical calculation. Therefore, when studying the effect of water injection and permeability enhancement in gas-bearing coal seams, the influence of initial damage and rheological damage should be considered comprehensively.

**Author Contributions:** Conceptualization, W.W. and Z.W.; methodology, Z.Y. and J.Q.; software, W.W., Z.W. and X.Y.; validation, W.W.; investigation, W.W.; resources, W.W.; data curation, W.W. and Z.W.; writing—original draft preparation, J.Q.; writing—review and editing, W.W., Z.Y. and X.Y.; supervision, J.Q.; project administration, Z.Y. All authors have read and agreed to the published version of the manuscript.

**Funding:** 1. National Key R&D Program (2023YFC3009003), Sponsor: Wenbin Wu, Zhen Wang, Zhuangzhuang Yao; 2. Special project of scientific and technological innovation venture capital of Tiandi Science and Technology Co., Ltd. (2022-2-TD-ZD008), Sponsor: Wenbin Wu, Zhuangzhuang Yao; 3. The General Program of Natural Science Foundation of Chongqing—Study on the Migration and Distribution Patterns of Hydraulic Fracturing Proppant in Methane-Bearing Coal and Its Conduction Mechanism (2024NSCQ-MSX1046), Sponsor: Zhuangzhuang Yao, Wenbin Wu; 4. the Key Project of Science and Technology Innovation and Entrepreneurship Fund of Tiandi Technology Co., Ltd. (2023-2-TD-ZD001), Sponsor: Wenbin Wu.

**Data Availability Statement:** The original contributions presented in the study are included in the article; further inquiries can be directed to the corresponding authors.

**Conflicts of Interest:** Author Jianyun Qin was employed by the company Kuche Yushuling Coal Mine Co., Ltd. The remaining authors declare that the research was conducted in the absence of any commercial or financial relationships that could be construed as a potential conflict of interest.

## References

1. Kang, Y.S.; Sun, L.Z.; Zhang, B.; Gu, J.Y.; Mao, D.L. Discussion on classification of coalbed reservoir permeability in China. *J. China Coal Soc.* **2017**, *42*, 186–194.
2. Zhang, Q.; Feng, S.; Yang, X. Basic reservoir characteristics and development strategies of coalbed methane resource in China. *J. China Coal Soc.* **2001**, *26*, 230–235.
3. Wang, Y.G.; Li, H.Y.; Qi, Q.X.; Peng, Y.W.; Li, C.R.; Deng, Z.G. The evolution of permeability and gas extraction technology in mining coal seam. *J. China Coal Soc.* **2010**, *35*, 406–410.
4. Xia, B.W.; Liu, C.W.; Lu, Y.Y.; Liu, Y.; Ge, Z.L.; Tang, J.R. Experimental study of propagation of directional fracture with slotting hydraulic blasting. *J. China Coal Soc.* **2016**, *41*, 432–438.
5. Lu, Y.; Liu, Y.; Li, X.; Kang, Y. A new method of drilling a long borehole in low permeability coal by improving its permeability. *Int. J. Coal Geol.* **2010**, *84*, 94–102. [CrossRef]
6. Yuan, L.; Qin, Y.; Cheng, Y.P.; Meng, J.B.; Shen, J. Scenario prediction of medium-long-term extraction scale of coalbed methane mines in China. *J. China Coal Soc.* **2013**, *38*, 529–534.
7. Jiang, Z.A.; Wang, L.F.; Zhang, J.J.; Liu, Q.; Chen, J. Influence of coal water injection on pore and methane adsorption/ desorption properties of raw coal. *J. China Coal Soc.* **2018**, *43*, 2780–2788.
8. Xiangjun, C.; Yuanping, C.; Tao, H.; Xin, L.I. Water injection impact on gas diffusion characteristic of coal. *J. Min. Saf. Eng.* **2013**, *30*, 443–448.

9. Guo, H.; Su, X. Research on the mechanism of gas emission inhibition in water-flooding coal seam. *J. China Coal Soc.* **2010**, *35*, 928–931.
10. Yang, H.; Cheng, W.M.; Liu, Z.; Wang, W.Y.; Zhao, D.W.; Wang, W.D. Fractal characteristics of effective seepage channel structure of water infusion coal based on NMR experiment. *J. Rock Soil Mech.* **2020**, *41*, 1279–1286.
11. Zhang, K.; Guo, J.; Teng, T. Experimental study on water injection softening and seepage characteristics of weakly cemented sandy mudstone-Taking Shendong mining area as an example. *Coal Sci. Technol.* **2022**, *50*, 195–201.
12. Biot, C.; Glorian, G.; Maciejewski, L.A.; Brocard, J.S.; Domarle, O.; Blampain, G.; Millet, P.; Georges, A.J.; Abessolo, H.; Dive, D.; et al. Synthesis and antimalarial activity in vitro and in vivo of a new ferrocene-chloroquine analogue. *J. Med. Chem.* **1997**, *40*, 3715–3718. [CrossRef] [PubMed]
13. Witherspoon, P.A. Investigations at Berkeley on fracture flow in rocks: From the parallel plate model to chaotic systems. *Am. Geophys. Union Geophys. Monogr. Ser.* **2013**, *122*, 760293.
14. Junqing, M.; Baisheng, N. Study on water seepage law of raw coal during loading process. *Math. Comput. Appl.* **2015**, *20*, 217–227. [CrossRef]
15. Liu, Z.; Hu, P.; Yang, H.; Yang, W.; Gu, Q. Coupling Mechanism of Coal Body Stress-Seepage around a Water Injection Borehole. *Sustainability* **2022**, *14*, 9599. [CrossRef]
16. Fu, J.W.; Zhu, W.S.; Zhang, D.F.; Jia, C. Numerical study of the damage and progressive failure process of rocks under the effect of seepage. *Hydrogeol. Eng. Geol.* **2015**, *42*, 53–59.
17. Wang, Y.L.; Liu, Z.L.; Lin, S.C.; Zhuang, Z. Finite element analysis of seepage in rock based on continuum damage evolution. *Eng. Mech.* **2016**, *33*, 29–37.
18. Chen, L.; Liu, J.F.; Wang, C.P.; Liu, J.; Su, R.; Wang, J. investigation on damage evolution characteristic of granite under compressive stress condition and its impact on permeability. *Rock Mech. Eng.* **2014**, *33*, 287–295.
19. Shanpo, J. Hydro-Mechanical Coupled Creep Damage Constitutive Model of Boom Clay, Back Analysis of Model Parameters and Its Engineering Application. Ph.D. Thesis, Graduate Institute of Chinese Academy of Sciences, Wuhan Institute of Geotechnical Mechanics, Wuhan, China, 2009.
20. Taicheng, W.; Qingwang, L.; Yunxia, Q. Research on the influence of lateral pressure coefficient based on FDM-DEM on coal seam water injection drilling. *Min. Res. Dev.* **2024**, *44*, 105–113.
21. Huang, B.X.; Huang, C.M.; Cheng, Q.Y.; Huang, C.H.; Xue, W.C. Hydraulic fracturing theory and technology framework of coal and rock mass. *J. Min. Saf. Eng.* **2011**, *28*, 167–173.
22. Liang, Y.; Shi, B.; Yue, J.; Zhang, C.; Han, Q. Anisotropic Damage Mechanism of Coal Seam Water Injection with Multiphase Coupling. *ACS Omega* **2024**, *9*, 16400–16410. [CrossRef] [PubMed]
23. Zhou, H.; Liu, Z.; Sun, X.; Ren, W.; Zhong, J.; Zhao, J.; Xue, D. The evolution characteristics of seepage channels in deep coal during water injection. *J. China Coal Soc.* **2021**, *46*, 867–875.
24. Liu, Z.; Wang, W.D.; Xu, W.B.; Yang, H.; Dong, B. Permeability model of coal seam water injection and numerical simulation study of hydraulic coupling influencing factors. *J. Min. Saf. Eng.* **2021**, *38*, 1250–1258.
25. Chunan, T. *Catastrophes in the Process of Rock Fracture*; Coal Industry Publishing House: Beijing, China, 1993.
26. Hongfa, X. Time dependent behaviours of strength and elasticity modulus of weak rock. *Chin. J. Rock Mech. Eng.* **1997**, *16*, 246.
27. Lemaitre, J. How to use damage mechanics. *Nucl. Eng. Des.* **1984**, *80*, 233–245. [CrossRef]
28. Cao, W.G.; Zhao, H.; Li, X.; Zhang, L. A statistical damage simulation method for rock full deformation process with consideration of the deformation characteristics of residual strength phase. *China Civ. Eng. J.* **2012**, *45*, 139–145.
29. Zhou, Y.Q.; Sheng, Q.; Leng, X.L.; Fu, X.D.; Li, L.F. Statistical constitutive model of elastic damage for rock considering residual strength and threshold. *J. Chang. River Sci. Res. Inst.* **2016**, *33*, 48–53.
30. Oliaei, M.N.; Pak, A.; Soga, K. A coupled hydro-mechanical analysis for prediction of hydraulic fracture propagation in saturated porous media using EFG mesh-less method. *Comput. Geotech.* **2014**, *55*, 254–266. [CrossRef]
31. Rutqvist, J.; Tsang, C.F. A study of caprock hydromechanical changes associated with CO<sub>2</sub>-injection into a brine formation. *Environ. Geol.* **2002**, *42*, 296–305. [CrossRef]
32. Brace, W.F.; Walsh, J.B.; Frangos, W.T. Permeability of granite under high pressure. *J. Geophys. Res.* **1968**, *73*, 2225–2236. [CrossRef]
33. Zhaoping, M.E.G.; Lu, Y. Experimental study on stress-permeability of high rank coal samples before and after hydraulic fracturing. *Coal Sci. Technol.* **2023**, *51*, 353–360.

**Disclaimer/Publisher’s Note:** The statements, opinions and data contained in all publications are solely those of the individual author(s) and contributor(s) and not of MDPI and/or the editor(s). MDPI and/or the editor(s) disclaim responsibility for any injury to people or property resulting from any ideas, methods, instructions or products referred to in the content.

Article

# Research on Intelligent Design and Visualization of Gas Extraction Drilling Based on PSO–LSTM

Yongming Yin <sup>1,2</sup>, Dacang Wang <sup>2,\*</sup>, Quanjie Zhu <sup>3</sup>, Guangyu Yang <sup>4,5</sup>, Xuexi Chen <sup>6</sup>, Xiaohui Liu <sup>6</sup> and Yongfeng Liu <sup>7</sup><sup>1</sup> China Academy of Safety Science and Technology, Beijing 100012, China<sup>2</sup> Cathay Safety Technology Co., Ltd., Beijing 100012, China<sup>3</sup> School of Emergency Technology and Management, North China Institute of Science and Technology, Sanhe 065201, China<sup>4</sup> Coal Mining Research Institute Co., Ltd. of CCTEG, Beijing 100013, China<sup>5</sup> State Key Laboratory of Coal Mining and Clean Utilization, Beijing 100013, China<sup>6</sup> School of Safety Engineering, North China Institute of Science and Technology, Sanhe 065201, China<sup>7</sup> School of Resources and Safety Engineering, Chongqing University, Chongqing 400044, China

\* Correspondence: wdc15102587295@163.com

**Abstract:** Under the background of intelligent construction of coal mines, gas extraction design is still based on manual design, which is complex, time-consuming, and error-prone, and its automation degree needs to be improved. In order to solve this problem, taking the 1302 working face of a mine in Shanxi Province as the research object, this paper carried out relevant research. Firstly, the influencing factors of gas extraction were determined, and the influence rules of different parameters on the extraction effect were studied by numerical simulation. Secondly, an intelligent optimization method of gas extraction drilling parameters based on deep mining called the PSO–LSTM model, is proposed. This model uses the PSO algorithm to optimize the parameters of the LSTM model, so as to improve the accuracy of the LSTM model results. Finally, a quantitative expression algorithm of 3D spatial information of gas extraction drilling holes based on Python is proposed, which can automatically generate 3D spatial models of bedding or through gas extraction drilling holes using optimized drilling parameters and known 3D information of coal seams. This study shows that the results obtained using the PSO–LSTM model are the same as the drilling parameters obtained using numerical simulation, which verifies the accuracy of the PSO–LSTM model. According to the optimized drilling parameters, a 3D model of gas extraction drilling is quickly generated, which greatly reduces the tedious work of drawing construction drawings for coal mine enterprises and improves the intelligence level of coal gas extraction drilling.

**Keywords:** gas extraction; drilling parameter optimization; PSO–LSTM; 3D model; Python

**Citation:** Yin, Y.; Wang, D.; Zhu, Q.; Yang, G.; Chen, X.; Liu, X.; Liu, Y. Research on Intelligent Design and Visualization of Gas Extraction Drilling Based on PSO–LSTM. *Processes* **2024**, *12*, 1691. <https://doi.org/10.3390/pr12081691>

Academic Editor: Yuhe Wang

Received: 2 July 2024

Revised: 2 August 2024

Accepted: 10 August 2024

Published: 13 August 2024



**Copyright:** © 2024 by the authors. Licensee MDPI, Basel, Switzerland. This article is an open access article distributed under the terms and conditions of the Creative Commons Attribution (CC BY) license (<https://creativecommons.org/licenses/by/4.0/>).

## 1. Introduction

Coal mine gas extraction is a systematic engineering process that includes the design and construction of extraction drilling holes, coal seam anti-reflection, monitoring and testing, standard evaluation, and other links. The design of the drilling hole is the main basis of drilling construction. The scientific and rational design of the drilling holes directly affects the difficulty of drilling construction and the amount of engineering, as well as the later extraction efficiency. The design of extraction drilling must be considered from various factors. It is a complex decision-making process that is limited by various factors such as coal seam gas geological conditions, drilling construction environment, drilling machine drilling tool performance, and so on. It is necessary to balance various needs, such as gas extraction standards, drilling construction difficulty, and drilling amount, so that the drilling layout scheme can achieve the overall optimization state. At present, the design of coal mine gas extraction drilling is mainly based on manual work. In addition to the large

workload, which is time-consuming and laborious, there are also the following problems. First, the design basis of the drilling hole is unreasonable. In addition to the inaccurate knowledge of gas geological conditions, key parameters, such as the effective extraction radius of the drilling hole, are mainly obtained through experimental measurement or experience, which are static and inaccurate. When the extraction location is transferred, and the coal seam gas geological conditions change significantly, the drilling hole design cannot be effectively supported. Secondly, the borehole design is not fine enough, and the whole extraction area is designed according to the same conditions without fully considering the differences in coal seam gas geological conditions and the length of gas pre-extraction time at different locations in the region. This can easily cause the borehole arrangement to be too thin or too dense, resulting in poor extraction effect, substandard extraction, increased drilling projects, and shortage of mining replacement. Therefore, the development trend of gas extraction drilling intelligent design is to carry out research on gas extraction drilling intelligent design technology, realize the fine automatic design of drilling parameters, and make the drilling layout reasonably match the extraction conditions and demand.

In recent years, with people's attention to gas extraction, research in the field of gas extraction is also carried out continuously. The optimization design of gas extraction parameters includes a variety of methods. One is a field test and data analysis. Gas extraction tests with different technological parameters are carried out at the coal mine site [1–6]. The field test can directly reflect the gas extraction effect under actual production conditions and provide real and reliable data for the optimization of process parameters. The second is numerical simulation and simulation analysis. Numerical simulation software is used to simulate and analyze the gas extraction process, and its influence on the extraction effect is observed by changing different technological parameters (such as drilling hole layout, drilling spacing, drilling diameter, etc.) so as to determine the optimal parameter combination [7–12]. This method can intuitively show the gas flow law, provide a scientific basis for parameter optimization, and reduce the blindness and cost of the field test. The third is intelligent control to optimize technology, the application of sensors, data acquisition technology, cloud computing, and other advanced technologies, and the establishment of intelligent gas monitoring and control systems. Through real-time monitoring of the gas concentration and operation parameters of the extraction equipment, the extraction process parameters can be automatically adjusted to realize intelligent control [13–18]. Intelligent control can significantly improve the response speed and accuracy of gas extraction systems, reduce the risk of human error, and improve the safety and stability of the system. Later, different scholars carried out research on gas extraction from the aspects of pressure relief [19–21], blasting [22], hole sealing [23], etc., so as to optimize the drilling horizon and improve the gas extraction efficiency.

In addition, other predecessors have also made visual presentations on gas extraction research. Xu Xuezhao et al. [24] used 3D modeling software and numerical simulation software to simulate the high-efficiency gas extraction range and used 3D modeling software and numerical simulation software to carry out a three-dimensional visual simulation of the through-layer gas extraction process. In terms of 3D visualization, Zhang Jilin et al. [25] developed a 3D visualization analysis software system for coal mine drilling holes, which realized intelligent design, automatic mapping of gas extraction drilling holes, and display of drilling shapes in a 3D environment. However, this type of software does not have the ability to identify the hidden dangers of hole arrangement. Therefore, Fan Kai [26] established a three-dimensional effect display and analysis platform for gas extraction drilling holes and applied the system to Sihe Coal Mine, realizing the timely discovery and complete elimination of hidden dangers of hole arrangement. However, the above gas extraction visualization system is difficult to develop for low-level personnel and difficult to popularize. Based on this, Zhu Quanjie et al. [27] used Blender, Python, and other open-source programs to build a rapid generation platform for 3D mine models based on parametric modeling ideas. Easy to grassroots development again: Users only need to input key data information to realize the rapid generation of a tunnel 3D model.



In the context of smart coal mine construction, gas drainage, as a fundamental solution to coal mine gas disasters, will emerge as a pivotal technology for addressing the challenges of gas disaster prevention and control in deep mining, thereby enhancing safety standards for coal mine operations. It constitutes a vital component of smart coal mine development. At present, the intelligence level of coal gas drainage technology and equipment in China is still very low. Overall, it is in the initial stage, and there is an urgent need to integrate modern information technology into the field of coal gas drainage and gradually realize the information, automation, and intelligence of gas drainage. For the application scenarios of coal mine gas extraction borehole design, drainage system regulation and maintenance, and drainage standard evaluation, the technologies of mine big data, coal mine 5G, and artificial intelligence are fully adopted to break through the key technologies of dynamic transparent gas geology, drilling intelligent design, drainage pipe network autonomous regulation and fault diagnosis, and drainage standard intelligent evaluation. The development direction of intelligent gas extraction is to form intelligent equipment and systems with the ability of accurate perception, autonomous decision-making, and automatic adaptation, and realize less or even no human operation in the whole process of gas extraction. Because the design and layout of a gas extraction drilling field are affected by coal seam occurrence, geological anomalies (such as faults), gas content, engineering layout, and other factors, the design of a reasonable and effective gas extraction drilling hole directly affects the gas extraction effect. Conventionally, technicians design drilling parameters and carry out construction according to the requirements of the "Rules for the Prevention and Control of Coal and Gas Outburst" (2019 edition) and other requirements, combined with the actual situation of the mine. This process runs throughout the gas coal seam mining process; the workload is large, complex, and time-consuming. With the gradual advancement of intelligent construction in coal mines, automation and intelligent construction of gas extraction work are on the agenda, and the automatic design and three-dimensional display of gas extraction drilling will become an important research topic in this field.

Based on the development trend of gas extraction toward precision, efficiency, and intelligence, the key technologies of intelligent design and visual display of gas extraction drilling holes are proposed. The research contents include influencing factors of gas extraction, the intelligent calculation method of key parameters, visualization of optimized drilling parameters, etc. This research not only provides a new method for the intelligent design of gas extraction drilling and intelligent generation of construction three-dimensional drawings but also has a positive guiding role for parameter design and on-site construction in this field.

## 2. Analysis of Factors Affecting Gas Extraction

### 2.1. Analysis of Influencing Factors

The effective drainage radius is the key index for evaluating the gas drainage effect, which directly reflects the effective range of the gas drainage drilling hole. Clarifying the factors influencing the effective extraction radius is of great significance for optimizing the gas extraction process and improving the extraction efficiency, and can also provide a clear direction for numerical simulation research on gas extraction.

According to the radial flow field law of gas migration, the initial intensity expression of gas emission from the drilling hole is as follows [28]:

$$q_0 = 2\pi m\lambda \frac{p_o^2 - p_l^2}{R \ln \frac{r}{r_o}} \quad (1)$$

The borehole gas emission intensity at time  $t$  is expressed as follows [28]:

$$q = q_0 e^{-at} \quad (2)$$

At time  $t$ , the total amount of gas extracted from the borehole is as follows [28]:

$$Q = \int_0^t q dt = \int_0^t q_0 e^{-\alpha t} dt = \frac{2\pi m \lambda (p_0^2 - p_1^2) (1 - e^{-\alpha t})}{\alpha \ln \frac{R}{r_0}} \quad (3)$$

For the range where the length and width of the extraction area are  $a$  and  $b$  respectively, the gas extraction amount is [28]

$$Q_{\text{Extraction}} = \eta Q_{\text{All}} = \eta a b m \gamma W \quad (4)$$

The number of boreholes required to have an effective extraction radius  $R$  is [28]

$$N = \frac{a}{2R} \cdot \frac{b}{2R} = \frac{ab}{4R^2} \quad (5)$$

From  $Q_{\text{Extraction}} = N Q_{\text{All}}$ , we can obtain [28]

$$R^2 = \frac{\pi \lambda (p_0^2 - p_1^2) (1 - e^{-\alpha t})}{2\alpha \eta \gamma W \ln \frac{R}{r_0}} \quad (6)$$

where:  $\eta$  represents extraction efficiency, %;  $q_0$  is the initial intensity of gas emission from the borehole,  $\text{m}^3/(\text{min} \cdot \text{hm})$ ;  $\alpha$  represents the attenuation coefficient of borehole gas flow,  $\text{d}^{-1}$ ;  $R$  represents the effective influence radius of gas extraction,  $m$ ;  $\lambda$  represents the permeability coefficient of coal seam,  $\text{m}^2/(\text{MPa}^2 \cdot \text{d})$ ;  $p_0$  is the initial pressure of coal seam gas, MPa;  $p_1$  represents the gas pressure in the borehole, MPa;  $r_0$  represents the borehole diameter,  $m$ ;  $\gamma$  is the bulk density of coal,  $\text{t}/\text{m}^3$ ;  $W$  is the original gas content of coal seam,  $\text{m}^3/\text{t}$ ;  $m$  is the borehole length,  $m$ ;  $P_{\text{std}}$  is standard atmosphere, MPa.

Through the analysis of Formula (6), we can gain insight into several core elements that affect the effective radius of extraction. Among them, the most important factors are the diameter of the drilling hole, the permeability of the coal seam, the initial gas pressure, the negative pressure of extraction, and the duration of extraction, which show a significant positive correlation with the effective extraction radius, which reveals a close relationship between them.

In the stage of coal seam gas pre-extraction, the three variables of drilling diameter, extraction negative pressure, and extraction time can be effectively regulated in the industrial production process. Therefore, with the help of advanced numerical simulation software, we can simulate how these controllable factors affect the effective extraction radius, which provides us with a deeper understanding of the extraction process and supports the optimization of the process.

## 2.2. Mesh Model and Coal Seam Parameters

In the 1302 working face of a mine in Shanxi Province, 94 mm drilling holes are used for gas extraction, the spacing of drilling holes is 5 m, the single arrangement of holes, and the extraction time is 120 days. A two-dimensional model with a length of 50 m and width of 5 m (as shown in Figure 1) was constructed using numerical simulation software to observe the effects of different parameters on the effective extraction radius. The parameters of the coal seam are shown in Table 1.

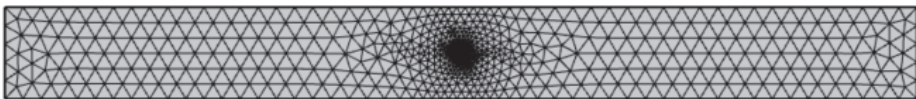


Figure 1. Single-hole extraction model grid.

**Table 1.** Parameter of coal seam.

Parameter	Parameter Value	Parameter	Parameter Value
Elastic modulus of coal	$2.415 \times 10^9$ Pa	Density of gas	$0.716 \text{ kg/m}^3$
Apparent density of coal	$1380 \text{ kg/m}^3$	Initial gas pressure	1.53 MPa
Moisture content	1.53%	Limit adsorption gas capacity	$15.53 \text{ m}^3/\text{t}$
Ash content	14.72%	Gas adsorption constant	$1.32 \text{ MPa}^{-1}$
Initial porosity	5.45%	Gas dynamic viscosity coefficient	$1.06 \times 10^{-5} \text{ Pa}\cdot\text{s}$
Initial permeability	$1.74 \times 10^{-16} \text{ m}^2$	Poisson's ratio	0.3

### 2.3. Influence of Different Parameters on Gas Extraction

In order to study the influence of different parameters on gas extraction, the following four groups of simulations were carried out:

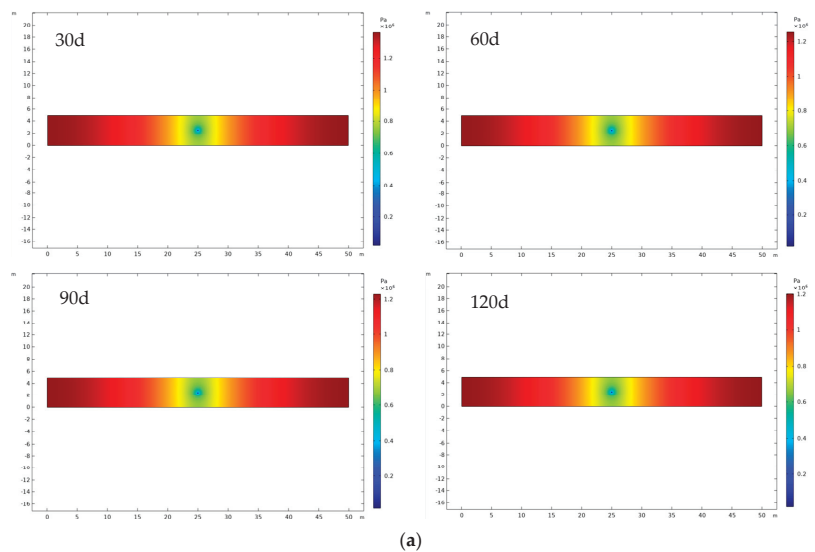
(1) In the actual gas extraction process, the gas extraction cycle is generally three to four months, so this paper takes 30 d, 60 d, 90 d, and 120 d as the extraction period to carry out numerical simulations to study the change in gas pressure.

(2) Boreholes with diameters of 75 mm, 94 mm, 133 mm, and 143 mm were used for numerical simulation, and the change in gas pressure was observed to study the relationship between borehole diameter and effective extraction radius.

(3) In order to study the relationship between the effective extraction radius and hole spacing, the gas pressure changes were simulated when the hole spacing was 2, 3, and 4 times the effective extraction radius.

(4) In order to explore the relationship between the negative drainage pressure and the effective drainage radius, the negative drainage pressures of 10 KPa, 20 KPa, 30 KPa, and 40 KPa were used for numerical simulation, and the gas pressure changes among them were observed.

The cloud diagram of the gas pressure variation under different parameters is shown in Figure 2, and the variation trend of the effective extraction radius under different parameters is shown in Figure 3. According to Figures 2 and 3, when other conditions remain unchanged, the effective extraction radius increases with the increase in extraction time, drilling diameter, and extraction negative pressure. In a certain range of content, the larger the drilling spacing, the larger the effective extraction range; however, beyond a certain range, the effective extraction range will not increase. According to the simulation results, the maximum drilling spacing is 6 m.

**Figure 2.** Cont.

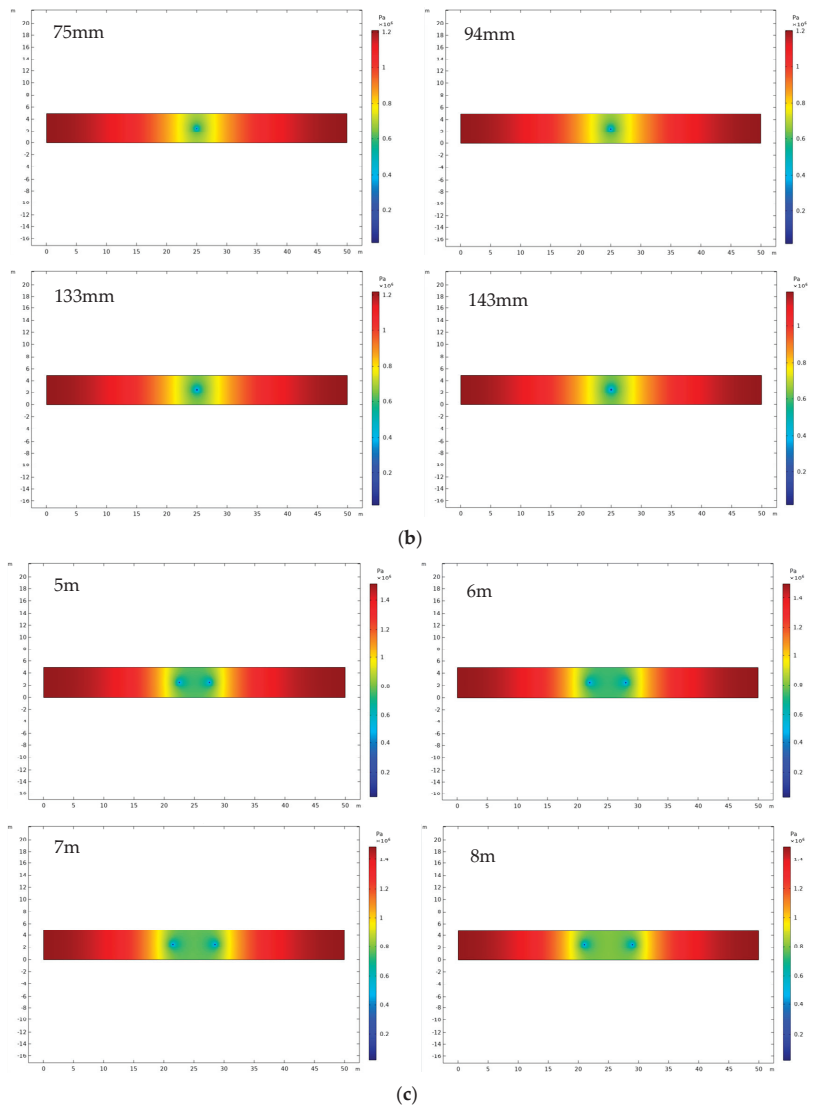
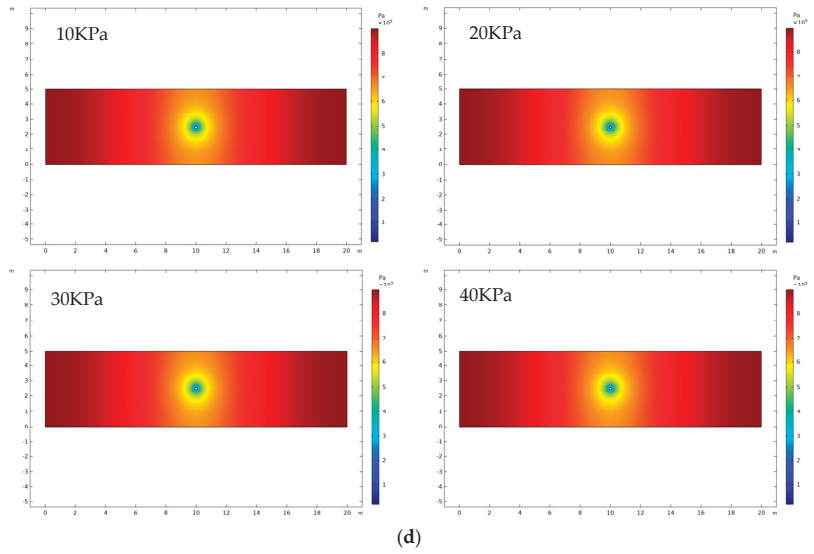
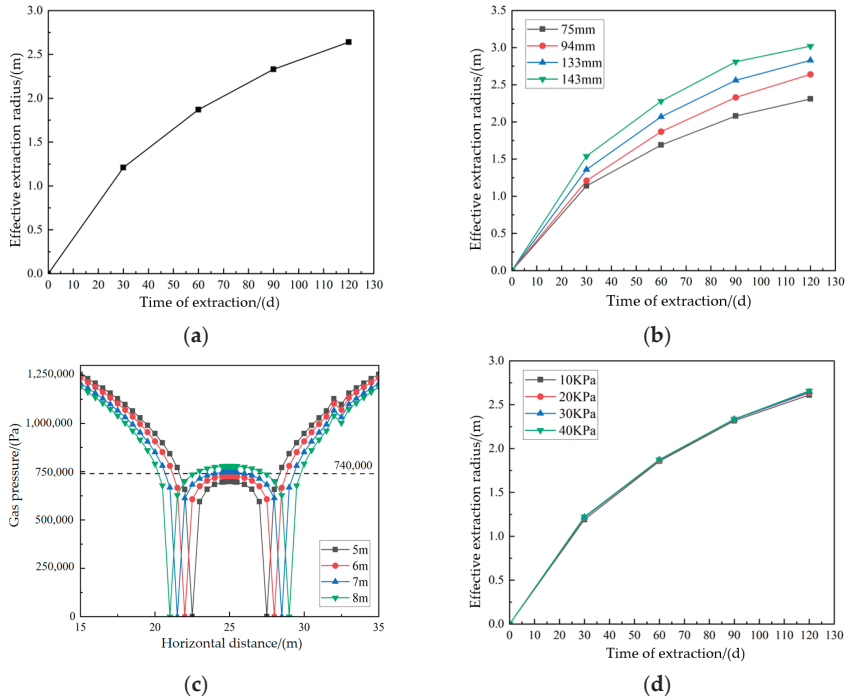


Figure 2. Cont.



**Figure 2.** Cloud diagram of gas pressure variation under different parameters. (a) Different extraction time; (b) Different extraction diameters; (c) Different hole spacing; (d) Different suction negative pressure.



**Figure 3.** Variation trend of the effective extraction radius under different parameters. (a) Different extraction time; (b) Different extraction diameters; (c) Different hole spacing; (d) Different suction negative pressure.

### 3. Research Methods and Ideas of the Thesis

This paper first studies the influence of different drilling parameters on the effective extraction radius and then constructs a gas extraction parameter optimization model to predict drilling parameters. Finally, a 3D drilling model was constructed to realize the optimized 3D drilling visualization display. Specific implementation methods and ideas are as follows:

#### 3.1. Parameter Optimization Algorithm (PSO–LSTM)

##### (1) PSO algorithm

The particle swarm optimization (PSO) algorithm is derived from research on bird predation behavior. The basic idea is to seek an optimal solution through mutual cooperation and information sharing among individuals within the group. In this algorithm, a massless particle is used to simulate an individual in a flock. There are only two attributes: velocity and position. Velocity represents the direction and distance of the next iteration, while position represents a solution to the problem. When PSO is initialized, all individuals in the flock forage in their own space. When the individuals find the food (the optimal solution of the problem), the solution is taken as the individual optimal solution ( $P_{id,pbest}$ ); All the individual optimal solutions in the group are shared, and the quality of the solutions is evaluated by the fitness function to obtain the group optimal solution ( $P_{d,gbest}$ ). In the next iteration, each individual updates its speed and position through the group optimal solution and continues foraging until a unique optimal solution is obtained [29]. The PSO algorithm flow is shown in Figure 4.

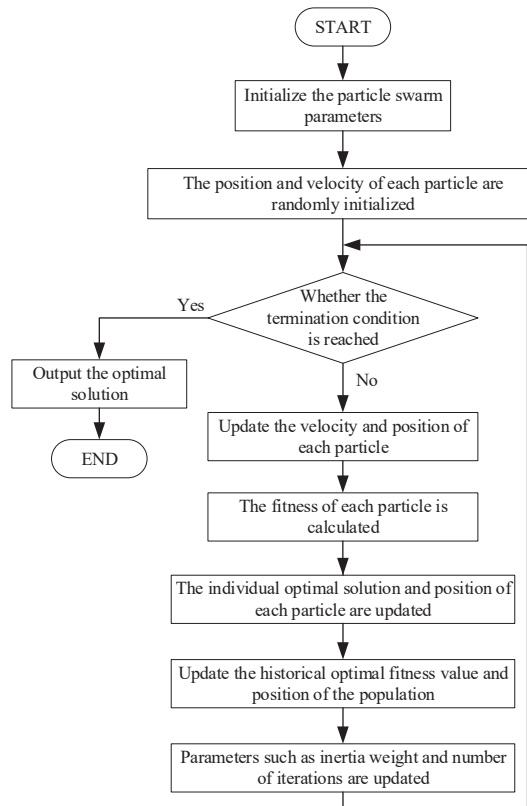


Figure 4. PSO algorithm flowchart.

Suppose there are  $N$  particles in the  $D$ -dimensional search space, and each particle represents a solution, then the position of the  $i$ th particle is  $X_{id} = \{x_{i1}, x_{i2}, \dots, x_{iD}\}$ , the velocity of the  $i$ th particle is  $V_{id} = \{v_{i1}, v_{i2}, \dots, v_{iD}\}$ , the optimal position searched by the  $i$ th particle (the individual optimal solution) is  $P_{id,pbest} = \{p_{i1}, p_{i2}, \dots, p_{iD}\}$ , the optimal position searched by the group (the group optimal solution) is  $P_{d,gbest} = \{p_{1,gbest}, p_{2,gbest}, \dots, p_{D,gbest}\}$ , and the individual historical optimal fitness value is  $f_p$ . The optimal population historical adaptation value is  $f_g$ . The algorithm is simple in structure, easy to implement, and has the advantages of high precision and short processing time.

Speed updating formula [29]:

$$v_{id}^{k+1} = wv_{id}^k + c_1r_1(P_{id,pbest}^k - x_{id}^k) + c_2r_2(P_{d,gbest}^k - x_{id}^k) \tag{7}$$

The location update formula is as follows [29]:

$$x_{id}^{k+1} = x_{id}^k + v_{id}^{k+1} \tag{8}$$

where  $i$  is the particle number,  $d$  is the particle dimension number,  $k$  is the number of iterations,  $w$  is the inertia weight,  $c_1$  is the individual learning factor,  $c_2$  is the group learning factor, and  $r_1$  and  $r_2$  are random numbers between 0 and 1. The velocity vector of particle  $i$  in the  $d$ -th dimension is the  $v_{id}^k$  in the  $k$ -th iteration. The position vector of particle  $i$  in the  $d$ -th dimension in the  $k$ -th iteration is the  $x_{id}^k$ . The historical optimal position of particle  $i$  in the  $d$ -th dimension in the  $k$ -th iteration is the  $P_{id,pbest}^k$ . The historical optimal position of the swarm in the  $d$ -th dimension in the  $k$ -th iteration is the  $P_{d,gbest}^k$ .

(2) LSTM model

The long short-term memory (LSTM) network model is composed of multiple repeated structural modules, and each structural module contains three gates: the forgetting gate, the input gate, and the output gate [30]. Figure 5 shows the LSTM model structure. The LSTM network realizes the control of three gates through the activation function so as to realize the retention and forgetting of historical information.

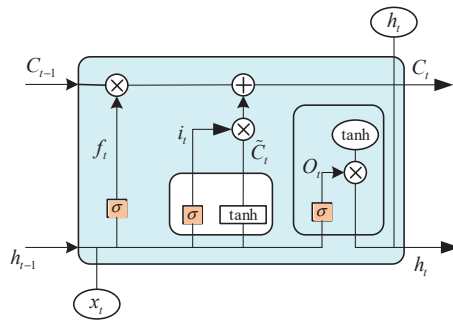


Figure 5. LSTM model structure diagram.

LSTM prediction model mainly includes three steps:

The forget gate  $f_t$  determined by the sigmoid function layer is calculated as follows:

$$f_t = \sigma(W_f[h_{t-1}, x_t] + b_f), \tag{9}$$

where, the sigmoid activation function is denoted by  $\sigma$ ; The forgetting gate weight matrix is denoted by  $W_f$ ; The neuron output is denoted by  $h$ ; The neuron input is denoted by  $x$ ; The current time is denoted by  $t$ . The previous time is denoted by  $t - 1$ ; The bias term is denoted by  $b_f$ .

The input gate to increase the amount of state is  $i_t$ , optionally updated. The calculation formula is shown in Equations (4)–(6):

$$i_t = \sigma(W_f[h_{t-1}, x_t] + b_i), \quad (10)$$

$$\tilde{C}_t = \tanh(W_c[h_{t-1}, x_t] + b_c), \quad (11)$$

$$C_t = f_t C_{t-1} + i_t \tilde{C}_t, \quad (12)$$

where, the alternative update information at time  $t$  is denoted by  $\tilde{C}_t$ ; The activation function is denoted by  $\tanh()$ .  $W_c$  represents the weight matrix of memory cells;  $C_t$  and  $C_{t-1}$  denote the memory cell state at time  $t$  and  $t - 1$ , respectively.

The output gate is denoted by  $O_t$  and is calculated as follows:

$$O_t = \sigma(W_o[h_{t-1}, x_t] + b_o), \quad (13)$$

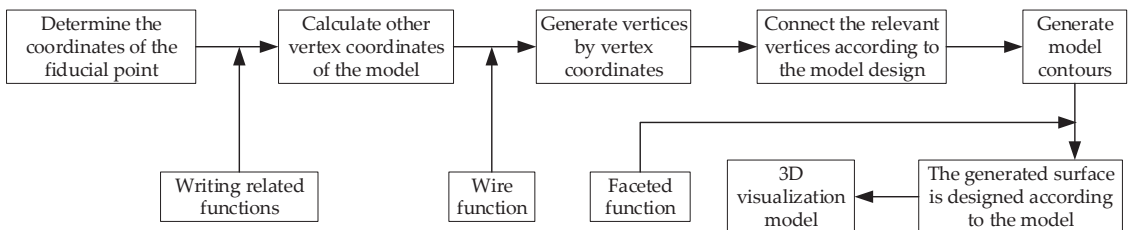
$$h_t = O_t \tanh C_t, \quad (14)$$

where, the output gate weight matrix is denoted by  $W_o$ .

### 3.2. Drilling 3D Model Construction Method

Python 3.7 is a major release of the Python programming language that introduces a number of new features and improvements that provide developers with a more powerful and flexible programming environment. The main characteristics of Python can be summarized as follows: it is simple and easy to learn, free source code, open source, and reduces the cost of learning; it has a wealth of high-quality libraries such as Pandas, Numpy, and Matplotlib that provide powerful support for data processing, computation, and plotting.

When generating the 3D model, the 3D coordinates of the reference point are determined, and the coordinates of the other vertices are calculated by the 3D spatial relationship between the other vertices of the model and the reference point. The scatter() function in Python was used to generate each vertex, and the wiring function was used to connect the relevant vertices according to the model design to generate the model contour. Then, the surface function is used to connect the contour lines in turn to form the model section and finally generate the three-dimensional space model. Figure 6 shows the rapid generation process of the 3D spatial model of the borehole.



**Figure 6.** Flowchart of rapid generation of 3D space model for drilling.

### 3.3. Specific Implementation Ideas

In order to realize the intelligent optimization of gas drilling parameters and the rapid generation of a three-dimensional space model based on big data mining technology, Python programming language, and MATLAB R2021b programming language are used to construct the intelligent optimization model of drilling parameters and the rapid generation algorithm of the three-dimensional space model. Specific research steps are as follows: in the process of borehole design, firstly, the regional gas extraction conditions are analyzed,



and according to the gas extraction law knowledge in the knowledge base, the gas extraction law of the extraction region is determined. Then, according to the law of gas extraction and the allowable time of gas pre-extraction, the spacing of the gas extraction holes at various points is determined. Then, according to the occurrence of the coal seam, the position of the drilling hole was determined by fully considering the performance of the drilling machine and drilling tool, and the azimuth Angle, dip Angle, and hole depth of each drilling hole were calculated by the spatial geometry method. Finally, according to the drilling design parameters, a drilling design map is automatically drawn to complete the intelligent drilling design. Its flowchart is shown in Figure 7.

1. Analysis of influencing factors of effective extraction radius: From the perspective of the theoretical formula of effective extraction radius, the influencing factors are analyzed. The factors that can be effectively controlled in the actual production process include extraction time, hole diameter, hole spacing, and extraction negative pressure. Therefore, numerical simulation software is used to construct geometric models and divide grids, and the gas pressure changes under different parameters are studied from these four aspects.
2. Intelligent optimization model of drilling parameters: in order to find more suitable drilling parameters, big data mining technology is used to learn the drilling experience of successful cases, and the long short-term memory neural network model of particle swarm optimization is constructed by MATLAB to determine the key parameters of the model and optimize the drilling parameters of gas extraction.
3. 3D space model generation algorithm: The Python open-source program is used as the compilation language, and the modeling idea of “generating lines from points, lines from surfaces, and surfaces from surfaces” is used to generate the corresponding 3D space model with the optimized parameters in step 2.

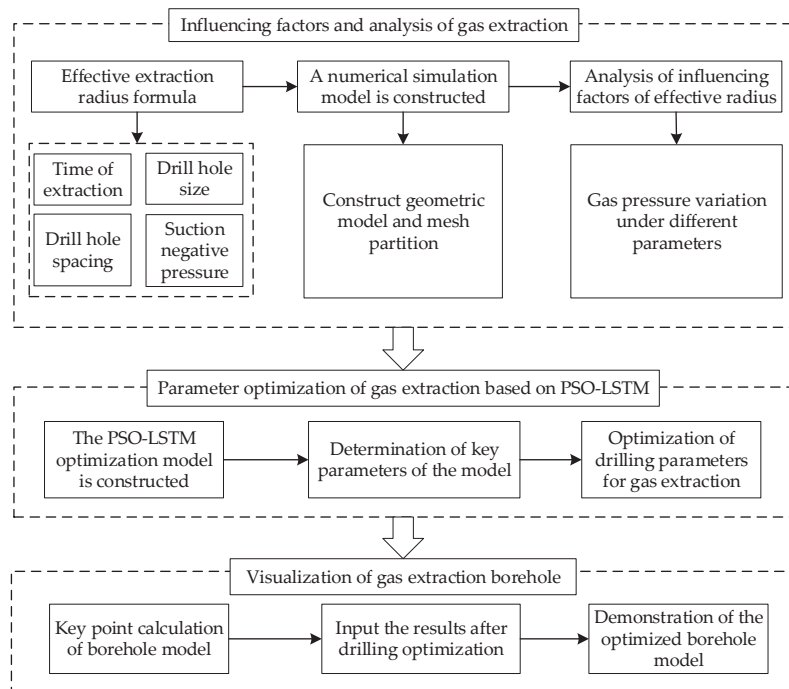


Figure 7. Basic Implementation Idea.

#### 4. Parameter Optimization Method of Gas Extraction Based on PSO–LSTM

The design of a drilling hole is the main basis of drilling construction. The scientific and rational design of drilling holes directly affects the difficulty of drilling construction and the amount of engineering, as well as the play of later extraction efficiency. The design of extraction drilling must be considered from various factors. It is a complex decision-making process that is limited by various factors such as coal seam gas geological conditions, drilling construction environment, drilling machine drilling tool performance and so on. It needs to balance various needs, such as gas extraction standards, drilling construction difficulty, drilling amount and so on, so that the drilling layout scheme can achieve the overall optimization state. To solve this black-box problem, it is an effective way to construct a long short-term memory neural network model based on particle swarm optimization. The model can fuse coal mine geological data, gas monitoring data, and other related information and realize transparent and intelligent analysis of gas geological conditions.

##### 4.1. Optimization Model Construction

Particle Swarm Optimization long short-term memory neural network model (PSO–LSTM) is a combination of Particle swarm optimization (PSO) and long short-term memory (LSTM). (LSTM) performs double training on gas drilling data and uses the optimization results of the PSO algorithm as the test set of the LSTM algorithm, which makes the training results of the LSTM algorithm more accurate [31], and the flow chart is shown in Figure 8.

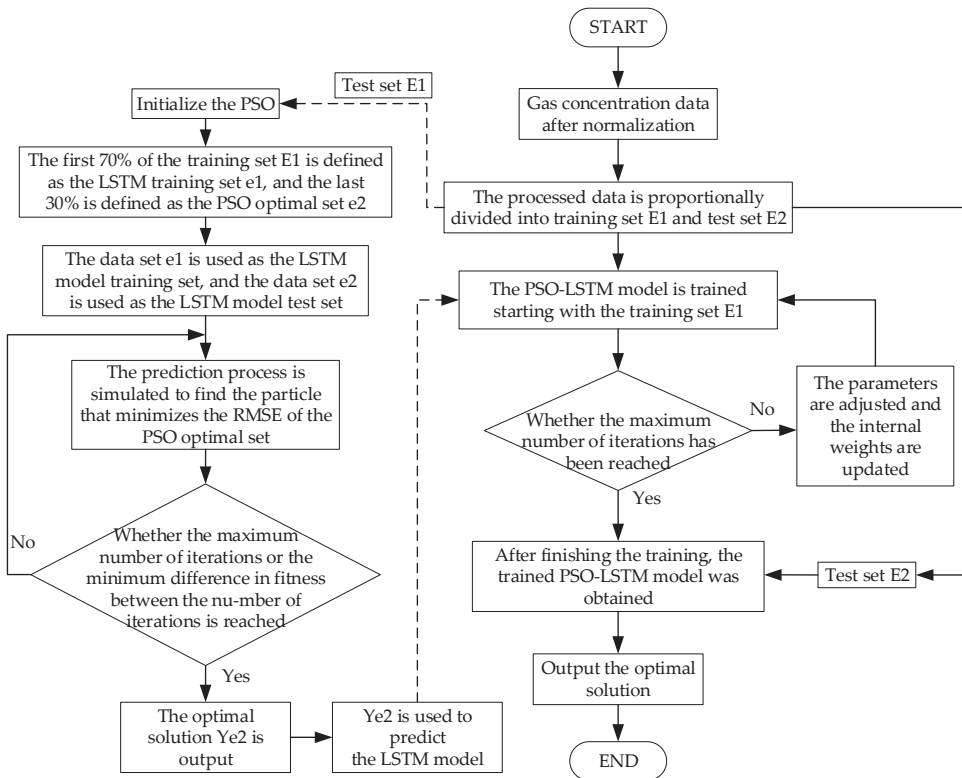


Figure 8. Flowchart of the PSO–LSTM model.

The specific process is as follows:

Step 1: The gas drilling data  $X_n$  is standardized according to the format so that it conforms to the data processing flow; The processed data is divided into training set  $E_1$  and test set  $E_2$  in proportion. In equations  $X_n$ ,  $E_1$ , and  $E_2$ ,  $R_i$  is the drilling radius,  $d_i$  is the drilling spacing, and  $i = \{1, 2, \dots, n\}$ .

Step 2: Start with the training set  $E_1$  and the PSO model to optimize and train the LSTM model. The specific process is as follows:

(1) The PSO algorithm is initialized to form an optimization community.

(2) The conventional prediction model divides the training set and the test set according to a ratio of 7:3. Therefore, the first 70% of the training set  $E_1$  is defined as the LSTM model training set  $e1 = (\sum_i^n R_i, \sum_i^n d_i)$ , and the last 30% is defined as the PSO model

optimization set  $e2 = (\sum_i^n R_i, \sum_i^n d_i)$ .

(3) The LSTM model training set  $e1$  is used as the training set of the LSTM model, and the optimal solution of the PSO model optimization set  $e2$  is used as the test set of the LSTM model.

(4) Start the simulation prediction process to find the particle that minimizes the RMSE of the PSO selection set (training result). Meanwhile, the training set  $e1$  is used to train the LSTM model.

Root Mean Square Error (RMSE) is used as the evaluation index to detect whether the PSO model training reaches the maximum number of iterations or the minimum difference in fitness between iterations.

$$RMSE = \sqrt{\frac{\sum_{i=1}^n (X_{obs,i} - X_{pre,i})^2}{n}} \quad (15)$$

(5) Output the optimal solution  $Y_{e2} = (\sum_i^n R_i, \sum_i^n d_i)$  of optimal set  $e2$  of PSO model,  $i = \{1, 2, \dots, n\}$ .

Step 3: Use the optimal solution  $Y_{e2} = (\sum_i^n R_i, \sum_i^n d_i)$  of the PSO model selection  $e2$  to predict and analyze the LSTM model that has been trained.

Step 4: Adjust the model parameters based on the predictions. If it does not, the parameters are adjusted, the internal weights are updated, and the PSO–LSTM model is returned for training again until the training result reaches the maximum number of iterations.

Step 5: After the training of the PSO–LSTM model, the test set  $E_2$  is used to predict and analyze the trained PSO–LSTM model.

Step 6: Output the PSO–LSTM model optimal solution  $Y_n = (\sum_i^n R_i, \sum_i^n d_i)$ ,  $i = \{1, 2, \dots, n\}$ .

#### 4.2. Determination of Key Parameters

When constructing the PSO–LSTM model, it is necessary to consider how to establish its key parameters and the influence of the data itself on the prediction accuracy so as to improve the performance of the model by reasonably establishing these parameters. The parameters of the PSO algorithm were as follows: the number of the initial populations was five, the dimension of the initial population was two, the maximum iteration number of the initial population was 10, the learning factor  $c_1 = c_2 = 2$ , the maximum inertia weight was 1.2, and the minimum inertia weight was 0.8. The parameters of the PSO–LSTM model are input layer dimension 2, output layer dimension 1, hidden layer neuron number 10~200, learning rate 0.01~0.15, iteration number 50, and stochastic gradient descent algorithm [32]. The key parameters are shown in Table 2.

Table 2. Key parameter table.

PSO Algorithm Parameter		PSO-LSTM Algorithm Parameter	
Parameter	Parameter Value	Parameter	Parameter Value
Initialize the number of groups	5	Input layer dimension	2
Initialize the group dimensions	2	Output layer dimension	1
Initialize the maximum number of swarm iterations	10	Number of neurons in the hidden layer	10~200
Learning factor $c_1$	2	LSTM layer solver	PSO optimization
Learning factor $c_2$	2	Learning rate	Adam
Maximum inertia weight	1.2	Number of iterations	Adaptive
Minimum inertia weight	0.8		50

5. Fast Generation Algorithm for 3D Borehole Model

According to the above-optimized drilling parameters and 3D coordinate information of coal seam, the rapid generation algorithm of 3D drilling space is realized based on the modeling idea of “generating lines from points, generating surfaces from lines, and generating bodies from surfaces”. It consists of two parts: the 3D model generation of bedding drilling and through drilling. Generate 3D models of boreholes covering necessary parts such as coal seams, laneways, and boreholes.

5.1. Key Point Calculation of Bedding Borehole Model

The 3D modeling of the working face is carried out by using the drilling of bedding on both sides of the strike. In the ideal state, the 3D drilling model of the inlet roadway and the return roadway is shown in Figure 9, in which the starting and ending coordinates of the intersection line between the working face and the bottom of the inlet roadway are  $A_1(x_{A_1}, y_{A_1}, z_{A_1})$  and  $B_1(x_{B_1}, y_{B_1}, z_{B_1})$  respectively, and the starting and ending coordinates of the intersection line between the working face and the bottom of the return roadway are  $C_1(x_{C_1}, y_{C_1}, z_{C_1})$  and  $D_1(x_{D_1}, y_{D_1}, z_{D_1})$  respectively. The length along coal seam strike is  $L_{Z1}$ , the slant width of working face is  $L_{W1}$ , the azimuth Angle of the roadway is  $\alpha_1$ , the Angle between coal seam strike and horizontal plane is  $\beta_1$ , the azimuth Angle of drill hole in inlet roadway is  $\theta_1$ , and the azimuth Angle of the drill hole in return roadway is  $\theta_2$ . A schematic diagram of the drill hole arrangement of the k unit is shown in Figure 10.

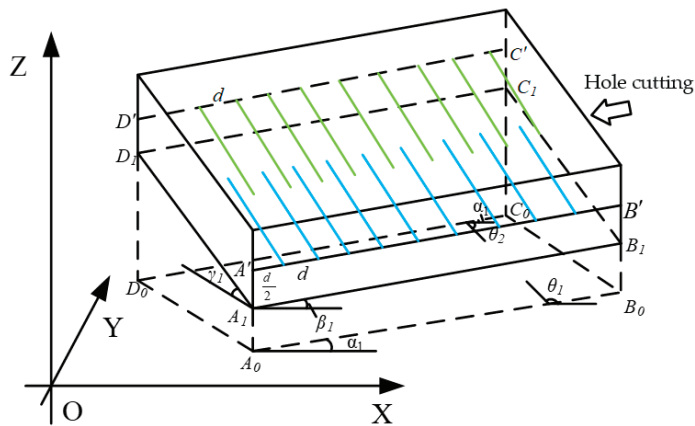


Figure 9. Schematic diagram of the 3D model of drilling in counterpunching bedding.

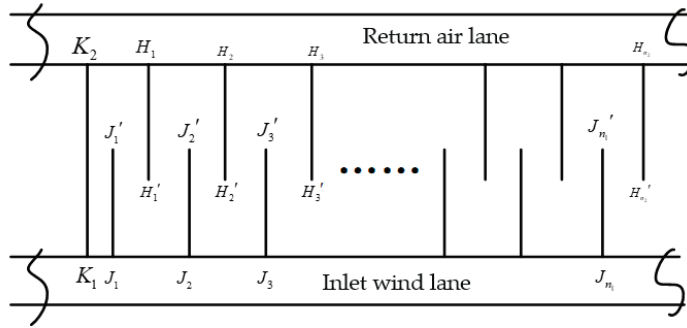


Figure 10. Diagram of drill hole arrangement in unit k.

The coordinate of the control point of the first unit of the inlet wind lane is  $(x_{A_1}, y_{A_1}, z_{A_1} + \frac{L_h}{2})$ .

(1) Coordinates of inlet lane

The coordinate of the  $n_1$  opening point of the KTH element is  $J_{n_1}(x_{J_{n_1}}, y_{J_{n_1}}, z_{J_{n_1}})$ :

$$\begin{cases} x_{J_{n_1}} = x_{A_1} + \sum_1^{k-1} L_k \cos(\beta_1) \cos(\alpha_1) + (n_1 - \frac{1}{2})d_k \cos(\beta_1) \cos(\alpha_1) \\ y_{J_{n_1}} = y_{A_1} + \sum_1^{k-1} L_k \cos(\beta_1) \sin(\alpha_1) + (n_1 - \frac{1}{2})d_k \cos(\beta_1) \sin(\alpha_1) \\ z_{J_{n_1}} = z_{A_1} + \frac{L_h}{2} + \sum_1^{k-1} L_k \sin(\beta_1) + (n_1 - \frac{1}{2})d_k \sin(\beta_1) \end{cases} \quad (16)$$

where,  $n_1$  represents the number of pumping holes in the inlet lane of unit k.

The coordinate of the  $n_1$  final hole point of the KTH element is  $J'_{n_1}(x_{J'_{n_1}}, y_{J'_{n_1}}, z_{J'_{n_1}})$ :

$$\begin{cases} x_{J'_{n_1}} = x_{A_1} + \sum_1^{k-1} L_k \cos(\beta_1) \cos(\alpha_1) + (n_1 - \frac{1}{2})d_k \cos(\beta_1) \cos(\alpha_1) - L_c \cos(\gamma_1) \sin(\alpha_1) \\ y_{J'_{n_1}} = y_{A_1} + \sum_1^{k-1} L_k \cos(\beta_1) \sin(\alpha_1) + (n_1 - \frac{1}{2})d_k \cos(\beta_1) \sin(\alpha_1) + L_c \cos(\gamma_1) \cos(\alpha_1) \\ z_{J'_{n_1}} = z_{A_1} + \frac{L_h}{2} + \sum_1^{k-1} L_k \sin(\beta_1) + (n_1 - \frac{1}{2})d_k \sin(\beta_1) + L_c \sin(\gamma_1) \end{cases} \quad (17)$$

where,  $\frac{L_h}{2}$  represents the distance between coal seam  $A_1$  and  $A_1'$ , m;  $\gamma$  is the dip Angle of coal seam, °;  $L_c$  is the length of the extraction drilling hole, m,  $L_c \geq L_w/2 + 5$ .

(2) Return air lane

The coordinate of the  $n_2$  opening point of the KTH element is  $H_{n_2}(x_{H_{n_2}}, y_{H_{n_2}}, z_{H_{n_2}})$ :

$$\begin{cases} x_{H_{n_2}} = x_{A_1} - L_{w1} \cos(\gamma_1) \sin(\alpha_1) + \sum_1^{k-1} L_k \cos(\beta_1) \sin(\alpha_1) + n_2 d_k \cos(\beta_1) \cos(\alpha_1) \\ y_{H_{n_2}} = y_{A_1} + L_{w1} \cos(\gamma_1) \cos(\alpha_1) + \sum_1^{k-1} L_k \cos(\beta_1) \cos(\alpha_1) + n_2 d_k \cos(\beta_1) \sin(\alpha_1) \\ z_{H_{n_2}} = z_{A_1} + \frac{L_h}{2} + L_{w1} \sin(\gamma_1) + \sum_1^{k-1} L_k \sin(\beta_1) + n_2 d_k \sin(\beta_1) \end{cases} \quad (18)$$

The coordinate of the  $n_2$  final hole point of the KTH element is  $H'_{n_2}(x_{H'_{n_2}}, y_{H'_{n_2}}, z_{H'_{n_2}})$ :

$$\begin{cases} x_{H'_{n_2}} = x_{A_1} - L_{w1} \cos(\gamma_1) \sin(\alpha_1) + \sum_1^{k-1} L_k \cos(\beta_1) \sin(\alpha_1) + n_2 d_k \cos(\beta_1) \cos(\alpha_1) + L_c \cos(\gamma_1) \sin(\alpha_1) \\ y_{H'_{n_2}} = y_{A_1} + L_{w1} \cos(\gamma_1) \cos(\alpha_1) + \sum_1^{k-1} L_k \cos(\beta_1) \cos(\alpha_1) + n_2 d_k \cos(\beta_1) \sin(\alpha_1) - L_c \cos(\gamma_1) \cos(\alpha_1) \\ z_{H'_{n_2}} = z_{A_1} + \frac{L_h}{2} + L_{w1} \sin(\gamma_1) + \sum_1^{k-1} L_k \sin(\beta_1) + n_2 d_k \sin(\beta_1) - L_c \sin(\gamma_1) \end{cases} \quad (19)$$

where,  $n_2$  represents the number of drilling holes in the return air lane of unit k.

### 5.2. Key Point Calculation of Through-Layer Drilling Model

A schematic diagram of the 3D model of through-layer drilling is shown in Figure 11, which is composed of four parts: the bottom coal pumping roadway with  $A_2B_2C_2D_2$  as the top surface, the pre-pumping coal seam with  $A_3B_3C_3D_3$  as the bottom surface, the pre-driving coal roadway with  $A_4B_4C_4D_4$  as the bottom surface, and the red and blue drilling trajectories. It is assumed that the inclination angles of the bottom pumping roadway, the pre-pumping coal seam and the pre-tunneling coal roadway are the same, and the bottom pumping roadway is  $A_2(x_{A_2}, y_{A_2}, z_{A_2}), B_2(x_{B_2}, y_{B_2}, z_{B_2}), C_2(x_{C_2}, y_{C_2}, z_{C_2})$  and  $D_2(x_{D_2}, y_{D_2}, z_{D_2})$ . Pre-pumped coal seam  $A_3(x_{A_3}, y_{A_3}, z_{A_3}), B_3(x_{B_3}, y_{B_3}, z_{B_3}), C_3(x_{C_3}, y_{C_3}, z_{C_3})$ ,  $D_3(x_{D_3}, y_{D_3}, z_{D_3})$ ; Coal roadway  $A_4(x_{A_4}, y_{A_4}, z_{A_4}), B_4(x_{B_4}, y_{B_4}, z_{B_4}), C_4(x_{C_4}, y_{C_4}, z_{C_4})$  and  $D_4(x_{D_4}, y_{D_4}, z_{D_4})$  were pre-tunneled. The length along the strike of the coal seam is  $L_{Z2}$ , the slant width of the working face is  $L_{W2}$ , the azimuth Angle of the roadway is  $\alpha_2$ , and the Angle between the strike of the coal seam and the horizontal plane is  $\beta_2$ .

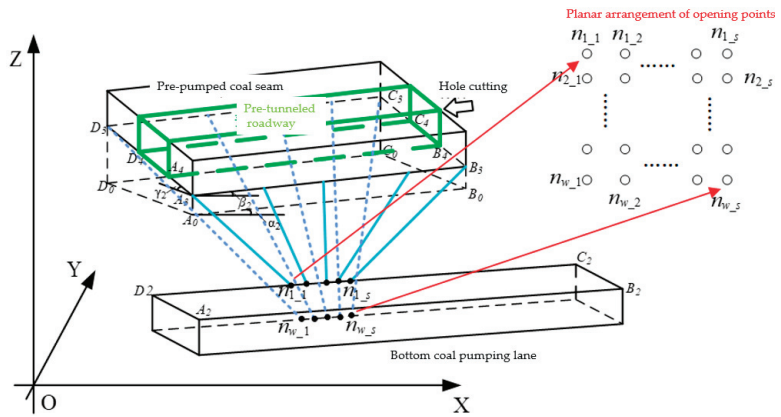


Figure 11. Schematic diagram of 3D model of through-layer drilling hole.

The planar diagram of the opening point is similar to that of the final hole point, as shown in “Opening point planar Arrangement” in Figure 11, where  $n_{w,s}$  represents the  $s$ -th drilled hole in the  $w$  row. The difference is that the opening point is located at the back side of the bottom extraction roadway, and the final hole point is located at the bottom of the pre-extraction seam.

(1) Coordinates of opening points

The  $s$  opening point in row  $w$  is  $K_{n_{w-s}}(x_{K_{n_{w-s}}}, y_{K_{n_{w-s}}}, z_{K_{n_{w-s}}})$ :

$$\begin{cases} x_{K_{n_{w-s}}} = x_{D_2} + K_{d_0} \cos(\beta_2) \cos(\alpha_2) + \sum_1^{s-1} K_{d_1} \cos(\beta_2) \cos(\alpha_2) + \sum_1^{s-1} K_{d_1} \cos(\beta_2) \cos(\alpha_2) \\ y_{K_{n_{w-s}}} = y_{D_2} + K_{d_0} \cos(\beta_2) \sin(\alpha_2) + \sum_1^{s-1} K_{d_1} \cos(\beta_2) \sin(\alpha_2) + \sum_1^{s-1} K_{d_1} \cos(\beta_2) \sin(\alpha_2) \\ z_{K_{n_{w-s}}} = z_{D_2} + K_{d_0} \sin(\beta_2) + \sum_1^{s-1} K_{d_1} \sin(\beta_2) - \sum_1^{w-1} K_{d_2} \sin(\beta_2) \end{cases} \quad (20)$$

where,  $K_{d_0}$  represents the distance between  $K_{n_{1-1}}$  and  $D_2$  point,  $m$ ;  $K_{d_1}$  represents the spacing of the opening point column,  $m$ ;  $K_{d_2}$  denotes the row spacing of the opening points,  $m$ .

(2) Final hole point coordinates

The  $s$ -th final hole point in row  $w$  is  $Z_{n_{w-s}}(x_{Z_{n_{w-s}}}, y_{Z_{n_{w-s}}}, z_{Z_{n_{w-s}}})$ :

$$\begin{cases} x_{Z_{n_{w-s}}} = x_{A_3} + \sum_1^{s-1} Z_{d_1} \cos(\beta_2) \cos(\alpha_2) - \sum_1^{w-1} Z_{d_2} \cos(\beta_2) \sin(\alpha_2) \\ y_{Z_{n_{w-s}}} = y_{A_3} + \sum_1^{s-1} Z_{d_1} \cos(\beta_2) \sin(\alpha_2) + \sum_1^{w-1} Z_{d_2} \cos(\beta_2) \cos(\alpha_2) \\ z_{Z_{n_{w-s}}} = z_{A_3} + \sum_1^{s-1} Z_{d_1} \sin(\beta_2) + \sum_1^{w-1} Z_{d_2} \sin(\gamma_2) \end{cases} \quad (21)$$

where,  $Z_{d1}$  represents the spacing of the final hole point column, m;  $Z_{d2}$  represents the row spacing of the terminal hole point, m.

## 6. Application Example and Effect Evaluation

### 6.1. Source of Cases

The test site was selected as the 1302 working face of a coal mine in Shanxi Province, with a coal seam thickness of 5.3 m and a coal seam dip Angle of  $16^\circ$ . There are two grooves in the working face, and there is a high extraction roadway below the coal seam. According to the actual demand of the mine, gas extraction work is carried out from two laneways, including gas extraction work of low through-layer drilling and gas extraction work of bedding drilling. Considering the complexity, time-consuming, and labor-intensive manual design of gas extraction drilling, a method of artificial intelligence is proposed to quickly design the parameters of gas extraction drilling, and the visual display of the gas extraction drilling field is realized by means of software programming.

### 6.2. Case 1 Result Analysis (Bedding Extraction)

#### (1) Optimization of drilling parameters

Based on the extraction records of the adjacent working face, 30 historical data points of the drilling holes along the layer were selected to verify the effectiveness of the above method, in which the diameter of the drilling holes along the layer was not less than 94 mm. The first 24 (80%) of each group of data were used as the training set, and the PSO-LSTM model was used to optimize and train the drilling parameters. The last six items (20%) were used as the test set to predict the optimization results. Among them, the first 17 (70%) items of the test set were used as the LSTM model training set, and the last seven (30%) items were used as the PSO model optimization set.

By defining the size, iteration number, inertia weight, acceleration coefficient, and other parameters of the particle swarm, the particle swarm is initialized, and the LSTM network structure is designed, including the input layer, hidden layer, and output layer, and relevant parameters such as the time step and the number of hidden layer units are set. PSO was combined with LSTM, the initial weights and hyperparameters of LSTM were optimized by PSO, and the model was trained until it converged to the optimal solution as shown in Table 3.

**Table 3.** Comparison of drilling parameter optimization results in bedding.

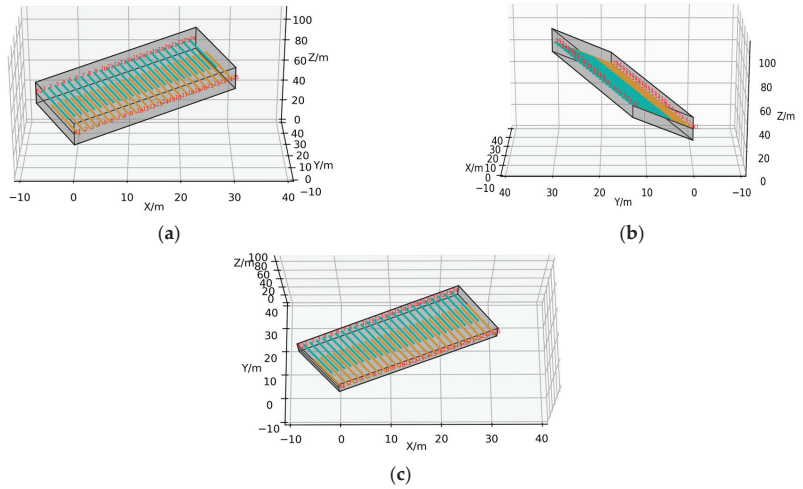
Serial Number	Data Types	Drill Hole Spacing/(m)	Drill Hole Depth/(m)	Inclination of Drill Hole/(°)	Borehole Azimuth/(°)
X1	Training set	9.1	28.7	18.17	29.87
X2	Training set	8.4	29.5	16.92	29.26
X3	Training set	8.8	30.0	17.91	30.08
T1	Test set	8.1	29.7	17.30	30.21
T2	Test set	8.3	28.7	17.11	30.15
T3	Test set	8.2	30.1	16.81	29.72
Y1	Design results	6	30.0	16.00	30.00

Table 3 shows that the drilling parameters designed using the PSO-LSTM optimization model are spacing 6 m, drilling hole depth 30 m, drilling dip Angle  $16^\circ$ , and azimuth Angle  $30^\circ$ . The design results are the same as the drilling parameters designed using numerical simulation, and the time consumption is shorter, which shows the accuracy and convenience of the method.

#### (2) Visual display of drill field

The design results in Table 3 are incorporated into the compiled drill-field visualization model, and the results are shown in Figure 12. It can be seen from Figure 12 that the drill

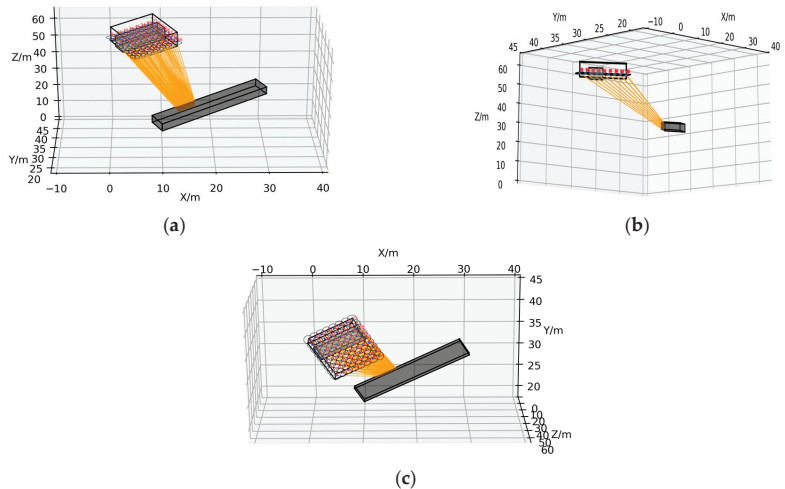
holes of the inlet and return air roadways are different, and the length of the drill holes is greater than half of the width of the extracted coal seam. This method of hole distribution can fully extract coal seam gas and avoid an excessive concentration of residual gas. The drill holes of the inlet lane and return lane are numbered. There are 25 drill holes in the inlet lane (lower side) and 24 drill holes in the return lane (upper side).



**Figure 12.** Renderings of 3D model of bedding borehole. (a) Main view; (b) Left view; (c) Top view.

6.3. Case 2 Result Analysis (Through-Layer Extraction)

3D visualization of the through-layer drilling holes is shown in Figure 13. There are 72 through-layer drilling holes (nine rows and eight columns), and the opening points and final hole points of the drilling holes are arranged neatly and numbered from 1 to 72. Figure 13c shows that the effective extraction range of the final hole point of each drilling hole overlaps with each other and is tightly connected, covering the whole pre-extracted coal seam, which can fully extract coal seam gas. Due to space limitations, the optimization process of through-layer drilling will not be described again.



**Figure 13.** 3D visualization rendering of through-layer drilling. (a) Main view; (b) Left view; (c) Top view.



#### 6.4. Discussion

With the gradual development of intelligent construction in mines, it is imperative to automate and intelligentize gas extraction. Based on this, this study proposes an intelligent optimization method based on PSO–LSTM and combines 3D visualization technology to carry out intelligent design and visual display research of extraction drilling parameters, which improves the scientific and intuitive design of gas extraction drilling and provides strong support for coal mine safety production. Through a later test, the above method is used to realize the rapid design of gas extraction parameters, drilling concentration, negative pressure, and other composite-related requirements. At the same time, the generation of a three-dimensional drilling field lays the foundation for the visual display of the gas extraction drilling field and ensures the safe and efficient recovery of the working face.

Gas extraction is a “four-dimensional” dynamic process, which needs to fully consider the dimensions of space and time. Differential borehole parameter design is an indispensable problem in gas extraction, and gas transparent geology technology is a key link. In order to improve the accuracy and timeliness of geological condition detection and coal seam gas measurement, advanced coal seam geological detection and coal seam gas parameter measurement techniques are studied for dynamic transparent gas geology. Establishing a GIS-based gas geological information platform, constructing a high-precision three-dimensional gas geological dynamic model, and accurately, intuitively, and dynamically displaying the gas geological conditions and their evolution process in the whole life cycle of gas extraction are the main development trends of gas geological security in intelligent gas extraction.

In the future, based on the above theoretical research, the team will further develop the automatic design platform of gas extraction drilling, improve the functions of extraction drilling design, 3D model generation, drawing output, and so on, and form a full-cycle control platform of “design–construction–acceptance–observation–enrichment–abandonment” of gas extraction drilling. It integrates the functions of auxiliary analysis of borehole spacing, automatic calculation of borehole parameters, automatic drawing of design drawings, three-dimensional display of design effects, etc., and realizes the automatic design of boreholes for common types of gas extraction in coal mines, such as through layers, along layers, and high positions. At the same time, it is further explored to combine other optimization algorithms with deep learning models to improve the intelligence level of drilling design and expand its application in other mine safety production fields.

#### 7. Conclusions

Aiming at the problems of low utilization rate of gas extraction parameters and long design cycle of the gas extraction scheme, an intelligent design and visualization method of gas extraction drilling based on PSO–LSTM was proposed. The PSO–LSTM model uses the PSO algorithm to optimize the parameters of the LSTM model and search for the most suitable LSTM model parameters to improve the accuracy of the LSTM algorithm.

1. From the perspective of the theoretical formula of extraction radius, the law of extraction radius with different drilling parameters is studied; that is, the extraction range increases with the increase in extraction time, drilling diameter, and extraction negative pressure. Within a certain range, the extraction range increases with an increase in borehole spacing, which provides a theoretical basis for the intelligent optimization of extraction parameters.
2. This paper proposes an intelligent optimization method for gas extraction drilling parameters based on depth mining. Using the experience of successful cases of gas extraction drilling in-depth mining by this method, taking the successful actual parameters as a reference, intelligent optimization of 1302 working face drilling parameters: drilling spacing 6 m, drilling depth 30 m, drilling Angle  $16^\circ$ , azimuth Angle  $30^\circ$ , improve the accuracy of the model.
3. The mathematical expressions of the gas extraction space models for the bedding and through-layer boreholes are summarized. Based on the modeling idea of the point–

generating line, line-generating surface, and surface-generating body”, through the intelligent optimization of drilling parameters and 3D coordinate information of the coal seam, a 3D space model of bedding and throughbed is generated. This method uses a Python open-source program as the basic modeling language, which overcomes the shortcomings of other modeling software with diverse operations and complexity. In addition, Python can automate the modeling process by writing scripts, reducing manual time and errors. This is particularly important for scenarios in which fast iterations are required, or a large number of models need to be processed.

4. Taking the 1302 working face of a coal mine in Shanxi Province as the research object, the drilling parameters are designed by numerical simulation and the PSO-LSTM model. The research in Section 5.2 shows that the drilling parameters designed by numerical simulation and the PSO-LSTM model are similar, which verifies the accuracy of the PSO-LSTM model and provides some support for the intelligent mining of coal mines.

**Author Contributions:** Conceptualization, Q.Z. and Y.Y.; methodology, Q.Z. and D.W.; software, G.Y.; validation, X.C.; resources, X.C.; data curation, Y.Y. and D.W.; writing—original draft preparation, D.W. and Y.Y.; writing—review and editing, X.L. and Y.L.; supervision, Q.Z. and Y.L.; project administration, Q.Z. All authors have read and agreed to the published version of the manuscript.

**Funding:** This work was supported and financed by Special Funds for Basic Research Business Fees of the China Academy of Safety Science and Technology (No. 2021JBKY11, No. 2023JBKY04), National Key Research and Development Program of China (No. 2021YFC3090403, No. 2021YFC3001904, No. 2021YFC3001905), the Hebei Natural Science Foundation, grant number E2023508021, the Fundamental Research Funds for the Central Universities, grant number 3142021002, S&T Program of Hebei, grant number 22375401D, General Program of National Natural Science Foundation of China, grant number 52074121.

**Data Availability Statement:** The data used to support the findings of this study were supplied by Dacang Wang under license and so cannot be made freely available. Requests for access to these data should be made to Dacang Wang (wdc15102587295@163.com).

**Conflicts of Interest:** Author Yongming Yin was employed by the China Academy of Safety Science and Technology, and Cathay Safety Technology Co., Ltd. Author Guangyu Yang was employed by the company Coal Mining Research Institute Co., Ltd. of CCTEG. The remaining authors declare that the research was conducted in the absence of any commercial or financial relationships that could be construed as potential conflicts of interest. The companies in affiliation and Funding had no role in the design of the study; in the collection, analyses, or interpretation of data; in the writing of the manuscript, or in the decision to publish the results.

## References

1. Wang, P.; Ni, H.; Wang, R.; Li, Z. Modulating downhole cuttings via a pulsed jet for efficient drilling-tool development and field testing. *J. Nat. Gas Sci. Eng.* **2015**, *27*, 1287–1295. [CrossRef]
2. Xue, Y.; Liu, J.; Ranjith, P.; Liang, X.; Wang, S. Investigation of the influence of gas fracturing on fracturing characteristics of coal mass and gas extraction efficiency based on a multi-physical field model. *J. Pet. Sci. Eng.* **2021**, *206*, 109018. [CrossRef]
3. Pan, H. Optimized design of gas extraction parameters by high-positioned drill-holes. *China Coal* **2009**, *35*, 106–107+115.
4. Li, T.; Wu, B.; Lei, B. Study on the optimization of a gas drainage borehole drainage horizon based on the evolution characteristics of mining fracture. *Energies* **2019**, *12*, 4499. [CrossRef]
5. Yan, Z.; Wang, Y.; Fan, J.; Huang, Y.; He, Y. Study on Key Parameters of Directional Long Borehole Layout in High-Gas Working Face. *Shock Vib.* **2021**, *2021*, 5579967. [CrossRef]
6. Huang, Y. Optimization study of hydraulic slotting parameters for soft coal seam in Yuwu Coal Mine. *Min. Saf. Environ. Prot.* **2022**, *49*, 61–65.
7. Wu, K.; Shi, S.; Lu, Y.; Li, H.; Li, M. Optimization of the Plastic Area of a Borehole Based on the Gas Extraction Effect and Its Engineering Application. *Geofluids* **2021**, *2021*, 8147366. [CrossRef]
8. Yang, X.; Wen, G.; Lu, T.; Wang, B.; Li, X.; Cao, J.; Lv, G.; Yuan, G. Optimization and field application of CO<sub>2</sub> gas fracturing technique for enhancing CBM extraction. *Nat. Resour. Res.* **2020**, *29*, 1875–1896. [CrossRef]
9. Wang, Y.; Zhang, Y. Study on optimization of layout parameters of high-level boreholes in Pingdingshan coal mine. *Sci. Rep.* **2023**, *13*, 19759. [CrossRef]

10. Jing, G.; Wang, Y.; Zhou, F.; Tan, Z. Numerical Simulation Study of Water Fracturing with Different Angle through Beds Holes Based on RFP2D. *Coal Min. Technol.* **2018**, *23*, 103–107.
11. Lin, H.; Ji, P.; Kong, X.; Li, S.; Dou, G.; Li, K. Precise borehole placement model and engineering practice for pre-draining coal seam gas by drilling along seam. *J. China Coal Soc.* **2022**, *47*, 1220–1234.
12. Luo, M.; Yang, L.; Wen, H.; Zhao, D.; Wang, K. Numerical Optimization of Drilling Parameters for Gas Predrainage and Excavating–Drainage Collaboration on Roadway Head. *Geofluids* **2022**, *2022*, 3241211. [CrossRef]
13. Lee, B.Y.; Liu, H.S.; Tarnq, Y.S. Modeling and optimization of drilling process. *J. Mater. Process. Technol.* **1998**, *74*, 149–157. [CrossRef]
14. Lipin, K.; Govindan, P. A review on multi objective optimization of drilling parameters using Taguchi methods. *AKGEC Int. J. Technol.* **2013**, *4*, 11–21.
15. Zhao, Y.; Noorbakhsh, A.; Koopalipoor, M.; Azizi, A.; Tahir, M.M. A new methodology for optimization and prediction of rate of penetration during drilling operations. *Eng. Comput.* **2020**, *36*, 587–595. [CrossRef]
16. Ashena, R.; Rabiei, M.; Rasouli, V.; Mohammadi, A.H.; Mishani, S. Drilling parameters optimization using an innovative artificial intelligence model. *J. Energy Resour. Technol.* **2021**, *143*, 052110. [CrossRef]
17. Xie, B.; Zhong, S.; Cao, X. Automatic optimization design and application of drilling parameters for gas drainage in cross cut coal uncovering. *J. Min. Sci. Technol.* **2021**, *6*, 678–687.
18. Qin, Z.; Shen, H.; Yuan, Y.; Gong, Z.; Chen, Z.; Xia, Y. Determination of Gas Extraction Borehole Parameters in Fractured Zone on ‘Borehole in Place of Roadway’ Based on RSM–GRA–GA. *Processes* **2022**, *10*, 1421. [CrossRef]
19. Ding, Y.; Zhu, B.; Li, S.; Lin, H.; Wei, Z.; Li, L.; Long, H.; Yi, Y. Accurate identification and efficient drainage of relieved methane in goaf of high outburst mine. *J. China Coal Soc.* **2021**, *46*, 3565–3577.
20. Zhao, P.; Kang, X.; Li, S.; Lin, H.; Gan, L.; An, X. Optimization of “hole–drift” collaborative drainage layout parameters and high efficient drainage in pressure relief gas migration area. *Coal Sci. Technol.* **2022**, *50*, 137–146.
21. Shi, Z.; Ye, D.; Hao, J.; Qin, B.; Li, G. Research on gas extraction and cut flow technology for lower slice pressure relief gas under slice mining of extra-thick coal seam. *ACS Omega* **2022**, *7*, 24531–24550. [CrossRef]
22. Xie, Z.; Zhang, D.; Song, Z.; Li, M.; Liu, C.; Sun, D. Optimization of Drilling Layouts Based on Controlled Presplitting Blasting through Strata for Gas Drainage in Coal Roadway Strips. *Energies* **2017**, *10*, 1228. [CrossRef]
23. Yi, M.; Wang, L.; Hao, C.; Liu, Q.; Wang, Z. Method for designing the optimal sealing depth in methane drainage boreholes to realize efficient drainage. *Int. J. Coal Sci. Technol.* **2021**, *8*, 1400–1410. [CrossRef]
24. Xu, X.; Meng, X.; Zhao, G.; Wang, X.; He, Y. Virtual simulation of gas drainage drilling through layers in stress–relaxation zone based on three–dimensional visualization. *J. Saf. Sci. Technol.* **2014**, *10*, 77–82.
25. Zhang, J.; Yue, J.; Tan, Y.; Zhang, D.; Zhang, Q.; Wang, Q. Construction and Application of 3D Borehole Visualization System. *Coal Technol.* **2017**, *36*, 106–108.
26. Fan, K. Application of 3D Visualization of Gas Drainage Borehole in Sihe Coal Mine. *Coal Technol.* **2017**, *36*, 185–187.
27. Zhu, Q.; Zhang, Z.; Liang, J.; Liu, X.; Gu, L.; Zhong, L. Fast generation method of 3D mine roadway model and its application. *China Saf. Sci. J.* **2022**, *32*, 48–57.
28. Zhang, F.; Shang, W.; Luo, H.; Wang, N.; Jia, J.; Li, B. Analysis on influential factors of effective radius of gas extraction from coal seam borehole. *Min. Saf. Environ. Prot.* **2022**, *49*, 137–142.
29. Tang, G.; Sheng, J.; Wang, D.; Men, S. Continuous Estimation of Human Upper Limb Joint Angles by Using PSO–LSTM Model. *IEEE Access* **2021**, *9*, 17986–17997. [CrossRef]
30. Xu, Y.; Hu, C.; Wu, Q.; Jian, S.; Li, Z.; Chen, Y.; Zhang, G.; Zhang, Z.; Wang, S. Research on Particle Swarm Optimization in LSTM Neural Networks for Rainfall–Runoff Simulation. *J. Hydrol.* **2022**, *608*, 127553. [CrossRef]
31. Gao, J.W.; Jia, Z.H.; Wang, X.Y.; Xing, H. Degradation trend prediction of proton exchange membrane fuel cell based on PSO–LSTM. *J. Jilin Univ. (Eng. Technol. Ed.)* **2022**, *52*, 2192–2202.
32. Yang, G.; Zhu, Q.; Wang, D.; Feng, Y.; Chen, X.; Li, Q. Method and Validation of Coal Mine Gas Concentration Prediction by Integrating PSO Algorithm and LSTM Network. *Processes* **2024**, *12*, 898. [CrossRef]

**Disclaimer/Publisher’s Note:** The statements, opinions and data contained in all publications are solely those of the individual author(s) and contributor(s) and not of MDPI and/or the editor(s). MDPI and/or the editor(s) disclaim responsibility for any injury to people or property resulting from any ideas, methods, instructions or products referred to in the content.

## Article

# A Study on the Effect of Different Charge Structures on the Permeability Enhancement of Coal Seam Blasting

Yunfei Zuo <sup>1,\*</sup>, Jianyu Zhang <sup>2</sup>, Lidong Yang <sup>3</sup>, Feiran Wang <sup>1,\*</sup> and Zhengang Wang <sup>4</sup>

<sup>1</sup> School of Emergency Management and Safety Engineering, China University of Mining and Technology (Beijing), Beijing 100083, China

<sup>2</sup> School of Materials and Chemical Engineering, Bengbu University, Bengbu 233030, China; zhangjianyuxs@163.com

<sup>3</sup> Kailuan Energy Chemical Co., Ltd., Tangshan 063003, China; ylsyds067001@163.com

<sup>4</sup> Jinneng Holding Coal Group Luxin Company, Hami 839000, China; fengyedaowang@163.com

\* Correspondence: zuoyunfei-cumtb@outlook.com (Y.Z.); wangfeiran2003@163.com (F.W.)

**Abstract:** With the increasing depth of coal mining, the ground stress of coal seams rises, the gas content rises, and the permeability decreases, which is unfavorable to gas extraction and increases the possibility of gas accidents in coal mines. Blasting technology is often used to improve the permeability of coal seams and increase the effect of gas extraction, but it is difficult to control the blasting effect of ordinary flux coils, and the direction of the fissure and the degree of development of randomness, so it is important to study the effect of different flux coil structures on the blasting of coal seams to increase the permeability of the coal seam, in this paper, first of all, through the numerical simulation to analyze the effect of the blasting of the ordinary structure flux coils and the fissure change in the polygonal structure flux coils, and then make the experimental module. Then, we make the test module, build the test platform, and analyze the effect of blasting penetration of different drug coil structures by comparing the strain after blasting and the change in resistivity before and after blasting of two kinds of drug coil structures, and the results show that the polymerized drug coil can play the role of directional fracturing, and compared with the ordinary structure of the drug coil, the polymerized drug shows a better effect of fracturing and penetration increase.

**Keywords:** ordinary blasting; energy-concentrated blasting; charge structure; permeability enhancement by blasting; coal seam fractures

**Citation:** Zuo, Y.; Zhang, J.; Yang, L.; Wang, F.; Wang, Z. A Study on the Effect of Different Charge Structures on the Permeability Enhancement of Coal Seam Blasting. *Processes* **2024**, *12*, 1645. <https://doi.org/10.3390/pr12081645>

Academic Editor: Qingbang Meng

Received: 7 July 2024

Revised: 27 July 2024

Accepted: 2 August 2024

Published: 5 August 2024



**Copyright:** © 2024 by the authors. Licensee MDPI, Basel, Switzerland. This article is an open access article distributed under the terms and conditions of the Creative Commons Attribution (CC BY) license (<https://creativecommons.org/licenses/by/4.0/>).

## 1. Introduction

Blasting technology is an important engineering technique that utilizes the tremendous energy generated by explosions to break rocks or structures, achieving predetermined engineering purposes. The application of blasting technology is extensive, including mining [1,2], shaft construction, [3], highway tunnel construction [4–6], underwater demolition of structures [7,8], and urban subway construction [9].

Due to China's energy resource situation characterized by "abundant coal, scarce oil, and limited gas", coal will continue to play a dominant role in the country's energy structure for a long time [10]. As the depth of coal mining continues to increase [11], the geological conditions of coal seams have significantly changed compared to shallow coal seams. These changes include higher ground stress, reduced permeability, and increased gas content [12]. These alterations lead to higher mining costs and reduced safety. Therefore, in deep coal seam mining, enhancing coal seam permeability and reducing gas content are crucial for the safe production of coal mines.

Currently, techniques such as hydraulic fracturing [13], hydraulic punching [14,15], and deep-hole blasting [16] are commonly used to improve the permeability of high-gas, low-permeability coal seams.

Li et al. monitored and characterized the spatial shapes of fractures induced by hydraulic fracturing in coal seams underground [17]. Peng et al. analyzed the changes in the physical fields during the hydraulic fracturing process and proposed a multiscale, multimodal detection method based on variations in wave velocity and resistivity caused by fracture propagation to determine the effective range of hydraulic fracturing in coal seams [13]. Huang et al. studied the influence of stress fields, coal seam inclination, and fracturing fluid displacement on the expansion patterns of hydraulic fractures in interlayer coal, analyzing the formation process and expansion mechanism of hydraulic fractures in interlayer coal [18]. Zhang et al. developed a permeability model for coal-containing hydraulic support fractures and concluded that the higher the mass concentration of coal powder in the suspension and the larger the volume fraction of deposited coal powder, the lower the porosity and permeability of the support fractures [19].

Liu et al. studied the parameters of hydraulic punching. The study results indicate that the variation in the flaw parameters changes the propagation pattern of cracks, resulting in different compressive strengths [20]. Zhao et al. developed a multifield model that integrates stress, damage, gas diffusion, and gas flow in heterogeneous coal. They simulated coal damage induced by stress release around slot-shaped boreholes and conducted engineering field validation [21]. Shi et al. proposed an enhanced coalbed methane (ECBM) synergistic extraction technology based on the combination of high-frequency and gas injection displacement (GD), which can eliminate the stress concentration zones (SC) generated by hydraulic fracturing (HF) and improve gas extraction efficiency [22]. Liu et al. established a gas flow-geomechanics coupling model based on an equivalent fractured coal model. The stress release zone, plastic zone, and permeability enhancement zone around boreholes in soft coal are significantly larger than those in hard coal. The degree of stress concentration and permeability reduction in soft coal are also greater than in hard coal [23].

Chen et al. applied deep-hole pre-splitting blasting technology at the Xinji No. 2 Mine, which doubled the gas drainage volume, confirming the effectiveness of this technology in enhancing coal seam permeability [24]. Liu et al., through numerical simulations and theoretical analysis, concluded that blasting in hard rock induces numerous fractures and significant displacements due to the explosive stress. Additionally, the desorption gas flow from the top coal cavities and along the fractures improves the gas extraction capability [25].

Directional blasting technology uses concentrated explosive energy and high-penetration shaped jets formed during the explosion to induce rock fractures [26–28]. Shaped charge blasting technology employs grooving on both sides of the charge to achieve directional fracture control [26,27]. Directional energy-concentrated blasting technology is mostly used in rock fracturing research and related engineering applications [28–31]. Zhu et al. investigated the synergistic effect of shaped charge blasting and control hole [32], as well as the mechanical impact of shaped charge jet in the process of coal fracturing [26].

In summary, there are many technical methods to increase the permeability of high gas coal seams, and blasting still occupies an important position, but blasting technology also has its shortcomings, such as too large a range of crushing zone, random distribution of fissure direction. Energy-concentrated blasting has the effect of directional fracturing, this technology is mainly used in other fields, it is rare to apply it to increase the permeability of coal seams, so it is of great significance to carry out the research on blasting penetration enhancement by changing the structure of the pill rolls for high-gas and low-permeability coal seams.

## 2. Numerical Simulation Study of Permeability Enhancement by Blasting

Using the ANSYS/LS-DYNA (v. 18.2) three-dimensional numerical simulation analysis software, a coal-rock model with dimensions of 50 cm × 50 cm × 50 cm was established. The model includes a roof thickness of 15 cm, a coal seam thickness of 20 cm, and a floor thickness of 15 cm. The blasting hole is located at the center of the coal seam with a diameter of 20 mm. Non-reflective boundary conditions were applied to all faces of the model. The explosive material was modeled using the high-energy material model

(MAT\_HIGH\_EXPLOSIVE\_BURN) available in ANSYS/LS-DYNA., and the JWL equation was chosen as the equation of state for the explosive [33,34]. The JWL equation is as follows:

$$P = A\left(1 - \frac{\omega}{R_1 V}\right)e^{-R_1 V} + B\left(1 - \frac{\omega}{R_2 V}\right)e^{-R_2 V} + \frac{\omega E_0}{V} \quad (1)$$

In the equation: A and B are explosive characteristic parameters in GPa.  $R_1$ ,  $R_2$ , and  $\omega$  are dimensionless explosive characteristic parameters. P is the pressure generated by the explosive detonation in MPa.  $E_0$  is the initial internal energy ratio of the detonation products in GPa. V is the relative volume in  $m^3$ .

In numerical calculations, the parameters of the coal-rock layer are as shown in Table 1, and the specific parameters of the explosive during the simulation process are shown in Table 2.

**Table 1.** Physical and mechanical parameters of coal and rock.

Medium	Elastic Modulus E/(GPa)	Poisson's Ratio	Compressive Strengths/(MPa)	Tensile Strength/(MPa)
coal seam	4.5	0.38	1.06	0.2
rock stratum	9.6	0.24	7.34	0.5

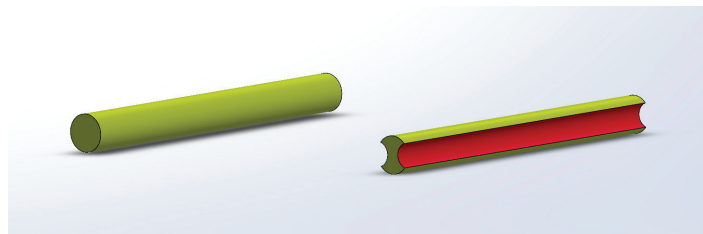
**Table 2.** Explosive material parameter.

$\rho/(g/cm^3)$	D/(m·s <sup>-1</sup> )	A/(GPa)	B/(GPa)	$R_1$	$R_2$	$\omega$	V
1.3	2800	0.36	28	4.15	0.95	0.3	1

The material of the shaped charge is copper, and the MAT\_JOHNSON\_COOK model is utilized. The EOS\_GRUNEISEN model is used to define its equation of state. The material parameters of the shaped charge are shown in Table 3, and the schematic diagram of different shaped charge structures is depicted in Figure 1.

**Table 3.** Material parameter table of shaped medicine rolls.

$\rho/(g/cm^3)$	C	$S_1$	$S_2$	$S_3$	$\gamma_0$	a	$E_0$	$V_0$
8.96	0.46	1.489	0	0	2.02	0.47	0	1



**Figure 1.** Schematic diagram of different shaped charge structures.

### 2.1. Comparative Analysis of Cloud Diagrams of Different Shaped Charge Structures after Blasting

Using the LS-Pre Post post-processing software to read the d3plot header file of the model and analyze the simulation results. Utilizing the post-processing software Fcomp to demonstrate the evolution process of effective stress near the blasting hole during the initial stage of blasting. The cloud diagrams of effective stress at different time points for two sets of models are shown in Figures 2 and 3.

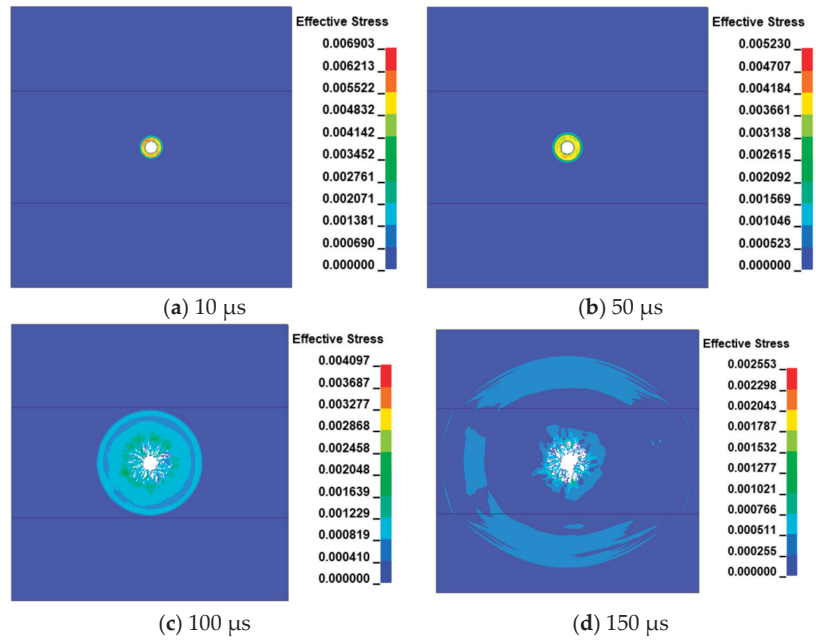


Figure 2. Stress cloud diagram at different time steps for conventional shaped charge.

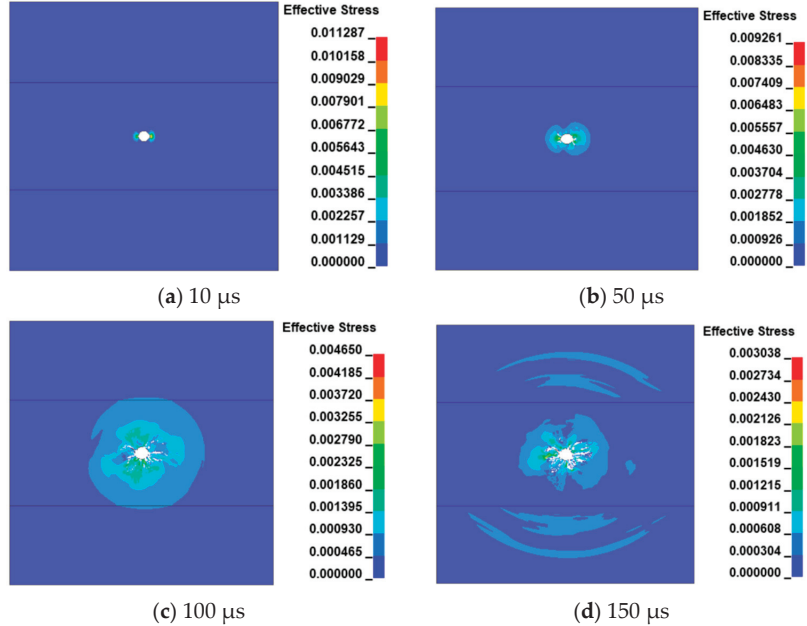


Figure 3. Stress cloud diagram at different time steps for shaped charge with energy concentration.

From Figure 2, it can be observed that after the conventional shaped charge detonates, the blasting shock wave first acts on the walls of the blasting hole, creating a large crushing zone around the blasting hole. As the stress wave continues to propagate, noticeable fracture development occurs around the blasting hole.

From Figure 3, it can be observed that after the detonation of the shaped charge with energy concentration, the energy focusing hood first forms a metal jet acting on the blasting hole, causing cracks to form in the direction of energy concentration, creating guiding fissures. The overall shape around the blasting hole appears to be elliptical.

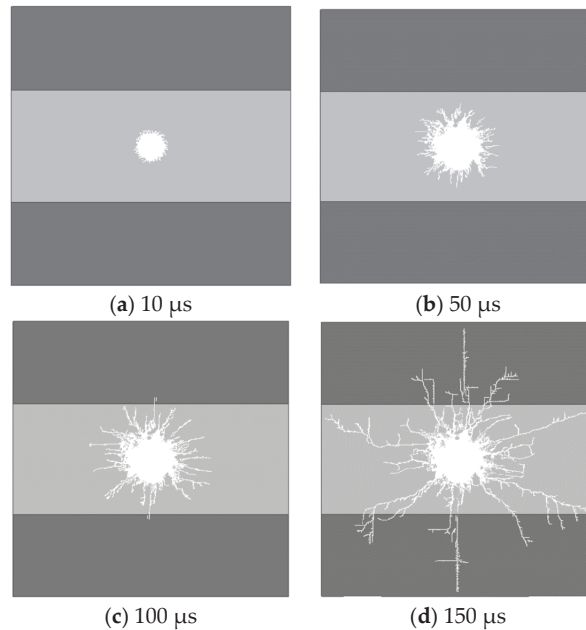
By comparing Figures 2 and 3, it can be seen that by changing the shaped charge structure, the evolution process of stress changes around the blasting hole can be altered. The fragmentation zone of the shaped charge with energy concentration is smaller than that of the conventional shaped charge. Therefore, the shaped charge with energy concentration can apply more energy to the generation and development of fractures.

## 2.2. Comparative Analysis of Fractures after Blasting with Different Shaped Charge Structures

Previously, we discussed the different stress cloud diagrams near the blasting hole due to different shaped charge structures during the blasting process. Through post-processing software, the development and expansion process of fractures within the model can be further displayed, as shown in Figures 4 and 5.

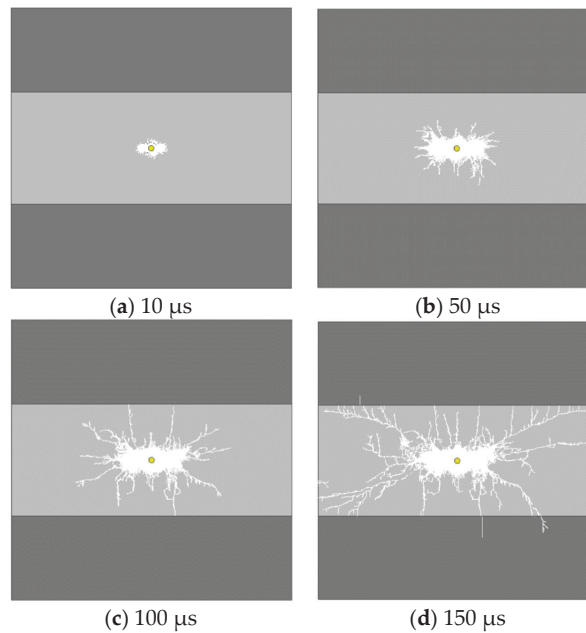
From Figure 4, it can be observed that after the detonation of the conventional shaped charge, fractures around the blasting hole develop sufficiently, but the direction of fractures is relatively random, exhibiting a radial pattern.

From Figure 5, it can be observed that after the detonation of the shaped charge with energy concentration, fractures initially occur in the direction of energy concentration around the blasting hole and continue to develop. The degree of fracture development in the direction of energy concentration is greater than in the non-energy concentration direction.



**Figure 4.** Development of fractures at different time steps for conventional shaped charge.





**Figure 5.** Development of fractures at different time steps for shaped charge with energy concentration.

Figures 4d and 5d were processed using Matlab to statistically calculate the fractal dimension of different roll structures, and the statistical results are shown in Table 4. According to the statistical results, it can be concluded that the fractal dimension of the coal seam is small and the fractal dimension of the top and bottom plate is large after blasting with ordinary drug rolls, and the fractal dimension of the coal seam is large and the fractal dimension of the top and bottom plate is small after blasting with polymerized drug rolls, which means that polymerized drug rolls enhance the destruction of the coal seam and reduce the damage of the top and bottom plate, and they can play a role of directional fracture effect.

**Table 4.** Fractal dimensions after blasting for different drug coil structures.

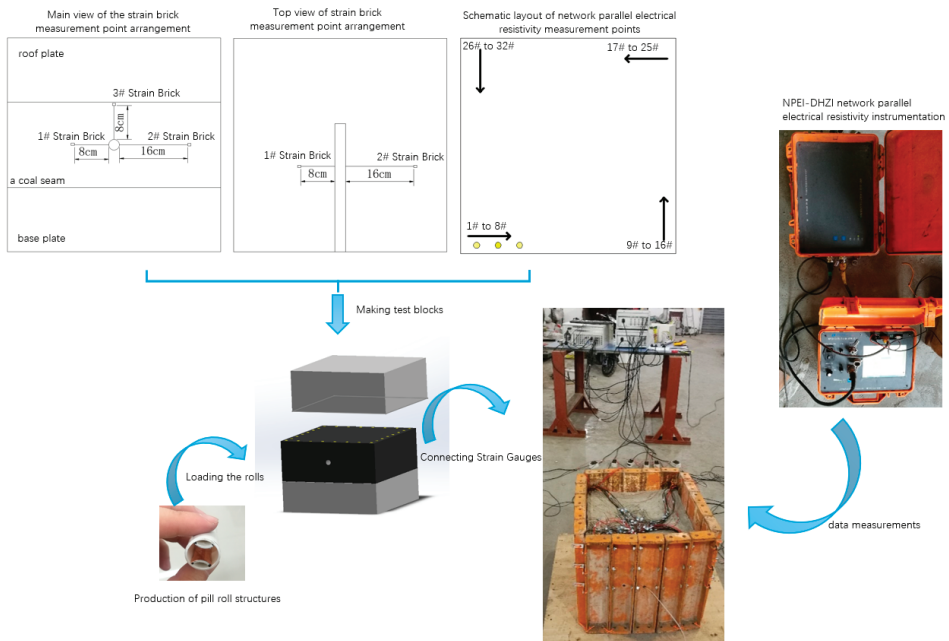
Structure of the Pill Rolls	Position	Fractal Dimension
Conventional Shaped Charge	Down (base plate)	1.1298
	Mid (a coal seam)	1.5397
	Up (roof plate)	1.1425
Shaped Charge with Energy Concentration	Down (base plate)	0.91685
	Mid (a coal seam)	1.5593
	Up (roof plate)	0.59612

Overall, from Figures 4 and 5, it can be concluded that changing the shaped charge structure can alter the degree of fracture development around the blasting hole. Shaped charges with energy concentration can play a role in directional fracturing.

### 3. Similar Simulation Study on Permeability Enhancement by Blasting

In order to investigate the permeability enhancement effect after blasting with different shaped charge structures, a similar simulation experiment on blasting-induced permeability enhancement was conducted. The experiment simulated a coal-rock formation at a certain location in the Pansan Mine, Anhui Province. After determining the similar materials and

proportions, an experimental platform was constructed, with the overall design scheme shown in in Figure 6. Firstly, the positions of strain collection points, parallel electrical method measurement points, and shaped charge structures were designed. Secondly, test blocks were fabricated according to the design scheme. Finally, blasting experiments were conducted, and data were collected. Before both blasting models completed the blasting tests, the NPEI-DHZI network parallel electrical resistivity instrumentation was used to conduct data measurements on the models after blasting.



**Figure 6.** Schematic of similar simulation experiment design for permeability enhancement by blasting.

According to the experimental plan, precast strain bricks measuring  $2\text{ cm} \times 2\text{ cm} \times 1\text{ cm}$  were prepared. During the production process of the blasting test blocks, the strain bricks were arranged in the coal seam. Specifically, strain brick 1 and strain brick 2 were horizontally placed on the left and right sides of the blasting hole, respectively, with the blasting hole as the axis. The distance between strain brick 1 and the blasting hole was 80 mm, while the distance between strain brick 2 and the blasting hole was 160 mm. Strain brick 3 was placed directly above the blasting hole, in the same plane as strain brick 1, and at a distance of 80 mm from the blasting hole.

Test module in the production of layered filling method, in the filling to the design of the height of the blast hole, pre-buried 25 mm diameter, length of 30 cm PVC pipe.

According to the experimental plan, the parallel electrical method measurement points were arranged at the interface between the coal seam and the roof. When filling the similar materials to the corresponding height, 32 measurement points were arranged in sequence, and each measurement point was numbered consecutively to prepare for the measurement of the electrical method before and after blasting.

The explosive charges used in this experiment are conventional shaped charges and directional energy-concentrated shaped charges. The main difference between them lies in the internal charge structure. For the directional energy-concentrated shaped charges, PVC pipes with a diameter of 20 mm, a wall thickness of 1 mm, and an inner diameter of

18 mm are used as the charge casing. The energy-concentrating hood inside the charge casing is made of 0.1 mm thick copper sheet. After the completion of the charge casing, it is filled with black powder and detonated using a detonator before the blasting experiment. Conventional shaped charges are also made using PVC pipes of the same specifications, with no special treatment to the internal structure.

After 28 days of curing in the similar model used for the experiment, the pre-embedded PVC pipes are removed to form blast holes. The depth of the holes is 30 cm, with a diameter of 25 mm. The experimentally self-made PVC pipe charges with a diameter of 20 mm are inserted into the blast holes, and a mixture of yellow clay, fine sand, and lime in certain proportions is used to seal the blast holes.

### 3.1. Comparative Analysis of Strain after Blasting with Different Shaped Charge Structures

The experiment collected strain data from different points using the SDY2107A super dynamic strain gauge. After organizing the collected strain data, it was plotted into Figures 7–9.

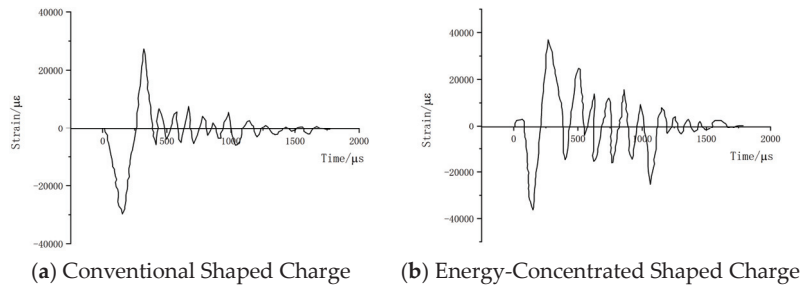


Figure 7. Strain curve for Point 1.

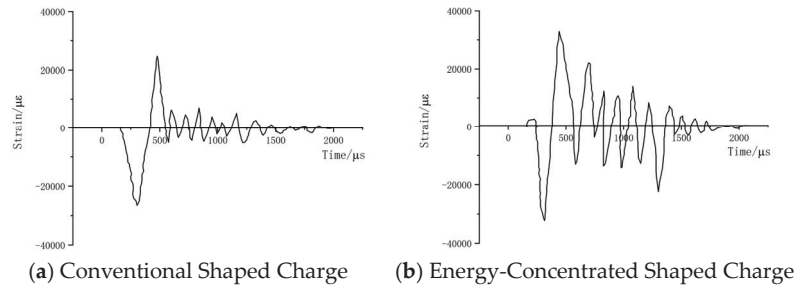


Figure 8. Strain curve for Point 2.

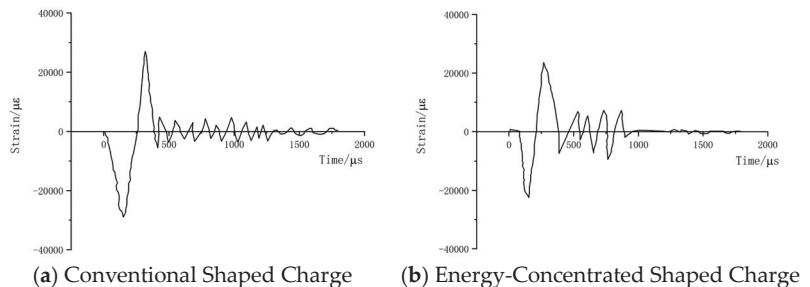


Figure 9. Strain curve for Point 3.

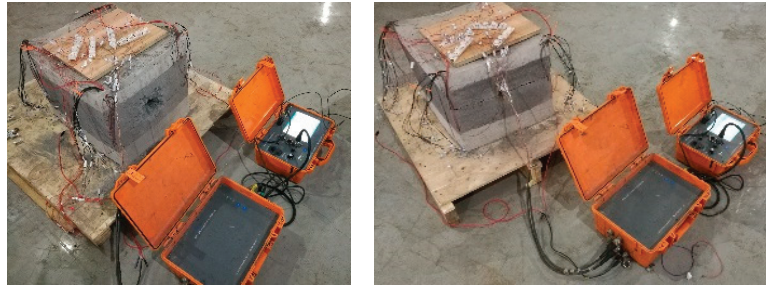
At Point 1 of the two similar model test blocks, a comparison between Figure 7a,b reveals that before 400  $\mu\text{s}$  is the dynamic loading phase of the blasting. During this phase, the coal body is mainly affected by the explosion stress wave, resulting in drastic changes in stress values. Both simulated test blocks showed two stress peaks during this phase. In the simulated test block filled with conventional shaped charges, the strain peak at Point 1 was  $-29,693 \mu\epsilon$ , while in the simulated test block filled with directional energy-concentrated shaped charges, the strain peak at Point 1 was  $-36,230 \mu\epsilon$ . It can be calculated that the strain peak in the horizontal energy-concentrating direction using directional energy-concentrated shaped charges is approximately 1.22 times that of conventional shaped charges. During the static loading phase, the coal body is mainly affected by the detonation gases, resulting in a smaller range of strain changes that gradually attenuate over time. In Figure 7a, the static loading phase of the model test block filled with conventional shaped charges is from 400 to 1000  $\mu\text{s}$ , with a duration of 600  $\mu\text{s}$ . In Figure 7b, the static loading phase of the model test block filled with directional energy-concentrated shaped charges is from 400 to 1200  $\mu\text{s}$ , with a duration of 800  $\mu\text{s}$ . This indicates that in the horizontal direction, the directional energy-concentrated shaped charges have a longer duration of detonation gas action compared to conventional shaped charges, extending the time by approximately 200  $\mu\text{s}$ , reflecting the ability of directional energy-concentrated shaped charges to guide more detonation gases towards the energy-concentrating direction.

At Point 2 of the two similar model test blocks, a comparison between Figure 8a,b reveals that before 600  $\mu\text{s}$  is the dynamic loading phase of the blasting. During this phase, the coal body is mainly affected by the explosion stress wave, resulting in drastic changes in stress values. Both simulated test blocks showed two stress peaks during this phase. In the simulated test block filled with conventional shaped charges, the strain peak at Point 2 was  $-26,511 \mu\epsilon$ , while in the simulated test block filled with directional energy-concentrated shaped charges, the strain peak at Point 2 was  $-32,304 \mu\epsilon$ . It can be calculated that the strain peak in the horizontal energy-concentrating direction using directional energy-concentrated shaped charges is approximately 1.22 times that of conventional shaped charges. During the static loading phase, in Figure 8a, the static loading phase of the model test block filled with conventional shaped charges is from 600  $\mu\text{s}$  to 1200  $\mu\text{s}$ , with a duration of 600  $\mu\text{s}$ . In Figure 8b, the static loading phase of the model test block filled with directional energy-concentrated shaped charges is from 600  $\mu\text{s}$  to 1400  $\mu\text{s}$ , with a duration of 800  $\mu\text{s}$ . This reflects that in the horizontal direction, directional energy-concentrated shaped charges can prolong the duration of detonation gas action, guiding more detonation gases towards the energy-concentrating direction.

At Point 3 of the two similar model test blocks, a comparison between Figure 9a,b reveals that before 400  $\mu\text{s}$  is the dynamic loading phase of the blasting. During this phase, the coal body is mainly affected by the explosion stress wave, resulting in drastic changes in stress values. Both simulated test blocks showed two stress peaks during this phase. In the simulated test block filled with conventional shaped charges, the strain peak at Point 3 was  $-28,974 \mu\epsilon$ , while in the simulated test block filled with directional energy-concentrated shaped charges, the strain peak at Point 3 was  $-22,378 \mu\epsilon$ . It can be observed that in the vertical direction, the strain peak of the conventional shaped charges is greater than that of the directional energy-concentrated shaped charges, approximately 1.29 times higher. During the static loading phase, in Figure 9a, the static loading phase of the model test block filled with conventional shaped charges is from 400  $\mu\text{s}$  to 1200  $\mu\text{s}$ , with a duration of 800  $\mu\text{s}$ . In Figure 9b, the static loading phase of the model test block filled with directional energy-concentrated shaped charges is from 400  $\mu\text{s}$  to 900  $\mu\text{s}$ , with a duration of 500  $\mu\text{s}$ . This indicates that in the vertical direction, the duration of detonation gas action for directional energy-concentrated shaped charges is shorter than that of conventional shaped charges, approximately 300  $\mu\text{s}$  less, indicating a weaker ability of energy-concentrated shaped charges to promote coal body fracture development in the non-energy-concentrating direction.

### 3.2. Analysis of Parallel Electrical Resistivity Instrumentation after Blasting with Different Cartridge Structures

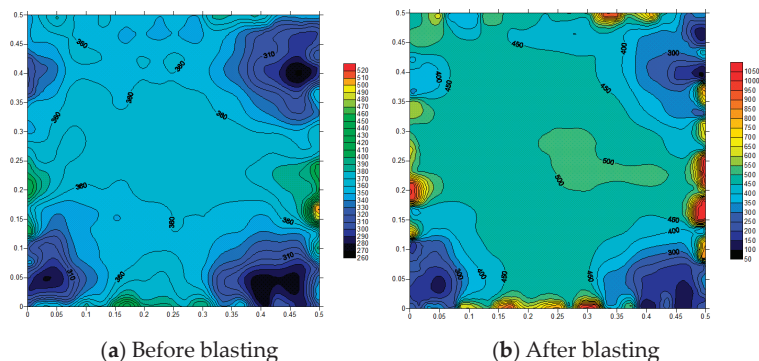
After both blasting models completed the blasting tests, the NPEI-DHZI network parallel electrical resistivity instrumentation was used to conduct data measurements on the models after blasting, as shown in Figure 10. The collected data were exported using software and decrypted using the corresponding decryption software.



**Figure 10.** Data collection using electrical resistivity instrument.

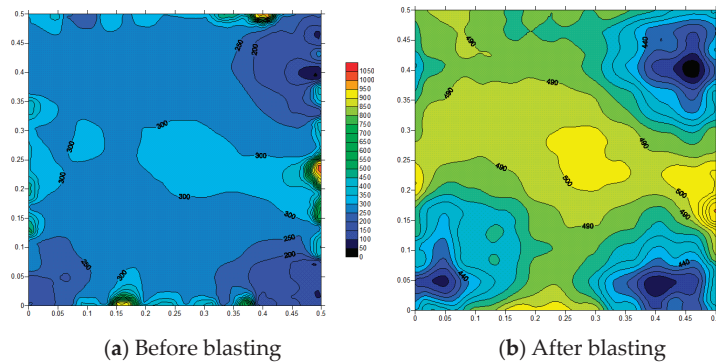
The decrypted data were imported into the WBD2.0 (Network Parallel Electrical Resistivity Processing System) software for slicing and extraction of data slices at a depth of 15 cm below the electrical resistivity instrument measurement points, corresponding to the XY plane of the blasting hole. The extracted data files were then processed in Surfer software to generate contour maps of electrical resistivity.

As shown above, where Figure 11a depicts the contour map of resistivity before blasting for the block with ordinary explosive charge, and Figure 11b shows the contour map of resistivity after blasting for the block with ordinary explosive charge. From Figure 11a, it can be observed that the resistivity in most areas is approximately 360  $\Omega\cdot\text{m}$ , distributed relatively uniformly. From Figure 11b, it can be seen that after blasting, the maximum resistivity at the center position is 500  $\Omega\cdot\text{m}$ , while the resistivity values around it are approximately 450  $\Omega\cdot\text{m}$ . Comparing Figure 11a,b, it is evident that after blasting with ordinary explosive charge, a crushed zone appears near the blasting hole. Therefore, the resistivity value at the center position is higher than that of its surroundings. The resistivity at the center position has increased by approximately 140  $\Omega\cdot\text{m}$  after blasting, representing an increase of approximately 38.9%. The resistivity around the center has increased by approximately 90  $\Omega\cdot\text{m}$ , representing an increase of approximately 38.9%. There is a slight increase in resistivity in the four corner areas, but the variation is relatively small compared to other positions.



**Figure 11.** Contour map of electrical resistivity of test block after conventional explosive detonation.

As shown above, Figure 12a displays the contour map of resistivity before blasting for the test block filled with directional energy-aggregated explosive charges, while Figure 12b shows the contour map of resistivity after blasting for the same block. From Figure 12a, it can be observed that the resistivity at the center of this plane is  $300 \Omega \cdot m$ , with values ranging between  $250 \Omega \cdot m$  and  $300 \Omega \cdot m$  in its vicinity. In Figure 12b, after blasting, the resistivity at the center of this plane is  $500 \Omega \cdot m$ , with surrounding resistivity ranging between  $480 \Omega \cdot m$  and  $490 \Omega \cdot m$ . By comparing Figure 12a,b, it is evident that the resistivity at the center of this plane has increased by approximately  $200 \Omega \cdot m$  after blasting, representing an increase of approximately 66.7%. The resistivity in the surrounding area has increased by approximately  $280 \Omega \cdot m$ , with an increase ranging from 93.3% to 112%, indicating sufficient development of fractures around the blasting hole. Although there is an increase in resistivity in the four corner regions, it is relatively smaller compared to the center. By comparing Figures 11b and 12b, it can be seen that there is a significant difference in the impact of the two types of charge structures on the surrounding fracture zones after blasting, with the directional energy-aggregated explosive charge demonstrating superior effectiveness in promoting fracture development in the direction of energy aggregation compared to the ordinary explosive charge.



**Figure 12.** Contour map of resistivity of the test block after directional energy-aggregated explosive charge blasting.

#### 4. Conclusions

In this study, the following conclusions were obtained from the previous numerical simulations and blasting tests:

- (1) Through numerical simulations and comparing the stress and fracture conditions after blasting with two types of explosive charges, it can be concluded that directional energy-aggregated explosive charges can achieve directional fracturing, reduce energy loss in the crushing zone, and promote higher degree of fracture development in the direction of energy aggregation.
- (2) Analysis of data at position 1# of the two test blocks leads to the following conclusions: During the dynamic loading phase, the coal body is mainly affected by the explosion stress wave, resulting in drastic changes in stress values. The peak strain value in the horizontal energy aggregation direction using directional energy-aggregated explosive charges is approximately 1.22 times that of ordinary explosive charges. Analysis of data at position 2# indicates that directional energy-aggregated explosive charges can prolong the action time of the explosion gas in the horizontal direction. Analysis of data at position 3# reveals that in the non-energy aggregation direction, the peak strain value of ordinary explosive charges is greater than that of directional energy-aggregated explosive charges, indicating a weakening effect of directional energy-aggregated explosive charges. The action time of directional energy-aggregated

- explosive charges in the non-energy aggregation direction is shorter than that of ordinary explosive charges.
- (3) Analysis of resistivity data inverted by the electrical resistivity instrument reveals that for the test block filled with ordinary explosive charges, the resistance jump amplitude on the selected plane ranges from 90  $\Omega \cdot m$  to 140  $\Omega \cdot m$ . For the test block filled with directional energy-aggregated explosive charges, the resistance jump amplitude on the selected plane ranges from 180  $\Omega \cdot m$  to 200  $\Omega \cdot m$ . Comparing the resistivity contour maps before and after the action of two different explosive charges, it can be concluded that directional energy-aggregated explosive charges are more effective in promoting fracture development in the direction of energy aggregation than ordinary explosive charges.
  - (4) Compared to ordinary explosive charges, directional energy-aggregated explosive charges demonstrate better directional fracturing effects, promote higher degree of coal seam fracture development, and are conducive to increasing coal seam permeability, thereby improving gas extraction efficiency.
  - (5) The gas content of the coal seam and gas pressure is also a factor that affects the effect of blasting penetration, limited by the test conditions, the research carried out in this paper will be simplified, to be continued in the future research.

**Author Contributions:** Y.Z.: Writing—original draft. J.Z.: Visualization. L.Y.: Writing—review & editing. F.W.: Writing—review & editing. Z.W.: Writing—review & editing. All authors have read and agreed to the published version of the manuscript.

**Funding:** This research received no external funding.

**Data Availability Statement:** The original contributions presented in the study are included in the article, further inquiries can be directed to the corresponding authors.

**Conflicts of Interest:** Author Lidong Yang was employed by the company Kailuan Energy Chemical Co., Ltd. Author Zhengang Wang was employed by the company Jinneng Holding Coal Group Luxin Company. The remaining authors declare that the research was conducted in the absence of any commercial or financial relationships that could be construed as a potential conflict of interest.

## References

1. Khademian, A. Optimization of blasting patterns in Esfordi phosphate mine using hybrid analysis of data envelopment analysis and multi-criteria decision making. *Eng. Appl. Artif. Intell.* **2024**, *133*, 108061. [CrossRef]
2. Nayak, N.P.; Jain, A.; Ranjan Mahapatra, S. Application of Mine Excellence software in flyrock prediction & mitigation. *Mater. Today Proc.* **2022**, *48*, 1271–1276.
3. Gan, E.C.J.; Remennikov, A. Blast propagation and hazard mapping outside coal mine tunnels and shafts. *Tunn. Undergr. Space Technol.* **2024**, *148*, 105749. [CrossRef]
4. Li, C.; Zhou, J. Prediction and optimization of adverse responses for a highway tunnel after blasting excavation using a novel hybrid multi-objective intelligent model. *Transp. Geotech.* **2024**, *45*, 101228. [CrossRef]
5. Li, X.; Liu, K.; Sha, Y.; Yang, J.; Hong, Z. Experimental and numerical investigation on rock fracturing in tunnel contour blasting under initial stress. *Int. J. Impact Eng.* **2024**, *185*, 104844. [CrossRef]
6. Song, S.; Li, S.; Li, L.; Shi, S.; Zhou, Z.; Liu, Z.; Shang, C.; Sun, H. Model test study on vibration blasting of large cross-section tunnel with small clearance in horizontal stratified surrounding rock. *Tunn. Undergr. Space Technol.* **2019**, *92*, 103013. [CrossRef]
7. Kumar Modi, S.; Murthy, V.M.S.R. Assessment of blasting impacts in underwater concrete berth demolition and development of a Hybrid Controlled Blasting (HCB) technique—A case study. *Structures* **2022**, *40*, 420–433. [CrossRef]
8. Pana, I.-F.; Puica, C.; Goga, D.-A.; Nuta, I. Numerical Studies Regarding Underwater Detonation. *Procedia Econ. Financ.* **2015**, *32*, 946–951. [CrossRef]
9. Shi, H.; Jiang, N.; Zhou, C.; Zhnag, Y.; Yao, Y.; Zhou, W.; Cai, Z. Safety assessment of ancient buddhist pagoda induced by underpass metro tunnel blasting vibration. *Eng. Fail. Anal.* **2023**, *145*, 107051. [CrossRef]
10. Chong, C.H.; Zhou, X.; Zhang, Y.; Ma, L.; Bhutta, M.S.; Li, Z.; Ni, W. LMDI decomposition of coal consumption in China based on the energy allocation diagram of coal flows: An update for 2005–2020 with improved sectoral resolutions. *Energy* **2023**, *285*, 129266. [CrossRef]
11. Kang, Y.; Liu, Q.; Gong, G.; Wang, H. Application of a combined support system to the weak floor reinforcement in deep underground coal mine. *Int. J. Rock Mech. Min.* **2014**, *71*, 143–150. [CrossRef]

12. Qiao, Z.; Li, C.; Wang, Q.; Xu, X. Principles of formulating measures regarding preventing coal and gas outbursts in deep mining: Based on stress distribution and failure characteristics. *Fuel* **2024**, *356*, 129578. [CrossRef]
13. Peng, Y.; Qiu, L.; Zhu, Y.; Liu, Q.; Song, D.; Cheng, X.; Wang, C.; Liu, Y.; Sun, Q. Multi-scale multivariate detection method for the effective impact range of hydraulic fracturing in coal seam. *J. Appl. Geophys.* **2023**, *215*, 105124. [CrossRef]
14. Zhang, H.; Cheng, Y.; Deng, C.; Jiang, J.; Zhang, L.; Yan, X.; Guo, J.; Wang, S. Stress-unloading and gas migration improvement mechanism in the soft and hard interbedded coal seam using directional hydraulic flushing technology. *Int. J. Min. Sci. Technol.* **2023**, *33*, 1165–1179. [CrossRef]
15. Lu, T.K.; Yu, H.; Zhou, T.Y.; Mao, J.S.; Guo, B.H. Improvement of methane drainage in high gassy coal seam using waterjet technique. *Int. J. Coal Geol.* **2009**, *79*, 40–48. [CrossRef]
16. Feng, C.; Zegong, L. Intensified extracting gas and rapidly diminishing outburst risk using deep-hole presplitting blast technology before opening coal seam in shaft influenced by fault. *Procedia Eng.* **2011**, *26*, 418–423. [CrossRef]
17. Li, N.; Fang, L.; Sun, W.; Zhang, X.; Chen, D. Evaluation of Borehole Hydraulic Fracturing in Coal Seam Using the Microseismic Monitoring Method. *Rock Mech. Rock Eng.* **2021**, *54*, 607–625. [CrossRef]
18. Huang, L.; Li, B.; Wu, B.; Li, C.; Wang, J.; Cai, H. Study on the extension mechanism of hydraulic fractures in bedding coal. *Theor. Appl. Fract. Mech.* **2024**, *131*, 104431. [CrossRef]
19. Zhang, X.; Hu, S.; Feng, G.; Li, G.; Li, S.; Sun, X.; Guo, S.; Chen, Z. A mathematical model for the permeability evolution of coal-bearing hydraulic propped fractures. *Adv. Powder Technol.* **2024**, *35*, 104373. [CrossRef]
20. Liu, T.; Lin, B.; Zheng, C.; Zou, Q.; Zhu, C.; Yan, F. Influence of coupled effect among flaw parameters on strength characteristic of precracked specimen: Application of response surface methodology and fractal method. *J. Nat. Gas Sci. Eng.* **2015**, *26*, 857–866. [CrossRef]
21. Zhao, Y.; Lin, B.; Liu, T.; Kong, J.; Zheng, Y. Gas flow in hydraulic slotting-disturbed coal seam considering stress relief induced damage. *J. Nat. Gas Sci. Eng.* **2020**, *75*, 103160. [CrossRef]
22. Shi, Y.; Lin, B.; Liu, T.; Zhao, Y.; Hao, Z. Synergistic ECBM extraction technology and engineering application based on hydraulic flushing combing gas injection displacement in low permeability coal seams. *Fuel* **2022**, *318*, 123688. [CrossRef]
23. Liu, T.; Lin, B.; Fu, X.; Zhao, Y.; Gao, Y.; Yang, W. Modeling coupled gas flow and geomechanics process in stimulated coal seam by hydraulic flushing. *Int. J. Rock Mech. Min.* **2021**, *142*, 104769. [CrossRef]
24. Chen, X.; Xue, S.; Yuan, L. Coal seam drainage enhancement using borehole presplitting blasting technology—A case study in Huainan. *Int. J. Min. Sci. Technol.* **2017**, *27*, 771–775. [CrossRef]
25. Liu, J.; Liu, Z.; Xue, J.; Gao, K.; Zhou, W. Application of deep borehole blasting on fully mechanized hard top-coal pre-splitting and gas extraction in the special thick seam. *Int. J. Min. Sci. Technol.* **2015**, *25*, 755–760. [CrossRef]
26. Zhu, F.; Liu, Z.; Huang, A.-C. The shaped blasting experimental study on damage and crack evolution of high stress coal seam. *J. Loss Prev. Process Ind.* **2023**, *83*, 105030. [CrossRef]
27. Yin, Y.; Sun, Q.; Zou, B.; Mu, Q. Numerical Study on an Innovative Shaped Charge Approach of Rock Blasting and the Timing Sequence Effect in Microsecond Magnitude. *Rock Mech. Rock Eng.* **2021**, *54*, 4523–4542. [CrossRef]
28. Li, Q.; Gao, Z.-H.; Xu, W.-L.; Wang, K.; Liu, S.; Ran, G.-F.; Hu, Y. Experimental research on the dynamic propagation process of mode I cracks in the rock under directional fracture blasting using the strain gauge method. *Eng. Fract. Mech.* **2020**, *235*, 107113. [CrossRef]
29. Xiao, J.; Zhang, X.; Guo, Z.; Wang, H. Enhanced Damage Effects of Multi-Layered Concrete Target Produced by Reactive Materials Liner. *Propellants Explos. Pyrotech.* **2018**, *43*, 955–961. [CrossRef]
30. Ma, T.-b.; Liu, J.; Wang, Q. Influence of shaped charge structure parameters on the formation of linear explosively formed projectiles. *Def. Technol.* **2022**, *18*, 1863–1874. [CrossRef]
31. Xie, L.X.; Lu, W.B.; Zhang, Q.B.; Jiang, Q.H.; Wang, G.H.; Zhao, J. Damage evolution mechanisms of rock in deep tunnels induced by cut blasting. *Tunn. Undergr. Space Technol.* **2016**, *58*, 257–270. [CrossRef]
32. Zhu, F.H.; Liu, Z.G.; Huang, A.C. Study on the coupling mechanism of shaped blasting and empty hole to crack coal body. *Process Saf. Environ.* **2023**, *175*, 644–653. [CrossRef]
33. Zhu, F.H.; Liu, Z.G.; Zuo, Y.F.; Yang, N. Damage and failure characteristics of coal and surrounding rock under shaped blasting. *Process Saf. Environ.* **2023**, *176*, 56–64. [CrossRef]
34. Jayasinghe, L.B.; Shang, J.; Zhao, Z.; Goh, A.T.C. Numerical investigation into the blasting-induced damage characteristics of rocks considering the role of in-situ stresses and discontinuity persistence. *Comput. Geotech.* **2019**, *116*, 103207. [CrossRef]

**Disclaimer/Publisher’s Note:** The statements, opinions and data contained in all publications are solely those of the individual author(s) and contributor(s) and not of MDPI and/or the editor(s). MDPI and/or the editor(s) disclaim responsibility for any injury to people or property resulting from any ideas, methods, instructions or products referred to in the content.



## Article

# Research on Gas Drainage Pipeline Leakage Detection and Localization Based on the Pressure Gradient Method

Huijie Zhang <sup>1,2,3</sup>, Maoliang Shen <sup>2,3,\*</sup>, Zhonggang Huo <sup>1,2,3</sup>, Yibin Zhang <sup>2</sup>, Longyong Shu <sup>2,3</sup> and Yang Li <sup>2,3</sup>

<sup>1</sup> College of Safety Science and Engineering, Liaoning Technical University, Fuxin 123000, China; zhjwell@126.com (H.Z.); huozhonggang@sohu.com (Z.H.)

<sup>2</sup> China Coal Research Institute, Beijing 100013, China; zhangyibin93@163.com (Y.Z.); slyccri@163.com (L.S.); liyanglg@163.com (Y.L.)

<sup>3</sup> State Key Laboratory of Coal Mine Disaster Prevention and Control, Beijing 100013, China

\* Correspondence: shensml2010@163.com

**Abstract:** Pipeline leakage seriously threatens the efficient and safe gas drainage in coal mines. To achieve the accurate detection and localization of gas drainage pipeline leakages, this study proposes a gas drainage pipeline leakage detection and localization approach based on the pressure gradient method. Firstly, the basic law of gas flow in the drainage pipeline was analyzed, and a pipeline network resistance correction formula was deduced based on the pressure gradient method. Then, a drainage pipeline model was established based on the realizable  $k-\varepsilon$  turbulence model, and the pressure and flow velocity distribution during pipeline leakage under different leakage degrees, leakage locations, and pipeline negative pressures were simulated and analyzed, thus verifying the feasibility of the pipeline leakage detection and localization method. It is concluded that the positioning errors of pipeline leakage points under different leakage degrees, different leakage positions, and different pipeline negative pressures were 0.88–1.08%, 0.88–1.49%, and 0.68–0.88%, respectively. Finally, field tests were conducted in the highly located drainage roadway 8421 of the Fifth Mine of Yangquan Coal Industry Group to verify the accuracy of the proposed pipeline leakage detection and localization method, and the relative error was about 8.2%. The results show that with increased pipeline leakage hole diameters, elevated pipeline negative pressures, and closer leakage positions to the pipeline center, the relative localization error was smaller, the localization accuracy was higher, and the stability was greater. The research results could lay the foundation for the fault diagnosis and localization of coal mine gas drainage pipeline networks and provide technical support for safe and efficient coal mine gas drainage.

**Keywords:** gas drainage; leakage detection; leakage localization; pipeline leakage; pressure gradient method

**Citation:** Zhang, H.; Shen, M.; Huo, Z.; Zhang, Y.; Shu, L.; Li, Y. Research on Gas Drainage Pipeline Leakage Detection and Localization Based on the Pressure Gradient Method. *Processes* **2024**, *12*, 1590. <https://doi.org/10.3390/pr12081590>

Academic Editor: Adam Smoliński

Received: 21 June 2024

Revised: 22 July 2024

Accepted: 26 July 2024

Published: 29 July 2024



**Copyright:** © 2024 by the authors. Licensee MDPI, Basel, Switzerland. This article is an open access article distributed under the terms and conditions of the Creative Commons Attribution (CC BY) license (<https://creativecommons.org/licenses/by/4.0/>).

## 1. Introduction

The occurrence conditions of coal seams in China are extremely complex. With the continuous increase in mining depth in recent years, the gas content and gas pressure of the working seam gradually increased, and the risks of gas emission quantity and coal and gas outburst grew continuously [1–3]. Gas accidents remain the greatest threat to coal mine safety.

Relevant policies and regulations clearly stipulate that coal mines with high gas contents and outburst risks must be equipped with a ground permanent gas extraction system or downhole temporary gas extraction system. Coal mine gas control practice in China shows that coal mine gas drainage is an effective and key measure to achieve coal seam gas control, effectively reduce coal seam gas content, and eliminate coal mine gas accidents [4–8]. The gas drainage pipeline network composed of drainage pipelines is an important part of coal mine gas drainage systems. Most of the gas drainage pipelines at the coal mine site are laid in the return airways with harsh environments and poor maintenance,

and the pipeline surface and the flange connection between pipelines are susceptible to factors such as roadway deformation, flooding, and corrosion, leading to pipeline corrosion damage, and bending deformation that, in turn, cause pipeline leakage [9,10]. In the case of gas leakage, the negative pressure in the gas drainage pipeline sucks in ambient air, thus decreasing the gas concentration and increasing oxygen content, which not only reduces the gas drainage efficiency, but also increases the risk of gas explosion. Therefore, gas drainage pipeline leakage detection and localization is an important prerequisite for safe and efficient gas drainage.

At present, insufficient attention is devoted to the leakage detection problem of underground gas drainage pipelines in China, with most of the mines still relying on manual inspection [11]. However, the length and complexity of the drainage pipeline gradually increased with the continuous increase in the mining depth, resulting in practical problems such as long detection time, large manpower consumption, and low efficiency. Therefore, the accurate fault diagnosis and localization of gas drainage pipelines using gas drainage multivariate information attracted the attention of researchers, and certain results were achieved.

Early pipeline leakage detection and localization technologies mainly focused on natural gas and oil transportation. According to previous data, the existing pipeline leakage detection and localization methods can be divided into two major categories: software-based methods and hardware-based methods [12–15]. Yin et al. [16] proposed a pipeline leakage detection algorithm based on the acoustic propagation characteristics of transverse and longitudinal waves to achieve non-destructive pipeline leakage detection and localization. Thang et al. [17] proposed a reliable method to detect leaks and recognize their various sizes in a gas pipeline based on the spectral portrait of acoustic emission (AE) signals. He et al. [18] proposes an improved model-based pipeline leakage detection and localization method based on compressed sensing (CS) and an event-triggered (ET) particle filter (ET-PF). Zhou et al. [19] proposed a gas extraction pipeline leakage diagnosis and location method based on the Simulated Annealing (SA) and Particle Swarm Optimization (PSO) collaborative optimization Back Propagation neural network. Zuo et al. [20] analyzed the research progress of pipeline leakage detection technology based on optical fiber sensing technology firstly and proposes an algorithm for monitoring gas pipeline leakage based on distributed optical fiber acoustic sensing (DAS) system. The algorithm can obtain the time domain signal characteristics of pipeline leakage to identify leaks, locate the leak points through frequency domain. Zhang et al. [21] proposed a novel hybrid technique based on the real-time transient modeling method and negative pressure wave method. An experimental bench for straight pipelines is set up to evaluate the performance of the proposed hybrid technique, and corresponding experimental test programs for gas leakage detection and location are designed and conducted. A mathematical model for the transient flow in pipelines was established and solved under different boundary conditions. Liu et al. [22] found that when negative pressure wave (NPW) signals are used to locate pipeline leaks, noise will increase the error of location estimation. Thus, an adaptive noise reduction method based on variational mode decomposition (ANR-VMD) was proposed to improve the accuracy of leak location. In terms of leakage detection and localization of coal mine gas drainage pipelines, She et al. [23] proposed a mathematical model for the gas flow state and leakage diagnosis of underground gas drainage pipelines. By experimentally studying the leakage characteristics of the main pipeline from the flow rate, oxygen concentration, and negative pressure aspects, Pei [11] proposed a multi-parameter comprehensive diagnosis method for main gas drainage pipeline leakage monitoring and a localization algorithm based on pressure distribution state. Lei et al. [24] proposed a method to evaluate the leakage and blockage state of the gas drainage pipeline based on the descending curve slope of the pipeline pressure square. Mao et al. [25] verified the principle of the pressure gradient method for pipeline leakage detection and used the on-site pipeline segmentation negative pressure monitoring method to conduct leakage detection analysis on the mine gas drainage system. Zhang et al. [26] combined the flow balance method,

negative pressure wave method, and wavelet noise reduction principle to propose a leakage localization method for underground main drainage pipelines based on the transient model and verified its accuracy through simulation analysis. Guo et al. [27] employed ultrasonic detection to detect the turbulence generated at the underground gas pipeline leakage and achieved underground drainage pipeline leakage localization by detecting the strength and source of the ultrasonic signal. Based on the OpenFOAM platform, Cai et al. [28] proposed a multi-factor gas drainage pipeline leakage and diffusion model capable of analyzing the leakage and diffusion characteristics within the pipeline and verified its practicality using data measured at the coal mine site. Zhao et al. [29] established a leakage diagnostic method for gas extraction pipelines based on the pressure gradient method and built a gas drainage pipeline network experimental platform for single pipeline blockage and leakage tests investigating the effect of main pipeline leakage on the negative pressure of branch pipelines and discussing the influence of the negative pressure changes of the temporary pumping station on the parallel pipelines. Cui et al. [30] proposed a cellular automata (CA) model to locate gas drainage pipeline leakages. With the rapid development of computer science and technology, machine learning methods were partially applied in pipeline leakage detection. Rodolfo Pinheiro da Cruz et al. [31] proposed a technique that combines acoustic sensors and machine learning algorithms to identify and locate leaks in low-pressure gas pipelines. Ullah Niamat et al. [32] proposed a machine learning-based platform for using acoustic emission (AE) sensor channel information to detect leaks of various pinhole sizes. Based on the principle of negative pressure wave leak detection, Lin [33] proposes a variety of deep learning methods for pipeline leakage detection. A negative pressure wave leakage detection method based on wavelet threshold denoising and deep belief network (Wavelet-DBN) is adopted to further improve the accuracy of oil pipeline leakage detection.

At present, some achievements were made in coal mine gas drainage pipeline leakage detection and localization methods. However, the existing studies on accurate identification and localization of gas drainage pipeline leakages are not mature, warranting further in-depth research. Moreover, inside the gas drainage pipeline is a negative pressure environment, and the gas flow state in the pipeline is relatively complex. The gas flow state of the pipeline should be considered to further improve the accuracy of leakage detection and localization.

In light of the above, this study employs the pressure gradient method of the steady-state model to address the issue. Firstly, the basic law of gas flow in the drainage pipeline is thoroughly analyzed. Then, a method for calculating the pipeline network resistance is proposed based on the pressure gradient method. Further, the feasibility of the pressure gradient method for gas drainage pipeline leakage detection and localization under negative pressure is verified via numerical simulation, and the accuracy of the proposed method is verified via downhole field tests. The research results could lay the theoretical foundation for the fault diagnosis and localization of coal mine gas drainage pipeline networks and provide technical support for safe and efficient coal mine gas drainage.

## 2. Analysis of the Basic Law of Gas Flow in the Drainage Pipeline

### 2.1. Basic Equations of Gas Flow in the Pipeline

#### 2.1.1. Pipeline Gas Flow Continuity Equation

Regarding the gas flow in the drainage pipeline, this study ignores the effects of changes in the vertical upward body forces on the average flow velocity in the pipeline and considers it a one-dimensional linear flow. Thus, the pipeline fluid continuity differential equation is expressed in Equation (1) [34]:

$$\frac{\partial \rho}{\partial t} + \frac{\partial(\rho u)}{\partial L} = 0 \quad (1)$$

where  $u$  is the flow velocity (m/s);  $t$  is the time (s);  $L$  is the pipeline length (m); and  $\rho$  is the density of the gas mixture (kg/m<sup>3</sup>).

### 2.1.2. Pipeline Gas Flow Energy Equation

According to the law of conservation of energy, the energy of the gas remains constant as it flows through the pipeline, and its energy equation is expressed in Equation (2) [35]:

$$\frac{\partial}{\partial t} \left[ \rho \left( u + \frac{v^2}{2} + gs \right) \right] + \frac{\partial}{\partial x} \left[ \rho v \left( h + \frac{v^2}{2} + gs \right) \right] + \rho v \frac{\partial Q}{\partial x} = 0 \quad (2)$$

where  $Q$  is the amount of heat emitted per unit mass of the gas to the outside world (J/kg);  $u$  is the internal energy of the gas (J/kg);  $h$  is the enthalpy of the gas (J/kg); and  $s$  is the height of the pipeline (m).

### 2.1.3. Pipeline Gas Flow Motion Equation

According to the law of conservation of momentum, the resultant force acting on the system from the external is the momentum change rate of the system, and the motion equation of the drainage pipeline built based on the principle of fluid dynamics is expressed in Equation (3):

$$\frac{\partial(\rho v)}{\partial t} + \left( \frac{\partial(\rho v^2)}{\partial x} \right) + g\rho \sin \theta + \frac{\partial p}{\partial x} + \frac{\lambda}{D} \frac{v^2}{2} \rho = 0 \quad (3)$$

where  $g$  is the gravitational acceleration ( $\text{m/s}^2$ );  $\lambda$  is the friction coefficient;  $p$  is the gas pressure in the pipeline (Pa);  $D$  is the pipeline diameter (m); and  $\theta$  is the angle between the pipeline and the horizontal plane (rad).

## 2.2. Pipeline Network Resistance Calculation Based on the Pressure Gradient Method

According to the fluid mechanics energy equation and dimensional analysis theory, the pipeline frictional resistance reflected by the wind flow pressure energy loss can be expressed as follows whether the flow is laminar or turbulent:

$$H = \lambda \frac{L}{d} \frac{v^2}{2} \rho \quad (4)$$

where  $H$  is the pipeline pressure loss (Pa);  $\lambda$  is the frictional resistance coefficient of the pipeline (dimensionless);  $L$  is the pipeline length (m);  $d$  is the inner diameter of the circular pipes or equivalent diameter of non-circular pipes (m);  $\rho$  is the density of the gas in the pipeline ( $\text{kg/m}^3$ ); and  $v$  is the average gas flow velocity in the pipeline (m/s).

Substituting  $v = \frac{4Q}{\pi d^2}$  into (4) yields:

$$H = \lambda \frac{L}{d} \frac{16Q^2}{2\pi^2 d^4} \rho = 0.81057 \lambda \frac{LQ^2}{d^5} \rho \quad (5)$$

where  $Q$  is the gas flow in the pipeline ( $\text{m}^3/\text{s}$ ).

The frictional resistance coefficient of steel pipes is calculated as:

$$\lambda = 0.11 \left( \frac{\Delta}{d} + 1923 \frac{vd}{Q} \right)^{0.25} \quad (6)$$

The general correction formula for the frictional resistance of steel pipes is:

$$H = 68.8 \left[ \frac{\Delta}{d} + 1923 \frac{v_0 d T_0 + C}{Q_0 T + C} \left[ \frac{T}{T_0} \right]^{1.5} \right]^{0.25} \frac{LQ_0^2}{d^5} \rho_0 \frac{p_0 T}{p T_0} \quad (7)$$

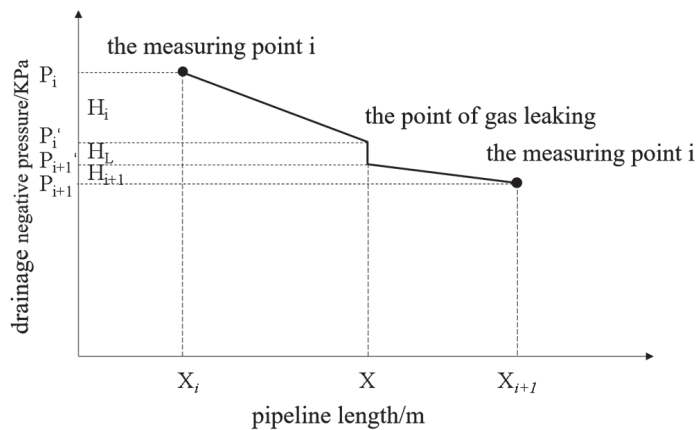
By converting the units of  $Q$  and pipeline inner diameter  $d$  to  $\text{m}^3/\text{h}$  and  $\text{cm}$  and considering the little effect of temperature on the kinematic viscosity, the general correction formula for the frictional resistance of steel pipes can be simplified as:

$$H = k_1 68.8 \left[ \frac{\Delta}{d} + 1923 \frac{v_0 d}{Q_0} \right]^{0.25} \frac{L Q_0^2}{d^5} \rho_0 \frac{p_0 T}{p T_0} \quad (8)$$

where  $v_0$  is the kinematic viscosity of the gas at standard temperature and pressure (STP;  $\text{m}^2/\text{s}$ );  $k_1$  is the local frictional resistance correction coefficient (1.1);  $Q_0$  is the gas flow in the pipeline at STP ( $\text{m}^3/\text{h}$ );  $T$  is the absolute temperature (K) of the gas in the pipeline at time  $t$ ;  $T_0$  is the absolute temperature at STP ( $T_0 = 273 \text{ K}$ );  $\rho_0$  is the gas density at STP ( $\text{kg}/\text{m}^3$ );  $p$  is the absolute pressure of the gas in the pipeline (Pa); and  $p_0$  is the atmospheric pressure at STP (Pa).

### 2.3. Principle of Pipeline Leakage Detection and Localization Based on the Pressure Gradient Method

This study assumes that the gas flow in the pipeline is a steady-state one. That is, the flow parameters at any point along the pipeline are only related to the position of that point and not to time. The pressure gradient method comparatively analyzes the gradient of pressure curve variations before and after pipeline leakage and locates the leakage by seeking the maximum gradient. Under stable flow conditions, the pressure inside the pipeline can be approximately considered to vary linearly along the pipeline. In the case of a sudden leakage, the external gas instantaneously enters the pipeline due to the negative pressure in it, causing a sharp pressure rise at the leakage point. As the steady state is reached again, the pressure distribution in the drainage pipeline will present an obvious polyline abrupt change, as shown in Figure 1, with the turning point indicating the pipeline leakage point.



**Figure 1.** Schematic diagram of the pressure gradient method-based localization.

According to the abrupt change characteristics of the pressure gradient before and after the pipeline leakage in Figure 1, the gas drainage negative pressure and other drainage parameters of the  $i$ th and  $(i + 1)$ th measuring points at a certain time, the following equation is used to calculate the pipeline length  $X$  from the leakage point to the pump:

$$\left\{ \begin{array}{l} H_i + H_{i+1} + H_L = P_i - P_{i+1} \\ H_i = k_1 68.8 \left( \frac{\Delta}{d} + 1923 \frac{v d}{Q_i} \right)^{0.25} \frac{\rho (X - X_i) Q_i^2}{d^5} + \rho g (h_i - h_X) \\ H_{i+1} = k_1 68.8 \left( \frac{\Delta}{d} + 1923 \frac{v d}{Q_{i+1}} \right)^{0.25} \frac{\rho (X_{i+1} - X) Q_{i+1}^2}{d^5} + \rho g (h_X - h_{i+1}) \\ H_L = \zeta \frac{2}{\pi^2} \frac{\rho Q_i^2}{d^4} \end{array} \right. \quad (9)$$

where  $\zeta$  is the local resistance coefficient at the leakage point; and  $h_x$  is the horizontal elevation of the leakage point (m).

### 3. Results and Discussion

#### 3.1. Numerical Simulation Study on the Leakage Detection and Localization Method Based on the Pressure Gradient Method

In this section, COMSOL Multiphysics 3.5 numerical simulation software is used to study the gas flow patterns in the underground coal mine gas drainage pipeline under different working conditions.

The simulation parameters affect the reliability of the simulation results. Therefore, the following points should be taken into account when selecting the simulation parameters:

(1) Because the extraction pipeline is affected by the compressibility of the fluid and the temperature transfer, the flow law of the fluid in the pipeline is extremely complex. It is difficult to accurately describe the internal flow law of the gas extraction pipeline, and the secondary influence of the field environment of the gas extraction pipeline on the simulation results should be ignored. Therefore, it is assumed that the gas extraction pipeline is a steady flow of one-dimensional incompressible gas, and the influence of temperature on the pipeline is not considered.

(2) Considering the high accuracy of large flow monitoring, an 800 mm diameter extraction pipeline was selected. In order to eliminate the influence of turbulent flow in the surrounding area of leakage point, the length of pipeline cannot be too short. Considering that 30~50 m is used as an extraction unit in a coal mine, it is necessary to select a pipeline with a length of at least 100 m.

(3) The velocity inlet was set to 13 m/s, and the pressure outlet was set to the relative pressure of  $-40,000$  Pa, which is in line with the actual situation of coal mine gas extraction.

(4) The degree of pipeline leakage, the location of the leakage point, and the pipeline pressure are important factors affecting the results of gas leakage detection, which represent the main causes of gas leakage, the location of gas leakage, and the condition of the extraction pipeline, respectively. The degree of pipeline leakage can be characterized by the radius of the leakage hole. The radius of 0.03 m, 0.05 m, and 0.08 m is reasonable. The location of the leakage point is set to 30 m, 50 m, and 70 m from the head of pipeline in turn, which is reasonable under simulation conditions. The leakage point pressure outlet is set to the relative pressure of  $-40,000$  Pa,  $-60,000$  Pa, and  $-80,000$  Pa, which is in line with the actual situation of the main pipeline of coal mine gas extraction.

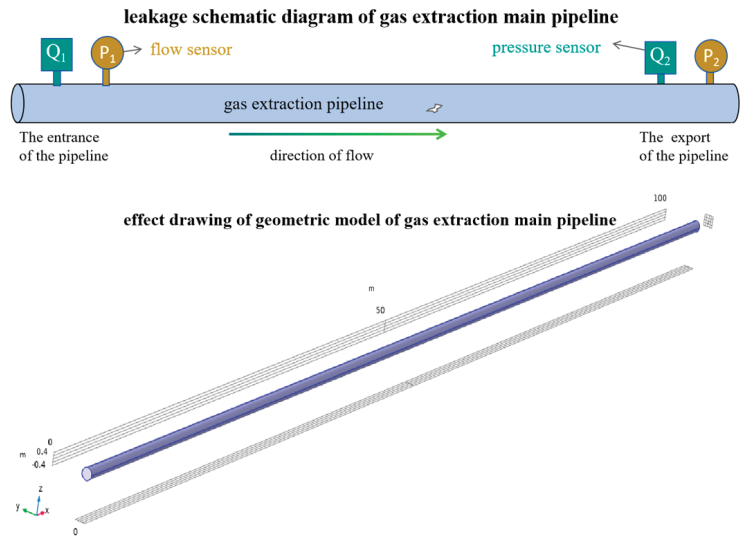
##### 3.1.1. Gas Drainage Pipeline Model Establishment

The following assumptions are made to study the fluid motion in the downhole gas drainage main pipeline under different working conditions:

(1) Inside the gas drainage pipeline is assumed to be a steady-state flow of a one-dimensional incompressible gas;

(2) The effect of temperature on the pipeline is not considered, and the gas flow in the pipeline is an isothermal one.

To simulate the fluid motion in the drainage pipeline under different working conditions, a three-dimensional simulation pipeline with a length of 100 m and a diameter of 800 mm was established based on the realizable  $k-\varepsilon$  turbulence model, with methane gas ( $\text{CH}_4$ ) as the material inside the pipeline. The simulation model obeys the laws of conservation of energy, mass, and momentum. The schematic and geometric renderings of the drainage pipeline leakage model are shown in Figure 2.



**Figure 2.** Drainage pipeline leakage model schematic and geometric renderings.

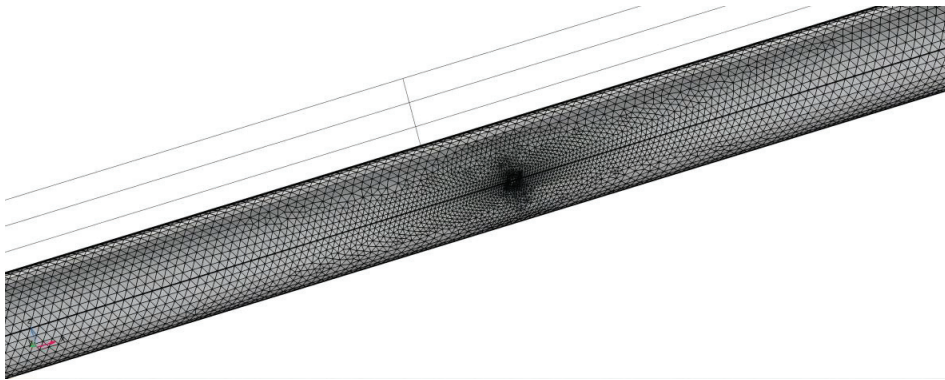
The realizable  $k$ - $\varepsilon$  turbulence model can be expressed as follows:

$$\begin{cases} \frac{\partial}{\partial t}(\rho k) + \frac{\partial}{\partial x_j}(\rho k u_j) = \frac{\partial}{\partial x_j} \left[ \left( \mu + \frac{\mu_t}{\sigma_k} \right) \frac{\partial k}{\partial x_j} \right] + P_k + P_b - \rho \varepsilon - Y_M + S_k \\ \frac{\partial}{\partial t}(\rho \varepsilon) + \frac{\partial}{\partial x_j}(\rho \varepsilon u_j) = \frac{\partial}{\partial x_j} \left[ \left( \mu + \frac{\mu_t}{\sigma_\varepsilon} \right) \frac{\partial \varepsilon}{\partial x_j} \right] + \rho C_1 S \varepsilon - \rho C_2 \frac{\varepsilon^2}{k + \sqrt{v \varepsilon}} + C_{1\varepsilon} \frac{\varepsilon}{k} C_{3\varepsilon} P_b + S_\varepsilon \\ C_1 = \max \left[ 0.43, \frac{\eta}{\eta + 5} \right] \\ \eta = S \frac{k}{\varepsilon} \\ S = \sqrt{2 S_{ij} S_{ij}} \end{cases} \quad (10)$$

where  $\rho$  is the gas density ( $\text{kg}/\text{m}^3$ );  $P_k$  is turbulent kinetic energy generated by the average velocity gradient (J);  $P_b$  is the turbulent kinetic energy generated by buoyancy (J);  $Y_M$  is the influence factor of the fluctuation expansion on the total dissipation rate;  $S$  is the simulated frontal area ( $\text{m}^2$ );  $v$  is the inflow velocity ( $\text{m}/\text{s}$ );  $\sigma_k$ ,  $\sigma_\varepsilon$ ,  $C_1$ ,  $C_2$ , and  $C_{1\varepsilon}$  are empirical constants;  $k$  is the turbulent kinetic energy (J); and  $\varepsilon$  is the turbulence dissipation rate.

### 3.1.2. Meshing and Boundary Condition Establishment

The model simulates the operation of the underground gas drainage main pipeline in different working conditions. According to the actual situation on site, a negative pressure is set inside the pipeline. The inlet of the pipeline is set as a speed inlet, the outlet of the pipeline is set as a pressure outlet, and the middle leakage point is set to a pressure outlet. The boundaries of the model are set as walls, and the pipe roughness is set to 0.0005. The model adopts free mesh triangulation for meshing, and the size of the physical field control mesh cell is selected as regular, resulting in 1,459,933 cells. The partial diagram of the meshing effect of the model is shown in Figure 3.



**Figure 3.** Partial diagram of pipeline leakage model meshing.

### 3.2. Drainage Pipeline Leakage Numerical Simulation Result Analysis

To verify the applicability and feasibility of the pressure gradient method under different working conditions and summarize the effects of these conditions, pipeline leakages under different working conditions (leakage degree, leakage position, and pipeline negative pressure) are numerically simulated, and a control model is established.

#### 3.2.1. Effect of Leakage Degree on Pipeline Fluid Motion State

A negative pressure gas drainage pipeline model is set up with a pipeline length of 100 m, a pipeline diameter of 800 mm, an inlet speed of 13 m/s, an outlet pressure of  $-40,000$  Pa relative pressure, an inlet pressure of 0 Pa at the leakage point, and a leakage point at 50 m (pipeline center). The leakage hole radius is set to 0.03 m, 0.05 m, and 0.08 m in turn, which are compared with the no-leakage condition. The specific simulation results are shown in Figures 4 and 5.

Figure 4 shows that the gas drainage pipeline in normal operation tends to have a constant flow velocity and evenly distributed flow lines within. With the increase in the leakage hole diameter, the flow lines in the pipeline become increasingly chaotic. Thus, with increased pipeline leakage degrees, the sudden velocity and pressure changes at the leakage point are more significant, and the turbulence effect is enhanced. Figure 5 shows that the pressure in the pipeline under normal operation decreases uniformly along the pipeline line. In the case of leakage, the pressure at the leakage point decreases significantly, and the decrements are larger as the pipeline leakage degree increases.

Based on the simulation results, the pressure distribution curve along the pipeline and the axial flow velocity distribution curve under different leakage degrees are plotted in Figure 6. It can be observed from Figure 6 that as the pipeline leakage degree increases, the turbulence in the pipeline surges, and the pressure distribution along the pipeline axis shows a complex trend from uniform decline to upward surge and downward plunge, with the pressure downstream the leakage point gradually increasing. In the case of leakage, the originally stable flow velocity along the pipeline fluctuates (starting from the leakage point), and the abrupt velocity changes at the leakage point increase with the increase in the leakage degree. However, the overall curve of velocity along the pipeline tends to be relatively stable.



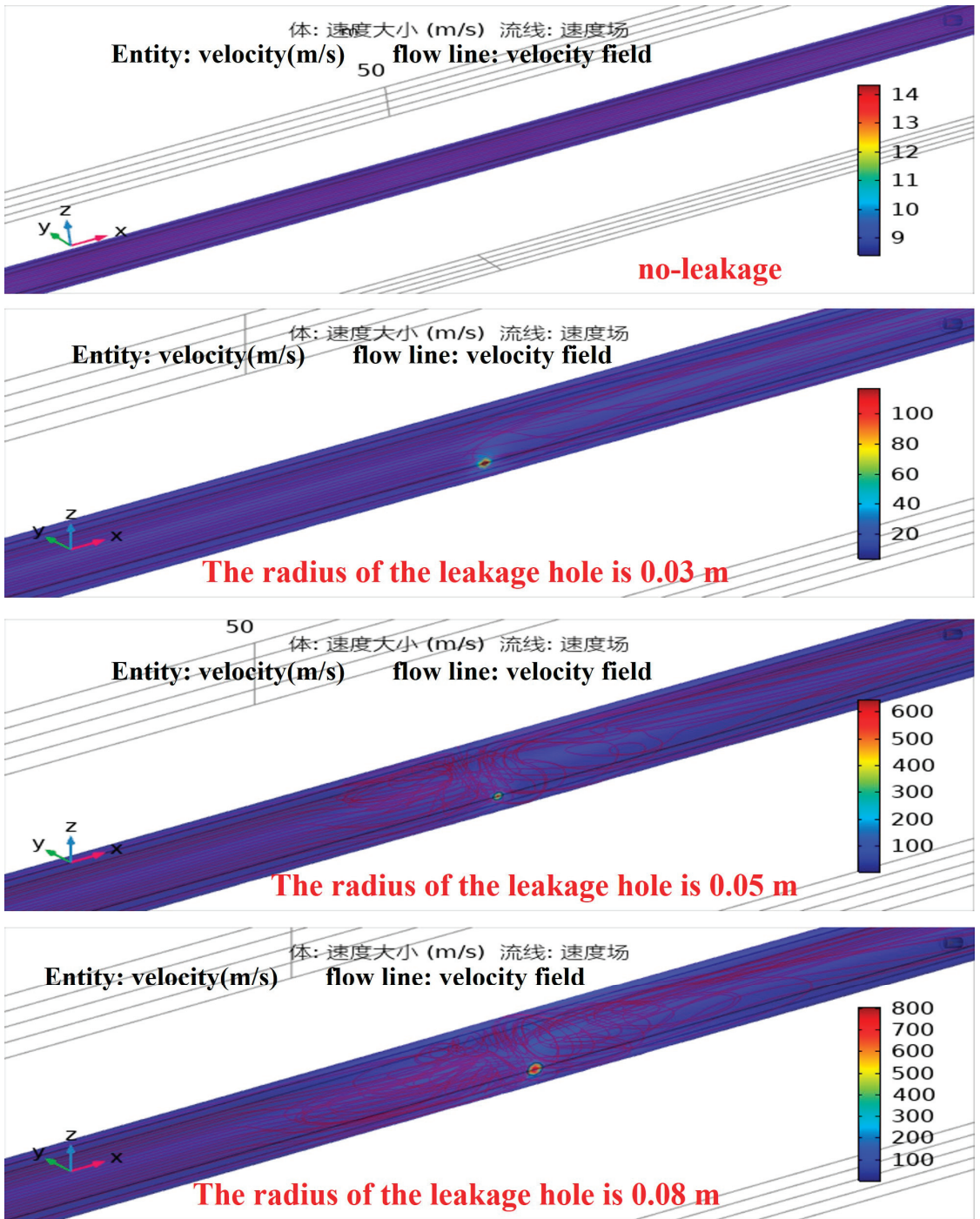


Figure 4. Cloud diagram of flow velocity in the pipeline under different leakage degrees.

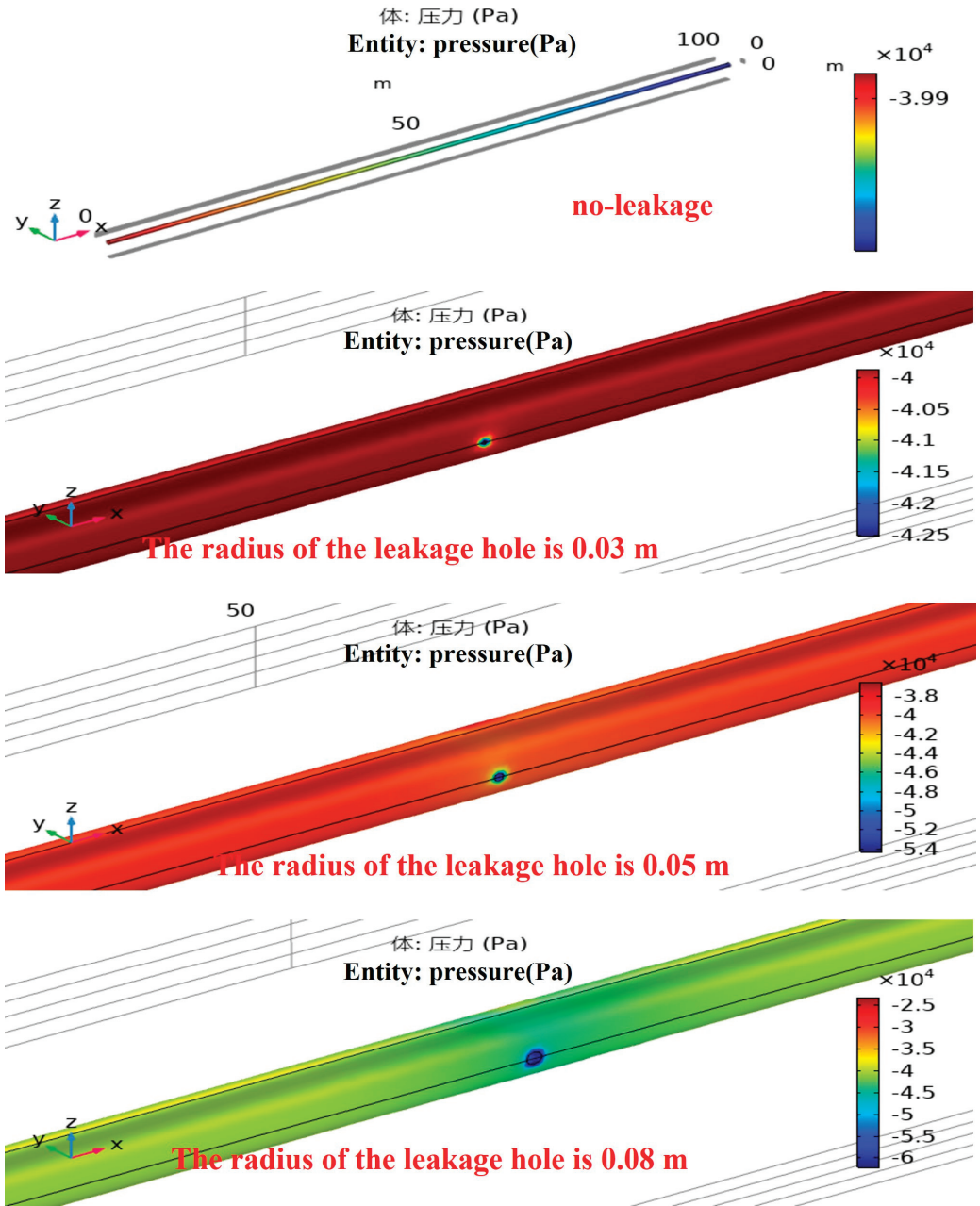
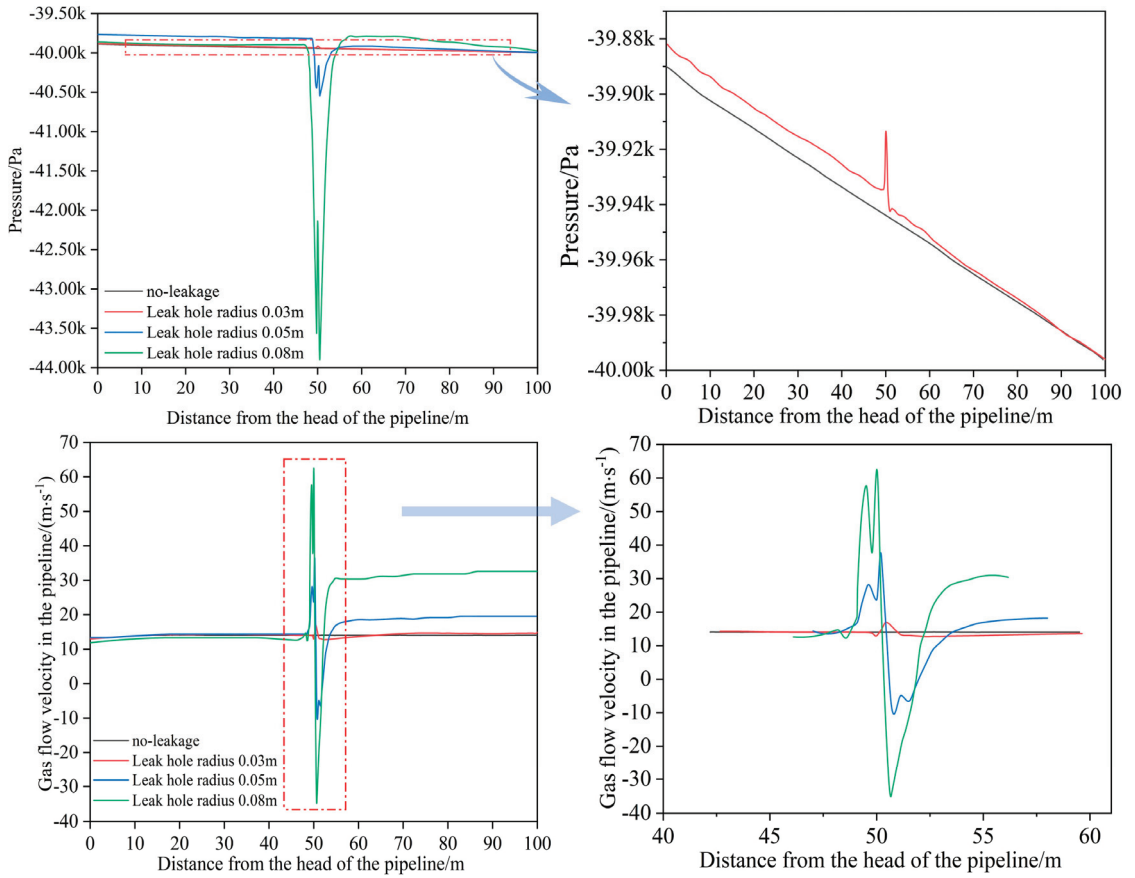


Figure 5. Cloud diagram of pressure in the pipeline under different leakage degrees.

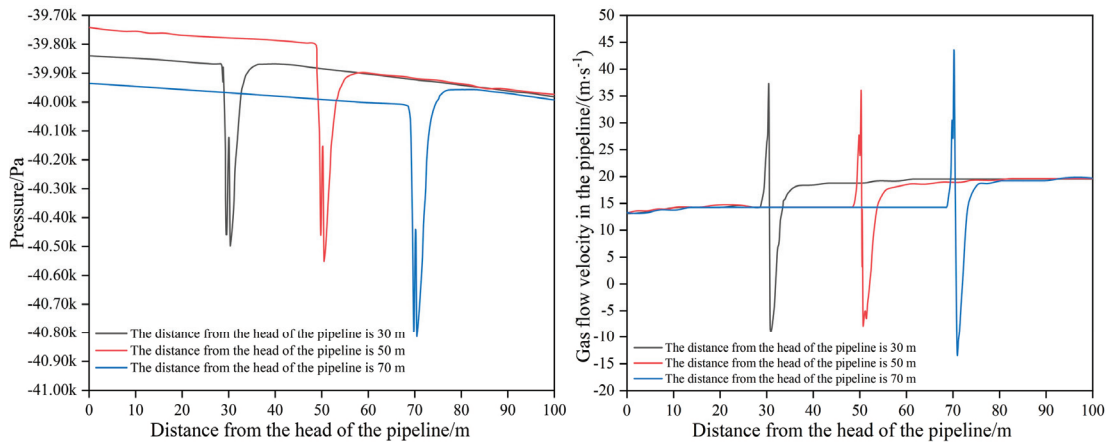


**Figure 6.** Pressure distribution and axial flow velocity distribution curves along the pipeline under different leakage degrees.

### 3.2.2. Effect of Leakage Position on Pipeline Fluid Motion State

A negative pressure gas drainage pipeline model is set up with a pipeline length of 100 m, a pipeline diameter of 800 mm, an inlet speed of 13 m/s, an outlet pressure of  $-40,000$  Pa relative pressure, an inlet pressure of 0 Pa at the leakage point, and a leakage hole radius of 0.05 m. The leakage position is set to 30 m, 50 m, and 70 m, in turn, from the start point of the pipeline. Based on the simulation results, the pipeline axial pressure and axial flow velocity distribution curves with different leakage positions are plotted, as shown in Figure 7.

With the same leakage degree, the pipeline leakage position (upstream, midstream, and downstream) has little effect on the distribution of the transversal pressure and velocity in the pipeline, all of which show abrupt changes at the leakage point. Among them, the pressure decays sharply at the leakage point, while the pressure elsewhere shows a uniform decline trend, which is consistent with the fluid dynamics law that the pipeline fluid decays under the influence of frictional resistance, viscous resistance, etc. The velocity curves with different pipeline leakage positions all trend upward and then downward. Elsewhere in the pipeline, the flow velocity rises slowly as the negative pressure drives external gas into the pipeline.



**Figure 7.** Pipeline axial pressure and axial flow velocity distribution curves with different leakage positions.

### 3.2.3. Effect of Negative Pressure on Pipeline Leakage Fluid Motion State

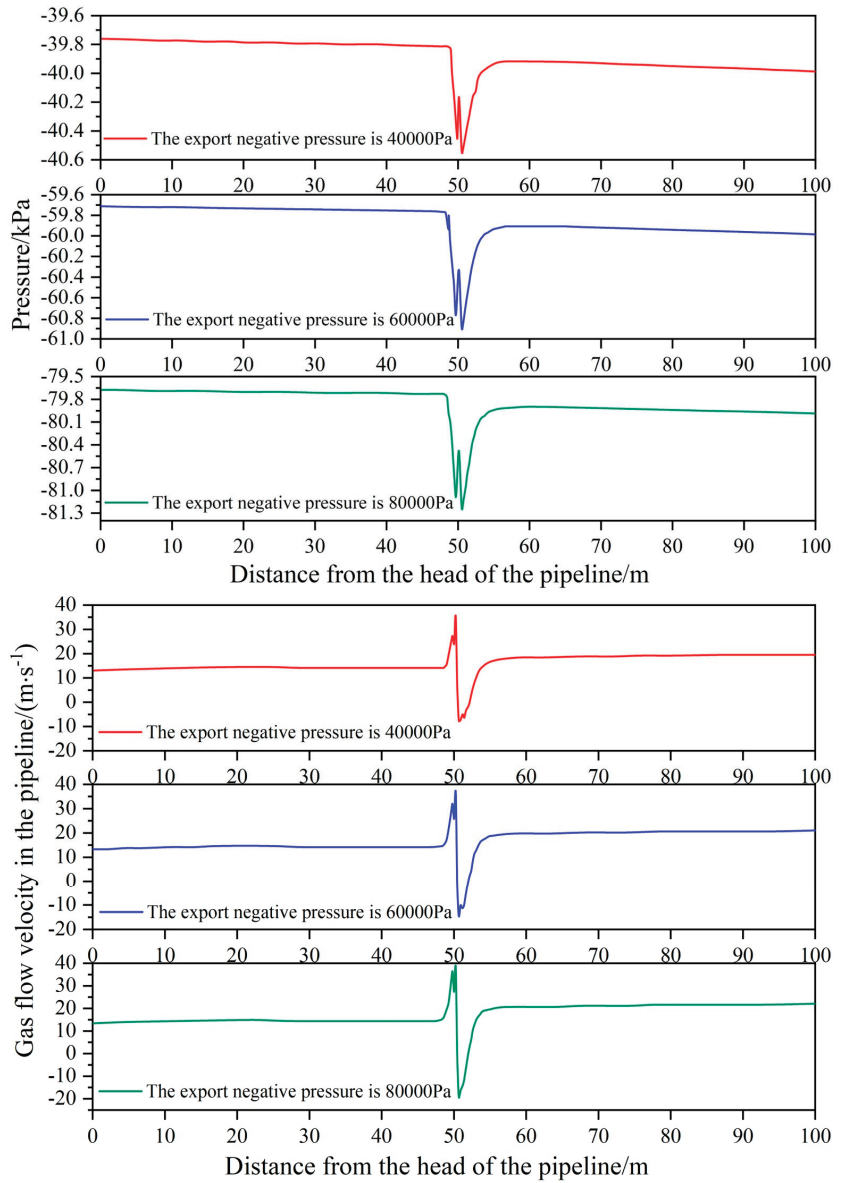
A negative pressure gas drainage pipeline model is set up with a pipeline length of 100 m, a pipeline diameter of 800 mm, an inlet speed of 13 m/s, an inlet pressure of 0 Pa at the leakage point, a leakage hole radius of 0.05 m, and a leakage position of 50 m from the start point of the pipeline. The leakage point is set as a pressure outlet, and the relative pressure is set to  $-40,000$  Pa,  $-60,000$  Pa, and  $-80,000$  Pa in turn. Based on the simulation results, the distribution curves of axial pressure and axial flow velocity during pipeline leakage under different drainage negative pressures are plotted in Figure 8.

Figure 8 shows that with other boundary conditions being consistent, decreasing the relative negative pressure (outlet pressure) of the pipeline causes abrupt changes in the transversal pressure and velocity distribution curves at the leakage point. As the relative pressure of the pipeline decreases, the absolute values of the sudden pressure and flow velocity change at the leakage point increase.

### 3.3. Accuracy Analysis of Gas Drainage Pipeline Leakage Detection and Localization Based on the Pressure Gradient Method

To verify the accuracy of drainage pipeline leakage detection and localization based on the pressure gradient method, the pressure data at the starting and end points of the pipeline at the same position are recorded under different working conditions (leakage degree, leakage position, and pipeline negative pressure) for fitting to derive the theoretical leakage point as the intersection point of the fitting equations of the starting and end points. The relative error between the theoretical leakage point and the actual leakage point is analyzed. The fitting curves are shown in Figure 9.

According to the comparative analysis between the actual leakage point and the theoretical leakage point obtained by fitting with the pressure data at the starting and end points of the pipeline at the same position under different working conditions (leakage degree, leakage position, and pipeline negative pressure), the relative error is derived, as shown in Figure 10.



**Figure 8.** Distribution curves of axial pressure and axial flow velocity during pipeline leakage under different drainage negative pressures.

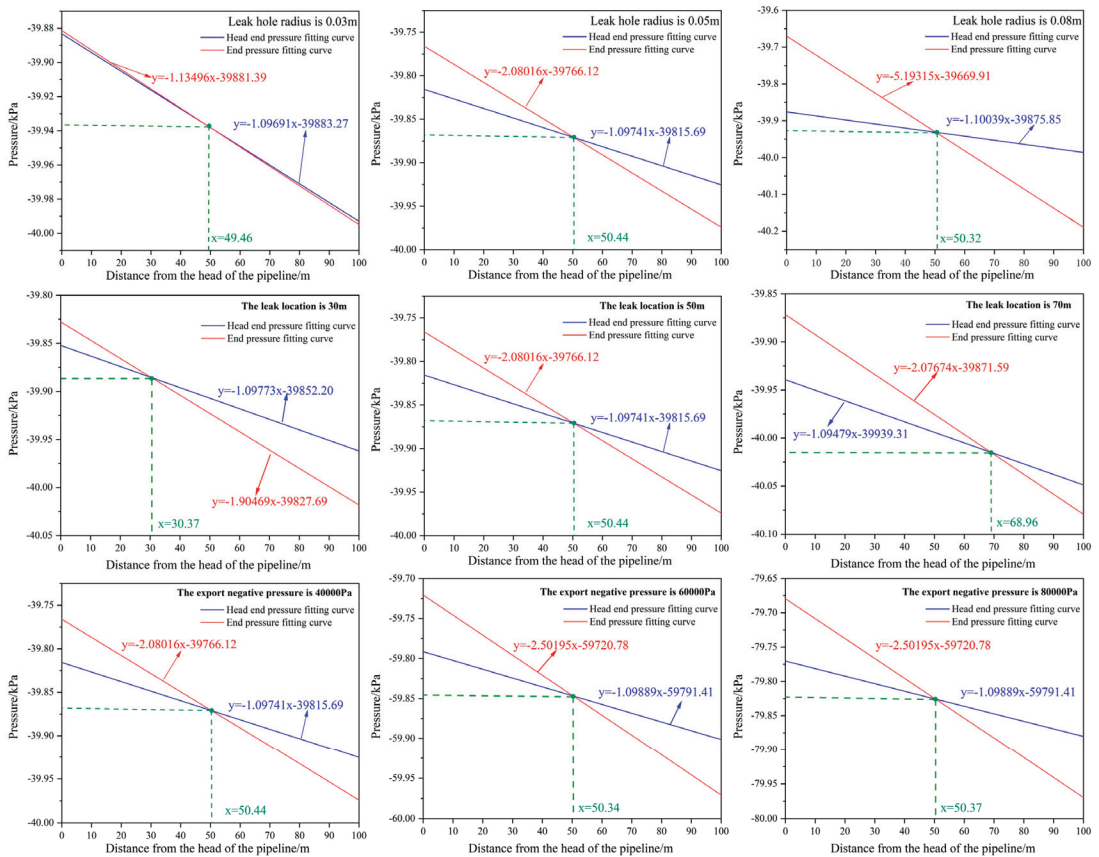
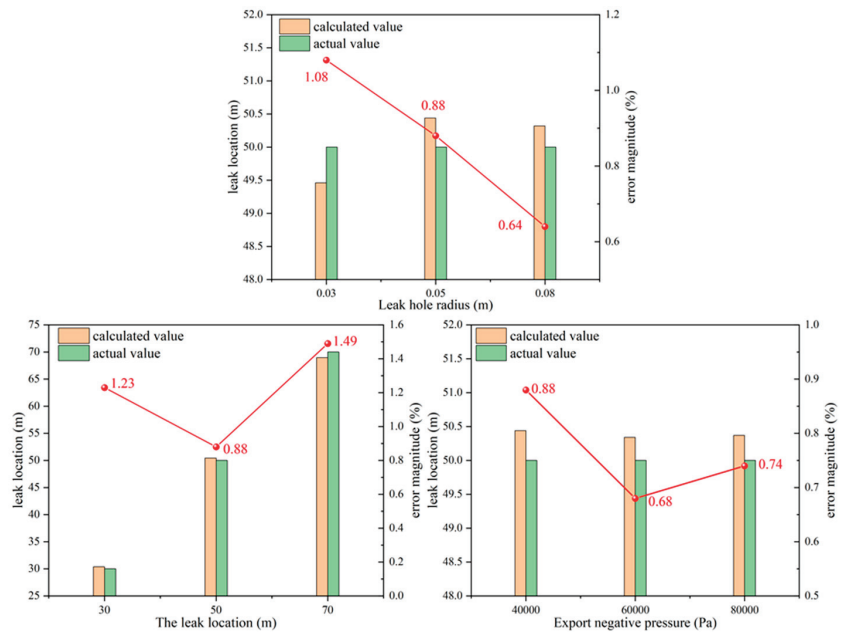


Figure 9. Starting and end point pressure fitting curves under different working conditions.

Figure 10 shows that the localization error under different leakage degrees is between 0.88% and 1.08%. Thus, changes in the size of the leakage point have a relatively large impact on the steady-state pipeline leakage detection and localization method. Moreover, the amount of pipe leakage is greater with the expansion of the leakage hole, leading to a smaller relative error of localization. That is, pipeline leakage detection and localization perform better as the pipeline leakage degree increases. The localization error with different leakage positions is between 0.88% and 1.49%. Thus, changes in the leakage position have a relatively significant impact on the steady-state pipeline leakage detection and localization method. Leakage points closer to the middle of the pipeline can better reduce the influence of the pipeline's starting and end points on the flow within. Therefore, the localization is more accurate when the leakage points are closer to the middle point of the pipeline. The localization error under different pipeline negative pressures is between 0.68% and 0.88%. Thus, the negative pressure at the pipeline outlet has relatively little effect on the steady-state leakage detection and localization method.



**Figure 10.** Leakage localization errors under different working conditions.

In order to further clarify the influence of leakage degree, leakage position, and pipeline negative pressure on the accuracy of leakage location by pressure gradient method, the statistical method was used to analyze the sample error between the theoretical value and the calculated value of simulation data by SPSS software (version 27). The results show that the standard deviations of the positioning error values under different leakage degrees, leakage locations, and pipeline negative pressure conditions are 0.22%, 0.31%, and 0.11%, respectively. The degree of leakage is negatively correlated with the positioning error, and the correlation coefficient is 0.998; that is, the greater the degree of leakage, the smaller the positioning error. The leakage position is positively correlated with the positioning error, and the correlation coefficient is 0.425; that is, the farther the leakage point is, the larger the positioning error is. The negative pressure of the pipeline is negatively correlated with the positioning error, and the correlation coefficient is 0.640; that is, the larger the negative pressure of the pipeline, the smaller the positioning error. The significance between different leakage degrees, leakage positions, pipeline negative pressures, and their corresponding positioning error values is 0.72, 0.55, and 0.04, respectively. It shows that the degree of leakage has the greatest influence on the positioning accuracy, and the influence of pipeline negative pressure on the positioning accuracy is not significant.

The above analyses indicate that without changing the other conditions of the gas extraction pipeline, merely changing the pipeline leakage hole diameter, leakage position, or pipeline negative pressure can impact the accuracy of the steady-state leakage detection and localization method. The influence of the leakage hole diameter is greater than that of the leakage position, and the influence of the leakage position is greater than that of the pipeline negative pressure. Since the leakage detection and localization errors under the influence of the three factors are within acceptable ranges, it is feasible and relatively accurate to use the pressure gradient method to detect and locate pipeline leakages.

### 3.4. On-Site Test Result Analysis of Leakage Detection and Localization Based on the Pressure Gradient Method

The proposed pipeline leakage detection and localization method is subjected to downhole field application tests in the 8421 highly located drainage roadway of the Fifth Mine of the Yangquan Coal Industry Group and its connected Xiaonanzhuang Pumping Station. The total length of the 8421 highly located drainage roadway is about 7542 m, and the pipeline diameter is 700 mm. Through downhole field investigations, the drainage pipeline of about 1685 m long with manual detection holes at the starting and end points was selected for the test. Figure 11 is the schematic diagram. Equation (10) is used to calculate the negative pressure loss of the pipeline in the test, and the required parameters are listed in Table 1. The application effect is analyzed based on the steady-state pressure gradient method, and the pipeline localization errors are compared.

$$H = 1.1 \times 1.17 \times 68.8 \left[ \frac{\Delta}{d} + 1923 \frac{v_0 d}{Q_0} \right]^{0.25} \frac{L Q_0^2}{d^5} \rho_0 \frac{p_0 T}{p T_0} \quad (11)$$

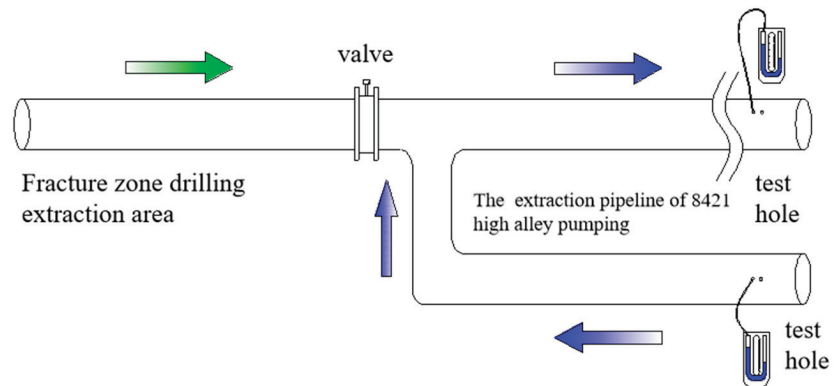


Figure 11. 8421 highly located drainage roadway inspection schematic diagram.

Table 1. Parameters required for calculating the resistance loss of the 8421 highly located drainage roadway pipeline.

Required Parameters	8421 Highly Located Drainage Roadway Measurement Starting Point	8421 Highly Located Drainage Roadway Measurement End Point
Local resistance coefficient ( $k_1$ )	1.1	1.1
Pipeline overall correction coefficient ( $k_2$ )	1.17	1.17
Pipeline length ( $L$ )	1685 m	1685 m
Pipeline roughness ( $\Delta$ )	0.0005 m	0.0005 m
Pipeline inner diameter ( $d$ )	70 cm	70 cm
STP gas viscosity ( $v_0$ )	$1.5787 \times 10^{-5} \text{ m}^2/\text{s}$	$1.5787 \times 10^{-5} \text{ m}^2/\text{s}$
STP pipeline flow ( $Q_0$ )	$19,440 \text{ m}^3/\text{h}$	$27,000 \text{ m}^3/\text{h}$
STP gas density ( $\rho_0$ )	$1.1350 \text{ kg}/\text{m}^3$	$1.1836 \text{ kg}/\text{m}^3$
STP absolute temperature ( $T_0$ )	273 K	273 K
Pipeline absolute temperature ( $T$ )	286.5 K	285.8 K
STP atmospheric pressure ( $P_0$ )	101,325 Pa	101,325 Pa
Pipeline absolute pressure ( $P$ )	95,159 Pa	87,065 Pa
Pipeline resistance loss ( $H$ )	4459.49 Pa	9062.87 Pa



As shown in Figure 11, a pair of detection holes are designed at the starting and end points of the 8421 highly located drainage roadway, and a U-type differential pressure gauge is used to detect the negative pressure and flow at the starting and end points of the pipeline. The downhole test site is shown in Figure 12. When the valve is closed, the 8421 highly located drainage roadway can be approximated as a leak-free negative pressure pipeline. When the valve is opened, the pipeline connecting the fracture zone extraction area starts to work. Since the gas concentration in the fracture zone is low, the leaked-in gas can be approximated as air. In this way, pipeline leakage can be simulated without damaging the on-site pipeline or affecting the normal operation of the drainage pipeline.



Figure 12. The downhole test site.

According to the field measurement data, the pressure loss curves at the starting and end points of the 8421 highly located drainage roadway pipeline are calculated, with that of the starting point being  $y = -2.6142x - 6170.2528$  and that of the end point being  $y = -5.3256x - 5197.8001$ . The intersection of the two lines is the calculated leakage point. The calculated leakage point is at 358.65 m, as shown in Figure 13.

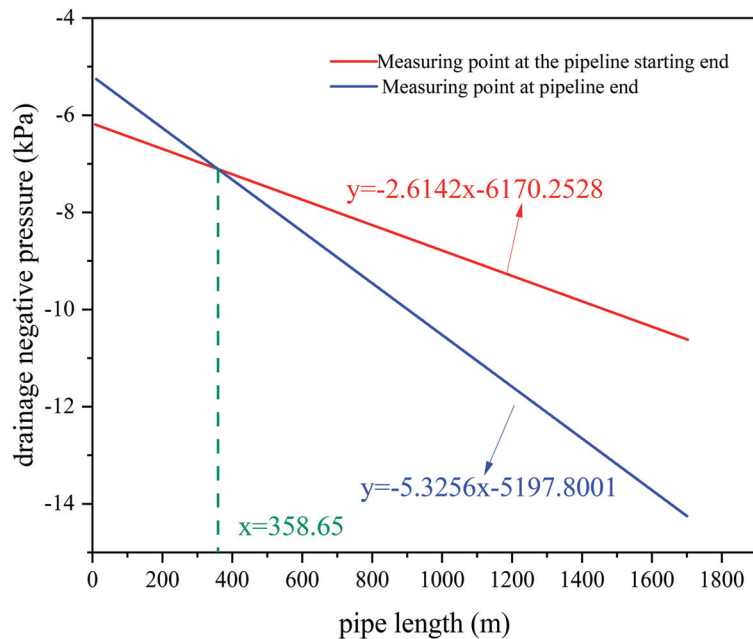


Figure 13. Negative pressure distribution curves at the starting and end points of the 8421 highly located drainage roadway pipeline.

In this downhole drainage pipeline leakage detection test on a 1685 m pipeline, the leakage position calculated based on the pressure gradient method is about 358 m away from the detection point at the starting point of the pipeline, which has an absolute error of about 138 m from the actual leakage position (220 m), and a relative error of about 8.2%. It can be concluded that downhole drainage pipeline leakage detection and localization based on the pressure gradient method has relatively high accuracy. Meanwhile, the following conclusions can be drawn based on the simulation analysis results in Section 3.2: with increased pipeline leakage hole diameters, elevated pipeline negative pressures, and closer leakage positions to the pipeline center, the relative localization error was smaller, the localization accuracy was higher, and the stability was greater.

At present, through simulation and field test, it is proved that the pressure gradient method has good accuracy in leakage detection and location of gas extraction pipeline. However, the accurate estimation method of local resistance at the leakage point and its relationship with parameters, such as leakage volume and leakage position, still need to be further studied and improved.

### *3.5. Thoughts and Prospects of Pressure Gradient Method Gas Drainage Pipeline Leakage Detection Technology*

The advantages of the pressure gradient method pipeline leakage detection and location technology proposed in this study are mainly reflected in the following three aspects: (1) the negative pressure monitoring of the gas extraction pipeline is part of the coal mine safety monitoring system and does not require additional economic costs; (2) real-time continuous monitoring can be realized, and the pipeline can be found in time after air leakage occurs; and (3) the theoretical method is relatively mature, which can help realize the qualitative and quantitative judgment of pipeline leakage.

This technology can be applied to pipelines that transport fluids, such as coal mine gas drainage pipelines in a negative pressure state, ground natural gas pipelines in a positive pressure state, and long-distance water pipelines. The pressure gradient method can be used to detect and locate pipeline faults.

The implementation of the pressure gradient method in the actual pipeline system is limited by the difference of pipeline resistance distribution and the sensitivity of the monitoring parameters in different application scenarios. This method also has room for improvement in accurate monitoring. The main challenge of using the pressure gradient method to carry out pipeline fault diagnosis and location is the accurate monitoring of gas flow in the pipeline and the arrangement spacing of monitoring points. The accurate monitoring of gas flow in the pipeline depends on the hardware level, and the accuracy of micro-flow monitoring is low at this stage. The spacing of monitoring points depends on the balance between the requirement of monitoring accuracy and the economic cost of monitoring.

## **4. Conclusions**

(1) Without leakage, the pressure along the gas drainage pipeline decreases uniformly, and the flow velocity tends to be stable. In the case of leakage, the gas pressure and flow velocity distribution along the axial direction of the pipeline change significantly, and the sudden change point is the leakage point.

(2) During pipeline leakage, the pressure at the leakage point shows an overall decreasing trend, and the pressure decrements are larger with the increase in the leakage degree. The impact of leakage position on the pressure and flow velocity distributions along the pipeline is relatively small. As the drainage negative pressure decreases, the magnitude of pressure and flow velocity changes at the leakage point increases.

(3) The pipeline leakage degree, leakage position, and pipeline negative pressure affect the accuracy of leakage localization based on the pressure gradient method. The leakage degree has the greatest impact on the localization accuracy, followed by the leakage position, and pipeline negative pressure has the least impact. The pipeline leakage localization

errors under different leakage degrees, leakage positions, and pipeline negative pressures are 0.88~1.08%, 0.88~1.49%, and 0.68~0.88%, respectively, indicating the relatively high feasibility and accuracy of gas drainage pipeline leakage detection and localization based on the pressure gradient method.

(4) On-site test results from the 1685 m drainage pipeline of the Yangquan Coal Industry Group show that the relative errors of leakage localization based on the pressure gradient method are about 8.2%, demonstrating the relatively high accuracy of underground drainage pipeline leakage detection and localization based on the pressure gradient method.

(5) With increased pipeline leakage degrees, elevated pipeline negative pressures, and closer leakage positions to the pipeline center, the relative localization error based on the pressure gradient method is smaller, the localization accuracy is higher, and the stability is greater.

**Author Contributions:** Conceptualization, H.Z. and M.S.; methodology, H.Z. and Z.H.; software, Y.Z.; validation, H.Z., Y.Z. and M.S.; formal analysis, L.S.; investigation, Y.L.; resources, Y.Z.; data curation, M.S.; writing—original draft preparation, H.Z.; writing—review and editing, M.S. and H.Z.; visualization, L.S.; supervision, Z.H.; project administration, Z.H.; funding acquisition, H.Z. All authors have read and agreed to the published version of the manuscript.

**Funding:** This study was supported by the China Coal Research Institute Technology Innovation Fund (2022CX-I-05) and the Special Project for Technology Innovation and Entrepreneurship Foundation of Tiandi Science & Technology Co., Ltd. (2021-2-TD-MS001).

**Data Availability Statement:** The data presented in this study are available on request from the corresponding author. The data are not publicly available due to containing information that could compromise the privacy of research participants.

**Conflicts of Interest:** The author Huijie Zhang has received research grants from China Coal Research Institute (the China Coal Research Institute Technology Innovation Fund, Number: 2022CX-I-05). The author Zhonggang Huo has received research grants from Tiandi Science & Technology Co., Ltd. (the Special Project for Technology Innovation and Entrepreneurship Foundation, Number: 2021-2-TD-MS001). All the authors declare no conflicts of interest.

## References

- Liu, Y.; Liang, Y.; Li, Q. Cause Analysis of Coal Mine Gas Accidents in China Based on Association Rules. *Appl. Sci.* **2023**, *13*, 9266. [CrossRef]
- Wang, C.; Yang, S.; Yang, D.; Li, X.; Jiang, C. Experimental analysis of the intensity and evolution of coal and gas outbursts. *Fuel* **2018**, *226*, 252–262. [CrossRef]
- Zhao, W.; Dong, H.; Yuan, Y.; Wang, K.; Song, Y. Evolution law of coal and gas outburst hole shapes with varying underground stress conditions: Numerical analysis and on-scene evidence. *Fuel* **2024**, *360*, 130531. [CrossRef]
- Zhou, A.; Xu, Z.; Wang, K.; Wang, Y.; An, J.; Shi, Z. Coal mine gas migration model establishment and gas extraction technology field application research. *Fuel* **2023**, *349*, 128650. [CrossRef]
- Wang, Z.; Sun, Y.; Wang, Y.; Zhang, J.; Sun, Z. A coupled model of air leakage in gas drainage and an active support sealing method for improving drainage performance. *Fuel* **2019**, *237*, 1217–1227. [CrossRef]
- Zhang, J.; Liu, Y.; Ren, P.; Han, H.; Zhang, S. A fully multifield coupling model of gas extraction and air leakage for in-seam borehole. *Energy Rep.* **2021**, *7*, 1293–1305. [CrossRef]
- Liu, T.; Lin, B.; Yang, W.; Liu, T.; Kong, J.; Huang, Z.; Wang, R.; Zhao, Y. Dynamic diffusion-based multifield coupling model for gas drainage. *J. Nat. Gas Sci. Eng.* **2017**, *44*, 233–249. [CrossRef]
- Shu, L. Study on Gas Extraction Technology for Goaf Using L-Shaped Borehole on the Ground. *Appl. Sci.* **2024**, *14*, 1594. [CrossRef]
- Yang, P. Cause Analysis and Repair Technology of Gas Leakage in Gas Extraction Pipeline. Master's Thesis, Xi'an University of Science and Technology, Xi'an, China, 2022.
- Han, Q.Z.; Xiang, J.; Shao, H. Research on leakage positioning technology of gas drainage pipelines. *China Coal* **2011**, *37*, 90–93.
- Pei, W. Experimental Study on the Leak Detection and Localization System of Main Methane Drainage Pipeline. Master's Thesis, China University of Mining and Technology, Xuzhou, China, 2014.
- Lu, H.; Iseley, T.; Behbahani, S.; Fu, L. Leakage detection techniques for oil and gas pipelines: State-of-the-art. *Tunn. Undergr. Space Technol.* **2020**, *98*, 103249. [CrossRef]
- Sekhavati, J.; Hashemabadi, S.H.; Soroush, M. Computational methods for pipeline leakage detection and localization: A review and comparative study. *J. Loss Prev. Process Ind.* **2022**, *77*, 104771. [CrossRef]

14. El-Shiekh, T.M. Leak Detection Methods in Transmission Pipelines. *Energy Sources Part A Recovery Util. Environ. Eff.* **2010**, *32*, 715–726. [CrossRef]
15. Tian, X.; Jiao, W.; Liu, T. Intelligent leak detection method for low-pressure gas pipeline inside buildings based on pressure fluctuation identification. *J. Civ. Struct. Health Monit.* **2022**, *12*, 1191–1208. [CrossRef]
16. Yin, S.; Liu, Y.; Han, W. Single-point location algorithm based on an acceleration sensor for pipeline leak detection. *Measurement* **2020**, *163*, 108021. [CrossRef]
17. Bui Quy, T.; Kim, J.-M. Leak detection in a gas pipeline using spectral portrait of acoustic emission signals. *Measurement* **2020**, *152*, 107403. [CrossRef]
18. He, N.; Qian, C.; Li, R.; Zhang, M. An improved pipeline leak detection and localization method based on compressed sensing and event-triggered particle filter. *J. Frankl. Inst.* **2021**, *358*, 8085–8108. [CrossRef]
19. Zhou, J.; Lin, H.; Li, S.; Jin, H.; Zhao, B.; Liu, S. Leakage diagnosis and localization of the gas extraction pipeline based on SA-PSO BP neural network. *Reliab. Eng. Syst. Saf.* **2023**, *232*, 109051. [CrossRef]
20. Zuo, J.; Zhang, Y.; Xu, H.; Zhu, X.; Zhao, Z.; Wei, X.; Wang, X. Pipeline Leak Detection Technology Based on Distributed Optical Fiber Acoustic Sensing System. *IEEE Access* **2020**, *8*, 30789–30796. [CrossRef]
21. Zhang, T.; Tan, Y.; Zhang, X.; Zhao, J. A novel hybrid technique for leak detection and location in straight pipelines. *J. Loss Prev. Process Ind.* **2015**, *35*, 157–168. [CrossRef]
22. Liu, B.; Jiang, Z.; Nie, W. Negative pressure wave denoising based on VMD and its application in pipeline leak location. *J. Mech. Sci. Technol.* **2021**, *35*, 5023–5032. [CrossRef]
23. She, X.Z.; Hou, Q.; Yang, L. Leak Detection Technology in Underground Gas Extraction Pipe Network. *Saf. Coal Mines* **2013**, *44*, 75–77.
24. Lei, B.W.; Li, X.; Liu, Z. Research on Diagnosis Method for Gas Drainage Pipeline Network Running State Based on Pressure Measurement. *Min. Saf. Environ. Prot.* **2017**, *44*, 32–35+52.
25. Mao, J.R.; Liu, X.; Wang, S. Leak Detection Analysis and Maintenance of Gas Extraction Pipeline Based on Pressure Gradient Method. *J. Kunming Metall. Coll.* **2020**, *36*, 15–19+46.
26. Zhang, Y.Z.; Zhang, L.; Zhang, H.; Li, W.; Liu, Y.; Sang, C. Research on leakage positioning method of underground gas extraction main pipeline based on transient model. *J. Mine Autom.* **2021**, *47*, 55–60.
27. Guo, S. A Leakage Detection Technology for Gas Drainage Pipeline Based on Ultrasonic Inspection. *Min. Saf. Environ. Prot.* **2014**, *41*, 88–91.
28. Cai, J.; Wu, J.; Yuan, S.; Liu, Z.; Kong, D. Numerical analysis of multi-factors effects on the leakage and gas diffusion of gas drainage pipeline in underground coal mines. *Process Saf. Environ. Prot.* **2021**, *151*, 166–181. [CrossRef]
29. Zhao, C.; He, B.; Wang, Y.; Wu, B. Experimental study on the diagnosis of operation state of gas extraction pipeline based on pressure gradient method. *Energy Sources Part A Recovery Util. Environ. Eff.* **2021**, 1–14. [CrossRef]
30. Cui, C.; Jiang, S.; He, X.; Wang, K.; Shao, H.; Wu, Z. Experimental study on the location of gas drainage pipeline leak using cellular automata. *J. Loss Prev. Process Ind.* **2018**, *56*, 68–77. [CrossRef]
31. da Cruz, R.P.; da Silva, F.V.; Fileti, A.M. Machine learning and acoustic method applied to leak detection and location in low-pressure gas pipelines. *Clean Technol. Environ. Policy* **2020**, *22*, 627–638. [CrossRef]
32. Ullah, N.; Ahmed, Z.; Kim, J.-M. Pipeline Leakage Detection Using Acoustic Emission and Machine Learning Algorithms. *Sensors* **2023**, *23*, 3226. [CrossRef]
33. Lin, R. Research on Oil Pipeline Leakage Detection Method Based on Deep Learning. Master's Thesis, Dalian University of Technology, Dalian, China, 2022.
34. Ren, H. Adaptive Control Model of Gas Drainage Parameters in Coal Mine. Master's Thesis, China University of Mining and Technology, Xuzhou, China, 2021.
35. Liu, Z. Experimental Research on the Optimizing Operation Methods of Pipe Network of Gas Extraction in Coal Mine. Ph.D. Thesis, China University of Mining and Technology (Beijing), Beijing, China, 2017.

**Disclaimer/Publisher's Note:** The statements, opinions and data contained in all publications are solely those of the individual author(s) and contributor(s) and not of MDPI and/or the editor(s). MDPI and/or the editor(s) disclaim responsibility for any injury to people or property resulting from any ideas, methods, instructions or products referred to in the content.

Article

# Response Surface Analysis on Multiple Parameter Effects on Borehole Gas Extraction Efficiency

Xiaoyu Cheng <sup>1,\*</sup>, Cheng Cheng <sup>1,2</sup>, Lu Xiao <sup>1</sup> and Xingying Ma <sup>1</sup>

<sup>1</sup> China Coal Energy Research Institute Co., Ltd., Xi'an 710054, China; 18717314036@163.com (C.C.); xiaolu8317@126.com (L.X.); mxy6629@163.com (X.M.)

<sup>2</sup> College of Safety Science and Engineering, Xi'an University of Science and Technology, Xi'an 710054, China

\* Correspondence: chengxiaoyu89@126.com

**Abstract:** To explore the impact of different factors on the effectiveness of borehole gas extraction, in situ stress tests were conducted in a test mining area. A theoretical model of gas migration within the coal matrix–fracture system was established. Based on field data, a numerical model was constructed to study the variation patterns of the effective extraction radius under different extraction conditions. Using the response surface methodology, the interactions of different factors and their impact on the effective extraction radius were analyzed, resulting in a response surface model for each factor and the effective extraction radius. The results indicate that the initial permeability of the coal seam has the greatest impact on the extraction radius, with a maximum range of 2.027 m. The influence of extraction time, extraction negative pressure, and borehole diameter decreases sequentially. The borehole diameter has the least impact, with a range of 0.608 m. The response surface model has good significance, with a coefficient of determination ( $R^2$ ) of 0.9957, and it can explain over 99.57% of the response values. The response surface between the initial permeability of the coal seam and extraction time shows the greatest degree of distortion, indicating a significant interaction effect on the extraction radius. In contrast, the response surface between extraction time and extraction negative pressure shows the least degree of distortion, indicating that their interaction effect is the least significant. These findings can provide a theoretical reference for improving borehole design and enhancing gas extraction efficiency.

**Citation:** Cheng, X.; Cheng, C.; Xiao, L.; Ma, X. Response Surface Analysis on Multiple Parameter Effects on Borehole Gas Extraction Efficiency. *Processes* **2024**, *12*, 1587. <https://doi.org/10.3390/pr12081587>

**Keywords:** in-seam boreholes; gas extraction; extraction parameters; influence characteristics; coal mine safety

Academic Editor: Carlos Sierra Fernández

Received: 26 June 2024  
Revised: 21 July 2024  
Accepted: 24 July 2024  
Published: 29 July 2024



**Copyright:** © 2024 by the authors. Licensee MDPI, Basel, Switzerland. This article is an open access article distributed under the terms and conditions of the Creative Commons Attribution (CC BY) license (<https://creativecommons.org/licenses/by/4.0/>).

## 1. Introduction

Coal accounts for 56.0% of China's total energy consumption. Compared with previous years, although the proportion of coal production and consumption has decreased, it still occupies a dominant position in China's energy structure and will continue to play an important role in China's future economic development [1,2]. With the increase in coal mining depth in China, geological conditions have become more and more complex, and the probability of coal mine disasters is also increasing [3]. Compared with other coal mine accidents, gas accidents have always been one of the largest types of accidents, with the largest danger and the highest death rate in coal mines [4], so the containment of gas accidents cannot be ignored. Gas extraction is one of the important methods to prevent gas accidents, and the effect of gas extraction is affected by many factors.

Based on theories of gas flow and elastic mechanics, Shang et al. [5] conducted numerical simulations to study the effects of extraction negative pressure, borehole diameter, extraction time, and the initial permeability of the coal seam on the effective extraction radius. A multiple linear regression model of the influencing factors on the effective extraction radius was established. Chen et al. [6] used COMSOL Multiphysics numerical software to establish a three-dimensional numerical model of gas extraction boreholes.

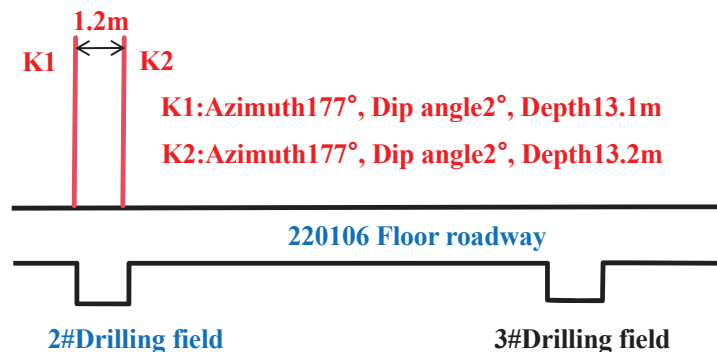
They analyzed the evolution pattern of gas pressure in the coal body and quantitatively studied the influence of borehole spacing on gas extraction effectiveness. Wang et al. [7] conducted qualitative and quantitative analyses of the extraction efficiency by examining three main factors influencing gas extraction: coal seam permeability, gas pressure, and burial depth. Fang et al. [8] used COMSOL software (version 6.2) to analyze the factors affecting gas occurrence and further investigated the impact of differences in gas pressure distribution on the effective extraction radius. Wang et al. [9] established a gas flow–solid coupling model based on stress and transport equations, used COMSOL software for numerical simulations of various factors affecting gas extraction efficiency, and obtained the distribution patterns of gas pressure. Wei et al. [10], addressing the creep characteristics of soft coal, established a flow–solid coupling mathematical model considering the creep characteristics of coal based on the permeability dynamic evolution equation that accounts for matrix shrinkage and effective stress. Using COMSOL Multiphysics software, they calculated the gas extraction volumes for single and multiple boreholes, optimized the gas extraction parameters, and conducted field trial applications. Zhang et al. [11] studied the relationship between gas geology (initial gas pressure, initial permeability, and burial depth) and the effective extraction radius, achieving precise borehole placement for gas extraction. Gao et al. [12] established a gas–air mixed flow model to study the effects of extraction time, negative extraction pressure, and extraction leakage on gas concentration, revealing the mechanism of gas extraction leakage. Xu et al. [13] established a gas seepage unit model around the borehole, derived the theoretical mathematical expression for calculating the effective extraction radius, conducted numerical simulations of gas extraction using computational fluid dynamics software, and obtained the effective extraction radius. To study the gas seepage characteristics in highly anisotropic coal seams, Nian et al. [14] established an anisotropic dual-porosity model and analyzed the impact of permeability anisotropy on gas pressure, gas extraction volume, and changes in the effective extraction radius. Additionally, they investigated the mechanisms by which ground stress, initial gas pressure, ultimate adsorption strain, and the Langmuir volume constant affect permeability anisotropy and gas extraction volume. Based on the gray correlation analysis of factors affecting gas extraction, such as borehole diameter, borehole spacing, and negative extraction pressure, Wang et al. [15] used orthogonal experimental design and COMSOL to simulate the effective extraction radius under different conditions. Zhang et al. [16] combined similarity simulation experiments and numerical simulations to analyze the impact of negative pressure changes on the gas seepage characteristics of coal. Kong et al. [17] analyzed the influence of multiple factors on the effective extraction radius of boreholes under hydraulic punching conditions by constructing a fluid–solid coupling numerical model.

Many scholars have achieved significant results in the sensitivity analysis of gas extraction efficiency. However, most previous studies have focused on the qualitative analysis of the impact of single factors on gas extraction efficiency. The variation patterns of gas extraction efficiency under the interaction of multiple factors require further quantitative analysis. Coal mine gas extraction is a complex system engineering project, where the effectiveness of its implementation is often influenced by multiple factors rather than a single factor. Therefore, studying only a single factor cannot fully reveal the mechanisms affecting gas extraction, nor can it reliably guide on-site gas extraction in coal mines. Based on previous research in this field and practical experience in coal mine gas extraction, this paper mainly selects initial coal seam permeability, extraction time, extraction negative pressure, and borehole diameter as the primary factors for study. This study is based on the Liuzhuang Mine of the China Coal Xinji Company. It employs the hole stress relief method for in situ stress testing in the mining area. Using a gas desorption–diffusion–seepage model and COMSOL Multiphysics numerical simulation software, the gas extraction process in boreholes is analyzed. Additionally, Minitab software (<https://www.minitab.com>) is used to design response surface experiments to investigate the impact of multi-factor interactions on borehole gas extraction efficiency. This research identifies the primary and secondary influencing factors and establishes the relationship between the effective extraction radius

of boreholes and multiple factors. The findings provide significant reference value for the design of gas extraction in underground coal mines. Specifically, through this study, the quantitative relationships between coal seam permeability, extraction time, extraction negative pressure, borehole diameter, and the effective extraction radius were established. This research reveals the key factors affecting gas extraction efficiency, making on-site gas extraction in coal mines more targeted and effective. For example, in the practical implementation of gas extraction projects in coal mines, measures such as enhancing coal seam permeability through hydraulic fracturing, reasonably increasing extraction time or negative pressure, and appropriately enlarging the borehole diameter can maximize gas extraction efficiency. The findings of this study can provide a reference for weighting these measures and guide the practical work on-site in coal mines.

## 2. In Situ Stress Testing

Permeability is a crucial factor affecting the coal seam gas extraction process, and it is closely related to the magnitude of in situ stress. Conducting in situ stress testing in the mining area provides essential stress data for constructing numerical models. Our field test employed the hole stress relief method to ensure the accuracy and reliability of the data. The advantage of the stress relief method for boreholes is that it is one of the most applicable and reliable methods for determining absolute stress. This method is not only technically mature but also provides accurate and reliable measurement results. Therefore, it has widespread application in the fields of rock mechanics and engineering. Two in situ stress measurement boreholes, K1 and K2, were arranged at the test site. Both boreholes were located on the south side of the roadway, approximately 1.5 m from the floor, with a spacing of about 1.2 m between them. The layout of the measurement boreholes is shown in Figure 1.



**Figure 1.** Schematic diagram of layout of in situ stress measuring boreholes.

Due to the fragmented nature of the core samples obtained during the in situ stress measurements, it was challenging to obtain the rock mechanical properties parameters for stress calculations through confining pressure tests. Therefore, rock blocks from boreholes K1 and K2 that were suitable for laboratory rock mechanics tests were processed into standard rock samples ( $\varphi 50 \text{ mm} \times 100 \text{ mm}$ ). Uniaxial compression tests were conducted on these samples using the RMT-150C rock mechanics testing machine (Wuhan, China) (Figure 2) to obtain the rock's elastic modulus, Poisson's ratio, and strength parameters. The test results are shown in Table 1.

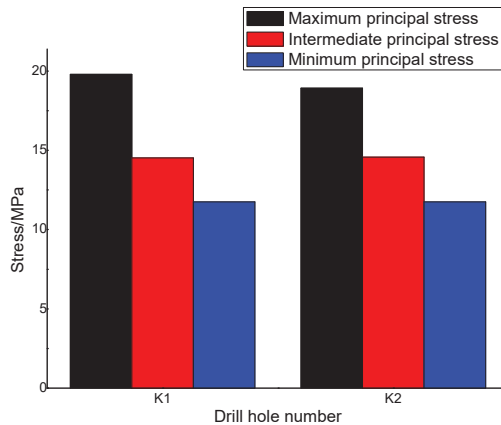
Based on the formula for the hole-core stress relief method and the measured rock mechanics parameters, the three-dimensional in situ stress measurement results for the measurement points were calculated, as shown in Figure 3.



**Figure 2.** RMT-150C test system for rock mechanical properties.

**Table 1.** Uniaxial compression test results of cores obtained from boreholes K1 and K2.

Number	Strength (MPa)	Elastic Modulus (GPa)	Poisson's Ratio
S1	69.789	24.865	0.208
S2	84.363	38.694	0.185
S3	64.322	34.477	0.183
Average value	74.158	34.012	0.192



**Figure 3.** The 3D in situ stress measurement results.

The results of the hole–core stress relief method for in situ stress testing at boreholes K1 and K2 indicate the following: The range of values for the maximum principal stress and intermediate principal stress at the measurement points on-site are 18.92 to 19.80 MPa and 14.52 to 14.57 MPa, respectively. The value for the minimum principal stress is 11.75 MPa. The azimuths are in the ranges of 265.9 to 266.4°, 74.6 to 88.6°, and 176.2 to 176.5°. The inclinations are in the ranges of 7.0 to 11.9°, 78.1 to 84.6°, and −0.43 to −4.44°. The horizontal stress exceeds the overburden stress, with the range of the maximum horizontal principal stress to overburden stress ratio being 1.38 to 1.41, indicating that the stress at the measurement points is predominantly tectonic. These in situ stress test results provide support for setting up stress conditions for subsequent numerical modeling.



### 3. Numerical Model Development

#### 3.1. Coal Seam Gas Migration Model

To effectively conduct numerical simulation research, the gas migration governing equations for the numerical model must first be theoretically constructed. The fractures in the coal seam divide the coal body into individual matrix elements. Adsorbed gas in the coal matrix desorbs and diffuses into the fractures, where it then flows through the fractures by seepage. This process is described by the dual-porosity gas migration model. When using this model, the matrix permeability is defined as a constant, only considering the dynamic changes in fracture permeability, simplifying the gas migration in the coal seam to a sequential process.

During the coal seam gas extraction process, the adsorbed gas within the coal matrix elements desorbs outward as a mass source, leading to continuous diffusion and seepage. The mass exchange equation between the coal matrix and fracture system is expressed as follows [18–20]:

$$Q_s = aD(c_m - c_f) = \frac{1}{\tau}(c_m - c_f) \quad (1)$$

In this equation,  $Q_s$  is the mass exchange rate between the unit volume of the coal matrix and the fracture system ( $\text{kg}/(\text{m}^3 \cdot \text{s})$ ).  $a$  is the matrix shape factor ( $\text{m}^{-2}$ ).  $D$  is the gas diffusion coefficient ( $\text{m}^2/\text{s}$ ).  $c_m$  is the gas concentration in the coal matrix ( $\text{kg}/\text{m}^3$ ).  $c_f$  is the gas concentration in the coal fractures ( $\text{kg}/\text{m}^3$ ).  $\tau$  is the adsorption time (s).

According to the ideal gas law, the relationship between gas concentration and pressure in the coal matrix and fractures is as follows:

$$c_m = \frac{M_g}{RT} p_m \quad (2)$$

$$c_f = \frac{M_g}{RT} p_f \quad (3)$$

In this equation,  $M_g$  is the molar mass of the gas ( $\text{kg}/\text{mol}$ ).  $R$  is the universal gas constant, with a value of  $8.314 \text{ J}/(\text{mol} \cdot \text{K})$ .  $T$  is the temperature of the coal seam (K).  $p_m$  is the gas pressure in the coal matrix (MPa).  $p_f$  is the gas pressure in the coal fractures (MPa).

Considering the adsorption time, the equation for gas diffusion from the coal matrix to the fractures can be modified to:

$$Q_s = \frac{M_g}{\tau RT} (p_m - p_f) \quad (4)$$

During the coal seam gas extraction process, the matrix system serves as a positive mass source for the fracture system, while the fracture system acts as a negative mass source for the matrix system. Therefore, according to the law of mass conservation, the mass exchange rate between the coal matrix and the fracture system should equal the rate of change in the gas mass in the coal matrix over time, which can be expressed as:

$$\frac{\partial m_m}{\partial t} = -\frac{M_g}{\tau RT} (p_m - p_f) \quad (5)$$

In this equation,  $m_m$  is the total gas content mass per unit volume in the coal matrix (kg).  $t$  is time (s).

The adsorption of gas only occurs in the coal matrix. The gas mass in the coal matrix includes both adsorbed gas and free gas. Therefore, the gas content mass per unit volume in the coal matrix can be expressed as follows [21]:

$$m_m = \phi_m \frac{M_g}{RT} p_m + (1 - \phi_m) \rho_n \rho_c \frac{V_L p_m}{p_m + P_L} \quad (6)$$

In this equation,  $\phi_m$  is the porosity of the coal matrix (%).  $\rho_n$  is the gas density at standard conditions ( $\text{kg}/\text{m}^3$ ).  $\rho_c$  is the bulk density of coal ( $\text{kg}/\text{m}^3$ ).  $V_L$  is the Langmuir volume constant ( $\text{m}^3/\text{t}$ ).  $P_L$  is the Langmuir pressure constant (MPa).

The gas density at standard conditions can be calculated using the following equation:

$$\rho_n = \frac{M_g}{V_m} \quad (7)$$

In this equation,  $V_m$  is the molar volume of the ideal gas at standard conditions ( $\text{m}^3/\text{mol}$ ).

By rearranging the above equations, we can obtain the governing equation for the change in gas pressure in the coal matrix over time:

$$\left[ \phi_m + (1 - \phi_m) \frac{\rho_c R T V_L P_L}{V_m (p_m + P_L)^2} \right] \frac{\partial p_m}{\partial t} = -\frac{1}{\tau} (p_m - p_f) \quad (8)$$

The mass balance equation for gas within the unit volume of the coal fracture system is:

$$\frac{\partial m_f}{\partial t} + \nabla \cdot (\rho_f \vec{q}) = (1 - \phi_f) Q_s \quad (9)$$

In this equation,  $m_f$  is the mass of free gas per unit volume in the coal fracture system (kg).  $\rho_f$  is the gas density in the coal fracture system ( $\text{kg}/\text{m}^3$ ).  $\vec{q}$  is the velocity vector according to Darcy's law (m/s).  $\phi_f$  is the porosity of the coal fracture system (%).

The mass of free gas per unit volume in the coal fracture system is:

$$m_f = \rho_f \phi_f \quad (10)$$

Since the mass of gas is very small, the effect of gravity on gas diffusion and flow in the coal seam can be ignored. According to Darcy's law, the velocity vector of the gas is given by:

$$\vec{q} = -\frac{k}{\mu} \nabla p_f \quad (11)$$

In this equation,  $k$  is the permeability of the coal ( $\text{m}^2$ ).  $\mu$  is the dynamic viscosity of the gas (Pa·s).

Finally, the governing equation for gas flow in the fracture system can be expressed as:

$$\phi_f \frac{\partial p_f}{\partial t} + p_f \frac{\partial \phi_f}{\partial t} - \nabla \cdot \left( \frac{k}{\mu} p_f \nabla p_f \right) = \frac{1}{\tau} (1 - \phi_f) (p_m - p_f) \quad (12)$$

Thus, the governing equation for gas migration in the dual-porosity medium model is:

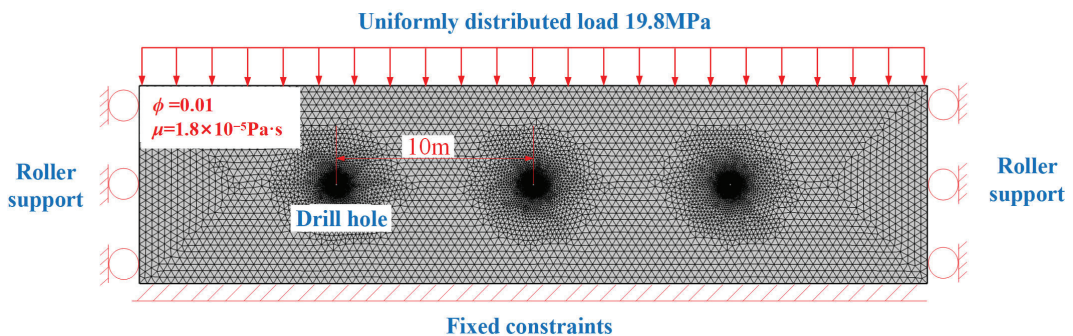
$$\begin{cases} \left( \phi_m + (1 - \phi_m) \frac{\rho_c R T V_L P_L}{V_m (p_m + P_L)^2} \right) \frac{\partial p_m}{\partial t} = -\frac{1}{\tau} (p_m - p_f) \\ \phi_f \frac{\partial p_f}{\partial t} + p_f \frac{\partial \phi_f}{\partial t} - \nabla \cdot \left( \frac{k}{\mu} p_f \nabla p_f \right) = \frac{1}{\tau} (1 - \phi_f) (p_m - p_f) \end{cases} \quad (13)$$

This model is used to control the gas flow process in numerical simulations of gas extraction, ensuring the accuracy of the sensitivity analysis of gas extraction parameters.

### 3.2. Geometric Model and Boundary Conditions

Based on the actual geological conditions of the mine, a numerical model was established with dimensions of 40 m in length, 10 m in height, and a distance of 10 m between boreholes. Regarding boundary conditions, roller supports were set on both sides of the model, and fixed constraints were applied to the bottom boundary of the model, allowing overall settlement. For the convenience of numerical model establishment and analysis,

it was assumed that the stress on the model is uniformly distributed, and the initial gas pressure and porosity within the model are also uniformly distributed. Since this study mainly focuses on the impact of coal seam permeability, extraction time, extraction negative pressure, and borehole diameter on the effectiveness of gas extraction, the influence of these assumptions, as well as the model grid division and boundary condition settings, on the study's error was within an acceptable range. According to collected coal seam parameter data, a uniformly distributed load pressure of 19.8 MPa was applied to the surface of the model. The initial gas pressure in the coal seam was 0.6 MPa, the porosity of the coal seam was 0.01, the gas density was  $0.716 \text{ kg/m}^3$ , and the gas dynamic viscosity was  $1.8 \times 10^{-5} \text{ Pa}\cdot\text{s}$ . At the beginning of the simulation experiment, gas extraction boreholes were set up. Once the model reached stress equilibrium, extraction negative pressure was applied for the calculation, and the simulation results under the influence of various parameters were obtained. A schematic diagram of the numerical model is shown in Figure 4.



**Figure 4.** Schematic diagram of numerical model.

## 4. Numerical Simulation Analysis and Discussion

### 4.1. Screening of Influencing Factors

In the 150,804 working faces of the 8th coal seam at Liuzhuang Mine, the coal seam gas pressure is 0.6 MPa. The effective extraction radius cannot be determined by the criterion of the gas pressure dropping below 0.74 MPa. According to the relative pressure index method, if the pre-extraction rate of the coal seam is 30%, the gas pressure reduction in the coal seam needs to reach 51%. When the simulated gas pressure at a certain point in the coal seam drops to 0.294 MPa, indicating a 51% reduction, the gas extraction at that point meets the standard. The distance from that point to the borehole is then considered the effective extraction radius.

In the multivariable orthogonal experiment method, range analysis is typically used to explore the influence of orthogonal experiment results. Range analysis can intuitively determine the strength of each factor's impact on the experimental data. This study uses an orthogonal experimental design to analyze the influence of borehole gas extraction parameters on extraction effectiveness, identifying the least significant factor. Using the effective extraction radius  $R$  as the response indicator, the study examines the effects of extraction time, the initial permeability of the coal seam, negative extraction pressure, and borehole diameter on the effective extraction radius. Each of these four factors was set at three levels, and a three-level, four-factor orthogonal design table  $L_9(3^4)$  was used, resulting in nine experimental schemes. The parameters in each experimental scheme were mainly set reasonably based on the actual conditions of the coal mine site and relevant industry standards, as shown in Table 2:

Table 2. Orthogonal test scheme.

Test Serial Number	Initial Permeability of the Coal Seam ( $10^{-15} \text{ m}^2$ )	Borehole Diameter (mm)	Extraction Time (d)	Negative Pressure for Gas Extraction (kPa)	Effective Extraction Radius (m)
1	0.01	64	60	13	0.328
2	0.01	94	120	23	0.596
3	0.01	124	180	33	0.850
4	0.10	64	120	33	0.630
5	0.10	94	180	13	0.956
6	0.10	124	60	23	1.034
7	1.00	64	180	23	3.322
8	1.00	94	60	33	1.482
9	1.00	124	120	13	3.050

The results of the orthogonal experiments were processed and analyzed by calculating the mean and range for each factor at each level, followed by normalization. Each factor was then ranked to understand the degree of influence on the response indicator. The calculated results are shown in Table 3:

Table 3. Range analysis of effective extraction radius.

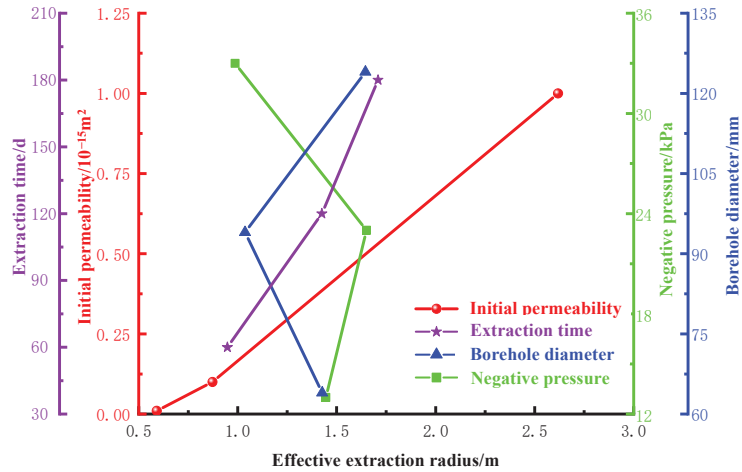
Level Group Number	Initial Permeability of the Coal Seam ( $10^{-15} \text{ m}^2$ )	Borehole Diameter (mm)	Extraction Time (d)	Negative Pressure for Gas Extraction (kPa)
1	1.774	4.280	2.844	4.334
2	2.620	3.112	4.276	4.952
3	7.854	4.934	5.128	2.962
Mean value 1	0.591	1.427	0.948	1.445
Mean value 2	0.873	1.037	1.425	1.651
Mean value 3	2.618	1.645	1.709	0.987
Range	2.027	0.608	0.761	0.664
Patch	1	4	2	3

Figure 5 shows the mean effective extraction radius under different levels of various factors. It is evident that the initial permeability of the coal seam has the largest mean difference across its three levels, indicating it has the greatest influence. The mean differences for extraction time and extraction negative pressure at the three levels are secondary, indicating that their impact is less significant than the initial permeability of the coal seam. In contrast, the borehole diameter has almost the same mean values across its three levels, indicating its influence is minimal. Additionally, combining the results from Table 3, it can be concluded that the four factors have varying degrees of influence on the effective extraction radius of the borehole. The factors ranked in descending order of influence are the initial permeability of the coal seam, extraction time, negative extraction pressure, and borehole diameter.

For the initial permeability of the coal seam, the maximum mean effective extraction radius is 2.618 m, and the minimum mean is 0.591 m, resulting in a range of 2.027 m, indicating its highest impact on the effective extraction radius. For the borehole diameter, the maximum mean effective extraction radius is 1.645 m, and the minimum mean is 1.037 m, resulting in a range of 0.608 m, indicating its lowest impact. Among the three levels of the extraction time factor, the maximum average effective extraction radius of the borehole is 1.709 m, and the minimum average is 0.948 m. The range of the effective extraction radius for extraction time is 0.761 m, indicating that its influence on the effective extraction radius of the borehole is less than that of the initial permeability of the coal seam. Among the three levels of the extraction negative pressure factor, the maximum average effective extraction radius of the borehole is 1.445 m, and the minimum average is 0.987 m.

The range of the effective extraction radius for extraction negative pressure is 0.664 m, indicating that its influence on the effective extraction radius of the borehole is less than that of extraction time.

Therefore, in the response surface experiments, the borehole diameter factor was excluded, and the focus was on analyzing the effects of initial coal seam permeability, extraction time, and negative extraction pressure on borehole gas extraction efficiency.



**Figure 5.** The mean value of effective extraction radius under different factors and their different levels.

#### 4.2. Response Surface Model

The response surface method (RSM) is a technique for parameter optimization using mathematical and statistical analysis. By fitting a first-order or second-order model between the response function and influencing factors as an approximation of the true response function, the RSM actively collects data based on multiple linear regressions to obtain a well-behaved regression equation. The established complex multi-dimensional space surface closely approximates actual conditions, requiring relatively few experimental runs. Commonly used design methods in the RSM are the central composite design (CCD) and the Box–Behnken design (BBD).

When the factors are the same, the Box–Behnken design requires fewer experimental runs than central composite design, has approximate rotatability, lacks sequentiality, and avoids experimental combinations where factors are simultaneously at high levels. Moreover, the Box–Behnken design has been successfully applied in similar research scenarios in recent years [22,23]. Therefore, the Box–Behnken design was adopted. The Box–Behnken design includes 15 experimental schemes, as shown in Table 4. The effective extraction radius of boreholes under different extraction parameter conditions was calculated using COMSOL software, and the results are presented in Table 4.

Based on the results, an effective extraction radius and multi-factor coupling relationship model can be established to assist in guiding the dynamic optimization and adjustment of extraction parameters. Using a response surface model with polynomial degrees higher than two would increase the number of higher-order coefficients and significantly increase the computational load. A quadratic polynomial is more flexible and simple, offers high fitting accuracy, and is widely used. Therefore, this study employs a quadratic polynomial to express the relationship.

Table 4. Response surface experimental design scheme and results.

Test Serial Number	Initial Permeability of the Coal Seam ( $10^{-15} \text{ m}^2$ )	Extraction Time (d)	Negative Pressure for Gas Extraction (kPa)	Effective Extraction Radius (m)
1	1.00	120	33	2.316
2	0.01	60	23	0.222
3	0.10	120	23	0.654
4	0.01	120	33	0.273
5	1.00	180	23	3.703
6	1.00	120	13	2.158
7	0.10	180	13	0.761
8	0.10	120	23	0.651
9	0.10	60	13	0.450
10	0.10	120	23	0.652
11	0.01	180	23	0.308
12	0.10	180	33	0.810
13	1.00	60	23	1.453
14	0.10	60	33	0.480
15	0.01	120	13	0.259

For the simulation results obtained in Table 4, a response surface experiment was conducted to perform a multi-factor regression fitting analysis. The polynomial response surface regression equation between the effective extraction radius and multiple factors was established as follows:

$$R = -0.093 + 2.069K - 0.00420T + 0.0454Q - 2.204K^2 + 0.000020T^2 - 0.000985Q^2 + 0.01802KT + 0.00689K \times Q + 0.00008T \times Q$$

In this equation, R represents the effective extraction radius, K represents the coal seam permeability, T represents the extraction time, and Q represents the negative extraction pressure.

#### 4.3. Response Surface Analysis of Effective Extraction Radius

The approximate function of the quadratic polynomial response surface model was transformed into a linear function in form through variable substitution. Then, the function values based on the response surface model were obtained through the parameter matrix of the experimental sample space. This allowed for the calculation of the error between the response values and the experimental values. The coefficients of the quadratic polynomial in the above equation were determined using the least squares method.

In the table, the  $p$ -value is a key analysis value for the significance of each term. The smaller the  $p$ -value, the less likely an extreme hypothetical situation occurs, indicating that the result is more significant.

The variance analysis of the regression equation is shown in Table 5. It can be observed that the  $p$ -value of the response surface model for the target function R is much less than 0.01, indicating excellent model significance. This means the polynomial regression equation accurately reflects the influence of various factors on the response value (effective extraction radius). The  $p$ -values for the initial permeability term, extraction time term, the square of the initial permeability term, and the interaction term between initial permeability and extraction time are all less than 0.05, indicating that these terms are significant in the model. The  $p$ -values for the other terms are not much greater than 0.05, suggesting that their significance is also acceptable. Although the significance of extraction negative pressure in the model is not high, considering that it is a key indicator for coal mine gas extraction and other potential uncertainties, extraction negative pressure was included in the construction and further analysis of this model. The coefficient of determination is 0.9957, indicating that over 99.57% of the response values can be explained by this model.

Table 5. Variance analysis.

Source	Degree of Freedom	Adj SS	Adj MS	F-Value	p-Value
Model	9	13.7142	1.52380	128.96	0.000
Linear	3	11.4241	3.80802	322.28	0.000
Initial permeability	1	9.1763	9.17633	776.62	0.000
The extraction time	1	2.2346	2.23458	189.12	0.000
Negative pressure for gas extraction square	3	0.1478	0.04927	4.17	0.079
Initial permeability and Initial permeability	1	0.0899	0.08994	7.61	0.040
Extraction time and Extraction time	1	0.0189	0.01885	1.60	0.262
Negative pressure and Negative pressure	1	0.0359	0.03585	3.03	0.142
Two-factor interaction	3	1.5356	0.51187	43.32	0.001
Initial permeability and Extraction time	1	1.5293	1.52932	129.43	0.000
Initial permeability and Negative pressure	1	0.0062	0.00621	0.53	0.501
Extraction time and Negative pressure	1	0.0001	0.00009	0.01	0.934
Error	5	0.0591	0.01182	...	...
Total	14	13.7732	...	...	...

Note: Significance is indicated by  $p < 0.05$ , and high significance by  $p < 0.01$ . The coefficient of determination is  $R^2 = 0.9957$ , and the adjusted coefficient of determination is  $R^2(\text{adjust}) = 0.988$ .

Based on the quadratic polynomial regression equation, response surfaces were plotted, as shown in Figures 6–8. These are three-dimensional surfaces resulting from the interaction effects of various independent variables on the response value. They allow for the analysis of the interaction between any two factors.

The response surface plots between pairs of the initial permeability of the coal seam, extraction time, and extraction negative pressure show that the effective extraction radius of the borehole changes the fastest along the initial permeability axis and the slowest along the extraction negative pressure axis. Among these, the response surface in Figure 6 has the most distortion, indicating a significant interaction between initial permeability and extraction time. The greater the initial permeability of the coal seam, the shorter the extraction time required to achieve the same extraction volume. The response surface in Figure 7 shows some distortion, suggesting a slightly significant interaction between initial permeability and extraction negative pressure. The greater the initial permeability of the coal seam, the lower the extraction negative pressure required to achieve the same extraction capacity. The response surface in Figure 8 shows no obvious distortion, indicating that the interaction between extraction time and extraction negative pressure is not significant. There is no clear interrelationship between extraction time and extraction negative pressure.

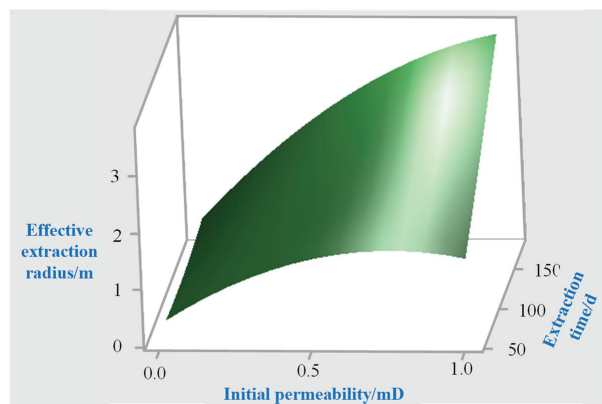


Figure 6. Response surface of initial permeability of coal seam and extraction time.

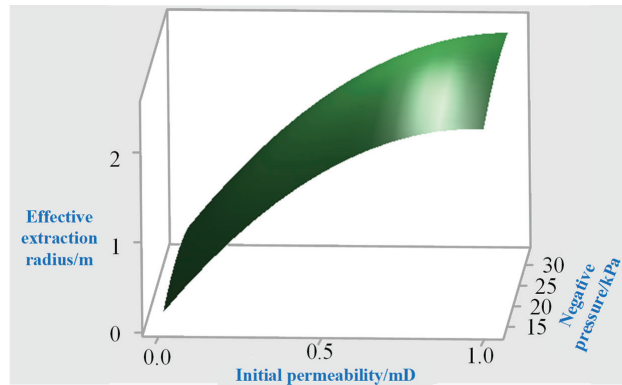


Figure 7. Response surface of initial permeability of coal seam and negative pressure.

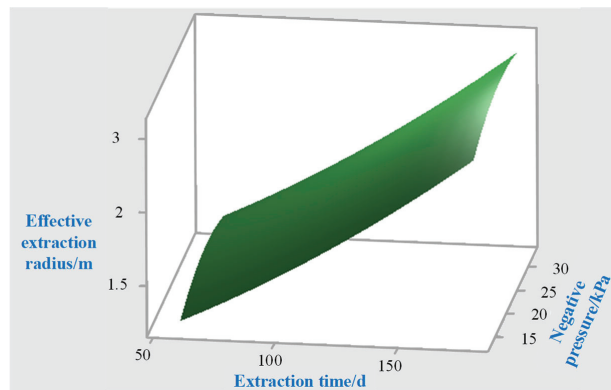


Figure 8. Response surface of extraction time and extraction negative pressure.

This also confirms that the initial permeability of the coal seam has a highly significant effect on the effective extraction radius of the borehole during gas extraction. The extraction time has a moderately significant effect, while the extraction negative pressure has a less significant effect. The most critical factor influencing borehole gas extraction is the permeability of the coal seam. When the permeability is high, the coal seam fractures are well-developed, allowing for higher permeability and making gas flow through the coal seam easier and more efficiently extracted by the borehole. The longer the extraction time, the more gas is extracted from the coal seam. However, due to the limitation of the initial permeability of the coal seam, the potential for improvement in gas extraction efficiency by extending the extraction time is limited. In actual coal mine production scenarios, an unreasonable increase in extraction time can negatively impact coal production. Increasing the extraction negative pressure can enhance the gas extraction capacity to some extent and accelerate the gas extraction rate from the coal seam. However, excessively high extraction negative pressure can lead to borehole leakage, adversely affecting gas extraction efficiency.

In summary, the factors affecting the effective extraction radius of the borehole, in order of significance, are initial permeability of the coal seam > extraction time > extraction negative pressure. This is consistent with the range analysis results of the orthogonal experiments. By comparing these results with other similar studies, it is found that for low-permeability coal seams, the primary factor affecting gas extraction efficiency is coal seam permeability. However, for coal seams with better permeability, the impact of coal seam permeability is not significant, and factors such as extraction time, borehole sealing quality, appropriate extraction negative pressure, and borehole diameter become the main



factors influencing gas extraction efficiency. Therefore, for low-permeability coal seams, it is crucial to implement measures to increase permeability before extraction, such as hydraulic slotting, protective layer mining, and loosening blasting. These measures can increase the permeability of low-permeability coal seams and improve gas extraction efficiency. When coal mines have conditions for protective seam mining, priority should be given to adopting protective seam extraction measures to increase coal seam permeability. For single low-permeability coal seams, further measures should be selected based on the characteristics of the coal seam, such as hydraulic fracturing, liquid carbon dioxide phase transition fracturing, or gas injection displacement, to enhance coal seam permeability and extraction efficiency and fundamentally improve gas extraction effectiveness.

It should be noted that different coal mines have varying geological conditions and gas extraction conditions. The main factors and their weights affecting gas extraction efficiency will also differ. In practical coal mine applications, further characteristic analysis should be conducted based on specific conditions to obtain research results that are more applicable to specific scenarios.

## 5. Conclusions

(1) Significance of Initial Permeability: Based on the orthogonal experiment results, the initial permeability of the coal seam has the greatest impact on the effective extraction radius, with a maximum range of 2.027 m. In contrast, the borehole diameter has the least impact, with a range of 0.608 m. The influence of the factors on the effective extraction radius of the borehole decreases in the following order: initial permeability of the coal seam, extraction time, extraction negative pressure, and borehole diameter;

(2) Response Surface Model: Using the response surface method, the relationship model between the initial permeability of the coal seam, extraction time, extraction negative pressure, and effective extraction radius was obtained. The  $p$ -value of this response surface model is less than 0.05, indicating its high significance. The model's determination coefficient is 0.9957, meaning it can explain over 99.57% of the response values;

(3) Interaction Effects: The interaction of multiple factors introduces new influences on the changes in the effective extraction radius. The initial permeability of the coal seam remains the most significant factor. The response surface between initial permeability and extraction time shows the greatest distortion, indicating the strongest interaction effect on the extraction radius. Conversely, the response surface between extraction time and extraction negative pressure shows the least distortion, indicating a negligible interaction effect. Therefore, increasing the permeability of the coal seam is one of the primary methods to enhance gas extraction efficiency;

(4) For coal seam gas extraction, especially in low-permeability coal seams, conducting pre-extraction coal seam fracturing to increase permeability can effectively enlarge the gas extraction radius, thereby significantly enhancing gas extraction efficiency.

**Author Contributions:** Conceptualization, X.C.; methodology, C.C.; validation, X.C., C.C. and L.X.; formal analysis, C.C.; investigation, X.M.; resources, C.C.; data curation, X.M.; writing—original draft preparation, X.C.; writing—review and editing, C.C.; visualization, C.C.; supervision, L.X.; project administration, X.C.; funding acquisition, X.C. All authors have read and agreed to the published version of the manuscript.

**Funding:** This research is funded by the National Key Research and Development Program of China, grant number 2023YFF0615404.

**Data Availability Statement:** The data used to support the findings of this study are available from the corresponding author upon request.

**Conflicts of Interest:** Author X.C., C.C., L.X. and X.M. were employed by the company China Coal Energy Research Institute Co., Ltd. The remaining authors declare that the research was conducted in the absence of any commercial or financial relationships that could be construed as a potential conflict of interest.

## References

- Xie, H.P.; Wu, L.X.; Zheng, D.Z. Prediction on the energy consumption and coal demand of China in 2025. *J. China Coal Soc.* **2019**, *44*, 1949–1960.
- Xie, H.P.; Ren, S.H.; Xie, Y.C. Development opportunities of the coal industry towards the goal of carbon neutrality. *J. China Coal Soc.* **2021**, *46*, 2197–2211.
- Yuan, L. Research progress of mining response and disaster prevention and control in deep coal mines. *J. China Coal Soc.* **2021**, *46*, 716–725.
- Liu, P.; Jing, J.B.; Wei, H.Z.; Yu, J.; Lu, X.; Liu, M. Construction of knowledge base and early warning inference of gas accident based on time-space constraints. *Coal Sci. Technol.* **2020**, *48*, 262–273.
- Shang, Y.Q.; Wu, G.Y.; Kong, D.Z. Research on influencing factors of effective gas extraction radius in coal mine based on multiple linear regression. *Adv. Mater. Sci. Eng.* **2022**, *2022*, 3013647. [CrossRef]
- Chen, X.J.; Cui, P.F.; Min, R. Numerical simulation study on influencing factors of hole spacing of hydraulic punching based on the effective extraction area. *Energy Rep.* **2023**, *9*, 3192–3203. [CrossRef]
- Wang, H.; Wang, E.Y.; Li, Z.H. Analysis of the difference of gas extraction quantity from coal seam under the influence of permeability, gas Pressure, and buried depth of coal seam: A case study. *Processes* **2023**, *11*, 3086. [CrossRef]
- Fang, H.H.; Zheng, C.S.; Qi, N. Coupling mechanism of THM fields and SLG phases during the gas extraction process and its application in numerical analysis of gas occurrence regularity and effective extraction radius. *Pet. Sci.* **2022**, *19*, 990–1006. [CrossRef]
- Wang, Y.; Zhao, C.G.; Wu, B. Study on gas migration law and influencing factors of gas drainage. *Int. J. Oil Gas Coal Technol.* **2022**, *31*, 406–423. [CrossRef]
- Wei, P.; Huang, C.W.; Li, X.L. Numerical simulation of boreholes for gas extraction and effective range of gas extraction in soft coal seams. *Energy Sci. Eng.* **2019**, *7*, 1632–1648. [CrossRef]
- Zhang, L.W.; Chu, Y.Y.; Zhou, Y. The in-hexagon borehole layout for the optimization of the effective radius of gas extraction. *Sustainability* **2023**, *15*, 12711. [CrossRef]
- Gao, H.; Du, F.; Cheng, X.Y. Study on the influence mechanism of air leakage on gas extraction effect—a numerical case study of the coal mine site in Anhui. *Processes* **2023**, *11*, 2161. [CrossRef]
- Xu, H.; Wang, G.; Yang, G.Y. Theoretical, numerical, and experimental analysis of effective extraction radius of coalbed methane boreholes by a gas seepage model based on defined criteria. *Energy Sci. Eng.* **2020**, *8*, 880–897. [CrossRef]
- Nian, F.T.; Ju, F.; Zheng, C.S.; Wu, H.; Cheng, X. Effects of coal permeability anisotropy on gas extraction performance. *Processes* **2023**, *11*, 1408. [CrossRef]
- Wang, Y.; Xu, M.T.; Kong, D.Z. Optimization of drilling parameters for coal seam gas extraction considering fluid-solid coupling and field application. *Energy Sci. Eng.* **2024**, *12*, 657–669.
- Zhang, T.J.; Pang, M.K.; Jiang, X.K.; Peng, W.Q.; Ji, X. Influence of negative pressure on gas percolation characteristics of coal body in perforated drilling hole. *Rock Soil Mech.* **2019**, *40*, 2517–2524.
- Kong, X.G.; Wang, E.Y.; Liu, X.F.; Li, N.; Chen, L.; Feng, J.; Liu, Q. Coupled analysis about multi-factors to the effective influence radius of hydraulic flushing: Application of response surface methodology. *J. Nat. Gas Sci. Eng.* **2016**, *32*, 538–548. [CrossRef]
- Warren, J.E.; Root, P.J. The behavior of naturally fractured reservoirs. *Soc. Pet. Eng. J.* **1963**, *3*, 245–255. [CrossRef]
- Liu, Q.Q.; Chu, P.; Huang, W.Y.; LV, B.; Wang, L.; Zhang, B.; Liu, Y. Gas desorption-diffusion hysteresis pressure and the matrix-fracture mass transfer function of dual-porosity coal. *J. China Coal Soc.* **2022**, *47*, 870–882.
- Liu, Y.X.; Ozbayoglu, E.M.; Upchurch, E.R.; Baldino, S. Computational fluid dynamics simulations of Taylor bubbles rising in vertical and inclined concentric annuli. *Int. J. Multiph. Flow* **2023**, *159*, 104333. [CrossRef]
- Saghafi, A.; Faiz, M.; Roberts, D. CO<sub>2</sub> storage and gas diffusivity properties of coals from Sydney Basin, Australia. *Int. J. Coal Geol.* **2007**, *70*, 240–254. [CrossRef]
- Oza, S.; Kodgire, P.; Kachhwaha, S.S. Analysis of RSM based BBD and CCD techniques applied for biodiesel production from waste cotton-seed cooking oil via ultrasound method. *Anal. Chem. Lett.* **2022**, *12*, 86–101. [CrossRef]
- Sukpancharoen, S.; Hansirisawat, P.; Srinophakun, T.R. Implementation of response surface to optimum biodiesel power plant derived from empty fruit bunch. *J. Energy Resour. Technol.* **2022**, *144*, 012101. [CrossRef]

**Disclaimer/Publisher’s Note:** The statements, opinions and data contained in all publications are solely those of the individual author(s) and contributor(s) and not of MDPI and/or the editor(s). MDPI and/or the editor(s) disclaim responsibility for any injury to people or property resulting from any ideas, methods, instructions or products referred to in the content.

Article

# Research on Gas Control Technology in Goaf Based on the Influence of Mining Speed

Cheng Cheng <sup>1,2,\*</sup>, Xiao-Yu Cheng <sup>1</sup>, Long Chen <sup>1</sup> and Xing-Ying Ma <sup>1</sup>

<sup>1</sup> China Coal Energy Research Institute Co., Ltd., Xi'an 710054, China; chengxiaoyu@chinacoal.com (X.-Y.C.); chenlong1@chinacoal.com (L.C.); mxy6629@123.com (X.-Y.M.)

<sup>2</sup> College of Safety Science and Engineering, Xi'an University of Science and Technology, Xi'an 710054, China

\* Correspondence: 18717314036@163.com

**Abstract:** To comprehensively understand the influence of mining speed on gas emissions in goaf during coal seam extraction, enhance gas extraction efficiency in goaf, manage gas emissions at the working face, and ensure safety in the mining production process. This study focuses on the No. 3 mining area of Wangjialing Mine, employing numerical simulations to analyze the evolution of mining-induced fractures and the characteristics of gas distribution in the overburden at varying mining speeds. Furthermore, by integrating actual gas emission and extraction data at the production face, this study examines the quantitative relationship between mining speed and gas emissions in the goaf, identifying optimal regions for high-position borehole layouts and conducting borehole optimization design and investigation. The results of this study indicate that the initial caving step distance of the goaf roof increases with the advancement speed of the working face. Conversely, the maximum height of through fractures in the overburden decreases as the mining speed increases, while delamination fractures are minimally affected by the advancement speed. By categorizing and averaging data on goaf mining speed, the impact of initial and periodic pressure on gas emissions can be effectively mitigated, revealing a linear correlation coefficient of 0.94 between goaf gas emissions and mining speed. At varying mining speeds of the working face, the efficient extraction layer and horizontal distance parameters of gas extraction boreholes in the goaf conform to the linear equation  $y = ax \pm b$ . Based on the research findings, an optimization design for mining face speed and high-level borehole parameters in the goaf was implemented. The average gas extraction rate of high-level directional boreholes reached 68% throughout the extraction period. Gas emissions at the working face were effectively controlled below  $10 \text{ m}^3/\text{min}$ , with the maximum gas concentration at the upper corners and return airflow kept below 0.8%. This effectively managed gas emissions at the working face, ensuring safe production in the mine, providing a theoretical basis for identifying gas-rich areas in the mining-induced overburden, and enhancing gas extraction efficiency at the working face.

**Keywords:** mining-induced fractures; mining speed; numerical simulation; gas extraction; high-level borehole optimization

**Citation:** Cheng, C.; Cheng, X.-Y.; Chen, L.; Ma, X.-Y. Research on Gas Control Technology in Goaf Based on the Influence of Mining Speed. *Processes* **2024**, *12*, 1528. <https://doi.org/10.3390/pr12071528>

Academic Editor: Guining Lu

Received: 28 June 2024

Revised: 16 July 2024

Accepted: 18 July 2024

Published: 20 July 2024



**Copyright:** © 2024 by the authors. Licensee MDPI, Basel, Switzerland. This article is an open access article distributed under the terms and conditions of the Creative Commons Attribution (CC BY) license (<https://creativecommons.org/licenses/by/4.0/>).

## 1. Introduction

Coal serves as the “ballast stone” of China’s energy security, and ensuring the safe and efficient extraction of coal mines is crucial for maintaining this security [1,2]. As the number of ten-million-ton mines in the country increases, the mining intensity of coal mines also rises. Due to high-intensity mining at the working face, gas emissions in mines escalate, making gas disasters a key factor restricting the safe production of coal mines [3–5]. Especially during high-intensity mining at the working face, gas emissions in the goaf increase sharply, causing gas over-limit at the coal mining face, upper corners, and return airflow, thereby posing significant safety hazards to the mine [6,7]. Therefore, to effectively carry out gas prevention and control in the goaf, it is first necessary to determine the emission and accumulation characteristics of gas in the goaf, enabling the implementation

of targeted measures. However, during mine production, the gas emission and migration characteristics in the goaf are influenced by the advancement speed of the working face. The collapse and fracture development of the mining-induced overburden in the goaf exhibit significant variations, complicating the accurate determination of gas-rich locations within the fracture zone. This results in inefficiencies in extracting gas from the fractures of the overburden through high-level directional long boreholes in the goaf [8]. Therefore, it is imperative to study the evolution of fractures in the overburden influenced by the mining face speed and the gas emission characteristics in the goaf to enhance the gas management capacity of the mine goaf.

Numerous scholars have extensively studied the characteristics of gas emission and migration in the goaf. Empirical evidence has shown that the main sources of gas in the goaf are residual coal, air leakage at the working face, and gas migration from adjacent strata. After being emitted, the gas migrates and accumulates in the fracture zones of the overburden in the goaf [9–13]. Therefore, examining the development characteristics of mining-induced overburden fractures can effectively elucidate the gas migration patterns in the goaf. Qian Minggao, Yuan Liang, Li Shugang, and others have proposed various theories on mining field movement, including the “O-ring”, “high-position annular body”, “vertical three zones”, and “elliptic parabolic zone” theories [14–16]. Building upon these theories, numerous scholars have further explored the evolution characteristics of overburden fractures in the goaf using methods such as numerical simulation, physical simulation, and field experiments. Islam [17] and Wu [18] employed numerical simulations to investigate the characteristics of overburden collapse during working face mining and analyzed the fracture zone development process. Lin [19] utilized physical similarity simulation methods to experimentally analyze the dynamic evolution process of overburden fractures during coal seam mining. Zhang [20] and Kang [21] respectively utilized peeping technology and borehole water injection experiments to analyze the development characteristics of the mining-induced fracture zone in the overburden on site. Yuan [22] and colleagues employed electromagnetic methods to conduct on-site testing and analysis of overburden fractures during coal seam mining based on the electrical characteristics of the overburden fractures. Zhang [23] conducted a comprehensive study on the evolution characteristics of overburden fractures in fully mechanized mining using a combination of theoretical analysis, numerical simulations, and field measurements. Concurrently, numerous scholars have studied the migration and distribution patterns of gas in the goaf based on research on mining-induced overburden fractures, providing fundamental theoretical support for gas management in the goaf. Zhou [24] and Qin [25] employed numerical simulations to analyze the gas migration characteristics within mining-induced fractures, obtaining the flow characteristics of gas in the annular high-permeability zones of the overburden under different working conditions. Guo [26] and colleagues utilized finite element simulations to analyze the dynamic interaction between stress, overburden fractures, and gas seepage during working face mining. Zhang [27] employed physical experiments to investigate the permeability evolution characteristics of fractured coal under different pressures, analyzing the gas seepage and migration patterns in the compaction and fracture zones of the goaf. Liu [28] and colleagues examined the migration and distribution characteristics of gas within overburden fracture zones under gas extraction conditions in the goaf.

The aforementioned research results have significantly advanced the understanding of mining-induced overburden fractures and gas accumulation characteristics in the goaf, and substantial progress has been made in gas management within the goaf. However, research on the characteristics of gas emission and distribution in the goaf considering the impact of the working face advancement speed has been limited. Additionally, there has been scant research on the gas accumulation characteristics in the mining-induced overburden fracture zone affected by the advancement speed, thereby limiting the guidance for on-site gas management. Therefore, it is imperative to further study the evolution of mining-induced overburden fractures and the characteristics of gas emission in the goaf under the influence of the mining speed. This will effectively guide the selection of areas

for high-level directional long borehole placement in the goaf and enhance the effectiveness of gas management in the mine goaf.

This paper employs numerical simulations to investigate the evolution of the fracture zone distribution range in the overburden layers of the goaf under varying mining speeds. It identifies the characteristics of gas accumulation in the goaf as influenced by the mining speed. Based on field measurement data, it analyzes the gas emission patterns in the goaf and quantifies the relationship between the optimal borehole layer and horizontal distance affected by the mining speed. According to the research results, it optimizes the parameters of high-level boreholes in the goaf and conducts field tests. The research findings provide theoretical support for identifying gas accumulation zones in mining-induced overburden and for optimizing high-level boreholes.

## 2. Evolution Characteristics of Mining-Induced Fractures and Gas Migration Patterns Affected by Mining Speed

### 2.1. Overview of Engineering Conditions in the Test Area and Establishment of the Numerical Model

Wangjialing Coal Mine, situated in Xiangning County, Shanxi Province, encompasses a mining field area of 119.7 km<sup>2</sup>. The mine utilizes primary and auxiliary inclined shafts for development and employs the longwall retreat mining method combined with fully mechanized top coal caving technology. It is a quintessential high-production, high-efficiency coal mine characterized by high gas emissions at the working face.

The selected test area is the third mining area of Wangjialing Coal Mine, characterized by an average coal thickness of 6 m and a simple coal seam structure. During the production process at the working face, gas emissions from the goaf constitute 45.5% of the total gas emissions at the working face. Gas in the goaf is primarily extracted using high-level directional long boreholes and buried pipes. However, during the mining process, due to a high mining intensity and inadequately matched borehole design parameters and construction, the gas extraction efficiency at the working face is suboptimal, leading to elevated gas concentration hazards in the return air corner. Therefore, determining an optimal working face mining speed and enhancing the gas extraction rate at the working face are critical issues that require urgent resolution in the mine.

UDEC 3.0 is a two-dimensional discrete element numerical calculation program for discontinuous medium models, typically used to solve engineering problems involving discontinuous rock masses, and it performs well in representing large discontinuous deformations in jointed rock masses. For the mechanical characteristics of discontinuous media under load, it can accurately simulate the joint and layer collapse processes of rock masses. Therefore, in this paper, UDEC 3.0 numerical simulation software was used to establish the numerical calculation model shown in Figure 1, simulating the evolution of mining-induced overlying rock fractures at mining speeds randomly set at 0–4 m/d, 4–8 m/d, and 8–12 m/d.

The values assigned to the strata at each level in the model are derived from the geological conditions and the physical–mechanical properties of the coal seam located in the No. 3 mining area of Wangjialing Coal Mine. The specific parameters are detailed in Table 1. The model dimensions are (XY): 500 × 420 m. A 100 m boundary protection coal pillar is left at each end of the model to mitigate the boundary effects of mining. The mining depth of the coal seam is 508.5 m. The weighted average bulk density of the overburden is 23.3 kN/m<sup>3</sup>, resulting in an overburden pressure of 23.3 kN/m<sup>3</sup> × 508.5 m = 11.85 MPa. The lateral pressure coefficient is set at 1, resulting in a lateral pressure of 11.85 MPa × 1 = 11.85 MPa. The model's boundary conditions are defined as follows: zero displacement is imposed on the bottom, left, and right boundaries, whereas the upper boundary is free. The “Mohr–Coulomb” slip model is utilized for coal-rock damage, while the Coulomb slip model is employed for joints and fractures. Joints are divided in the horizontal and vertical directions within the model to simulate the distribution of joints in real rock strata, with a gravitational acceleration of 9.8 m/s<sup>2</sup>. During the experiment, stepwise excavation is conducted along the strike, with a cycle progress of 0.80 m, totaling 279.6 m of excavation.

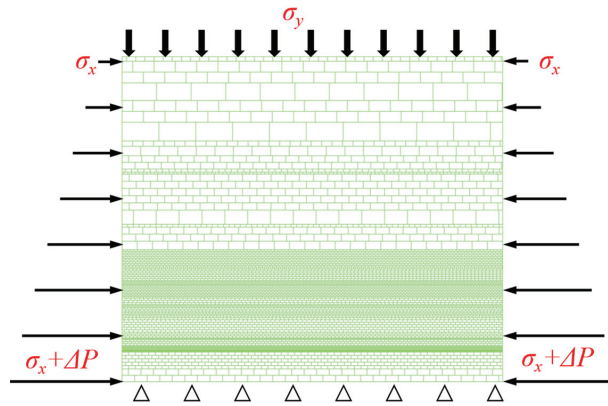


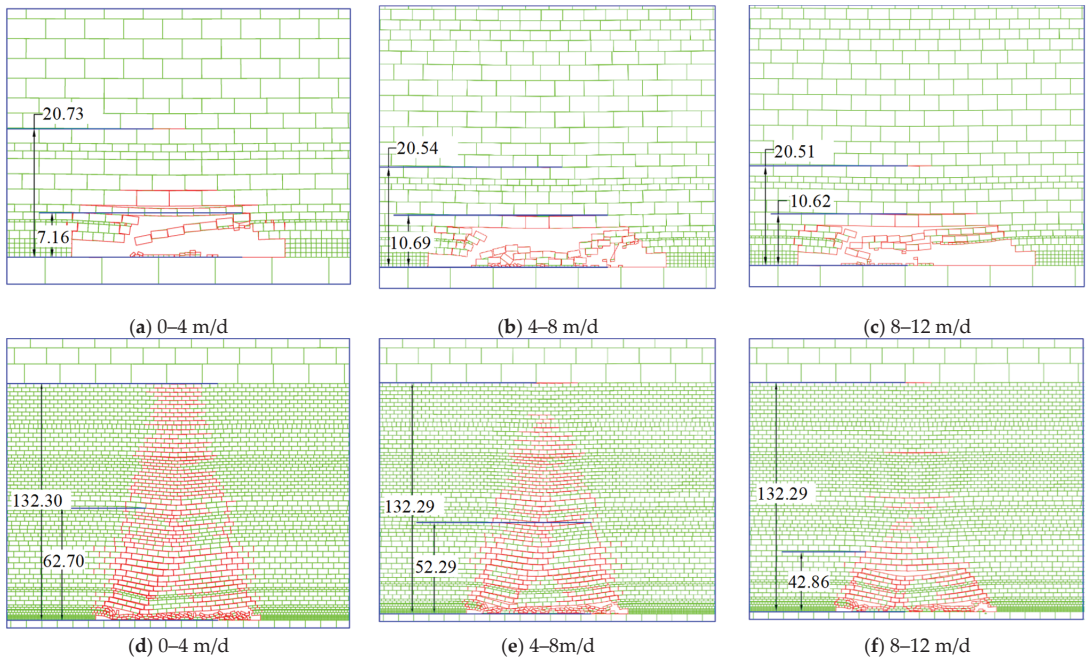
Figure 1. Numerical simulation model.

Table 1. Physical and mechanical parameters of coal and rock strata.

Lithology	Strata Thickness (m)	Elastic Modulus (GPa)	Angle of Internal Friction (°)	Tensile Strength (MPa)	Density ( $\text{kg}\cdot\text{m}^{-3}$ )
Loess	40.87	/	/	/	1800
Sandy mudstone	36	5.62	35	2.91	2635
Sandy mudstone	25.56	5.62	35	2.91	2635
Mudstone	21.7	4.35	33.5	2.88	2643
Siltstone	25.75	9.86	35	2.67	2660
Sandy mudstone	5.35	5.62	35	2.91	2635
Siltstone	55	9.86	35	2.67	2660
Sandy mudstone	27.4	5.62	35	2.91	2635
Sandy mudstone	18.4	5.62	35	2.91	2635
Siltstone	32.8	9.86	35	2.67	2660
Mudstone	3.15	4.35	33.5	2.88	2643
Siltstone	1.8	9.86	35	2.67	2660
Medium-grained sandstone	7.35	8.76	42	7.92	2652
Mudstone	17.85	4.35	33.5	2.88	2643
Sandy mudstone	33.42	5.62	35	2.91	2635
Fine-grained sandstone	22.85	7.86	32	2.98	2645
Sandy mudstone	16	5.62	35	2.91	2635
Fine-grained sandstone	7.25	7.86	32	2.98	2645
Sandy mudstone	2.5	5.62	35	2.91	2635
Fine-grained sandstone	7.4	7.86	32	2.98	2645
Sandy mudstone	2.5	5.62	35	2.91	2635
#2 Coal seam	5.69	2.37	24	0.18	1390
Siltstone	0.86	9.86	35	2.67	2660
Sandy mudstone	2.22	5.62	35	2.91	2635
#3 Coal seam	0.33	2.37	24	0.18	1390

## 2.2. Influence of Working Face Advancement Speed on the Evolution of Mining-Induced Fractures

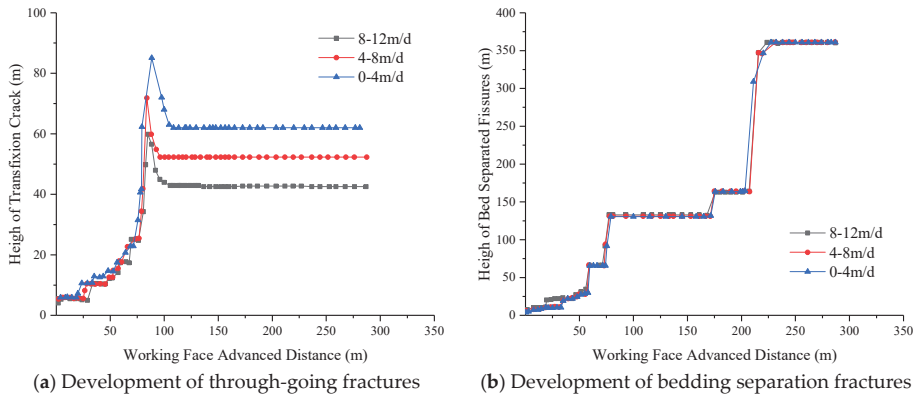
Figure 2a–c illustrate the characteristics of direct roof fracture development under varying mining speeds. At a mining speed of 0–4 m/d, when the working face advances 19.6 m, the direct roof collapses into the goaf, with a fracture height of 7.16 m and a delamination fracture height of 20.73 m. At a mining speed of 4–8 m/d, the collapse step distance increases to 26.8 m, with a fracture height of 10.69 m and a delamination fracture height of 20.54 m. When the working face advances at a speed of 8–12 m/d and reaches 33.2 m, the direct roof initially collapses, with both the fracture and delamination fracture heights developing to 10.62 m. Compared to the 4–8 m/d advancement speed, the maximum fracture and delamination fracture heights remain consistent.



**Figure 2.** Effect of mining speed on the characteristics of mining-induced fractures in overlying strata.

Figure 2d–f depict the evolution characteristics of composite key layer fractures influenced by various mining speeds. During the mining process at varying speeds, mining-induced fractures continuously develop and close. The rock strata in the middle of the goaf gradually compact, forming a compaction zone, while a trapezoidal mining-induced fracture network forms on both sides of the goaf. After the third periodic pressure, the development height of the mining-induced overburden fractures gradually stabilizes. Influenced by varying mining speeds, there are significant differences in the final heights of through-going fractures after mining stabilizes. The maximum heights of through-going fractures are 62.70 m, 52.29 m, and 42.86 m at mining speeds of 0–4 m/d, 4–8 m/d, and 8–12 m/d, respectively.

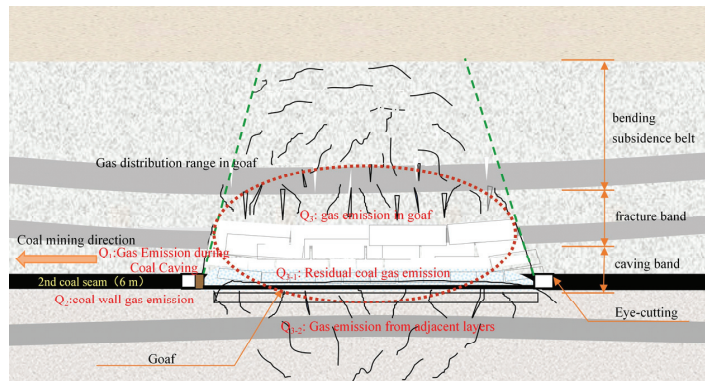
Plot the maximum height curves of through-going fractures and delamination fractures at varying mining speeds, as depicted in Figure 3. The overall trend of through-going and delamination fracture development remains consistent across the three different advancement speeds. However, due to varying mining speeds, the initial collapse step distance of the direct roof varies, increasing with higher speeds. When the through-going fractures reach their maximum height, it is greatest at a mining speed of 0–4 m/d. As the mining speed increases, the maximum height of through-going fractures gradually decreases. This is due to the subsidence of the overlying soft rock and the mutual compression of adjacent strata, which cause the original fractures to close. Regarding delamination fractures, when the working face advances to the third periodic pressure, the delamination fractures stabilize at around 132 m and remain stable for an extended period. They start developing again when the working face advances to 175.6 m, with the development trend and height remaining highly consistent. The development of delamination fractures is generally less influenced by mining speed.



**Figure 3.** Maximum height curves of through-going fractures and separation fractures.

### 2.3. Gas Distribution Characteristics in Goaf Affected by Mining

The composition of gas sources in the fully mechanized caving face is illustrated in Figure 4, primarily comprising  $Q_1$  gas emissions from caving coal,  $Q_2$  gas emissions from the coal wall, and  $Q_3$  gas emissions from the goaf. Among these, gas emissions from the goaf consist of emissions from residual coal and adjacent layers. Therefore, for gas emissions from the goaf in the fully mechanized caving face, factors such as the coal seam gas content and the volume of residual coal in the goaf significantly influence the emission situation. Additionally, given the extensive spatial range of the goaf and the substantial accumulation of gas, scenarios like the initial pressure of the main roof, periodic pressure, large-scale roof collapse, and goaf leakage can all induce substantial gas emissions from the goaf.



**Figure 4.** Composition diagram of gas sources in a fully mechanized caving mining face.

During the mining process at the working face, gas migration in the goaf can be divided into three main stages. The first stage involves gas release due to decompression, which rises upwards. The migration and storage areas of decompressed gas are primarily in the surrounding and top fracture zones of the overlying strata. The second stage occurs when decompressed gas in the top fracture zone becomes saturated, diffusing into the mining-induced fracture area and gradually filling the fracture and compaction zones. The rock strata in the compaction zone of the mining-induced fracture field become compacted, reducing porosity and hindering the migration of decompressed gas. At this stage, decompressed gas primarily migrates within the fracture zone of the fracture belt. The third stage involves emitted gas flowing through fractures into the deeper parts of the



goaf, merging with gas from residual caving coal, the coal wall, and adjacent working face coal seams, causing the gas concentration in the deeper goaf to gradually increase.

During the gas migration process of decompressed gas in the working face of Wangjialing Coal Mine's third mining area, as the working face advances, the gradual destruction of the immediate roof and the composite key layer in the goaf causes the gas to rise and accumulate in the fracture zone of the overlying strata. When the roof fracture stabilizes, part of the rock layer subsides, causing the original fractures and delamination cracks to close. Once the fractures close, their porosity sharply decreases. The cantilever of the overlying strata increases, and during rock layer breakage, newly formed fractures and delamination cracks become the main channels for decompressed gas migration. Although the porosity sharply decreases after the rock layer closes, gas can still migrate within, forming a complex mining-induced fracture network that permeates the entire fracture field. Decompressed gas gradually accumulates at the top of the fracture zone along the mining-induced fracture network. When decompressed gas in the top fracture zone reaches saturation, it gradually fills the entire mining-induced fracture field. Due to the gradual compaction of the central rock layer in the goaf, decompressed gas primarily migrates within the fracture zone. Additionally, with the continuous influx of fresh airflow, leakage airflow carries decompressed gas into the deeper parts of the goaf.

According to the numerical simulation results of mining-induced fracture evolution, the gas migration and distribution characteristics in the goaf at different advancing speeds are presented in Table 2.

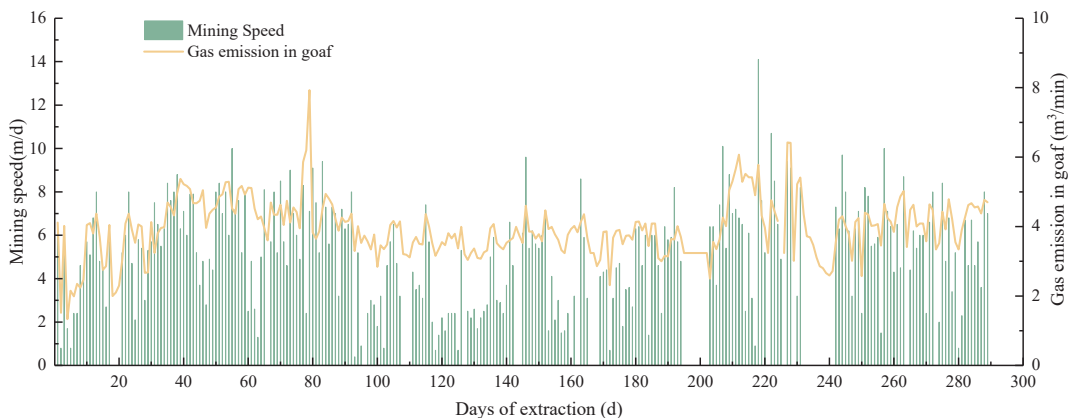
**Table 2.** Gas accumulation height in the fully mechanized caving mining face.

Mining Speed m/d	Height of Gas Aggregation/m			
	Initial Weighting	Second Weighting	Third Weighting	Stope Stability
0–4	7.16	22.84 m	41.76	62.70
4–8	10.69	17.96	34.66	52.29
8–12	10.62	14.53	25.30	42.86

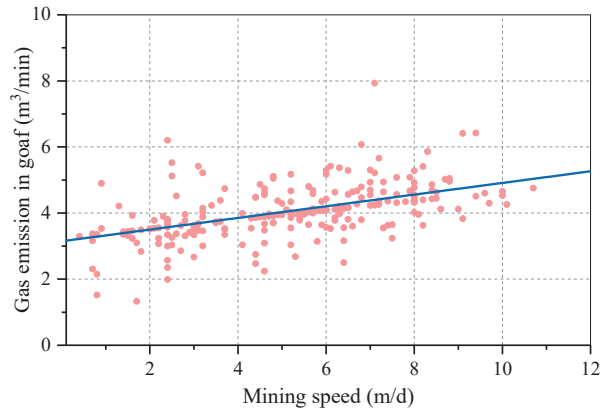
### 3. Influence of Mining Speed on Goaf Gas Emission and Accumulation Characteristics

#### 3.1. Correlation Analysis Between Mining Speed and Goaf Gas Emission

To investigate the impact of the working face mining speed on gas emissions from the goaf, this study statistically analyzes historical data on gas emissions and mining speeds from the third mining area of Wangjialing Mine. The variation curves of gas emissions with the mining speed are plotted in Figures 5 and 6.



**Figure 5.** Evolution curve of goaf gas emission and mining speed.

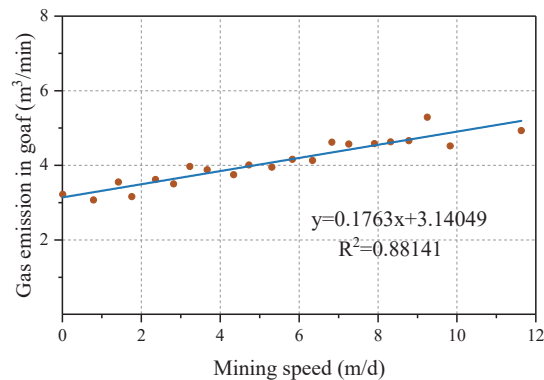


**Figure 6.** Correlation between goaf gas emission and mining speed.

To further elucidate the influence of mining speed on gas emissions and minimize the impact of confounding factors, the mining speed was categorized into stages at specific intervals. The average values of the mining speed and gas emissions within these intervals were calculated and are presented in Table 3, with a linear relationship plotted in Figure 7.

**Table 3.** Data statistics for speed interval classification.

Velocity Range (m·d <sup>-1</sup> )	Sample Size	Mining Speed (m·d <sup>-1</sup> )	Gas Emission Quantity (m <sup>3</sup> ·min <sup>-1</sup> )	Velocity Range (m·d <sup>-1</sup> )	Sample Size	Mining Speed (m·d <sup>-1</sup> )	Gas Emission Quantity (m <sup>3</sup> ·min <sup>-1</sup> )
0.0~0.5	40	0.01	3.22	5.6~6.0	28	5.83	4.16
0.6~1.0	9	0.79	3.07	6.1~6.5	23	6.34	4.13
1.1~1.5	5	1.42	3.55	6.6~7.0	13	6.83	4.62
1.6~2.0	9	1.76	3.16	7.1~7.5	14	7.26	4.57
2.1~2.5	22	2.36	3.62	7.6~8.0	17	7.91	4.58
2.6~3.0	12	2.82	3.50	8.1~8.5	10	8.32	4.63
3.1~3.5	13	3.23	3.97	8.6~9.0	5	8.78	4.66
3.6~4.0	6	3.67	3.88	9.1~9.5	4	9.25	5.29
4.1~4.5	12	4.34	3.75	9.6~10.0	4	9.83	4.52
4.6~5.0	21	4.73	4.01	>10.0	3	11.63	4.93
5.1~5.5	19	5.31	3.95	correlation coefficient		0.94	



**Figure 7.** Linear relationship between mining speed and goaf gas emission.

After classifying and analyzing the mining speed, the correlation between the gas emissions from the goaf and the mining speed markedly increased from 0.60 to 0.94. This indicates that initial and periodic pressures during the mining process significantly impact gas emission volumes. Figure 7 presents the scatter plot and fitting curve of gas emissions from the goaf and the mining speed after data classification. The figure clearly shows that gas emissions from the goaf are influenced by the mining speed, exhibiting a linear relationship and indicating a strong correlation.

Due to the implementation of the fully mechanized top-coal caving method, residual coal remains in the goaf during mining, and gas from adjacent layers infiltrates the goaf through fracture channels. This results in significant gas accumulation in the goaf and fracture zone. Therefore, even at low mining speeds or during stoppage periods, gas emission volumes can still be maintained at a certain level. As gas emission attenuates over time, the emission capacity of residual coal at the same depth varies with different mining speeds. When the mining speed increases, the gas emission volume of residual coal correspondingly increases, exhibiting linear growth.

### 3.2. Optimal Zones for Gas Extraction Boreholes in Overburden Affected by Mining Speed

The mining speed of the working face significantly influences the collapse and fracture development of the overlying strata. The collapse and fracture development of the overlying strata vary with different mining speeds of the working face. Therefore, the optimal layer and horizontal distance of gas extraction boreholes in the goaf can be determined based on historical mining speeds.

Based on the recovery conditions of the mining face in the experimental mine, historical data on borehole design layers/horizontal distance and gas extraction volumes were collected for recovery speeds of 0–4 m/d, 4–8 m/d, and 8–12 m/d. The relationship between the gas extraction volume and layer/horizontal distance at different recovery speeds was then analyzed, as presented in the first and second columns of Table 4. The borehole layers and horizontal distance that exhibited better extraction effects at different recovery speeds were subsequently selected, and a scatter plot was drawn, as shown in the third column of Table 4. The relationship between the borehole layers and horizontal distance was fitted to obtain the quantitative relationship of the optimal layers and horizontal distance for extraction boreholes at different recovery speeds, as also shown in Table 5.

**Table 4.** Relationship between borehole extraction capacity and layer/horizontal distance at different mining speeds.

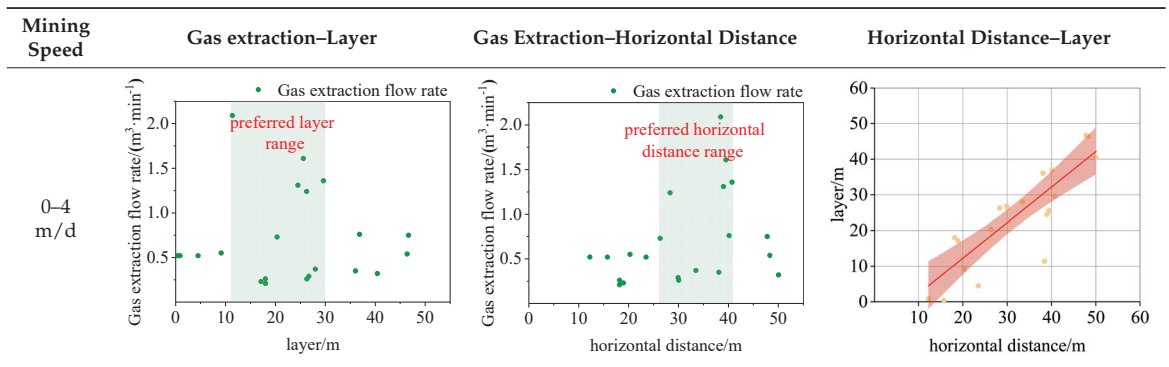


Table 4. Cont.

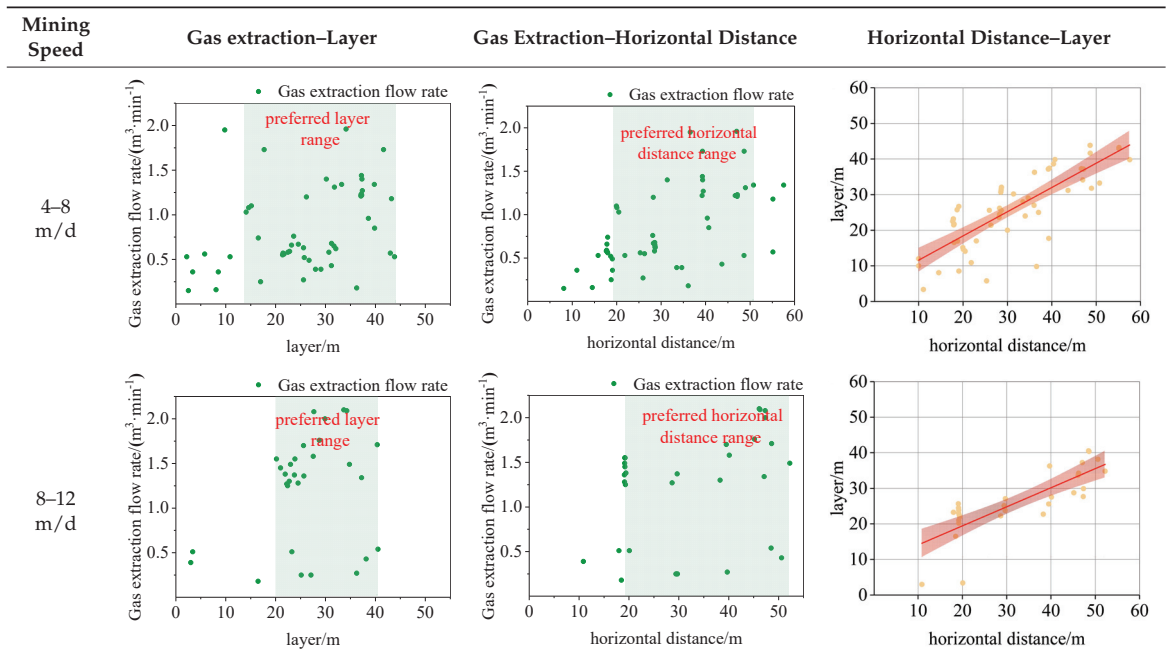


Table 5. Optimal borehole layer/horizontal distance for different mining speeds.

Mining Speed m/d	Preferred Layer /m	Preferred Horizontal Distance /m	Quantitative Relationship	R <sup>2</sup>
0–4	12–30	26–41	$y = 0.9959x - 7.6928$	0.7152
4–8	14–44	17–51	$y = 0.8199x + 4.0584$	0.6461
8–12	21–41	21–52	$y = 0.5360x + 8.7194$	0.6354

Tables 4 and 5 illustrate that the optimal layer of boreholes with enhanced extraction effects vary with different mining speeds. Overall, as the mining speed of the working face increases, the optimal layer and horizontal distance of boreholes also increase. The optimal borehole layer and horizontal distance at different mining speeds fit a linear equation  $y = ax \pm b$ , with a good fit ( $R^2 > 0.6$ ). Therefore, these quantitative relationships of the optimal borehole layer and horizontal distance under different mining speeds can be utilized to optimize the parameters of high-level boreholes.

#### 4. Optimization of Goaf Gas Extraction Technology in the Production Working Face

##### 4.1. Optimization of High-Level Directional Borehole Parameters Considering Advance Speed

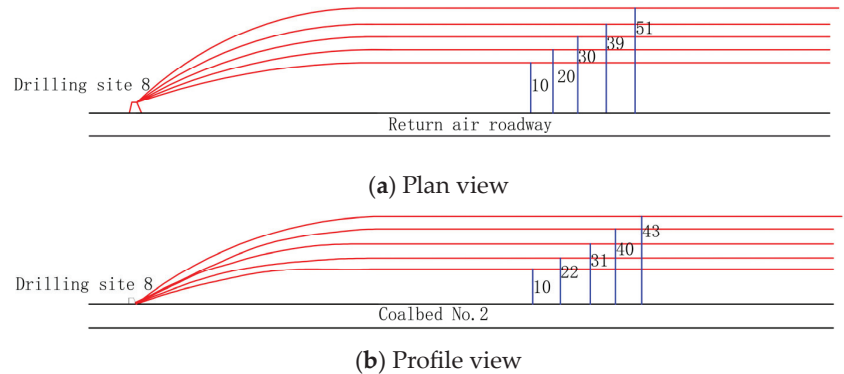
According to statistical data on the gas emission and return corner gas concentration in the No. 3 mining area of the experimental mine, when the gas emission from the working face is less than  $10 \text{ m}^3/\text{min}$ , it can be effectively controlled below the limit through face ventilation and goaf gas extraction. During production, the gas emission from the goaf accounts for 45.5% of the total gas emission at the working face, implying that the goaf gas emission should be less than  $4.55 \text{ m}^3/\text{min}$ . Based on the aforementioned linear relationship between the mining speed and goaf gas emission, to ensure that working face gas emissions do not exceed the limit, the mining speed should be controlled within 8 m/d. At low mining speeds, no specific design is required. Therefore, when designing high-level gas

extraction boreholes in the goaf, the parameters should primarily focus on mining speeds of 4–8 m/d.

Based on the quantitative analysis of optimal drilling positions and spacing for a mining speed of 4–8 m per day, and taking into account the uniformity of drilling distribution, optimization and verification were conducted at the 12,302 working face of the mine. The elevation of the working face was +570~+640 m, the strike length was 2604 m, and the inclination length was 310 m. Further, the working face caving ratio was 1:1, with a bulk density of 1.44 t/m<sup>3</sup> and a recovery ratio of 88%. It utilizes a “U”-shaped ventilation system with an average air volume of 2400 m<sup>3</sup>/min, and the coal seam gas content is 3.1 m<sup>3</sup>/t. Eight drilling sites were established in the working face. For the experimental phase, the No. 8 drilling site of the 12,302 working face was selected for optimization and verification, with five boreholes arranged at this site. The parameters of the boreholes are detailed in Table 6, and the borehole trajectories are illustrated in Figure 8.

**Table 6.** Drilling parameters of the No. 8 drilling site.

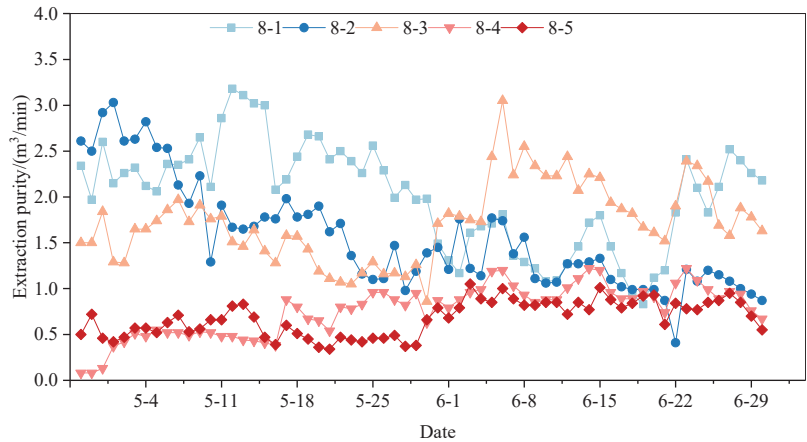
Drilling Site	Drilling Number	Horizontal Distance/m	Layer/m	Length/m
8#	8-1	51	43	471
	8-2	39	40	468
	8-3	30	31	465
	8-4	20	22	462
	8-5	10	10	459



**Figure 8.** Schematic diagram of actual high-level drilling at a daily advancement distance of 4–8 m/d.

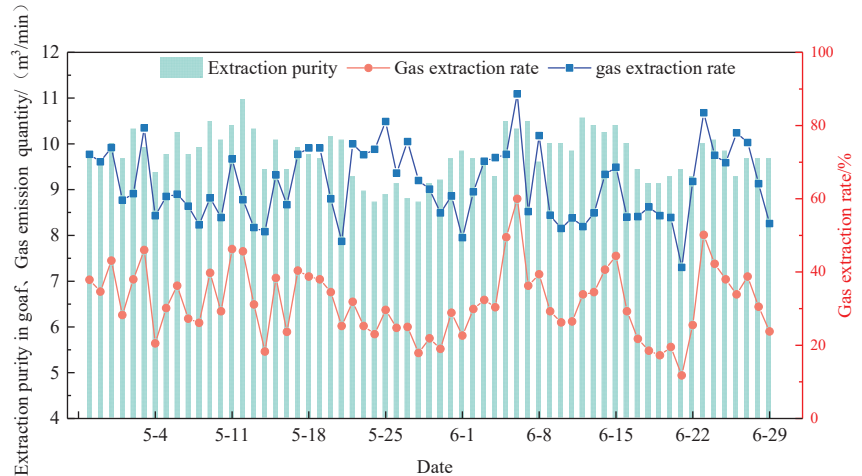
#### 4.2. Investigation of Gas Extraction and Control Effectiveness

The individual borehole gas extraction volumes at drilling site No. 8 are depicted in Figure 9. As illustrated in Figure 9, the extraction volumes of each borehole group exhibit some fluctuations. The maximum gas extraction flow rate of borehole 8-1 reached 3.18 m<sup>3</sup>/min, representing a 51% increase compared to the maximum single borehole gas extraction volume at other drilling sites prior to optimization. The average gas extraction volumes for boreholes 8-1, 8-2, 8-3, 8-4, and 8-5 were 2.01, 1.55, 1.73, 0.76, and 0.68 m<sup>3</sup>/min, respectively. Compared to borehole 8-5, the extraction volumes of the other four boreholes were higher, thus verifying the rationality and feasibility of this method.



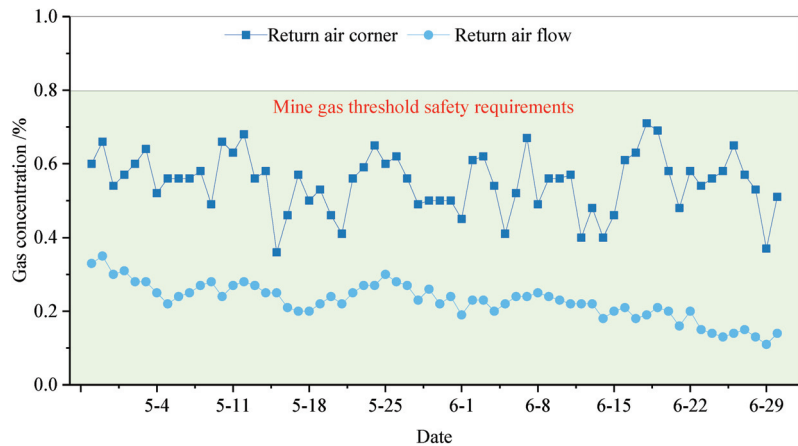
**Figure 9.** Variation characteristics of borehole gas extraction volume.

The daily gas extraction volumes of high-level directional boreholes, along with the gas emission volumes and gas extraction rates of the working face, are depicted in Figure 10. When the working face advance speed was below 8 m/d, the gas emission volume at the working face was generally maintained within 10 m<sup>3</sup>/min, with only five days exceeding this threshold. The average gas extraction rate of high-level directional boreholes reached 68%, with the extraction volumes of these boreholes playing a crucial role in controlling the gas emissions at the working face.



**Figure 10.** Variation characteristics of extraction volume, gas emission volume, and extraction rate.

The gas concentrations in the upper corner and the return airflow during the extraction period of high-level directional boreholes are illustrated in Figure 11. As illustrated in Figure 11, the maximum gas concentrations in the upper corner ranged from 0.35% to 0.7%, and the maximum gas concentrations in the return airflow ranged from 0.11% to 0.35%. Both the upper corner and return airflow gas concentrations were maintained below 0.8%, achieving the expected goal of gas control at the working face. This ensures the safe and efficient production of the mine, thus proving the feasibility of optimizing the design of high-level boreholes considering the effect of advance speed and highlighting its significant role in ensuring the safe mining of the working face.



**Figure 11.** Variation characteristics of the gas concentration in upper corners and return airflow.

## 5. Discussion

“Intelligentization” and “clean low-carbon” development will be the primary directions for future mine advancements. The coal mining process is progressively entering the intelligent stage. To ensure production safety at the working face during intelligent mining, it is imperative to establish reasonable mining parameters. This study aims to offer insights and technical support for determining the mining speed and gas extraction process parameters in the intelligent mining of the working face.

This paper utilizes numerical simulation experiments and field tests to analyze the impact of the mining face speed on the development characteristics of mining-induced overburden fractures, as well as the emission and migration characteristics of gas in the goaf. Based on the results of numerical simulations and field data analysis, the influence of varying mining speeds on overburden fractures in the goaf during production and their impact on gas migration and enrichment characteristics in the goaf were determined. Furthermore, by analyzing gas enrichment characteristics, the parameters of gas extraction boreholes in the goaf were optimized, thereby improving the gas extraction capacity in the goaf.

This study primarily focuses on the impact of mining speed on the development of overburden fractures and gas migration characteristics in the goaf under fixed conditions. However, in actual mining processes, numerous factors influence mining-induced overburden fractures and gas migration characteristics in the goaf, such as variations in coal and rock properties, geological features, and gas occurrence characteristics. The impact of these factors on mining-induced overburden fractures and gas migration in the goaf requires further investigation to enhance the gas extraction capacity in the goaf.

## 6. Conclusions

- (1) Numerical simulations were employed to model the fracture development characteristics of the overlying strata under different working face advance speeds. The initial collapse step distance increased with the working face advance speed, whereas the maximum height of through fractures in the goaf decreased as the advance speed increased. In contrast, the development of separation fractures was primarily influenced by the advance distance of the working face and had little relationship with the advance speed.
- (2) The working face advance speed exhibits a linear correlation with gas emissions in the goaf. By categorizing and averaging gas emissions and advance speeds, the influence of factors such as the initial pressure and periodic pressure on gas emissions in the goaf can be effectively reduced, thereby increasing the correlation from 0.60 to 0.94.

The optimal drilling layer and horizontal distance of boreholes at different advance speeds also exhibit a linear relationship. As the daily advance speed increases, the slope of the line gradually decreases, while the intercept increases.

- (3) Based on the gas emission characteristics of the working face, a safe advance speed for the working face was determined. Subsequently, the parameters for high-level boreholes in the working face were optimized and applied. Consequently, the gas emission volume at the working face was effectively controlled below 10 m<sup>3</sup>/min. Throughout the entire extraction period, the average gas extraction rate of high-level directional boreholes reached 68%, and the maximum gas concentrations in the upper corner and return airflow during production remained below 0.8%.

**Author Contributions:** Conceptualization, C.C.; methodology, X.-Y.C.; validation, C.C., X.-Y.C. and L.C.; formal analysis, C.C.; investigation, X.-Y.C.; resources, X.-Y.C.; data curation, X.-Y.M.; writing—original draft preparation, X.-Y.C.; writing—review and editing, C.C.; visualization, C.C.; supervision, L.C.; project administration, C.C.; funding acquisition, C.C. All authors have read and agreed to the published version of the manuscript.

**Funding:** This research is funded by the National Key Research and Development Program of China, grant number 2023YFF0615404.

**Data Availability Statement:** The data used to support the findings of this study are available from the corresponding author upon request.

**Conflicts of Interest:** Authors Cheng Cheng, Xiao-Yu Cheng, Long Chen and Xing-Ying Ma were employed by the company China Coal Energy Research Institute Co., Ltd. They declare that the research was conducted in the absence of any commercial or financial relationships that could be construed as a potential conflict of interest. The company had no role in the design of the study; in the collection, analyses, or interpretation of data; in the writing of the manuscript, or in the decision to publish the results.

## References

1. Capuano, L. *International Energy Outlook 2018 (IEO2018)*; US Energy Information Administration (EIA): Washington, DC, USA, 2018; p. 21.
2. Jiang, D.; Chen, S.; Liu, W.; Ren, Y.; Guo, P.; Li, Z. Underground hydro-pumped energy storage using coal mine goafs: System performance analysis and a case study for China. *Front. Earth Sci.* **2021**, *9*, 760464. [CrossRef]
3. Kurnia, J.C.; Sasmito, A.P.; Mujumdar, A.S. CFD simulation of methane dispersion and innovative methane management in underground mining faces. *Appl. Math. Model.* **2014**, *38*, 3467–3484. [CrossRef]
4. Zhou, W.; Yuan, L.; Zhang, G.L.; Du, H.L.; Xue, S.; He, G.H.; Han, Y.C. A new method for determining the individual sources of goaf gas emissions: A case study in Sihe Coal Mine. *J. China Coal Soc.* **2018**, *43*, 1016–1023.
5. Brodny, J.; Tutak, M. Determination of the zone endangered by methane explosion in goaf with caving of longwalls ventilated on “Y” system. *Manag. Syst. Prod. Eng.* **2016**, *24*, 247–251. [CrossRef]
6. Cheng, J.; Mei, J.; Peng, S.; Qi, C.; Shi, Y. Comprehensive consultation model for explosion risk in mine atmosphere—CCMER. *Saf. Sci.* **2019**, *120*, 798–812. [CrossRef]
7. Chen, H.; Qi, H.; Long, R.; Zhang, M. Research on 10-year tendency of China coal mine accidents and the characteristics of human factors. *Saf. Sci.* **2012**, *50*, 745–750. [CrossRef]
8. Yu, X.; Gao, M.; Zhao, H.; Zhao, S.; Zhao, H. Research on the Laws of Overlying Rock Fracture and Energy Release under Different Mining Speeds. *Appl. Sci.* **2024**, *14*, 3222. [CrossRef]
9. Whittles, D.N.; Lowndes, I.S.; Kingman, S.W.; Yates, C.; Jobling, S. Influence of geotechnical factors on gas flow experienced in a UK longwall coal mine panel. *Int. J. Rock Mech. Min. Sci.* **2006**, *43*, 369–387. [CrossRef]
10. Raabe, D. The materials science behind sustainable metals and alloys. *Chem. Rev.* **2023**, *123*, 2436–2608. [CrossRef]
11. Yang, M.; Guo, L.; Wu, X.; Li, N.; Li, X.; Zhang, N. Subpore-mediated tunable water absorption in nanoparticle-based materials. *Int. J. Heat Mass Transf.* **2024**, *231*, 125811. [CrossRef]
12. Wang, L.; Wang, Z.; Xu, S.; Zhou, W.; Wu, J. A field investigation of the deformation of protected coal and its application for CBM extraction in the Qinglong coalmine in China. *J. Nat. Gas Sci. Eng.* **2015**, *27*, 367–373. [CrossRef]
13. Bondarev, A.; Mihai, S.; Pântea, O.; Neagoe, S. Use of biopolymers for the removal of metal ion contaminants from water. In *Macromolecular Symposia*; WILEY-VCH: Weinheim, Germany, 2011; Volume 303, pp. 78–84.
14. Qian, M.G.; Xu, J.L. Study on the “O-shape” circle distribution characteristics of mining induced fractures in the overlying strata. *J. China Coal Soc.* **1998**, *23*, 466–469.



15. Yuan, L.; Guo, H.; Shen, B.T.; Qu, Q.D.; Xue, J.H. Circular overlying zone at longwall panel for efficient methane capture of multiple coal seams with low permeability. *J. China Coal Soc.* **2011**, *36*, 357–365.
16. Li, S.G.; Shi, P.W.; Qian, M.G. Study on the dynamic distribution features of mining fissure elliptic paraboloid zone. *Ground Press. Strat. Control* **1999**, *3*, 44–46.
17. Islam, M.R.; Hayashi, D.; Kamruzzaman, A.B.M. Finite element modeling of stress distributions and problems for multi-slice longwall mining in Bangladesh, with special reference to the Barapukuria coal mine. *Int. J. Coal Geol.* **2009**, *78*, 91–109. [CrossRef]
18. Wu, W.D.; Bai, J.B.; Wang, X.Y.; Yan, S.; Wu, S.X. Numerical study of failure mechanisms and control techniques for a gob-side yield pillar in the Sijiazhuang coal mine, China. *Rock Mech. Rock Eng.* **2019**, *52*, 1231–1245. [CrossRef]
19. Lin, H.F.; Li, S.G.; Cheng, L.H.; Wang, H.S. Experimental analysis of dynamic evolution model of mining-induced fissure zone in overlying strata. *J. Min. Saf. Eng.* **2011**, *28*, 298–303.
20. Yujun, Z.; Huaxing, Z.; Peipei, C. Visual exploration of fissure field of overburden and rock. *J. China Coal Soc.* **2008**, *33*, 1216–1219.
21. Kang, Y.; Wang, J.; Kong, F.; Liu, X.E.; Jin, R.C.; Zheng, J.Q. Bore hole survey method for overburden failure. *Coal Sci. Technol.* **2002**, *30*, 26–28.
22. Yang, Y.; Liang, P. The detection technology of goaf overburden rock damage of based on EH4 electromagnetic imaging system. *Chin. J. Geol. Hazard. Control* **2013**, *24*, 68–71.
23. Zhang, H.W.; Zhu, Z.J.; Huo, L.J.; Chen, Y.; Huo, B.J. Overburden failure height of superhigh seam by fully mechanized caving method. *J. China Coal Soc.* **2014**, *39*, 816–821.
24. Zhou, H.; Liu, J.; Xue, D.; Yi, H.; Xue, J. Numerical simulation of gas flow process in mining-induced crack network. *Int. J. Min. Sci. Technol.* **2012**, *22*, 793–799. [CrossRef]
25. Qin, Z.; Yuan, L.; Guo, H.; Qu, Q. Investigation of longwall goaf gas flows and borehole drainage performance by CFD simulation. *Int. J. Coal Geol.* **2015**, *150*, 51–63. [CrossRef]
26. Guo, H.; Yuan, L.; Shen, B.; Qu, Q.; Xue, J. Mining-induced strata stress changes, fractures and gas flow dynamics in multi-seam longwall mining. *Int. J. Rock Mech. Min. Sci.* **2012**, *54*, 129–139. [CrossRef]
27. Zhang, C.; Chen, Y.; Ren, Z.; Wang, F. Compaction and seepage characteristics of broken coal and rock masses in coal mining: A review in laboratory tests. *Rock Mech. Bull.* **2024**, *3*, 100102. [CrossRef]
28. Liu, Y.; Shao, S.; Wang, X.; Chang, L.; Cui, G.; Zhou, F. Gas flow analysis for the impact of gob gas ventholes on coalbed methane drainage from a longwall gob. *J. Nat. Gas Sci. Eng.* **2016**, *36*, 1312–1325. [CrossRef]

**Disclaimer/Publisher’s Note:** The statements, opinions and data contained in all publications are solely those of the individual author(s) and contributor(s) and not of MDPI and/or the editor(s). MDPI and/or the editor(s) disclaim responsibility for any injury to people or property resulting from any ideas, methods, instructions or products referred to in the content.

Article

# Distriformer: Research on a Distributed Training Rockburst Prediction Method

Yu Zhang <sup>1,2</sup>, Kongyi Fang <sup>1,\*</sup> and Zhengjia Guo <sup>3</sup>

<sup>1</sup> School of Electrical and Information Engineering, Beijing University of Civil Engineering and Architecture, Beijing 100044, China; yuzhang@bucea.edu.cn

<sup>2</sup> State Key Laboratory in China for GeoMechanics and Deep Underground Engineering, China University of Mining & Technology, Beijing 100083, China

<sup>3</sup> Thomas Lord Department of Computer Science, University of Southern California, Los Angeles, CA 90007, USA; zgao7940@usc.edu

\* Correspondence: kongyif1999@163.com; Tel.: +86-15778883202

**Abstract:** The precise forecasting of rockburst is fundamental for safeguarding human lives and property, upholding national energy security, and protecting social welfare. Traditional methods for predicting rockburst suffer from poor accuracy and extended model training durations. This paper proposes a distributed training rockburst prediction method called Distriformer, which uses deep learning technology combined with distributed training methods to predict rockburst. To assess the efficacy of the Distriformer rockburst model proposed herein, five datasets were used to compare the proposed method with Transformer and Informer. The experimental results indicate that, compared with Transformer, the proposed method reduces the mean absolute error by 44.4% and the root mean square error by 30.7% on average. In terms of training time, the proposed method achieves an average acceleration ratio of 1.72. The Distriformer rockburst model enhances the accuracy of rockburst prediction, reduces training time, and serves as a reference for development of subsequent real-time prediction models for extensive rockburst data.

**Keywords:** rockburst; distributed training; rockburst prediction

**Citation:** Zhang, Y.; Fang, K.; Guo, Z. Distriformer: Research on a Distributed Training Rockburst Prediction Method. *Processes* **2024**, *12*, 1205. <https://doi.org/10.3390/pr12061205>

Academic Editor: Chunhui Zhao

Received: 9 May 2024

Revised: 8 June 2024

Accepted: 9 June 2024

Published: 12 June 2024



**Copyright:** © 2024 by the authors. Licensee MDPI, Basel, Switzerland. This article is an open access article distributed under the terms and conditions of the Creative Commons Attribution (CC BY) license (<https://creativecommons.org/licenses/by/4.0/>).

## 1. Introduction

Since the initial documentation of rockburst in the 17th century [1], these events have progressively gained attention within the scientific community. Rockburst occurs during the mining process due to external disturbances, prompting the release of elastic potential energy, resulting in rock rupture, often accompanied by audible explosion phenomena [2]. The phenomenon of rockburst is characterized by its sudden and unpredictable nature, as it is influenced by a multitude of intricate factors, such as the inherent structure of the rock, the surrounding topography, and the stress within the crust, making it a challenging task for humans to foresee promptly. Coal has traditionally served as the primary energy source in China [3]. With ongoing societal advancement, resource demands have surged, leading to annual escalations in both the scale and frequency of coal mining, consequently resulting in a rise in rockburst accidents as well [4]. Rockburst disasters endanger human lives, property, national energy security, and societal welfare. Hence, there is an urgent need to investigate efficient and accurate methods for predicting rockburst.

Rockburst prediction has perennially attracted significant research attention within this domain. Over the decades, scholars have investigated diverse facets of rockburst prediction methodologies. Existing methods for predicting rockburst encompass both traditional prediction methods and those leveraging artificial intelligence techniques. The microseismic method [5], acoustic emission method [6], and electromagnetic radiation method [7] are categorized as traditional rockburst prediction methods. These methods investigate and forecast rockburst based on rock parameters and characteristics gathered through

monitoring. Traditional rockburst prediction methods exhibit significant limitations in practical applications. Hence, researchers endeavor to integrate artificial intelligence techniques into rockburst prediction endeavors [8]. Traditional machine learning algorithms such as support vector machine [9,10], decision tree [11], and random forest [12,13] have also been employed to address the nonlinear challenges inherent in rockburst prediction. Furthermore, deep learning methods have garnered attention due to their enhanced nonlinear processing capabilities. Artificial neural network [14,15], self-organizing neural network [16], and long short-term memory recurrent neural network [17] are pivotal in rockburst prediction. They significantly enhance predictive accuracy. The accuracy of rockburst prediction has significantly improved from traditional methods to those leveraging artificial intelligence techniques.

Most of the aforementioned methods focus on predicting rockburst intensity levels. There is limited research on using artificial intelligence techniques to predict acoustic emission time series. At the same time, the above studies often do not pay attention to the time issue of model training. In addition to accuracy, timeliness is a crucial indicator in rockburst prediction, as it determines whether preventive measures can be implemented promptly to mitigate disaster-related losses. Therefore, temporality is also a focus of this study. Accurate and rapid predictions are particularly important.

The proposal of Transformer [18] has led to excellence in multiple domains. The original Transformer architecture encounters challenges related to time complexity and memory usage as model sizes expand and the necessity to handle long sequential data escalates. Research scholars have put forth a refined architecture known as Informer, which stems from Transformer and integrates the ProbSparse self-attention mechanism along with the self-attention distilling mechanism to effectively address these challenges. This model effectively reduces both the computational and memory demands, thereby significantly enhancing prediction accuracy across a diverse array of tasks. Consequently, researchers have also undertaken efforts to introduce this crucial aspect into the realm of rockburst prediction.

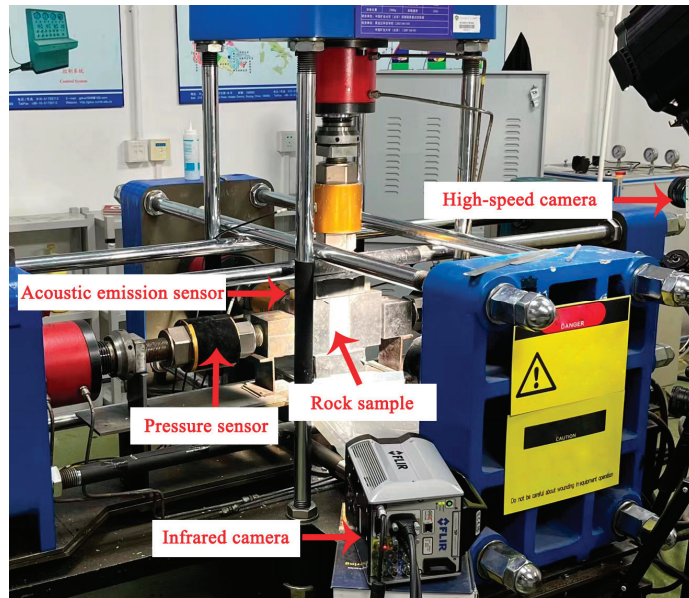
Furthermore, to enhance the performance of deep learning algorithms in real-world scenarios, there is a tendency for datasets to undergo expansion, deep learning models to become more intricate, and training duration to undergo escalation. In recent years, distributed training has emerged as a primary method for accelerating the training of deep learning models, garnering significant attention from both domestic and international research scholars to reduce training time.

This paper proposes a distributed training rockburst prediction method called Distributed Transformer. Distributed training methods are innovatively introduced into the field of rockburst prediction for the first time. Initially, the rockburst data and the model are allocated across multiple GPUs. Furthermore, distributed training is employed to optimize the rockburst prediction model during the training phase. Finally, the trained model for predicting rockburst will be applied. The method was applied to five rockburst datasets for experimentation, demonstrating optimal model performance. On average, the mean absolute error decreases by 44.4% and the root mean square error decreases by 30.7% for accuracy. Additionally, it achieves an average acceleration ratio of 1.72 for timeliness. The method proposed in this paper effectively solves the accuracy and timeliness problems encountered in rockburst prediction.

## 2. Experimental System and Data Sources

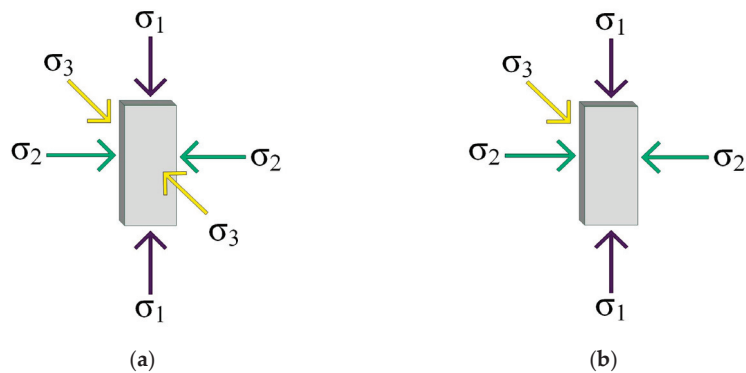
The experimental apparatus utilized in this study originates from the strain rockburst physical simulation test system autonomously designed by China University of Mining and Technology. The system comprises three components: the mainframe, the loading control system, and the data acquisition system. The strain rockburst physical simulation test system is shown in Figure 1. The system is capable of simulating rockburst occurrence indoors and capturing it via an acoustic emission sensor, a pressure sensor, and a high-

speed camera to monitor the data changes throughout the entire rockburst process of the rock samples.



**Figure 1.** The strain rockburst physical simulation test system.

The rock specimens utilized in this experiment comprise ROCKBURST\_S1, ROCKBURST\_S2, ROCKBURST\_S3, ROCKBURST\_S4, and ROCKBURST\_S5. Uniform and well-integrated rocks were prepared by cutting them into samples of specified dimensions and subsequently positioned at the designated loading point within the experimental setup. Initially, the loading control system employs a three-phase and six-sided force on the rock samples to replicate the pre-construction force state of the rock at the site. The forces on the rock sample are shown in Figure 2a. The loading control system was incrementally loaded to a predetermined level, followed by rapid unloading along a specified side to simulate the rock's force state during construction, persisting until the occurrence of rockburst. The unloaded state of the rock sample is shown in Figure 2b.



**Figure 2.** Stress state of rock samples: (a) force state of the rock sample and (b) unloaded state of the rock sample.

Firstly, the indoor simulated rockburst experiment will yield a substantial volume of experimental data, which will be stored in text files by the data acquisition system. Each text file comprises numerous datasets encompassing metric information for multiple parameters across different time intervals. Then, the extensive rockburst dataset was subjected to feature extraction. Important features like count, amplitude, peak frequency, and absolute energy are extracted at different moments during indoor simulated rockburst. Lastly, the text file containing the primary characteristic parameters of the indoor simulated rockburst experiment is generated.

### 3. Methodology

#### 3.1. Informer Model

The Informer model is a Transformer-based architecture designed for time series prediction. It comprises two primary components: an encoder and a decoder [19]. Leveraging the Transformer architecture, it optimizes both the encoding and decoding layers to address its three primary challenges. The three primary enhancements are outlined below: to reduce the computational complexity of the traditional self-attention mechanism, multi-head ProbSparse self-attention is proposed at the encoder layer; self-attention distilling is employed to emphasize primary attention while reducing the input of the cascade layer by half; and to enhance prediction speed for lengthy sequences, a generative decoder mechanism is introduced at the decoding layer to generate the prediction output in a single step.

(1) ProbSparse self-attention mechanism: The conventional self-attention mechanism conducts the scaling dot product operation through the query–key–value triad, executing a scaled dot product operation. The dot product formula is as follows:

$$A(Q, K, V) = \text{Softmax}\left(\frac{QK^T}{\sqrt{d}}\right)V \quad (1)$$

where  $Q$  is the matrix of the query,  $K$  is the matrix of the key,  $V$  is the matrix of the value,  $d$  is the dimensionality of the input variables, and  $\text{Softmax}$  is the activation function.

During self-attention computation, it is not always the case that one element of the input exhibits a high correlation with all other elements. To minimize computational overhead, the ProbSparse self-attention mechanism initially assesses the sparsity of the overall query vector. Then, the number of query vectors used for dot product computation is determined, and the values corresponding to the remaining unchecked query vectors are directly assigned to the mean. The formula for computing the correlation  $\bar{M}$  between the  $i$ -th query vector  $q_i$  and the key matrix  $k$  is:

$$\bar{M}(q_i, k) = \max_j \left\{ \frac{q_i k_j^T}{\sqrt{d}} \right\} - \frac{1}{L_k} \sum_{j=1}^{L_k} \frac{q_i k_j^T}{\sqrt{d}}, \quad (2)$$

Thus, the formulation of the ProbSparse self-attention mechanism is established as:

$$A_m(Q, K, V) = \text{Softmax}\left(\frac{\bar{Q}K^T}{\sqrt{d}}\right)V \quad (3)$$

where  $\bar{Q}$  is a new sparse query matrix composed of  $u$  query vectors with the highest scores selected by sparsity computation.

(2) Self-attention distilling: Incorporating a distilling layer prior to the self-attention mechanism enables the extraction of prominent features, thereby facilitating the allocation of increased weights to these salient features. This process reduces the network parameter size, resulting in a halving of the input sequence length with each layer. The distilling operation from self-attention layer  $j$  to layer  $j + 1$  is calculated as:

$$X_{j+1}^t = \text{MaxPool}\left(\text{ELU}\left(\text{Conv1d}\left(\left[X_j^t\right]_{AB}\right)\right)\right) \quad (4)$$

where MaxPool is the maximum pooling layer operation, ELU is the activation function, Conv1d is the one-dimensional convolution operation, and  $\left[ X_j^t \right]_{AB}$  includes the basic operations of the attention block and sparse self-attention mechanism.

(3) Generative decoder mechanism: It employs a masked multi-head ProbSparse self-attention mechanism to prevent the incorporation of future unknown information into the current prediction. The generative decoder mechanism concurrently generates the complete prediction, significantly enhancing prediction speed. The input sequence to the decoder comprises historical load sequence, denoted as  $X_{token}^t$ , serving as a reference, alongside the predicted sequence  $X_0^t$ , which requires masking from future contextual factors. The input sequence formula for the decoder is as follows:

$$X_{de}^t = \text{Concat}(X_{token}^t, X_0^t) \in \mathbb{R}^{(L_{token}+L_y)d_{model}} \quad (5)$$

where  $X_{de}^t$  is the t-th input sequence in the decoder,  $X_{token}^t$  is the start token of the t-th sequence, and  $X_0^t$  is a placeholder for the target sequence of the t-th sequence.

### 3.2. Distributed Training

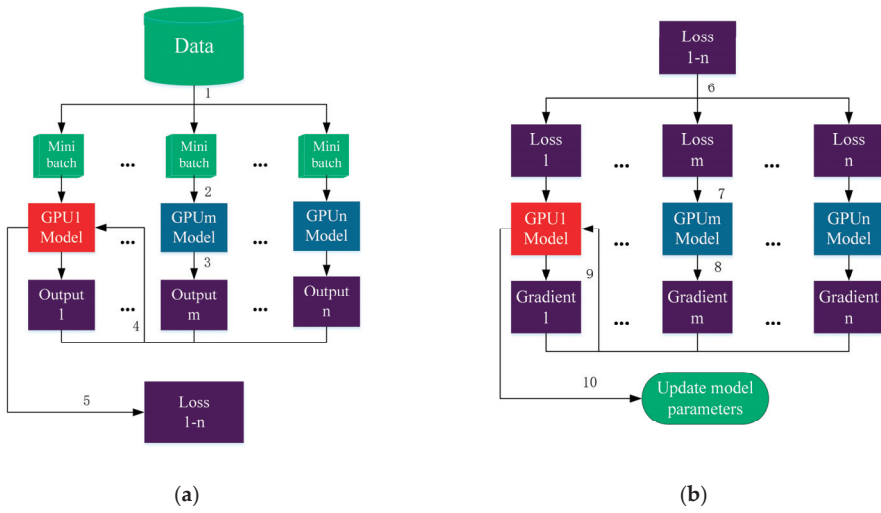
In recent years, the continuous advancement of graphics processing units (GPUs) has led to significant breakthroughs in areas such as big data analysis, deep learning, and large-scale model training, owing to their formidable computational capabilities. Consequently, an increasing number of researchers and scholars opt for GPUs over CPUs in deep learning training. Moreover, to expedite training, distributed training methods are employed. Model parallelism and data parallelism are the two predominant parallel schemes employed in distributed training [20]. Typically, the latter incurs lower communication overhead compared to the former [21]. Considering the model's structure and the associated parallelism overhead, the data parallelism approach was chosen.

The essence of employing the data parallelism approach in distributed training is to address the challenge of handling excessive data with limited GPU memory, thereby enhancing training efficiency. The hardware setup must include multiple GPUs, each equipped with a complete and identical copy of the model. The data need to be partitioned and scattered to different GPUs for parallel training prior to training. Forward and backward propagation are central components of the process. The forward propagation process focuses on the fact that the data are scattered to each GPU and the GPUs all acquire models with consistent parameters. Subsequently, the GPUs collectively engage in training the model concurrently, with each GPU producing an output. The primary GPU (labeled as GPU1 in Figure 3a,b) is responsible for gathering outputs from each GPU, computing loss, and generating n loss. Backpropagation involves the primary GPU scattering each of the n losses to corresponding GPUs for gradient computation, followed by gathering the gradients and updating the model parameters. Then, the new model parameters are updated on each GPU for subsequent iteration. The schematic diagrams illustrating distributed training are depicted in Figure 3.

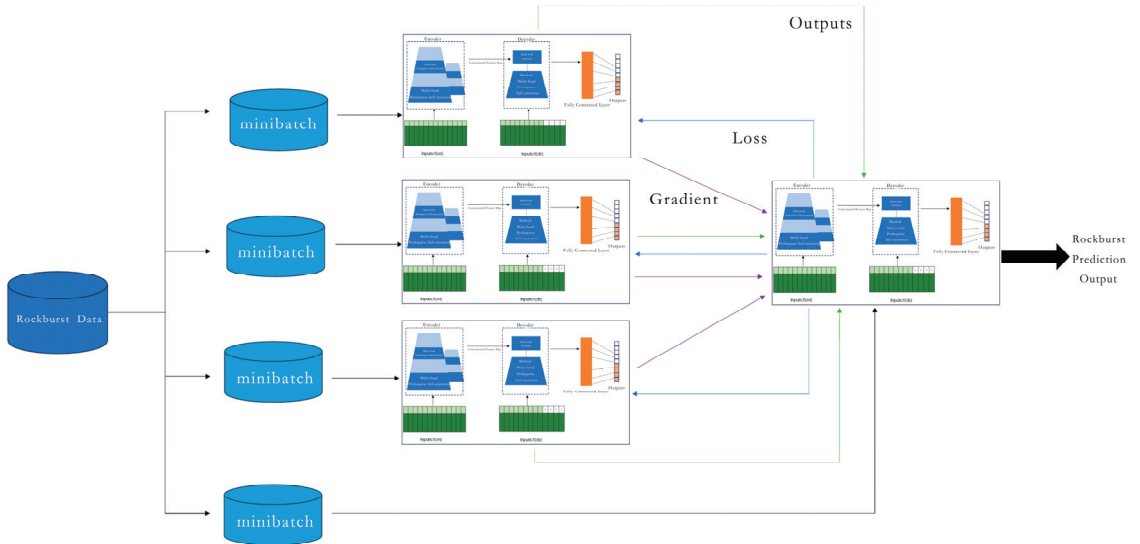
### 3.3. Distriformer Rockburst Prediction Model

In predicting rockburst, precision and timeliness are critical, as even a slight advance in detection time could prevent substantial losses in both assets and human lives. Thus, this paper proposes a distributed training model for rockburst prediction called Distriformer, with the aim of enhancing prediction accuracy and reducing prediction time.

The Distriformer rockburst prediction model enhances the self-attention mechanism by introducing the ProbSparse self-attention mechanism and self-attention distilling. This aims to reduce computational complexity while effectively capturing long-distance dependencies and improving prediction accuracy. In addition, the model uses a distributed training strategy to accelerate model training through parallel data processing across multiple computing nodes. The overall schematic diagram of the Distriformer rockburst prediction model is presented in Figure 4.



**Figure 3.** Distributed training flowchart: (a) forward propagation schematic and (b) backward propagation schematic.



**Figure 4.** Schematic diagram of the Distriformer rockburst prediction model.

The rockburst data are initially partitioned into an equal number of segments corresponding to the number of GPUs and then distributed among the GPUs. Each GPU is equipped with an identical rockburst model and its parameters. GPUs start training the rockburst model. The rockburst data first pass through the Encoder layer. The ProbSparse self-attention layer uses a novel attention calculation mechanism to optimize computational efficiency. And self-attention distilling compresses the rockburst features to reduce the dimensionality and the number of network parameters. The Encoder layer enhances the robustness of the rockburst prediction model by stacking the aforementioned two operations. Subsequently, it traverses the Decoder layer, undergoes masked self-attention, and culminates in the single-step generation of the rockburst prediction outcome. The primary GPU summarizes the values and calculates the loss and gradient. During the

backpropagation process, each GPU receives the loss values computed by the rockburst model and calculates the corresponding gradient, which is subsequently aggregated onto the primary GPU. The primary GPU distributes updated model parameters to individual GPUs for continual model optimization. Subsequently, the trained rockburst prediction model is employed to forecast the final rockburst outcomes.

## 4. Experiments and Analysis

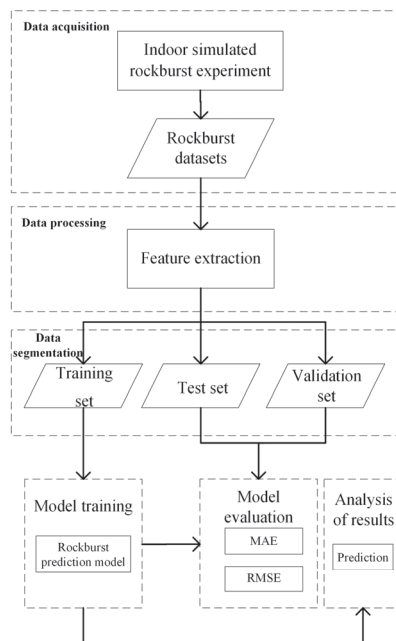
### 4.1. Experimental Setup

The experimental configurations are detailed in Table 1 below.

**Table 1.** Experimental configurations table.

Environment	Name	Configuration Information
Hardware environment	CPU	Intel(R) Core (TM) i9-7900X CPU@4.6 GHz
	Random Access Memory	64GB
	GPU	4*NVIDIA GeForce GTX 1080
Software environment	Operating System	Ubuntu 18.04
	Programming Language	Python 3.7
	Basic Framework	Pytorch 1.10
	Programming Software	Pycharm

The foundational experimental framework of the rockburst prediction method outlined in this paper comprises six essential components: data acquisition, data processing, data segmentation, model training, model evaluation, and analysis of results, visually depicted in Figure 5.



**Figure 5.** Experimental framework diagram.

Data acquisition was carried out using the acoustic emission system in the indoor simulated rockburst experiments to collect the corresponding raw rockburst datasets. Subsequently, following data processing, pertinent data features were extracted, constituting



the rockburst datasets for this experiment. The training set was utilized for model training, whereas the test and validation sets were employed for model evaluation. Three types of rockburst prediction models, namely Transformer, Informer, and Distriformer, underwent comparative analysis during model training to ascertain the optimal performer. The model evaluation process employed two widely used error assessment techniques: mean absolute error (MAE) and root mean square error (RMSE). The training time was measured by the average time taken for one epoch and the acceleration ratio. Finally, the results of the experiment were analyzed.

This paper employs two evaluation indices, namely MAE and RMSE, to assess the efficacy of rockburst prediction. The formulas for their calculation are as follows:

$$\text{MAE}(y, \tilde{y}) = \frac{1}{n} \sum_{i=0}^{n-1} |y_i - \tilde{y}_i| \quad (6)$$

$$\text{RMSE}(y, \tilde{y}) = \sqrt{\frac{1}{n} \sum_{i=0}^{n-1} (y_i - \tilde{y}_i)^2} \quad (7)$$

where  $\tilde{y}$  represents the predicted value of rockburst,  $y$  denotes the true value of rockburst, and  $n$  signifies the total number of predicted points.

The experiments employed an acceleration ratio to quantify the duration needed for training the rockburst prediction model. The acceleration ratio is defined as the ratio of the average time per epoch required to train the two models. The formula is as follows:

$$S = \frac{T_1}{T_2} \quad (8)$$

where  $S$  represents the acceleration ratio,  $T_1$  denotes the longer average training duration per epoch, and  $T_2$  denotes the shorter average training duration per epoch.

#### 4.2. Experimental Data

The present study encompasses an analysis of five distinct rockburst datasets, each with a substantial volume of samples to ensure robust predictive modeling. Specifically, the dataset ROCKBURST\_S1 comprises 13,962 samples, ROCKBURST\_S2 contains 27,572 samples, ROCKBURST\_S3 encompasses 22,804 samples, ROCKBURST\_S4 includes 31,210 samples, and ROCKBURST\_S5 consists of 12,010 samples. Table 2 shows the specific sample number of each rockburst dataset.

**Table 2.** Rockburst dataset sample sizes.

Dataset	Number of Samples
ROCKBURST_S1	13,962
ROCKBURST_S2	27,572
ROCKBURST_S3	22,804
ROCKBURST_S4	31,210
ROCKBURST_S5	12,010

#### 4.3. Result Analysis

##### 4.3.1. Accuracy Analysis

Table 3 presents the evaluation metrics for each rockburst prediction model, assessed using the MAE and RMSE metrics. Lower values denote increased accuracy in model predictions.

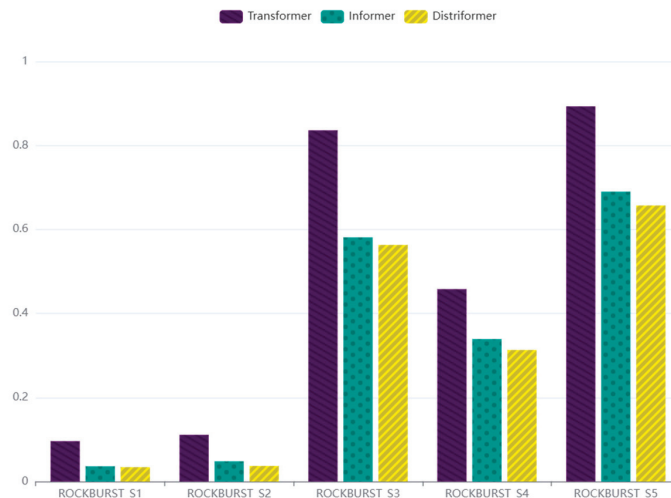
Table 3 illustrates that the Distriformer model outperforms the Transformer model significantly in both MAE and RMSE, exhibiting a considerable improvement. It reduces the MAE by 64.6%, 66.7%, 32.7%, 31.7%, and 26.4% and the RMSE by 62.4%, 24.4%, 31.1%, 14.2%, and 21.5%. The experimental results indicate that the Distriformer model

exhibits reduced error compared to the baseline model (Informer), resulting in enhanced overall performance.

**Table 3.** Rockburst model accuracy assessment.

Dataset	Model	MAE	RMSE
ROCKBURST_S1	Transformer	0.096	0.101
	Informer	0.036	0.042
	Distriformer	0.034	0.038
ROCKBURST_S2	Transformer	0.111	0.160
	Informer	0.048	0.131
	Distriformer	0.037	0.121
ROCKBURST_S3	Transformer	0.836	10.604
	Informer	0.581	7.326
	Distriformer	0.563	7.302
ROCKBURST_S4	Transformer	0.458	9.928
	Informer	0.339	8.725
	Distriformer	0.313	8.521
ROCKBURST_S5	Transformer	0.893	6.719
	Informer	0.690	5.314
	Distriformer	0.657	5.272

Figures 6 and 7 illustrate the performance of the rockburst prediction model in terms of Mean MAE and RMSE across five datasets depicted in a bar chart. The figure also illustrates the superior performance of the Distriformer model.



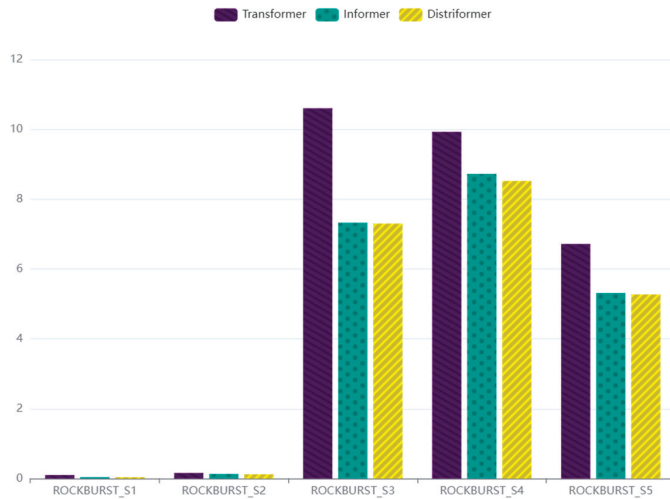
**Figure 6.** Status of MAE assessment indicators.

#### 4.3.2. Training Time Analysis

To facilitate a comparison of model training duration, the average time required for training one epoch was measured, and the acceleration ratio was introduced for emphasis. Table 4 displays the mean duration necessary for training per epoch across various rockburst prediction models.

As indicated in Table 4, the experimentations across all five datasets revealed that Informer required the longest duration, followed by Transformer, with Distriformer exhibiting the shortest time. Thus, the acceleration ratio of the Informer model was set as 1 for

each dataset, while the acceleration ratios of the remaining two models were computed and juxtaposed for comparison. The acceleration ratio of the Transformer model ranges from 1.11 to 1.14, whereas the Distriformer model exhibits a minimum ratio of 1.63 and a maximum of 1.87. The Distriformer model decreases processing time by 38.8% to 46.4% compared to that of the Informer model.



**Figure 7.** Status of RMSE assessment indicators.

**Table 4.** Time required for model training.

Dataset	Model	Average Time Taken for One Epoch (s)	Acceleration Ratio
ROCKBURST_S1	Transformer	12.3	1.11
	Informer	13.6	1
	Distriformer	8.0	1.70
ROCKBURST_S2	Transformer	24.4	1.11
	Informer	27.1	1
	Distriformer	15.9	1.70
ROCKBURST_S3	Transformer	19.7	1.14
	Informer	22.5	1
	Distriformer	13.3	1.69
ROCKBURST_S4	Transformer	27.1	1.14
	Informer	30.8	1
	Distriformer	16.5	1.87
ROCKBURST_S5	Transformer	10.3	1.13
	Informer	11.6	1
	Distriformer	7.1	1.63

Figure 8 illustrates a comparison of the average epoch training times for the model, providing a clearer visualization of the time disparities among the three. The x-axis of the graph represents time in seconds, while the y-axis denotes the corresponding dataset. The time disparity between the Transformer and Informer models is marginal, whereas the Distriformer model significantly diminishes training duration.

Figure 9 shows the line graph of the acceleration ratio for each model. The figure illustrates that the Distriformer model achieved the highest acceleration ratio across all datasets, implying the efficacy of the proposed model in reducing training time for rockburst prediction.

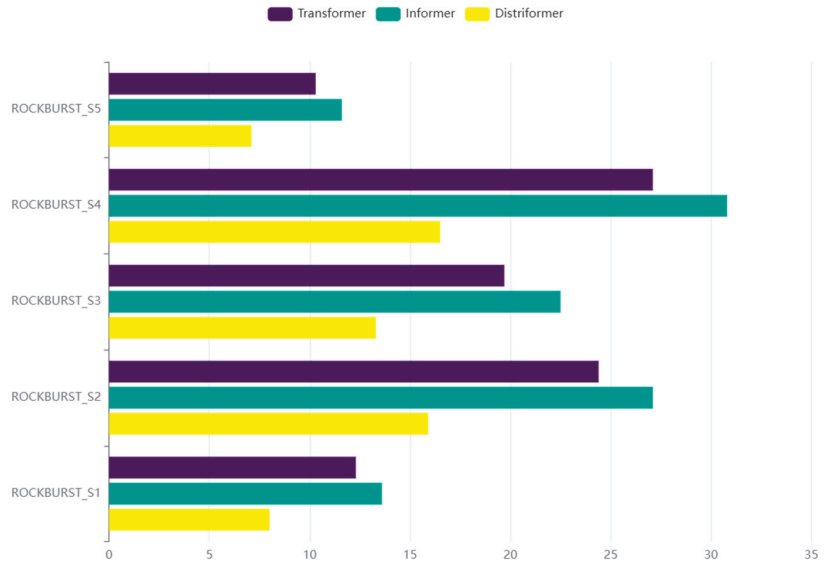


Figure 8. Comparison graph of model training time.

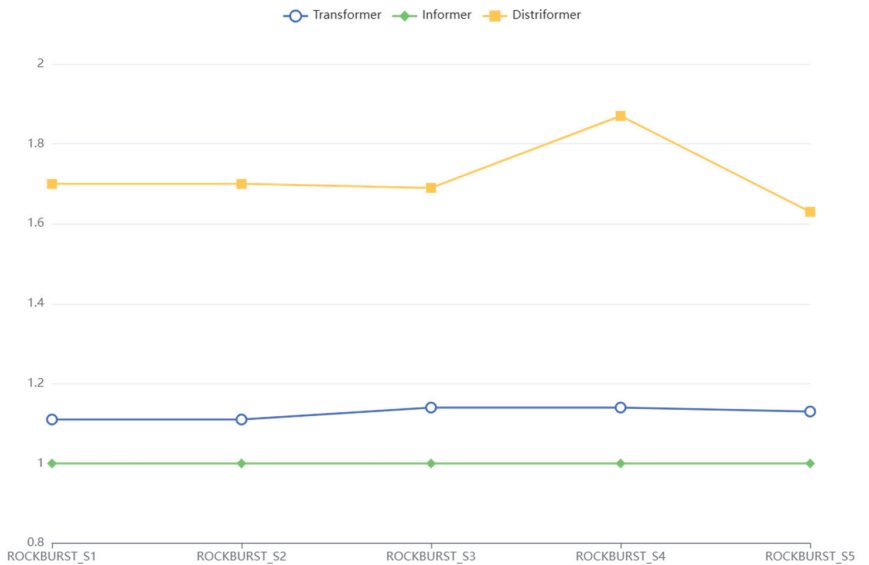


Figure 9. Acceleration ratio line graph.

In summary, the Distriformer rockburst prediction model has excellent performance. The Distriformer model with distributed training outperforms the original Informer model across all measurement indices, confirming the efficacy of distributed training for Informer. This method enhances the accuracy of rockburst prediction, resulting in an average decrease of 44.4% in MAE and 30.7% in RMSE. Furthermore, it accelerates the training process for predicting rockburst, achieving an average acceleration ratio of 1.72. The issue of low model accuracy and extended model training duration has been partially addressed.

## 5. Conclusions and Outlook

This paper innovatively introduces distributed training methods into rockburst prediction to solve the problem of training time. The Distriformer model for rockburst prediction achieves a balance between prediction accuracy and timeliness, as evidenced by experimental results validating its feasibility. Application of this method in real-world scenarios holds the potential to enhance rockburst prediction accuracy, bolster mining operation safety, and reduce model training time. Simultaneously, it establishes the groundwork for subsequent rockburst prediction, facilitating the online prediction and processing of substantial volumes of rockburst data.

Nevertheless, the research presented in this paper is not without its limitations. Future research endeavors could be enhanced by focusing on the following areas.

(1) Data sources: This study exclusively employed data generated from indoor simulated rockburst. Future research endeavors can leverage real-time training and prediction using rockburst data from operational mines.

(2) Federated Learning: Employing federated learning techniques enables collaborative training and data sharing among units, safeguarding individual data privacy, and thereby enhancing the precision and applicability of rockburst prediction models.

**Author Contributions:** Conceptualization, Y.Z., K.F. and Z.G.; methodology, Y.Z., K.F. and Z.G.; validation, Y.Z.; formal analysis, K.F.; investigation, Y.Z., K.F. and Z.G.; resources, Y.Z.; data curation, Y.Z., K.F. and Z.G.; writing—original draft preparation, Y.Z., K.F. and Z.G.; writing—review and editing, Y.Z. and K.F.; visualization, K.F.; supervision, K.F.; project administration, Y.Z. and K.F.; funding acquisition, Y.Z. All authors have read and agreed to the published version of the manuscript.

**Funding:** This research was funded by the Institute for Deep Underground Science and Engineering, grant number XD2021021, the BUCEA Post Graduate Innovation Project, grant number PG2024099, and the Postgraduate education and teaching quality improvement project of Beijing University of Civil Engineering and Architecture, grant number J2022003.

**Data Availability Statement:** The data presented in this study are available on request from the corresponding author. The data are not publicly available due to privacy.

**Conflicts of Interest:** The authors declare no conflicts of interest.

## References

1. Wu, M.; Ye, Y.; Wang, Q.; Hu, N. Development of rockburst research: A comprehensive review. *Appl. Sci.* **2022**, *12*, 974. [CrossRef]
2. Li, K.; Wu, Y.; Du, F.; Zhang, X.; Wang, Y. Prediction of rockburst intensity grade based on convolutional neural network. *Coal Geol. Explor.* **2023**, *51*, 94–103. [CrossRef]
3. Zhang, J.; Xu, K.; Reniers, G.; You, G. Statistical analysis the characteristics of extraordinarily severe coal mine accidents (ESCMAs) in China from 1950 to 2018. *Process Saf. Environ. Prot.* **2020**, *133*, 332–340. [CrossRef]
4. Liu, J.; Gao, Y.; Chen, F.; Cao, Z. Mechanism Study and Tendency Judgement of Rockburst in Deep-Buried Underground Engineering. *Minerals* **2022**, *12*, 1241. [CrossRef]
5. Li, X.; Chen, D.; Fu, J.; Liu, S.; Geng, X. Construction and application of fuzzy comprehensive evaluation model for rockburst based on microseismic monitoring. *Appl. Sci.* **2023**, *13*, 12013. [CrossRef]
6. Luo, D.; Lu, S.; Su, G.; Tao, H. Experimental study on rock burst of granite with prefabricated single crack under true-triaxial stress condition with a free face. *Rock Soil Mech.* **2023**, *44*, 75–87. [CrossRef]
7. Liu, X.; Zhang, S.; Wang, E.; Zhang, Z.; Wang, Y.; Yang, S. Multi-index geophysical monitoring and early warning for rockburst in coalmine: A case study. *Int. J. Environ. Res. Public Health* **2022**, *20*, 392. [CrossRef] [PubMed]
8. Liu, H.; Zhao, G.; Xiao, P.; Yin, Y. Ensemble tree model for long-term rockburst prediction in incomplete datasets. *Minerals* **2023**, *13*, 103. [CrossRef]
9. Jin, A.; Basnet, P.M.S.; Mahtab, S. Microseismicity-based short-term rockburst prediction using non-linear support vector machine. *Acta Geophys.* **2022**, *70*, 1717–1736. [CrossRef]
10. Jia, Z.; Wang, Y.; Wang, J.; Pei, Q.; Zhang, Y. Rockburst Intensity Grade Prediction Based on Data Preprocessing Techniques and Multi-model Ensemble Learning Algorithms. *Rock Mech. Rock Eng.* **2024**, 1–21. [CrossRef]
11. Owusu-Ansah, D.; Tinoco, J.; Lohrasb, F.; Martins, F.; Matos, J. A decision tree for rockburst conditions prediction. *Appl. Sci.* **2023**, *13*, 6655. [CrossRef]
12. Sun, J.; Wang, W.; Xie, L. Predicting Short-Term Rockburst Using RF-CRITIC and Improved Cloud Model. *Nat. Resour. Res.* **2024**, *33*, 471–494. [CrossRef]

13. Liu, J.; Zhou, Z. Rockburst Grade Prediction Based on Modified Scatter Graph Matrix and Random Forest. *Nonferrous Met. Eng.* **2022**, *12*, 120–128. [CrossRef]
14. Zhou, J.; Guo, H.; Koopialipoor, M.; Jahed Armaghani, D.; Tahir, M.M. Investigating the effective parameters on the risk levels of rockburst phenomena by developing a hybrid heuristic algorithm. *Eng. Comput.* **2021**, *37*, 1679–1694. [CrossRef]
15. Zhang, W.; Bi, X.; Hu, L.; Li, P.; Yao, Z. Performance and Applicability of Recognizing Microseismic Waveforms Using Neural Networks in Tunnels. *KSCE J. Civ. Eng.* **2024**, *28*, 951–966. [CrossRef]
16. Yang, X.; Pei, Y.; Cheng, H.; Hou, X.; Lu, J. Prediction method of rockburst intensity grade based on SOFM neural network model. *Chin. J. Rock Mech. Eng.* **2021**, *40*, 2708–2715. [CrossRef]
17. Di, Y.; Wang, E.; Li, Z.; Liu, X.; Huang, T.; Yao, J. Comprehensive early warning method of microseismic, acoustic emission, and electromagnetic radiation signals of rock burst based on deep learning. *Int. J. Rock Mech. Min. Sci.* **2023**, *170*, 105519. [CrossRef]
18. Vaswani, A.; Shazeer, N.; Parmar, N.; Uszkoreit, J.; Jones, L.; Gomez, A.N.; Kaiser, L.; Polosukhin, I. Attention is all you need. *Adv. Neural Inf. Process. Syst.* **2017**, *30*. [CrossRef]
19. Zhou, H.; Zhang, S.; Peng, J.; Zhang, S.; Li, J.; Xiong, H.; Zhang, W. Informer: Beyond efficient transformer for long sequence time-series forecasting. *Proc. AAAI Conf. Artif. Intell.* **2021**, *12*, 11106–11115. [CrossRef]
20. Dai, M.; Yuan, J.; Huang, Q.; Lin, X.; Wang, H. Distributed Encoding and Updating for SAZD Coded Distributed Training. *IEEE Trans. Parallel Distrib. Syst.* **2023**, *7*, 2124–2137. [CrossRef]
21. Wei, J.; Zhang, X.; Wang, L.; Zhao, M.; Dong, X. MC<sup>2</sup> Energy Consumption Model for Massively Distributed Data Parallel Training of Deep Neural Networks. *J. Comput. Res. Dev.* **2023**, 1–21. [CrossRef]

**Disclaimer/Publisher’s Note:** The statements, opinions and data contained in all publications are solely those of the individual author(s) and contributor(s) and not of MDPI and/or the editor(s). MDPI and/or the editor(s) disclaim responsibility for any injury to people or property resulting from any ideas, methods, instructions or products referred to in the content.

Article

# Decision Intelligence-Based Predictive Modelling of Hard Rock Pillar Stability Using K-Nearest Neighbour Coupled with Grey Wolf Optimization Algorithm

Muhammad Kamran <sup>1,\*</sup>, Waseem Chaudhry <sup>2</sup>, Blessing Olamide Taiwo <sup>3</sup>, Shahab Hosseini <sup>4</sup> and Hafeezur Rehman <sup>5</sup>

<sup>1</sup> College of Science and Engineering, University of Tasmania, Hobart, TAS 7001, Australia

<sup>2</sup> Department of Petroleum Engineering, Institute Technology of Bandung, Bandung 40132, Indonesia; wasim\_ch2@hotmail.com

<sup>3</sup> Department of Mining Engineering, Federal University of Technology Akure, Gage 340110, Nigeria; taiwoblessing199@gmail.com

<sup>4</sup> Faculty of Engineering, Tarbiat Modares University, Tehran 14115-175, Iran; h.seyyedshahab@modares.ac.ir

<sup>5</sup> Department of Mining Engineering, Faculty of Engineering and Architecture, Balochistan University of Information Technology, Engineering and Management Sciences (BUIITEMS), Quetta 87300, Pakistan; hafeezur.rehman@buitms.edu.pk

\* Correspondence: m.kamran@utas.edu.au

**Abstract:** Pillar stability is of paramount importance in ensuring the safety of underground rock engineering structures. The stability of pillars directly influences the structural integrity of the mine and mitigates the risk of collapses or accidents. Therefore, assessing pillar stability is crucial for safe, productive, reliable, and profitable underground mining engineering processes. This study developed the application of decision intelligence-based predictive modelling of hard rock pillar stability in underground engineering structures using K-Nearest Neighbour coupled with the grey wolf optimization algorithm (KNN-GWO). Initially, a substantial dataset consisting of 236 different pillar cases was collected from seven underground hard rock mining engineering projects. This dataset was gathered by considering five significant input variables, namely pillar width, pillar height, pillar width/height ratio, uniaxial compressive strength, and average pillar stress. Secondly, the original hard rock pillar stability level has been classified into three types: failed, unstable, and stable, based on the pillar's instability mechanism and failure process. Thirdly, several visual relationships were established in order to ascertain the correlation between input variables and the corresponding pillar stability level. Fourthly, the entire pillar database was randomly divided into a training dataset and testing dataset with a 70:30 sampling method. Moreover, the (KNN-GWO) model was developed to predict the stability of pillars in hard rock mining. Lastly, the performance of the suggested predictive model was evaluated using accuracy, precision, recall, F1-score, and a confusion matrix. The findings of the proposed model offer a superior benchmark for accurately predicting the stability of hard rock pillars. Therefore, it is recommended to employ decision intelligence models in mining engineering in order to effectively prioritise safety measures and improve the efficiency of operational processes, risk management, and decision-making related to underground engineering structures.

**Keywords:** pillar stability; safety; grey wolf optimization; decision-making; underground structures; KNN

**Citation:** Kamran, M.; Chaudhry, W.; Taiwo, B.O.; Hosseini, S.; Rehman, H. Decision Intelligence-Based Predictive Modelling of Hard Rock Pillar Stability Using K-Nearest Neighbour Coupled with Grey Wolf Optimization Algorithm. *Processes* **2024**, *12*, 783. <https://doi.org/10.3390/pr12040783>

Academic Editors: Feng Du, Aitao Zhou and Bo Li

Received: 17 February 2024

Revised: 5 April 2024

Accepted: 9 April 2024

Published: 13 April 2024



**Copyright:** © 2024 by the authors. Licensee MDPI, Basel, Switzerland. This article is an open access article distributed under the terms and conditions of the Creative Commons Attribution (CC BY) license (<https://creativecommons.org/licenses/by/4.0/>).

## 1. Introduction

In underground hard rock mining, pillars are crucial structural elements for mine safety. One of the primary functions of underground engineering processes is to provide safe access to work areas, while another is to support the weight of overburden materials to ensure global stability [1]. The presence of unstable pillars poses a significant threat to worker safety, as it has the potential to result in extensive collapses [2]. In the event of a pillar failure, the remaining pillars are required to bear an increased load. If the

load surpasses the strength of the nearby pillars, it may result in a failure. The potential exists for the initiation of a rapid and extensive cascade, analogous to the phenomenon known as the domino effect. Moreover, empirical evidence suggests that an increase in the depth of mining operations corresponds to a rise in ground stress levels, thereby causing a greater frequency of pillar instability-related incidents [3,4]. The maintenance of stability in underground pillars is of paramount importance in safeguarding the integrity and safety of underground mining engineering operations. Implementing effective evaluation and control measures regarding pillar stability can mitigate hazardous events and protect the surrounding environment. Ground control is rendered impossible in the absence of stable pillars. Hence, the evaluation of pillar stability has significant importance in ensuring the effectiveness, safety, efficiency, and profitability of underground hard rock mining.

Pillar stability assessment in hard rock mining involves one of three methods. The first strategy is referred to as the safety factor (SF) ratio. The SF is an approach indicating the ratio of pillar stability/stress [5]. By employing this methodology, it is possible to determine the strength of the pillar, the stress exerted on the pillar, and the safety threshold. Several experimental methods have been proposed to analyse the calculation of pillar strength. These approaches include the linear shape effect, the power shape effect, the size effect, and the Hoek–Brown methods [6]. The determination of pillar stress involves the utilisation of two approaches, namely the tributary area model and numerical modelling [7]. The determination of the safety factor necessitates the consideration of both the applied force and the structural integrity of the pillar. Increasing the SF will result in the enhanced strength of the pillar. Theoretically, the bearable degree of risk is deemed as equal to unity. According to Cauvin et al. (2009), a pillar is deemed stable when the SF exceeds one; however, in other contexts, it is regarded as unstable [8]. When considering the potential variations of this technique, it is generally necessary for the safety threshold to exceed one in order to provide user protection during practical implementation. Although the SF technique is convenient to apply, there is still a lack of recognised unified equations for pillar strength and safety thresholds.

Numerical modelling serves as an alternative method for ascertaining the value of pillar stability. Numerical modelling approaches have gained extensive use due to their ability to account for the intricate boundaries and rock-mass properties. In order to examine the failure mechanism and non-linear displacement of rock pillars, Mortazavi et al. [9] employed an immediate Lagrangian analysis of continuum approach. Shnorhokian et al. [10] employed FLAC3D to assess the performance of the pillar stability in different mining sequence circumstances. In their study, Elmo and Stead [11] examined the failure characteristics of naturally fractured pillars. To do this, they employed a hybrid approach that integrated the finite element method (FEM) with the discrete element method (DEM). Li et al. utilised rock failure process analysis to ascertain the pillar stability in the presence of coupled thermo-hydrologic-mechanical conditions [12]. Jaiswal et al. utilised the boundary element approach to replicate the asymmetry observed in the produced stresses exerted on pillars [13]. Li et al. introduced the finite discrete element method (FDEM) to investigate the mechanical characteristics of the pillars and the variables contributing to their failure [14]. Moreover, a number of scholars employed numerical modelling in conjunction with other computational methodologies in order to examine the pillar stability phenomenon. The optimisation of the pillars' structure was achieved by the utilisation of the finite element method (FEM), artificial neural network (ANN), and reliability evaluation methodologies [15]. Griffiths et al. employed the random field concept, elastoplastic finite element method (FEM), and Monte Carlo simulation in their study of the likelihoods associated with pillar collapse [16]. Numerical modelling methods offer the capability to replicate the intricate failure behaviours shown by pillars, hence enabling the acquisition of valuable insights on the underlying mechanisms of failures and their associated ranges. However, accurately determining the model inputs and constitutive formulae might present difficulties because of the complex non-linear characteristics and anisotropic nature of the rock mass [17]. Consequently, the use of the theoretical framework becomes



challenging. Consequently, the validity of the implications that can be derived from this methodology is constrained.

Over the past decade, a multitude of soft computing techniques have been widely utilized to address engineering challenges, showcasing superior accuracy in predictive modelling [18–23]. Jian et al. employed support vector regression (SVR) to estimate pillar stability for mining in underground spaces chosen from a variety of coals and rock mines [24]. By utilising a range of metrics, it was determined that SVR possesses an adequate capability, which makes it a valuable method for predicting pillar stability. Random forests and C4.5 decision trees are two techniques that were suggested by Ahmad et al. for predicting pillar stability of underground mines; these models were capable of estimating pillar stability with a level of precision that was considered to be satisfactory [25]. In order to estimate the stability of hard rock pillars, Liang et al. applied the gradient algorithms and discovered that all three models provided an excellent capacity for predicting the pillar stability [26]. Ghasemi et al. obtained a high potential for performance in their development of pillar stability by employing two distinct intelligent categorisation strategies [27]. Zhou et al. evaluated the effectiveness of several metaheuristic algorithms to optimize ANN technique in terms of their ability to anticipate pillar stress [28]. Tawadrous and Katsabanis employed ANNs to examine the stability of surface crown pillars [29], whereas Wattimena applied multinomial logistic regression for pillar stability estimation [30]. Ding et al. used an algorithm known as stochastic gradient boosting (SGB) to predict and model pillar stability [31]. The proposed approach shows a superior accuracy compared to the other developed models. Zhou et al. assessed the effectiveness of six artificial intelligence techniques in determining the potential of the pillar stability predictive model [6]. A recent study utilized t-distributed stochastic neighbour embedding (t-SNE), k-means clustering, and support vector classifier to predict pillar stability [32]. Table 1 depicts the recent advances in the field of artificial intelligence for predicting pillar stability. Despite the fact that various machine learning methods can address pillar stability prediction problems to some degree, none of them can be used in all engineering scenarios. A universally accepted standardized algorithm for mining professionals has not yet been developed.

**Table 1.** Recent advances in the field of artificial intelligence to predict pillar stability.

Machine Learning Algorithms	Number of Datasets	Accuracy (%)	References
Multinomial logistic regression	84	79	[30]
Logistic Model Trees	178	79.1 and 80.5	[33]
ANN-BP model with Ensemble Learning	423	87.98	[34]
Stochastic Gradient Boosting Technique	205	90	[31]
Random Forest	205	85	[31]
GBDT	236	83	[26]
XGBoost	236	83	[26]
Support Vector Machine	251	83.2	[6]
Artificial Neural Network	251	80.9	[6]
Logistic regression model	80	81.25	[1]
Fuzzy logic model	80	87.50	[1]

Researchers have made significant advancements in their understanding of methods and mechanisms by using innovative approaches in recent years. The practical relevance of the learned knowledge has been empirically proven in the fields of engineering, environment, and risk analysis [35–38]. However, our present level of scientific understanding is insufficient to create underground engineering projects that possess the essential qualities of safety, reliability, environmental sustainability, and the ability to sustain innovative solutions, especially in situations where rigorous testing is not feasible. There is a significant amount of data that demonstrates a link between these advancements and the engineering fields that are responsible for protecting mining environments and maintaining the integrity of underground engineering processes.

In addition, the initiatives intending to predict pillar stability in hard rock mining have rarely incorporated the implementation of cutting-edge decision intelligence models. In this study, K-nearest neighbour coupled with grey wolf optimization algorithm (KNN-GWO) would be utilised to develop an early warning system for pillar stability. This research proposes a novel and state-of-the-art system for identifying and evaluating pillar stability in deep underground projects. Its novel features include an algorithm derived from observations that permits continuous evaluation of the pillar's stability and its predictions. In turn, the learning process of the data-driven network allows the model to continuously adapt to the underground mining production process in which it will be implemented. Consequently, this provides the opportunity for extremely precise and immediate outcomes, both of which are essential in the mining industry and in the case of pillar stability.

The application of the KNN-GWO algorithm for pillar stability entails determining the most effective design characteristics for deep hard rock mining. The grey wolf optimization algorithm (GWO) algorithm imitates the social behaviour of grey wolves to find the optimal solution, whereas the K-nearest neighbour (KNN) aids in assessing the stability of pillars based on the characteristics of surrounding pillars. This integrated method enhances the accuracy and effectiveness of pillar stability analysis, thereby contributing to the design of safer and more stable underground mining operations.

The remaining part of the paper is structured as follows: The second section presents the data curation and visualization. The third section provides an overview of the proposed methodology, including GWO, KNN, and their mathematical model. The fourth section illustrates decision intelligence and its application in the discipline of mining engineering. The fifth section subsequently discusses the results and discussion. In the sixth section, the limitations of the proposed paradigm and future possibilities are discussed. The conclusion is finally drawn in the last section.

## 2. Data Curation and Visualization

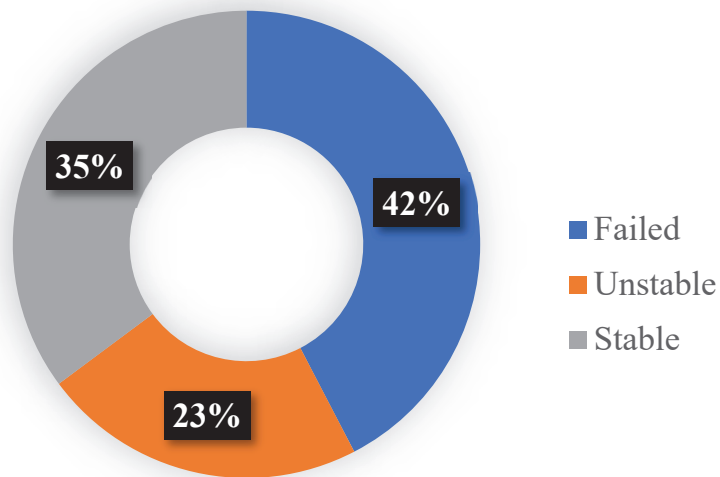
In order to create an accurate prediction model, historical data on hard rock pillar incidents must be gathered from real-life events. In the framework of the present study, a total of 236 instances were obtained from seven subsurface hard rock mining sites [5,7,39]. These mines include the Elliot Lake uranium mine, the Selebi-Phikwe mine, the Open stope mine, the Zinkgruvan mine, and the Westmin Resources Ltd.'s H-W mine, the Marble mine, and the Stone mine. Table 2 lists the statistics for the dataset related to pillar stability. The input variables were pillar width in meters (represented by Z1), pillar height in meters (represented by Z2), the ratio of pillar width to pillar height (represented by Z4), uniaxial compressive strength in MPa (represented by Z4), and average pillar stress in MPa (represented by Z5). The pillar stability level was the output variable, failed pillars (represented by 0), unstable pillars (represented by 1), and stable pillars (represented by 2), based on the failure process and instability mechanism of pillars. Researchers broadly acknowledge that the input criteria selected by Liang et al. [26] constitute a comprehensive and appropriate dataset for predicting pillar stability. When designing room-and-pillar or stope-and-pillar systems, the strength of a pillar, which refers to its loading capacity, is just as crucial as the stability of the roof and walls [40]. The failure mechanisms for a naturally fractured pillar include: (a) failure due to the lateral release of pre-formed blocks under increasing vertical load and inadequate confinement, (b) failure caused by the development of inclined shear fractures reducing through the pillar, particularly in pillars with a low Z1/Z2 ratio, and (c) failure involving transgressive fractures where the fracture inclination angle surpasses the angle of friction with the main loading axis of the pillar. The mechanical response of a pillar in these mechanisms is closely linked to the geological features of the ground, with the most significant impacts observed in slender pillars. Wider pillars are prone to collapsing due to a combination of brittle and shearing mechanisms. Geological discontinuities in rock layers are crucial for studying the strength, permeability, and deformability. Understanding the discontinuity in geometry, such as

spatial connectivity, persistence length, and aperture, is crucial for comprehending the behaviour of rock masses [41]. Discontinuities in rock profiles are widely recognized to have a significant impact on their strength qualities. Several examples from the pertinent rock failure literature could be identified due to an incorrect assessment of the impact of discontinuities on rock strength. Jessu and Spearing found that discontinuities have a significant impact on pillar inclination, even at higher Z1/Z2 ratios [42]. Shang et al. aimed to tackle issues related to the tensile strength of initial rock fractures and measured this characteristic using data from tests conducted in laboratories [43]. Data collection poses the greatest obstacle to the applicability of these variables, which are regarded as the primary variables for quantitatively identifying the occurrence of rock mass mechanical responses within the pillar. Thus, in the present study, the five variables are taken into account.

**Table 2.** Descriptive statistics of the pillar stability dataset.

Influential Variables	Mean	Standard Deviation	Minimum	Maximum
Z1 (m)	11.51	7.75	1.90	45
Z2 (m)	12.58	11.34	2.4	61
Z3	1.17	0.61	0.21	4.50
Z4 (MPa)	141.06	64.62	61	316
Z5 (MPa)	41.50	31.41	0.14	127.60

A robust Python library designed for machine learning, Scikit-learn [44], provides numerous tools, including those for data pre-processing, classification, regression, and clustering. Jupyter notebooks facilitate data exploration, analysis, and visualization through the integration of code, text, and multimedia components in an interactive environment [45]. To analyse the data related to pillar stability in hard rock mining, the Scikit-learn library was utilized to perform the computations in Jupyter notebook. Figure 1 displays the distribution of the pillar database based on the failure process and instability mechanism of pillars.



**Figure 1.** The donut chart of hard rock pillar stability levels.

Figure 2 depicts the diagonal correlations between the influencing variables and the pillar stability level. In order to display the correlation coefficient of the relevant variables of the pillar stability database, a seaborn correlation heatmap developed using Python has been utilised. Overall, the relationship coefficients between the influential variables and the pillar stability level are comparatively small. Hence, all the variables have been included

in this study to optimize the performance of the final model for predicting the stability of pillars in deep hard rock mining.

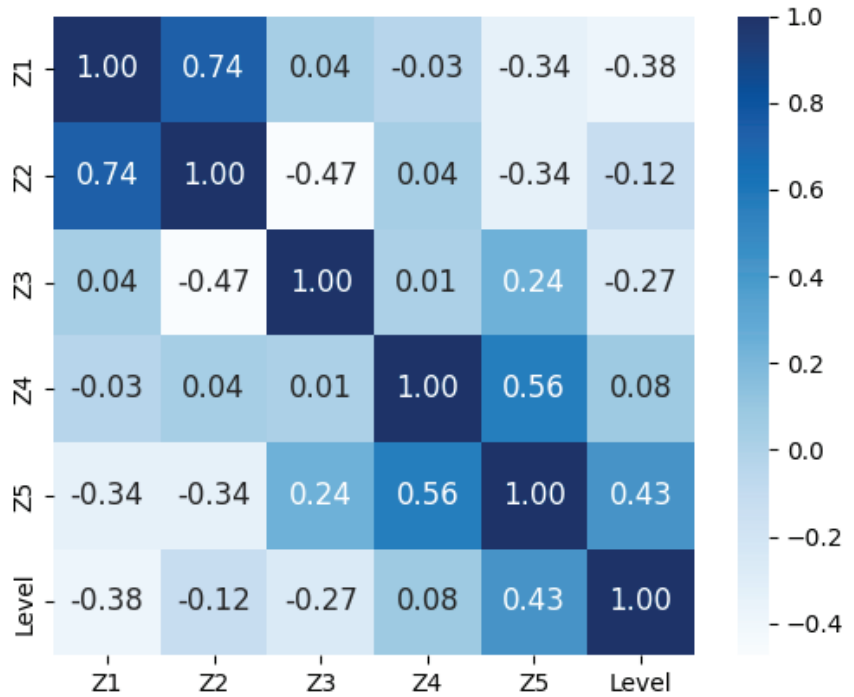
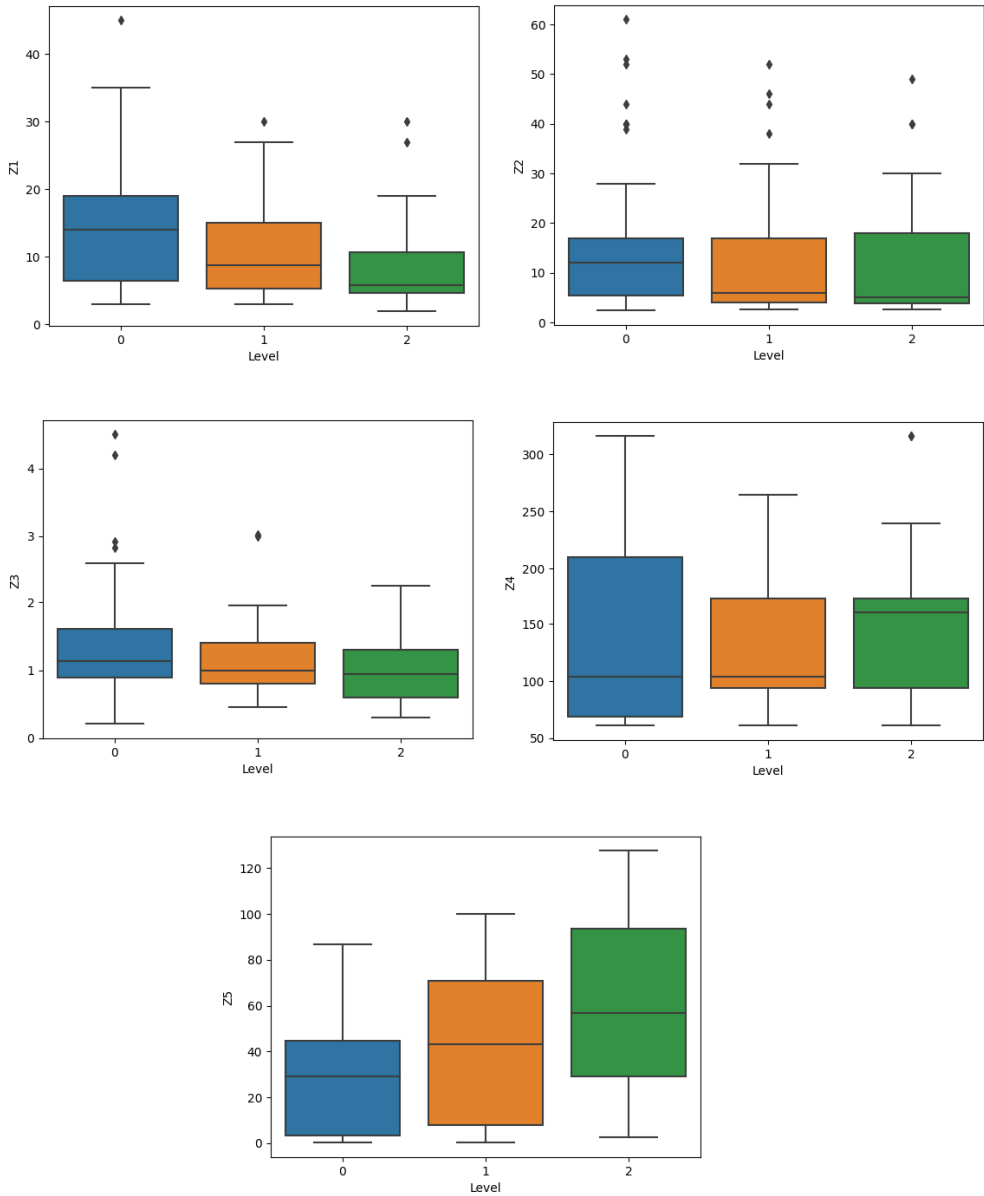


Figure 2. Correlation heatmap of pillar stability database.

Figure 3 illustrates the box plot representing the distribution of each variable across different degrees of pillar stability level. The data depicted in Figure 3 exhibit several interesting characteristics. Initially, it should be noted that each variable encompasses a certain quantity of outliers. Furthermore, the stability level of the pillar has a negative correlation with Z1 and Z3, but a positive correlation with Z5. Nevertheless, there are no evident relationships between Z2 and Z4. Also, the variances between the top and lower quartiles exhibit variability across different levels of the same variables. It should be noted that there exists an overlapping region within the ranges of results for several variables. Likewise, it is worth noting that the median does not coincide with the precise midpoint of the box, suggesting a lack of uniformity in the distribution of variable values. Therefore, these scenarios illustrate the intricate characteristics of the pillar stability phenomena.

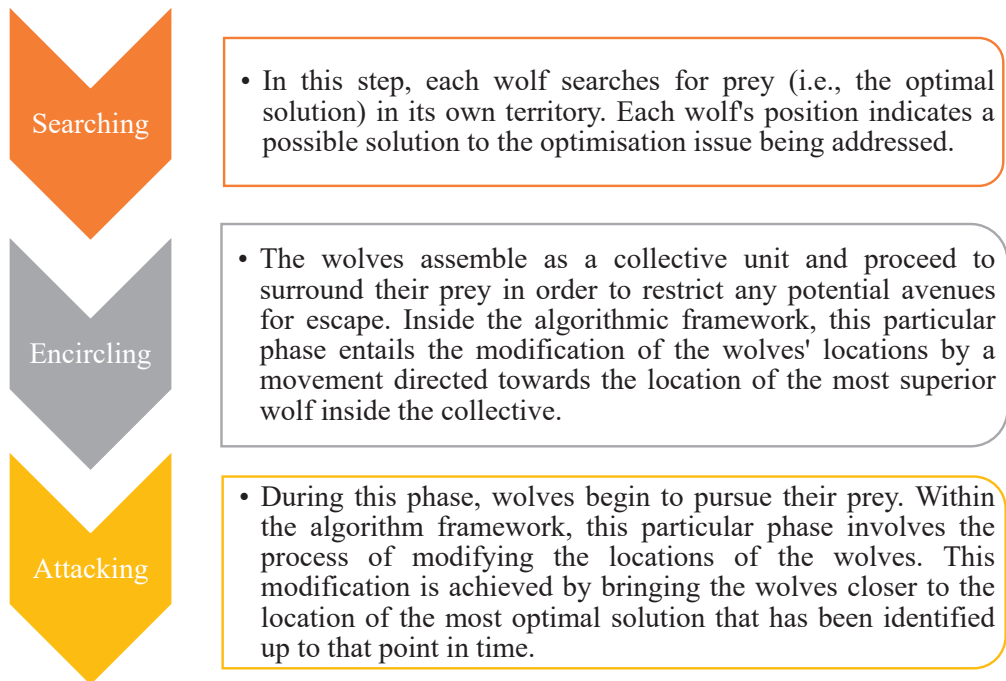


**Figure 3.** Boxplot of each of the parameters for different pillar stability levels.

### 3. Methodology

#### 3.1. Grey Wolf Optimization Algorithm (GWO)

A metaheuristic algorithm called Grey Wolf Optimization algorithm (GWO) was developed in order to model the social foraging behaviour of grey wolves in the wild [46]. Beginning with a base population of grey wolves, the GWO algorithm iteratively modifies the population by simulating wolf social behaviour [47,48]. The steps required to update the wolf population during the hunting process are shown in Figure 4.



**Figure 4.** Steps for Updating GWO population during training [49].

Mirjalili et al. modified the multi-objective technique in GWO for the first time to optimise situations with various goals [50]. In order to save and retrieve optimum solutions, a fixed-size external archive has been added within the GWO. Gupta and Deep presented the concept of random walks (RW-GWO) as a modified algorithm to increase Grey Wolf's search capacity [51]. The modified RW-GWO algorithm was found to be an efficient and reliable solution for handling both continuous and real-world optimization issues. Nadimi-Shahraki et al. developed an enhanced the GWO method to address the lack of population inclusion, the disparity among exploitation and exploration, as well as the GWO algorithm's early convergence [52]. The I-GWO algorithm utilises a dimension learning-based hunting (DLH) seeking approach, a new movement technique derived from the hunting behaviour of wild wolves. In the newly designed GWO, the DLH strategy employs a distinct method for developing a neighbourhood around every wolf whereby details about its neighbours are able to be disseminated. The software models wolf social structure. The wolves are classified as alpha, beta, or delta according to this method. The alpha wolves lead the pack and make choices, while the beta wolves provide assistance (see Figure 5). Delta wolves are subservient to alpha and beta wolves. The circling of their prey begins the hunting staging phase. Equations (1)–(6) contain the algorithm for outlining expressions.

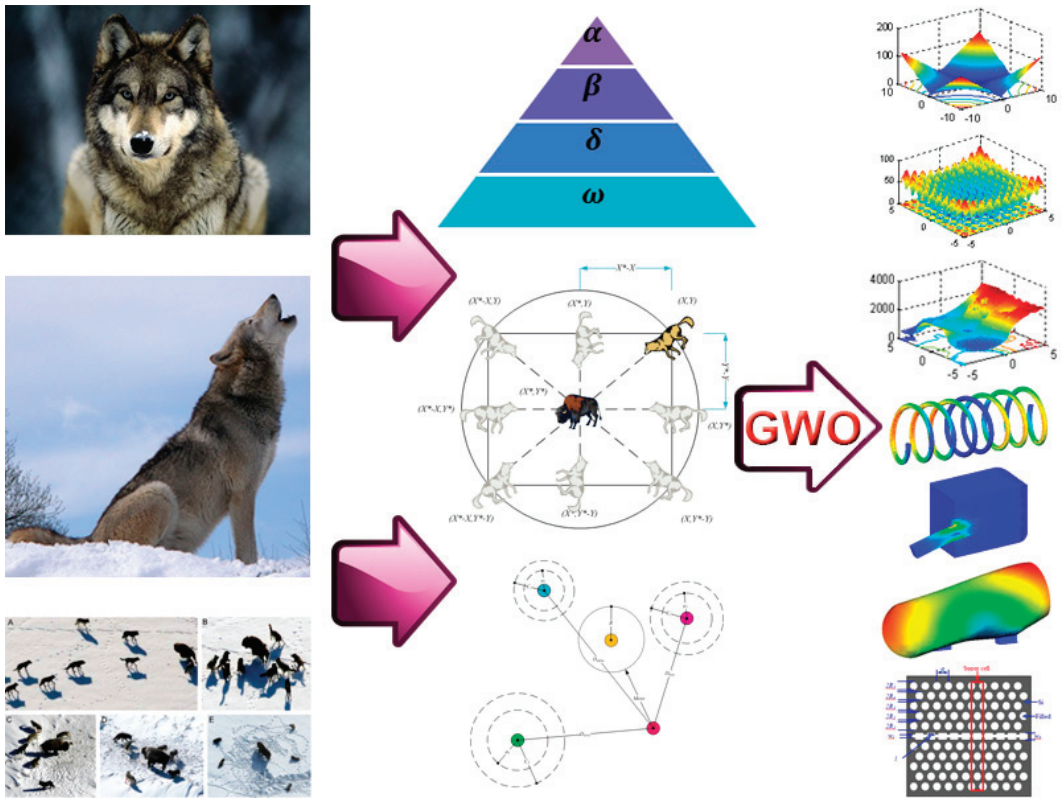


Figure 5. Pivot point illustration of GWO position update equations [53].

The mechanism of wolf positioning is represented by Equation (1)

$$Z(n + 1) = Z_p(n) + A \times D \tag{1}$$

$$D = |c \times Z_p(n + 1) - Z_p(n)| \tag{2}$$

$$I = 2 \times a \times v_1 - a \tag{3}$$

$$C = 2 \times v_2 \tag{4}$$

$$a = 2 - n \left( \frac{2}{Nn} \right) \tag{5}$$

where  $Z$  represents the position of the grey wolf,  $n$  depicts the total quantity of cycles,  $Z_p$  is the position of the prey, and  $D$  and  $A$  can both be determined using Equations (2) and (3).  $I$  depicts the iteration number ranging from zero to two,  $N_n$  represents the entire number of occurrences, and  $v_1$  and  $v_2$  are randomly selected vectors for the hunting process simulation, ranging between  $[0, 1]$ . As shown in Equation (6), there is an optimal prey location that provides the best hunting result at each position adopted by the wolves. The

method iterates until a stopping criterion, such as a limit on the number of iterations or a desired degree of solution quality, is fulfilled.

$$Z(t+1) = (Z_1 + Z_2 + Z_3)/3 \quad (6)$$

The position of each prey within the space field ( $Z_1$ ,  $Z_2$ , and  $Z_3$ ) are computed using Equations (7)–(9), respectively.

$$Z_1 = [Z_\alpha - A_1 \times D_\alpha] \quad (7)$$

$$Z_2 = [Z_\beta - A_2 \times D_\beta] \quad (8)$$

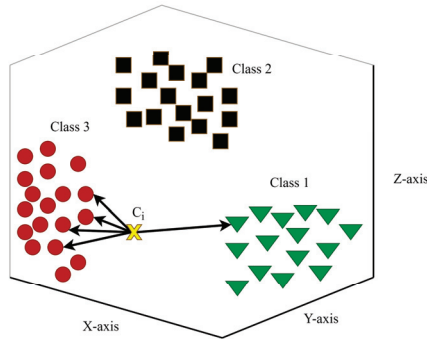
$$Z_3 = [Z_\delta - A_3 \times D_\delta] \quad (9)$$

The GWO as an optimization technique has found applicability in a variety of scientific disciplines. Ahmed et al. [54] developed predictive models for determining the compressive strength of ground granulated blast furnace slag concrete using 268 samples and six soft computing models. GWO constitutes a single of the utilised methods to optimise the support vector regression method with a 0.9522 correlation coefficient [54]. Adithiyaa et al., used k-nearest neighbours (KNN) along with GWO to optimise the manufacturing variables involved in stirring-squeeze moulding of augmented composites from metal matrix material [55]. A composite predictive algorithm has been developed for building power consumption by employing a machine learning strategy based on the fuzzy C-means clustering algorithm-GWO- back propagation neural network. To enhance the efficacy of the optimizer, Tian et al. clustered previous electrical usage data based on statistical distribution characteristics using the fuzzy C-means clustering technique [56]. In addition, Chen et al. utilised the step-wise weight assessment ratio analysis technique to determine the starting weight of every category of Chinese landslide-affecting variables in order to develop a combined landslide-illustrating structure that combines an adaptive neuro-fuzzy inference system (ANFIS) with GWO optimizer techniques [57]. Fattahi and Hasanipناه developed intelligent ground vibration models using 95 Malaysia quarry datasets by combining relevance vector regression (RVR) with GWO [58]. Additionally, the GWO method has been shown to be effective for a variety of optimization tasks, such as engineering design, image processing, and machine learning [52].

### 3.2. K-Nearest Neighbor (KNN) Algorithm

The K-Nearest Neighbour (KNN) technique is a popular classification and regression machine learning algorithm [59]. The fundamental principle of KNN is to locate the K training data points which are closest to the particular test data point and use their labels (in classification) or values (in regression) to predict the test data point's label or value [60]. The KNN classification constitutes one of the most elementary and easy-to-use approaches to classification and ought to be one of the first alternatives when one has no previous expertise regarding the data dispersion. The inspiration behind the development of KNN classification was the need for discriminant evaluation in cases where accurate parametric computations of probability densities are not accessible or undetermined [61]. Figure 6 illustrates the fundamental mechanism of the KNN algorithm.





**Figure 6.** A basic multi-class KNN model for three-dimensional spaces.

The KNN algorithm can be summarized as follows:

1. Choose the number of  $K$  neighbours to consider.
2. Calculate the distance between the test data point and each point in the training set using a distance metric (e.g., Euclidean distance).
3. The distance metric can be computed using Equations (10)–(13)

$$d(x, y) = \sqrt{\sum_{i=1}^n (Y_i - X_i)^2} \quad (10)$$

where  $d(x, y)$  is the Euclidean straight-line distance between the query point ( $Y_i$ ) and the other point being measured ( $X_i$ ).

$$Md(x, y) = \sum_{i=1}^m |X_i - Y_i| \quad (11)$$

where  $Md(x, y)$  is the navigating Manhattan distance from point  $X_i$  to another point  $Y_i$ .

$$Kd(x, y) = \left( \sum_{i=1}^n |X_i - Y_i| \right)^{1/p} \quad (12)$$

where  $Kd(x, y)$  is the navigating Minkowski distance from point  $X_i$  to another point  $Y_i$ .

$$Dh(x, y) = \left( \sum_{i=1}^k |X_i - Y_i| \right) \quad X = Y, Dh = 0, X \neq Y, Dh \neq 1 \quad (13)$$

where  $Dh(x, y)$  is the navigating Hamming distance from point  $X_i$  to another point  $Y_i$ .

1. Select the  $K$  data points in the training set that are closest to the test data point.
2. For classification tasks, determine the class label of the test data point based on the majority class of the KNN. For regression tasks, estimate the value of the test data point based on the average value of the KNN.
3. Return the predicted class label or value [61].

As a criterion, the kernel function is applied to configure the KNN model, which includes quartic (Equation (14)), tri-weight (Equation (15)), and cosine (Equation (16)) [62].

$$K(u) = \frac{15}{16} (1 - u^2)^2 \quad (14)$$

$$K(u) = \frac{35}{32} (1 - u^2)^3 \quad (15)$$

$$K(u) = \frac{\pi}{4} \cos\left(\frac{\pi}{2}u\right)^1 \quad (16)$$

Guo et al. noted that KNN technique can be used to solve issues involving binary and multi-class classification, as well as regression [63]. It is a non-parametric method,

which implies no inferences are established regarding the distribution of the underlying data. To achieve optimum performance, both the distance measure and the number of neighbours must be selected with consideration. Alkhatib et al. utilised the KNN and a non-linear regression approach to forecast the price of stocks for a sample of six major Jordanian companies to assist shareholders, executives, decision makers, and consumers in order to reach accurate and well-informed choices regarding investments [64]. Adaptive KNN was presented by Subramaniaswamy and Logesh as an innovative version of the KNN method for constructing a knowledge-driven, domain-dependent taxonomy for the creation of personalised recommendations using a collaborative filtering-based recommender system [65].

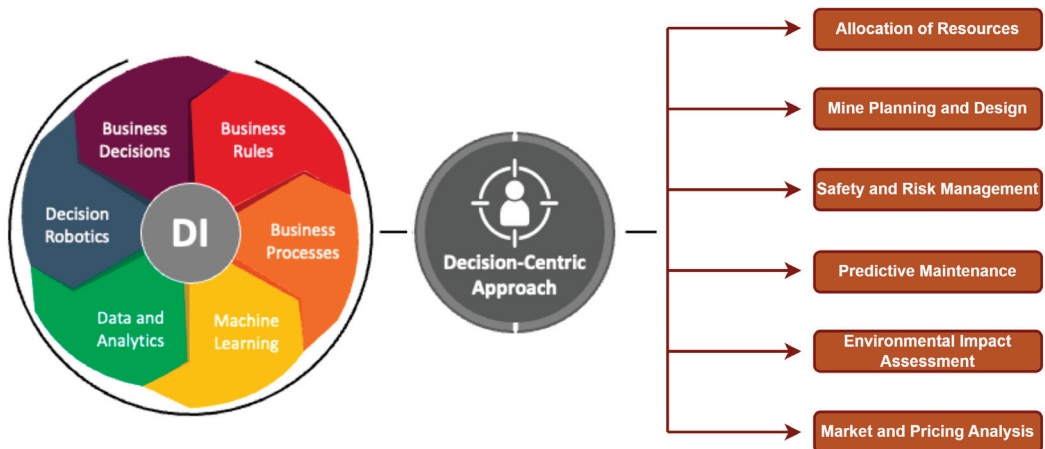
#### 4. Decision Intelligence and Its Application in Mining Industry

The emerging discipline of “Decision Intelligence” integrates artificial intelligence, decision theory, and the behavioural sciences to enhance the decision-making processes employed by organizations. Decision Intelligence, often referred to as decision management and decision analytics, is an alternative term used to describe the field of study and practice concerned with making informed decisions. The use of decision intelligence holds potential for several domains, including engineering, finance, healthcare, and cybersecurity. This tool proves to be highly advantageous for both overarching strategic decisions and more specific individual selections. The concept of “decision intelligence” pertains to the use of information and expertise to enhance the calibre of decision-making, particularly in intricate situations. Decision intelligence encompasses a range of methodologies, including machine learning, data analytics, optimisation, and game theory. These strategies are advantageous in facilitating the comparison of prospective outcomes across different scenarios and assessing the relative significance of various components [66].

The use of decision intelligence in the field of mining engineering involves the utilisation of data science and machine learning techniques, leading to useful results. The domains of rock engineering and rock mechanics can benefit greatly from the use of decision intelligence when it comes to various scenarios and decision-making procedures. Figure 7 depicts the practical use of decision intelligence within the domain of mining engineering. A few strategies that mining companies could employ to effectively utilize decision intelligence are as follows:

- (1) **Resource Allocation:** The efficient use of limited resources to attain desired objectives is a core component of decision intelligence [67,68]. Allocating resources like labour, money, and equipment may be performed more efficiently by mining businesses with the use of decision intelligence. This approach facilitates the optimisation of resource allocation and scheduling, resulting in better operational efficiency.
- (2) **Safety and Risk Management:** The application of decision intelligence has the potential to facilitate risk assessment and safety supervision by means of analysing data obtained from sensors, previous event reports, and geological surveys [69]. The underground mining engineering sector faces various hazards, such as rock bursts, gases, poor air quality, high temperatures, ventilation issues, and the presence of toxic chemicals. Decision intelligence models have the ability to aid in the implementation of preventive measures, risk management, and incident response by analysing instances.
- (3) **Mine Planning and Design:** The process of mine planning and design necessitates the involvement of mining engineers, who possess the necessary skills to make crucial decisions pertaining to many aspects, such as the layout of the mine, extraction methods, and production scheduling. The analysis of geological data, geotechnical constraints, and economic variables can be facilitated by the application of decision intelligence methodologies, hence aiding in the process of decision-making in this context [70]. The enhancement of mine planning and design may be achieved via the application of models that facilitate the simulation of various situations, enable the comparison of alternative strategies, and identify the most optimal techniques.

- (4) **Predictive Maintenance:** Mining equipment plays a crucial role in operational activities; nonetheless, equipment failures can incur significant costs. In order to enhance the accuracy of maintenance estimations and optimise maintenance schedules, the use of decision intelligence may be employed to analyse sensor data, historical maintenance records, and equipment performance [71]. The use of a preventative maintenance strategy in mining enterprises has the potential to optimise operating efficiency, prolong the lifespan of equipment, and minimise instances of downtime.
- (5) **Environmental Impact Assessment:** The implementation of decision intelligence can enhance the assessment and efficient handling of the environmental impacts linked to mining activities [72]. The understanding of probable consequences arising from mining operations can be improved by employing analytical models that evaluate environmental data related to air quality, water quality, and biological attributes. This comprehension adds to the improvement of waste management practices, land restoration endeavours, and compliance with environmental standards.
- (6) **Market and Pricing Analysis:** Decision intelligence technologies may be employed to examine market trends, dynamics of pricing, and scenarios of supply and demand [73]. The models can offer valuable insights into production quantities, pricing strategies, and market positioning through the incorporation of market data, sales records, and economic variables.



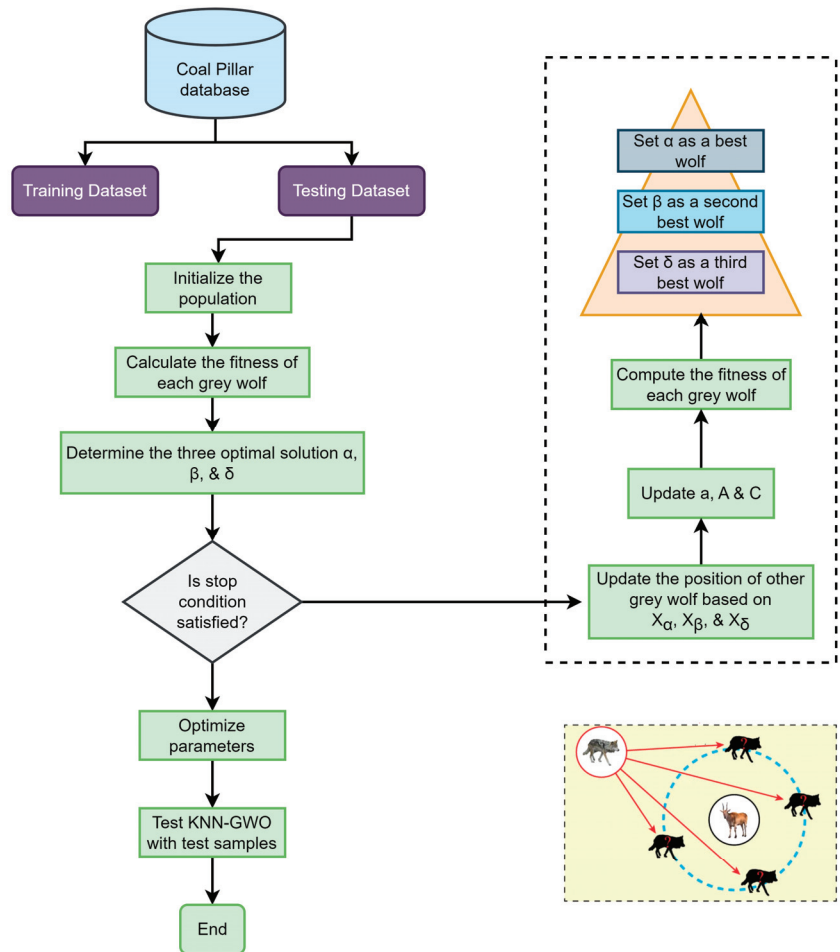
**Figure 7.** Application of decision intelligence in the field of mining engineering.

By incorporating decision intelligence approaches into mining engineering practices, mining businesses may make data-driven decisions, optimise operations, increase safety, reduce environmental impact, and boost overall productivity and profitability.

## 5. Results and Discussion

Python is a widely used programming language that has undergone significant expansion in recent years. It is used in the task of undertaking scientific and computational studies on enormous databases. Python is a language for programmers that is capable of being employed for assisting with procedures and algorithms that focus on the sorting and organising stages of the data mining process [74]. When it comes to creating flexible applications, this option is among the best options to choose because it provides such a wide variety of valuable perks. Python has become the language of choice for developers working on a wide variety of challenges due to its ease of use, extensive library support, and thriving community. This means that large datasets associated with pillar stability data may be studied using big data analysis techniques in order to produce reliable outcomes.

In this study, two decision intelligence models are developed to evaluate the stability of pillars in underground rock mining. Firstly, the KNN model has been developed to classify the different levels of 1 pillar stability levels. Moreover, in order to further enhance the accuracy of the proposed model, the KNN-GWO approach has been utilized. This approach combines the social behaviour of grey wolves, as simulated by the GWO optimization algorithm, with the KNN to aid in determining pillar stability based on the characteristics of adjacent pillars. By utilizing this optimization technique, we trained the machine learning model using the training data sent by the GWO. Several studies have confirmed that optimizing hyperparameters using the GWO algorithm can significantly enhance machine learning performance [75,76]. Figure 8 provides a depiction of the overall structure of the KNN-GWO technique that has been proposed in this study.



**Figure 8.** The structure of the KNN-GWO technique employed in this study.

The prediction summary of a classification-based data driven model is shown as a confusion matrix [77–79]. It summarises the algorithm’s predictions and evaluates how well they match up with the true values of the intended variable. The confusion matrix is often displayed as a table where rows represent predictions and columns reflect actual values. It displays the number of accurate and wrong predictions made for each class. The entire number of attributes that the data-driven framework is capable of accurately

predicting is shown in the cells that are diagonal to the primary diagonal of the matrix. The number of attributes that the data-driven framework incorrectly categorised is shown by the number of classes that are located outside of the diagonal. The projected classes from the data-driven framework can be viewed along the axis that is horizontal to the confusion metric, while the ground truth can be viewed along the vertical axis of the metric. We can extrapolate from this that a reliable model will have more information along the diagonal.

In addition, researchers have used a variety of performance indices to assess the performance of a classification centred around a data model [66,78,80]. In this study, four evaluation standards are utilised to define the relationship between the true and predicted values. These assessment criteria are accuracy, precision, specificity, and sensitivity.

### 5.1. Accuracy

Accuracy is computed by taking the total number of correct predictions and dividing it by the sum of the numbers of true positives and true negatives. If the simulation is adequate, this is a straightforward portrayal of actuality. In the event that there is an imbalance between the classes, the results will not be appropriate.

$$Accuracy = \frac{TP + TN}{TP + FP + FN + TN} \quad (17)$$

### 5.2. Precision

The term “precision” refers to a classifier’s ability to abstain from classifying input as positive when it is negative. The ratio of the number of true positives to the combined number of true and false positives is how each class’s precision value is defined.

$$Precision = \frac{TP}{TP + FP} \quad (18)$$

### 5.3. Recall

The potential of a classification algorithm to determine each successful instance is referred to as its recall. At each level, the proportion of true positives to the combined total of true positives and false negatives is referred to as the “Recall.”

$$Recall = \frac{TP}{TP + FN} \quad (19)$$

### 5.4. F<sub>1</sub> Score

The F1 score is a weighted harmonic mean, and its value may vary, ranging from 0.0 to 1.0. It is important to keep in mind that F1 scores are derived by incorporating both precision and recall into their calculations, which is one reason why they frequently perform worse than accuracy measurements. When evaluating classifier models, the weighted average of F1 is often suggested rather than total accuracy because of its more sophisticated nature.

$$F1 - score = 2 \frac{Precision * Recall}{Precision + Recall} \quad (20)$$

The swarm sizes and the number of iterations must be set as the GWO’s parameters. The right choice of these parameters can efficiently and rapidly produce the best outcomes. The swarm sizes for each optimisation procedure are set to 50, 100, 150, and 200, respectively, after building the model numerous times. The number of iterations is set at 1000.

The KNN-GWO model has been utilized as follows to predict pillar stability levels in hard rock mining.

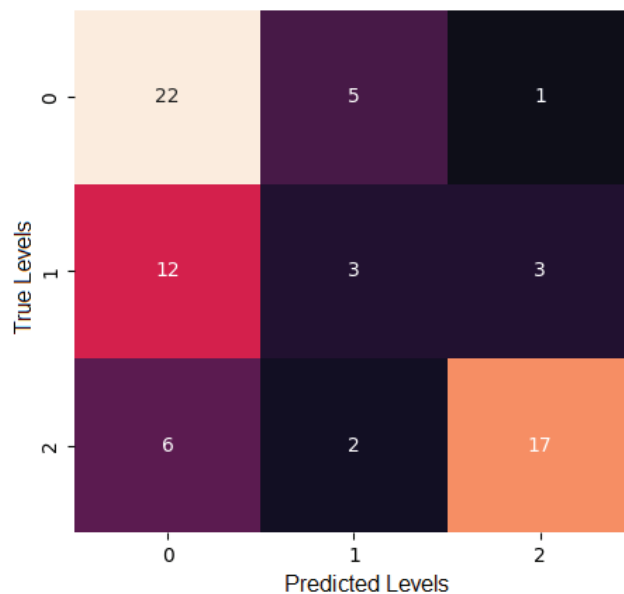
- (1) Data preparation: The raw data were arbitrarily partitioned into two subsets: the training set, which comprised 70% of the records, and the testing set, which comprised the remaining 30%.

- (2) Data pre-processing: To prepare the dataset for model training, we employed a pre-processing scheme. The first step was to apply the standardization technique.
- (3) Fitness assessment: The population's fitness value has been and then save the best fitness value before beginning the subsequent iteration.
- (4) Parameters adjustments: The fitness value has been adjusted based on each iteration's results in an effort to capture the best outcomes.
- (5) Retention requirements check: The optimal solutions of the weights of KNN are attained when the ideal fitness value no longer changes, or the maximum number of trials is reached.

The Python default configuration is used to develop the KNN algorithm. The KNN algorithm demonstrated a significant degree of accuracy in predicting outcomes across the 71 instances of the pillar. Overall, the KNN's performance accuracy was 60%. The performance evaluation matrices used in the testing datasets for pillar stability in underground hard rock mines are presented in Table 3. In addition, the confusion matrix of the proposed KNN algorithm is shown in Figure 9. As the pillar stability instances are small and the data points are disproportional, this impacts the model's consistency, reliability, and universality. As a result, the KNN-GWO model has been incorporated into this investigation in order to provide a model that is more accurate for the stability of underground pillars stability in hard rock mines.

**Table 3.** Performance evaluation indices of KNN algorithm.

	Precision (%)	Recall (%)	F1-Score (%)
Failed	55	79	65
Unstable	30	17	21
Stable	81	68	74



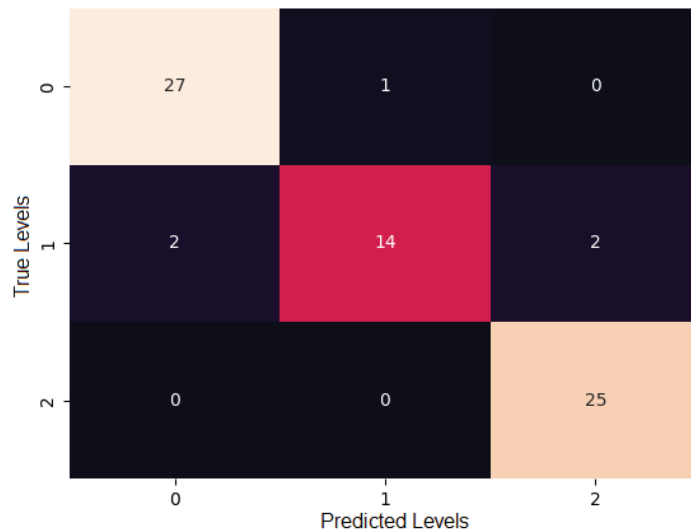
**Figure 9.** Confusion matrix of KNN algorithm based on pillar stability database.

An adequate predictive model was developed by using the KNN-GWO for each of the different levels of hard rock pillar stability. The parameters and their settings that were utilised for this approach are outlined in Table 4, where the iterations, wolves, dimension

numbers, and search domain are identified. The  $a$  and  $b$  fitness function parameters are specified. As can be seen in Figure 10, the KNN-GWO results in the inaccurate prediction of only five levels within the entire testing datasets, whereas the KNN-GWO algorithm generated accurate predictions for the 66 pillar instances. In addition, the same assessment attributes were employed in the implementation of the KNN-GWO performance analysis. The values of the three within-class KNN-GWO measures for each pillar stability level are displayed in Table 5. The KNN-GWO has a total accuracy of 93%, which signifies that it executes satisfactorily in predicting the level of pillar stability in deep hard rock mines. In addition, as shown by the comprehensive assessment in Table 1, the KNN-GWO model demonstrated an excellent degree of performance that surpassed all the other models reported previously in the literature to predict pillar stability. Hence, it is suggested that the proposed KNN-GWO mechanism is adequate for predicting the stability of pillars in underground hard rock mining.

**Table 4.** The setting of the parameters for the proposed method.

Parameters	Numbers
Number of iterations	100
Number of Wolves	5
Number of Dimensions	14
Search domain	[0, 1]
$\alpha$ in fitness function	0.99
$\beta$ in fitness function	0.01



**Figure 10.** Confusion matrix of KNN-GWO algorithm based on pillar stability database.

**Table 5.** Performance evaluation indices of KNN-GWO algorithm.

	Precision (%)	Recall (%)	F1-Score (%)
Failed	93	96	95
Unstable	93	78	85
Stable	93	100	96

The practical use of decision intelligence in underground mining has been shown to be a highly effective methodology for accurately predicting the stability of pillars.

The implementation of decision intelligence may be employed to effectively acquire and analyse data from the monitoring system in real-time, aiding in the identification of possible stability issues associated with the pillar. Upon the acquisition of pertinent data, the rock engineer and technician are able to ascertain the optimal approach for mitigating roof collapse while ensuring the integrity of the pillars remains intact.

It may be possible to predict pillar stability in underground mining production processes using artificial intelligence that takes into account past data from continuous monitoring. The machine learning system possesses the capability to discern data instances and attributes that might potentially signify an elevated susceptibility to instability. The implementation of decision intelligence, monitoring systems, and artificial intelligence has the potential to enhance the safety of underground mining operations. By making judgements based on better information, it is feasible to decrease the probability of employee injuries and minimise the duration of delays.

The risk assessment method may be enhanced by incorporating a comprehensive evaluation of many elements that influence the stability of pillars. The integration of the proposed model into decision support systems has the potential to enhance efficiency and safety in several aspects of mine planning, pillar design, and mining sequencing for engineers and stakeholders. Optimization algorithms can aid in identifying the most effective mining procedures that encompass production requirements, safety concerns, and environmental considerations.

## 6. Limitations of the Proposed Model and Possible Developments for the Future

Although the suggested decision intelligence technique exhibits a certain degree of reliability in its outcomes, it is crucial to recognise that there are certain constraints that should be addressed in future studies.

- (1) A discrepancy exists in the quantity and distribution of the pillar stability dataset. The prediction performance of machine learning algorithms is greatly impacted by the volume and quality of the datasets that are accessible. In the majority of instances, the extent to which a predictive algorithm can be applied to different contexts, and its reliability, will be compromised when working with a dataset that is constrained in terms of size or scope. The potential for enhanced prediction outcomes may be observed with an expanded dataset, notwithstanding the effective performance of the GWO in conjunction with the KNN algorithm when applied to smaller datasets. This phenomenon can be attributed to the fact that larger databases tend to include a greater amount of practical data. The dataset exhibits numerous discrepancies, particularly in relation to the varying degrees of quality across the samples. This exemplifies the potential impact that might arise from the use of erroneous data in drawing conclusions. Hence, the acquisition of a comprehensive and diverse database for pillar stability prediction is of utmost importance.
- (2) The predictive model's outcome may be influenced by external influences. While this study employs five variables to enhance the identification of fundamental stability conditions of pillars, it is crucial to acknowledge that the inclusion of these measures does not necessarily indicate the exclusion of other variables that might potentially affect the predictability of pillar stability. Hence, it is crucial to thoroughly analyse the impact of additional influential variables on the projected outcomes.

## 7. Conclusions

Pillar collapse is a significant and catastrophic risk in underground rock engineering processes. This practice poses a threat to the safety and wellbeing of workers, leading to substantial financial and material damages. The implementation of thorough assessment and periodic maintenance of pillar stability is crucial in mitigating potential risks and protecting the integrity of the surrounding environment. Therefore, the evaluation of pillar stability has significant importance in ensuring the effectiveness, safety, productivity, and profitability of underground hard rock mining engineering operations. The research



strategy is based on the KNN-GWO algorithm, showcasing the utilisation of innovative scientific methodologies for addressing a practical problem. The suggested model has shown superior performance in predicting the stability of pillars in hard rock mining, surpassing other models previously reported in the literature.

The assessment of pillar stability is a crucial factor that necessitates meticulous consideration in the context of underground mining activities. Regular failure checks are of utmost importance in underground processes to guarantee the safety of employees engaged in underground structures. Despite modest progress, the present initiatives undertaken by mining enterprises to tackle pillar failure have proven to be insufficient. The objective of this study is to address the query, “Does the collapse of underground mining structures pose a risk to miners?” The suggested decision intelligence paradigm represents a notable progression in the field due to its capacity to provide greater flexibility in programming and centralised monitoring. The design strictly adheres to the notion of zero-occurrence. In order to guarantee the enduring viability of production and the safety of mining facilities, it is important to possess a thorough comprehension of the hazards that are inherent to mining operations. The methodology presented facilitates the timely detection of pillar failure, hence allowing the emergency response team additional response time and enabling the implementation of environmentally friendly advancements in underground mining operations.

The application of advanced decision intelligence methods has the potential to improve the stability of hard rock pillars in underground engineering structures. Decision intelligence facilitates continual monitoring of mining circumstances, anticipation of pillar stability, and the effective distribution of resources through the utilization of optimization techniques, advanced machine learning algorithms, and methodologies for data analytics. The aforementioned features facilitate enhanced risk management, increased safety protocols, improved productivity, and reliable decision-making within underground rock engineering processes.

**Author Contributions:** Conceptualization, M.K.; Methodology, M.K. and H.R.; Software, M.K.; Validation, M.K.; Formal analysis, M.K.; Investigation, B.O.T. and S.H.; Resources, W.C. and H.R.; Data curation, M.K.; Writing—original draft, M.K. and S.H.; Writing—review & editing, W.C. and B.O.T.; Visualization, M.K.; Supervision, M.K.; Project administration, H.R.; Funding acquisition, H.R. All authors have read and agreed to the published version of the manuscript.

**Funding:** This research received no external funding.

**Data Availability Statement:** Data are contained within the article.

**Conflicts of Interest:** The authors declare no conflict of interest.

## References

1. Ghasemi, E.; Ataei, M.; Shahriar, K. Prediction of global stability in room and pillar coal mines. *Nat. Hazards* **2014**, *72*, 405–422. [CrossRef]
2. Wang, J.A.; Shang, X.C.; Ma, H.T. Investigation of catastrophic ground collapse in Xingtai gypsum mines in China. *Int. J. Rock Mech. Min. Sci.* **2008**, *45*, 1480–1499. [CrossRef]
3. Zhou, Y.; Li, M.; Xu, X.; Li, X.; Ma, Y.; Ma, Z. Research on catastrophic pillar instability in room and pillar gypsum mining. *Sustainability* **2018**, *10*, 3773. [CrossRef]
4. Liang, W.; Zhao, G.; Wu, H.; Chen, Y. Assessing the risk degree of goafs by employing hybrid TODIM method under uncertainty. *Bull. Eng. Geol. Environ.* **2019**, *78*, 3767–3782. [CrossRef]
5. González-Nicieza, C.; Álvarez-Fernández, M.I.; Menéndez-Díaz, A.; Álvarez-Vigil, A.E. A comparative analysis of pillar design methods and its application to marble mines. *Rock Mech. Rock Eng.* **2006**, *39*, 421–444. [CrossRef]
6. Zhou, J.; Li, X.; Mitri, H.S. Comparative performance of six supervised learning methods for the development of models of hard rock pillar stability prediction. *Nat. Hazards* **2015**, *79*, 291–316. [CrossRef]
7. Lunder, P.J. Hard Rock Pillar Strength Estimation an Applied Empirical Approach. Ph.D. Dissertation, University of British Columbia, Vancouver, BC, Canada, 1994.
8. Cauvin, M.; Verdel, T.; Salmon, R. Modeling uncertainties in mining pillar stability analysis. *Risk Anal.* **2009**, *29*, 1371–1380. [CrossRef] [PubMed]
9. Mortazavi, A.; Hassani, F.P.; Shabani, M. A numerical investigation of rock pillar failure mechanism in underground openings. *Comput. Geotech.* **2009**, *36*, 691–697. [CrossRef]

10. Shnorhokian, S.; Mitri, H.S.; Moreau-Verlaan, L. Stability assessment of stope sequence scenarios in a diminishing ore pillar. *Int. J. Rock Mech. Min. Sci.* **2015**, *74*, 103–118. [CrossRef]
11. Elmo, D.; Stead, D. An integrated numerical modelling-discrete fracture network approach applied to the characterisation of rock mass strength of naturally fractured pillars. *Rock Mech. Rock Eng.* **2010**, *43*, 3–19. [CrossRef]
12. Li, L.C.; Tang, C.A.; Wang, S.Y.; Yu, J. A coupled thermo-hydrologic-mechanical damage model and associated application in a stability analysis on a rock pillar. *Tunn. Undergr. Space Technol.* **2013**, *34*, 38–53. [CrossRef]
13. Jaiswal, A.; Sharma, S.K.; Shrivastva, B.K. Numerical modeling study of asymmetry in the induced stresses over coal mine pillars with advancement of the goaf line. *Int. J. Rock Mech. Min. Sci.* **2004**, *41*, 859–864. [CrossRef]
14. Li, X.; Kim, E.; Walton, G. A study of rock pillar behaviors in laboratory and in-situ scales using combined finite-discrete element method models. *Int. J. Rock Mech. Min. Sci.* **2019**, *118*, 21–32. [CrossRef]
15. Deng, J.; Yue, Z.Q.; Tham, L.G.; Zhu, H.H. Pillar design by combining finite element methods, neural networks and reliability: A case study of the Feng Huangshan copper mine, China. *Int. J. Rock Mech. Min. Sci.* **2003**, *40*, 585–599. [CrossRef]
16. Griffiths, D.V.; Fenton, G.A.; Lemons, C.B. Probabilistic analysis of underground pillar stability. *Int. J. Numer. Anal. Methods Geomech.* **2002**, *26*, 775–791. [CrossRef]
17. Amato, F.; Moscato, V.; Picariello, A.; Sperli'i, G. Extreme events management using multimedia social networks. *Futur. Gener. Comput. Syst.* **2019**, *94*, 444–452. [CrossRef]
18. Liu, Q.; Wang, X.; Huang, X.; Yin, X. Prediction model of rock mass class using classification and regression tree integrated AdaBoost algorithm based on TBM driving data. *Tunn. Undergr. Space Technol.* **2020**, *106*, 103595. [CrossRef]
19. Taiwo, B.O. Improvement of small-scale dolomite blasting productivity: Comparison of existing empirical models with image analysis software and artificial neural network models. *J. Min. Environ.* **2022**, *13*, 627–641.
20. Hosseini, S.; Khatti, J.; Taiwo, B.O.; Fissaha, Y.; Grover, K.S.; Ikeda, H.; Pushkarna, M.; Berhanu, M.; Ali, M. Assessment of the ground vibration during blasting in mining projects using different computational approaches. *Sci. Rep.* **2023**, *13*, 18582. [CrossRef]
21. Taiwo, B.O.; Ajibona, A.I.; Idowu, K.; Babatunde, A.S.; Ogunyemi, B.O. Improvement of small scale mine blast operation: A comparative application of hunter-point artificial neural network, support vector machine, and regression analysis models. *Int. J. Min. Geo-Eng.* **2023**, *57*, 205–213.
22. Bo, Y.; Liu, Q.; Huang, X.; Pan, Y. Real-time hard-rock tunnel prediction model for rock mass classification using CatBoost integrated with Sequential Model-Based Optimization. *Tunn. Undergr. Space Technol.* **2022**, *124*, 104448. [CrossRef]
23. Taiwo, B.O. Improvement of small-scale dolomite mine blast fragmentation efficiency using hybrid artificial intelligence and soft computing approaches—A case study. *Arab. J. Geosci.* **2023**, *16*, 668. [CrossRef]
24. Zhou, J.; Li, X.B.; Shi, X.Z.; Wei, W.; Wu, B.B. Predicting pillar stability for underground mine using Fisher discriminant analysis and SVM methods. *Trans. Nonferrous Met. Soc. China* **2011**, *21*, 2734–2743. [CrossRef]
25. Ahmad, M.; Al-Shayea, N.A.; Tang, X.W.; Jamal, A.; Al-Ahmadi, H.M.; Ahmad, F. Predicting the pillar stability of underground mines with random trees and C4.5 decision trees. *Appl. Sci.* **2020**, *10*, 6486. [CrossRef]
26. Liang, W.; Luo, S.; Zhao, G.; Wu, H. Predicting hard rock pillar stability using GBDT, XGBoost, and LightGBM algorithms. *Mathematics* **2020**, *8*, 765. [CrossRef]
27. Ghasemi, E.; Kalthori, H.; Bagherpour, R. Stability assessment of hard rock pillars using two intelligent classification techniques: A comparative study. *Tunn. Undergr. Space Technol.* **2017**, *68*, 32–37. [CrossRef]
28. Zhou, J.; Chen, Y.; Chen, H.; Khandelwal, M.; Monjezi, M.; Peng, K. Hybridizing five neural-metaheuristic paradigms to predict the pillar stress in bord and pillar method. *Front. Public Health* **2023**, *11*, 1119580. [CrossRef]
29. Tawadrous, A.S.; Katsabanis, P.D. Prediction of surface crown pillar stability using artificial neural networks. *Int. J. Numer. Anal. Methods Geomech.* **2007**, *31*, 917–931. [CrossRef]
30. Wattimena, R.K. Predicting the stability of hard rock pillars using multinomial logistic regression. *Int. J. Rock Mech. Min. Sci.* **2014**, *71*, 33–40. [CrossRef]
31. Ding, H.; Li, G.; Dong, X.; Lin, Y. Prediction of Pillar Stability for Underground Mines Using the Stochastic Gradient Boosting Technique. *IEEE Access* **2018**, *6*, 69253–69264. [CrossRef]
32. Kamran, M.; Shahani, N.M. Decision support system for the prediction of mine fire levels in underground coal mining using machine learning approaches. *Min. Metall. Explor.* **2022**, *39*, 591–601. [CrossRef]
33. Li, N.; Zare, M.; Yi, C.; Jimenez, R. Stability risk assessment of underground rock pillars using logistic model trees. *Int. J. Environ. Res. Public Health* **2022**, *19*, 2136. [CrossRef] [PubMed]
34. Mendrofa, G.A.; Hertono, G.F.; Handari, B.D. Ensemble Learning Model on Artificial Neural Network-Backpropagation (ANN-BP) Architecture for Coal Pillar Stability Classification. *arXiv* **2023**, arXiv:2303.16524. [CrossRef]
35. Eker, H. Investigation of the usability of industrial mining wastes in agriculture. *Front. Environ. Sci.* **2023**, *11*, 1248188. [CrossRef]
36. Chen, S.; Xiang, Z.; Eker, H. Curing stress influences the mechanical characteristics of cemented paste backfill and its damage constitutive model. *Buildings* **2022**, *12*, 1607. [CrossRef]
37. Yin, X.; Liu, Q.; Pan, Y.; Huang, X.; Wu, J.; Wang, X. Strength of stacking technique of ensemble learning in rockburst prediction with imbalanced data: Comparison of eight single and ensemble models. *Nat. Resour. Res.* **2021**, *30*, 1795–1815. [CrossRef]
38. Janusz, A.; Grzegorowski, M.; Michalak, M.; Wróbel, Ł.; Sikora, M.; Ślęzak, D. Predicting seismic events in coal mines based on underground sensor measurements. *Eng. Appl. Artif. Intell.* **2017**, *64*, 83–94. [CrossRef]

39. Esterhuizen, G.S.; Dolinar, D.R.; Ellenberger, J.L. Pillar strength in underground stone mines in the United States. *Int. J. Rock Mech. Min. Sci.* **2011**, *48*, 42–50. [CrossRef]
40. Nordlund, E.; Radberg, G.; Jing, L. Determination of failure modes in jointed pillars by numerical modelling. In Proceedings of the Conference on Fractured and Jointed Rock Masses, Lake Tahoe, CA, USA, 3 June 1992; Taylor & Francis: Washington, DC, USA, 1995; pp. 345–350.
41. Shang, J.; West, L.J.; Hencher, S.R.; Zhao, Z. Geological discontinuity persistence: Implications and quantification. *Eng. Geol.* **2018**, *241*, 41–54. [CrossRef]
42. Jessu, K.V.; Spearing, A.J.S. Performance of inclined pillars with a major discontinuity. *Int. J. Min. Sci. Technol.* **2019**, *29*, 437–443. [CrossRef]
43. Shang, J.; Hencher, S.R.; West, L.J. Tensile strength of geological discontinuities including incipient bedding, rock joints and mineral veins. *Rock Mech. Rock Eng.* **2016**, *49*, 4213–4225. [CrossRef]
44. Pedregosa, F.; Varoquaux, G.; Gramfort, A.; Michel, V.; Thirion, B.; Grisel, O.; Duchesnay, E. Scikit-learn: Machine learning in Python. *J. Mach. Learn. Res.* **2011**, *12*, 2825–2830.
45. Kluyver, T.; Ragan-Kelley, B.; Pérez, F.; Granger, B.E.; Bussonnier, M.; Frederic, J.; Kelley, K.; Hamrick, J.B.; Grout, J.; Corlay, S.; et al. *Jupyter Notebooks—A Publishing Format for Reproducible Computational Workflows*; IOS Press: Amsterdam, The Netherlands, 2016; Volume 2016, pp. 87–90.
46. Mirjalili, S.; Mirjalili, S.M.; Lewis, A. Grey wolf optimizer. *Adv. Eng. Softw.* **2014**, *69*, 46–61. [CrossRef]
47. Lang, X.; Li, P.; Zhang, B.; Cao, J.; Guo, Y.; Kan, Z.; Lu, S. Localization of multiple leaks in a fluid pipeline based on ultrasound velocity and improved GWO. *Process Saf. Environ. Prot.* **2020**, *137*, 1–7.
48. Zhou, J.; Huang, S.; Qiu, Y. Optimization of random forest through the use of MVO, GWO and MFO in evaluating the stability of underground entry-type excavations. *Tunn. Undergr. Space Technol.* **2022**, *124*, 104494. [CrossRef]
49. Emary, E.; Zawbaa, H.M.; Hassanien, A.E. Binary grey wolf optimization approaches for feature selection. *Neurocomputing* **2016**, *172*, 371–381. [CrossRef]
50. Mirjalili, S.; Saremi, S.; Mirjalili, S.M.; Coelho, L.D.S. Multi-objective grey wolf optimizer: A novel algorithm for multi-criterion optimization. *Expert Syst. Appl.* **2016**, *47*, 106–119. [CrossRef]
51. Gupta, S.; Deep, K. A novel random walk grey wolf optimizer. *Swarm Evol. Comput.* **2019**, *44*, 101–112. [CrossRef]
52. Nadimi-Shahraki, M.H.; Taghian, S.; Mirjalili, S. An improved grey wolf optimizer for solving engineering problems. *Expert Syst. Appl.* **2021**, *166*, 113917. [CrossRef]
53. Faris, H.; Aljarah, I.; Al-Betar, M.A.; Mirjalili, S. Grey wolf optimizer: A review of recent variants and applications. *Neural Comput. Appl.* **2018**, *30*, 413–435. [CrossRef]
54. Ahmed, H.U.; Mostafa, R.R.; Mohammed, A.; Sihag, P.; Qadir, A. Support vector regression (SVR) and grey wolf optimization (GWO) to predict the compressive strength of GGBFS-based geopolymer concrete. *Neural Comput. Appl.* **2023**, *35*, 2909–2926. [CrossRef]
55. Adithiyaa, T.; Chandramohan, D.; Sathish, T. Optimal prediction of process parameters by GWO-KNN in stirring-squeeze casting of AA2219 reinforced metal matrix composites. *Mater. Today: Proc.* **2020**, *21*, 1000–1007. [CrossRef]
56. Tian, Y.; Yu, J.; Zhao, A. Predictive model of energy consumption for office building by using improved GWO-BP. *Energy Rep.* **2020**, *6*, 620–627. [CrossRef]
57. Chen, W.; Hong, H.; Panahi, M.; Shahabi, H.; Wang, Y.; Shirzadi, A.; Pirasteh, S.; Alesheikh, A.A.; Khosravi, K.; Panahi, S.; et al. Spatial prediction of landslide susceptibility using gis-based data mining techniques of anfis with whale optimization algorithm (woa) and grey wolf optimizer (gwo). *Appl. Sci.* **2019**, *9*, 3755. [CrossRef]
58. Fattahi, H.; Hasanipanah, M. Prediction of blast-induced ground vibration in a mine using relevance vector regression optimized by metaheuristic algorithms. *Nat. Resour. Res.* **2021**, *30*, 1849–1863. [CrossRef]
59. Elsheikh, A.H. Applications of machine learning in friction stir welding: Prediction of joint properties, real-time control and tool failure diagnosis. *Eng. Appl. Artif. Intell.* **2023**, *121*, 105961. [CrossRef]
60. Yin, Q.; Sun, Z.; Zhang, M.; He, G.; Chen, Y.; Wang, Q.; Yan, M. Structure and electrical properties of  $K_{0.5}Na_{0.5}Nb_{0.94-x}Sb_{0.06}Sn_xO_3$  lead-free piezoelectric ceramics. *J. Alloys Compd.* **2015**, *622*, 132–136. [CrossRef]
61. Pandey, A.; Jain, A. Comparative analysis of KNN algorithm using various normalization techniques. *Int. J. Comput. Netw. Inf. Secur.* **2017**, *11*, 36. [CrossRef]
62. Bui, X.N.; Jaroonpattanapong, P.; Nguyen, H.; Tran, Q.H.; Long, N.Q. A novel hybrid model for predicting blast-induced ground vibration based on k-nearest neighbors and particle swarm optimization. *Sci. Rep.* **2019**, *9*, 13971. [CrossRef]
63. Guo, H.; Li, Y.; Li, Y.; Liu, X.; Li, J. BPSO-Adaboost-KNN ensemble learning algorithm for multi-class imbalanced data classification. *Eng. Appl. Artif. Intell.* **2016**, *49*, 176–193.
64. Alkhatib, K.; Najadat, H.; Hmeidi, I.; Shatnawi, M.K.A. Stock price prediction using k-nearest neighbor (kNN) algorithm. *Int. J. Bus. Humanit. Technol.* **2013**, *3*, 32–44.
65. Subramaniaswamy, V.; Logesh, R. Adaptive KNN based recommender system through mining of user preferences. *Wirel. Pers. Commun.* **2017**, *97*, 2229–2247. [CrossRef]
66. Kamran, M.; Wattimena, R.K.; Armaghani, D.J.; Asteris, P.G.; Jiskani, I.M.; Mohamad, E.T. Intelligent Based Decision-Making Strategy to Predict Fire Intensity in Subsurface Engineering Environments. *Process Saf. Environ. Prot.* **2023**, *171*, 374–384. [CrossRef]
67. Noriega, R.; Pourrahimian, Y. A systematic review of artificial intelligence and data-driven approaches in strategic open-pit mine planning. *Resour. Policy* **2022**, *77*, 102727. [CrossRef]

68. Sharma, R.; Mithas, S.; Kankanhalli, A. Transforming decision-making processes: A research agenda for understanding the impact of business analytics on organisations. *Eur. J. Inf. Syst.* **2014**, *23*, 433–441. [CrossRef]
69. Patriarca, R.; Di Gravio, G.; Cioponea, R.; Licu, A. Safety intelligence: Incremental proactive risk management for holistic aviation safety performance. *Saf. Sci.* **2019**, *118*, 551–567. [CrossRef]
70. Chen, L.; Hu, X.; Wang, G.; Cao, D.; Li, L.; Wang, F.Y. Parallel mining operating systems: From digital twins to mining intelligence. In Proceedings of the 2021 IEEE 1st International Conference on Digital Twins and Parallel Intelligence (DTPI), Beijing, China, 15 July–15 August 2021; pp. 469–473.
71. Kaparathi, S.; Bumblauskas, D. Designing predictive maintenance systems using decision tree-based machine learning techniques. *Int. J. Qual. Reliab. Manag.* **2020**, *37*, 659–686. [CrossRef]
72. Faz-Mendoza, A.; Gamboa-Rosales, N.K.; Castorena-Robles, A.; Cobo, M.J.; Castañeda-Miranda, R.; López-Robles, J.R. Strategic Intelligence and Knowledge Management as drivers of Decision-Making in Mining Industry: An analysis of the literature. In Proceedings of the 2020 International Conference on Decision aid Sciences and Application (DASA), Sakheer, Bahrain, 8–9 November 2020; pp. 536–540.
73. Khoshalan, H.A.; Shakeri, J.; Najmoddini, I.; Asadizadeh, M. Forecasting copper price by application of robust artificial intelligence techniques. *Resour. Policy* **2021**, *73*, 102239. [CrossRef]
74. Kamran, M.; Chaudhry, W.; Wattimena, R.K.; Rehman, H.; Martyushev, D.A. A Multi-Criteria Decision Intelligence Framework to Predict Fire Danger Ratings in Underground Engineering Structures. *Fire* **2023**, *6*, 412. [CrossRef]
75. Shahin, I.; Alomari, O.A.; Nassif, A.B.; Afyouni, I.; Hashem, I.A.; Elnagar, A. An efficient feature selection method for arabic and english speech emotion recognition using Grey Wolf Optimizer. *Appl. Acoust.* **2023**, *205*, 109279. [CrossRef]
76. Akyol, S.; Yildirim, M.; Alatas, B. Multi-feature fusion and improved BO and IGWO metaheuristics based models for automatically diagnosing the sleep disorders from sleep sounds. *Comput. Biol. Med.* **2023**, *157*, 106768. [CrossRef] [PubMed]
77. Kidega, R.; Ondiaka, M.N.; Maina, D.; Jonah KA, T.; Kamran, M. Decision based uncertainty model to predict rockburst in underground engineering structures using gradient boosting algorithms. *Geomech. Eng.* **2022**, *30*, 259.
78. Kamran, M.; Shahani, N.M.; Armaghani, D.J. Decision support system for underground coal pillar stability using unsupervised and supervised machine learning approaches. *Geomech. Eng.* **2022**, *30*, 107.
79. Mazumder, R.K.; Salman, A.M.; Li, Y. Failure risk analysis of pipelines using data-driven machine learning algorithms. *Struct. Saf.* **2021**, *89*, 102047. [CrossRef]
80. Kamran, M.; Ullah, B.; Ahmad, M.; Sabri, M.M.S. Application of KNN-based isometric mapping and fuzzy c-means algorithm to predict short-term rockburst risk in deep underground projects. *Front. Public Health* **2022**, *10*, 1023890. [CrossRef]

**Disclaimer/Publisher’s Note:** The statements, opinions and data contained in all publications are solely those of the individual author(s) and contributor(s) and not of MDPI and/or the editor(s). MDPI and/or the editor(s) disclaim responsibility for any injury to people or property resulting from any ideas, methods, instructions or products referred to in the content.

## Article

# Analysis of Rock Burst Mechanism in Extra-Thick Coal Seam Controlled by Thrust Fault under Mining Disturbance

Suihan Yang<sup>1</sup>, Xiangzhi Wei<sup>1</sup>, Linlin Chen<sup>1</sup>, Zhiliu Wang<sup>2,\*</sup> and Wen Wang<sup>3</sup>

- <sup>1</sup> Henan Dayou Energy Co Ltd., Gencun Coal Mine, Sanmenxia 472400, China; 15188337902@163.com (S.Y.); hmx13262059661@126.com (X.W.); chenlinlin8925@163.com (L.C.)
- <sup>2</sup> School of Civil Engineering & Architecture, Zhongyuan University of Technology, Zhengzhou 450007, China
- <sup>3</sup> School of Energy Science & Engineering, Henan Polytechnic University, Jiaozuo 454000, China; wangwen2006@hpu.edu.cn
- \* Correspondence: 6855@zut.edu.cn

**Abstract:** A fault is a common geological structure encountered in underground coal mining. Interactions between the discontinuous structure of a fault and mining activities are the key factors in controlling the rock bursts induced by the fault. It is of great importance to study the rock burst mechanism of an extra-thick coal seam under the combined influence of reverse faults and coal mining for the prediction and prevention of rock burst. In this study, we establish a sliding dynamics model of rock mass in a fault zone and analyze the mechanical distribution of fault-induced rock bursts under the combined action of mining disturbances. Additionally, we utilize theoretical calculation and a 3D numerical simulation method to clarify the rockburst mechanism in an extra-thick coal seam controlled by a thrust fault under mining disturbance and a fault. The results showed that the distribution range of the shear stress increment in the fault footwall was larger than that in the hanging wall, revealing a skewed distribution. The fault dip angle and mining thickness exhibit significant influence on the structure around the fault. With increases in the dip angle of the fault and mining thickness, the maximum vertical stress and peak stress first increase and then decrease. A position 80 m away from the fault is the dividing line between the fault-non-affected area and the fault-affected area. The 13,200 working face of the Gencun coal mine is used as a case study to study the influence of mining disturbances on microseismic events. The results of this study are in good agreement with the theoretical calculations and numerical simulation results.

**Keywords:** thrust fault; mining disturbance; strata behaviors; extra-thick coal seam; rock burst mechanism

**Citation:** Yang, S.; Wei, X.; Chen, L.; Wang, Z.; Wang, W. Analysis of Rock Burst Mechanism in Extra-Thick Coal Seam Controlled by Thrust Fault under Mining Disturbance. *Processes* **2024**, *12*, 320. <https://doi.org/10.3390/pr12020320>

Academic Editor: Carlos Sierra Fernández

Received: 18 December 2023  
Revised: 22 January 2024  
Accepted: 26 January 2024  
Published: 2 February 2024



**Copyright:** © 2024 by the authors. Licensee MDPI, Basel, Switzerland. This article is an open access article distributed under the terms and conditions of the Creative Commons Attribution (CC BY) license (<https://creativecommons.org/licenses/by/4.0/>).

## 1. Introduction

Coal geological conditions and mining disturbances have an important influence on the stress distribution of a longwall face [1,2]. With the increase in coal mining depth, the geological conditions gradually deteriorate. A rock burst is a serious disaster and a dynamic instability phenomenon that can occur during the process of coal mining [3–5]. Mining in ultra-deep coal mines leads to frequent rock burst accidents, which restricts the safety and highly effective production of coal mines. A rock burst is influenced by many factors, such as fault geological structure, coal mining disturbance, and mining depth [6–8].

When coal is close to a fault structure, coal stress increases, and a rock burst is easily induced [9–11]. In Central and Western China, coal mining is characterized by thick roofs, large mining depths, high ground stresses, and complex structural conditions which may lead to rock burst disasters. For example, an “11·3” rock burst accident occurred in the Qianqiu coal mine in 2011. This was caused by working face mining near an F16 large-scale reverse fault. In 2012, a “4·12” accident occurred in the Chaoyang coal mine at the intersection of a 3110 isolated island working face with two faults (F3110-1 and F3109-1). In 2013, a “3·15” rock burst accident occurred in the Junde coal mine. This was caused by F1 and L1 faults. An “8·2” rock burst accident was caused by an F5010 fault and a syncline

structure in the Tangshan Mine in 2019. In 2020, a “5·24” rock burst accident occurred in Mengcun Lane, which was affected by a DF29 fault and a fold. The above accidents have resulted in casualties and huge property losses.

A large number of scholars have researched the influence of geological structures on the stress distribution of surrounding rocks and rock burst occurrences. He et al. [12] pointed out that a roadway rock burst is closely linked to fault tectonic stress concentration and fault activation. Wang et al. [13] inverted the influence of fault structures on the appearance of roadway rock bursts using seismic tomography technology, putting forward a prediction method for rock burst disasters. Li and Yang et al. [14,15] emphasized that faults, lateral roof structures, and periodic roof failures have important influences on the emergence of rock burst disasters. Digital imaging technology has been used to study the evolution of fault structures during coal mining [16]. Physical similarity model tests have been carried out to study the effect of fault angles on surrounding rock stress [17]. Sainoki and Mitri [18] comprehensively considered factors such as fault dip and fall, revealing the sliding instability mechanism of fault structures under the influence of mining.

Fracture mechanics theory has also been used to study fracture damage development and fault slip mechanisms. Mechanical models of fault fracture damage and rock mass slip have been established, and the main factors affecting fault activation have been extensively analyzed [19,20]. Lv et al. [21] developed a simplified mechanical model dominated by horizontal tectonic stress. They emphasized that fault activation has an important influence on the stress analysis of stopes, revealing the rock burst mechanism in a roadway under the superimposed action of ground stress and mining. Wu et al. [22] developed a mechanical model of overburden movement in graben tectonic regions. A criterion formula for calculating the starting energy of a rock burst was given, and anti-scour technology for “breaking chain and increasing consumption” was proposed. Kong and Ji et al. [23,24] have researched the influence of different mining layouts on fault reactivation. They highlighted that mining disturbance has a significant effect on induced fault activation, noting, in particular, that mining activity perpendicular to the fault strike has a larger disturbance effect. By analyzing numerous accidents, Zhao et al. [25,26] have pointed out that rock burst accidents are influenced by many factors, highlighting that the combined action of multiple structures has a greater impact on the appearance of rock bursts. Cao et al. [27] hypothesized that the width of a coal pillar has an important influence on fault activation instability and energy variation within faults. Jiao et al. [28] suggested that there was a positive correlation between the risk of rock bursts in the surrounding rock near the fault and the mining depth. Tong and Zhao et al. [29,30] proposed criteria for evaluating structural activity using activation coefficients and damage factors, with the heterogeneity and non-uniform deformation of the rock considered in the criteria. Sainoki and Orlecka et al. [31–33] simulated the influence of joint roughness on fault activation and highlighted the effect of mining disturbances on the maximum shear displacement and energy of a fault. Similar simulation tests have also been carried out to identify the influence of footwall mining on fault dislocation instability, revealing that mining disturbance can induce fault activation instability [34–36]. Wang et al. [37–39] quantitatively analyzed the migration rule of overlying rock using digital speckle, highlighting that the coupled action of working face advancements and fault presence has a significant influence on rock burst occurrence.

Moreover, many scholars have also carried out research on rock burst evaluation methods to prevent and control the occurrence of rock bursts in coal mines. Based on changes in strain energy in coal and rock masses, Kidybifski et al. proposed evaluation indices for rock bursts and determined the values of different mining pressure development indices through laboratory tests [40]. Smoliński and Malashkevych found that mining conditions have an important effect on pressure production in working faces, and quantitative-qualitative indicators of mining were proposed to improve the efficiency of mining [41,42]. Mohamadali and Wojtecki et al. used conventional and numerical methods to assess rock burst disasters [43,44]. Konicek and Filippov et al. proposed monitoring rock bursts through acoustic signals and the use of energy absorption support to prevent rock bursts [45,46].

Kopytov et al. suggested that blasting and drilling for pressure relief could prevent stress accumulation in coal and rock masses [47]. Zhou et al. compared and analyzed research achievements and limitations, as well as future research directions for different rock burst evaluation methods [48]. A rock burst risk assessment method combining tomography and microseismic monitoring was established. It has been pointed out that longitudinal wave velocity can reflect the strength, energy, and dynamic load criteria of rock bursts [49]. A rock burst monitoring system based on stress and energy monitoring was established to prevent and control rock bursts in coal mines, and a critical stress index evaluation method for rock burst risk was proposed [50].

In summary, tectonic stress and fault activation are the primary factors influencing rock bursts in roadway construction. The phenomenon of fault reactivation induced by mining activities has been verified using theoretical analysis, model tests, field observations, and numerical calculations. However, few studies have considered the mechanics of rock bursts induced by the coupling of mining disturbances and thrust faults under the geological conditions of extra-thick conglomerates. In addition, most experimental, physical, and mechanical studies of fault activation have only focused on vibration mechanisms, and the influence of mining disturbance and thrust fault structure coupling on the stress distribution of the surrounding rock has been largely ignored. Therefore, the mechanism of rock bursts under these conditions requires further study. It can provide insights for predicting and preventing rock bursts in extra-thick coal seams subjected to thrust faults and mining activities. In this study, a sliding mechanical model of a rock mass in a fault zone is constructed and solved to obtain the stress distribution of a reverse fault. The stress distribution on the surrounding rock of the working face under different geological structures and mining conditions, including the influence of faults on this stress distribution, is clarified. By combining theoretical calculations and numerical analyses, the quantitative relationship between mining disturbance, fault activity, microseismic event monitoring, and rock bursts were revealed. The influence law of tectonic stress is analyzed, and the influence zone of the F16 fault is determined. We expound on the rock burst mechanism of extra-thick coal seams influenced by thrust faults and mining disturbances. Finally, the research results are verified by comparing them with the field monitoring results.

## 2. Engineering Background

### (1) Geological structural characteristics of the Gengcun coal mine

The Gengcun coal mine is located in Mianchi County, Sanmenxia City. It is 3.2 km north of Mianchi County and 15 km northeast of Yima City. It is 53 km west of Sanmenxia City and 69 km east of Luoyang City. The Gengcun coal mine benefits from convenient transportation. The Longhai Railway, 310 National Highway, and Lianhuo Expressway pass through the northern edge of Jingtian. The Mianchi Station is connected to the Longhai Railway via a special railway line.

There is an outcrop of 2–3 coal seams to the north and an F16 fault to the south of the coal mine. Prospecting line 41 is bound via the Qianqiu and Yuejin Mines to the east. The mining area is 11,503 km<sup>2</sup>.

The 13,200 working face is adjacent to the 13,180 and 13,230 working faces. To the west and south are 2–3 unmined coal entities. The designed mining length and inclined length are 749 m and 249 m, respectively. The maximum mining depth is 630 m. The coal seam thickness is approximately 19.3 m.

### (2) Developmental characteristics of the F16 fault

The strata were subjected to nappe tectonic stress, which caused the Triassic strata to push upward along the deep coal seam to form the F16 fault. Moreover, part of the coal seam under the nappe surface was shoveled away. The coal seam under the nappe surface becomes thinner, while the coal thickness in the nappe zone increases significantly. The 13,200 working face area is greatly affected by F16 fault thrust. The coal seam thicknesses at both ends of the 13,200 open cutting are both 13–15 m, which is less than that in the

cutting hole. The upper and lower thrust lines of the F16 fault are the boundaries of the thick coal seam. The thick seam belt runs obliquely through the 13,200 working face. The lower thrust line of the F16 fault intersects with the lower roadway at 160 m, and the upper thrust line of the F16 fault intersects with the lower roadway at 620 m.

The roof structure exhibits a close relationship with the F16 fault. As a result, the roof structure changes with the advancement of the working face. The upper wall of the F16 fault is a Triassic rock layer with an angle of 50–75°. The immediate roof on the northern side of the upper thrust line of the F16 fault is Jurassic mudstone with a thickness of 25 m. The range of influence of the Jurassic immediate roof gradually increases from the open cutting to the end. The immediate roof on the south side of the downthrust nappe line of the F16 fault is a Triassic formation, which is grayish-white sandstone with a thickness of 7 m. The area affected by the immediate roof of the Triassic system gradually decreases by 160 m in front of the stop.

### 3. Mechanical Analysis

#### 3.1. Mechanical Model

The generation of concentrated stress during mining is a significant factor contributing to rock bursts induced by reverse faults. Figure 1 shows the rock burst distribution of a working face influenced by a reverse fault.

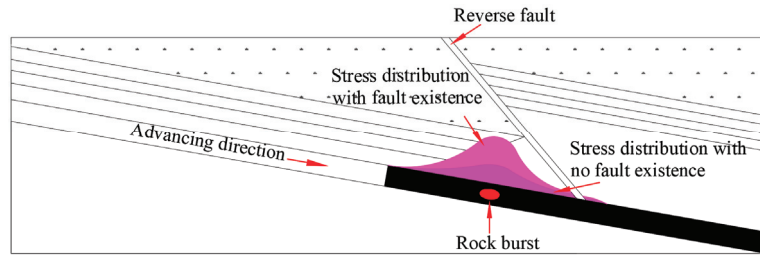


Figure 1. Rock burst distribution influenced by the reverse fault.

According to a study by Wang et al. [51], it is believed that the tectonic stress of a fault is influenced by the fault length, fault dip angle, mining disturbance, and ground stress. The dip profile of the F16 fault in the Gengcun Mine is regarded as an elliptical formation fracture, and a complex coordinate system  $z = x + iy$  is established by combining the fault angle ( $\theta$ ) and the center of the ellipse (see Figure 2). The infinite region outside the crack is transformed into a polar circle of the coordinate system ( $\zeta = \zeta + i\eta = \rho e^{i\varphi}$ ) through the conformal transformation of the complex potential function [51,52]. In Figure 2,  $\rho$  is the length of the point at the edge of the ellipse hole and the line at the center of the ellipse,  $m$ ;  $\varphi$  is the angle between the line of the edge point of the ellipse hole and the center of the ellipse, and the major axis of the ellipse ( $^\circ$ ).  $\rho$  and  $\varphi$  form the polar coordinate system.

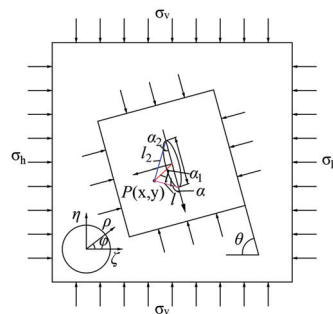


Figure 2. Mechanical model of structural stress increment for thrust fault.



Complex functions and polar coordinate functions can be converted as follows:

$$z = x + iy = \omega(\zeta) = \frac{a}{2}(1/\zeta + \zeta) \quad (1)$$

where,  $\omega(\zeta)$  is the variogram function.  $x$  and  $y$  are the horizontal and vertical coordinates in the cartesian coordinate system with the major and minor axes of the ellipse, respectively. The complex variables and boundary conditions of the stress component are as follows:

$$\sigma_x + \sigma_y = 4\text{Re}\varphi'(z) \quad (2)$$

$$\sigma_y - \sigma_x + 2i\tau_{xy} = 2[\bar{z}\varphi''(z) + \psi'(z)] \quad (3)$$

$$\varphi'(z) + z\overline{\varphi'(z)} + \overline{\psi'(z)} = i \int (\bar{f}_x + if_y) ds \quad (4)$$

where,  $\sigma_x$  is the tectonic stress in the x direction, Pa;  $\sigma_y$  is the tectonic stress in the y direction;  $\tau_{xy}$  is the shear stress, Pa;  $\varphi(z)$  and  $\psi(z)$  are reset potential functions;  $\bar{f}_x + if_y$  is the complex number of boundary surface forces.

By combining Equations (1)–(4), we can obtain:

$$\sigma_\varphi + \sigma_\rho = 4\text{Re}\phi(\zeta) \quad (5)$$

$$\sigma_\varphi - \sigma_\rho + 2i\tau_{\rho\varphi} = \frac{2\zeta^2}{\rho^2\omega'(\zeta)} [\bar{\epsilon}(\zeta)\phi'(\zeta) + \omega'(\zeta)\Psi(\zeta)] \quad (6)$$

$$i \int (\bar{f}_x + if_y) ds = \Phi(\zeta) + \omega(\zeta) / [\omega'(\zeta)\phi'(\zeta) + \Psi(\zeta)] \quad (7)$$

where,  $\sigma_\varphi$  is the hoop stress in the polar coordinates, Pa;  $\sigma_\rho$  is radial stress in the polar coordinates, Pa;  $\tau_{\rho\varphi}$  is shear stress in the polar coordinates, Pa;  $\text{Re}(z)$  is the real part of the complex number  $z$ .

Moreover, Equation (8) can be represented as follows:

$$\phi(\zeta) = \varphi(z) \quad (8)$$

By using derivation, we can obtain the following:

$$\varphi'(z) = \phi'(\zeta) / \omega'(\zeta) = \Psi(\zeta) \quad (9)$$

Furthermore, Equation (8) can be obtained using coordinate transformation:

$$\psi(\zeta) = \psi(z) \quad (10)$$

By using derivation, we can obtain the following:

$$\psi'(z) = \psi'(\zeta) / \omega'(\zeta) = \Psi(\zeta) \quad (11)$$

The complex functions are:

$$\phi(\zeta) = \frac{1+v}{8\pi} (\bar{F}_x + i\bar{F}_y) \ln \zeta + B\omega(\zeta) + \varphi_0(\zeta) \quad (12)$$

$$\Psi(\zeta) = \frac{3-v}{8\pi} (\bar{F}_x - i\bar{F}_y) \ln \zeta + (B' + iC')\omega(\zeta) + \psi_0(\zeta) \quad (13)$$

$$\varphi_0(\zeta) = \sum_{n=1}^{\infty} b_n \zeta^n \quad (14)$$

$$\psi_0(\zeta) = \sum_{n=1}^{\infty} c_n \zeta^n \quad (15)$$

Based on the distribution of the ground stress field and boundary conditions (see Figure 2), we can obtain the following:

$$B = (\sigma_1 + \sigma_2)/4; B' = -(\sigma_2 - \sigma_1)/2; C' = 0; (\overline{f_x} + i\overline{f_y})ds = 0 \quad (16)$$

$$\overline{F_x} = \overline{F_y} = 0 \quad (17)$$

$$\varphi'(z) = \frac{\sigma_1}{2} \left( \frac{z}{\sqrt{z^2 - a^2}} \right) + \frac{\sigma_2}{4} - \frac{\sigma_1}{4}, \psi'(z) = -\frac{\sigma_1 + \sigma_2}{2} \quad (18)$$

Assuming that  $\alpha$ ,  $\alpha_1$ ,  $\alpha_2$ , and  $l$ ,  $l_1$ ,  $l_2$  are the angles and distances between A and the left, middle, and right ends of the fault, the increment of structural stress at point A can be obtained by using Equations (19) and (20).

$$\Delta\sigma_x = -\sigma_1(D - E - 1) \quad (19)$$

$$\Delta\sigma_y = -\sigma_2(1 - D - E), \Delta\tau_{xy} = -\sigma_1 F \quad (20)$$

$$D = (l_1 / \sqrt{l_1^2}) \cos[\alpha_1 - (\alpha + \alpha_2)/2] \quad (21)$$

$$E = [a^2 l_1 / \sqrt{(l_2)^3}] \sin \alpha \sin[3(\alpha + \alpha_2)/2] \quad (22)$$

$$F = -[a^2 l_1 / \sqrt{(l_2)^3}] \sin \alpha \cos[3(\alpha + \alpha_2)/2] \quad (23)$$

As mentioned above,  $\sigma_1, \sigma_3$  are the initial ground stresses, respectively, which can be obtained by ignoring the fault inclination  $\theta$ ,

$$\sigma_1 = \frac{\sigma_h + \sigma_v}{2} - \frac{\sigma_h - \sigma_v}{2} \cos 2\theta \quad (24)$$

$$\sigma_3 = \frac{\sigma_h + \sigma_v}{2} + \frac{\sigma_h - \sigma_v}{2} \cos 2\theta \quad (25)$$

Here,  $\sigma_h$  is the horizontal stress of rock mass in the fault zone, Pa.  $\sigma_v$  is the vertical stress of rock mass in the fault zone, Pa.

The field measurement results showed the horizontal principal stress of the Gengcun coal mine was perpendicular to the fault structure. The horizontal stress ( $\sigma_h$ ) and vertical stress ( $\sigma_v$ ) are 15.8 MPa and 14.60 MPa, respectively. The geometric parameters of the F16 fault were substituted into Equations (15)–(20), and then the conversion formula of stress and the stress increment cloud map were combined. Figure 3 shows the vertical tectonic stress increment distribution of the fault.

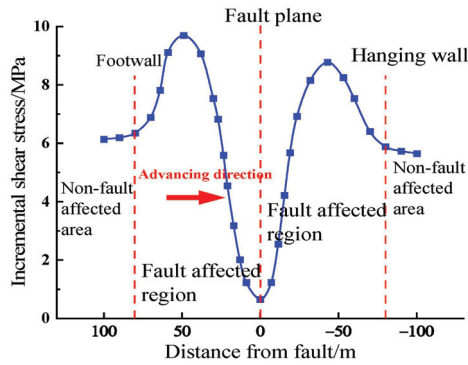


Figure 3. Shear stress increment field of the fault structure.

Figure 3 shows that the distribution range of the shear stress increment in the footwall of the fault is larger than that in the hanging wall, exhibiting an asymmetric distribution. The maximum shear stress increment in the footwall is 9.69 MPa, and the maximum value is located 49 m away from the fault plane. The maximum increment in shear stress in the hanging wall is 8.78 MPa, and the maximum value is located 43 m away from the fault plane. The shear stress increment in the hanging wall is less than that in the footwall, the main reason being that mining disturbance has a greater impact on the footwall of the fault. The shear stress of the lower wall changes when the working face is 80 m away from the fault plane. As the distance from the fault decreases, the shear stress slowly increases at first and then rapidly decreases. Because the working face is significantly farther away from the fault plane, the shear stress of the hanging wall shows an initial rapid increase followed by a slow decrease. When the mining face is 80 m away from the fault plane, the shear stress no longer changes significantly.

3.2. Rock Burst Mechanism

The “three-factor” induction theory for rock bursts was proposed by Qi et al. [53,54], which suggests that the three key factors affecting the evolution and occurrence of rock bursts are divided into force source, physical property, and structural factors (see Figure 4).

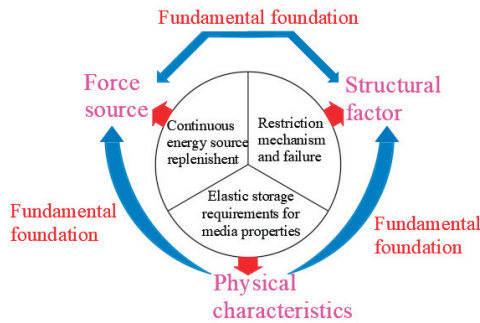


Figure 4. Theoretical framework of “three factors” [48].

The 13,200 working face of the Gengcun coal mine is utilized as a case study. The redistribution and concentration stresses caused by coal mining disturbances are the main sources of force. The concentration stress is caused by the increment in structural stress in the tectonic-affected area, and the coefficient of structural stress concentration significantly increases. This provides a fundamental driving force for rock burst formation, thus resulting in the deformation and destruction of rock masses in the working face and roadway. This

also creates ideal conditions for the accumulation of elastic energy in the surrounding rock, serving as an important basis for measuring the burst risk of the surrounding rock.

From the perspective of physical properties, the spatial structure of the hard roofs in the surrounding goaf and the 13,200 working faces induces a high concentration of stress in the working faces. From a structural perspective, the F16 fault structure disrupts the uniformity and continuity of the surrounding rock mass and forms a new spatial system. When the influence of mining disturbance reaches the limit state of the spatial structure, failure will occur, thus inducing a rock burst.

From the perspective of rock burst types, the 13,200 working face is affected by several primary factors, such as the significant burial depth, hard roofs, fault structures, and mining disturbance. Coal mining and ground stress load cause energy accumulation in the surrounding rock. The dynamic load induced by the fracture of the hard roof induces energy release, resulting in coal pillar failure and, thus, a rock burst.

It can be concluded that the tectonic stress generated by the F16 fault structure has an important influence on the roadway, as shown in Figure 5. In other words, roadway support and tectonic stresses jointly affect static loads in the structural area. The static stress load of coal near the roadway in a single structural area can be represented as  $\sigma_S + \sigma_T + \sigma_D$ .

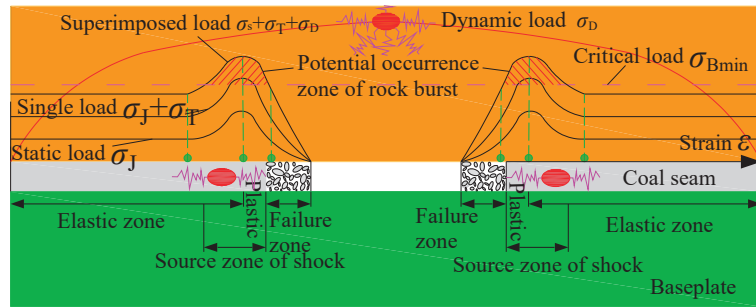


Figure 5. Rock burst mechanism of a roadway in a tectonic zone.

Here,  $\sigma_S$  is the roadway support stress,  $\sigma_T$  is the structural stress, and  $\sigma_D$  is the dynamic load stress of the coal seam roof. Compared to areas with no structure, the increments in static load stress and the superimposed stress of the coal body caused by the structure exceed the impact source area of the critical stress. Moreover, the dynamic load caused by coal seam mining disturbances leads to a higher peak value for the superimposed load. This increases both shock risk and the range of shock sources.

In general, the static load consists of the original rock stress and abutment stress (Equation (26)).

$$\sigma_j = \sigma_{j1} + \sigma_{j2} = (k + \lambda)\gamma H \tag{26}$$

where  $\gamma$  is the bulk density of overlying strata;  $H$  is the overlying strata thickness;  $\lambda$  is the coefficient of structural stress concentration; and  $k$  is the abutment pressure concentration coefficient.

The primary source of dynamic load in coal mining is the substantial stress change caused by mining activities, which manifests as rock burst activity. When the superimposed stress, formed by the static load of mining surrounding rock and the dynamic load induced by mine earthquakes, exceeds the critical load of coal and rock, the coal and rock mass is dynamically damaged, resulting in rock bursts.

#### 4. Numerical Simulation

##### 4.1. Model Construction and Rock Mechanics Parameters

In order to further study the mechanism of rock burst induced by an extra-thick conglomerate and a thrust fault, the surrounding rock deformation and fault tectonic stress

distribution are simulated for a 13,200 working face using FLAC-3D software (version 6.0, ITASCA, Minneapolis, MN, USA, 2017). Based on the mining and geological conditions of the F16 fault in the Gengcun coal mine, a FLAC-3D numerical model is constructed considering a thrust fault and mining disturbance.

The model contains 449,280 elements and has a size of 700 m × 500 m × 200 m (see Figure 6). In the construction process of the model, the dip angle of the Jurassic roof strata in the footwall of the F16 fault is set to 10°, with the dip angle of the Triassic strata in the upper fault set to 50°. The extremely thick seam zone is simplified into a triangular area with a length of 150 m and a height of 60 m. In the model, a built-in interface module of FLAC 3D is used to simulate the F16 fault structure. The fault inclination is set to 50°, with the starting coordinates of the lower end of the fault plane set to (520, 0, 50). The physical and mechanical parameters were measured using laboratory tests for simulations, as shown in Table 1. The mechanical properties of the fault are shown in Table 2. The boundary conditions of the model are set as follows: normal displacement constraints are applied around the model, the bottom boundary is set to a fixed boundary, the displacement in the X, Y, and Z directions is zero, and the upper boundary is set as a free boundary (see Figure 7). A uniform load of 10.75 MPa is utilized to simulate the overlying rock pressure, with a height of 430 m. In order to simplify the spatial relationship between the 13,200 working face and the F16 fault in the simulation process, the F16 fault in the model is fixed, and the excavation step is 20 m along the coal seam inclination. Moreover, the excavation is stopped near the fault in the lower roadway due to frequent microseismic events. The influence of mining disturbance, seam thickness, fault dip angle, and other factors on the structural stress of the coal seam is studied.

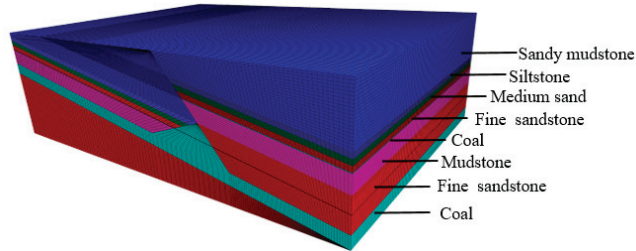


Figure 6. Numerical calculation model.

Table 1. Mechanical properties of rock masses.

Lithology	Density (kg/m <sup>3</sup> )	Bulk (GPa)	Shear (GPa)	Tensile Strength (MPa)	Poisson Ratio	Internal Friction Angle (°)	Cohesion (MPa)
Coal	1344	1.6	1.4	0.4	0.25	30	2.08
Mudstone	2450	10.4	7.3	2.1	0.24	35	4
Sandy mudstone	2550	12.1	9.5	2.6	0.26	37	4.66
Siltstone	2600	12.4	9.2	3.1	0.24	34	4.7
Fine sandstone	2650	16.3	12.5	4.3	0.3	38	7.5
Medium sandstone	2600	13.5	10.1	3	0.24	35	5

Table 2. Mechanical properties of the fault.

Lithology	Density/kg/m <sup>3</sup>	Bulk/GPa	Shear/GPa	Tensile Strength/MPa	Poisson Ratio	Internal Friction Angle/°
Fault	1344	1.78	1.28	0.4	0.25	30

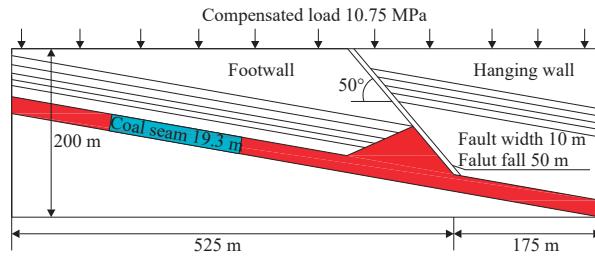


Figure 7. Boundary condition of the model.

#### 4.2. Simulation Results and Discussion

##### 4.2.1. Evolutionary Law of Supporting Stress and Surrounding Rock Stress of the F16 Fault

In order to obtain the stress distribution law of surrounding rock at different positions in front of the coal wall during coal mining, the working face is inclined along the coal seam, and the length of each excavation is set to 10 m. The monitoring line is set at the 10 m position of the roof, with monitoring points spaced at 10 m intervals (see Figure 7). The stress distribution curves of the surrounding rock are obtained at different positions in front of the coal wall, as shown in Figure 8. The excavation positions are 100 m, 80 m, 70 m, 60 m, 50 m, 40 m, 30 m, and 10 m away from the fault.

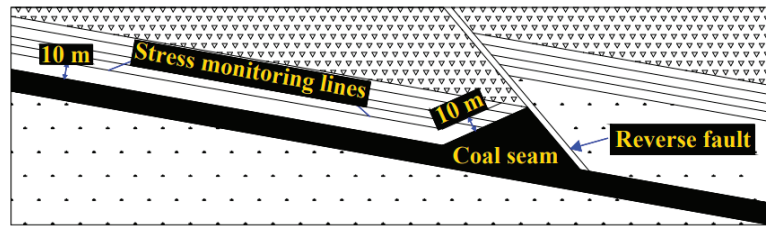


Figure 8. Monitoring point arrangement.

The following stress distribution law during the advancement of the working face can be obtained from Figures 9–11.

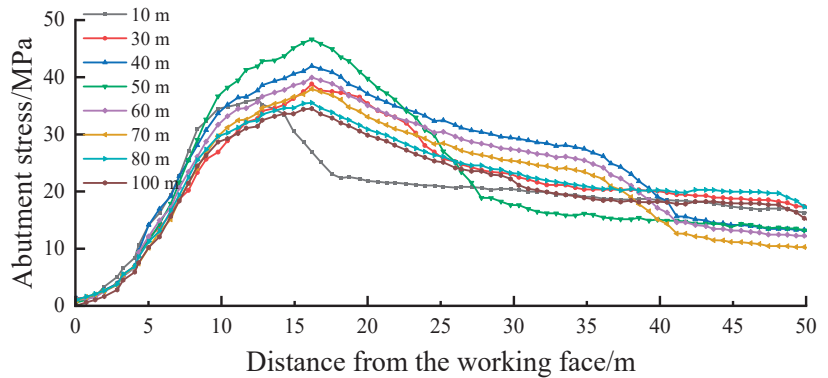


Figure 9. Abutment stress at different distances in front of the working face.

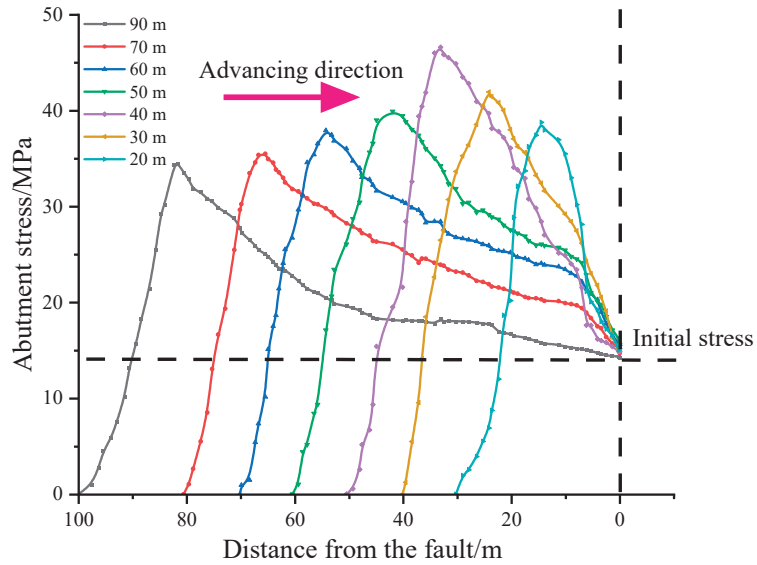


Figure 10. Abutment stress at different distances away from the fault plane.

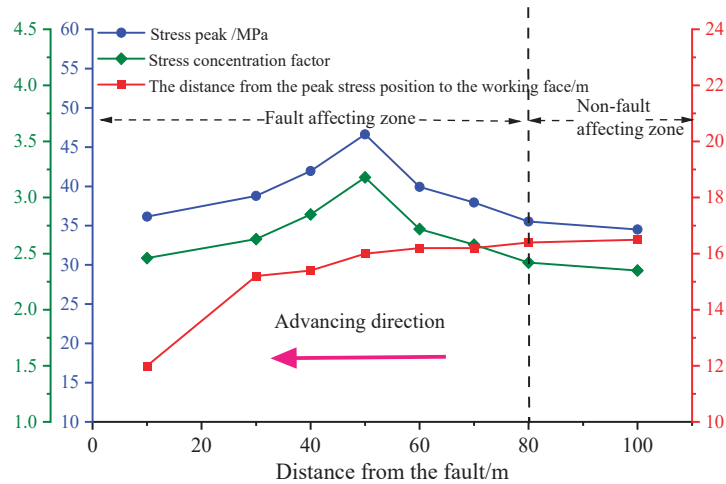


Figure 11. Stress peak and stress concentration factor at different positions from the fault plane.

- (1) Figure 9 shows that stress concentration is likely to occur, with peak stress located 13–17 m in front of the working face. The stress peak value is higher than 35 MPa, and the stress concentration coefficient is larger than 2.42. Due to the thick and hard rock in the upper part of the mining area, a large overhanging roof is formed behind the goaf, and the phenomenon of stress concentration appears.
- (2) With the increase in mining distance, both stress peak and stress concentration coefficient values first increase and then decrease (see Figures 10 and 11), with maximum values of 46.62 MPa and 3.17, respectively, located 50 m away from the working face. When the distances from the fault are 100 m and 80 m, the peak stress values are 34.51 MPa and 35.52 MPa, respectively. The distribution law of the advanced supporting pressure of the working face is similar. When the distance is less than 80 m, the stress peak value increases significantly. With the advancement of the working

face toward the fault direction, the influence of the fault on the working face becomes increasingly obvious. The stress reaches its maximum value at a distance of 50 m from the fault, and at a distance of 80 m from the fault, it is divided into a fault-affected zone and a fault non-affected zone. When the distance from the fault is less than 50 m, the increasing trend of the stress peak and stress concentration coefficient decreases. When the working face is excavated 10 m away from the fault, the stress on the coal far exceeds the compressive strength because of the small distance between the fault and the working face. Consequently, coal failure occurs, and the peak stress is reduced by 36.14 MPa. The fault reduces the supporting stress range and forms a large stress gradient between the coal wall and the fault, which results in a rock burst.

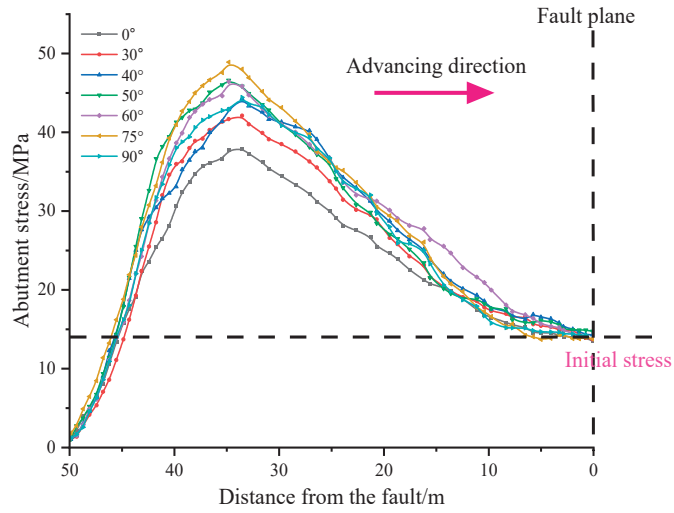
#### 4.2.2. Supporting Stress and Surrounding Rock Stress of the F16 Fault for Different Fault Dip Angles

In order to obtain the stress distribution law of the surrounding rock under the coupling effect of mining disturbance and a fault at different dip angles, we conducted simulations for fault inclinations of  $0^\circ$ ,  $30^\circ$ ,  $40^\circ$ ,  $50^\circ$ ,  $60^\circ$ ,  $70^\circ$ , and  $80^\circ$ . Moreover, the monitoring line was set at the 10 m position of the coal seam roof, with monitoring points spaced at 10 m intervals. The stress distribution of the surrounding rock at different positions in front of the coal wall was obtained when the working face was 50 m away from the fault (see Figure 12). Moreover, the stress variation trend of the surrounding rock for different fault angles was obtained. The variation laws of the stress peak value and stress concentration coefficient for different positions near the fault are shown in Figures 13 and 14.

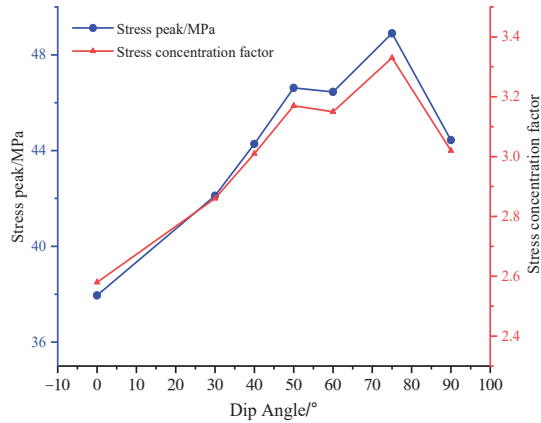


**Figure 12.** Abutment stress in front of the working face for different fault dip angles.





**Figure 13.** Abutment stress at different positions from the fault for different fault dip angles.



**Figure 14.** Stress peak and stress concentration factor from the fault for different dip angles.

The following stress distribution law for different dip angles can be obtained from Figures 12–14.

- (1) Figure 12 shows that peak stress occurs 12–17 m in front of the working face and is less affected by the fault dip angle. For different fault dip angles, the vertical stress near the fault plane is maintained at about 14.7 MPa, and the difference is small.
- (2) Figures 13 and 14 show that the stress concentration coefficient and stress peak at different positions show a similar trend for different fault dip angles. With an increase in the dip angle, the stress concentration coefficient and stress peak first increase and then decrease. When the maximum dip angle is 75°, the stress concentration coefficient and peak stress values are 3.33 and 48.9 MPa, respectively. The simulation results show that the dip angle of the fault has an obvious effect on the tectonic stress of the fault.

#### 4.2.3. Supporting Stress and Surrounding Rock Stress of the F16 Fault for Different Mining Thickness

In order to study the influence of the coupled effect of mining disturbance and faults on the stress of the surrounding rock, we simulated stress distribution using mining thicknesses of 8 m, 13 m, 17 m, 19 m, 21 m, and 26 m (see Figure 15). The monitoring line was set at the 10 m position of the roof, with monitoring points spaced at 10 m intervals. The stress variation trend of the surrounding rock for different mining thicknesses was obtained. The variation laws of the stress peak and stress concentration coefficient for different positions near the fault are shown in Figures 16 and 17.

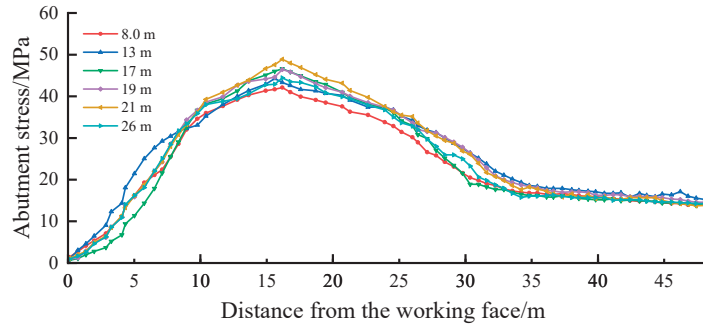


Figure 15. Abutment stress in front of the working face for different thicknesses.

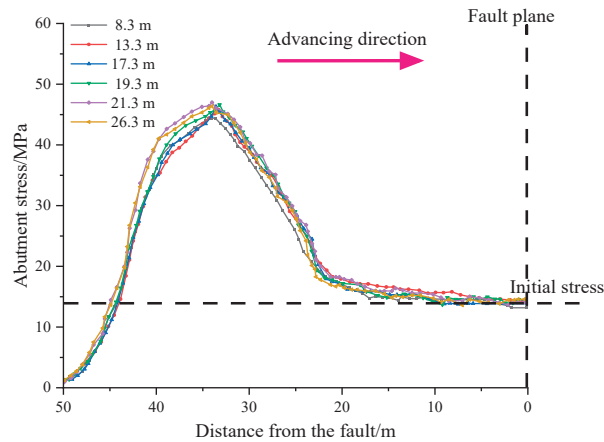
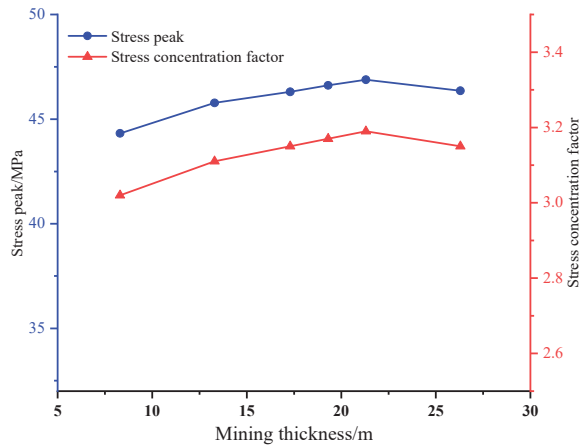


Figure 16. Abutment stress at different positions from the fault for different mining thicknesses.



**Figure 17.** Stress peak and stress concentration factor from the fault for different mining thicknesses.

The following stress distribution law for different mining thicknesses can be obtained from Figures 15–17.

- (1) Figure 15 shows that peak stress occurs 12–17 m in front of the working face and is less affected by the mining thickness. For different mining thicknesses, the vertical stress near the fault plane is maintained at about 14 MPa, and the difference is small.
- (2) Figures 16 and 17 show that the stress concentration coefficient and stress peak at different positions show a similar trend for different mining thicknesses. With an increase in mining thickness, the stress concentration coefficient and stress peak first increase and then decrease. When the maximum mining thickness is 21.3 m, the stress concentration coefficient and peak stress values are 3.19 and 46.89 MPa, respectively. When the minimum mining thickness is 8.3 m, the stress concentration coefficient and peak stress values are 3.01 and 44.32 MPa, respectively. The difference in the stress peak value is 2.57 MPa. Therefore, the simulation results show that mining thickness significantly affects the tectonic stress of a fault.

## 5. Case Study

### 5.1. The Law of Shock Instability in the Working Face under the Influence of “Fault Structure”

Microseismic events in front of the “fault” tectonic area were counted to further verify the mechanisms of rock burst for extra-thick coal influenced by a large conglomerate and a thrust fault. Microseismic events are defined as high-energy events when  $E > 10^6$  J; conversely, microseismic events are defined as low-energy events when  $E \leq 10^6$  J.

Two high-energy events occurred on 1 February and 6 March 2021, accompanied by a large number of microseismic events ( $E = 10^5$ ) in their vicinity, indicating that the highly static coal body in the structural area is significantly influenced by mining disturbance.

The spatio-temporal relationship between the distribution of microseismic events and the advancement of the working face shows that the tectonic influence area is 0–80 m in front of the fault, with microseismic events being more active in this area (Figures 18 and 19). High-energy microseismic events frequently occur 30–60 m in front of the fault. The non-affected area of the fault structure is more than 80 m away from the fault, representing the balance area of microseismic events. The influence range of the fault structure is consistent with the above theoretical calculation and numerical simulation results. There are many factors affecting rock bursts. In this paper, the influences of fault dip, seam thickness, and mining disturbance on rock burst are mainly considered. It is necessary to comprehensively and thoroughly study the correlation between more relevant data on in-situ mine pressure manifestation and rockburst occurrence. In future investigations, deep learning theories will be used to analyze comprehensive field data, such as overburden movement, surface

subsidence, support pressure, displacement, and microseismic events, and their correlations will be clarified. The probability of rock bursts will be predicted, thus providing guidance for the prevention and control of rock bursts.

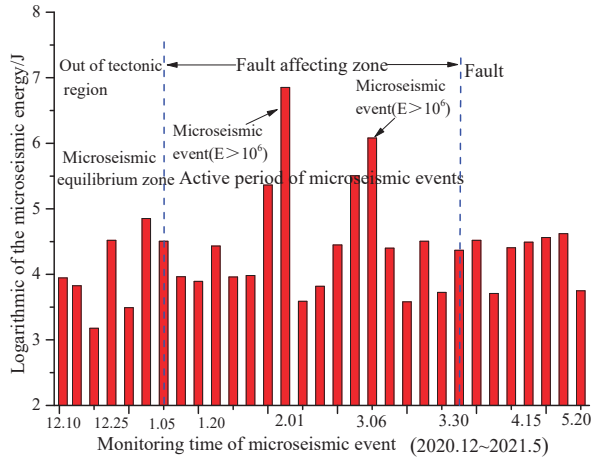


Figure 18. Field microseismic events near faults at different times.

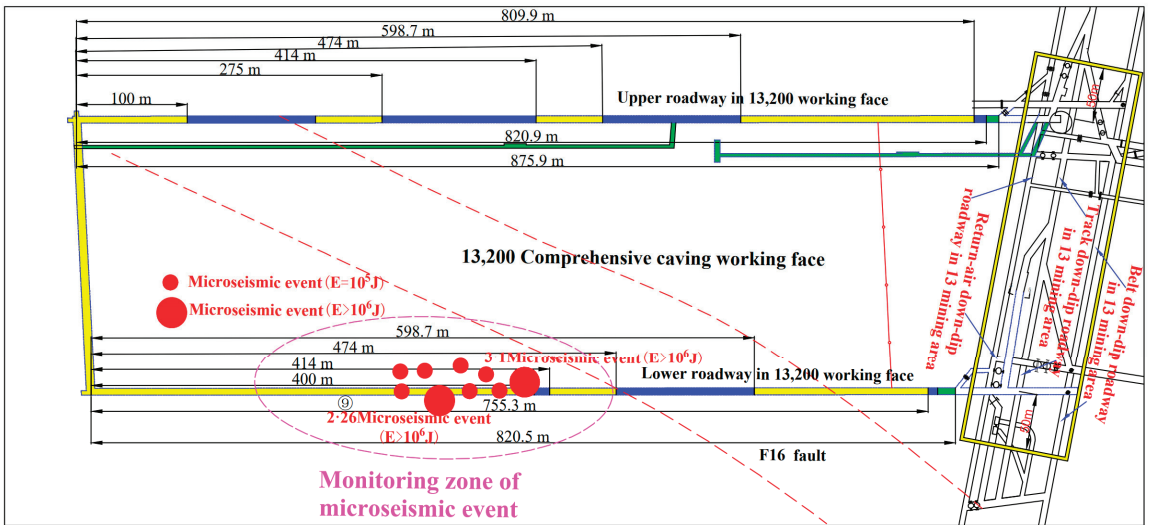


Figure 19. Impact dangerous area in 13,200 fully mechanized caving face.

### 5.2. Prevention and Control of Rock Burst under the Influence of “Fault” Structure

The mechanism of rock bursts in a fault tectonic area involves abutment pressure and tectonic stress, resulting in the formation of high static load stress. When high static loads exceed the critical stress, the energy accumulated in the coal body is released in a nonlinear manner. When a roadway with a high static load is disturbed by mining activities, the superimposed load on the coal body far exceeds the critical stress. The rock burst risk source area is larger, and the microseismic activity is more intense. Moreover, the impact and microseismic events of the roadway are concentrated in areas with high structural stress. Therefore, the prevention and control of roadway rock bursts in “fault” structural areas can be carried out considering two aspects. On the one hand, the static load stress of coal should be decreased. Pressure relief measures, such as large-diameter drilling and

blasting, should be adopted to reduce the concentration of structural stress. On the other hand, efforts should be made to reduce or avoid dynamic load disturbances in structural areas of roadways. In the process of coal mining, increasing the width of coal pillars can isolate mining faces from the structural areas of roadways. This can extend the propagation path of dynamic load stress waves. Thus, the influence of disturbed dynamic loads on the surrounding rock of roadways can be decreased or avoided.

## 6. Conclusions

The following conclusions can be drawn:

- (1) In this paper, a mechanical model of structural stress increment for a thrust fault is established and solved. The results show that the stress distribution around the fault is significantly influenced by the depth of coal, the stress concentration coefficient of the stope, the lateral pressure coefficient, and the fault dip angle. The fault tectonic stress field in the Gengcun coal mine is asymmetrically distributed under the ground stress and dip angle of the fault. The shear stress increment range in the footwall of the fault is larger than that in the hanging wall. The shear stress in the hanging wall is greater than that in the footwall, and the impact risk is higher.
- (2) A 3D numerical simulation method is used to reveal the distribution law of the bearing stress in front of the working face during mining. The results show that stress concentration is likely to occur in front of the working face under mining disturbance. The stress distribution is relatively regular, and the peak stress is generally located 13–17 m in front of the working face. The stress peak value is greater than 35 MPa, and the stress concentration coefficient is greater than 2.42. Due to the thick and hard rock layer in the upper part of the mining area, a large overhanging roof and stress concentration occur at the back of the goaf.
- (3) The stress peak value and stress concentration coefficient vary for different distances from the fault. As the working face is excavated and approaches the fault-affected area, the stress first increases and then decreases. The peak stress and maximum stress concentration coefficient values are 46.62 MPa and 3.17, respectively, at a 50 m distance from the working face. Under the influence of mining disturbance, an 80 m distance from the fault is the dividing line between the fault non-affected area and the fault-affected area.
- (4) The fault dip angle and mining thickness have significant influences on the structure around the fault. With an increase in the dip angle, the maximum vertical stress and peak stress first increase and then decrease. For a maximum angle of  $75^\circ$ , the stress concentration coefficient and peak stress values are 3.33 and 48.9 MPa, respectively. For a minimum value of  $0^\circ$ , the stress concentration coefficient and peak stress values are 2.58 and 37.95 MPa, respectively. Moreover, with an increase in mining thickness, the peak stress and stress concentration coefficients show a trend of first increasing and then decreasing. For mining thicknesses of 8 m and 21 m, the corresponding stress concentration coefficient and peak stress values are 3.01 and 44.32 MPa and 3.19 and 46.89 MPa, respectively.
- (5) The 13,200 working face of the Gengcun coal mine is used as a case study, and field microseismic events are analyzed. The field microseismic events mainly occur at a distance of 0–80 m from the footwall of the fault, with the energy and frequency of microseismic events reaching their maximums at a distance of 30–50 m from the footwall. This is in good agreement with the simulated results of the stress concentration area. When the working face is located in the influence zone of the tectonic area, microseismic events occur more frequently and with greater energy.

**Author Contributions:** Conceptualization, S.Y.; supervision, S.Y.; writing-original draf, S.Y., X.W. and Z.W.; investigation, X.W.; software, X.W., L.C. and W.W.; resources, L.C.; data curation, L.C. and W.W.; formal analysis, Z.W.; funding acquisition, Z.W.; writing-review & editing, Z.W.; All authors have read and agreed to the published version of the manuscript.

**Funding:** This research was funded by the Scientific and Technological Project of Henan Province (222102320060), the strength improvement plan of the advantageous disciplines of Zhongyuan University of Technology (SD202232), and the Young backbone teacher project of Zhongyuan University of Technology (2023XQG14).

**Data Availability Statement:** Data are contained within the article.

**Conflicts of Interest:** Author Suihan Yang, Xiangzhi Wei and Linlin Chen were employed by the company Henan Dayou Energy Co Ltd., Gencun Coal Mine. The remaining authors declare that the research was conducted in the absence of any commercial or financial relationships that could be construed as a potential conflict of interest.

### List of Symbols

Symbol	Explanation	Unit	Symbol	Explanation	Unit
$x$	Horizontal coordinates in the cartesian coordinate system with the major axes of the ellipse	m	$y$	Vertical coordinates in the cartesian coordinate system with the minor axes of the ellipse	m
$\varphi$	Angle between the line of the ellipse edge point, the ellipse center, and the major axis of the ellipse	°	$\rho$	Length of the point at the edge of the ellipse hole and the line at the center of the ellipse	m
$\omega(\zeta)$	The variogram function	1	$\text{Re}(z)$	The real part of the complex number $z$	1
$\sigma_x$	Tectonic stress in the x direction	Pa	$\sigma_\varphi$	Hoop stress in the polar coordinates	Pa
$\sigma_y$	tectonic stress in the y direction	Pa	$\sigma_\rho$	Radial stress in the polar coordinates	Pa
$\bar{f}_x + i\bar{f}_y$	Complex number of boundary surface forces	Pa	$\tau_{\rho\varphi}$	Shear stress in the polar coordinates	Pa
$\sigma_1$	Initial ground stresses	Pa	$\sigma_3$	Initial ground stresses	Pa
$\sigma_h$	Horizontal stress of rock mass in the fault zone	Pa	$\sigma_v$	Vertical stress of rock mass in the fault zone	Pa

### References

- Vu, T.T. Solutions to prevent face spall and roof falling in fully mechanized longwall at underground mines, Vietnam. *Min. Miner. Deposits*. **2022**, *16*, 127–134. [CrossRef]
- Babets, D.; Sdvyzhkova, O.; Hapieiev, S.; Shashenko, O.; Prykhodchenko, V. Multifactorial analysis of a gateroad stability at goaf interface during longwall coal mining—A case study. *Min. Miner. Deposits*. **2023**, *17*, 9–19. [CrossRef]
- Barański, A.; Drzewiecki, J.; Dubiński, J.; Kabiesz, J.; Konopko, W.; Kornowski, J.; Kurzeja, J.; Lurka, A.; Makówka, J.; Mutke, G.; et al. *Principles of Using the Complex Method and Detailed Methods for Assessing the State of Rockburst Hazard in Hard Coal Mines, Instruction No. 22*; Central Mining Institute: Katowice, Poland, 2012.
- Wojtecki, L.; Iwaszenko, S.; Apel, D.B.; Bukowska, M.; Makówka, J. Use of machine learning algorithms to assess the state of rockburst hazard in underground coal mine openings. *J. Rock Mech. Geotech.* **2022**, *14*, 703–713. [CrossRef]
- Konicek, P.; Ptacek, J.; Waclawik, P.; Kajzar, V. Long-Term Czech Experiences with Rockbursts with Applicability to Today's Underground Coal Mines. *Rock Mech. Rock Eng.* **2019**, *52*, 1447–1458. [CrossRef]
- Pu, Y.; Apel, D.B.; Lingga, B. Rockburst prediction in kimberlite using decision tree with incomplete data. *J. Sustain. Min.* **2018**, *17*, 158–165. [CrossRef]
- Chen, J.; Shi, K.W.; Pu, Y.Y.; Apel, D.B.; Zhang, C.; Zuo, Y.; Chen, J.; Xu, L.; Gui, Z.; Song, L. Study on instability fracture and simulation of surrounding rock induced by fault activation under mining influence. *Rock Mech. Bull.* **2023**, *2*, 10003. [CrossRef]
- Dou, L.M.; Tian, X.Y.; Cao, A.Y.; Gong, S.Y.; He, H.; He, J.; Cai, W.; Li, X.W. Present situation and problems of coal mine rock burst prevention and control in China. *J. China Coal Soc.* **2022**, *47*, 152–171.
- Zhang, J.W.; Dong, X.K.; Chai, H.T.; Song, Z.X.; Fan, W.B.; Wang, Q.; Lv, Y.L.; Zheng, B.; Bai, J.J.; Liu, Z.G.; et al. The mechanism and prevention of rock burst caused by the collapse of low-level thick hard rock seam at full mining height in thick coal seam. *J. China Coal Soc.* **2022**, *47*, 734–744.
- Li, C.C.; Zhao, T.; Zhang, Y.; Wan, W. A study on the energy sources and the role of the surrounding rock mass in strain burst. *Int. J. Rock Mech. Min. Sci.* **2022**, *154*, 105–114. [CrossRef]
- Kong, P.; Liu, R.; Xing, L.Y.; Wan, W.K. Study on the dynamic response and the hazard of rock burst under the influence of fault slip. *Front. Earth Sci.* **2023**, *10*, 1034332. [CrossRef]
- He, J.; Dou, L.; Gong, S.; Li, J.; Ma, Z. Rock burst assessment and prediction by dynamic and static stress analysis based on micro-seismic monitoring. *Int. J. Rock Mech. Min. Sci.* **2017**, *93*, 46–53. [CrossRef]
- Wang, C.; Cao, A.; Zhu, G.; Jing, G.; Li, J.; Chen, T. Mechanism of rock burst induced by fault slip in an island coal panel and hazard assessment using seismic tomography: A case study from Xuzhuang colliery, Xuzhou, China. *Geosci. J.* **2017**, *21*, 469–481. [CrossRef]
- Li, K.; Chen, J.; Zhao, Z.; Yan, R.; Du, T.T. Study on disaster-causing factors and evolution process of rock burst in roadway near gob. *Coal Sci. Technol.* **2019**, *47*, 76–82.

15. Yang, W.L.; Lin, Q.; Wei, Q.D.; Qu, X.C.; Wang, J.C.; Liu, X. Mechanism of rockburst induced by fault coal pillars with different widths indeep shaft. *Coal Eng.* **2020**, *52*, 112–116.
16. Jagger, L.J.; McClay, K.R. Analogue modelling of inverted domino-style basement fault systems. *Basin Res.* **2018**, *30*, 363–381. [CrossRef]
17. Bonini, L.; Basili, R.; Toscani, G.; Burrato, P.; Seno, S.; Valensise, G. The role of pre-existing discontinuities in the development of extensional faults: An analog modeling perspective. *J. Struct. Geol.* **2015**, *74*, 145–158. [CrossRef]
18. Sainoki, A.; Mitri, H.S. Dynamic behaviour of mining-induced fault slip. *Int. J. Rock Mech. Min. Sci.* **2014**, *66*, 19–29. [CrossRef]
19. Wang, P.; Jiang, L.S.; Jiang, J.Q.; Zheng, P.Q.; Li, W. Strata behaviors and rock Burst-Inducing Mechanism under the coupling effect of a hard, thick stratum and a normal fault. *Int. J. Geomech.* **2018**, *18*, 04017135. [CrossRef]
20. Yu, Q.G.; Zhang, H.X.; Zhang, Y.J.; Deng, W.N.; Zhang, G.Y. Analysis of fault activation mechanism and influencing factors caused by mining. *J. China Coal Soc.* **2019**, *44*, 18–30.
21. Lv, J.G.; Nan, C.Q.; Zhang, Y.; Qiao, Y.G.; Tang, Z. Coal bump mechanism in Yima coalfield mining near thrustfault. *J. Min. Saf. Eng.* **2018**, *35*, 567–574.
22. Wu, Z.H.; Pan, P.Z.; Pan, J.F.; Wang, Z.F.; Gao, J.M. Analysis of mechanism of rock burst and law of mining induced events in graben structural area. *Rock Soil Mech.* **2021**, *42*, 2225–2238.
23. Kong, P.; Jiang, L.; Shu, J.; Wang, L. Mining stress distribution and fault-slip behavior: A case study of fault-influenced longwall coal mining. *Energies* **2019**, *12*, 2494. [CrossRef]
24. Ji, H.G.; Ma, H.S.; Wang, J.A. Mining disturbance effect and mining arrangements analysis of near-fault mining in high tectonic stress region. *Saf. Sci.* **2012**, *50*, 649–654. [CrossRef]
25. Zhao, T.B.; Guo, W.Y.; Tan, Y.L.; Lu, C.P.; Wang, C.W. Casehistories of rock bursts under complicated geological conditions. *Bull. Eng. Geol. Environ.* **2018**, *77*, 1529–1545. [CrossRef]
26. Zhao, S.K.; Deng, Z.G.; Ji, W.B.; Li, Z.; Zhang, G.; Li, Y. Effects of multi-stage tectonic movement on regional tectonic stress characteristics and rockburst. *J. Min. Saf. Eng.* **2019**, *36*, 306–314.
27. Cao, M.H.; Liu, F.; Wang, T.X. Numerical simulation study of fault activation process and coal pillar instability mechanism. *J. Shandong Univ. Sci. Technol. Nat. Sci.* **2020**, *39*, 61–68.
28. Jiao, Z.; Yuan, Q.; Zou, P.; Shi, B.J. Case Study of the Characteristics and Mechanism of Rock Burst near Fault in Yima Coalfield, China. *Shock. Vib.* **2021**, *2021*, 9950273. [CrossRef]
29. Tong, H.M.; Cai, D.S.; Yongping, W.U.; Li, X.G. Activity criterion of pre-existing fabrics in non-homogeneous deformation domain. *Sci. China Earth Sci.* **2010**, *53*, 1115–1125. [CrossRef]
30. Zhao, Y.X.; Lu, Z.G.; Zhu, G.P.; Jiao, Z.H.; Wang, H.; Gao, N. Fault reactive induced by the principal stress rotation for the underground coal mining. *J. China Univ. Min. Technol.* **2018**, *47*, 73–80.
31. Sainoki, A. Dynamic modelling of fault-slip with Barton’s shear strength model. *Int. J. Rock Mech. Min. Sci.* **2014**, *67*, 155–163. [CrossRef]
32. Sainoki, A.; Mitri, H.S. Effect of slip-weakening distance on selected seismic source parameters of mining induced fault-slip. *Int. J. Rock Mech. Min. Sci.* **2015**, *73*, 115–122. [CrossRef]
33. Orlecka-Sikora, B.; Lasocki, S.; Lizurek, G.; Rudziński, L. Response of seismic activity in mines to the stress changes due to mining induced strong seismic events. *Int. J. Rock Mech. Min. Sci.* **2012**, *53*, 151–158. [CrossRef]
34. Zhao, Y.X.; Wang, H.; Jiao, Z.H.; Lu, Z.G.; Zhang, X. Experimental study of the activities of reverse fault induced by footwall coal mining. *J. China Coal Soc.* **2018**, *43*, 914–922.
35. Zhao, S.K. Experiments on the characteristics of thrust fault activation influenced by mining operation. *J. Min. Saf. Eng.* **2016**, *33*, 354–360.
36. Wang, T.; You, S. The influence of different mining modes on the evolution law of stress in fault surrounding rock. *J. Min. Saf. Eng.* **2017**, *34*, 276–281.
37. Wang, H.W.; Wang, Q.; Shi, R.M.; Jiang, Y.D.; Tian, Z. A review on the interaction mechanism between coal burstsand fault structure instability from the perspective of multi-physical field. *J. China Coal Soc.* **2022**, *47*, 762–790.
38. Wang, H.; Jiang, Y.; Xue, S.; Mao, L.T.; Lin, Z.N.; Deng, D.X.; Zhang, D.Q. Influence of fault slip on mining-induced pressure and optimization of roadway support design in fault-influenced zone. *J. Rock Mech. Geotech. Eng.* **2016**, *8*, 660–671. [CrossRef]
39. Wang, H.W.; Shao, M.M.; Wang, G.; Deng, D.X. Characteristics of stress evolution on the thrust fault plane during the coal mining. *J. China Coal Soc.* **2019**, *44*, 2318–2327.
40. Kidybiński, A. Bursting liability indices of coal. *Int. J. Rock Mech. Min. Sci. Geomech. Abstr.* **1981**, *18*, 295–304. [CrossRef]
41. Smoliński, A.; Malashkevych, D.; Petlovanyi, M.; Rysbekov, K.; Lozynskiy, V.; Sai, K. Research into Impact of Leaving Waste Rocks in the Mined-Out Space on the Geomechanical State of the Rock Mass Surrounding the Longwall Face. *Energies* **2022**, *15*, 9522. [CrossRef]
42. Malashkevych, D.; Petlovanyi, M.; Sai, K.; Zubko, S. Research into the coal quality with a new selective mining technology of the waste rock accumulation in the mined-out area. *Min. Miner. Depos.* **2022**, *16*, 103–114. [CrossRef]
43. Sepehri, M.; Apel, D.B.; Adeeb, S.; Leveille, P.; Hall, R.A. Evaluation of mining-induced energy and rockburst prediction at a diamond mine in Canada using a full 3D elastoplastic finite element model-ScienceDirect. *Eng. Geol.* **2020**, *266*, 105457. [CrossRef]

44. Wojtecki, L.; Konicek, P. Estimation of active rockburst prevention effectiveness during longwall mining under disadvantageous geological and mining conditions. *J. Sustain. Min.* **2016**, *15*, 1–7. [CrossRef]
45. Konicek, P.; Schreiber, J. Heavy rockbursts due to longwall mining near protective pillars: A case study. *Int. J. Min. Sci. Technol.* **2018**, *28*, 799–805. [CrossRef]
46. Filippov, V.N.; Eremenko, A.A.; Khristolyubov, E.A. Extraction of ore reserves from safety pillars in rockburst-hazardous conditions of tashtagol and sheregesh deposits. *J. Min. Sci.* **2021**, *57*, 57–65. [CrossRef]
47. Kopytov, A.I.; Eremenko, A.A.; Shaposhnik, Y.N. Design of support systems for rockburst-hazardous underground mines in Gornaya Shorial. *J. Min. Sci.* **2020**, *56*, 567–574. [CrossRef]
48. Zhou, J.; Li, X.B.; Mitri, H.S. Evaluation method of rockburst: State-of-the-art literature review. *Tunn. Undergr. Space Technol.* **2018**, *81*, 632–659. [CrossRef]
49. Wu, C.; Dou, L.M.; Si, G.Y.; Cao, A.Y.; Gong, S.Y.; Wang, G.F.; Yuan, S.S. A new seismic-based strain energy methodology for coal burst forecasting in underground coal mines. *Int. J. Rock Mech. Min. Sci.* **2019**, *123*, 104086.
50. Pan, Y.S.; Wang, A. Disturbance response instability theory of rock bursts in coal mines and its application. *Geohazard Mech.* **2022**, *1*, 1–17. [CrossRef]
51. Wang, L.H.; Cao, A.Y.; Guo, W.H.; Dou, L.M.; Wen, Y.Y.; Xue, C.C.; Hu, Y.; Lv, D.Z. Rock burst mechanism and characteristics of roadway in “faulu-fold” structure area. *J. Min. Saf. Eng.* **2023**, *40*, 69–81.
52. Liu, Z.C.; Liu, X.R.; Li, Y.K.; Zhang, H. Mechanism of faults acting on in-situ stress field direction. *Oil Gas Geol.* **2016**, *37*, 387–393.
53. Qi, Q.X.; Ma, S.Z.; Sun, X.K.; Zhao, S.K.; Li, Y.P.; Li, H.T.; Yu, B.; Pan, Z.P.; Wang, S.G.; Li, H.; et al. Theory and technical framework of coal mine rock burst origin prevention. *J. China Coal Soc.* **2018**, *43*, 1801–1810.
54. Cai, W.; Dou, L.M.; Wang, G.F. Mechanism of fault reactivation and its induced coal burst caused by coal mining activities. *J. Min. Saf. Eng.* **2019**, *36*, 1193–1202.

**Disclaimer/Publisher’s Note:** The statements, opinions and data contained in all publications are solely those of the individual author(s) and contributor(s) and not of MDPI and/or the editor(s). MDPI and/or the editor(s) disclaim responsibility for any injury to people or property resulting from any ideas, methods, instructions or products referred to in the content.



## Article

# Study on the Effectiveness of the Integral Emergency Response System for Coal Mine Water Hazard Accidents Based on Combination Weighting

Yu Hao<sup>1,2</sup>, Huanhuan Yang<sup>3</sup>, Lijun Zhang<sup>1,2</sup> and Chaolun Sun<sup>1,2,4,\*</sup>

<sup>1</sup> Emergency Management School, Henan Polytechnic University, Jiaozuo 454000, China; haoyu\_he@163.com (Y.H.); zl13849117460@163.com (L.Z.)

<sup>2</sup> Safety and Emergency Management Research Center, Henan Polytechnic University, Jiaozuo 454000, China

<sup>3</sup> Emergency Management Training Center, Party School of the CPC Central Committee (Chinese Academy of Governance), Beijing 100091, China; 18639748698@163.com

<sup>4</sup> State Key Laboratory Cultivation Base for Gas Geology and Gas Control, Henan Polytechnic University, Jiaozuo 454000, China

\* Correspondence: suncl@hpu.edu.cn

**Abstract:** Improving the emergency response effectiveness of coal mines in response to water hazard accidents not only plays a vital part in minimizing the resultant losses, but also functions as an important index for evaluating the emergency response capability of coal mines. Therefore, it is of great necessity to test the emergency response capability of coal mines. In this study, an effectiveness measurement index system for the emergency response system that comprises two primary indexes (i.e., response capability and service capability) and six secondary indexes (i.e., accident information transmission, emergency command and control, emergency rescue and mitigation, emergency management, personnel team, and prevention and preparation) was constructed. Additionally, a technique for order preference by similarity to ideal solution (TOPSIS) model for evaluating the effectiveness of the integral emergency response system for coal mine water hazard accidents, based on combination weighting, was put forward. Both the empirical evaluation and model validation of the emergency response system for water hazard accidents were carried out by taking five coal mines attached to Henan Coking Coal Group as research objects. The findings suggest that the effectiveness of the emergency response system for water hazard accidents in the Guhanshan Coal Mine and the Zhongmachun Coal Mine is rated as “average”, while those in the Jiulishan Coal Mine, Zhaogu No. 1 Coal Mine, and Zhaogu No. 2 Coal Mine are graded as “good”. This result is consistent with the actual situation, which verifies the capacity of the proposed TOPSIS model to evaluate the emergency response system scientifically and efficiently for coal mine water hazard accidents. This study not only offers new ideas for how to enhance the comprehensive emergency response capability of coal mines with respect to water hazard accidents, but also provides support for making decisions concerning the upgrading of the emergency response capacity of coal mines.

**Citation:** Hao, Y.; Yang, H.; Zhang, L.; Sun, C. Study on the Effectiveness of the Integral Emergency Response System for Coal Mine Water Hazard Accidents Based on Combination Weighting. *Processes* **2024**, *12*, 235. <https://doi.org/10.3390/pr12010235>

Academic Editors: Chi-Min Shu

Received: 19 December 2023

Revised: 10 January 2024

Accepted: 18 January 2024

Published: 22 January 2024

**Keywords:** coal mine safety; water hazard accidents; emergency response; effectiveness measurement



**Copyright:** © 2024 by the authors. Licensee MDPI, Basel, Switzerland. This article is an open access article distributed under the terms and conditions of the Creative Commons Attribution (CC BY) license (<https://creativecommons.org/licenses/by/4.0/>).

## 1. Introduction

The abundant coal resources carry great weight in China’s national economy. After more than a century of mining, most of the mines in China intend to switch their attention to the mining of lower coal groups [1]. As the mining time and depth increase, the hydrogeological conditions of mines in China have become increasingly complex. As such, China has become one of the countries suffering from the most serious coal mine water hazard accidents in the world [2,3]. The statistical materials analysis shows that a total of three major water hazard accidents and six less serious water hazard accidents took place in coal mines across the country from 2020 to 2022, claiming the lives of 78 people.

Additionally, multiple water-related accidents also occurred in the meantime [4]. Accident emergency response plays a vital role throughout accident emergency management. It can not only reflect whether prevention and preparation before the accident are in place but can also speed up emergency response and rescue. Raising the emergency response speed of coal mine water hazard accidents proves to be the key to reducing its severity. For this purpose, coal mining enterprises are urged to make greater efforts to enhance their emergency response capabilities. On this account, measuring and evaluating the effectiveness of accident emergency response systems in coal mining enterprises serves as a touchstone for testing the quality of emergency management in related coal mining enterprises. This work is of prime importance for implementing coal mine safety production requirements and supervising coal mine safety production emergency management.

Water hazard accidents are one of the five most commonly seen disasters in coal mines. In this regard, scholars all over the world have chiefly focused on the influence of waterproof mechanisms and structural cracks on water hazard accidents, as well as water hazard accident mechanisms during pressurized mining. Snow and Louise et al. [5,6], to name a few, applied the method for calculating permeability tensor to coal mine water hazard accidents and constructed an anisotropic fractured medium seepage model. Santos and Bieniawski et al., centering on the mechanism of bottom plate failure, introduced the concept of “critical capacity release point” and widened the application range of the water disaster causation theory by refining the Hoek–Brown rock strength criterion [7–10]. As for Chinese scholars, they have focused their research on analyzing why water hazard accidents happen and how they evolve. For instance, Wang, after giving a detailed analysis on the causes of water hazard accidents, classified the causal factors into five categories and constructed a coal mine accident causation model based on management errors [11]. Zhang et al. set up a three-dimensional water disaster prevention and control technology system and refined it into two subsystems: surface water and groundwater [12]. Zhao conducted fuzzy clustering analysis on the causes of water hazard accidents with the aid of MATLAB. Following the analysis, four types of water disasters in coal mines were identified, which greatly accelerates the judgement on the causes of water hazard accidents [13]. Miao et al. [14] looked at the basic situation and the problems of coal mine water hazard accidents in China in 2020 and attributed the disasters to six aspects of factors. Sun et al. [15] compiled data from 2000 to 2015 and found that the number of deaths in a single major water accident ranked first. Wei et al. [16] conducted a hierarchical and classified statistical analysis on the relevant information on coal mine water hazard accidents that occurred in China from 2001 to 2013, further clarifying the relationship between relevant factors and coal mine water hazard accidents. Yin et al. [17] investigated the main reasons for water hazard accidents and proposed corresponding technical measures to standardize the process of detecting and releasing water with pilot holes. Zhang et al. [18] collected and researched the information on water hazard disasters in China between 2008 and 2020. In addition, Bascetin et al. reduced the cost of tailings pond leakage prevention from the perspective of improvement of seepage control materials, which provided a new management idea for the prevention of water damage accidents in coal mines [19]. Based on the results, the provinces where water hazard accidents frequently occurred were realized.

Coal mining is not only severely restricted by water resources, but also has more and more obvious influence on groundwater resources. Jia Xin, He Ruimin et al. revealed the influence and rule of surface cracks formed by coal mining on the vertical gradient of surface water content by monitoring the evolution process of ecological environment and the dynamic distribution of surface cracks in different periods of collapse [20]. Lu Zhen, Guo Yangnan et al. adopted the CCME-WQI method to carry out the water quality assessment of different water bodies in mining areas, and established water quality health risk assessment models to analyze water quality health risks of different populations in mining areas and their spatial distribution characteristics, so as to grasp the water quality characteristics and health risks of various water bodies in mining areas, which is of great significance for rational development and utilization of water resources in mining

areas [21]. Li Qiming, Zhai Lijuan et al. proposed that the damage types of karst aquifer caused by coal mining could be divided into three types: direct damage, indirect damage, and non-impact damage; the damage modes of aquifer caused by coal mining could be divided into three types: “roof pore water destruction”, “floor karst water destruction”, and “karst water, fissure water, pore water destruction” [22]. Cao Zhiguo, He Ruimin et al. summarized three types of groundwater migration laws in four stages of stability in pre-mining, mid-mining, post-mining, post-mining under large-scale, and high-intensity modern coal mining conditions [23]. Ning Jianhong, Jia Xirong et al. discussed the method of determining the work grade of groundwater environmental impact assessment in the coal mine area combined with the type of deposit exploration [24]. Fan Limin, Kou Guide et al. have studied the variation law of shallow groundwater flow field under coal mining conditions [25], and these results have provided references for the scientific protection and rational utilization of water resources in mining areas.

China is one of the most serious countries suffering from mine water [26]. The underground water rushes into the underground mining space by means of the roof and floor water channel, causing great casualties and property losses. Therefore, one of the key scientific issues to realize the scientific mining of coal mines is the prevention and control of water disasters and the protection and utilization of water resources [27,28]. In recent years, China has made great achievements, solved many problems, and achieved great benefits in the prevention and control of water hazards in coal mines. Many scholars at home and abroad have also made rich achievements in the theoretical research of water damage control in coal mining. These studies mainly focus on the hydrogeological characteristics of coal mining, the risk assessment of water disaster in coal mining, and the comprehensive water disaster prevention technology in coal mining, etc. For example, in terms of hydrogeological characteristics of coal mining, ZhaopingMeng and GuoqingLi [29] studied the permeability behavior and influencing factors of high grade coal in the early depletion process of coalbed methane. DongshengZhang et al. [30,31] pointed out that the large-scale mining of shallow coal seams has an important impact on the overlying aquifer and the surface ecological environment. In order to protect the aquifer and maximize the exploitation of coal resources, field tests were carried out during the mining of LW32201 in Bulianta Coal Mine, Shandong. ZhenHuang et al. [32,33] found that the hydraulic characteristics of the strata under the floor of coal seams were an important factor in evaluating the water inrush risk of the floor, but the laboratory hydraulic test could not accurately determine the water inrush risk of the floor. In the study of coal mining flood risk assessment, water inrush coefficient is often used to predict flood risk in the world, such as the Kriging interpolation method [34,35]. In terms of comprehensive water disaster prevention and control technology in coal mines, the active protection method is mainly adopted in foreign countries to prevent and control water inrush, using vertical ground drilling and submersible pumps with high lift (1000 m), large displacement (5000 m<sup>3</sup>/h), and high power (2000 KW) to drain aquifers [29]. Domestic coal mine water prevention and control technology mainly has two aspects: one is blocking, the other is sparse; these can be present in combination with one another. For example, Hu Weiyue [36], starting with the spatio-temporal changes of coal seam mining and the evolution process of underground water flow, proposed that the water filled in the roof aquifer during shallow coal seam mining is composed of fluctuating static storage water release and incremental dynamic recharge water, and proposed a spatio-temporal dynamic prediction method of mine water inrush with the mining process. TieLi et al. [37] took a water-bearing alluvial layer as an example and evaluated the stress redistribution, formation failure, and enhanced water conductivity caused by coal mining in Daliuta Coal Mine in Shaanxi Province through field investigation, physical simulation, and numerical analysis.

Through a review of the literature, it is found that current research on coal mine water hazard accidents primarily focuses on the prediction, exploration, management, monitoring, and early warning of water hazard accidents. By contrast, there is scarce research on the emergency response capability of coal mining enterprises to water hazard

accidents. As one of the five major disasters in coal mines, water hazard accidents have risen to be the second largest “killer”, second only to gas accidents in terms of threatening coal mine safety production and personnel life safety.

Coal mine accidents are characterized by suddenness, uncertainty, disastrous, and secondary nature. Effective emergency response serves as a vital approach to mitigate losses brought by major disasters and accidents and prevent further damage [38]. In this paper, an evaluation system targeting the effectiveness of the integrated emergency response system for coal mine water hazard accidents was constructed to test and assess the emergency system response efficiency of coal mining enterprises. This move aims to promote coal mining enterprises to upgrade their emergency response capabilities for accidents and disasters, thus maximizing the efficiency of coal production and disaster prevention and control. Moreover, this paper provides ideas for safe and efficient mining, water disaster prevention, and control in coal mines.

## 2. Construction of the Effectiveness Measurement Index System

### 2.1. Connotation of the Integrated Emergency Response System for Coal Mine Water Hazard Accidents

The emergency response system for coal mine water hazard accidents is a collection of various organizational personnel, equipment, emergency treatment steps, plans, and their interrelationships involved in the response and disposal by coal mining enterprises in the face of water hazard accidents. By this token, it is also the interaction between accident classification and response levels. The integrated emergency response system for coal mine water hazard accidents is a highly targeted, interconnected, and complex giant system that links the stages of emergency life cycle management, covering preparation, prevention, response, and recovery. In the production and operation activities of coal mining enterprises, numerous cases of accidents being exacerbated by delayed emergency response crop up here and there, indicating an urgent need for coal mining enterprises to optimize their current accident emergency response systems, as well as their normalized emergency services and abnormal emergency response capabilities.

Guo, Zhang, and Zhang et al. divided the integrated emergency response system into response capability and service capability in the estimation of added value for integrated emergency response systems [39]. Given the fact that the emergency response process and steps for different accidents are similar, this paper transforms the evaluation of the emergency response capability for coal mine water hazard accidents into a measurement of the effectiveness of the integrated emergency response system for coal mine water hazard accidents. The measurement covers two dimensions: abnormal response capability and normalized service capability. Evaluations of these two capabilities can not only reflect the efficacy of emergency management prevention and preparation in coal mining enterprises, but also detect the effectiveness of emergency management monitoring and early warning in coal mining enterprises. Furthermore, it also plays a role in affecting the scale, speed, results, and effectiveness of emergency response and rescue, as well as recovery and reconstruction in coal mining enterprises. Therefore, this paper takes advantage of response capability and service capability in order to measure the effectiveness of the integrated emergency response system of coal mining enterprises.

### 2.2. Construction of the Effectiveness Measurement Index System for the Integrated Emergency Response System for Coal Mine Water Hazard Accidents

With respect to effectiveness measurement of the integrated emergency response system for coal mine water hazard accidents, the number of indexes is not the only factor that matters; the applicability and appropriateness of measurement indexes also make a difference to the accuracy of the results. Therefore, in accordance with the principles of independence, scientificity, and data availability, as well as existing research results and suggestions from experts in the field of coal mine safety emergency response, this paper provides an in-depth analysis of the construction of the validity measurement index system based on the AHP methodology (Table 1) [40].

**Table 1.** Efficiency measurement index system of comprehensive emergency response system for coal mine water disaster accidents.

Target Layer	Criterion Layer	Sub-Criterion Layer	Index Level	AHP Weight	Entropy Method Weight	Combined Weight
Efficiency measurement index system of comprehensive emergency response system for coal mine flooding accident	B <sub>1</sub> Responsiveness	C <sub>1</sub> Accident information transmission	Hazard identification capability C <sub>11</sub>	0.0419	0.0378	0.03985
			Prediction ability of water exploration and release C <sub>12</sub>	0.0496	0.0541	0.05185
			Water damage cause analysis capacity C <sub>13</sub>	0.0463	0.0490	0.04765
			Accident information alarm capability C <sub>14</sub>	0.0371	0.0356	0.03635
			Accident information reporting ability C <sub>15</sub>	0.0325	0.0309	0.0317
		C <sub>2</sub> Emergency command and control	Accident identification and control handling capability C <sub>21</sub>	0.0341	0.0309	0.0325
			The emergency broadcast system is scientific C <sub>22</sub>	0.0301	0.0356	0.03285
			Emergency command authority activation capability C <sub>23</sub>	0.0445	0.0378	0.04115
			Disaster relief command and coordination ability C <sub>24</sub>	0.0381	0.0425	0.0403
			C <sub>3</sub> Emergency rescue and mitigation	Quality of rescue team C <sub>31</sub>	0.0474	0.0464
		Medical security level C <sub>32</sub>		0.0299	0.0464	0.03815
		Technical support C <sub>33</sub>		0.0315	0.0309	0.0312
		Security monitoring system running status C <sub>34</sub>		0.0464	0.0309	0.03865
		Video surveillance system running status C <sub>35</sub>		0.0303	0.0309	0.0306

Table 1. Cont.

Target Layer	Criterion Layer	Sub-Criterion Layer	Index Level	AHP Weight	Entropy Method Weight	Combined Weight
Efficiency measurement index system of comprehensive emergency response system for coal mine flooding accident	B <sub>2</sub> Service capability	C <sub>4</sub> Emergency management dimension	Safety input level of coal mine C <sub>41</sub>	0.0253	0.0253	0.0253
			Completeness of emergency response system C <sub>42</sub>	0.0253	0.0283	0.0268
			Perfection of emergency materials reserve management system C <sub>43</sub>	0.0253	0.0253	0.0253
			Framework of the responsibility system for preventing and controlling water C <sub>44</sub>	0.0283	0.0253	0.0268
			Contingency plan preparation, training, and exercise rationality C <sub>45</sub>	0.0283	0.0283	0.0283
		C <sub>5</sub> Personnel team dimension	Knowledge level of water damage accidents C <sub>51</sub>	0.0303	0.0283	0.0293
			Safety accident attitude concept C <sub>52</sub>	0.0407	0.0427	0.0417
			Code of conduct for work safety C <sub>53</sub>	0.0283	0.0283	0.0283
			Rationality of mine drainage system C <sub>61</sub>	0.0493	0.0483	0.0488
			Water safety training and warning education level C <sub>62</sub>	0.0387	0.0366	0.03765
		C <sub>6</sub> Prevention of preparation dimension	Emergency rescue equipment and materials level C <sub>63</sub>	0.0472	0.0503	0.04875
			Spatial accessibility of emergency supplies C <sub>64</sub>	0.0425	0.0412	0.04185
			Emergency response exercise and summary normative C <sub>65</sub>	0.0508	0.0521	0.05145

### 2.3. Determination of Combination Weights of the Effectiveness Measurement Indexes for Emergency Response System

#### 2.3.1. AHP Method for Determining Subjective Weights of Measurement Indexes

The subjective weights discussed in this paper are determined according to the following procedure.

Step 1: divide the selected and integrated measurement indexes into levels and construct a tree-shaped decision-making framework consisting of the “target-criterion”

layer, the “criterion-sub criterion” layer, and the “sub-criterion-index” layer (as exhibited in Table 1).

Step 2: Invite 25 experts in the field of coal mine water hazard accidents to compare the relative importance of the established indexes pairwise, according to the 1–9 scale method created by Schaty. According to the results, a judgment matrix  $F_1$  between adjacent levels is hereby constructed. This step is designed to make the subjective weights of indexes more convincing and credible.

Step 3: Based on the comparison results, figure out the relative importance of each index under established conditions and determine the judgment matrix of the “index-target” layer, and then work out the objective weights of each level. It is noteworthy that the concept of “established conditions” here refers to the relative importance of each index in the corresponding (sub) criterion layer (single hierarchical ranking) and in the target layer (total hierarchical ranking). Among them, relative importance can be converted to weight in light of the rule that the stronger the relative importance, the greater the corresponding weight.

Step 4: Consistency test. This means testing the logical rationality of the determined index weights. Following programming and calculation in MATLAB 2021, as well as continuous adjustment and correction of the judgment matrix, all matrices were subjected to the consistency test. The subjective weights of each index were also determined (as presented in Table 1).

### 2.3.2. Entropy Method for Determining Objective Weights of Measurement Indexes

The entropy method functions as an objective evaluation method, and its underlying rule is the greater the amount of information, the smaller the uncertainty, and the lower the entropy value, and vice versa [41,42]. The objective weights are determined on the strength of the standardized initial matrix  $E$ . This study adopts the “backward induction” method to calculate objective weights (Table 1). The specific calculation process is introduced here:

$$W_{E_j} = \frac{1 - e_j}{\sum_{j=1}^n (1 - e_j)} \quad (1)$$

where  $e_j$  is the entropy value of the influencing factor. Since the value of weight  $W$  depends on the proportion of the entropy value of the index, working out the entropy value of the index is a must, which can be counted by the equation below:

$$e_j = -\frac{1}{\ln m} \sum_{i=1}^m Q_{ij} \times \ln Q_{ij} \quad (2)$$

where  $Q_{ij}$  is the proportion of the index, and it can be expressed as:

$$Q_{ij} = \frac{E_{ij}}{\sum_{i=1}^m E_{ij}}, Q_{ij} \in [0, 1] \quad (3)$$

where  $E_{ij}$  is the term of the standard matrix.

### 2.3.3. AHP and Entropy Methods for Determining Combination Weights by Establishing a Combination Weighting Model

The AHP method determines weights by means of comparing the preferences and importance of every two indexes, usually adopting a 1–9 scale. Differently, the determination of objective weights through the entropy method relies on calculating the entropy value of the collected data. The key to AHP is quantifying human subjective judgments, so that the index weights determined by AHP are more subjective, while the entropy method puts greater emphasis on the quantitative calculation of the data. Consequently, the index

weights determined by the entropy method fail to reflect which index the evaluator prefers. Even worse, the results may contradict the actual situation.

In summary, this paper adopts both AHP and entropy methods for combination weighting, effectively minimizing subjective influence and objective data defects, and enhancing the scientificity and rationality of the index weight values. In addition, the Lagrangian function, based on the AHP and entropy methods for weights, was also introduced to facilitate the construction of the decision model, and the Euclidean distance function was employed to construct the relationship equation between subjective and objective weights and preference coefficients. With these measures, the optimal combination weight comes into being [42].

The decision model can be represented as:

$$\begin{cases} W_j = \beta W_{Aj} + \lambda W_{Bj} \\ \beta + \lambda = 1 \end{cases} \quad (4)$$

where  $W_{Aj}$  is the subjective weight;  $W_{Bj}$  is the objective weight;  $\beta$  and  $\lambda$  are preference coefficients for the subjective and objective weights.

The Euclidean distance can be calculated as follows:

$$\begin{cases} M(W_{Aj} - W_{Bj}) = \sqrt{\sum_{j=1}^n (W_{Aj} - W_{Bj})^2} \\ M(W_{Aj} - W_{Bj})^2 = (\beta - \lambda)^2 \end{cases} \quad (5)$$

#### 2.4. Grading of Emergency Response System Effectiveness for Coal Mine Water Hazard Accidents

Based on the connotation of the effectiveness of the emergency response system in coal mining enterprises, this paper considers the measurement variable value range of the effectiveness of the emergency response system in coal mining enterprises as  $[0, 1]$ . In light of the standard of the five-level evaluation method, as well as suggestions from experts in the field of emergency response to coal mine water hazard accidents, the emergency response capacity of coal mining enterprises for water hazard accidents falls into five levels (Table 2).

**Table 2.** Standard set of efficiency classification of emergency response system in coal mine enterprises.

Evaluation Level	Rank Scale	Equal Efficiency Score Interval
optimal	I	(0.9, 1.0]
good	II	(0.8, 0.9]
normal	III	(0.7, 0.8]
range	IV	(0.6, 0.7]
Very bad	V	[0, 0.6]

### 3. Construction of a Fuzzy Evaluation Model for the Effectiveness of Integrated Emergency Response System for Coal Mine Water Hazard Accidents

#### 3.1. Establishment of a Dimensionless Original Data Matrix

As previously discussed, the measurement model constructed in this paper utilizes multiple indexes for comprehensive evaluation. For this reason, to eliminate the influence of diversity from evaluation indexes with different dimensions and orders of magnitude, the first step is to standardize the original data. Only in this way can the reliability of the results be enhanced. The specific standardization steps are as follows:

Step 1: Store the original data in the form of a spatial matrix and accordingly establish a spatial matrix  $D$ . Among them, each row represents a coal mine, and each column stands for an index. That is, matrix  $D$  is composed of  $m$  coal mines and  $n$  indexes;

Step 2: Standardize the data (dimensionless processing);



Step 3: Output a new matrix  $E$ , which serves as the source data for subsequent measurement.

The expression of the matrix is:

$$D = [D_{ij}]_{m \times n}; i = 1, 2, 3, \dots, m; j = 1, 2, 3, \dots, n \quad (6)$$

The calculation formula for standardized processing in Step 2 is as follows:

The formula for standardizing positive indexes:

$$E_{ij} = \frac{C_{ij} - \min(C_j)}{\max(C_j) - \min(C_j)} \quad (7)$$

The formula for standardizing negative indexes:

$$E_{ij} = \frac{\max(C_j) - C_{ij}}{\max(C_j) - \min(C_j)} \quad (8)$$

The output new matrix  $E$  can be represented as:

$$E = [E_{ij}]_{m \times n}; i = 1, 2, 3, \dots, m; j = 1, 2, 3, \dots, n \quad (9)$$

### 3.2. Calculation of the TOPSIS Model

The technique for order preference by similarity to ideal solution (TOPSIS) method [43], which is commonly used in the multi-objective analysis of practical solutions in systems engineering, has been extensively applied in numerous fields. The basic idea behind this method is that the positive and negative ideals of the final solution form a space based on a normalized initial data matrix, and the evaluated solution is regarded as a point in this space. By calculating the distance between this point and the positive and negative ideal solution, the relative closeness,  $d_i$ , between the evaluated scheme and the positive or negative ideal scheme can be deduced, and the effectiveness of the scheme can therefore be realized.

Single index evaluation: supposing that the weight distributed to indexes in  $C_x$  is  $Q$ , and that  $L$  is the single index evaluation matrix of  $C_x$ , then

$$K_i = Q \cdot L = (k_1, k_2, \dots, k_y) \quad (10)$$

where  $K_i$  is the evaluation result of a single index in  $C_x$ .

Multi-index sequential evaluation: since indexes to be evaluated in this study are great in number, this paper adopts a calculation scheme of deriving evaluation results step by step by dividing them into different levels. The dominating evaluation principle is to determine the evaluation matrix of the index layer, the single, and the total ranking of the levels, and to conduct a comprehensive evaluation of each level using the "onion peeling" method.

Finally, the evaluation results are standardized to obtain the final scores of each evaluation object.

$$K'_i = \frac{K_i - \min(K_i)}{\max(K_i) - \min(K_i)} \quad (11)$$

## 4. Empirical Analysis on Coal Mines

On the grounds of factors like type of work, type of enterprise, and safety production standardization level, research samples are selected from four primary coal mines: Jiulishan Coal Mine, Guhanshan Coal Mine, Zhaogu No.1 Coal Mine, and Zhaogu No. 2 Coal Mine, and one secondary coal mine, i.e., Zhongmachun Coal Mine. These five coal mines, which are located in Jiaozuo City, Henan Province, Chiam, are chosen as the research objects for this study. Targeting safety management personnel, mine water prevention and control

professionals, general practitioners, and other workers, extensive research was conducted. In addition, the effectiveness measurement index system and model of the emergency response system for water hazard accidents in coal mining enterprises constructed in this paper are adopted to empirically evaluate the five coal mines. Based on the results, the rationality of the theoretical model is further verified. This practice enjoys strong practical implications.

#### 4.1. Data Source and Processing

The survey method adopted in this paper is questionnaire retention and collection, and the samples are collected from the five coal mines mentioned above. From September to October 2023, a total of 190 questionnaires were distributed on safety training sites, and 185 were collected back, among which 183 questionnaires were valid. Therefore, the response rate is 97.37%, and the effective response rate is 96.32% (Table 3).

**Table 3.** Statistical table of questionnaire data.

Number of Copies Issued	Recycled Copies	Recovery	Effective Copies	Effective Recovery
190	185	97.37%	183	96.32%

#### 4.2. Questionnaire Reliability and Validity Test

An analysis on the reliability of the overall questionnaire reveals that  $\alpha = 0.987$ , greater than 0.9. The reliability analysis is also performed to target accident information transmission, emergency command and control, emergency rescue and mitigation, emergency management, personnel team, and prevention and preparation. The calculated  $\alpha$  reads 0.906, 0.954, 0.944, 0.971, 0.917, and 0.978, respectively (Table 4), all exceeding 0.9, indicating that the questionnaire is highly consistent and valid.

**Table 4.** Questionnaire reliability analysis table.

Variable (Layer/Level)	Kronbach Coefficient	Item
Accident information transfer	0.906	5
Emergency command and control	0.954	4
Emergency rescue and mitigation	0.944	5
Emergency management dimension	0.971	5
Personnel team dimension	0.917	3
Preventive preparedness dimension	0.978	5
Overall questionnaire	0.987	27

The scale section of the questionnaire is subjected to KMO and Bartlett's tests. The results presented in Table 5 suggest that KMO values of both the total scale and various sub-scales are all greater than 0.7, with no significant difference (less than 0.05). That is, the questionnaire scale section turns out to be applicable for exploratory factor analysis.

**Table 5.** KMO and Bartlett test tables.

Variable (Layer/Level)	KMO		Bartlett Sphericity Test	
	Exponent	Approximate Chi-Square	Degree of Freedom	Significance
Accident information transfer	0.755	242.547	10	0.000
Emergency command and control	0.818	298.787	6	0.000
Emergency rescue and mitigation	0.826	203.129	5	0.000
Emergency management dimension	0.754	201.075	10	0.000
Personnel team dimension	0.712	150.939	3	0.000
Preventive preparedness dimension	0.844	584.668	10	0.000

### 4.3. Result Analysis

#### 4.3.1. Scores-Based Comprehensive Evaluation

The TOPSIS method is employed to comprehensively evaluate the five coal mines, and the comprehensive evaluation and ranking results are given in Table 6.

**Table 6.** Efficiency measurement of emergency response system for water disaster.

Symbol	Comprehensive Integral	Positive Ideal Solution Distance	Negative Ideal Solution Distance	Relative Proximity	Sort Result
A	78.78	7.544	0.000	0.000	5
B	81.31	3.960	3.584	0.475	2
C	80.02	0.000	7.544	1.000	3
D	84.12	5.790	1.754	0.232	1
E	79.64	6.329	1.216	0.161	4

Where A, B, C, D, and E, respectively, represent Guhanshan Mine, Jiulishan Mine, Zhaogu No. 2 Mine, Zhaogu No. 1 Mine, and Zhongmacun Mine.

It is evident in Table 6 that the comprehensive scores of the emergency response systems for water hazard accidents in the five coal mines are all above 75. Among them, the comprehensive score of the D Coal Mine ranks highest (84.12), while the A Coal Mine comes in last (78.78). By calculation, the average comprehensive score of the five coal mines is 80.77, and the standard deviation is 1.86. These values somewhat reflect that the emergency response ability for coal mine water hazard accidents in Jiaozuo is rated as “good”. Apart from the above efforts, the effectiveness of the emergency response system for coal mine water hazard accidents is also investigated from the perspective of the ownership of mines. After calculation, the following results are obtained:

- (1) the average comprehensive score of the A Coal Mine, B Coal Mine, and E Coal Mine, which belong to the Coking Coal Group, is 79.91, with a standard deviation of 1.05;
- (2) that of the C Coal Mine and D Coal Mine, which are members of Henan Coal Chemical Group, is 82.07, with a standard deviation of 2.05.

These figures disclose that the effectiveness of the emergency response system for water hazard accidents in the coal mines under the Coking Coal Group is slightly lower than that of the coal mines under the Henan Coal Chemical Group. Nevertheless, in terms of the differences in the effectiveness of the emergency response system for water hazard accidents among coal mines owned by them, the Coking Coal Group witnesses less difference. In summary, coal mines under the Coking Coal Group boast more sufficient ability for coordinated development than those attached to the Henan Coal Chemical Group.

The two indexes on the criterion level of the five coal mines include response capability  $B_1$  and service capability  $B_2$ , and their measurement scores and comparison can be found in Figure 1.

Figure 1 gives a clear message that the response and service capabilities of the emergency response systems for water hazard accidents in the five coal mines all exceed 75. Among them, the response and service capabilities of the emergency response system for water hazard accidents in the D Coal Mine are evaluated as “good”. It is also the only mine among the five coal mines whose  $B_1$  and  $B_2$  scores reach 80 or above. Hence, other coal mines are highly recommended in order to learn from their construction experience, identify, and fill in gaps, in the hope of improving the effectiveness of the emergency response system. In addition, it is also revealed that the service capacity  $B_2$  score of the C Coal Mine is relatively weak, which means obvious weak links exist in one or more dimensions, such as emergency management, staff allocation, and prevention preparation. For the A Coal Mine, its response capability  $B_1$  score is relatively poor, which is reflected in one or more aspects of accident information transmission, emergency command and control, and emergency rescue and mitigation.

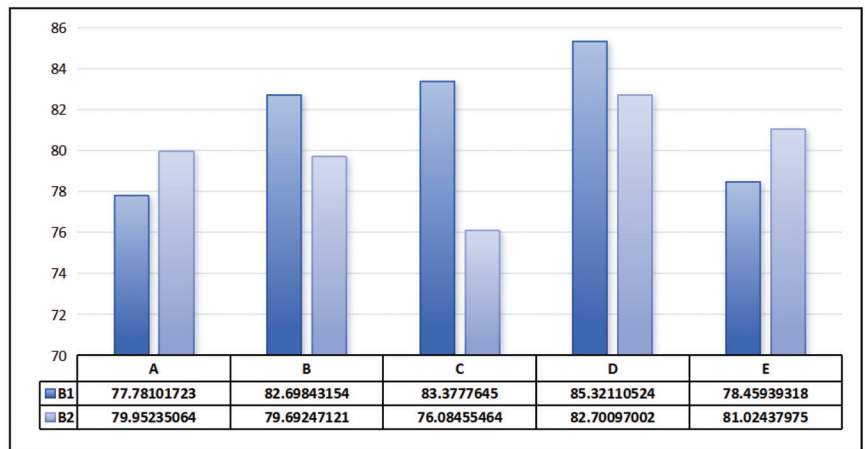


Figure 1. Statistical chart of index measurement scores at the criterion level.

The six indexes at the sub-criterion level of the five coal mines are made up of accident information transmission, emergency command and control, emergency rescue and mitigation, emergency management, personnel team, as well as prevention and preparation. The measurement scores and comparison are presented in Figure 2.

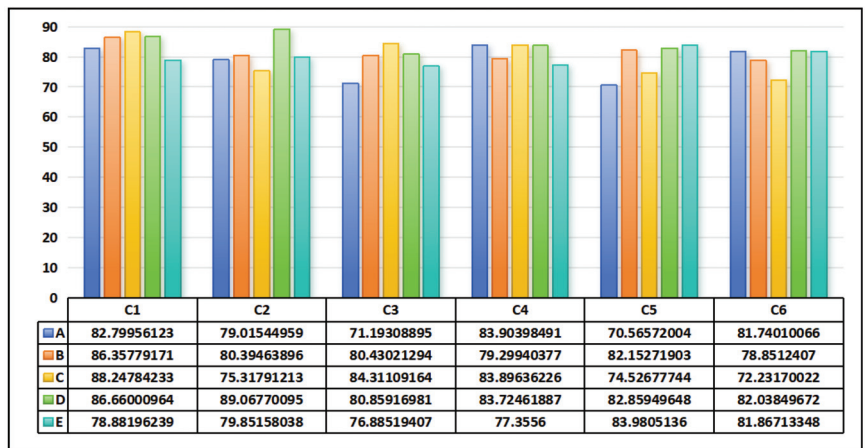


Figure 2. Statistical chart of index measure score of sub-criteria layer.

Based on the data shown in Figure 2, it is apparent that the six indexes at the sub-criterion level of the emergency response systems for water hazard accidents in the five coal mines are all rated above 75. Among them, the average scores of C<sub>1</sub>~C<sub>6</sub> are 84.59, 80.73, 78.74, 81.64, 78.82, and 79.35, respectively, all of which are greater than 75. However, it is noteworthy that the average scores of C<sub>3</sub>, C<sub>5</sub>, and C<sub>6</sub> are less than 80, indicating that the development of the emergency response system for coal mine water hazard accidents lags behind on emergency rescue and mitigation, personnel team, as well as prevention and preparation. It is urgent for each coal mine to identify deficiencies and accelerate construction.

The effectiveness scores and ranking results after the standardization of the criterion and sub-criterion layers are counted and displayed in Table 7.

**Table 7.** Evaluation results of criterion level and sub-criterion level of water disaster emergency response system effectiveness measurement.

Symbol	Responsiveness B <sub>1</sub>	Ranking	Symbol	Service Capability B <sub>2</sub>	Ranking
A	0	5	A	0.58457	3
B	0.65216	3	B	0.54529	4
C	0.74226	2	C	0	5
D	1	1	D	1	1
E	0.08996	4	E	0.74660	2
Symbol	Accident Information Transmission C <sub>1</sub>	Ranking	Symbol	Emergency Command and Control C <sub>2</sub>	Ranking
A	0.41828	4	A	0.26892	4
B	0.79819	3	B	0.36922	2
C	1	1	C	0	5
D	0.83046	2	D	1	1
E	0	5	E	0.32973	3
Symbol	Emergency Rescue and Mitigation C <sub>3</sub>	Ranking	Symbol	Emergency Management C <sub>4</sub>	Ranking
A	0	5	A	1	1
B	0.70415	3	B	0.29683	4
C	1	1	C	0.99883	2
D	0.73658	2	D	0.97260	3
E	0.43391	4	E	0	5
Symbol	Personnel Team C <sub>5</sub>	Ranking	Symbol	Prevention of Preparation C <sub>6</sub>	Ranking
A	0	5	A	0.96957	3
B	0.86374	3	B	0.67499	4
C	0.29527	4	C	0	5
D	0.91643	2	D	1	1
E	1	1	E	0.98252	2

Frequency statistics are performed on the data in Table 7, and the results reveal that the highest score of a single criterion or dimension appears twice in the C Coal Mine and D Coal Mine, contributing them to rank first. Furthermore, the A Coal Mine comes out number one in emergency management, and E is in first place in the personnel team. Based on this difference, it is revealed that the five coal mines involved in this paper have their own strengths in the development of emergency response systems for water hazard accidents. As a consequence, it is highly desirable that every coal mine can enhance its accident emergency response capabilities on the basis of the actual situation, together with typical experience and practices.

#### 4.3.2. Determination of Effectiveness Scores and Evaluation of Capability Grades

The calculated comprehensive scores of the emergency response systems for water hazard accidents of the five coal mines are scaled to the range of [0, 1] and graded according to effectiveness levels for emergency response systems of coal mining enterprises in Table 2. These practices aim to identify the corresponding capabilities of the five coal mines (Table 8).

The effectiveness of emergency response systems for water hazard accidents in five coal mines is evaluated comprehensively with a view to identifying their existing weaknesses in emergency response. Furthermore, this paper provides ideas for how to make up for these weaknesses in the hope of urging these coal mines to augment their overall emergency response capabilities.

**Table 8.** Evaluation table of each dimension index grade of system measurement of coal mine flooding accident.

Water Hazard Accidents Emergency Response System Effectiveness (A)						
Symbol					Lv.	
	A		0.7878		normal	
	B		0.8131		good	
	C		0.8002		good	
	D		0.8412		good	
	E		0.7964		normal	
Symbol	Responsiveness B <sub>1</sub>	Lv.	Symbol	Service Capability B <sub>2</sub>	Lv.	
	A	0.7778	normal	A	0.7995	normal
	B	0.8270	good	B	0.7969	normal
	C	0.8532	good	C	0.8270	good
	D	0.8338	good	D	0.7608	normal
	E	78.50	normal	E	0.8102	good
Symbol	Information Transmission C <sub>1</sub>	Lv.	Symbol	Command and Control C <sub>2</sub>	Lv.	
	A	0.8280	good	A	0.7902	normal
	B	0.8636	good	B	0.8039	good
	C	0.8666	good	C	0.8907	good
	D	0.8825	good	D	0.7532	normal
	E	0.7888	normal	E	0.7985	normal
Symbol	Rescue and Mitigation C <sub>3</sub>	Lv.	Symbol	Emergency Management C <sub>4</sub>	Lv.	
	A	0.7419	normal	A	0.8390	good
	B	0.8043	good	B	0.7930	normal
	C	0.8086	good	C	0.8372	good
	D	0.8431	good	D	0.8390	good
	E	0.7689	normal	E	0.7736	normal
Symbol	Personnel Team C <sub>5</sub>	Lv.	Symbol	Prevention of Preparation C <sub>6</sub>	Lv.	
	A	0.7057	normal	A	0.8174	good
	B	0.8215	good	B	0.7885	normal
	C	0.8286	normal	C	0.8204	good
	D	0.7453	good	D	0.7223	normal
	E	0.8398	good	E	0.8187	good

## 5. Conclusions

This paper mainly takes the emergency response ability of coal mine water disaster accidents as the research object. By constructing a comprehensive emergency response evaluation system of coal mine water disaster accidents, the response efficiency of the emergency response system of coal mine enterprises is tested and evaluated, with a view to promote coal mine enterprises in order to improve their own emergency response ability of accidents and disasters and provide references for safe and efficient coal mining and water disaster prevention and management. Firstly, according to the research status at home and abroad, collect data and read a lot of the relevant literature in order to elaborate the characteristics and trends of the current research on water damage in coal mines. Secondly, according to the influencing factors of coal mine water disaster accidents, the literature, and expert suggestions, the evaluation indicators are screened and improved, and the final evaluation index system of coal mine water disaster emergency response efficiency is obtained. Thirdly, the subjective and objective combination weighting model is established by the AHP+ entropy method in order to determine the index weight, and the TOPSIS fuzzy

comprehensive evaluation model is derived based on the fuzzy comprehensive evaluation model. Finally, five coal mines under the Coking Coal Group were selected for example analysis, focusing on the evaluation and optimization of the emergency response ability of coal mine water disasters. The main conclusions are as follows:

- (1) The efficiency measurement index system of the comprehensive emergency response system for coal mine water disaster accidents can be divided into two parts: normal emergency service capacity and non-normal emergency response capacity, and is then detailed into six secondary indexes, including accident information transmission, emergency command and control, emergency rescue and mitigation, emergency management dimension, personnel team dimension, and prevention and preparedness dimension. It is further divided into 27 three-level indexes, which can avoid the general concept of coal mine accidents and make the evaluation more targeted.
- (2) AHP method and entropy method are used to combine and empower the measurement indicators of the emergency response system of water disaster accidents in coal mine enterprises. TOPSIS evaluation model is introduced to build a comprehensive evaluation model of the emergency response ability of water disaster accidents in coal mine enterprises, which avoids too strong subjective thoughts and too simple methods, and enriches the evaluation methods of coal mine accident emergency response ability.
- (3) Taking five coal mines under Henan Coking Coal Group as examples, the empirical evaluation of water disaster emergency response system was carried out. According to the evaluation results, the comprehensive evaluation of water disaster emergency response system efficiency of Guhanshan Mine and Zhongma Cun Mine was in "average", while the comprehensive evaluation of water disaster emergency response system efficiency of Jiulishan Mine, Zhaogu No.1 Mine and Zhaogu II mine was in "good". The evaluation results are consistent with the actual situation, indicating that the evaluation model constructed in this paper has good practical significance, can evaluate the efficiency of the emergency response system of water disaster accidents in coal mines scientifically and effectively and provide a new way to improve the efficiency evaluation of the emergency response system of water disaster accidents in coal mines.
- (4) To comprehensively evaluate the effectiveness of the emergency response system for water disaster accidents in five coal mines, with the purpose of finding out the deficiencies in the emergency response for water disaster accidents, and taking corresponding rectification measures to improve their overall emergency response capability. Of course, this paper also has some limitations. First of all, there are many factors affecting the emergency response efficiency of coal mine water disaster accidents, so how to scientifically and reasonably select the evaluation index needs further in-depth research. Secondly, there are many evaluation methods for coal mine emergency response capability, and more excellent evaluation methods should be combined. In the future, a more perfect and reasonable evaluation model should be built to continuously optimize and improve.

## 6. Discussion

Based on the evaluation of the efficacy of the emergency response system for five coal mine water accidents, this paper discusses the following recommendations for rectification:

- (1) In the area of accident information transmission, the coal mine water hazard accident source management should be strengthened as far as possible in order to reduce the probability of accidents. Starting from upgrading their abilities to identify hazards, coal mines are encouraged to focus on strengthening their capabilities of predicting water detection and release, as well as on sourcing the causes of water hazard accident, with a view to refining technologies on accident prediction and early warning, reporting accident information more timely, and ensuring the smooth transmission of accident information continuously and effectively. To increase collaboration with

meteorological, water conservancy, flood prevention, and other departments, establish a disaster weather warning and prevention mechanism, pay close attention to the warning information of disaster weather forecasting, timely grasp information on heavy rainfall and flood hazards that may jeopardize the production of coal mines, and take safety precautions. In the meantime, it is also necessary to strengthen information communication with adjacent mines in the surrounding area, when it is found that the water damage of the mine may affect the adjacent mine, an immediate warning is issued to the adjacent mine.

- (2) In the emergency command and control, coal mining enterprises are advised to deepen the multidimensional efforts concept and the integrated establishment of water hazard accident underground personnel timely evacuation systems. Greater efforts should be made to enhance the emergency command and control quality of the coal mine personnel, and accelerate the design of scientific and reasonable emergency broadcasting systems. Coal mining should vigorously carry out accident drills, take advantage of safety training, and exchange learning and other opportunities in order to standardize the process steps, such as accident identification and control, emergency command agency activation, disaster relief command coordination, clear start-up criteria, and command departing.
- (3) In the emergency relief and mitigation, one should adhere to the “fast, effective, detract” course of action, committed to creating a skilled, rapid action rescue team. With the emphasis of building special and combined emergency rescue teams, set up emergency material reserves and infrastructure emergency temporary deployment points, master rescue technology and equipment, and optimize the current rescue plan. Water damage in coal mines may cause secondary disasters, such as secondary water burst and toxic and harmful gas leakages. Therefore, rescue programs should be systematically built with expert guidance. Perform accident emergency rescue and mitigation work need to pay attention to the combination of peace and war. In other words, the capacity-building of emergency services and the capacity of emergency responses should be both enhanced. What calls for special attention is the operational status of the security monitoring system and the video monitoring system, both of which play an irreplaceable role in guaranteeing the scientificity and effectiveness of emergency rescue and mitigation.
- (4) In the emergency management dimension, the emergency response capacity of coal mine water accident mainly depends on the frequency of emergency drills, the scientific nature of emergency preparedness planning and modification drills, the completeness of various systems at all levels, and the proficiency of personnel cooperation. It is recommended that coal mining enterprises organize special drills for water hazards in accordance with the provisions of the “Regulations on Water Prevention and Control” [44] in order to improve the proficiency of material deployment and personnel coordination. Coal mining enterprises are supposed to invest more funds in safety technology based on their actual situation, and establish and optimize management systems of different levels including emergency response systems for water hazard accidents, emergency material reserve management systems, responsibility systems for preventing and controlling water hazard accidents, and water disaster investigation and treatment systems. Besides, it is a must to clarify the responsibilities of the personnel involved with the intention of greatly avoiding disorderly and inefficient emergency response.
- (5) In the personnel dimension, coal mining enterprises are expected to increase their knowledge concerning water hazard accidents, clarify a concept of safe development, standardize daily production, and commit themselves to creating a sound situation featuring unified knowledge, belief, and actions for all employees. Set up incentive mechanisms of reward and punishment: employ punishment mechanisms to strengthen the knowledge and skills of personnel in water hazard accidents, and use rewards to inspire employees to learn. At the same time, strengthen the construction



- of enterprise safety cultures, cultivate the internal safety motivation of employees, and create a good production safety atmosphere.
- (6) In the prevention preparedness dimension, coal mining enterprises should strengthen ties with universities and scientific research institutes, update existing drainage and drainage technology equipment, introduce advanced equipment for mining, monitoring, warning, etc., actively introduce geophysical satellite systems to monitor groundwater flows, and deploy seismic sensors to detect underground bumps. In order to judge groundwater flow and verify the rationality of mine drainage systems, and to improve the graded control ability of underground water hazard risk, all-round improvement of the coal mine water accident detection system and early warning capabilities are desired.

**Author Contributions:** Conceptualization, Y.H.; methodology, Y.H.; validation, H.Y.; resources, H.Y.; data curation, C.S. and L.Z.; writing—original draft preparation, Y.H.; writing—review and editing, H.Y.; supervision, C.S. and L.Z. All authors have read and agreed to the published version of the manuscript.

**Funding:** This research is funded by the National Natural Science Foundation of China (NSFC) (52374196), the Strategic Research and Consulting Project of the Chinese Academy of Sciences (2023HENZDB05), the Philosophy and Social Science Innovation Team of Colleges in Henan Province (2023-CXTD-06), and the Humanities and Social Sciences Foundation of Henan Polytechnic University (SKYJ2021-01).

**Data Availability Statement:** The data used to support the findings of this study are available from the first author or corresponding author upon request.

**Conflicts of Interest:** The authors declare that they have no conflicts of interest with respect to the research, authorship, and/or publication of this article.

## References

- National Development and Reform Commission. *Coal Industry Development “13th Five-Year Plan”*; National Energy Administration: Beijing, China, 2016. Available online: [http://www.nea.gov.cn/2016-12/30/c\\_135944439.htm](http://www.nea.gov.cn/2016-12/30/c_135944439.htm) (accessed on 30 December 2016).
- Ge, L.T.; Ye, G.J.; Gang, H.L. *Hydrogeology of Coal Fields in China*; Coal Industry Press: Beijing, China, 2001; pp. 1–12.
- Wang, H.; Liu, B. *Control Technology of Mine Water Damage*; Coal Industry Press: Beijing, China, 2007; pp. 90–127.
- Zeng, Y.; Wu, Q.; Zhao, S.; Miao, Y.W.; Zhang, Y.; Mei, A.S.; Meng, S.H.; Liu, X.X. Characteristics, causes, and prevention measures of coal mine water hazard accidents in China. *Coal Sci. Technol.* **2023**, *51*, 1–14.
- David, T. Rock fracture spacings, openings, and porosities. *J. Soil Mech. Found. Div.* **1968**, *94*, 73–91. [CrossRef]
- Louis, C. Groundwater flow in rock masses and its influence on stability. *Rock Mech. Res.* **1969**.
- Meng, S.; Gao, Y.; Lu, A.H. *Theory and Method of Mine Water Inrush Risk Assessment*; Science Press: Beijing, China, 2001; pp. 74–77.
- Kong, H.L.; Miao, X.X.; Wang, L.Z.; Zhang, Y.; Chen, Z.Q. Analysis of the harmfulness of water-inrush from coal seam floor based on seepage instability theory. *J. China Univ. Min. Technol.* **2007**, *17*, 453–458. [CrossRef]
- Vutukuri, V.S.; Singh, R.N. Mine inundation-case histories. *Mine Water Environ.* **1994**, *14*, 107–130. [CrossRef]
- Yan, Z.; Zhang, H.; Du, P. Application of SVM in analyzing the headstream of gushing water in coal mine. *J. China Univ. Min. Technol.* **2006**, *16*, 433–438. [CrossRef]
- Wang, S. Research on construction of theoretical model of coal mine accident cause. *Coal Sci. Technol.* **2007**, *12*, 106–108. [CrossRef]
- Zhang, Z.L.; Gao, Y.; Wu, Q.; Wei, S.M. Technical system of three-dimensional control of mine water damage. *J. China Coal Soc.* **2013**, *38*, 378–383. [CrossRef]
- Zhao, B.F. Control of mine water disaster based on MATLAB fuzzy clustering analysis. *Coal Sci. Technol.* **2013**, *41*, 89–92. [CrossRef]
- Miao, Y.W.; Ye, L. Analysis and prevention countermeasures of coal mine water disaster in China in 2020. *China Coal* **2021**, *47*, 51–54.
- Sun, W.J.; Han, Q.; Li, S.Q. Analysis on water inrush accidents in China’s coal mines 2000–2015. *Coal Eng.* **2017**, *49*, 95–98.
- Wei, J.C.; Xiao, L.L.; Niu, C.; Yin, H.Y.; Shi, L.Q.; Han, J.; Duan, F.T. Characteristics analysis of the correlation factors of China mine water hazard accidents in 2001–2013. *China Sci.* **2015**, *10*, 336–341.
- Yin, S.X.; Wang, Y.; Li, W. Cause, countermeasures and solutions of water hazards in coal mines in China. *Coal Geol. Explor.* **2023**, *51*, 20.
- Zhang, P.; Li, F.; Zhu, H.; Niu, H.; Li, X. Statistical analysis and prevention countermeasures of coal mine accidents from 2008 to 2020. *Min. Saf. Environ. Prot.* **2022**, *49*, 128–134.
- Bascetin, A.; Adiguzel, D.; Eker, H.; Tuylu, S. The investigation of geochemical and geomechanical properties in surface paste disposal by pilot-scale tests. *Int. J. Min. Reclam. Environ.* **2022**, *36*, 537–551. [CrossRef]

20. Jia, X.; He, R.M.; Yao, H. Study on law of mining-induced surface crack affected to surface water in Shendong Mining Area. *Coal Sci. Technol.* **2017**, *45*, 17–22.
21. Lu, Z.; Guo, Y.N.; Li, G.Q.; Wang, L.; Li, F.Z.; Zhang, Z. Water quality and health risk of surface water, groundwater and mine water in Shendong mining area. *Saf. Environ. Eng.* **2023**, *30*, 222–234. [CrossRef]
22. Li, Q.M.; Zhai, L.J.; Fu, Y.J.; Ma, X.F.; Tang, Y.B.; Li, J.Y.; Li, H.; Meng, Y.P.; Ma, Y.L. A Study on Coal Mining Aquifer Destruction Mode in North China Typed Coalfields. *Coal Geol. China* **2012**, *24*, 38–43. [CrossRef]
23. Cao, Z.G.; He, R.M.; Wang, X.F. Coal Mining Affected to Underground Water and Underground Water Storage and Utilization Technology. *Coal Sci. Technol.* **2014**, *42*, 113–116+128. [CrossRef]
24. Ning, J.H.; Jia, X.R. Discussion on Working Grade Determination Method for Environmental Impact Assessment of Groundwater in Coal Mine area. *Coal Geol. Explor.* **2004**, *32*, 153–154. [CrossRef]
25. Fan, L.M.; Kou, G.D.; Jiang, Z.Q.; Wang, Z.Z. The variation law of groundwater flow field during the mining process of shallow buried coal seam. *Shaanxi Coal* **2003**, *1*, 26–28.
26. Dong, S.N.; Hu, W.Y. Basic characteristics and main controlling factors of coal mine water hazard in China. *Coal Geol. Explor.* **2007**, *5*, 34–38.
27. Wu, Q.; Shen, J.J.; Wang, Y. Mining techniques and engineering application for “Coal-Walter” dual-resources mine. *J. China Coal Soc.* **2017**, *42*, 8–16. [CrossRef]
28. Wang, S.M.; Huang, Q.X.; Fan, L.M.; Yang, Z.Y.; Shen, T. Study on overburden aquiclude and water protection mining regionization in the ecological fragile mining area. *J. China Coal Soc.* **2010**, *35*, 7–14. [CrossRef]
29. Zhao, P.M.; Guo, Q.L. Experimental research on the permeability of high-rank coal under a varying stress and its influencing factors. *Int. J. Coal Geol.* **2013**, *162*, 108–117. [CrossRef]
30. Dong, S.Z.; Gang, W.F.; Yu, D.L.; Li, Q.M. Field trials of aquifer protection in longwall mining of shallow coal seams in China. *Int. J. Rock. Mech. Min.* **2010**, *47*, 908–914. [CrossRef]
31. Qiang, S.; Ji, X.Z.; Nan, Z. Study and discussion of short-strip coal pillar recovery with cemented paste backfill. *Int. J. Rock. Mech. Min.* **2018**, *104*, 147–155. [CrossRef]
32. Zhen, H.; Zhen, Q.J.; Shu, Y.Z.; Zi, W.Q.; Ding, T.C. Characterizing the hydraulic conductivity of rock formations between deep coal and aquifers. *Int. J. Rock. Mech. Min.* **2014**, *71*, 12–18. [CrossRef]
33. Hua, G.; Liang, Y.; Bao, T.S.; Qing, D.Q.; Jun, H.X. Mining-induced strata stress changes, fractures and gas flow dynamics in multi-seam longwall mining. *Int. J. Rock. Mech. Min.* **2012**, *54*, 129–139. [CrossRef]
34. Zhang, Q.; Zhang, H.T.; Guo, L.; Du, P.Y.; Li, L.W.; Li, R.J.; Tang, X.F. Spatial distribution of soil heavy metal Cu content using Cokriging interpolation model combined with principal component analysis. *J. Huazhong Agric. Univ.* **2016**, *35*, 60–69. [CrossRef]
35. Zhang, G.F.; Yang, L.R.; QU, M.K.; Chen, H.L. Interpolation of daily mean temperature by using geographically weighted regression-Kriging. *Chin. J. Appl. Ecol.* **2015**, *26*, 1531–1535. [CrossRef]
36. Hu, W.Y. Water inflows prediction technique of water inflow from roof aquifer during extraction of shallow seam. *Coal Geol. Explor.* **2016**, *44*, 91–96. [CrossRef]
37. Tie, L.; Ting, T.M.; Xue, H.S.; Yu, G.L.; Ji, Q.S.; Ming, C. A study on a water-inrush incident at Laohutai coalmine. *Int. J. Rock. Mech. Min.* **2013**, *59*, 151–159. [CrossRef]
38. Gao, L.; Wu, Q.; Li, Y.; Ding, D.; Hao, Y.; Cui, Y.; Sun, H. How prepared are hospitals’ emergency management capacity? Factors influencing efficiency of disaster rescue. *Disaster Med. Public Health Prep.* **2018**, *12*, 176–183. [CrossRef] [PubMed]
39. Guo, Y.; Zhang, S.; Zhang, Z.; Meng, Q. Estimating Added Values of the Integrated Emergency Response System for Airport Accident: Improved Responsiveness and Increased Service Capacity. *Math. Probl. Eng.* **2018**, *2018*, 3960242. [CrossRef]
40. Ordu, M.; Der, O. Polymeric Materials Selection for Flexible Pulsating Heat Pipe Manufacturing Using a Comparative Hybrid MCDM Approach. *Polymers* **2023**, *15*, 2933. [CrossRef]
41. Zhou, Q.C.; Zhang, H.Q.; Jiao, Y.; Yu, B.; Guo, J. Evaluation of the risk of water inrush from coal roof based on combination weighting method. *Sci. Technol. Eng.* **2022**, *22*, 3497–3503.
42. Chen, G.B.; Teng, P.C.; Li, T.; Wang, C.Y.; Chen, S.J.; Zhang, G.H. Evaluation model of rock burst in coal mine and its application. *J. Taiyuan Univ. Technol.* **2021**, *52*, 966–973.
43. Kumar, A.; Sah, B.; Singh, A.R.; Deng, Y.; He, X.; Kumar, P.; Bansal, R.C. A review of multi criteria decision making (MCDM) towards sustainable renewable energy development. *Renew. Sust. Energy. Rev.* **2017**, *69*, 596–609. [CrossRef]
44. The Central People’s Government of the People’s Republic of China. Rules on Water Control in Coal Mines. 2018. Available online: [https://www.gov.cn/zhengce/zhengceku/2018-12/31/content\\_5448431.htm](https://www.gov.cn/zhengce/zhengceku/2018-12/31/content_5448431.htm) (accessed on 31 December 2018).

**Disclaimer/Publisher’s Note:** The statements, opinions and data contained in all publications are solely those of the individual author(s) and contributor(s) and not of MDPI and/or the editor(s). MDPI and/or the editor(s) disclaim responsibility for any injury to people or property resulting from any ideas, methods, instructions or products referred to in the content.

## Article

# Numerical Simulation Analysis of Acoustic Emission Characteristics during the Drilling Pressure Relief Process in Coal Seams under Different Influencing Factors

Ji Ma <sup>1,\*</sup>, Jiashuo Li <sup>1</sup>, Shuai Zhang <sup>2,3</sup>, Shengtao Yang <sup>4</sup>, Xiaohang Dong <sup>1</sup> and Dongsheng Liu <sup>1</sup>

- <sup>1</sup> School of Safety Science and Engineering, Henan Polytechnic University, Jiaozuo 454003, China; lijiaoshuo990308@gmail.com (J.L.); jack666jack666jack666@outlook.com (X.D.); liu1426098061@163.com (D.L.)
- <sup>2</sup> School of Civil Engineering, Beijing Jiaotong University, Beijing 100044, China; 9331@bjtu.edu.cn
- <sup>3</sup> Key Laboratory of Safety and Risk Management on Transport Infrastructures of Ministry of Transport, Beijing 100044, China
- <sup>4</sup> College of Construction Engineering, Jilin University, Changchun 130026, China; taoyang20@mails.jlu.edu.cn
- \* Correspondence: showsma@hpu.edu.cn

**Abstract:** Drilling pressure relief is a widely recognized and applied key technique to reduce the risk of rock burst occurrence, and its field-applied effects are also obvious. In this paper, the values of micro parameters required for discrete element method (DEM) simulations were first determined through indoor experiments and parameter calibration. Then, drilling pressure relief numerical simulations were conducted with different drilling diameters, drilling angles, and drilling depths. The results show that as the depth and diameter of the borehole increase, the peak strength of the coal sample first rapidly decreases, and then slowly decreases. The 30 mm depth and 14 mm diameter of the borehole are, respectively, the critical thresholds for the transition of the peak strength decrease rate; as the drilling angle increases, the peak strength of the coal sample first rapidly decreases and then increases, and the drilling angle of 25° is the critical threshold for the peak strength transformation. At the same time, the type of coal sample failure also changes from conjugate shear fracture to single slope shear fracture with the increase of three drilling parameters; shear and tensile cracks are the main types of micro fractures in coal samples. The research results are of great significance for improving the pressure relief plan of coal seam drilling and preventing and controlling rock burst disasters.

**Citation:** Ma, J.; Li, J.; Zhang, S.; Yang, S.; Dong, X.; Liu, D. Numerical Simulation Analysis of Acoustic Emission Characteristics during the Drilling Pressure Relief Process in Coal Seams under Different Influencing Factors. *Processes* **2023**, *11*, 3277. <https://doi.org/10.3390/pr11123277>

Academic Editor: Jose Carlos Pinto

Received: 22 October 2023

Revised: 6 November 2023

Accepted: 16 November 2023

Published: 23 November 2023



**Copyright:** © 2023 by the authors. Licensee MDPI, Basel, Switzerland. This article is an open access article distributed under the terms and conditions of the Creative Commons Attribution (CC BY) license (<https://creativecommons.org/licenses/by/4.0/>).

**Keywords:** rockburst; acoustic emission (AE); drilling pressure relief; moment tensor; discrete element method

## 1. Introduction

With the gradual deepening of coal resource mining, the geological environment and conditions in coal mines have become more complex, and the incidence and severity of coal and rock dynamic disasters such as rock bursts have significantly increased. It is extremely important to prevent and control coal and rock dynamic disasters in deep mines [1]. Drilling pressure relief is an effective method for preventing and controlling rock bursts [2,3]. It has been included in the criteria for rock bursts in China and is the first step to be carried out in the mining work of rock burst mines. For the study of controlling rock burst disasters through drilling pressure relief, the efficiency of drilling pressure relief is a key scientific issue of primary concern [4].

The essence of this key issue is to grasp the damage and deterioration characteristics of the surrounding rock mass during the process of drilling pressure relief, to formulate the optimal scheme for the physical parameter layout of drilling. Thus, a system of evaluation parameter indexes before and after the drilling pressure relief during the mining process of the working face can be developed. Therefore, scholars and experts in this field have

conducted a large amount of practical study and theoretical work, and have achieved a large number of related outcomes. The method of drilling pressure relief is considered the most convenient and efficient method in Europe and America, while in Germany, this method is the only measure approved by national departments [4,5]. In the last century, the former Soviet Union has also done a lot of work on the study of drilling pressure relief [6], and the influence of different drilling intervals and drilling diameters on the pressure relief effect was obtained through experimental research. Ortlepp and Stacey [7] analyzed the prevention and control mechanism of drilling pressure relief technology for rock burst disasters from the test results. Reyes and Einstein [8] carried out physical simulation tests of coal and rock mechanics. Refs. [9,10] conducted a systematic study on the influence of drilling shape on the mechanical properties and fracture characteristics of porous rocks under uniaxial loading. Refs. [11,12] studied the elastic energy dissipation, angle of stress transfer, and plastic behavior of large-diameter decompression drilling in coal seams under high stress conditions. A reasonable drilling pressure relief plan has been determined. Refs. [10,13] conducted uniaxial compression tests on drilled coal materials to study the changes in parameters such as strength and the energy dissipation index, and analyzed the crack propagation characteristics of rocks around the drilled holes in the experiments. Zhang et al. [12] found experimentally that variable diameter drilling can enhance the plasticity of the sample while weakening the brittleness, so that the impact tendency can be reduced. Zhang et al. [13] studied the shear failure characteristics caused by compressive stress concentration around non-circular drilling. Li et al. [14] investigated the energy, stress, and impact tendency of the pressure relief principle of drilling. The method of using electromagnetic wave CT detection technology to test the pressure relief effect of drilling was proposed and verified.

With the emergence of numerical simulation technology, the problem of the “black box” is transparent, and the study of the drilling pressure relief process can be realized. Refs. [15–17] used numerical simulation to study the pressure relief effect under different drilling intervals and diameters. Based on the theory of energy propagation attenuation, Refs. [17,18] found through numerical simulation of rock samples with different borehole diameters that an increase in borehole diameter can lead to better pressure relief effects in the borehole. Refs. [19,20] used numerical simulation software to model the process of drilling and unloading pressure in rock burst tunnels, and compared and analyzed the stress field of the surrounding rock with and without unloading pressure. Pressure relief is achieved by the energy accumulated in the high stress zone after drilling, which causes the rock mass between the boreholes to be damaged. Refs. [18,21] used numerical simulation software to simulate the stress concentration zone in the excavation direction of deep coal tunnels, and obtained the pressure relief effects of directional drilling, roof stratification, and axial force changes of anchor rods. Wen et al. [20] studied the number and the propagation law of fractures for coal samples in the process of drilling pressure relief under different parameter conditions by numerical simulation software. However, there are few reports on the microscopic mechanism of pressure relief by drilling in coal seams, and studies on the pressure relief scheme of drilling under the influence of different physical factors are also extremely rare.

Based on the above, this paper focuses on the macroscopic and microscopic mechanical properties and the optimal physical parameters of drilling in the process of pressure relief in coal seams. This study is based on the Hulusu Coal Mine located in Ordos City, Inner Mongolia Autonomous Region, China, with engineering technology as the background. Experimental and numerical simulation studies on the pressure relief of drilling in coal seams under the influence of different physical factors were carried out. The findings of the study can be beneficial for the revelation of the microscopic mechanism and the proposal of the optimization scheme of the pressure relief in coal seams. In this article, a combination of indoor tests and numerical simulations was used to study the failure mode and acoustic emission characteristics of borehole pressure relief in coal seams. These findings from

the current work can provide data support for the practical application and promotion of borehole pressure relief technology.

## 2. Engineering Overview and Pressure Relief Mechanism of Drilling

Introduction to the Hulusu Coal Mine (the research object of the current study): in recent years, dynamic disaster accidents have occurred frequently in mines in Shaanxi and Inner Mongolia. For example, on 18 November 2017, there was a strong dynamic force in the return airway of the 21,103 working face of Hulusu Coal Mine in Huijierte Mining Area, which caused a side heave of the coal pillar instantaneously, with a maximum displacement of 0.7 m. The safety exit of the tail section of the working face was blocked, and 10 single bodies were bent instantaneously. Subsequently, on 6 February 2018, the 21,103 working face was advanced by 85–133 m. The large-scale floor heave, drum side, and coal pillar side of the return air roadway were broken, 10 single pillars of coal pillar side were thrown to the solid side, 17 wooden stacks were overturned, and coal body burst from the floor.

As shown in Figure 1, the Hulusu Mine belongs to the Huijierte Mining Area. The entire mining area is located in Ordos, Inner Mongolia Autonomous Region, and is under the jurisdiction of Tuke Town, Wushen Banner and Taige Sumu, Yijinhuoluo Banner. The east–west tilt width of the Hulusu Mine is 13.0 km, the north–south length is 7.4 km, and the total area is about 92.76 km<sup>2</sup>. The production progress of Hulusu Mine is in the recovery of a 2-1 coal seam. The overall trend of the coal seam is northeast, and it is inclined to the northwest; the formation dip angle is 1~4°. The depth of the 2-1 coal seam is more than 600 m, and its roof lithology is mainly siltstone and sandy mudstone, followed by medium and fine sandstone. The floor lithology is mainly siltstone and sandy mudstone. According to the ‘Hulusu Coal Mine 2-1 Coal Rock Burst Tendency Identification Report’, the 2-1 coal seam has a strong burst tendency, and the roof and floor have a weak burst tendency. The second panel is located in the central west of the Hulusu Mine. On the north side of the area, there are three main roadways of the 2-1 coal seam, covered with Quaternary aeolian sand, with less vegetation in the area. It is a desert and semidesert area, and its surface is a plateau-accumulated hilly landform. The ground elevation of the second panel is +1304.50~+1341.20 m, the underground elevation is +655~+680 m, and the buried depth is 624~685 m.

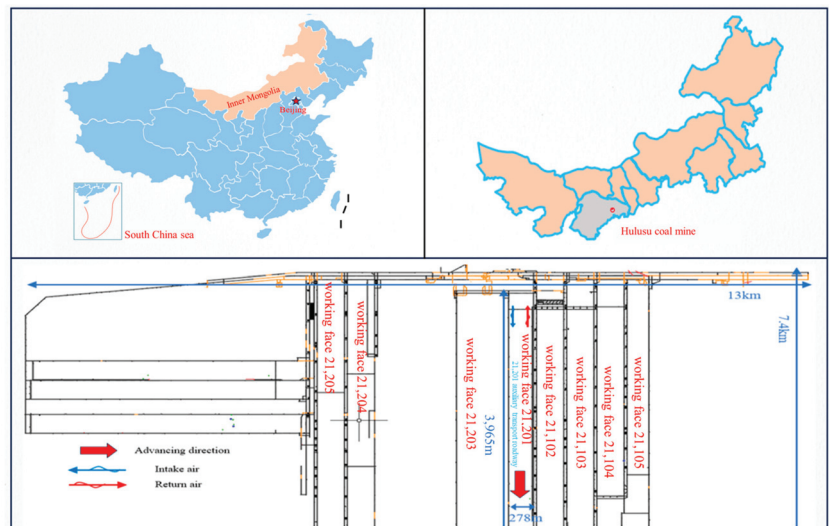
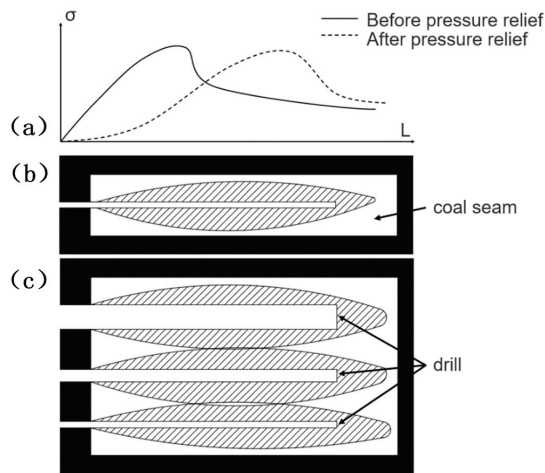


Figure 1. Schematic diagram of the location of Hulusu Coal Mine.

The 21,201 working face is located in the eastern part of the second panel. During the initial mining period, the surface width was 293 m. Mining work is 480 m, the surface width is 278 m, and the advancing length is 3965 m. Due to hidden factors such as the rock burst tendency of coal-rock, erosion zones, faults, goaf field and folds, a comprehensive evaluation has shown that there is a risk of a rock burst disaster during the mining of the 21,201 working face.

As a classic rock burst prevention and control method, the principle of drilling pressure relief is to reduce the stress concentration in the target area by drilling in the coal seam, or to change the mechanical properties of the coal within the target area so that the stable and controllable failure process of the coal can replace the unstable failures of the coal that may occur, which can effectively eliminate or reduce the risk of deformation and instability of the surrounding rock of the roadway. As shown in Figure 2b, when drilling is carried out in high-stress coal seams, cracks and ruptures occur in the coal near the borehole under the action of stress, resulting in a crushing zone of the coal near the borehole that is much larger than the diameters of the borehole. After multiple drills, these crushing zones can intersect with each other and generate a large-scale pressure relief zone in the entire coal seam, thereby effectively reducing the peak value of stress concentration and transferring the stress concentration zone to the deep area, as in Figure 2c. On the one hand, the fracture zone formed by drilling reduces the stress concentration of the coal seam, thus greatly reducing the impact risk and playing a role in pressure relief; on the other hand, drilling also changes the mechanical properties of coal seams and weakens the ability of coal seams to store elastic energy, thus reducing the risk of rock burst disasters. The pressure relief principle of drilling in coal is shown in Figure 2a.



**Figure 2.** Schematic of coal seam drilling relief [22]. (a) Stress changes before and after pressure relief; (b) The influence range of single borehole pressure relief; (c) The influence range of pressure relief of multiple boreholes with different diameters.

### 3. Numerical Model Diagram and Sample

#### 3.1. Basic Concept

The DEM model of coal samples in this paper is modeled by the PFC numerical simulation software, including the particles and contact between particles, as shown in Figure 3. The particles of the coal specimen were modeled as rigid spheres with a certain range of particle sizes. The contacts between the coal particles were chosen through the parallel bond model [21]. As a mechanical interaction law between particles in PFC software Version 6.0, the principle of this law is equivalent to establishing two sets of microscopic vertical spring units between two particles, including springs perpendicular to the contact

surface (normal springs) and springs parallel to the contact surface (tangential springs). Through the action of force, the maximum tensile and shear stresses generated between the two particles on the parallel bond are as follows [23,24]:

$$\bar{\sigma}_{\max} = \frac{-\bar{F}_n}{A} + \frac{|\bar{M}_s|\bar{R}}{I} < \bar{\sigma} \tag{1}$$

$$\bar{\tau}_{\max} = \frac{-\bar{F}_s}{A} + \frac{|\bar{M}_n|\bar{R}}{J} < \bar{\tau} \tag{2}$$

where  $\bar{F}_n$  is the normal force,  $\bar{F}_s$  is the tangential force;  $\bar{M}_n$  is the bending moment, and  $\bar{M}_s$  is the torque;  $J$ ,  $A$ ,  $I$  are the polar moment of inertia, the contact area, and the moment of inertia.

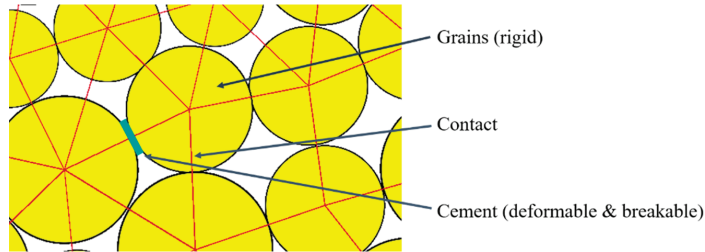


Figure 3. Bonded-particle model [23].

For the parallel bond contact model, the microscopic parameters mainly used to describe the physical properties are: normal strength  $\bar{\sigma}$  and tangential strength  $\bar{\tau}$ , particle normal stiffness  $k_n$  and tangential stiffness  $k_s$ , bonding normal stiffness  $\bar{k}_n$  and bonding tangential stiffness  $\bar{k}_s$  friction coefficient. When the shear stress on the contact exceeds the shear strength, the micro-spring between the particles is tangentially destroyed, the shear strength of the contact between the particles is reduced to the residual strength, and the normal force and friction factors affect the residual strength. When the tensile stress on the contact exceeds the tensile strength, the micro-spring between the particles breaks and tensile cracks appear, and the contact between the particles loses the tensile strength, as shown in Figure 4 [22].

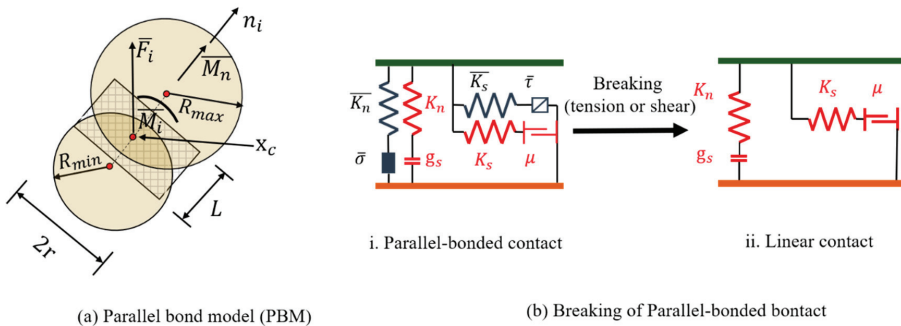


Figure 4. Parallel bond model and bond breaking [23].

Here is a description of the contact method (primarily the change of force and moment updated as the timestep) in the parallel bond contact model. The contact force is resolved into linear force  $F^l$ , dashpot force  $F^d$ , and the parallel-bond force  $\bar{F}$ . The contact moment  $M_c$  is the parallel-bond moment  $\bar{M}$ , which can be resolved into torsional moment  $\bar{M}_t$  and bending moment  $\bar{M}_b$ .

For the force group, including linear force  $F^l$ , dashpot force  $F^d$  and parallel-bond force  $\bar{F}$  can be resolved into a normal component and shear component. These three forces can be updated as follows:

For the linear force  $F^l$ :

$$F_n^l = k_n \times \Delta g_n \text{ (normal); } F_s^l = k_s \times \Delta g_s \text{ (shear)}$$

where  $k$  is the stiffness and  $\Delta g$  is the variational quantity in distance of ball–ball or ball–wall.

For the dashpot force  $F^d$ :

$$F_n^d = (2\beta_n \sqrt{m_c k_n}) \times \dot{\delta}_n \text{ (normal); } F_s^d = (2\beta_s \sqrt{m_c k_s}) \times \dot{\delta}_s \text{ (shear); } m_c = \frac{m_1 m_2}{m_1 + m_2}$$

where  $m_1$  and  $m_2$  are the mass of contact balls,  $\beta$  is the damping ratio,  $\dot{\delta}$  is the relative translational velocity of ball–ball or ball–wall.

For the parallel-bond force  $\bar{F}$ :

$$\bar{F}_n = -(\bar{F}_n)_0 + \bar{k}_n \bar{A} \Delta \delta_n \text{ (normal); } \bar{F}_s = -(\bar{F}_s)_0 + \bar{k}_s \bar{A} \Delta \delta_s \text{ (shear)}$$

where  $(\bar{F})_0$  is the parallel component force at the beginning of the time step,  $\bar{A}$  is the area of the bond,  $\bar{k}$  is the stiffness, and  $\Delta \delta$  is the relative normal displacement increment.

For the moment group, the parallel-bond moment  $\bar{M}$  can be resolved into a torsional component and bending group.

The torsional moment is updated:

$$\bar{M}_t = -(\bar{M}_t)_0 + \bar{k}_s \bar{J} \Delta \theta_t,$$

where  $(\bar{M}_t)_0$  is the twisting moment at the beginning of the time step,  $\bar{J}$  is the polar moment of inertia of the bond, and  $\Delta \theta_s$  is the relative twist rotation.

The bending moment is updated:

$$\bar{M}_b = -(\bar{M}_b)_0 + \bar{k}_n \bar{I} \Delta \theta_b,$$

where  $(\bar{M}_b)_0$  is the bending moment at the beginning of the time step,  $\bar{I}$  is the moment of inertia of the bond, and  $\Delta \theta_b$  is the bend–rotation increment.

### 3.2. AE Simulation Method Based on Moment Tensor

This section presents a moment tensor-based acoustic emission simulation method. It is assumed that the AE event is composed of a bond rupture event in a specified space–time range. The derivation [25] is as follows:

According to the variation of the contact force of the particles in the fracture zone, the moment tensor is obtained [26,27]:

$$M_{ij} = \sum_s \Delta F_i R_j \quad (3)$$

where  $\Delta F_i$  is the  $i$  direction component of the change value of the contact force and  $R_j$  is the  $j$  direction component of the distance between the contact point and the event center.  $S$  is the path enclosed by all contacts of the source particles (bonded broken particles).

The moment tensor with the maximum scalar moment value is used as the moment tensor of each AE event and stored. The expression of the scalar moment is [28]:

$$M_0 = \left( \sum_{j=1}^3 m_j^2 / 2 \right)^{1/2} \quad (4)$$

where  $m_j$  is the No.  $j$  eigenvalue of the moment tensor matrix.



The rupture strength of acoustic emission events can be calculated by the following formula [29]:

$$M_w = \frac{2}{3} \lg M_0 - 6 \quad (5)$$

After the shear fracture occurs, the time for the generated wave to be transmitted to the crack boundary is twice the duration of the micro-crack. During this period, the value of the moment tensor is recalculated and updated at each step. If no new micro-cracks appear during this period, it is considered that there is only one micro-crack in this AE event; if a new micro-crack is generated during this period, and the influence range of the new and old cracks is staggered, the micro-crack is attributed to the same AE event, that is, multiple micro-cracks appear in this AE event, and the calculation and extension of the duration of the micro-crack are updated.

Wang et al. [30] proposed to characterize the rupture type of AE events by the isotropic and anisotropic components of the moment tensor, namely:

$$R = \frac{\text{tr}(M) \times 100}{|\text{tr}(M)| + \sum |m_i^*|} \quad (6)$$

$$\text{tr}(M) = m_1 + m_2 + m_3 \quad (7)$$

$$m_i^* = m_i - \text{tr}(M)/3 \quad (8)$$

where  $\text{tr}(M)$  is the trace of a tensor;  $m_i$  is the eigenvalue of the tensor; and  $m_i^*$  is the eigenvalue partial tensor.

The specific criteria are as follows:  $R > 30\%$ , tensile failure;  $-30\% \leq R \leq 30\%$ , shear failure; and  $R < -30\%$ , mixed failure.

Because there is an exponential relationship between the amplitude of the acoustic emission event  $M$  and its value  $N$ , the relationship is described by the Gutenberg–Richter formula [31]:

$$\lg N = a - bM \quad (9)$$

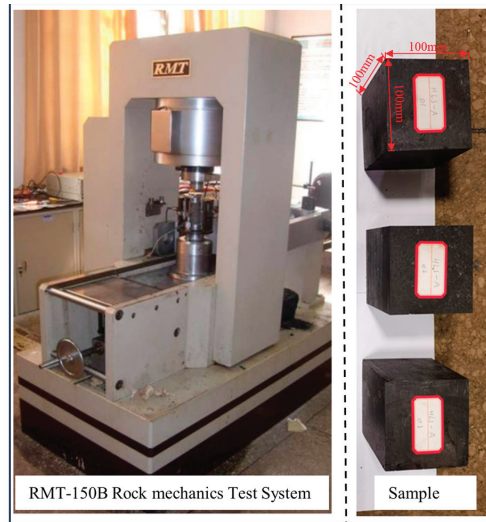
where  $N$  is the number of AE events with a moment tensor amplitude greater than  $M$ . For the slope  $b$  when the proportion of signal components with large energy is large, the  $b$  value is small; when the proportion of signal components with large energy is small, the  $b$  value is larger.

### 3.3. Sample Preparation and Parameter Calibration

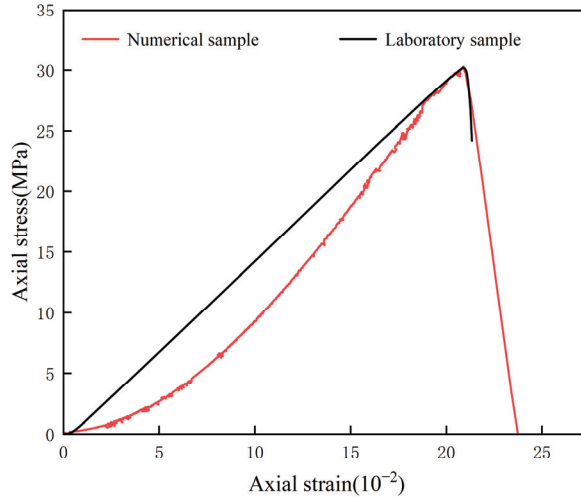
The calibration of microscopic parameters is the primary matter in the application of DEM software 6.0 to simulate coal and rock problems. The microscopic parameters involved in DEM software can not be obtained by tests. Therefore, it is necessary to continuously verify the macroscopic data such as the Poisson ratio, uniaxial compressive strength, and elastic modulus obtained by tests. Based on the experience of predecessors and their own experience, the microscopic parameters are repeatedly adjusted by the trial and error method to calibrate, so that the overall parameters of the numerical model are in line with the actual results. Firstly, an indoor uniaxial compression test is needed to obtain the macroscopic mechanical parameters of the coal.

The experimental coal sample was taken from Hulusu Coal Mine. In order to be more in line with the actual situation of the site, the original bulk coal sample was directly drilled in the coal mine, and the sample was cut into  $100 \times 100 \times 100$  (mm) standard cubes. The standard cube samples were three groups. The specific size and shape are shown in Figure 5. The RMT-150B (Institute of Rock and Soil Mechanics, Chinese Academy of Sciences, Wuhan, China) rock mechanics test system was used in the experiment. The axial load was measured by a 1000 kN force sensor with a load accuracy of  $1.0 \times 10^{-3}$  kN. The axial compression deformation was measured by a 5.0 mm displacement sensor. The circumferential deformation was measured by two 2.5 mm displacement sensors with a

deformation accuracy of  $1.0 \times 10^{-3}$  mm. The stress–strain curve obtained by the experiment is shown in Figure 6.



**Figure 5.** RMT-150B rock mechanics testing system (left) and experimental specimens (right).



**Figure 6.** The contrast of stress–strain curves between numerical simulations and laboratory tests.

A rock sample with diameters of  $\Phi 100 \text{ mm} \times 100 \text{ mm} \times 100 \text{ mm}$  was established. For the rock particles, a normal distribution was used for a particle radius range from 1.5 to 1.7 mm. A range of maximum and minimum particle radii with small differences ensured a more homogeneous generation of rock samples. Rock particles with a density of  $2700 \text{ kg/m}^3$  and an elastic modulus of 0.775 GPa were adopted to be close to the characteristics of the actual sample. The contact model between the rock particles adopted parallel bonding contact. The parameters of the parallel bonding contact are listed in Table 1. It was confirmed from numerous pre-tests that the peak value and rise ascent of simulated stress were significantly affected by the friction coefficient and effective modulus of rock particles, respectively. For this experience, the parameters shown in Table 1 were regulated by continuously modifying until the stress–strain characteristics of the numerical

simulation matched the experiments. From Figure 6, it can be seen that the simulated values are very close to the measured values, indicating that the microscopic parameters can accurately simulate the mechanical properties of coal. The proposed DEM parameters are shown in Table 1, which can better capture the mechanical behavior of the rock sample in this study. The effective modulus of the linear group and parallel bond group are all equal to  $0.87 \times 10^9$  Pa. The friction coefficient and normal to shear stiffness ratio are equal to 0.1 and 1.5, respectively. In addition, the tensile strength and cohesion of the contact are equal to  $2.2137 \times 10^7$  and  $8.1989 \times 10^6$ , respectively.

**Table 1.** Micromechanical parameters of the DEM model.

BPM Properties	Parameter	Value
Grain	Density ( $\text{kg}/\text{m}^3$ )	2700
	$R_{\min}$ (mm)	0.0015
	$R_{\max}$ (mm)	0.0017
	Elastic modulus (GPa)	0.775
Contact	Effective modulus of the linear group (Pa)	$0.87 \times 10^9$
	Effective modulus of the parallel bond group (Pa)	$0.87 \times 10^9$
	Normal to shear stiffness ratio	1.5
	Tensile strength of the parallel bond group (Pa)	$2.2137 \times 10^7$
	Cohesion of the parallel bond group (Pa)	$8.1989 \times 10^6$
	Friction coefficient	0.1

In this section, the influence of different drilling diameters and depths on the strength of the test block and the form of surrounding crack propagation were studied by means of laboratory tests and DEM simulation, so as to understand the mechanism of drilling pressure relief more comprehensively.

#### 4. Drilling Pressure Relief Test Scheme and Model Establishment

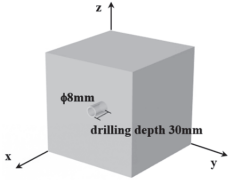
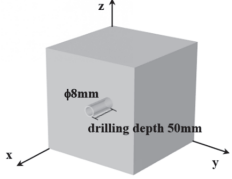
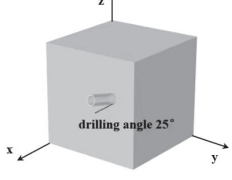
The influence of drilling depths, drilling diameters, and drilling angles on the effect of drilling pressure relief cannot be ignored. This experiment attempted to study the AE characteristics and physical influencing factors of different drilling depths, drilling diameters, and drilling angles in the process of drilling pressure relief. The influence of different parameters on the strength and AE characteristics of the sample under uniaxial compression was compared and analyzed. The specific experimental scheme is shown in Table 2.

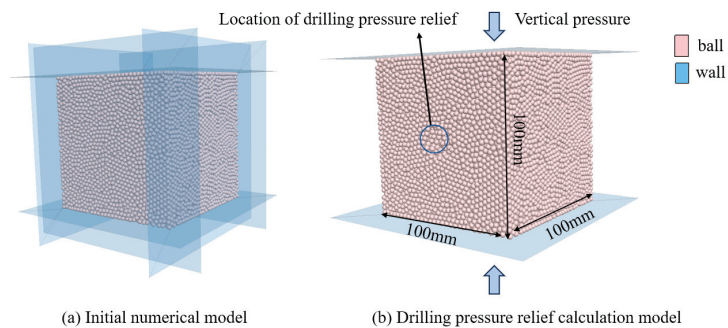
In this section, a standard cube numerical model of  $100 \times 100 \times 100$  (mm) has been established, and the microscopic parameters have been calibrated according to the results of the uniaxial loading compression tests. The numerical model is consistent with the macroscopic parameters of indoor experiment coal samples.

The dynamic excavation unloading process experiment of the numerical model under uniaxial loading conditions is shown in Figure 7. Initially, numerical specimens were prepared in the area surrounded by the walls (as shown in Figure 7a). To subject the numerical specimens to the pressure equivalent to the field specimens buried in the subsurface at an appropriate location, a confining pressure setting of 40 kPa in all directions was performed for the numerical specimens. In other words, a more compact rock sample was generated after the process of confining the specimen in all directions. Once the specimen with a specified strength was generated, the lateral walls were deleted and the activity of the rock sample in the lateral direction was no longer restricted. Then, a borehole was drilled, located in the middle of the front after the removal of the lateral walls. Finally, the uniaxial monotonic compressive testing using the axial displacement control method was carried out, and the loading rate was set to 0.005 mm/s. The loading method was as follows: The experimental loading rate was 0.005 mm/s, loading to 50% of the uniaxial peak strength, stopping loading to keep the deformation unchanged, drilling, keeping the deformation unchanged for 5 min, and then loading until the sample was destroyed. The dynamic

drilling unloading experiment was carried out on the numerical model following the above procedure.

**Table 2.** Experimental plan design.

Serial Number	Protocol	Parameter	Conceptual Drawing (Example)
I	Different drilling diameters	6, 8, 12, 14, 18, 20 mm	
II	Different drilling depths	10, 30, 50, 70, 90, 100 mm	
III	Different drilling angles	5, 15, 25, 35, 45°	



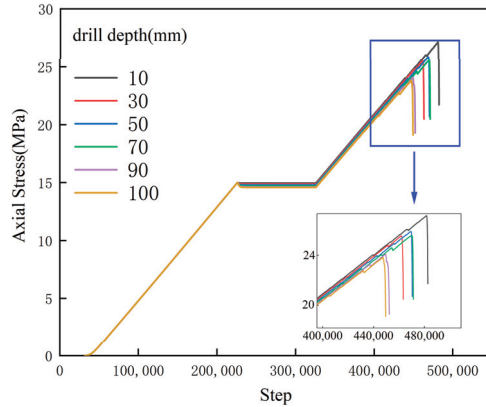
**Figure 7.** Pressure relief model for drilling.

## 5. Numerical Calculation Results

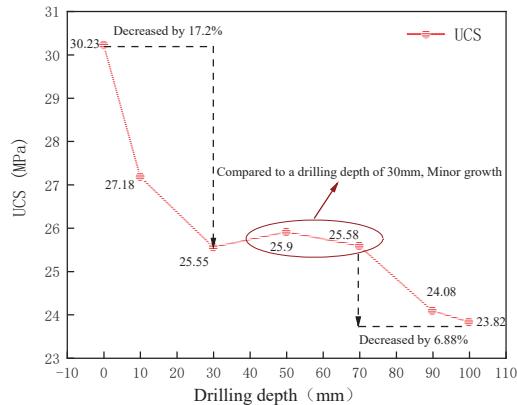
### 5.1. Strength Analysis of Samples under the Influence of Different Physical Factors

Figures 8 and 9 show the stress–strain curve of the sample under different drilling depths (the drilling radius was 8 mm). It can be seen from Figure 9 that the peak strength of the undrilled sample reached 30.23 MPa. After drilling at different depths, the peak strength of the sample decreased rapidly with the increase of the drilling depths (the drilling depths were 10 and 30 mm, respectively), then increased slowly (the drilling depths were 50 and 70 mm, respectively), and finally decreased slowly (the drilling depths were 90 and 100 mm, respectively). When the drilling depth was close to the central position of the sample, the influence scope ranges of the unloading zone were slightly weakened, indicating that the intersection of the lateral drilling unloading stress axis and the axial loading stress axis promoted the increase of sample strength. The peak strength of the sample with a

drilling depth of 30 mm was 17.2% lower than that of the sample without drilling, and the peak strength of the sample with a drilling depth of 100 mm was 6.88% lower than that of the sample with a drilling depth of 70 mm. Based on the above description, it can be seen that under uniaxial compression conditions, with the increase of drilling depths, when the drilling depth was below 30 mm, the pressure relief effect was the best.



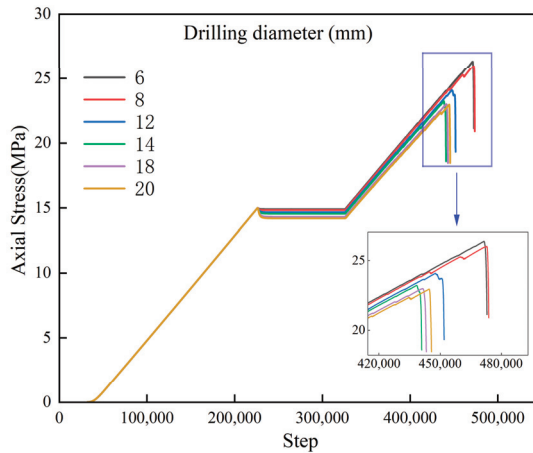
**Figure 8.** Stress–strain curve of samples under different drilling depths.



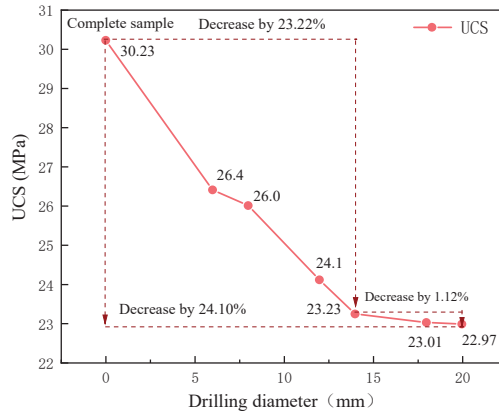
**Figure 9.** Curve of peak strength variation of samples under the influence of drilling depths.

Figures 10 and 11 are the stress–strain curves of the sample under different drilling diameters (the drilling depth was 30 mm). It can be seen from Figure 11 that the peak strength of the undrilled sample reached 30.23 MPa. After drilling with different diameters, the peak strength of the sample decreased with the increase of the borehole diameters (the drilling diameters were 6, 8, 12, 14, 18, and 20 mm, respectively) to 26.4, 26.0, 24.1, 23.23, and 23.01 MPa, respectively. It can be clearly seen that the strength of the sample decreased significantly with the increase of the drilling diameters. At the same time, it can be noted that the peak strength of the sample decreased rapidly with the increase of the diameters of the drilling (the depths of the drilling were 6, 8, 12, and 14 mm, respectively), and then decreased slowly (the depths of the drilling were 18 and 20 mm, respectively). The increase of the volume range of the borehole pressure relief area exacerbated the overall strength reduction of the sample. Based on the above description, it can be seen that under uniaxial loading, with other conditions unchanged, and with the increase of drilling diameters, the pressure relief effect of drilling increased with the increase of drilling diameters. The drilling diameter of 14 mm was the critical threshold. When the drilling diameter was

higher than this value, although the pressure relief effect of the drilling gradually increased, the effect gradually slowed down.



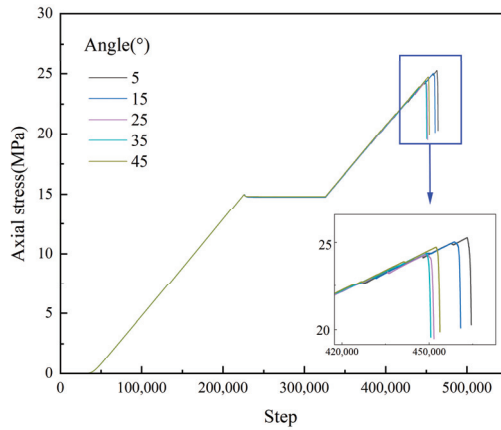
**Figure 10.** Stress–strain curve of samples under different drilling diameters.



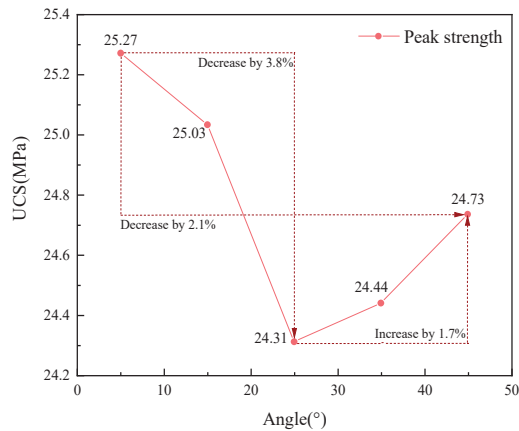
**Figure 11.** Curve of peak strength variation of samples under the influence of drilling diameters.

Figures 12 and 13 are the stress–strain curves of the sample under different drilling angles. The peak strength of the undrilled sample reached 30.23 MPa. After drilling with different angles, the peak strength of the sample decreased with the increase of the drilling angles (the drilling angles were 5°, 15°, and 25°, respectively) to 25.27 MPa, 25.08 MPa, and 24.31 MPa, which had a significant downward trend. Then, the peak strength of the sample increased with the increase of the drilling angles (the drilling angles were 35° and 45°, respectively) to 24.44 MPa and 24.73 MPa, and the upward trend was also obvious. The volume range of the unloading zone increased from the beginning to gradually decrease with the increase of the angle, and the overall strength weakening also showed a trend of first decreasing and then increasing with the change of the unloading zone range. The peak strength of the sample with a drilling angle of 25° was 3.8% lower than that of the 5° sample, while the peak strength of the sample with a drilling angle of 45° was 1.7% higher than that of the 25° sample. Based on the above analysis, it can be seen that under uniaxial loading, with other conditions unchanged, and with the increase of drilling angles, the pressure relief effect of drilling increased first and then decreased with the increase of drilling angles. The drilling angle of 25° was the critical threshold. When the drilling angle

exceeded  $25^\circ$ , the pressure relief effect of drilling gradually decreased. In summary, the pressure relief effect was best when the drilling angle was about  $25^\circ$ .



**Figure 12.** Stress–strain curve of samples under different drilling angles.



**Figure 13.** Curve of peak strength variation of samples under the influence of drilling angles.

### 5.2. Failure Mode Analysis of Samples under the Influence of Different Parameters

Figures 14–16 are the force chain contact diagrams of the samples under different drilling depths, different drilling diameters, and different drilling angles. From the three figures, it can be seen that the position of the failure crack and the distribution of the force chain in the surrounding area are more evacuated. The color of the force chain is deeper and the size of the force chain is smaller, which proves that this area had a better pressure relief effect. It can be seen from Figure 14 that when the drilling depth was 10–70 mm, the sample had a large pressure relief area. When the drilling depth was 90–100 mm, the pressure relief area of the sample was small, and when the drilling depth was 30 mm, the pressure relief area was the largest and the pressure relief effect was the best. It can be seen from Figure 15 that the sample had a large pressure relief area under different drilling diameters. When the borehole diameter was 14 mm, the pressure relief area was relatively large, the pressure relief effect was better, and the force chain distribution was more symmetrical. It can be seen from Figure 16 that the sample had a large pressure relief area under different drilling diameters, and the pressure relief area of the sample was relatively large when the drilling angle was  $25^\circ$ , and the pressure relief effect was better.

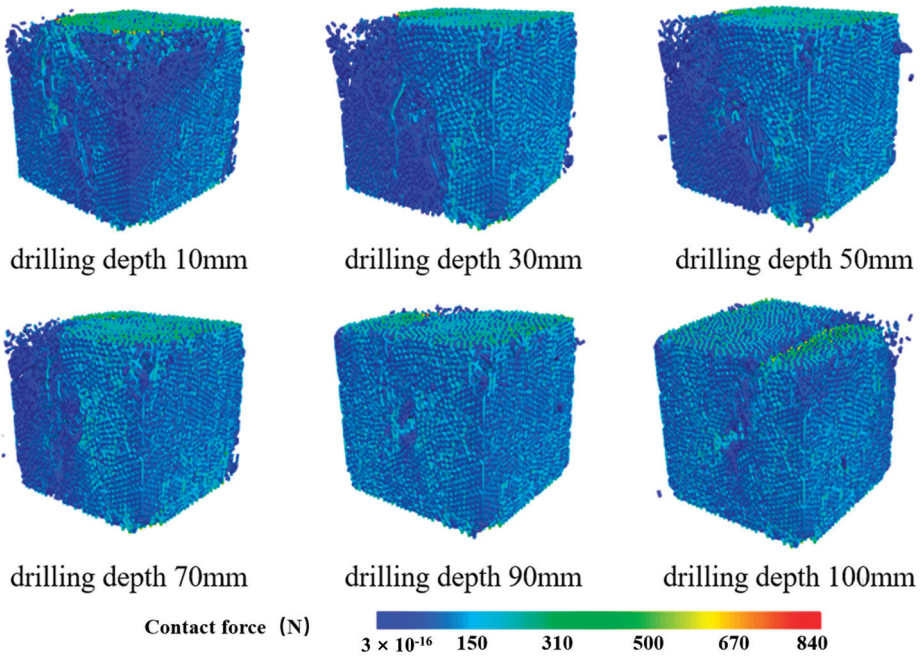


Figure 14. Contact diagram of force chains with different drilling depths.

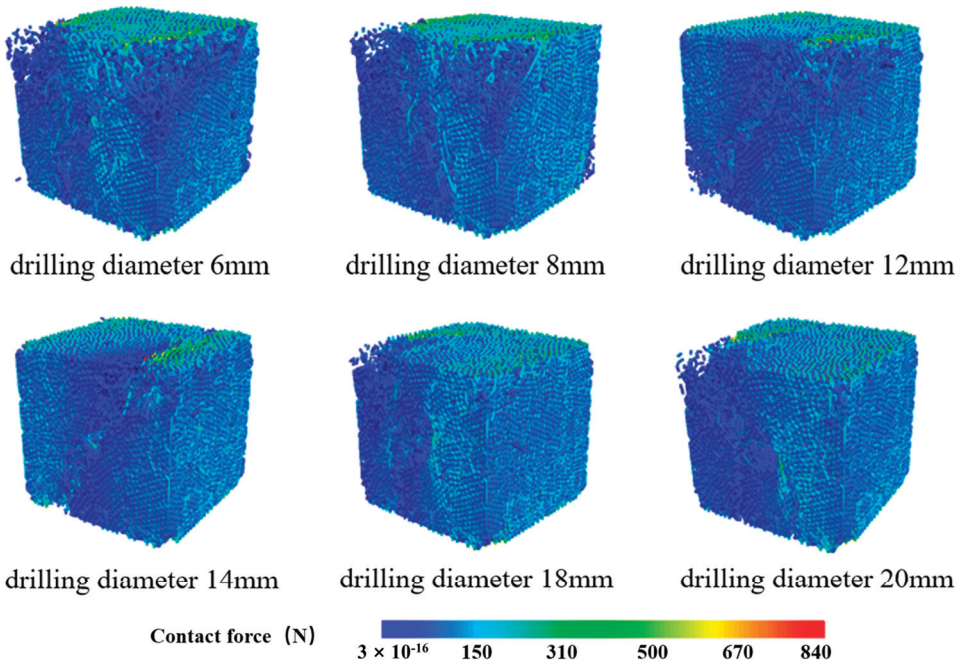
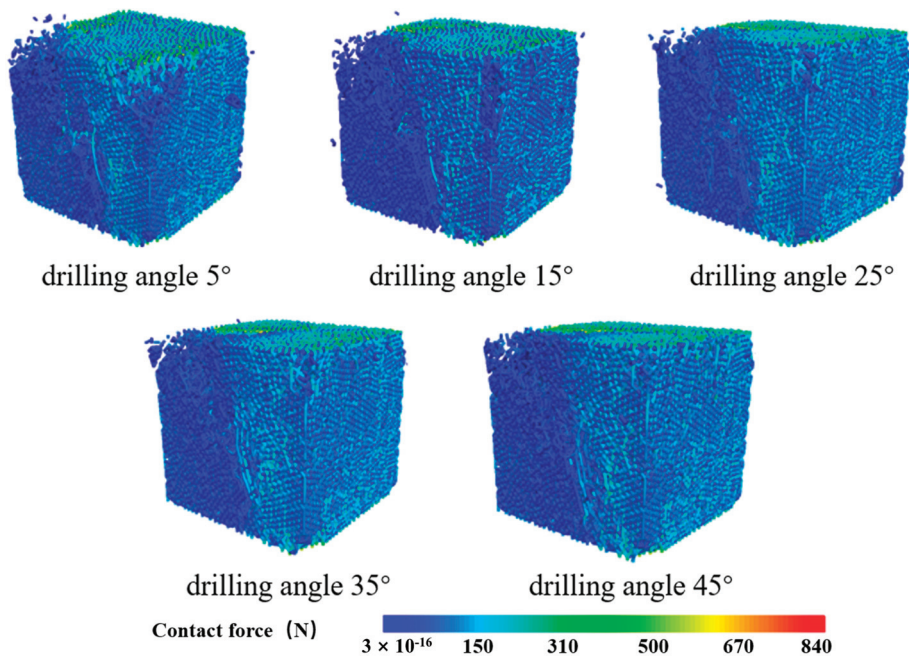


Figure 15. Contact diagram of force chains with different drilling diameters.

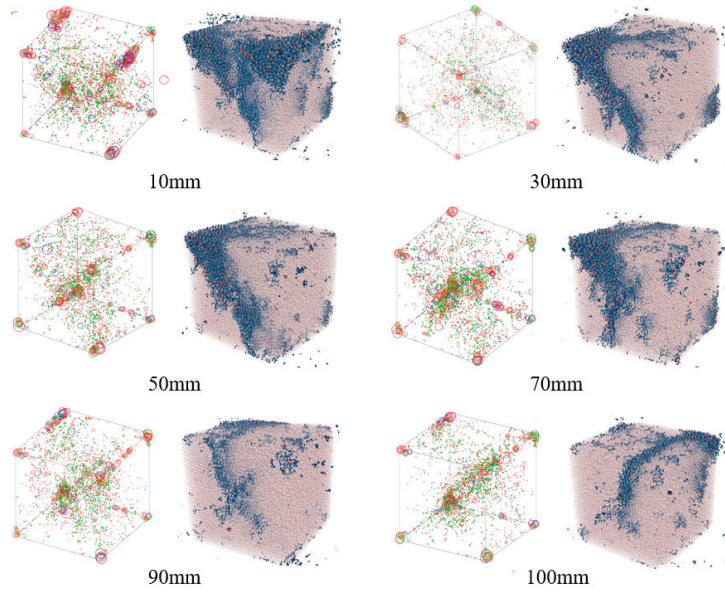




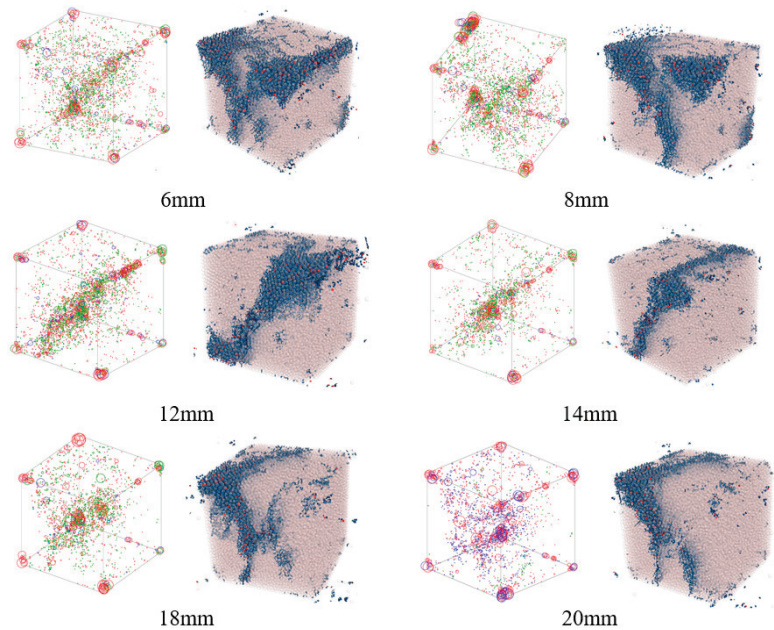
**Figure 16.** Contact diagram of force chains with different drilling angles.

Figure 17 shows the spatial distribution of the source and crack of the sample under different drilling depths. It can be seen from the diagram that the spatial distribution of the source and the spatial distribution of the crack had a high coincidence. This is because the crack generation process was accompanied by internal damage and vibration, so the area on the specimen surface where the macro-crack was generated had a large number and dense source distribution. When the drilling depth of the sample was 10 mm, the crack appeared as a conjugate shear fracture. As the drilling depth increased to 30 mm, the crack appeared as a single inclined plane shear fracture extending from the upper left corner to the lower right corner. From the drilling depth of 70 mm, the crack was still a single slope shear fracture, but its direction had changed from the upper right to the lower left. The critical value of drilling depths from the conjugate shear fracture to the single inclined plane shear fracture was 30 mm, which is consistent with the critical value of drilling depths when the optimal pressure relief effect is taken above.

Figure 18 shows the spatial distribution of the source and crack of the sample under different drilling diameters (the drilling depth was X mm, and the drilling angles was X°). It can be seen from the figure that the spatial distribution of the source and the spatial distribution of the crack also had a high coincidence. When the drilling diameter of the sample was 6–12 mm, the crack was characterized by a conjugate shear fracture. When the drilling diameter was 14 mm, the crack appeared as a single inclined plane shear fracture extending from the upper right corner to the lower left corner. From the drilling diameter to 18 mm, the direction of the shear fracture of the single inclined plane changed, and the trend of extending from the upper left to the lower right appeared. The critical value of drilling diameters from the conjugate shear fracture to the single inclined plane shear fracture was 14 mm, which is consistent with the critical value of drilling diameters when the optimal pressure relief effect is taken above.

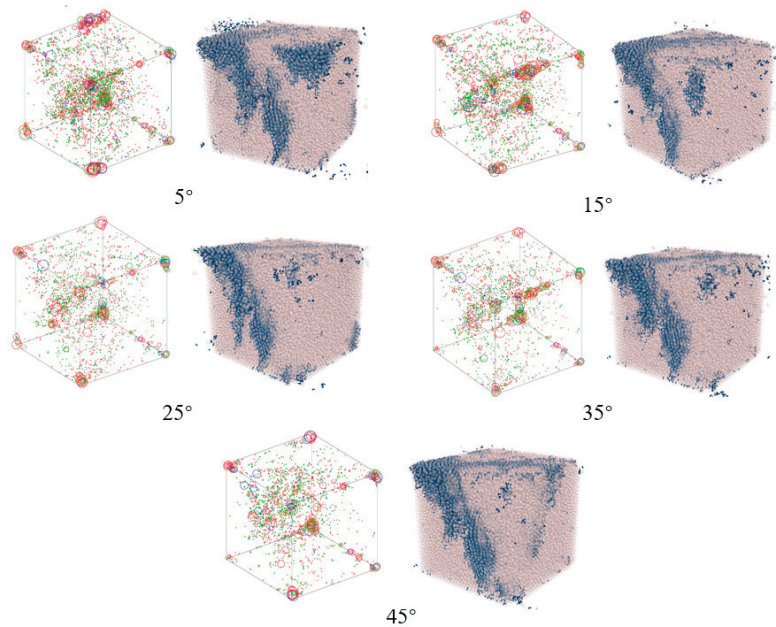


**Figure 17.** Spatial distribution of cracks and seismic sources under different drilling depths. Circles represent the location of seismic sources, where red indicates the deviatoric source; blue indicates the implosive source; green indicates the explosive source; and the size of the circle indicates the intensity of the seismic source.



**Figure 18.** Spatial distribution of cracks and seismic sources under different drilling diameters. Circles represent the location of seismic sources, where red indicates the deviatoric source; blue indicates the implosive source; green indicates the explosive source; and the size of the circle indicates the intensity of the seismic source.

Figure 19 is the spatial distribution map of the source and crack of the sample under different drilling angles. It can be seen from the figure that the spatial distribution of the source and the spatial distribution of the crack also had a high coincidence. When the drilling angles were  $5^\circ$  and  $15^\circ$ , the crack appeared as a conjugate shear fracture. When the drilling angle was  $25^\circ$ , the crack appeared as a single inclined plane shear fracture extending from the upper left corner to the lower right corner. From the drilling angle to  $35^\circ$ , the direction of the shear fracture of the single inclined plane changed, and the trend of extending from the upper right to the lower left appeared. The critical value of drilling depths from the conjugate shear fracture to the single inclined plane shear fracture was  $25^\circ$ , which is consistent with the critical value of drilling angles when the better pressure relief effect is taken above.

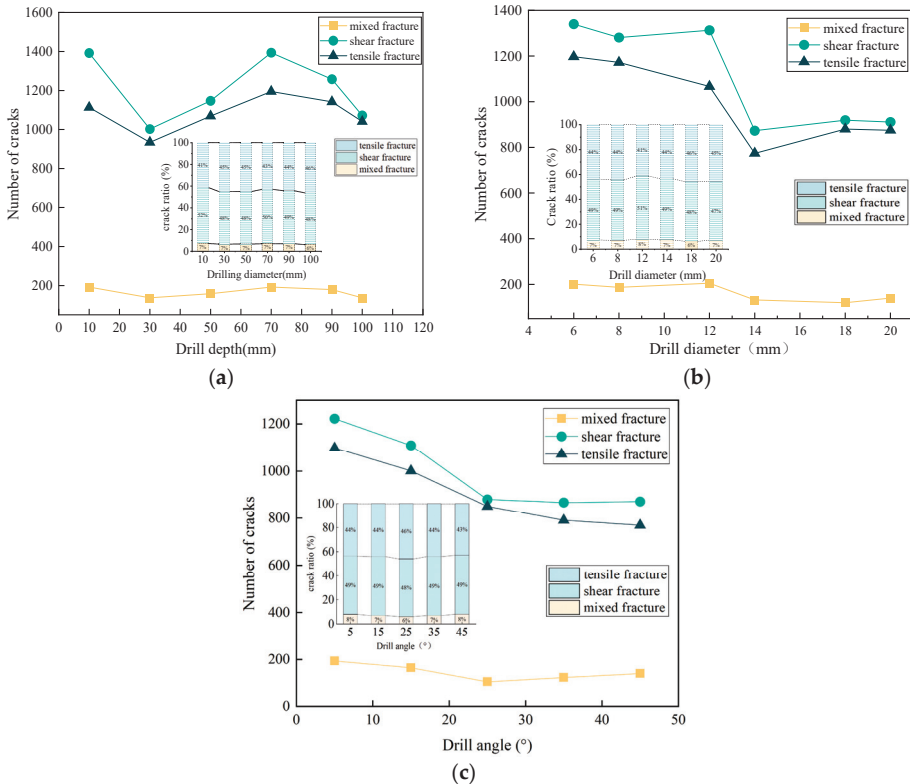


**Figure 19.** Spatial distribution of cracks and seismic sources under different drilling angles. Circles represent the location of seismic sources, where red indicates the deviatoric source; blue indicates the implosive source; green indicates the explosive source; and the size of the circle indicates the intensity of the seismic source.

### 5.3. Analysis of Acoustic Emission Characteristics under the Influence of Different Parameters

Figure 20 shows the proportion and number of cracks after the final failure of the coal body with different drilling depths, drilling diameters, and drilling angles. It can be seen from Figure 20 that the above three physical factors had little effect on the proportion of cracks after the final failure of coal. With the increase in drilling depths, drilling diameters, and drilling angles, the mixed fractures were kept at a low proportion (less than 10%), and the proportion of tensile fractures and shear fractures reached more than 90%, indicating that in the process of pressure relief of drilling, the failure forms were mainly tensile and shear failure. However, the drilling depths, drilling diameters, and drilling angles had a significant effect on the number of cracks after the final failure of the coal body. With the increase of drilling depths, the three kinds of fractures showed a trend of decreasing first, then increasing, and then decreasing in Figure 20a. When the drilling depth was 30 mm, the number of cracks was the lowest, which is consistent with the optimal critical value of the pressure relief effect with the drilling depth of 30 mm. With the increase of the diameter of the drilling, the three kinds of fractures showed a trend of decreasing slowly at first, then

decreasing rapidly, and finally remaining unchanged in Figure 20b. When the diameter of the drilling was 14 mm, the number of cracks was at a low level, which is consistent with the critical value of the pressure relief effect of the previous borehole diameters of 14 mm. With the increase of the drilling angles, the three fractures all showed a trend of decreasing rapidly first, then decreasing rapidly, and finally remaining unchanged in Figure 20c. When the drilling diameter was 25°, the the number of cracks was at a low level, which is consistent with the critical value of the pressure relief effect of the previous drilling angles of 25°.



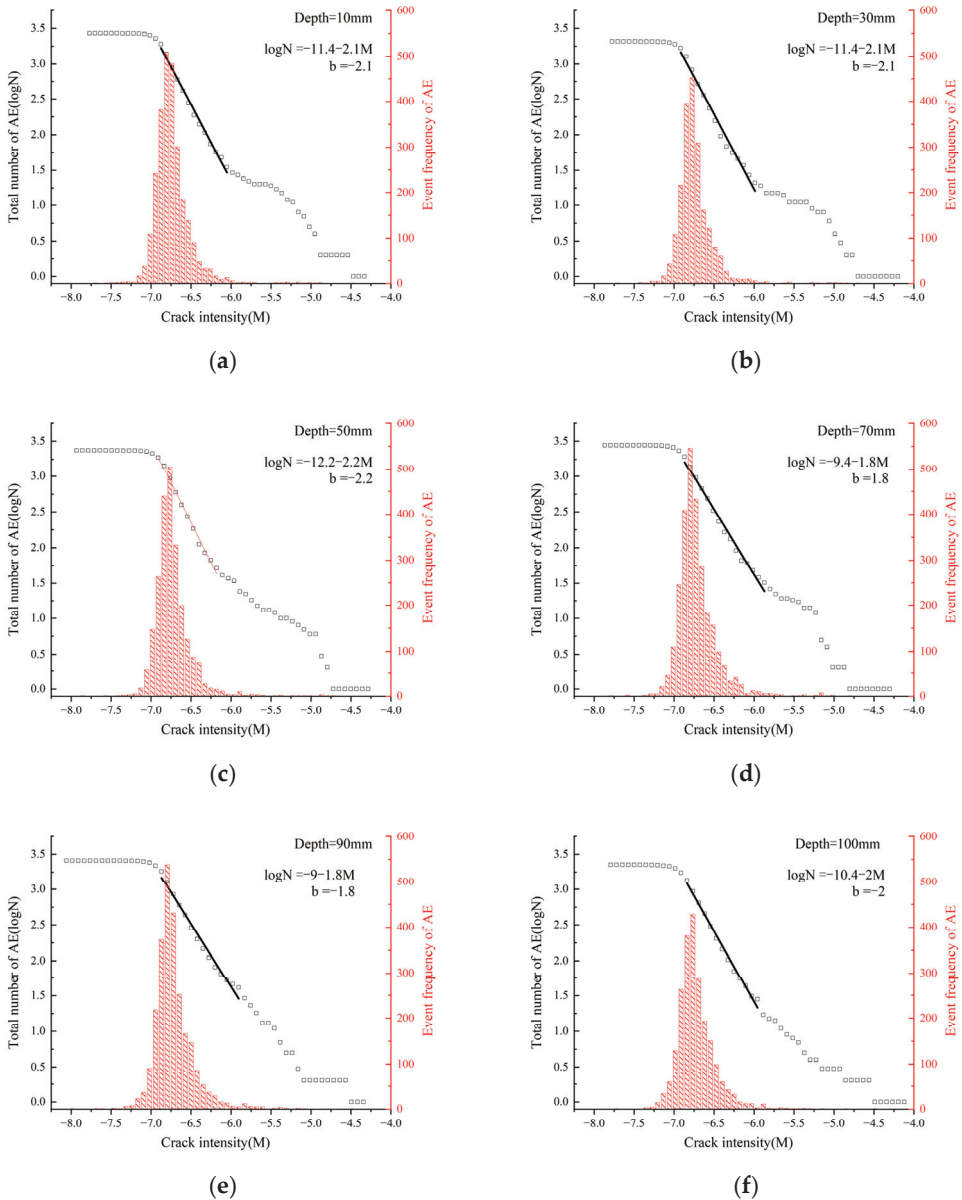
**Figure 20.** The proportion of cracks under the influence of different parameters. (a) Different drilling depth. (b) Different drilling diameter. (c) Different drilling angle.

From Figures 21–23, the moment tensor characteristics, AE characteristics, and b-value characteristics under different diameters, drilling depths, and drilling angles can be obtained. The specific analysis is as follows:

(1) Under different drilling diameters, the moment tensor amplitude of coal was mainly distributed in  $-7.75\sim-4.75$ , and the peak value appeared in  $-6.75\sim-6.5$ . Under different drilling depths, the moment tensor amplitude of coal was mainly distributed in  $-7.5\sim-5.0$ , and the peak value appeared in  $-6.75\sim-6.5$ . Under different drilling angles, the moment tensor amplitude of coal was mainly distributed in  $-7.25\sim-5.5$ , and the peak value appeared in  $-7.0\sim-6.75$ . Under different conditions, the relationship between the moment tensor size and the number of AE events obeyed the normal distribution.

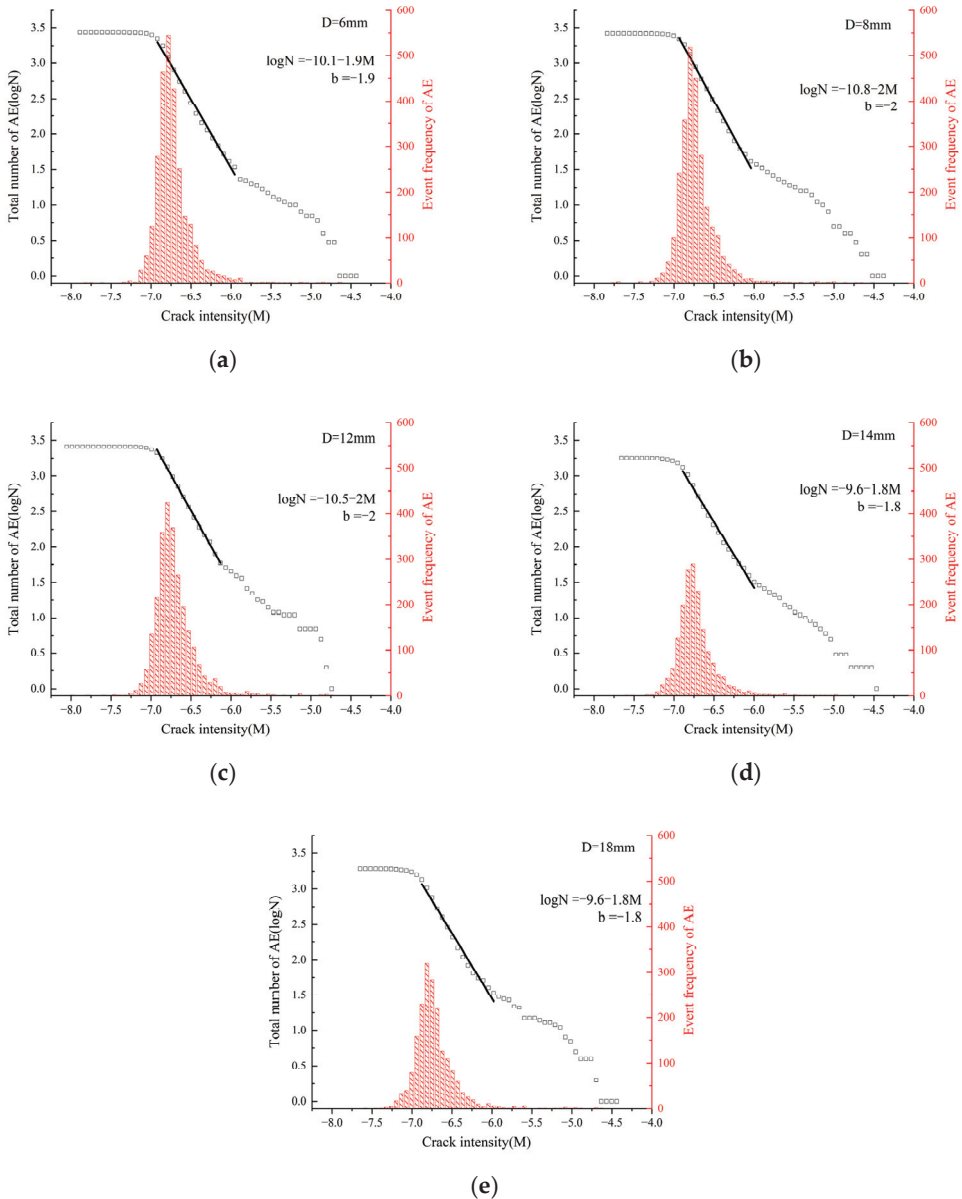
(2) In the same amplitude range, the number of AE events was affected by the drilling diameters, drilling depths, and drilling angles. When the drilling diameter was 6–14 mm, the number of AE events showed a decreasing trend with the increase of the drilling diameter. When the drilling diameter was 14–20 mm, the number of AE events increased with the increase of aperture. When the drilling depth was 10–30 mm, the number

of AE events shows a decreasing trend with the increase of the drilling diameter. When the drilling diameter was 30~100 mm, the number of AE events increased first and then decreased with the increase of drilling diameter. When the drilling angle was 5~25°, the number of AE events decreased with the increase of the drilling angle. When the drilling angle was 25~45°, the number of AE events increased first and then decreased with the increase of the drilling angle.

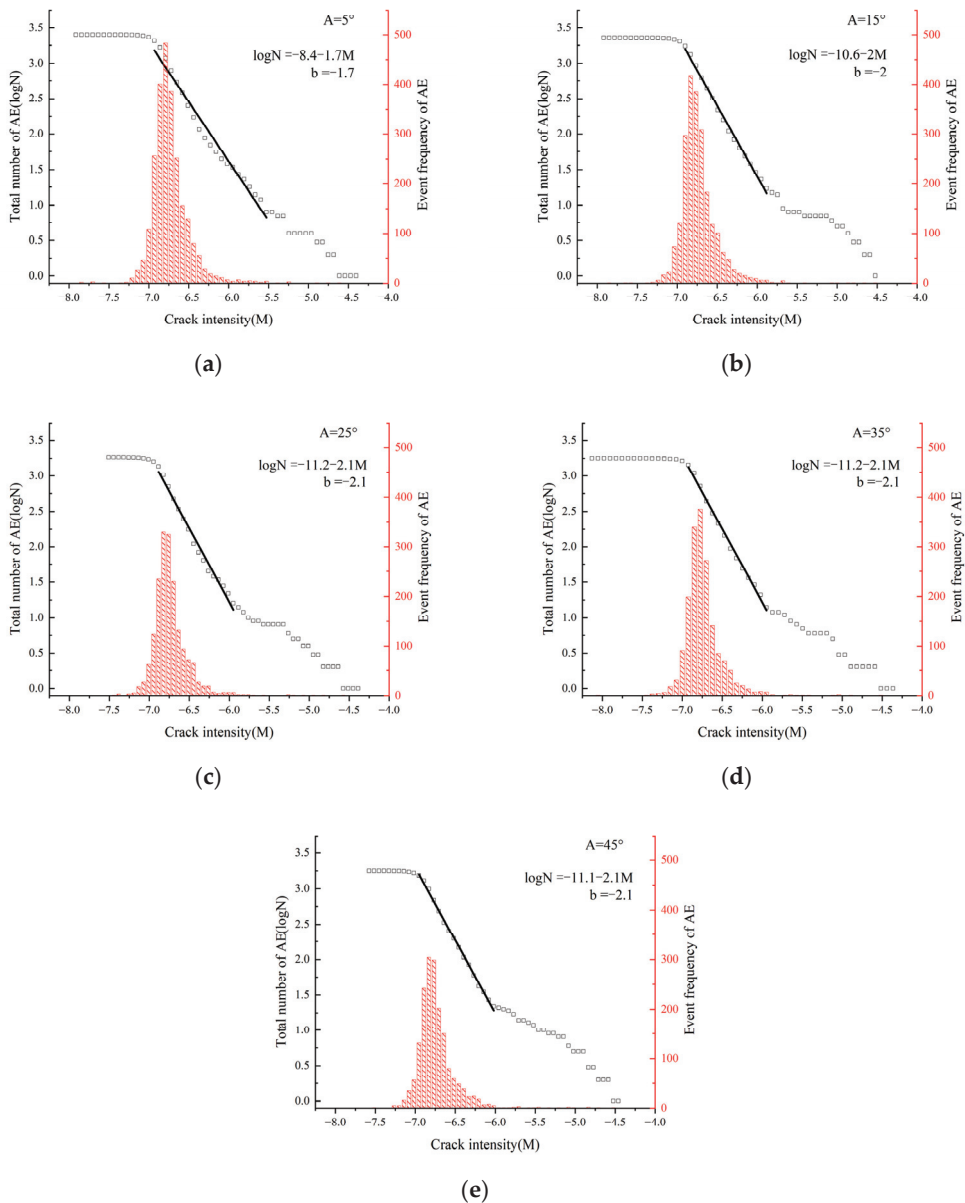


**Figure 21.** Distribution of moment tensor amplitude for different drilling depths. (a) 10 mm, (b) 30 mm, (c) 50 mm, (d) 70 mm, (e) 90 mm, (f) 100 mm.

(3) The changing trend of the b-value was closely related to the drilling diameters, drilling depths, and drilling angles. As shown in Figure 21, With the increase of drilling depths, the b-value increased first, then decreased, and finally increased again. With the increase of drilling diameters in Figure 22, the b-value generally showed a trend of increasing first, then decreasing, and finally stabilizing. With the increase of drilling angles in Figure 23, the b-value generally showed a trend of increasing first and then stabilizing.



**Figure 22.** Distribution of moment tensor amplitude for different drilling diameters. (a) 6 mm, (b) 8 mm, (c) 12 mm, (d) 14 mm, (e) 18 mm.



**Figure 23.** Distribution of moment tensor amplitude for different drilling angles. (a)  $5^\circ$ , (b)  $15^\circ$ , (c)  $25^\circ$ , (d)  $35^\circ$ , (e)  $45^\circ$ .

## 6. Conclusions

This paper is based on the basic principle of drilling pressure relief to prevent rock bursts, as well as considering the scale-independent properties of the damage localization mechanical behavior and the fracture process of rock-like material catastrophe. On the basis of the uniaxial compression mechanical behavior of coal samples at the laboratory scale, the PFC particle flow theory was applied to explore the changes in acoustic emission and the overall strength weakening effect during drilling pressure relief under different

physical influencing factors. The purpose was to clarify the effect of drilling pressure relief under various physical influencing factors, and to provide a regular understanding of the optimal parameter scheme for the construction of a single borehole. The main conclusions are as follows:

(1) With the increase of drilling depth, the peak strength of coal samples decreases rapidly first and then increases slowly, and then decreases slowly. With the increase of drilling diameter, the peak strength of coal samples decreases rapidly and then decreases slowly. With the increase of drilling angle, the peak strength of coal samples decreases first and then increases. Among them, the drilling depth of 30 mm, the drilling diameter of 14 mm, and the drilling angle of  $25^\circ$  are the critical thresholds when the above peak strength is low, indicating that when these values are taken, the drilling pressure relief effect is relatively good.

(2) When the coal sample is under the condition of a drilling depth of 30 mm, a drilling diameter of 14 mm, and a drilling angle of  $25^\circ$ , the location of the failure crack and the distribution of the force chain in the surrounding area are evacuated, and the color of the force chain is darker and the size of the force chain is smaller, which proves that this area has a better pressure relief effect, which is consistent with the above conclusions. The spatial distribution of cracks in coal samples is consistent with the spatial distribution of seismic sources. With the increase of hole depth, drilling diameter, and drilling angle, the cracks show the characteristics of changing from conjugate shear fractures to single inclined plane shear fractures, and the critical thresholds of transition are a drilling depth of 30 mm, a drilling diameter of 14 mm, and a drilling angle of  $25^\circ$ .

(3) Under various conditions, shear fractures and tensile fractures account for a very high proportion, indicating that these two fracture modes are the main types of microscopic fracture of coal samples, and the proportion of shear fractures is slightly higher than that of tensile fractures. When the drilling depth is 30 mm, the drilling diameters is 14 mm, and the drilling angle is  $25^\circ$ , the number of cracks is at a lower level.

(4) The moment tensor values of coal sample drilling are mainly distributed in the range of  $-7.5\sim-5.0$ , and the peak values mainly appear in the range of  $-7.0\sim-6.5$ . The relationship between the M value and N value is generally subject to normal distribution. When the drilling depth is 30 mm, the drilling diameter is 14 mm, and the drilling angle is  $25^\circ$ , the number of AE events is relatively low. With the increase of the hole diameter, the b value first increases and then decreases, and finally tends to be stable. With the increase of the drilling depth, the b-value first increases and then decreases, and finally increases again. With the increase of the drilling angle, the b-value first increases and then stabilizes. It shows that the events with small AE energy account for a large proportion when the drilling depth, drilling diameter, and drilling angle are small.

**Author Contributions:** Methodology, S.Z.; Software, S.Y.; Formal analysis, J.M. and J.L.; Investigation, J.M., J.L., S.Z., S.Y. and X.D.; Data curation, J.L., S.Y., X.D. and D.L.; Writing—original draft, J.M.; Writing—review & editing, J.M.; Visualization, J.L., X.D. and D.L.; Supervision, J.M., S.Z. and S.Y. All authors have read and agreed to the published version of the manuscript.

**Funding:** This research was funded by National Natural Science Foundation of China grant number 52274186.

**Data Availability Statement:** Data are contained within the article.

**Conflicts of Interest:** The authors declare no conflict of interest.

## References

1. Zhao, T.B.; Guo, W.Y.; Tan, Y.L.; Yin, Y.C.; Cai, L.S.; Pan, J.F. Case Studies of Rock Bursts Under Complicated Geological Conditions During Multi-seam Mining at a Depth of 800 m. *Rock Mech. Rock Eng.* **2018**, *51*, 1539–1564. [CrossRef]
2. Zhou, F.B.; Xia, T.Q.; Wang, X.X.; Zhang, Y.F.; Sun, Y.N.; Liu, J.S. Recent developments in coal mine methane extraction and utilization in China: A review. *J. Nat. Gas Sci. Eng.* **2016**, *31*, 437–458. [CrossRef]
3. Gong, F.Q.; Yan, J.Y.; Li, X.B.; Luo, S. A peak-strength strain energy storage index for rock burst proneness of rock materials. *Int. J. Rock Mech. Min. Sci.* **2019**, *117*, 76–89. [CrossRef]



4. Yin, Y.C.; Zhou, H.J.; Zhang, Y.B.; Wang, C.; Deng, Y.H.; Chen, B.A. Anchorage weakening effect of coal roadway sidewall with different destressing borehole diameters. *Energy Sci. Eng.* **2023**, *11*, 1325–1335. [CrossRef]
5. Chen, M.; Zhang, Y.L.; Zang, C.W.; Zhang, G.C.; Li, Q.; Jiang, B.Z. Experimental Investigation on Pressure Relief Mechanism of Specimens with Prefabricated Reaming Boreholes. *Rock Mech. Rock Eng.* **2023**, *56*, 2949–2966. [CrossRef]
6. Lan, Y.W.; Zhang, Y.J.; Gao, H.M. Research on the Mechanism of Floor Heave of Roadway in Deep Mining. *Kuangye Yanjiu Yu Kaifa Min. Res. Dev.* **2005**, *25*, 34–36.
7. Ortlepp, W.; Stacey, T. Rockburst mechanisms in tunnels and shafts. *Tunn. Undergr. Space Technol.* **1994**, *9*, 59–65. [CrossRef]
8. Reyes, O.; Einstein, H. Failure mechanisms of fractured rock—a fracture coalescence model. In Proceedings of the 7th ISRM Congress, Aachen, Germany, 16–20 September 1991.
9. Pan, Y.; Zhao, G.M.; Meng, X.R. Elastic-plastic analysis of roadway surrounding rock under non-uniform stress field. *J. China Coal Soc.* **2011**, *36*, 53–57.
10. Wu, H.; Zhao, G.Y.; Liang, W.Z. Mechanical properties and fracture characteristics of pre-holed rocks subjected to uniaxial loading: A comparative analysis of five hole shapes. *Theor. Appl. Fract. Mech.* **2020**, *105*, 18. [CrossRef]
11. Liu, J.H.; Jiang, F.X.; Wang, N.G. *Roof Movement Disaster Control of Long Fully Mechanized Caving Face in Deep Topsoil*; Beijing Science Press: Beijing, China, 2013.
12. Zhang, H.; Li, T.; Ouyang, Z.H.; Liu, S.; Yi, H.Y. Research on Optimization of Coal Pressure Relief Borehole Parameters under High-Stress Conditions. *Geofluids* **2021**, *2021*, 13. [CrossRef]
13. Zhang, S.C.; Li, Y.Y.; Shen, B.T.; Sun, X.Z.; Gao, L.Q. Effective evaluation of pressure relief drilling for reducing rock bursts and its application in underground coal mines. *Int. J. Rock Mech. Min. Sci.* **2019**, *114*, 7–16. [CrossRef]
14. Li, Y.Y.; Guo, R.W.; Zhang, S.C.; Chen, B.; Yan, H.; Meng, W.; Zheng, D. Experimental Study on Pressure Relief Mechanism of Variable-Diameter Borehole and Energy Evolution Characteristics of the Surrounding Rock. *Energies* **2022**, *15*, 6596. [CrossRef]
15. Bahrehdar, M.; Lakirouhani, A. Effect of eccentricity on breakout propagation around noncircular boreholes. *Adv. Civ. Eng.* **2023**, *2023*, 6962648. [CrossRef]
16. Qin, Z.H. Study of Pressure Relief with Large Diameter Drilling Hole and Results Verified. *J. Min. Strat. Control* **2018**, *23*, 77–80.
17. Liu, H.G.; He, Y.N.; Xu, J.H.; Han, L.J. Numerical simulation and industrial test of boreholes destressing technology in deep coal tunnel. *J. China Coal Soc.* **2007**, *32*, 33–37.
18. Liang, S.W.; Zhang, L.; Ge, D.; Wang, Q. Study on Pressure Relief Effect and Rock Failure Characteristics with Different Borehole Diameters. *Shock Vib.* **2021**, *2021*, 10. [CrossRef]
19. Liu, H.G.; Xu, J.H. Numerical simulation and application of borehole pressure relief mechanism in coal roadway. *Coal Sci. Technol. Mag.* **2003**, *4*, 37–38.
20. Wen, Y.L.; Zhang, G.J.; Zhang, Z.Q. Numerical experiments of drilling pressure relief preventing roadway rock burst. In Proceedings of the 3rd International Conference on Civil Engineering, Architecture and Building Materials (CEABM 2013), Jinan, China, 24–26 May 2013; pp. 1583–1587.
21. Wang, T.X.; Cao, H.J.; Zhang, Z.Y. Numerical Simulation and Field Practice of Pressure-relief Borehole to Prevent Coal Burst in Deep-seated Coal Roadway. In Proceedings of the 2nd International Conference on Mine Hazards Prevention and Control, Qingdao, China, 15–17 October 2010; pp. 1583–1587.
22. Jia, C.Y.; Jiang, Y.J.; Zhang, X.P.; Wang, D.; Luan, H.J.; Wang, C.S. Laboratory and numerical experiments on pressure relief mechanism of large-diameter boreholes. *Chin. J. Geotech. Eng.* **2017**, *39*, 1115–1122.
23. Itasca. *PFC 6.0 Documentation, User's Guide*, Version 6.00.13; Itasca Consulting Group: Minneapolis, MN, USA, 2019.
24. Potyondy, D.O. Simulating stress corrosion with a bonded-particle model for rock—ScienceDirect. *Int. J. Rock Mech. Min. Sci.* **2007**, *44*, 677–691. [CrossRef]
25. Potyondy, D.O.; Cundall, P. A bonded-particle model for rock. *Int. J. Rock Mech. Min. Sci.* **2004**, *41*, 1329–1364. [CrossRef]
26. Hazzard, J.F.; Young, R.P. Moment tensors and micromechanical models. *Tectonophysics* **2002**, *356*, 181–197. [CrossRef]
27. Hazzard, J.F.; Young, R.P. Dynamic modelling of induced seismicity. *Int. J. Rock Mech. Min. Sci.* **2004**, *41*, 1365–1376. [CrossRef]
28. Silver, P.G.; Jordan, T.H. Optimal estimation of scalar seismic moment. *Geophys. J. Int.* **2010**, *70*, 755–787. [CrossRef]
29. Hanks, T.C.; Kanamori, H. A moment magnitude scale. *J. Geophys. Res.* **1979**, *84*, 2348. [CrossRef]
30. Wang, K.; Zhang, X.; Du, F.; Li, K.N.; Sun, J.Z.; Wang, Y.Q. Numerical study on damage response and failure mechanism of gas-containing coal-rock combination under confining pressure effect. *Fuel* **2023**, *349*, 17. [CrossRef]
31. Yu, W.; Yu, L.; Yao, D. A bonded-particle model for rock. *J. Chengdu Univ. Technol. Sci. Technol. Ed.* **2021**, *48*, 714–722.

**Disclaimer/Publisher's Note:** The statements, opinions and data contained in all publications are solely those of the individual author(s) and contributor(s) and not of MDPI and/or the editor(s). MDPI and/or the editor(s) disclaim responsibility for any injury to people or property resulting from any ideas, methods, instructions or products referred to in the content.

## Article

# Study on the Spatiotemporal Dynamic Evolution Law of a Deep Thick Hard Roof and Coal Seam

Zhigang Zhang<sup>1,2</sup>, Linchao Dai<sup>1,2,\*</sup>, Haitao Sun<sup>1,2,\*</sup>, Yanbao Liu<sup>1,2</sup>, Huiming Yang<sup>1,2</sup>, Rifu Li<sup>1,2</sup> and Yi Zhang<sup>1,2</sup>

<sup>1</sup> State Key Laboratory of the Gas Disaster Detecting, Preventing and Emergency Controlling, Chongqing 400037, China; zzg-2@163.com (Z.Z.); yanbao\_liu@163.com (Y.L.); yhm3380@163.com (H.Y.); cqlirifu@163.com (R.L.); zy15896750887@126.com (Y.Z.)

<sup>2</sup> China Coal Technology and Engineering Group, Chongqing Research Institute, Chongqing 400037, China

\* Correspondence: 20212001047g@cqu.edu.cn (L.D.); dreamsht@163.com (H.S.); Tel.: +86-02365239611 (L.D.)

**Abstract:** Underground mining in coal mines causes strong disturbance to geological structures and releases a large amount of elastic strain energy. When the roof is a hard and thick rock layer, it is easy to cause dynamic disasters such as rock burst. To analyze the impact of a deep thick and hard roof fracture on the safe mining of thick coal seams, this paper studied the dynamic evolution process of the stress field, displacement field, energy field, and plastic zone of the coal seam and overlying strata during the mining process using FLAC3D numerical simulation. The results show that as the working face continues to be mined, the concentrated stress in the overlying strata first increases and then decreases, and the support pressure in front of the working face continues to increase. When it advances to 100 m, collapse occurs, and the stress increases sharply; the bottom plate undergoes plastic failure, resulting in floor heave. The overlying strata mass in the top plate exhibits downward vertical displacement, while the rock mass in the bottom plate exhibits upward vertical displacement, with a maximum subsidence of 4.51 m; energy concentration areas are generated around the working face roadway, forming an inverted “U” shape. When collapse occurs, the energy density decreases slightly; the direction of the plastic zone changes from “saddle shaped” to complete failure of the upper rock layer, and the overlying strata is mainly shear failure, which expands with the increase in mining distance. The research results have important practical significance for guiding the safe mining of deep thick and hard roof working faces.

**Keywords:** impact pressure; deep thick hard top plate; mining disturbances; numerical simulation

**Citation:** Zhang, Z.; Dai, L.; Sun, H.; Liu, Y.; Yang, H.; Li, R.; Zhang, Y. Study on the Spatiotemporal Dynamic Evolution Law of a Deep Thick Hard Roof and Coal Seam. *Processes* **2023**, *11*, 3173.

<https://doi.org/10.3390/pr11113173>

Academic Editors: Carlos Sierra Fernández, Feng Du, Aitao Zhou and Bo Li

Received: 18 October 2023

Revised: 2 November 2023

Accepted: 6 November 2023

Published: 7 November 2023



**Copyright:** © 2023 by the authors. Licensee MDPI, Basel, Switzerland. This article is an open access article distributed under the terms and conditions of the Creative Commons Attribution (CC BY) license (<https://creativecommons.org/licenses/by/4.0/>).

## 1. Introduction

China has abundant coal resources and a wide distribution area. Coal occupies a dominant position in the composition of disposable energy in China. With the rapid development of the social economy and the improvement in people’s living standards, the demand for raw coal is also increasing year by year [1,2]. In recent years, with the gradual depletion in shallow mineral resources in mining areas in eastern China, deep mining has become an inevitable trend for future development. Due to various factors such as tectonic stress, self-weight of overlying load, and complex geological structure, there are significant differences in the stress field of the original rock in deep coal seams compared to shallow coal seams. The deep environment accumulates more elastic energy in the coal seam, roof, and floor, and their combined structures during coal seam disturbance, resulting in high energy in the deep and frequent occurrence of large-scale coal rock dynamic disasters [3–7]. Thick and hard roof slabs are distributed in more than half of China’s mining areas, and the occurrence conditions of coal seams are relatively complex. Today, with the widespread use of fully mechanized mining technology, nearly 40% of fully mechanized mining faces have experienced the phenomenon of thick and hard roof falling violently for the first time [8–10].

Therefore, it is particularly important to master the temporal and spatial evolution law of overlying strata movement and energy under the condition of a deep thick and hard roof.

In recent years, many researchers at home and abroad have done a lot of work for the mining of coal seams under thick and hard roof conditions [11–13]. Ma et al. [14] used a variety of research methods to reveal the deformation and failure mechanism of roadway-surrounding rock in a gently inclined soft coal seam under different factors under the condition of a thick and hard roof, and put forward corresponding treatment plans. Wang et al. [15] studied the ground pressure behavior law of a fully mechanized top coal caving face under the condition of a shallow buried thick hard roof, and used fracturing technology to pre-crack the thick hard roof of the face, and achieved good results. Tan et al. [16] studied the mechanism of hard-roof-type rock burst, and the results showed that the two characteristics of stress mutation and energy increase can serve as important indicators of precursor information of rock burst. Zhang et al. [17] used a comprehensive research method to study the distribution law of mining-induced stress during the mining process of the working face. The results showed that the thick and hard roof overlying the coal seam is the main influencing factor of mining-induced stress, and the closer the coal seam is to the thick and hard roof, the more concentrated the mining-induced stress is. Kang et al. [18] used a comprehensive research method to study the failure and movement patterns of thick and hard roof structures, and obtained the deformation and stress distribution patterns of the roof. Liang et al. [19] established a mechanical analysis model to study the relationship between different influencing factors on the advanced fracture position and initial fracture distance of a thick and hard roof, and compared the analysis results with on-site monitoring data to verify the accuracy of the model. Li et al. [20] used five working faces of Chenghe No.2 Coal Mine as an example to study the failure mechanism of the roof and floor of the No.2 coal seam using a combination of on-site testing and numerical simulation. They also analyzed the distribution patterns of stress and displacement fields and plastic zone evolution characteristics of the roof and floor with different degrees of advancement of the working face. Xiong et al. [21] established a mechanical model for coal face failure under repeated mining conditions. Through similar simulation experiments and numerical simulation methods, the development of coal seam roof structure and surrounding rock fractures under repeated mining conditions was studied. The results showed that under the same roof pressure, the development of coal face fractures was more complete, the coal strength was lower, and the coal face was more prone to failure. Yang et al. [22] constructed a 3D physical simulation test under the condition of a thick and hard roof, and obtained the evolution law of the overburden displacement field and the dynamic evolution characteristics of “three belts” during thick seam mining. Bu et al. [23] constructed a mechanical model for the mining bearing capacity of a thick and hard roof, and from the perspective of energy, analyzed the relationship between the energy accumulated due to the fracture of the thick and hard roof in the mining area and the strong dynamic pressure manifestation, revealing the characteristics of the impact of the fracture instability of the thick and hard roof on the strong rock pressure manifestation.

In summary, when researching the instability of a coal seam under the conditions of a thick, hard roof, researchers both domestically and internationally primarily concentrate on one or two of the stress field, displacement field, and energy field, ignoring the investigation of the space–time evolution law of multiple fields. Numerical simulation techniques for engineering geology are maturing and getting better with the broad usage of computer technology. These techniques are also gradually being applied to solve engineering geological problems. The mutual verification between the results of numerical simulation calculations, experimental findings, and engineering practice has expanded the scope of problem solving in engineering geology, deepened the exploration of research topics, and effectively advanced the quantitative advancement of the engineering geological discipline [24–26]. Therefore, during the mining process of deep, thick, and hard roof working faces, this research employs FLAC3D V4.0 numerical simulation software to simulate and

examine the dynamic evolution process of the stress field, displacement field, energy field, and plastic zone of the coal seam and overlaying strata. Additionally, the distribution law and process of mining stress and thick hard impact roof impact on the alteration of coal elastic energy under deep high-stress conditions were examined. Under the limit conditions of gas containing coal failure and instability (outburst), obtain the dynamic distribution state, dynamic transfer process, and superposition effect with the high-energy elastic performance of the thick and hard roof. Then, analyze the spatial dynamic evolution law of the stress field and energy field. The study's findings can serve as a guide for safe mining in comparable circumstances.

## 2. Three-Dimensional Numerical Model of Coal Seam in Deep Thick and Hard Roof Working Face

A growing number of researchers are turning to numerical simulation techniques to address engineering geology-related issues as the field's numerical simulation technology matures. Using three-dimensional rapid Lagrangian analysis technology, FLAC3D is a numerical modeling tool that accurately models the behavior of materials in yield, plastic flow, softening, and massive deformation. The program is extensively used because of its strong functionality and good universality. Its distinctive advantages have been shown, particularly in the research on major deformation, simulation of construction processes, and material elasticity and plasticity analyses. Because of this reason, this study analyzes the working face mining process using FLAC3D V4.0 software while a thick, hard ceiling is present.

### 2.1. Selection of Constitutive Model

The rock mass in this simulation is mainly composed of sandstone and mudstone, which exhibit obvious elastic–plastic deformation characteristics under different confining pressures. The failure modes of the rock include plastic failure, tensile failure, and shear failure. Therefore, a Mohr–Coulomb constitutive model can be used [27].

#### 2.1.1. Mohr–Coulomb Incremental Elasticity Theory

The Mohr–Coulomb criterion in FLAC3D is represented by principal stress  $\sigma_1$ ,  $\sigma_2$ ,  $\sigma_3$  and strain increment  $\Delta\varepsilon_1$ ,  $\Delta\varepsilon_2$ ,  $\Delta\varepsilon_3$ , respectively. The incremental expression of Hooke's law in terms of generalized stress and stress has the following form:

$$\begin{cases} \Delta\sigma_1 = \alpha_1\Delta\varepsilon_1^e + \alpha_2(\Delta\varepsilon_2^e + \Delta\varepsilon_3^e) \\ \Delta\sigma_2 = \alpha_1\Delta\varepsilon_2^e + \alpha_2(\Delta\varepsilon_1^e + \Delta\varepsilon_3^e) \\ \Delta\sigma_3 = \alpha_1\Delta\varepsilon_3^e + \alpha_2(\Delta\varepsilon_1^e + \Delta\varepsilon_2^e) \end{cases} \quad (1)$$

In the formula,  $\Delta\varepsilon_i^e$  represents the increment of elastic strain;  $\alpha_1$  and  $\alpha_2$  are material constants defined in terms of the shear modulus,  $G$ , and bulk modulus,  $K$ , as follows:

$$\alpha_1 = K + (4/3)G \quad (2)$$

$$\alpha_2 = K - (2/3)G \quad (3)$$

#### 2.1.2. Mohr–Coulomb Yield Criterion

The failure envelope defined by the Mohr–Coulomb yield function from point A to point B is

$$f^s = \sigma_1 - \sigma_3 N_\phi + 2c\sqrt{N_\phi} \quad (4)$$

The yield function of tensile stress from point B to point C is defined as

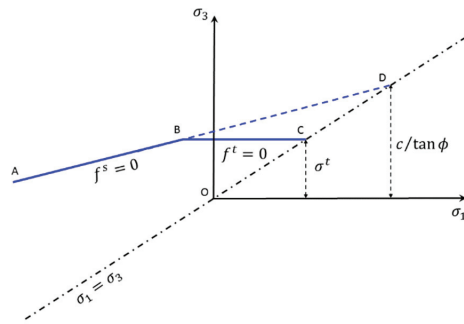
$$f^t = \sigma^t - \sigma_3 \quad (5)$$

In the formula,  $\phi$  is the friction angle,  $c$  is the cohesion force, and  $\sigma^t$  is the tensile strength, and

$$N_\phi = \frac{1 + \sin \phi}{1 - \sin \phi} \tag{6}$$

As shown in Figure 1, when  $f^s \geq 0$ , the material will undergo shear failure. After reaching the yield limit, the material undergoes plastic deformation at a constant stress level [28]. In the state of tensile stress, if the tensile stress exceeds the tensile strength of the material, the material will fail. And the strength of the material cannot exceed the  $\sigma_{\max}^t$  value defined below, namely

$$\sigma_{\max}^t = \frac{c}{\tan \phi} \tag{7}$$



**Figure 1.** Mohr–Coulomb model of geotechnical materials and failure criteria.

### 2.1.3. Mohr–Coulomb Flow Criterion

The shear potential function  $g^s$  corresponds to the non-correlated flow law, namely

$$g^s = \sigma_1 - \sigma_3 N_\phi \tag{8}$$

The potential function  $g^t$  corresponds to the correlated flow law of tensile stress failure, namely

$$g^t = -\sigma_3 \tag{9}$$

For the case of shear tensile stress near the boundary, the flow criterion of the Mohr–Coulomb model can be used to calculate by defining a mixed yield function near the boundary in a three-dimensional stress space. Define function  $h(\sigma_1, \sigma_3) = 0$  to represent the diagonal of the curves represented by  $f^s = 0$  and  $f^t = 0$  in the  $(\sigma_1, \sigma_3)$  plane. The expression for this function is

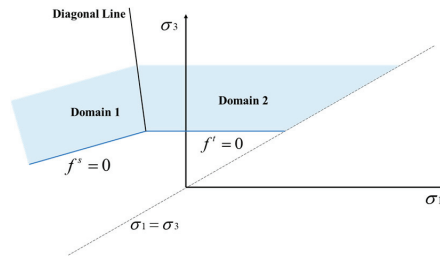
$$h = \sigma_3 - \sigma^t + a^p(\sigma_1 - \sigma^p) \tag{10}$$

In the formula

$$a^p = \sqrt{1 + N_\phi} + N_\phi \tag{11}$$

$$\sigma^p = \sigma^t N_\phi - 2c\sqrt{N_\phi} \tag{12}$$

The form of damage is represented by Zone 1 or Zone 2 in the  $(\sigma_1, \sigma_3)$  plane in Figure 2. If located in Zone 1, it is shear failure. Applying the flow criterion determined with potential function  $g^s$ , the stress points are regressed to the curve of  $f^s = 0$ . If located in Zone 2, it is tensile stress failure. Applying the flow criterion determined with potential function  $g^t$ , the stress points are regressed to the curve of  $f^t = 0$  [29].

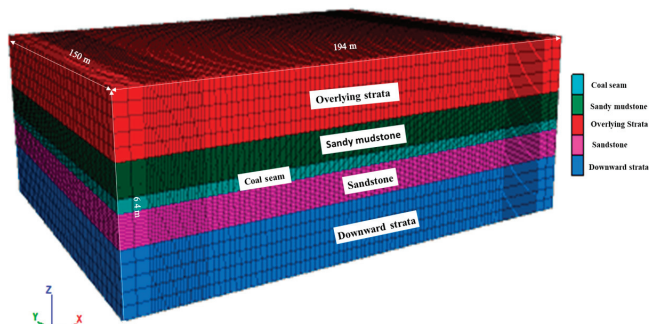


**Figure 2.** The area used in the Mohr–Coulomb model to define the flow criterion.

## 2.2. Establishment of a Three-Dimensional Numerical Model

The coal seam mined using a fully mechanized mining face in a certain coal mine had a gentle attitude and well-developed fractures. The thickness of the coal seam was 3.1–5.7 m, with a local thickness of 6.2 m and an average coal thickness of 4 m. The structure of the coal seam was relatively complex, containing 1–3 layers of gangue, and the lithology of the gangue was mostly siltstone. The dip angle of the coal seam was 0–10°, with an average of 4°. It was a nearly horizontal coal seam. The length of the working face was 150 m, and the burial depth of the working face was about 670 m. The roof of the coal seam was mainly composed of sandy mudstone and mudstone, while the floor was mainly composed of sandstone.

Taking the production geological conditions of the mining face as an example, a FLAC3D numerical physical model was established, as shown in Figure 3. The model size was 194 m × 150 m × 64 m, totally divided into five layers, of which the coal seam was 4 m thick. Because the coal seam was near horizontal, this simulation did not consider the issue of dip angle, and the dip angle of the coal seam was 0°. The number of zones generated was 159,840, and the number of grid points was 173,600. The X-axis direction of the model was defined as the inclination of the working face. The negative direction of the Y-axis was defined as the strike of the working face. The direction of rock deposits and reserves was defined as the Z-axis. A 10 m protective coal pillar was left in both the inclined and strike directions. This simulation used the Mohr–Coulomb constitutive model and activated the large deformation mode. Advance the mining along the Y-axis direction (mining direction of the working face), with a starting line of Y = 10 m and a mining step distance of 100 m. The mining was completed five times with a mining distance of 20 m. The boundaries around the model restricted horizontal displacement, with a fixed bottom and a free boundary at the top. A stress of 16 MPa was applied at the top to simulate the self-weight of the overlying strata. The lateral pressure coefficient was 1.1. The average unit weight of rock was 25 KN/m<sup>3</sup>. The gas pressure was taken as 0.5 MPa [30,31]. The mechanical parameters used in the model are shown in Table 1.



**Figure 3.** FLAC3D numerical physics model.

**Table 1.** Mechanical parameters of coal seam roof and floor.

Rock Strata	Thickness/ (m)	Density/ (kg·m <sup>-3</sup> )	Friction Angle/(°)	Cohesion/ MPa	Bulk Modulus/MPa	Shear Modulus/MPa	Tensile Strength/MPa
Overlying strata	20	1914	46.5	5.45	3.12	2.41	5.51
Sandy mudstone	10	2544.45	37.5	4.40	3.48	2.26	4.29
Coal seam	4	1625.75	24	3.30	1.52	0.81	1.25
Sandstone	10	2454	38.5	4.55	2.67	2.25	3.99
Downward strata	20	2314	46.5	5.45	2.41	2.41	5.41

### 3. Analysis of Numerical Simulation Results

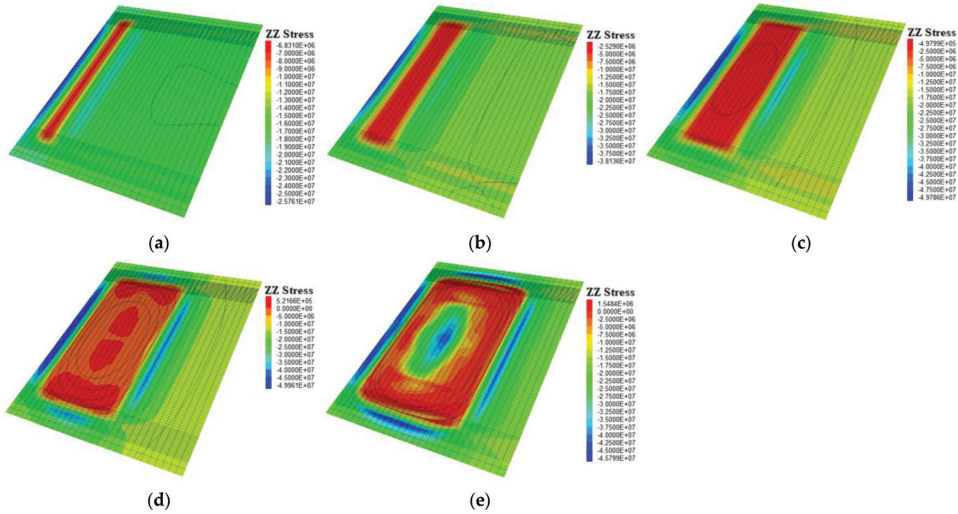
This simulation studied the spatiotemporal evolution of the stress field, displacement field, energy field, and plastic zone in the coal seam and overlying strata of the deep thick and hard roof working face during the excavation process of the model  $Y = 10$  m to  $Y = 110$  m, with a mining distance of 100 m. In order to better display the spatiotemporal evolution laws of the stress field, displacement field, energy field, and plastic zone of the coal seam and overlying strata during the mining period of the deep thick and hard roof working face from multiple angles, a horizontal section is made for the overlying strata above the parallel coal seam, a vertical section is made for the parallel advancing direction, and monitoring lines are arranged at different distances from the bottom of the coal seam to monitor the changes in stress, displacement, and energy of the coal seam and overlying strata in real time every 20 m of advancing of the working face [32]. Three monitoring lines are arranged at  $Y = 115$  m, with distances of 2 m, 12 m, and 22 m from the bottom of the coal seam, respectively; the total length of the monitoring line is 150 m, with a total of 16 monitoring points per layer, with a spacing of 10 m.

#### 3.1. The Spatiotemporal Evolution Law of the Stress Field in the Coal Seam and Overlying Strata during the Mining Period of the Working Face

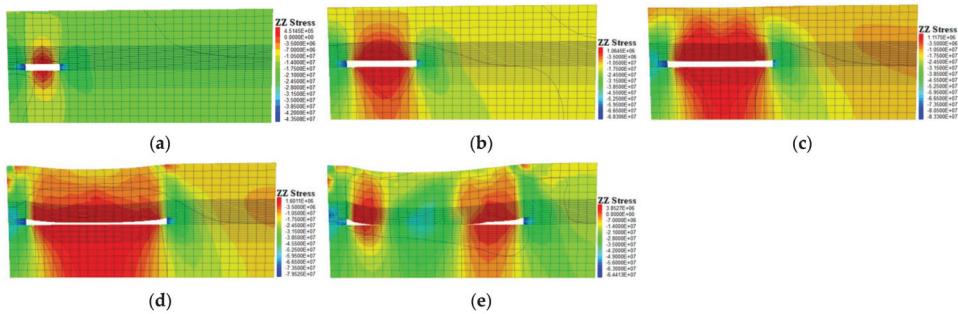
During the mining process of the working face, the stress field distribution of the overlying strata in the parallel and vertical directions of the working face is shown in Figures 4 and 5, respectively. The stress distribution of the overlying strata at different distances from the coal seam floor is shown in Figure 6.

As shown in Figures 4–6, as the working face continues to be mined, the support pressure in front of the working face continues to increase, leading to a gradual expansion of the scope of overlying strata failure; the farther away from the coal seam, the smaller the changes in overlying strata stress and displacement due to mining disturbance. As shown in Figure 4, as the working face advances, the stress concentration area of the overlying strata continues to expand, and the concentrated stress shows a trend of first increasing and then decreasing (it has increased from 25.7 MPa to 49.9 MPa and then decreased to 45.8 MPa). This is because collapse occurred when the excavation reached 100 m, resulting in partial stress release and a small decrease in concentrated stress. The overlying strata stress is mainly concentrated in the front of the working face and on both sides of the roadway. The stress in the overlying strata at the goaf is relatively low, which is the result of the movement of overlying strata during the extraction of coal seams. From Figure 4e, it can be seen that the mining of coal forms a goaf, and the stress in the surrounding coal and rock mass redistributes. The vertical stress around the mining face increases. As the roof collapses, the interior of the goaf is filled until it returns to the original rock stress state. From Figure 5, it can be seen that as the mining face continues to advance, the stress in the overlying strata behind the face gradually decreases, and the stress reduction area continues to expand. The overlying strata has a pressure relief zone, and the stress value gradually decreases with the coal seam mining and develops upwards. When the working face advances 100 m, collapse occurs and the stress increases sharply. As shown in Figure 6, when the advancing distance of the working face reaches 60 m, the stress in the overlying strata remains almost unchanged. When the advancing distance reaches 80 m, the stress increases slightly. When the advancing distance reaches 100 m, the stress at 2 m and 12 m

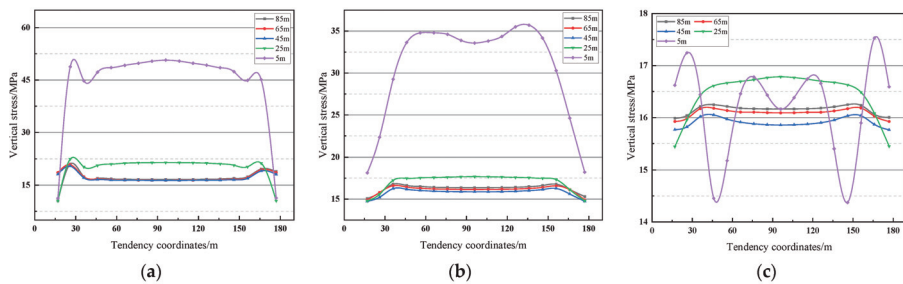
away from the coal seam floor increases significantly, and the stress in the overlying strata at 22 m away from the coal seam floor changes sharply.



**Figure 4.** Spatial distribution of overburden stress at 12 m from the bottom of the coal seam during the remining period of the working face: (a) 20 m; (b) 40 m; (c) 60 m; (d) 80 m; (e) 100 m.



**Figure 5.** Overlying stress cloud along the direction of face advancement during face remining: (a) 20 m; (b) 40 m; (c) 60 m; (d) 80 m; (e) 100 m.

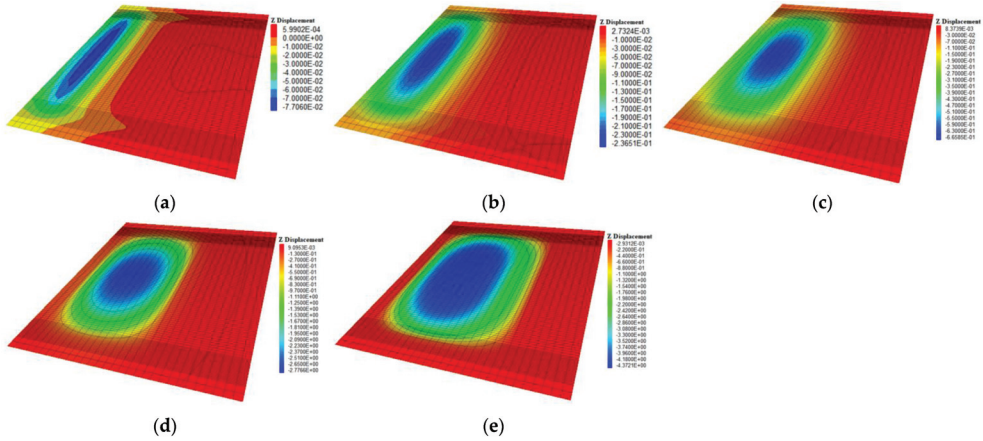


**Figure 6.** Vertical stress evolution results of overlying strata at different distances from the bottom of the coal seam during face remining: (a) 2 m; (b) 12 m; (c) 22 m.

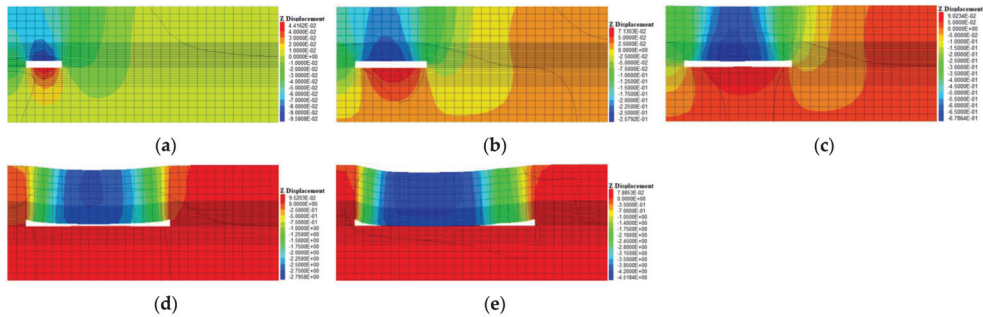


### 3.2. The Spatiotemporal Evolution Law of the Displacement Field of Coal Seams and Overlying Strata during the Mining Period of the Working Face

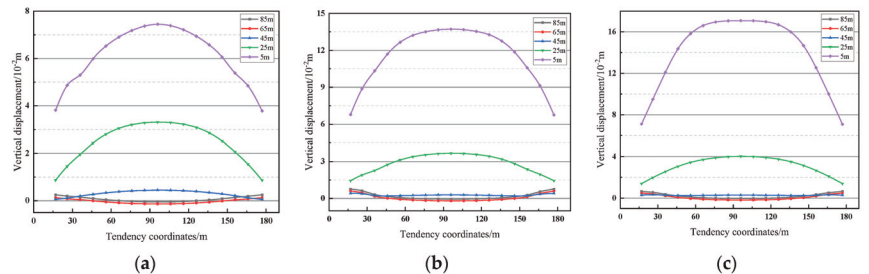
During the mining process of the working face, the distribution of the displacement field of the overlying strata in the parallel and vertical directions of the working face is shown in Figures 7 and 8, and the distribution of the displacement curve of the overlying strata at different distances from the coal seam floor is shown in Figure 9.



**Figure 7.** Spatial distribution of overburden movement at 12 m from the coal seam floor at different distances of the working face: (a) 20 m; (b) 40 m; (c) 60 m; (d) 80 m; (e) 100 m.



**Figure 8.** Overlying displacement cloud along the advance direction of the working face during the remining of the working face: (a) 20 m; (b) 40 m; (c) 60 m; (d) 80 m; (e) 100 m.



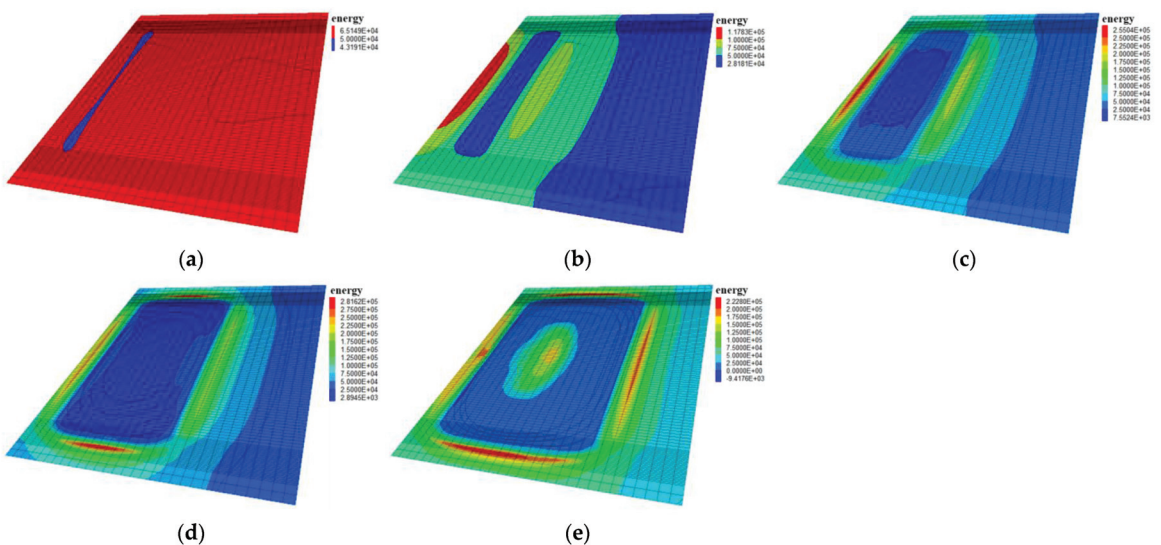
**Figure 9.** Evolution results of vertical displacement of overlying strata at different distances from the bottom of coal seam during the remining period of the working face: (a) 2 m; (b) 12 m; (c) 22 m.

From Figures 7 and 8, it can be seen that with the continuous mining of the working face, the rock mass on the top and bottom of the coal seam exhibits obvious displacement characteristics. The overlying strata mass in the working face roof mainly exhibits downward vertical displacement, while the rock mass in the bottom plate mainly exhibits upward vertical displacement. The displacement of the roof increases as the working face advances. When the working face advances to 80 m, there is a significant collapse, and when it advances to 100 m, there is a complete collapse with a maximum subsidence of 4.51 m. There was a significant upward displacement of the bottom plate at a distance of 80 m, increasing from 4.4 mm to the final 7.8 mm. This indicates that as the working face advances, the bottom plate undergoes plastic failure and produces a phenomenon of floor heave. From Figure 9, it can be seen that when the working face advances to 60 m, the displacement of the roof does not change significantly. When it advances to 80 m, the displacement slightly increases, while when it advances to 100 m, the displacement increases significantly. In addition, as the distance between the roof and the coal seam floor increases, its displacement also increases.

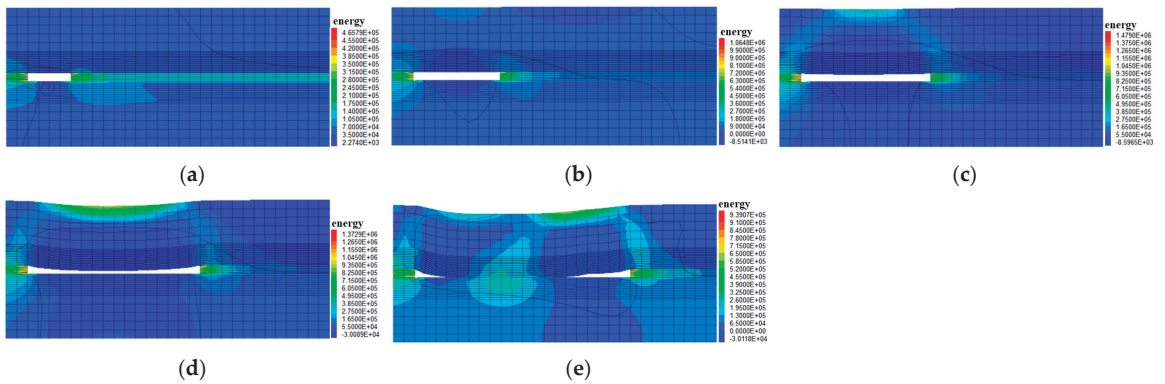
### 3.3. The Spatiotemporal Evolution Law of the Energy Field of Coal Seams and Overlying Strata during the Mining Period of the Working Face

During the mining process of this working face, the energy field distribution of the overlying strata in the parallel and vertical directions of the working face is shown in Figures 10 and 11, and the elastic energy distribution of the overlying strata at different distances from the coal seam floor is shown in Figure 12. The formula for calculating the elastic energy of the roof and coal seam is as follows:

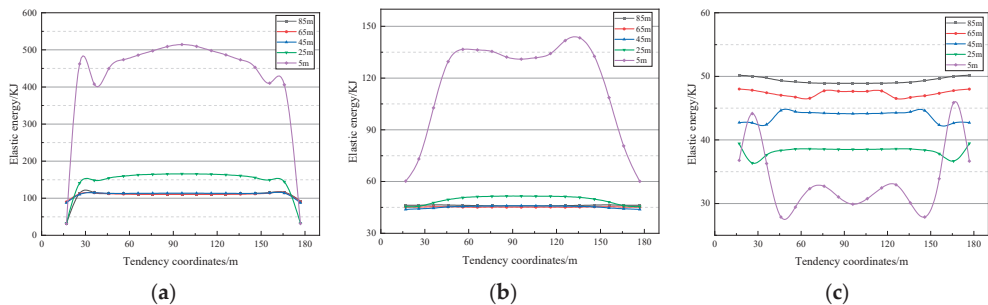
$$U = \frac{\sigma_1^2 + \sigma_2^2 + \sigma_3^2 - 2\nu(\sigma_1\sigma_2 + \sigma_1\sigma_3 + \sigma_2\sigma_3)}{2E} \quad (13)$$



**Figure 10.** Energy distribution of overburden at 12 m from the bottom of the coal seam during the remaining period of the working face: (a) 20 m; (b) 40 m; (c) 60 m; (d) 80 m; (e) 100 m.



**Figure 11.** Cloud map of overlying elastic energy along the direction of face advancement during face remining: (a) 20 m; (b) 40 m; (c) 60 m; (d) 80 m; (e) 100 m.



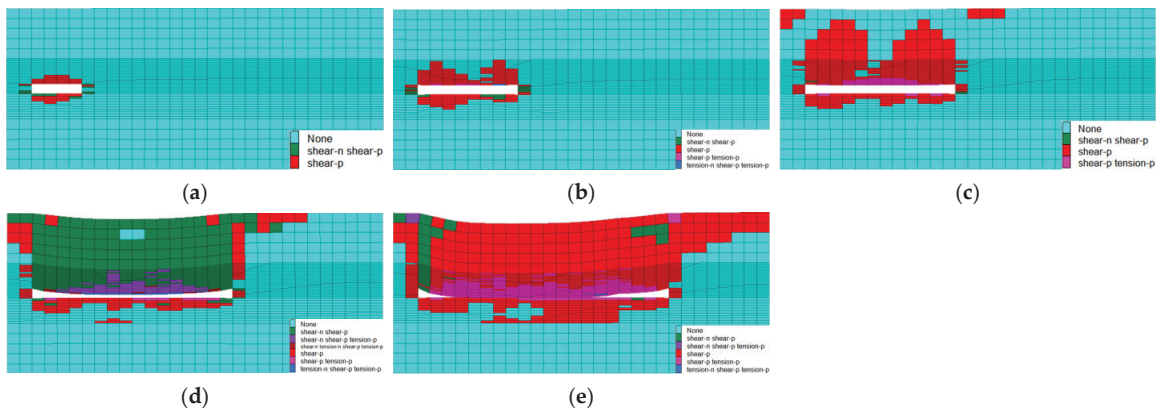
**Figure 12.** Evolution of elastic energy of overlying strata at different distances from the bottom of the coal seam during the recovery of the working face: (a) 2 m; (b) 12 m; (c) 22 m.

From Figures 10 and 11, it can be seen that the elastic energy after coal seam excavation is mainly concentrated in the overlying strata behind the working face and on both sides of the tunnel. Due to the soft nature of the coal body, the elastic deformation generated with the force is relatively large, and the stored elastic energy is relatively high, with a high energy density. Once the overlying strata is broken, the large amount of elastic energy stored in the coal and rock mass due to self-weight will be suddenly released, causing dangerous accidents. It can be seen that with the continuous mining of the working face, there is a significant energy concentration area around the working face roadway. When the working face is mined to 60 m, energy is connected at both ends of the roadway and the roof, forming an inverted “U” shape. And during the continuous mining process, this area also expands accordingly, reaching its maximum value when the working face advances to 100 m, but collapse occurs at this time and the energy density decreases slightly. From Figure 12, it can be seen that the upper and lower end areas are affected by the concentrated lateral support pressure of the mining face, resulting in energy accumulation. At a distance of 2 m and 12 m from the coal seam floor, a large amount of energy accumulation is generated in front of the working face due to mining disturbance, and the energy accumulation is relatively small at a distance of 22 m from the coal seam floor. Overall, the closer to the coal seam floor, the higher the accumulated elastic energy.

### 3.4. Plastic Failure Characteristics of Overlying Strata during Mining

From Figure 13, it can be seen that when the mining distance of the working face is short, the top and bottom rock layers undergo shear failure, a small portion undergoes

tensile failure, and shear failure occurs in front of the coal wall and at the opening of the working face. As the working face continues to be mined, the height of plastic zone damage gradually increases, and the scope of damage gradually expands; when the working face is mined to a depth of 20 m, shear failure occurs in the top and bottom rock layers of the goaf. When mined to a depth of 40 m, a small amount of tensile failure occurs in the overlying strata of the roof. As the working face continues to advance, the scope of tensile failure gradually expands; as shown in Figure 13c, when the working face is mined to 60 m, the plastic zone of the overlying rock above the entire goaf presents a “saddle shaped” shape with high ends and a low middle, and the plastic zone is mainly characterized by shear failure. As shown in Figure 13d,e, with the mining of the working face, the plastic zone changes from “saddle shaped” to a direction where all the rock layers in the upper part of the goaf are destroyed. This is because when the mining reaches 80 m, the overlying strata above the goaf undergoes significant subsidence, the stress balance of the surrounding rock is disrupted, and the stress is redistributed, leading to further expansion of the height of the plastic zone on the roof until it penetrates.

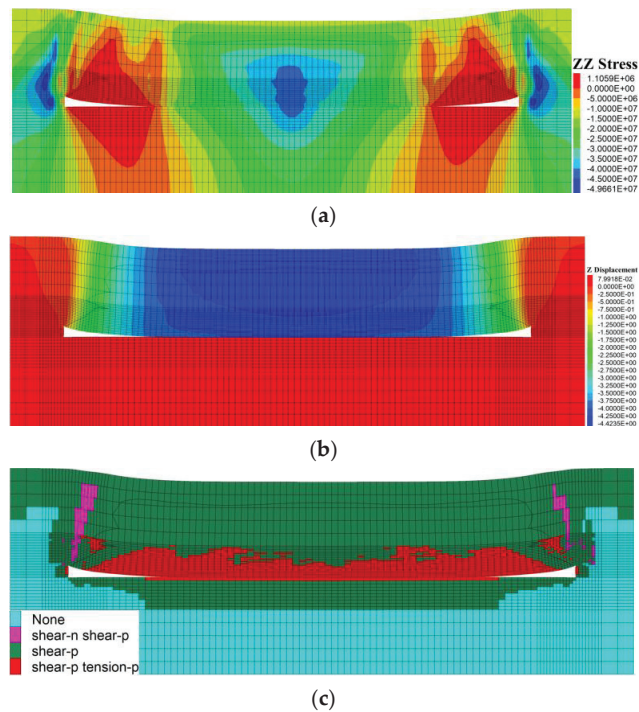


**Figure 13.** Development characteristics of overlying plastic zone above goaf during face remining: (a) 20 m; (b) 40 m; (c) 60 m; (d) 80 m; (e) 100 m.

### 3.5. The Distribution Characteristics of Stress, Displacement, and Plastic Zone in the Coal Seam and Overlying Strata in the Central Goaf

When the working face is mined to a depth of  $Y = 110$  m, the vertical stress, displacement, and plastic zone distribution of the overlying rock in the middle of the goaf at  $Y = 60$  m are shown in Figure 14.

From Figure 14a,b, it can be seen that in the middle of the working face, the overlying strata completely collapses and its vertical stress and displacement reach their maximum, decreasing towards both sides. From Figure 14c, it can be seen that the plastic zone exhibits a typical symmetrical distribution pattern with a larger range of roof failure and smaller two sides. The top plate undergoes tensile shear failure, the overlying strata undergoes large-scale shear failure, and the bottom plate undergoes small-scale shear failure.



**Figure 14.** Distribution of stress, displacement, and plastic zone of the surrounding rock of the top and bottom slabs in the goaf area behind the working face: (a) Vertical stress diagram of overlying strata in goaf; (b) Displacement map of overlying strata in goaf; (c) Distribution of plastic zone of overlying strata in goaf.

#### 4. Discussion

This study introduces the stress, displacement, and energy evolution characteristics of coal seam mining under the condition of a thick and hard roof. FLAC3D, as a simulation research tool, utilizes three-dimensional fast Lagrangian analysis technology and built-in multiple rock mechanics models. It can simulate the mechanical behavior of different types of rocks and soils, accurately simulating the behavior of materials in yield, plastic flow, softening, and large deformation. Moreover, it provides an intuitive graphical user interface that supports parallel computing, greatly improving work efficiency and demonstrating its unique advantages. Therefore, this article systematically analyzes the dynamic evolution process of the stress field, displacement field, energy field, and plastic zone of the coal seam and overlying rock during the mining process of the working face using FLAC3D V4.0 simulation software. The influence process and distribution law of mining stress and thick hard roof fracture on the elastic energy change in coal under a deep high-stress environment were studied, and the dynamic distribution state of high-energy elastic performance accumulation in a thick hard roof under the condition of gas containing coal instability and failure was obtained.

The rock deformation and fracture caused by coal mining may lead to the formation of stress concentration areas and high-stress areas in specific areas, which may lead to rock instability and other problems. Through simulation research, we can understand the stress changes in coal seams and overlying strata during the mining process of deep thick and hard roof working faces, which is of great significance for evaluating the possible stress concentration areas, high-stress areas, and stress transmission mechanisms in coal mining. At the same time, the study analyzed the change process and distribution law of a thick and

hard roof on the elastic energy of coal, which helps to understand the impact of a thick and hard roof on the safety of coal seam mining and provides a basis for designing reasonable support methods and mining processes.

The underground mining activities in coal mines result in the accumulation of a large amount of elastic strain energy in coal layers, especially when the top plate is a hard and thick rock layer, which can easily cause dynamic disasters. Therefore, the safe mining of coal seams under a thick and hard roof is of great significance, but there is currently little research on the spatiotemporal evolution law of multiple fields, and a systematic analysis of the dynamic evolution law of the stress field, displacement field, energy field, and plastic zone during the mining process of deep thick and hard roof working faces. In addition, although the numerical simulation research results are not as accurate as the on-site measurement results, their general trend is the same. Compared to the on-site measurement, the numerical simulation requires less manpower, energy, and financial investment. The results can be mutually verified with the on-site measurement results, providing scientific basis for safety management and coal mining technology in coal mine production.

In this study, the working face is a nearly horizontal coal seam. Due to the simplification of the model, the dip angle of the coal seam in the model is taken as  $0^\circ$ . But even in nearly horizontal coal seams, there may still be some slight tilting or non-uniformity in actual situations. These small inclinations or non-uniformities may have a certain impact on stress distribution, roof stability, and gas extraction. In terms of direction, the mesh division of the model is not dense, and the height of the model is also simplified to a certain extent, which has a certain impact on the analysis of the plastic zone.

## 5. Conclusions

Thick and hard roofs are widely distributed in more than half of China's mining areas. When the roof is a hard and thick rock layer, it is easy to accumulate a large amount of elastic energy during coal seam mining, leading to dynamic disasters such as rock burst. This study utilized FLAC3D V4.0 numerical simulation software to simulate the dynamic evolution process of the stress field, displacement field, energy field, and plastic zone in coal seams and overlying strata during the mining process of deep thick and hard roof working faces, and analyzed the influence process and distribution law of mining stress and a thick hard impact roof on the change in coal elastic energy under a deep high-stress environment. The corresponding conclusions are as follows:

- (1) With the continuous mining of the working face, the support pressure in front of the working face continues to increase, the stress in the overlying strata behind the working face continues to decrease, and the range of overlying strata failure continues to expand; the farther away from the coal seam, the smaller the impact of overlying strata stress due to mining disturbance.
- (2) With the continuous mining of the working face, the rock mass on the top and bottom of the coal seam shows obvious displacement characteristics: the overlying strata mass inside the working face roof mainly shows downward vertical displacement, and the rock mass inside the bottom plate produces floor heave, mainly showing upward vertical displacement.
- (3) With the continuous mining of the working face, there is a clear energy concentration area around the working face roadway. When the working face is mined to 60 m, the energy at both ends of the roadway intersects with the roof, forming an inverted "U" shape. The area expands as the mining distance of the working face increases, reaching its maximum at 100 m. At this point, collapse occurs and the energy density decreases slightly.
- (4) With the continuous mining of the working face, the damage range of the plastic zone of the rock layer gradually expands. When the working face is mined to 60 m, the plastic zone presents a "saddle shaped" distribution, mainly characterized by shear failure. After mining to 80 m, the rock layer above the goaf shows significant

subsidence, and the surrounding rock stress is redistributed. The plastic zone is divided into penetrating the top, and the tensile failure gradually increases.

**Author Contributions:** Conceptualization, Z.Z. and H.S.; methodology, Z.Z., L.D., H.S., Y.L., H.Y. and R.L.; validation, Z.Z., L.D., H.S., Y.L., H.Y., R.L. and Y.Z.; formal analysis, L.D. and H.Y.; investigation, L.D., Y.L., H.Y., R.L. and Y.Z.; resources, Z.Z. and H.S.; data curation, L.D., Y.L. and R.L.; writing—original draft preparation, Z.Z., L.D., H.S., Y.L., H.Y., R.L. and Y.Z.; writing—review and editing, Z.Z., L.D., H.S., Y.L., H.Y., R.L. and Y.Z.; visualization, L.D., H.S., Y.L. and H.Y.; supervision, Z.Z. and H.S.; project administration, Z.Z., L.D. and H.S.; funding acquisition, Z.Z., H.S. and L.D. All authors have read and agreed to the published version of the manuscript.

**Funding:** This research was funded by Natural Science Foundation of Chongqing (No. CSTB2022NSCQ-MSX1080, No. cstc2021jcyj-msxmX1149, No. cstc2021jcyj-msxmX0564), Key Project of Science and Technology Innovation and Entrepreneurship Fund of Tiandi Technology Co., Ltd. (No. 2023-2-TD-ZD001), National Natural Science Foundation of China (No. 52274246), Open Research Fund of State Key Laboratory of Gas Disaster Detecting, Preventing and Emergency Controlling (No. 2022SKLKF11), and Chongqing Science Fund for Distinguished Young Scholars (No. cstc2019jcyjX0019).

**Institutional Review Board Statement:** The study did not require ethical approval.

**Informed Consent Statement:** Informed consent was obtained from all subjects involved in the study.

**Data Availability Statement:** All data and/or models used in the study appear in the submitted article.

**Conflicts of Interest:** The authors declare no conflict of interest.

## References

- Wei, J.B.; Wang, S.M.; Song, S.J.; Sun, Q.; Yang, T. Experiment and numerical simulation of over-burden and surface damage law in shallow coal seam mining under the gully. *Bull. Eng. Geol. Environ.* **2022**, *81*, 207. [CrossRef]
- Xie, H.P.; Gao, F.; Ju, Y. Research and development of rock mechanics in deep ground engineering. *Chin. J. Rock Mech. Eng.* **2015**, *34*, 2161–2178.
- Wang, F.; Jie, Z.Q.; Ma, B.; Zhu, W.H.; Chen, T. Influence of Upper Seam Extraction on Abutment Pressure Distribution during Lower Seam Extraction in Deep Mining. *Adv. Civ. Eng.* **2021**, *2021*, 8331293. [CrossRef]
- Tang, Y.S.; Sun, W.C.; Zhang, X.; Liu, P.J. Effect of Advancing Direction of Working Face on Mining Stress Distribution in Deep Coal Mine. *Adv. Civ. Eng.* **2021**, *2021*, 7402164.
- Li, C.Y.; Cui, C.Y.; Lei, G.R.; Zuo, J.P.; He, T.; Li, X.S.; Du, W.S. Tensile fracture mechanism of rock mass induced by the unloading-seeping of confining pressure in deep coal mining. *J. China Coal Soc.* **2022**, *47*, 3069–3082.
- Dai, L.C.; Zhang, Z.G.; Sun, H.T.; Gao, H.L. Research on Mechanical Properties and Energy Evolution Law of Coal-Rock Assemblage with Different Gas Pressures. *Sustainability* **2022**, *14*, 9904. [CrossRef]
- Du, F.; Wang, K.; Guo, Y.Y.; Wang, G.D.; Wang, L.; Wang, Y.H. The mechanism of rockburst-outburst coupling disaster considering the coal-rock combination: An experiment study. *Geomech. Eng.* **2020**, *22*, 255–264.
- Li, J.W.; Fu, B.J.; Zhang, H.L.; Zhao, Q.C.; Bu, Q.W. Study on Fracture Behavior of Directly Covered Thick Hard Roof Based on Bearing Capacity of Supports. *Appl. Sci.* **2023**, *13*, 2546. [CrossRef]
- Zhang, H.W.; Zhao, S.F.; Guan, L.G.; Chen, Z.; Gao, M.S.; Wang, X.Y.; Zhang, H.F. Characteristics of strong mining pressure in 6.0 m high mining height and thick hard roof working face. *J. Min. Strat. Control Eng.* **2022**, *4*, 37–46.
- Zhang, G.F.; Liu, J.T.; Chang, A.P.; Zhang, W.L. Study on Key Parameters of Gob-Side Entry Retaining by Cutting Thick and Hard Roof in Inclined Coal Seam of Dongbaowei Coal Mine. *Min. Res. Dev.* **2021**, *41*, 111–116.
- He, Z.L.; Lu, C.P.; Zhang, X.F.; Guo, Y.; Meng, Z.H.; Xia, L. Numerical and Field Investigations of Rockburst Mechanisms Triggered by Thick-Hard Roof Fracturing. *Rock Mech. Rock Eng.* **2022**, *55*, 6863–6886. [CrossRef]
- Guo, Y.; Lu, C.P.; He, Z.L.; Song, J.F. Numerical and Field Investigations of Tremors Induced by Thick-Hard Strata Fracture. *Appl. Sci.* **2022**, *12*, 11151. [CrossRef]
- Gao, R.; Yang, J.X.; Kuang, T.J.; Liu, H.J. Investigation on the Ground Pressure Induced by Hard Roof Fracturing at Different Layers during Extra Thick Coal Seam Mining. *Geofluids* **2020**, *2020*, 8834235. [CrossRef]
- Ma, B.P.; Zhang, J.B.; Liu, Y.H.; Liu, S.W.; Liao, W.L.; Li, J. Deformation mechanism and control of surrounding rock in soft gently inclined coal seam roadway with thick hard roof. *Coal Eng.* **2022**, *54*, 109–116.
- Wang, R.; Liu, Q.J.; Cheng, L.; Ding, W.B.; Feng, Y.T.; Zhang, Z.; Liu, X.G. Strong mine pressure behavior law and control technology of longwall top-coal caving face in shallow extra-thick coal seam with thick hard roof. *Coal Eng.* **2023**, *55*, 47–52.

16. Tan, Y.L.; Zhang, M.; Xu, Q.; Guo, W.Y.; Yu, F.H.; Gu, S.T. Study on occurrence mechanism and monitoring and early warning of rock burst caused by hard roof. *Coal Sci. Technol.* **2019**, *47*, 166–172.
17. Zhang, C.N.; Cao, A.Y.; Li, W.D.; Li, Z.L.; Ma, Y.Z.; Wang, Q.; Li, Y.Y. Study on Stress Distribution Law and Its Influencing Factors in Mining of Coal Seam with Large Cover Depth, Thick Topsoil and Hard-Thick Roof Conditions. *Coal Technol.* **2023**, *42*, 86–91.
18. Kang, Z.P.; Zhao, J.; Duan, C.R. Overburden structure failure and movement law of thick and hard roof in slicing mining. *Coal Eng.* **2022**, *54*, 78–83.
19. Liang, S.P.; Lu, Y.L.; Guo, P.; Wu, B.Z. Mechanical Analysis of the First Fracture Characteristics of Hard Roof of Extra-thick Coal Seam. *Saf. Coal Mines* **2020**, *51*, 245–250.
20. Li, A.; Ma, Q.; Lian, Y.Q.; Ma, L.; Mu, Q.; Chen, J.B. Numerical simulation and experimental study on floor failure mechanism of typical working face in thick coal seam in Chenghe mining area of Weibei, China. *Environ. Earth Sci.* **2020**, *79*, 118. [CrossRef]
21. Xiong, Y.; Kong, D.Z.; Wen, Z.J.; Wu, G.Y.; Liu, Q.Z. Analysis of coal face stability of lower coal seam under repeated mining in close coal seams group. *Sci. Rep.* **2022**, *12*, 509. [CrossRef] [PubMed]
22. Yang, K.; Liu, W.J.; Jiao, B.; Zhang, Q.H.; Liu, S.; Zhang, Z.N. Three-dimensional physical simulation of overburden migration in deep thick hard roof fully-mechanized caving mining. *Chin. J. Geotech. Eng.* **2021**, *43*, 85–93.
23. Bu, Q.W.; Tu, M.; Zhang, X.Y.; Yuan, B.Q.; Zhao, Q.C.; Dang, J.X. Study on fracture instability and energy accumulation-release evolution of thick-hard roof in stope. *J. Min. Saf. Eng.* **2022**, *39*, 867–878.
24. Li, T.; Li, Z.; Sun, J.D. Study on Dynamic Evolution of Overburden Rock Movement and Mining-Induced Stress of Ultra-high Working Face. *Shock. Vib.* **2022**, *2022*, 2271635. [CrossRef]
25. Xie, J.L.; Ning, S.; Zhu, W.B.; Wang, X.Z.; Hou, T. Influence of Key Strata on the Evolution Law of Mining-Induced Stress in the Working Face under Deep and Large-Scale. *Mining. Minerals* **2023**, *13*, 983. [CrossRef]
26. Li, W.T.; Li, X.M.; Mei, Y.C.; Wang, G.; Yang, W.D.; Wang, H.T. A numerical simulation approach of energy-absorbing anchor bolts for rock engineering. *Int. J. Rock Mech. Min. Sci.* **2022**, *158*, 105188. [CrossRef]
27. Yang, Z.Q.; Liu, C.; Zhu, H.Z.; Xie, F.X.; Dou, L.M.; Chen, J.H. Mechanism of rock burst caused by fracture of key strata during irregular working face mining and its prevention methods. *Int. J. Min. Sci. Technol.* **2019**, *29*, 889–897. [CrossRef]
28. Shao, X.N. *Research of Fracture Law and Deep Hole Advance Blasting Technology in Hard Thick Sandstone Roof*; Anhui University of Science and Technology: Huainan, China, 2014.
29. Wu, Q.H. *Analyzing Stability Synthetically and Researching Treatment Methods on the Complicated Multi-Layer Mine-Out Areas*; Central South University: Changsha, China, 2010.
30. Ye, Q.; Wang, W.J.; Wang, G.; Jia, Z.Z. Numerical simulation on tendency mining fracture evolution characteristics of overlying strata and coal seams above working face with large inclination angle and mining depth. *Arab. J. Geosci.* **2017**, *10*, 82. [CrossRef]
31. Wen, X.L.; Ge, Z.C.; Zhang, F.Y. Study on the Migration Law of Overlying Rock in the Upward Layered Continuous Mining Face of Thick Coal Seam with Paste Backfill Mining. *Math. Probl. Eng.* **2022**, *2022*, 7297477. [CrossRef]
32. Shi, B.W.; Bai, J.P.; Hao, C.S.; Yang, C.Y.; Yao, J.B. Three-dimensional Simulation of Dynamic Evolution of Mining-induced Overburden Fractures. *Saf. Coal Mines* **2019**, *50*, 259–262.

**Disclaimer/Publisher’s Note:** The statements, opinions and data contained in all publications are solely those of the individual author(s) and contributor(s) and not of MDPI and/or the editor(s). MDPI and/or the editor(s) disclaim responsibility for any injury to people or property resulting from any ideas, methods, instructions or products referred to in the content.



Article

# Study of Overlying Rock Structure and Intensive Pressure Control Technology of Island Longwall Panel in Extra-Thick Coal Seams

Yaochuang Wang<sup>1</sup>, Pengkun Chen<sup>2</sup> and Shen Wang<sup>2,3,\*</sup>

<sup>1</sup> ZhongYun International Engineering Co., Ltd., Zhengzhou 450007, China

<sup>2</sup> School of Energy Science and Engineering, Henan Polytechnic University, Jiaozuo 454003, China

<sup>3</sup> Collaborative Innovation Center for Safe Production and Clean and Efficient Utilization of Coal, Jiaozuo 454003, China

\* Correspondence: wangshen@hpu.edu.cn

**Abstract:** In response to the severe occurrence of mining pressure in the fully mechanized top coal caving face of the extra-thick coal seam and the problem of strong rock pressure caused by the remaining coal pillars in the mining area on the isolated island fully mechanized top coal caving face, taking the 8102 isolated island working face of Tongxin Coal Mine as the background and by using methods such as on-site measurement and numerical simulation experiments, the characteristics of roof mining in the island longwall panel of extra-thick coal seams were analyzed. Establishing a mechanical model for the mining stress and overlying rock stress arch of an isolated working face, the mechanical characteristics of the isolated working face under special conditions were obtained. The results show that the longwall panel no. 8102 has an asymmetric long-arm T-shaped covering layer structure before mining and a C-shaped covering rock structure during mining, which will exacerbate the degree of mining pressure manifestation in the working face. Directional high-pressure hydraulic fracturing was implemented in the gob of longwall panel no. 8102, and the pressure reduction effect of the advance support section of the gob was obvious, ensuring the safety of the working face.

**Keywords:** extra-thick coal seam; strong rock pressure; island longwall panel; C-shaped overlying rock structure

**Citation:** Wang, Y.; Chen, P.; Wang, S. Study of Overlying Rock Structure and Intensive Pressure Control Technology of Island Longwall Panel in Extra-Thick Coal Seams. *Processes* **2023**, *11*, 3083. <https://doi.org/10.3390/pr11113083>

Academic Editors: Raymond Cecil Everson, Feng Du, Aitao Zhou and Bo Li

Received: 6 September 2023

Revised: 19 October 2023

Accepted: 23 October 2023

Published: 26 October 2023



**Copyright:** © 2023 by the authors. Licensee MDPI, Basel, Switzerland. This article is an open access article distributed under the terms and conditions of the Creative Commons Attribution (CC BY) license (<https://creativecommons.org/licenses/by/4.0/>).

## 1. Introduction

During the mining process of the fully mechanized top coal caving face in extremely thick coal seams, due to the large thickness of the coal seam extracted at one time, a large-scale mining space is formed, and the stable masonry beam structure is formed in the higher layers of rock layers, resulting in a strong rock pressure phenomenon in the fully mechanized top coal caving face. When there are residual coal pillars in the gob, the isolated island fully mechanized top coal caving face of the extra-thick coal seam where the pillar is extracted has a significant impact on its mining due to the combined influence of original rock stress and advanced support pressure.

On this basis, many scholars have conducted extensive research on the distribution law of mining-induced stress under different conditions and have achieved rich results.

Xingyun Ren [1] proposed to reduce the support pressure of the working face and protect the main roadway through roof cutting and pressure relief. Mingshi Gao [2] proposed a support plan that combines “active anchor cable support, hydraulic lifting support, and soft structure energy absorption”. Peng Wang [3] analyzed the deformation and instability characteristics of a composite roof coal roadway under different influencing conditions. Houqiang Yang [4] proposed and implemented the equidistant double bearing ring support technology. Zeng-Qiang Yang [5] proposed feasible methods for preventing rock burst using pressurized water jet technology. Xiaojie Yang [6] proposed the concept

of “cutting and reducing pressure on adjacent tunnel roof”. Xuyang Chen [7] studied the constitutive equation of the creep behavior of sandy mudstone and proposed corresponding solutions to improve the stability of the tunnel. Ming Ji [8] analyzed the radial variation of stress and displacement in tunnel surrounding rock.

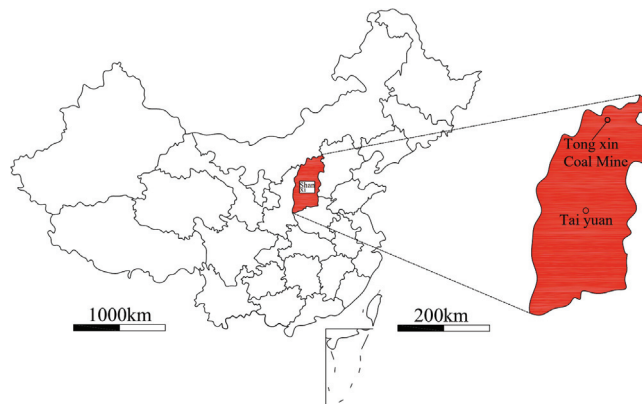
Yuxin Yuan [9] proposed thick anchor crossing boundary support under strong mining conditions and its engineering application. Deyu Qian [10] revealed the deformation and damage characteristics and distribution law of the surrounding rock of a stress-intensive roadway. Kai Wang [11] analyzed the use of microcrack grouting under high rock pressure conditions to quantitatively describe the changes in grout permeability distance and crack opening. Yunhai Cheng [12] proposed to reduce the impact of strong dynamic pressure on the roadway floor by changing the energy accumulation of the roadway floor. Jolfaei S [13] analyzed a large database and found that among the parameters that affect borehole fracture, the internal friction angle of the rock has the greatest impact on the fracture size. Jingxuan Yang [14] proposed measures to prevent strong rock using water-filled deep hole restricted blasting technology. Rui Gao [15] reveals the combined effect of a gob side relief zone and OCP stress concentration on final stress. Lu Chen [16] proposed a new type of energy-absorbing anchor rod with a small consumption of energy stored under high stress.

In the case of extremely thick coal seams, most previous studies have reflected the law of rock pressure behavior under a single condition. Therefore, this paper analyzes the roof structure of the island-shaped comprehensively placed working face of the extra-thick coal seam, simulates the mining stress and overburden rock stress arch of the working face for the special situation of the longwall panel no. 8102 of Tongxin Coal Mine, and puts forward the key technology of controlling the roof in the island-shaped comprehensively placed working face of the extra-thick coal seam on the basis of the key technology of controlling the roof of the extra-thick coal seam. The reliability of this simulation is verified based on on-site observation results.

## 2. Roof Structure of Island Longwall Panel in Extra-Thick Coal Seams

### 2.1. Engineering Geological Conditions

Located in the southwest of Datong City (Figure 1), Tongxin Coal Mine is 14.29 km from east to west and 10.36 km from south to north. The isolated longwall panel no. 8102 is located on the east side of the coal mining area no. 1. The eastern part is a solid coal area, the northern part is an 8103 goaf, the western part is a three-panel roadway, and the southern part is an 8101 goaf. Due to the fact that the adjacent working face 8102 has already been mined out, and a 6 m coal pillar has been left behind in the goaf, a situation of isolated working faces with goafs on both sides has been formed. The schematic diagram of the working face position is shown in Figure 2.



**Figure 1.** Location map of Tongxin Coal Mine.



**Figure 2.** Principle of automatic hydraulic bracket following machine.

The burial depth of longwall panel no. 8102 is 437.1–491.6 m, with an average coal thickness of 17 m. This coal seam is a semi-dark type with a middle layer of semi-bright coal, which is brittle and fragile. Overall, the coal seams in this working face have a relatively high floor near the panel roadway and cutting hole, while the middle floor is relatively low. There are 5–10 dirt bands in the coal seam, and the lithology is generally kaolinite, sandy mudstone, and carbonaceous mudstone, with occasional siltstone or fine sandstone. The dip angle of the coal seam is 0–4°, with an average of 1°. The overburden of longwall panel no. 8102 mainly consists of fine sandstone, siltstone, and medium sandstone, with good integrity, high hardness, and high strength. The rock column diagram of longwall panel no. 8102 is shown in Figure 3. There are multiple layers of thick and high-strength sandstone layers distributed in the range of 100 m above the working face.

The mining roadway of longwall panel no. 8102 is a rectangular roadway. Within it, the excavation width of Lane 2102 is 5500 mm, the height is 3700 mm, the tunnel section is 20.35 m<sup>2</sup>, and the total length is 1822.66 m. The excavation width of Lane 5102 is 5200 mm, the height is 3950 mm, the tunnel section is 20.54 m<sup>2</sup>, and the total length is 1831.05 m. The excavation width of 8102 top extraction roadway is 4200 mm, the height is 2700 mm, the roadway section is 11.34 m<sup>2</sup>, and the total length is 1827.38 m. The cross-sectional diagram of the 8102 mining roadway is shown in Figure 4.

## 2.2. Full Mining Conditions on Both Sides of the Isolated Working Face

### (1) History of adjacent roadway mining

After the excavation of the working face, the cracks in the overlying rock gradually develop from bottom to top, with the lower rock layer stabilizing first and the surface rock layer stabilizing later. If the surface rock layer area is stable, then it can be inferred that the activity of the lower rock layer has stabilized. The 8101 working face was completed in 2010, about 8 years before this study. The 8103 working face was completed in 2015, about 3 years before this study. The adjacent working face 8102 has already been mined out, resulting in an isolated island working face with both sides being mined out.

### (2) Settlement status of overlying rock

Through on-site research, it was found that the longwall panel no. 8102 has the following crack characteristics: ① there are both tension-type cracks and shear cracks on the surface; ② the direction of most of the cracks is roughly related to the contour of the working face of seams 3–5 #, indicating that the cracks were caused by the mining of seams 3–5 #; ③ in the early stage, some cracks were filled, but in the later stage, the cracks began to propagate, partly due to atmospheric precipitation and partly due to crack activation; ④ some cracks become closed cracks, which may be formed during the mining process of the overlying coal seam and closed due to the mining of coal seams 3–5. In addition, some

tension joints closed due to the effects of secondary mining. Figure 5 shows the distribution of the investigated fractures: workings 8101 and 8103 on either side of workings 8102 were completed in October 2010 and March 2015, respectively. It has been at least 8 years since then, and it can be inferred that the overlying rock activity has tended to be stationary and formed new overlying rock structures.


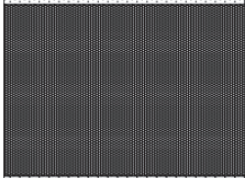


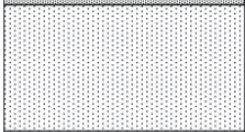



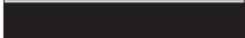








Columnar	Thickness/m	Buried depth/m	Rock properties
	1.60	375.20	Coarse grained sandstone
	19.30	394.50	Siltstone
	10.90	405.40	Glutenite
	1.10	406.50	Fine grained sandstone
	17.28	423.78	Glutenite
	1.90	425.68	Fine grained rock
	2.36	428.40	Fine grained sandstone
	10.27	438.31	Interbedded mudstone and sandstone
	2.00	440.31	No.4 coal
	3.44	443.75	Siltstone
	4.20	447.95	Fine grained sandstone
	7.00	454.95	Coarse grained sandstone
	3.65	458.60	Interbedded mudstone and sandstone
	4.53	463.13	Sandy mudstone
	1.80	464.93	No.2 coal
	0.90	465.84	Carbonaceous mudstone
	18.59	484.43	No.3-5 coal

Figure 3. Rock stratum histogram of longwall panel no. 8102.

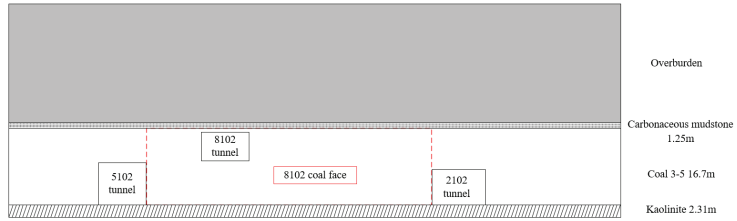


Figure 4. Section diagram of 8102 mining roadway.

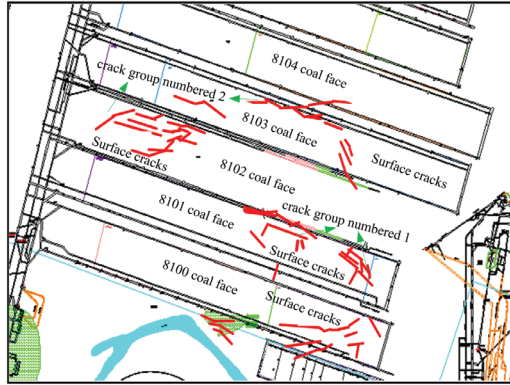


Figure 5. Crack investigation map.

It is speculated that the crack group numbered 1 in Figure 5 is a tension-type crack group that can be caused by the mining of working face 8101, while the crack group numbered 2 is caused by the joint mining of working faces 8101, 8103, and 8104. The distance between crack group 1 and the edge of working face 8101 is about 280 m, indicating that the fracture angle is approximately:

$$\phi = 90^\circ - \arctan(D/H) = 90^\circ - \arctan(280/484) = 59.95^\circ \quad (1)$$

The calculation principle of crack angle is shown in Figure 6. From this, it can be inferred that the overlying rock structure characteristics of a panel working face are inclined along the working face.

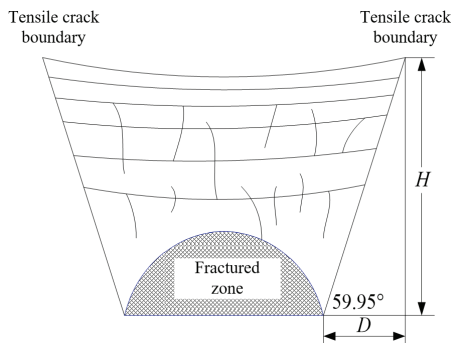


Figure 6. The influence range and structural diagram of the overlying rock along the dip after mining in a panel working face.

In addition, the structural characteristics of the stratigraphy overlying strata on the existing 8101 working face are inferred based on the discovered surface cracks. From Figure 6, it can be seen that ① the cracks on one side of the 8101 working face are cut along the direction of the 8101 roadway; ② the development of crack groups in the area near the main roadway of longwall panel no. 8102 indicates that after multiple mining impacts, there are many mining cracks in the overlying rock here; ③ the cracks on one side of the 8103 working face are mostly developed in the middle of the 8103 working face and near the junction of the 8103–8104 working face, and the distribution of cracks in the inclined direction shows asymmetric characteristics; ④ there are significantly more strike fractures than dip fractures, indicating that across the width of this working face, there are fewer developed dip fractures due to the hard and complete overlying rock.

This suggests that the longwall panel no. 8102 was mined with a longer length of overhanging roof along the direction of the workings, and if it suddenly breaks, there is a high possibility of causing strong impact on the working face.

Based on the above analysis, the following results can be summarized: the overlying rock structure of longwall panel no. 8102 is asymmetric, with a longer cantilever structure on the side near 8103 and a relatively shorter cantilever structure on the side near the 8101 working face. The near absence of inclined cracks in the overlying rock under these working face width conditions indicates the length of the hard rock strata suspended during the advance of the working face.

### 2.3. Full Mining Discrimination on Both Sides of Longwall Panel No. 8102

In order to analyze the temporal and spatial movement characteristics of the overlying rock strata of the Tongxin Coal Mine, the movement status of the underlying strata can be inferred from the surface subsidence law. Therefore, based on the mining subsidence characteristics of the 8105 working face, the spatiotemporal movement characteristics of the overlying strata in a panel can be inferred.

The 8105 working face belongs to a level northern area, with an average elevation of 797 m. The working face is a small anticline structure, with a gentle slope of 1–3° on both wings of the anticline. The eastern part of the working face is a solid coal area. The northern part is the 8106 working face, which has been mined out; There are three main alleys in the western region. The southern part is the 8104 working face.

The basic structural form of the mine field is a monocline trending northeast and tilting northwest, with a stratigraphic dip angle of 3–10° generally, and the southeast and south coal seam outcrops become steeper, reaching 30–80° and local vertical inversion; There are few faults, with a small amount of wide and gentle folds and collapse columns.

In addition, there are oil lampblack intrusions on both the east and west sides of the mine, which have a significant impact on the coal quality of the coal seam. There is moderate to simple construction complexity.

The roof, floor, and solid rock of coal seams are generally semi-hard to hard rocks with good engineering geological conditions, belonging to a simple type. The gas content is usually low but locally high. The specific conditions of the top and bottom plates of the 8105 working face are shown in Table 1. The mining parameters of the 8105 working face in Tongxin Coal Mine are shown in Table 2.

**Table 1.** Lithological characteristics of the top and bottom plates of working face 8105.

Name of Top and Bottom Plates	Rock Name	Thickness (m)	Lithological Characteristics
Main roof	Silty fine sandstone and gravelly gritstone	11.39	Grayish white gravelly gritstone, mainly composed of quartz, followed by feldspar, mica, and dark minerals, which is of subangular shape, poor sorting, and hard structure

Table 1. Cont.

Name of Top and Bottom Plates	Rock Name	Thickness (m)	Lithological Characteristics
Immediate roof	Siltstone and carbonaceous mudstone	3.35	Siltstone: horizontal bedding and coal chips; carbonaceous mudstone: block shaped, easily stains hands, containing plant stem and leaf fossils
Immediate floor	Mudstone	1.94	It is dark gray, massive, loose, and fragile, containing a small amount of siltstone

Table 2. Mining parameters of 8105 working face.

Name	Technical Parameter Values	
Working surface parameters	Strike length D <sub>3</sub>	1757 m
	Inclination length D <sub>1</sub>	200 m
Boundary mining depth	Downhill direction H <sub>1</sub>	460.0 m
	Uphill direction H <sub>2</sub>	470.0 m
	Open-off cut H <sub>3</sub>	400.0 m
	Stop line H <sub>4</sub>	490.0 m
Average dip angle of coal seam	1~3°	
Coal seam thickness	13.12–22.85 (average 16.85)	
Working face direction	107°	
Working face inclination	197°	
Coal-mining methods	Comprehensive mechanized coal mining	
Roof management methods	Total collapse method for roof management	

The 8105 working face surface movement and deformation observation station is equipped with three observation lines, A, B, and C. One main section-monitoring line of strike, two dip observation lines, eighty-four deformation-monitoring points, eight control points, and ninety-two total observation points are set. The average distance between observation points on the observation line is taken as 30 m. Taking into account the parameters of ground fissures, surface morphology damage, and surface movement and deformation, the following conclusions are drawn:

① According to the on-site investigation of surface cracks in a certain area, it can be seen that the surface cracks extend relatively far, with most of them developing along the advancing direction but exhibiting discontinuous characteristics. Fracture development in the direction of the working face is relatively small, suggesting that the impact of mining on the surface is limited in a given area due to the hard rock formations in the strata.

② According to on-site research, no subsidence basins were clearly observed due to the influence of terrain.

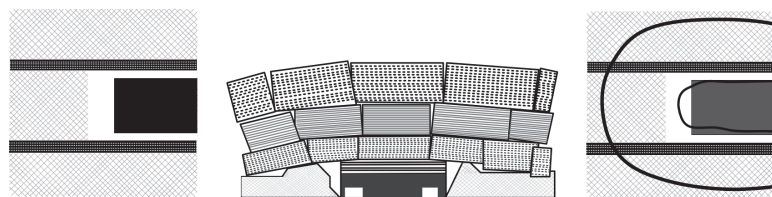
③ According to the observation of surface rock movement in the 8105 working face with one side of the gob, the maximum subsidence is only 4.994 m, and the expected subsidence coefficient is 0.4. This indicates that under the geological structure characteristics and mining conditions of a panel, one side of the gob is not fully mined after mining, and the strata have not fully settled.

#### 2.4. Evolution of Overlying Rock Spatial Structure during the Mining Process of Fully Mechanized Top Coal Caving Face in Extra-Thick Coal Seams

For multiface mining, whether the overlying rocks in two adjacent gob areas can form an interactive spatial structure mainly depends on the width of the coal pillar between the two. A large coal pillar can effectively isolate the connection between the overlying rock fractures in the gob. Generally, a coal pillar of more than 20 m between the working faces can isolate the movement of the overlying rock between the two working faces. Therefore, when the coal pillar of the working face is smaller than a certain value, the overlying rock between the working faces will form a collaborative movement, forming an interactive spatial structure. A small coal pillar 6 m wide was left between the 8102 face and the section of the mining area on both sides. Therefore, this small coal pillar cannot separate the overlying rock structure of the longwall panel no. 8102 from the overlying rock structure above the gob areas on both sides but rather forms an interactive spatial structure.

Generally, the spatial structure of the overlying rock in the mining area is divided into four types: the overlying rock spatial structure during the advancement of the surrounding solid coal working face, the overlying rock spatial structure during the advancement of the working face with one side of the gob, the overlying rock spatial structure during the advancement of the isolated island working face with both sides of the gob, and the overlying rock spatial structure of the isolated island working face with four sides of the gob. The longwall panel no. 8102 is an isolated island working face with gob on both sides, and its spatial structure shows a “C” shape.

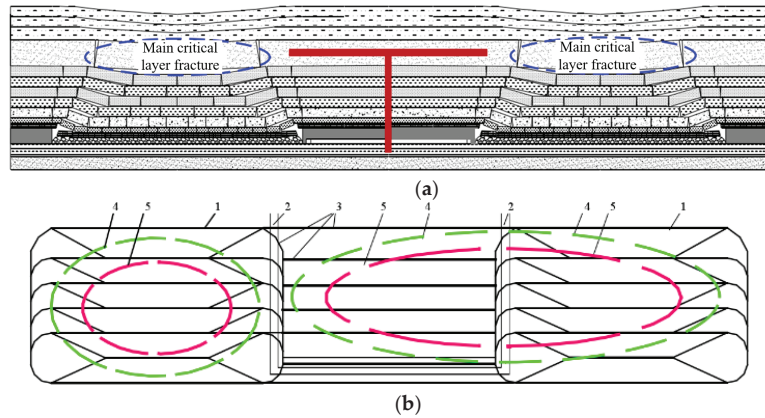
The formation process of C-type: this type of slope is an isolated working face left behind by skip mining. In recent years, the roadway support of the synthesized isolated working face has become a very difficult problem. Some working faces have advanced support pressure that affects a distance of up to 120 m, and roadway repair engineering has become a “bottleneck” for advancing the working face. There is still a problem of large-scale peeling in the deep working face. Figure 7 shows the spatial structure of the overlying rocks in this type of mining area. The rock layers above the main roof slabs of the three mining areas have been connected into a similar “C”-shaped spatial structure, and the large-scale movement of the “C”-shaped spatial structure is the main reason why the influence distance of the pressure on the overhanging support in the isolation workings is 2–3 times larger than that of the ordinary workings [17].



**Figure 7.** Schematic diagram of the spatial structure of the C-shaped overlying rock.

According to surface subsidence observation data and surface crack research, the insufficient settlement of the gob on both sides indicates that the longwall panel no. 8102 will form a long-arm T-shaped structure, and the asymmetric distribution of cracks indicates that the overlying rock of longwall panel no. 8102 will form an asymmetric longwall T-shaped structure (Figure 8a,b). The rock pressure manifestation under this structure is the most severe, equivalent to the cantilever of hard rock being completely above the working face. During the mining period, the basic roof of the longwall panel no. 8102 will form a C-shaped overlying rock structure.





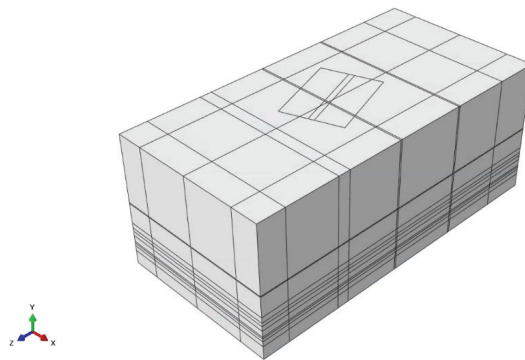
**Figure 8.** Schematic diagram of T-shaped overlying rock spatial structure. (a) Schematic diagram of symmetrical short-arm T-shaped overlying rock structure section. (b) Schematic Plan of Symmetrical Short-Arm T Overburden Structure.

### 3. Numerical Simulation of Mining Stress and Overlying Rock Stress Arch in Working Face

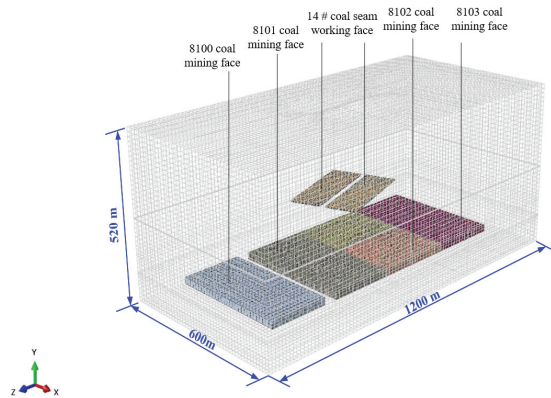
Longwall panel no. 8102 is an isolated island working face, and its advanced coal body stress state and overlying rock stress state are closely related to the possibility of dynamic disasters. This time, ABAQUS numerical calculation software was used to calculate the distribution of mining stress in the working face no. 8102, taking into account the impact of adjacent gobs (8100, 8103 gobs, and the overlying coal seam gob 14 #), providing a basis for evaluating the risk of dynamic disasters.

#### 3.1. Numerical Simulation Establishment

A three-dimensional numerical model was established using ABAQUS/CAE pre-processing software, the geometric model is shown in Figure 9, and the mesh model is shown in Figure 10. The Mohr–Coulomb softening model can be defined directly in ABAQUS/CAE. Among them, the width dimensions of each working face and coal pillar in the coal seams 3–5 # are established based on the actual dimensions. In order to reduce the computational complexity, appropriate selection of the forward length of the working face is necessary to ensure representativeness. Finally, the forward length of the working face was chosen to be 400 m.



**Figure 9.** Geometric model.



**Figure 10.** Grid model.

By comparing the corresponding relationship between the gob of coal seam 14 # and the longwall panel no. 8102, it can be seen that: ① the angle between the direction of coal seam 14 # working face and the direction of the longwall panel no. 8102 is about  $48^\circ$ ; ② 15–30 m wide coal pillar is left in the 4-seam mining area; ③ the width of the gob in coal seam 14 # is approximately 100 m. Based on the above spatial relationships and geometric parameter conditions, in this numerical simulation, the angle between the working face direction of seam 14 # and the direction of longwall panel no. 8102 is about  $48^\circ$ , and the working face width of seam 14 # is 100 m, and 20 m coal pillars are reserved in the section. To reduce computational complexity and minimize the impact of boundary conditions, only two working faces of coal seam 14 # are considered. The coal seam 14 # working face spans above the 8102 and 8101 working faces.

The numerical model is 1200 m long, 600 m wide, and 520 m high. It is divided into about 331,600 hexahedron elements. The element type is C3D8, that is, a three-dimensional eight-node full integration element. In the model, the displacement constraint in the x-direction of the two boundary interfaces perpendicular to the x-direction is  $U1 = 0$ . The z-direction displacement constraint of the two boundary interfaces perpendicular to the z-direction is  $U3 = 0$ . The y-direction displacement constraint of the bottom surface perpendicular to the y-direction is  $U2 = 0$ .

### 3.2. Numerical Simulation Parameters

#### (1) Constitutive model of rock strata

Dynamical problems involve the transfer of energy from elastic energy to kinetic energy in the subsurface. Based on the stress and strain components, the elastic energy in a solid finite element can be calculated. Therefore, selecting a relatively accurate model to reflect the stress–strain relationship and energy characteristics of rocks is the key to simulating roof impact problems. In addition, for numerical simulation, the final output parameter values were evaluated and determined from numerical simulation results and field observations. Therefore, rock deformation needs to be carefully considered in numerical simulations again.

In this study, the Mohr–Coulomb strain-softening model is selected to describe the rock deformation behavior caused by the unloading effect of underground coal seam mining. The stress–strain relationship in the elastic phase of the Mohr–Coulomb strain-softening model is the same as that of the Mohr–Coulomb model, while the stress–strain relationship in the plastic stage is different, as shown in Figure 11. In the Mohr–Coulomb model, the stress component after the yield point increases with the increase in the strain component, which is called the ideal elastic–plastic model. In the Mohr–Coulomb strain-softening model, the cohesion, friction angle, and tensile strength decrease with increasing plastic

strain. In Figure 11, U1 represents the elastic energy at the yield point, while U2 and U3 represent the elastic energy in the post-peak phase of the ideal elastic–plastic and strain-softening models, respectively. Obviously, the Mohr–Coulomb model cannot reflect the actual deformation behavior and elastic energy release, while the Mohr–Coulomb strain-softening model can describe the softening behavior and elastic energy release process ( $U1 > U3$ ).

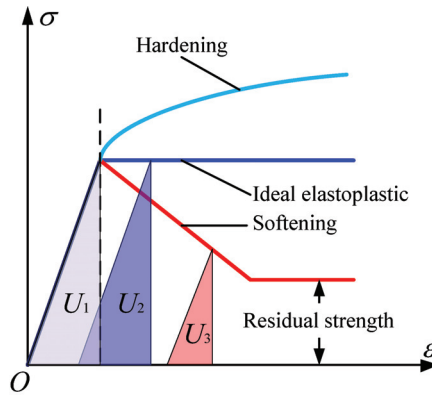


Figure 11. Schematic diagram of the Mohr–Coulomb model and its softening model.

In the elastic stage, the total strain tensor is equal to the elastic strain tensor, as follows:

$$\epsilon = \epsilon^e \tag{2}$$

In the post-peak phase, the total strain tensor is equal to the sum of the elastic and plastic strain tensor. The plastic strain tensor can be divided into two parts: the plastic shear strain tensor and the plastic tensile strain tensor. Therefore, the total strain tensor can also be expressed as:

$$\epsilon = \epsilon^e + \epsilon^{ps} + \epsilon^{pt} \tag{3}$$

The shear yield function  $F^s$  in the Mohr–Coulomb softening model is expressed as:

$$F^s = \sigma_1 - \sigma_3 N_\phi + 2c\sqrt{N_\phi} \tag{4}$$

In the equation,  $\sigma_1$  is the maximum principal stress,  $\sigma_3$  is the minimum principal stress,  $c$  is the cohesion force, and  $\phi$  is the friction angle.

The tensile yield function  $F^t$  is:

$$F^t = \sigma_t - \sigma_3 \tag{5}$$

In the formula,  $t$  is the tensile strength.

The shear plastic potential function  $g^s$  is based on the noncorrelated flow rule, while the tensile plastic potential function  $g^t$  is based on the correlated flow rule.

$$g^s = \sigma_1 - \sigma_3 N_\phi \tag{6}$$

$$g^t = -\sigma_3 \tag{7}$$

When shear failure occurs, the increase in shear plasticity can be calculated as:

$$\Delta\epsilon_i^{ps} = \lambda^s \frac{\partial g^s}{\partial \sigma_i} \tag{8}$$

When tensile failure occurs, the increase in tensile plasticity can be calculated as:

$$\Delta \varepsilon_i^{pt} = \lambda^t \frac{\partial \sigma_i^t}{\partial \sigma_i} \tag{9}$$

In the above equation,  $\Delta \varepsilon_i^p$  is the plastic strain increment, and  $\lambda^s$  and  $\lambda^t$  are undetermined coefficients.

By introducing Equation (6) into Equation (8), the plastic strain increment component  $\Delta \varepsilon_i^p$  under shear failure can be calculated as follows:

$$\begin{cases} \Delta \varepsilon_1^{ps} = \lambda^s \\ \Delta \varepsilon_2^{ps} = 0 \\ \Delta \varepsilon_3^{ps} = -\lambda^s N_\phi \end{cases} \tag{10}$$

For isotropic materials, the relationship between the principal stress increment and the principal strain increment according to the generalized Hooke’s law is:

$$\begin{cases} \Delta \sigma_1 = \alpha \Delta \varepsilon_1 + \beta (\Delta \varepsilon_2 + \Delta \varepsilon_3) \\ \Delta \sigma_2 = \alpha \Delta \varepsilon_2 + \beta (\Delta \varepsilon_1 + \Delta \varepsilon_3) \\ \Delta \sigma_3 = \alpha \Delta \varepsilon_3 + \beta (\Delta \varepsilon_1 + \Delta \varepsilon_2) \end{cases} \tag{11}$$

In the formula,  $\sigma_1$ ,  $\sigma_2$ , and  $\sigma_3$  are the maximum, middle, and minimum principal stress increments, respectively;  $\varepsilon_1$ ,  $\varepsilon_2$ , and  $\varepsilon_3$  are the maximum, middle, and minimum principal strain increments, respectively;  $\alpha$  and  $\beta$  are elastic constants, which can be calculated by Young’s modulus and Poisson’s ratio.

According to Equations (3), (9) and (10), the stress component under shear failure mode can be updated to:

$$\begin{cases} \sigma_1^N = \sigma_1^O - \lambda^s (\alpha - \beta N_\phi) \\ \sigma_2^N = \sigma_2^O - \beta \lambda^s (1 - N_\phi) \\ \sigma_3^N = \sigma_3^O - \lambda^s (\beta - \alpha N_\phi) \end{cases} \tag{12}$$

In the equation,  $\sigma_i^N$  and  $\sigma_i^O$  are the new and old stress states,  $i = 1, 2$ , and  $3$ , respectively. Similarly, the stress component under tensile failure mode can be updated to:

$$\begin{cases} \sigma_1^N = \sigma_1^O + \lambda^t \beta \\ \sigma_2^N = \sigma_2^O + \lambda^t \beta \\ \sigma_3^N = \sigma_3^O + \lambda^t \alpha \end{cases} \tag{13}$$

The initial shear expansion angle is taken as  $1/3-1/2$  of the friction angle. In ABAQUS, the strain-softening function is defined as a table function of. The cohesion and friction angle decay linearly with increasing plastic strain. When the plastic strain reaches  $5 \times 10^{-3}$ , the cohesion and friction angle decay to the original 25%. The attenuation slope is determined by displacement back analysis. Afterwards, the cohesion and friction angle remain unchanged, characterizing the residual strength of the rock.

(2) Bedding model and parameters

The mechanical behavior of bedding is divided into tangential and normal behaviors, as shown in Figure 12. In ABAQUS, the Coulomb friction model is used to simulate the tangential behavior of bedding. The normal behavior is defined as a hard contact model with initial tensile strength. Bedding stiffness is determined using the penalty function method; therefore, when the bedding shear stress is less than the shear strength, ABAQUS is also required to give an allowable initial elastic slip that is less than 0.05 times the characteristic length of the member. Typically, the tensile strength of rock formations is significantly lower than that of rocks and is often difficult to measure accurately. The initial tensile strength is set to 0.01 MPa and the initial coefficient of friction is set to 0.30.

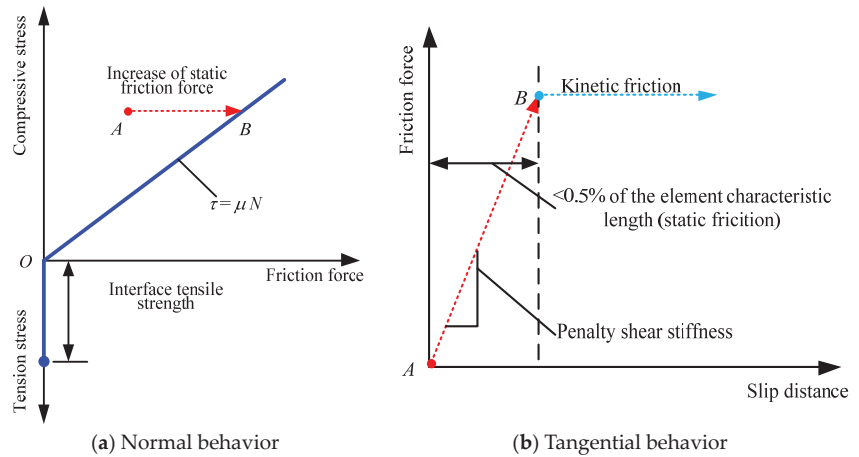


Figure 12. Mechanical behavior of bedding.

(3) Gob model

The compression process of gob is an important simulation part in the numerical simulation of longwall mining, which will significantly affect the settlement and migration laws of overlying rocks. In this simulation, the gob model proposed by Salamon in 1991 [18] was used. In this model, the vertical stress in the extraction zone increases with increasing vertical strain as shown in the following equation:

$$\sigma_v = \frac{E_{gob}\epsilon_v}{\epsilon_{gob} - \epsilon_v} \tag{14}$$

In the formula,  $E_{gob}$  is the initial deformation modulus of the gob, and  $\epsilon_{gob}$  is the ultimate vertical strain of the gob.

The initial values of deformation modulus and ultimate vertical strain are  $E_{gob} = 3.5$  MPa and  $\epsilon_{gob} = 0.5$ , respectively. Therefore, according to the above equation, the gob is a nonlinear elastic material. The bulk modulus of the gob continues to increase with the volume strain of the gob, and the bulk modulus can be calculated by the following formula:

$$K = \frac{1.75}{0.5 - \epsilon_z} \tag{15}$$

In the formula,  $\epsilon_z$  is the vertical strain component of the gob unit.

As the longwall face advances, collapse zones, fracture zones, and continuous deformation zones are formed above the coal seam. The height of the collapse zone gradually decreases as the veinstone filling in the mining airspace is gradually compressed. The final compression height of the collapse zone can be calculated as:

$$h_c^f = \frac{100M}{2.1M + 16} \pm 2.5 \tag{16}$$

In the formula,  $h_c^f$  is the final compression height of the collapse zone, and  $M$  is the mining thickness. According to Equation (16), the final compression height of longwall panel no. 8102 is 31.48–36.48 m.

The coefficient of collapse and expansion in the collapse zone is:

$$k_c = \frac{H_c}{H_r} \tag{17}$$

In the formula,  $k_c$  is the coefficient of collapse and expansion,  $H_c$  is the height of the collapse zone, and  $H_r$  is the direct top height before collapse.

As the gob is compacted, the coefficient of fragmentation and swelling in the collapsed zone gradually decreases. It is assumed that the initial and final breakup coefficients are 1.25 and 1.05. The initial height of the gob can be calculated as:

$$h_c^i = \frac{k_c^i}{k_c^f} h_c^f \quad (18)$$

According to Equation (18), it is between 37.48 and 43.43 m, and the average value of 40.46 m is taken in this numerical simulation.

The above gob constitution is programmed using the user subroutine UMAT and executed in ABAQUS/Standard.

#### (4) Simulation method for excavation of working face

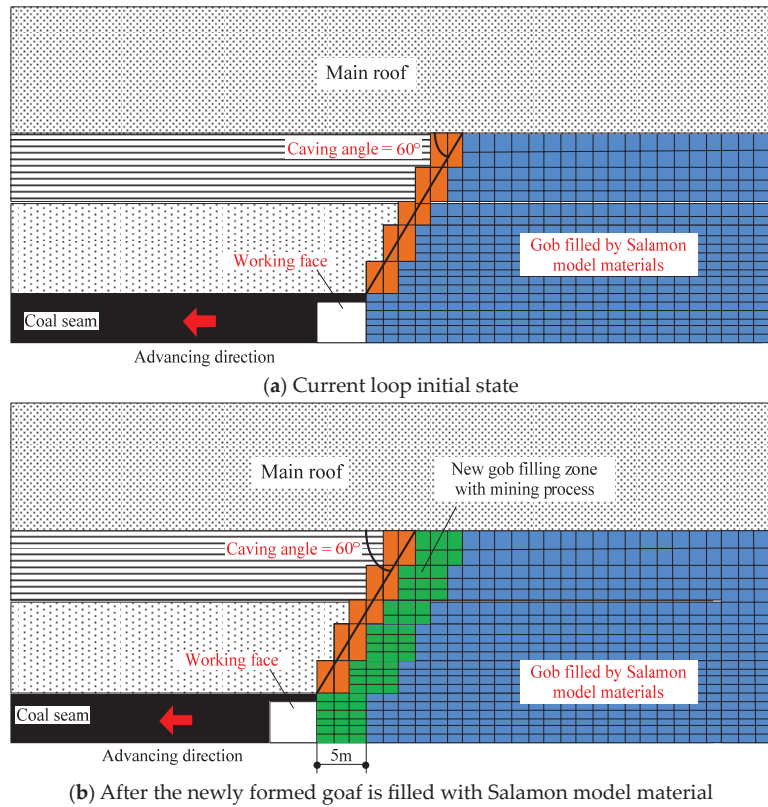
The longwall mining process was simulated using the “Static/General” solver mode and the “Standard” solver in ABAQUS. The matrix storage of finite element equation solving is asymmetric. The solution method is Newton–Raphson’s method. In order to improve the convergence of nonlinear analysis, the viscosity coefficient of the C3D8 element is set to 0.0001. The global numerical damping is set to 0.05.

In the simulation software, the coal seam 14 # working face, 8101 working face, 8200 working face, 8103 working face, and longwall panel no. 8102 were excavated in sequence. The stress distribution in an elastic body is independent of the loading or unloading path. However, the loading and unloading paths have a significant effect on the stress–strain evolution of the plasticizer. Therefore, the failure and deformation of the roof rock layer are influenced by the mining sequence. Therefore, implementing the mining process in ABAQUS is the most necessary in the actual mining process of coal mines. Figure 13 shows a typical cycle in the numerical mining process. The advance distance of each step in the simulation should be less than the main roof rupture distance of 12–32 m to avoid its influence on the main roof rupture behavior and pressure change characteristics. Therefore, the mining step length of one cycle was set to 5 m; the material properties of the extraction zone were converted to the Salamon model at a rate of 5 m/cycle.

#### (5) Numerical simulation verification

In order to analyze the stress–strain characteristics of coal under different surrounding rock pressure conditions, lime fine Taiyuan Group 3–5 coal samples were taken in Tongxin Coal Mine and processed into standard specimens along the coal seam layer direction [19], with a length of 100 mm and a diameter of 50 mm. Due to the low strength of the coal seam in the working face, it is not possible to drill cylindrical samples. The coal samples collected on site are processed into cylindrical samples.

The processed standard coal and rock samples were numbered, the dimensions were measured with a vernier caliper, and they were weighed with an electronic balance. The physical and mechanical parameters of coal and rock were obtained through the RMT-150B rock mechanics testing system, and uniaxial compression tests were conducted on the processed coal and rock samples. Some coal samples and testing equipment are shown in Figure 14.

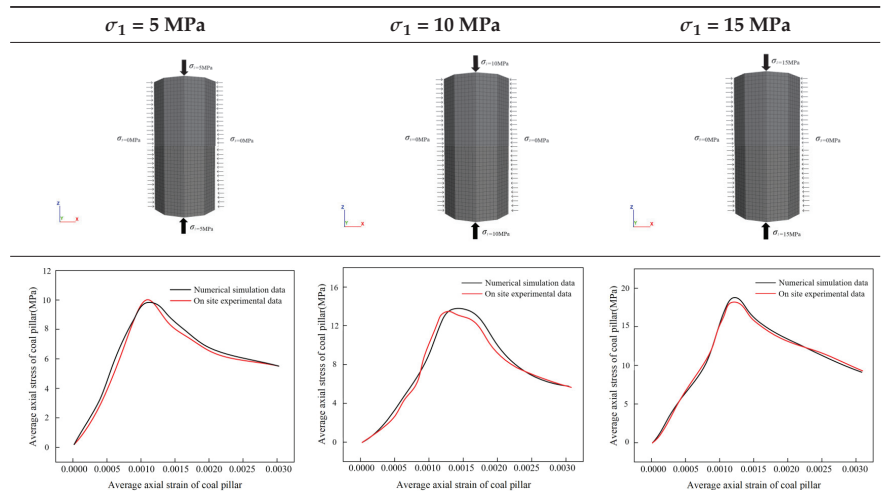


**Figure 13.** Schematic diagram of excavation simulation method for working face.



**Figure 14.** Partial coal samples and testing equipment.

At the same time, ABAQUS software is used to simulate the scenario of uniaxial compression of coal samples. Firstly, the displacement of the model in the normal direction is limited, and the displacement in the vertical normal direction is also limited. Then, the vertical displacement at the bottom of the model is set to zero. Finally, a constant velocity is applied to the top of the model in the negative z-direction to generate vertical loads on the model. For the on-site uniaxial compression test, 5 MPa, 10 MPa, and 15 MPa were selected as the applied load values in the numerical simulation. The numerical simulation diagrams and data comparison under different load conditions are shown in Table 3.

**Table 3.** Numerical simulation diagrams and data comparison under different load conditions.

By extracting on-site data from uniaxial compression tests and data from numerical simulations, it can be seen that the stress–strain curves of coal samples have similar variation characteristics. The deformation and failure process of coal samples can be divided into three stages: pore compression and elastic deformation stage, plastic deformation stage, and failure and instability stage. And the on-site data and numerical simulation data are basically consistent, proving that the numerical simulation data in this study can be used as a basis for distinguishing the mining stress and overlying rock stress arch of the working face.

### 3.3. The Results of Numerical Simulation

#### (1) Advance support stress distribution

Figure 15 shows the distribution cloud and curve of vertical stress and maximum principal stress during the mining process of longwall panel no. 8102. As shown in the figure, ① longwall panel no. 8102 end overrun coal body stress concentration is obvious, the maximum stress concentration is 27.42 MPa, stress concentration factor is 2.61; ② the two small coal pillars in the 8102 gob are in a state of pressure relief and cannot be carried; ③ the vertical stress of the 8100 gob, 8101 gob, and 8103 gob does not exceed 5 MPa and has not been fully compacted, which confirms the current situation of incomplete mining in a panel and indicates that there are upper hard rock layers bearing it, forming a large structure; ④ the stress concentration of the coal body at the front end is higher on the side close to the 8101 mining area than on the side close to the 8103 working face; ⑤ the direction of the vertical stress vector is relatively close to the direction of the maximum principal stress vector, indicating that the vertical stress becomes the point of maximum principal stress after mining (in the original rock stress state before mining, the horizontal stress is the maximum principal stress map).

#### (2) Distribution of plastic state of coal body

Figure 16 shows the distribution of plastic zones during the mining of the longwall panel no. 8102. As shown in the figure, ① the plastic deformation of the coal body in the longwall panel no. 8102 is the most severe, especially the advanced coal body on one side of the 8101 gob; ② during the mining process of longwall panel no. 8102, the overlying rock forms a C-shaped overlying rock structure, which will exacerbate the degree of mining pressure manifestation in the working face; ③ the maximum plastic principal strain direction of the leading coal body in longwall panel no. 8102 is near horizontal, which



indicates that the middling coal wall is prone to wall spalling during mining; ④ the elastic strain in the gob is relatively high, showing a situation of high strain in the middle and low strain around it, indicating that the Salomon model used has successfully simulated the compaction behavior of the gob.

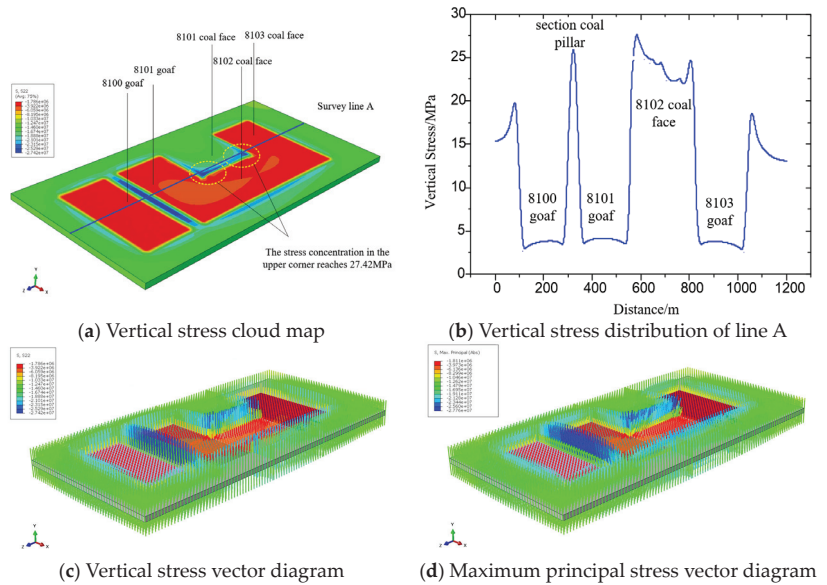


Figure 15. Vertical stress and maximum principal stress distribution diagram.

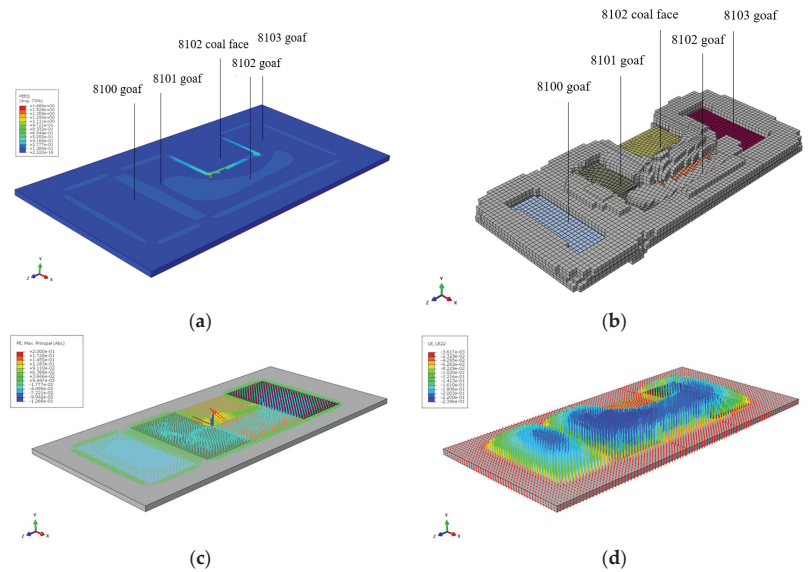
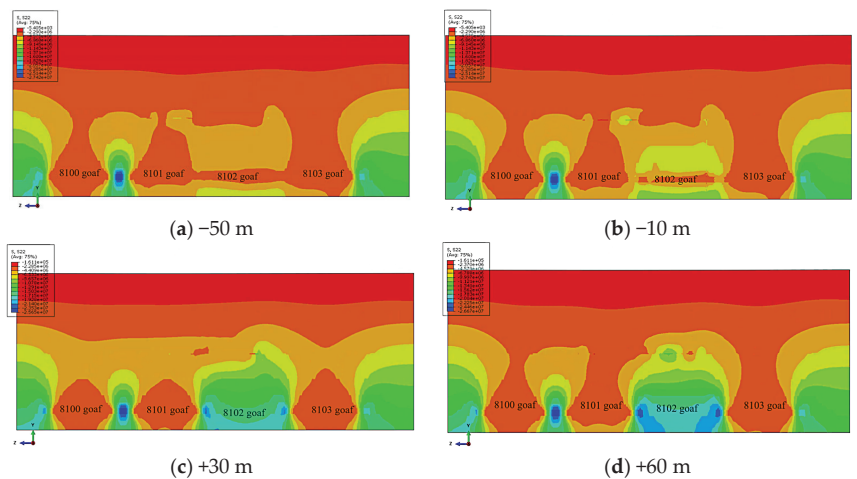


Figure 16. Simulation results of plastic zone distribution during the mining process of longwall panel no. 8102. (a) Distribution of plastic zone. (b) 8102 isolated island working face overlying rock C-shaped structure. (c) Vector plot of maximum plastic principal strain. (d) Vertical strain vector distribution of plasticity.

(3) Analysis of overlying rock stress arch structure

Figure 17 shows the stress cloud for slices at different locations along the working face direction. In the figure, the negative sign represents the rear of longwall panel no. 8102, and the positive sign represents the front of longwall panel no. 8102. From the figure, obviously ① the pressure is relieved behind the longwall panel no. 8102, but it is not fully relieved after 10 m, indicating that this area is affected by the “C”-shaped structure formed by the fracture of the hard top plate; ② the vertical stress is highest at 20 m in front of the working face; ③ stress arch structures with horizontal stress concentrations are formed 50 m above the 8100, 8101, 8102, and 8103 extraction zones, which are interconnected. This stress arch structure will be destroyed with the mining of longwall panel no. 8102, indicating that longwall panel no. 8102 is a key working face. The mining of longwall panel no. 8102 will cause the instability of the entire stress arch structure.



**Figure 17.** Slice stress cloud maps at different positions along the working face direction.

#### 4. Key Techniques for Hydraulic Fracturing and Pressure Relief of the Roof in the Island Fully Mechanized Caving Face of Extra-Thick Coal Seams

##### 4.1. Safety Risk Analysis of Longwall Panel No. 8102

The longwall panel no. 8102 is an isolated island working face, and the factors that are not conducive to the management of the working face roof and the prevention and control of dynamic phenomena in the working face are as follows:

① The overlying rocks are mostly sandstone layers with high hardness and few cracks, which suddenly break and induce impact loads; ② the mining thickness of the working face is large, the disturbance range of the overlying rock is large, the balance structure of the overlying rock moves upward, and the static load borne by the support is large; ③ on both sides of the longwall panel no. 8102 are gob areas. According to the observation results of surface cracks, there is an asymmetric long-arm suspended sandstone structure overlying the working face; ④ the coal seam is relatively hard and has the possibility of impact.

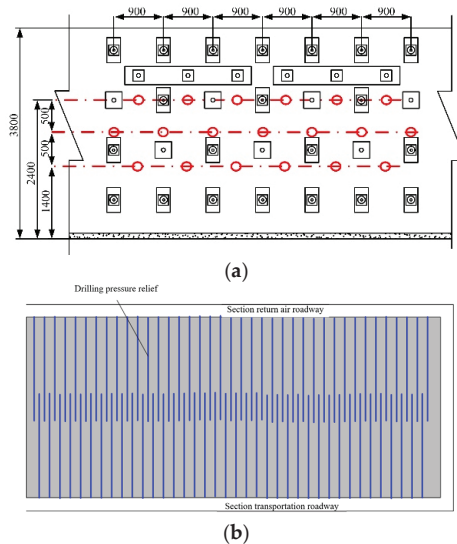
Therefore, 8102 island working face mining has the risk of strong dynamic pressure on the roof of the working face and rock burst in the coal seam, especially when the working face is first square and second square. In addition to increasing the working resistance of the hydraulic support, a series of technical measures for safety assurance should also be taken, including the pressure relief of the coal body drilling in front of the working face, the pre-cracking of the hard roof plate of the horizontal branch drilling under the well, the dynamic monitoring and early warning of microseisms, the dynamic monitoring of the support status, the dynamic monitoring of the advanced coal body stress, and the corresponding dynamic pressure prevention and control plan measures.

#### 4.2. Pressure Relief Plan for Coal Body Drilling in Front of the Working Face

In order to avoid the risk of sudden fracture of the hard overhanging roof slab rock strata causing impact on the coal body in front of the workings, large-diameter drilling was carried out from two roadways to relieve the pressure of the coal body in front of the workings.

Using a crawler-type drilling rig to drill large-diameter holes in the coal-mining slope construction, the diameter of the drill bit is 200 mm, and after expansion, the diameter is 200 mm. The drilling depth is not less than 120 m, forming a staggered layout of two alleys to eliminate the pressure relief void in the middle of the working face.

The pressure relief drilling construction is carried out in the central area of the coal-mining slope of the roadway, with a horizontal spacing of 900 mm and a vertical spacing of 500 mm between the drilling holes. The opening heights are 1400 mm and 2400 mm, respectively. After the drilling construction is completed, yellow mud is used to seal the hole for 300 mm to prevent gas from overflowing inside the hole. Several observation boreholes can be reserved. The drilling should be scheduled in advance, at least within 100 m of the working face, and the unpressurized drilling arrangement is shown in Figure 18.



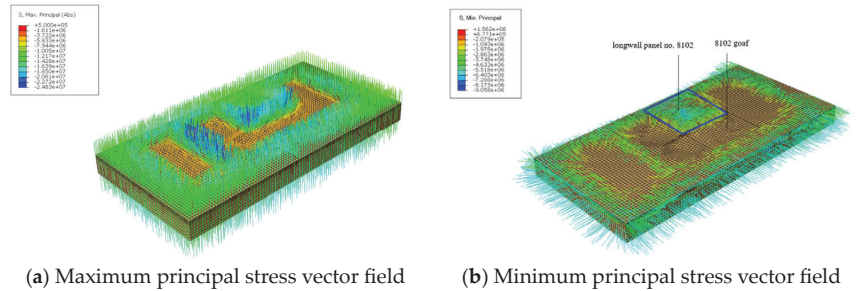
**Figure 18.** Layout of Pressure Relief Drilling in Section 1. (a) Layout of pressure relief drilling holes in the coal mining slope. (b) Interlaced arrangement of drilling holes for construction of two alleys.

#### 4.3. Pre-Splitting of Hard Roof Plate for Horizontal Branch Drilling

##### (1) Analysis of stress field environment of overburden rock in longwall panel no. 8102

In intact hard rock formations, the direction of propagation of hydraulic fractures is most significantly influenced by the ground stress field. Generally, the propagation surface of hydraulic fractures is perpendicular to the direction of the minimum principal stress and towards the direction of the maximum principal stress. The direction of the maximum principal stresses on the roof of the longwall panel no. 8102 has changed considerably due to the influence of the mountain packs on both sides. Figure 19 shows the distribution characteristics of the maximum and minimum principal stress vectors in the longwall panel no. 8102. From Figure 19a, it can clearly be seen that the direction of the maximum principal stress is approximately vertical during the mining of the longwall panel no. 8102, and the maximum principal stress near the end of the working face reaches 24.83 MPa, which is slightly inclined towards the gob. From Figure 19b, it can be seen that the minimum

principal stress direction in the coal body within 180 m of the longwall panel no. 8102 is roughly parallel to the advancing direction of the working face, which makes it easy to form vertical joints parallel to the working face. The minimum principal stress of the coal body 180 m away from the working face is parallel to the inclined direction of the working face, which is due to the release of constraints due to the gob on both sides. In this case, it is easy to form vertical joints parallel to the forward direction of the working face.

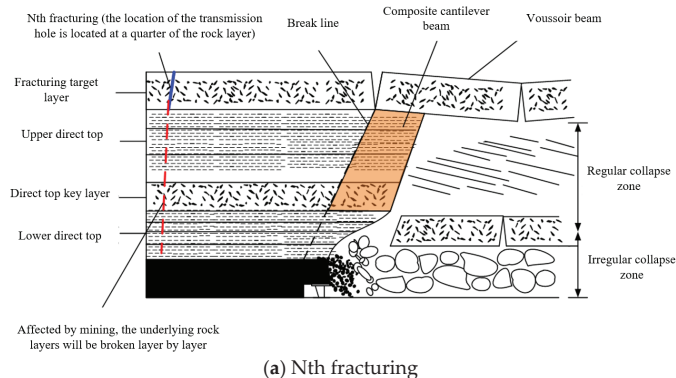


**Figure 19.** Numerical calculation results of maximum and minimum principal stress vector fields in longwall panel no. 8102.

If hydraulic fractures parallel to the working face are to be formed, it is suitable to conduct fracturing within 180 m of the working face in advance. If hydraulic fractures are to be formed parallel to the advancing direction of the working face, it is desirable to fracture within 180 m outside the advancing working face. The hydraulic fractures formed by both fracturing methods are vertical fractures.

## (2) Fracturing target layer

There are multiple layers of thick and hard rock layers in the overlying strata of Tongxin Coal Mine, which are the target layers for cracking. The 7 m thick K3 sandstone layer at 454.95 m buried depth, the 17.28 m thick sandy gravel layer at 423.78 m buried depth, the 10.9 m thick sandy gravel layer at 405.40 m buried depth, the 19.3 m thick silty sand layer at 394.5 m buried depth, the 9.55 m thick sandy gravel layer at 366.90 m buried depth, and the 10.95 m thick silty sand layer at 357.35 m buried depth may have a direct impact on the ground pressure of the working face. It is recommended to conduct fracturing in the 17.28 m thick sandy gravel layer at 423.78 m. The initial fracture is formed by perforation, and the perforation location should be within the upper 1/4 of the silty sand layer (as shown in Figure 20), so as to make the rock layer fracture under the action of ground pressure. When this rock layer fractures, the hard rock layer below it will also fracture.



**Figure 20.** Cont.

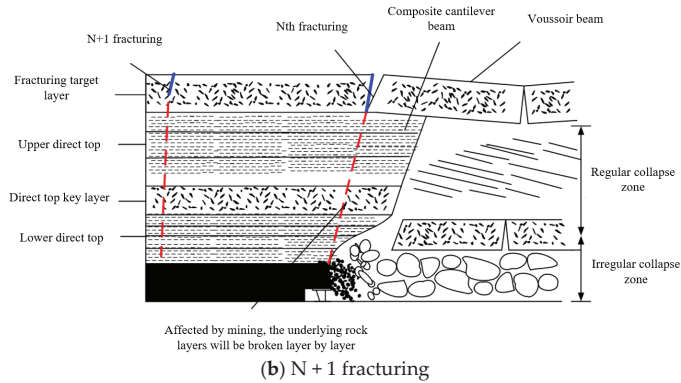
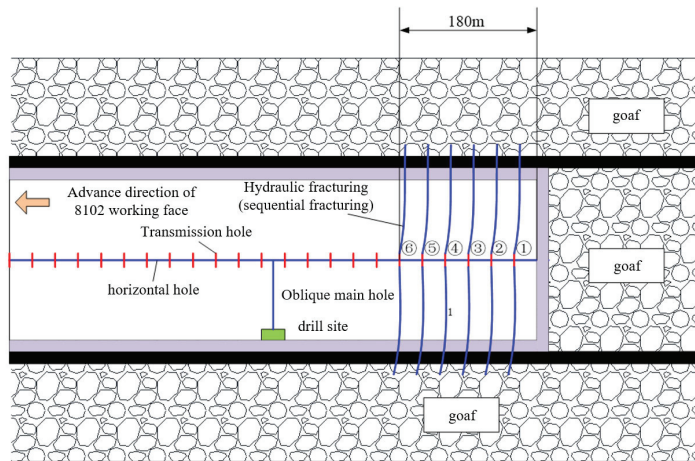


Figure 20. Fracturing target layer and perforation location.

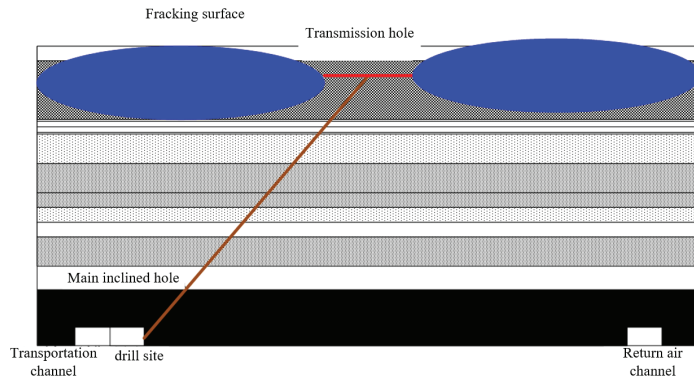
(3) Borehole layout of downhole fracking horizontal branch

In the transportation channel tunnel, starting from the cutting hole, fracturing drilling chambers are drilled every 500 m. The main fracturing hole is drilled diagonally upwards to the 17.28 m thick gravel layer buried at a depth of 423.78 m, which is 2 m from the top surface. The main oblique hole is projected parallel to the working face on the horizontal plane, and the final hole is located in the center of the working face, as shown in Figure 21. Then, horizontal holes are made parallel to the advancing direction of the working face, and the horizontal holes are arranged in this gravel rock layer. Horizontal holes are perforated in sequence with a spacing of 20 m, and then sequential fracturing is used to gradually fracture along the advancing direction from the opening of the cutting hole. To form vertical fractures parallel to the working face, fracturing should always be maintained within 180 m of the working face and should not be carried out in advance. The ultimate goal is to reduce the initial pressure step distance, cut off the cantilever structure of hard rock layers, and reduce the risk of working face impact.



(a) Layout plan of fracking boreholes on roof of longwall panel no. 8102

Figure 21. Cont.



(b) Profile diagram of fracking

**Figure 21.** Layout of fracking boreholes in longwall panel no. 8102.

## (4) Calculation of working resistance of hydraulic support on working face no. 8102

The 3rd to 5th coal seams of Tongxin Coal Mine are extra-thick coal seams with high mining height and integrated mining. The working face no. 8102 is also an isolated island working face in one panel. According to statistical analysis of the rock pressure behavior of other working faces in one panel, it can be concluded that: under the condition of using a 15,000 kN hydraulic support in one panel, it can basically meet the needs of roof management, however, there are still some serious pressure-bearing phenomena, indicating that the 15,000 kN hydraulic support is generally adaptable to the solid coal working face on both sides of the panel or the working face in one side of the air-mining zone. The application of 15,000 kN hydraulic support to the 8102 isolated island working face may face insufficient support resistance. The overlying strata structure of the coal seam is shown in Table 4.

**Table 4.** Structure of overlying strata in coal seams.

Layer Number	Thickness/m	Rock Name	Layer Number	Thickness/m	Rock Name
C1	0.90	Carbonaceous mudstone	C9	10.27	Interbedded mudstone and sandstone
C2	1.80	Coal	C10	2.36	Fine sandstone
C3	4.53	Sandy mudstone	C11	1.90	Glutenite
C4	3.65	Interbedded mudstone and sandstone	C12	17.28	Fine sandstone
C5	7.00	Coarse-grained sandstone	C13	1.10	Glutenite
C6	4.20	Fine sandstone	C14	10.9	Glutenite
C7	3.44	Siltstone	C15	19.30	Siltstone
C8	2	Coal	C16	1.6	Coarse-grained sandstone

The theoretical analysis method was used to determine the working resistance of the 8102 high mining height synthesized stent.

The roof rock layer that meets condition  $\Delta_j - \Delta_m \leq 0$  is the rock layer that needs to be controlled. The top slate layer that meets condition  $\Delta_j - \Delta_m > 0$  is the main roof rock layer.  $\Delta_j$  is the ultimate settlement;  $\Delta_m$  is the possible sinking amount;  $\Delta_m = (h_c + h_f)(1 - p_1) + (1 - k_p)h_m$ ;  $p_1$  is the coal loss rate;  $h_c$  is the coal-cutting height;  $h_f$  is the coal

discharge height;  $k_p$  is the direct crushing expansion coefficient;  $h_m$  is the thickness of a certain continuous roof rock layer.

(1) Determination based on the criteria for controlling rock layers:

$$\begin{aligned}\Delta_{m1} &= 19 \times (1 - 0.2) + (1 - 1.2) \times 0.9 = 15.02 \text{ m} \\ \Delta_{j1} &= h - \frac{ql^2}{2kh[\sigma_c]} < \Delta_{m1}\end{aligned}\quad (19)$$

So, the C1 rock layer is the rock layer that needs to be controlled,

$$\begin{aligned}\Delta_{m2} &= 19 \times (1 - 0.2) + (1 - 1.2) \times 2.7 = 14.66 \text{ m} \\ \Delta_{j2} &= h - \frac{ql^2}{2kh[\sigma_c]} < \Delta_{m2}\end{aligned}\quad (20)$$

So, the C2 rock layer is the rock layer that needs to be controlled,

$$\begin{aligned}\Delta_{m3} &= 19 \times (1 - 0.2) + (1 - 1.2) \times 7.23 = 13.754 \text{ m} \\ \Delta_{j3} &= h - \frac{ql^2}{2kh[\sigma_c]} < \Delta_{m3}\end{aligned}\quad (21)$$

So, the C3 rock layer is the rock layer that needs to be controlled.

By analogy, it is calculated that the C4, C5, C6, C7, C8, C9, C11, C12, and C13 strata are controlled strata, while the C14 stratum and above are the basic roof strata.

(2) Determination of rock layers without deformation pressure:

$$\sum_{i=1}^n (\Delta_j)_i = \Delta_d \quad (22)$$

$\Delta_d$  is the total deformation of the top coal body in the control zone,  $\Delta_d = \eta h_d(1 + \lambda)$ ,  $\eta$  is the porosity, and  $\lambda$  is the lateral pressure coefficient. After calculation, it was found that  $\Delta_d = 6.41$  m, and the C1~C5 rock layers can offset the deformation of the top coal. Therefore, the basic data of C6, C7, ..., C14 are brought into the following equation to calculate the working resistance.

$$P_z = G_d + Q = L_d h_d \gamma + \frac{f \sum_{i=1}^{j+1} P_i (l_i + h_i \cdot ctg\alpha) - 2(Q_B - K \cdot s)(h_{j+1} - \Delta)}{2cf} \quad (23)$$

In consideration of the factor of safety, the maximum value of the static resistance can be obtained, given by

$$P_z = G_d + Q = L_d h_d \gamma + \frac{f \sum_{i=1}^{j+1} P_i (l_i + h_i \cdot ctg\alpha)}{2cf} = 2643.8 + 7789.4 = 11, 843.2 \text{ kN} \quad (24)$$

The impact resistance coefficient of the support is taken as 2, which can determine that the working resistance of the hydraulic support should not be less than 20,866.4 kN, and the final value is 21,000 kN.

Appropriately increasing the bracket height of the hydraulic support is conducive to reducing the size of the coal block and improving the capacity of comprehensive release. However, the longwall panel no. 8102 is an isolated island working face. Increasing the mining height increases the working resistance of the stent, even in the case of an integrated working face. Therefore, it is not recommended to increase the height of the support. Therefore, a support height of 3.8 m is adopted, with a support structure height of 2.75~4.2 m.

In summary, ZFY21000/27.5/42 hydraulic support is selected. The working resistance of this type of hydraulic support is 21,000 kN, and it is necessary to pre-crack the roof rock layer in advance and manually create cracks along the working face. The hard roof shall be pre-cracked in advance by means of surface L-shaped horizontal wells or fracking by means of horizontal branch holes under the well.

## 5. Conclusions

- (1) The leading coal body at the end of the longwall working face in an extra-thick coal seam showed significant stress concentration, with a stress concentration coefficient of 2.61. Under the structural characteristics of the strata and the mining conditions in the one-panel area, one side of the hollow workings was mined over for nonsufficient mining and the strata failed to settle sufficiently.
- (2) During the mining process, the overlying strata undergo extensive and intense movement, inducing strong rock pressure. In this case, the structure of the overlying strata undergoes deformation from an asymmetric long-arm “T” before mining into a C-shaped structure during the mining process. The asymmetric T-shaped structure of the hard rock cantilever is located above the working face, causing significant rock pressure after fracture.
- (3) The directional hydraulic fracturing roof control technology was successfully implemented in Tongxin Coal Mine, achieving high stress transfer in the mining roadway of the working face. The appropriate hydraulic support resistance was determined through calculation, and the corresponding hydraulic support was successfully selected.

**Author Contributions:** Methodology, Y.W.; Software, P.C.; Formal analysis, Y.W. and S.W.; Resources, S.W. All authors have read and agreed to the published version of the manuscript.

**Funding:** This study was supported by the National Natural Science Foundation of China (No. 52204090).

**Data Availability Statement:** Not applicable.

**Conflicts of Interest:** The authors declare no conflict of interest.

## References

1. Ren, X.; Hao, B.; Wang, H.; Zhao, J.; Zhang, J.; Zhang, C. Roadway Protection by Roof-Cutting in the Support Removing Channel of the Long-Wall Mining Face. *Shock Vib.* **2022**, *2022*, 8116399. [CrossRef]
2. Gao, M.; He, Y.; Xu, D.; Yu, X. A New Theoretical Model of Rock Burst-Prone Roadway Support and Its Application. *Geofluids* **2021**, *2021*, 5549875. [CrossRef]
3. Wang, P.; Zhang, N.; Kan, J.; Xu, X.; Cui, G. Instability Mode and Control Technology of Surrounding Rock in Composite Roof Coal Roadway under Multiple Dynamic Pressure Disturbances. *Geofluids* **2022**, *2022*, 8694325. [CrossRef]
4. Yang, H.; Zhang, N.; Han, C.; Sun, C.; Song, G.; Sun, Y.; Sun, K. Stability Control of Deep Coal Roadway under the Pressure Relief Effect of Adjacent Roadway with Large Deformation: A Case Study. *Sustainability* **2021**, *13*, 4412. [CrossRef]
5. Yang, Z.-Q.; Liu, C.; Jin, H.-W. Study on Pressure Relief Zone Formed Inside Roadway Rib by Rotary Cutting with Pressurized Water Jet for Preventing Rock Burst. *Adv. Civ. Eng.* **2022**, *2022*, 9647029. [CrossRef]
6. Yang, X.; Hu, C.; He, M.; Wang, H.; Zhou, Y.; Liu, X.; Zhen, E.; Ma, X. Study on Presplitting Blasting the Roof Strata of Adjacent Roadway to Control Roadway Deformation. *Shock Vib.* **2019**, *2019*, 3174898. [CrossRef]
7. Chen, X.; Wang, X.; Zhang, D.; Qin, D.; Wang, Y.; Wang, J.; Chang, Z. Creep and Control of the Deep Soft Rock Roadway (DSRR): Insights from Laboratory Testing and Practice in Pingdingshan Mining Area. *Rock Mech. Rock Eng.* **2022**, *55*, 363–378. [CrossRef]
8. Ji, M.; Guo, H. Influence of In-Situ Rock Stress on the Stability of Roadway Surrounding Rock: A Case Study. *J. Geophys. Eng.* **2020**, *17*, 138–147. [CrossRef]
9. Yuan, Y.; Han, C.; Zhang, N.; Feng, X.; Wang, P.; Song, K.; Wei, M. Zonal Disintegration Characteristics of Roadway Roof Under Strong Mining Conditions and Mechanism of Thick Anchored and Trans-Boundary Supporting. *Rock Mech. Rock Eng.* **2022**, *55*, 297–315. [CrossRef]
10. Qian, D.; Deng, J.; Wang, S.; Yang, X.; Cui, Q.; Li, Z.; Jin, S.; Liu, W. Deformation Characteristics and Control Countermeasures for Surrounding Rock of Deep Roadway under Mining Disturbance: A Case Study. *Shock Vib.* **2022**, *2022*, 9878557. [CrossRef]
11. Wang, K.; Wang, L.; Ren, B.; Fan, H. Study on Seepage Simulation of High Pressure Grouting in Microfractured Rock Mass. *Geofluids* **2021**, *2021*, 6696882. [CrossRef]



12. Cheng, Y.; Bai, J.; Ma, Y.; Sun, J.; Liang, Y.; Jiang, F. Control Mechanism of Rock Burst in the Floor of Roadway Driven along Next Gob in Thick Coal Seam with Large Obliquity Angle in Deep Well. *Shock Vib.* **2015**, *2015*, 750807. [CrossRef]
13. Jolfaei, S.; Lakirouhani, A. Sensitivity Analysis of Effective Parameters in Borehole Failure, Using Neural Network. *Adv. Civ. Eng.* **2022**, *2022*, 4958004. [CrossRef]
14. Yang, J.; Liu, C.; Yu, B. Application of Confined Blasting in Water-Filled Deep Holes to Control Strong Rock Pressure in Hard Rock Mines. *Energies* **2017**, *10*, 1874. [CrossRef]
15. Gao, R.; Yu, B.; Meng, X. Stress Distribution and Surrounding Rock Control of Mining near to the Overlying Coal Pillar in the Working Face. *Int. J. Min. Sci. Technol.* **2019**, *29*, 881–887. [CrossRef]
16. Chen, L.; Li, Q.; Yang, J.; Qiao, L. Laboratory Testing on Energy Absorption of High-Damping Rubber in a New Bolt for Preventing Rockburst in Deep Hard Rock Mass. *Shock Vib.* **2018**, *2018*, 7214821. [CrossRef]
17. Jiang, F.X. Viewpoint of Spatial Structures of Overlying Strata and Its Application in Coal Mine. *J. Min. Saf. Eng.* **2006**, *23*, 30–33.
18. Salamon, M.D.G. Mechanism of caving in longwall coal mining. In Proceedings of the 31st U.S. Symposium of Rock Mechanics, Golden, CO, USA, 18–20 June 1990; West Virginia University Press: Morgantown, WA, USA, 1990.
19. Wang, H.; Poulsen, B.A.; Shen, B.; Xue, S.; Jiang, Y. The influence of roadway backfill on coal pillar strength by numerical investigation. *Int. J. Rock Mech. Min. Sci.* **2011**, *48*, 443–450. [CrossRef]

**Disclaimer/Publisher’s Note:** The statements, opinions and data contained in all publications are solely those of the individual author(s) and contributor(s) and not of MDPI and/or the editor(s). MDPI and/or the editor(s) disclaim responsibility for any injury to people or property resulting from any ideas, methods, instructions or products referred to in the content.

## Article

# Study on Performance Optimization of Water-Rich Grouting Materials Based on Response Surface Methodology

Xiaoping Li <sup>1</sup>, Guoping Han <sup>1</sup>, Yong Wang <sup>1</sup>, Jie Xu <sup>1</sup>, Jie Du <sup>1</sup>, Bo Yang <sup>1</sup>, Min Zhang <sup>1</sup>, Tao Li <sup>1</sup> and Bo Li <sup>2,\*</sup>

<sup>1</sup> Tunlan Mine, Shanxi Coking Coal Group Co., Ltd., Gujiao 030206, China; lixiaoping7526@163.com (X.L.); hanguoping0802@163.com (G.H.); wangyong202308@163.com (Y.W.); ky921899@126.com (J.X.); dujie20220502@163.com (J.D.); yangbo202308@163.com (B.Y.); chenycumt@sina.com (M.Z.); aqkygc@126.com (T.L.)

<sup>2</sup> School of Safety Science and Engineering, Henan Polytechnic University, Jiaozuo 454003, China

\* Correspondence: anquanlibo@163.com

**Abstract:** The quality of borehole sealing is a key factor affecting the efficiency of gas production. A new water-rich grouting material (RW) with composite coagulant and other additives was prepared in this study to overcome the disadvantages of long setting time and low stone rate of traditional cement materials. When the coagulants A is 4 g and coagulants B is 2 g, the setting time of RW material was reduced by 60.85% and 50.62%, which significantly shortened the setting time of the RW material, respectively. Based on the orthogonal method, 29 groups of comparative experiments were designed to investigate the interaction mechanism between different additives on the performance index of RW, including setting time, water secretion rate, and compressive strength. Quadratic regression equations were fitted using the response surface method. All the correlation coefficients  $R^2$  of each response model were greater than 0.97,  $R^2$  and  $R^2_{\text{adj}}$  were less than 0.2 through variance analysis, indicating a high correlation between the actual and prediction results. The water–cement ratio had the most significant effect among all factors on setting time, water secretion rate, and compressive strength of the RW material. The scanning electron microscope (SEM) was used to compare the micromorphological characteristics of RW and conventional Portland cement material (PC). The results showed that the hydration products of RW were mostly smectite, calcium silicate hydrate gel, and calcium hydroxide, which interweaved with each other to form a network structure that was denser than the PC material. Furthermore, the interface bonding degree between RW and injected coal was tighter than that of PC, without obvious cracks at the slurry–coal interface. The results indicate that the addition of composite coagulant can significantly accelerate the hydration process of RW material and also enhance the interface strength of injected coal, which is conducive to improving the grouting quality and sealing effect of the extraction borehole.

**Keywords:** gas extraction; water-rich grouting materials; orthogonal experiment methodology; response surface methodology; scanning electron microscope

**Citation:** Li, X.; Han, G.; Wang, Y.; Xu, J.; Du, J.; Yang, B.; Zhang, M.; Li, T.; Li, B. Study on Performance Optimization of Water-Rich Grouting Materials Based on Response Surface Methodology. *Processes* **2023**, *11*, 2789. <https://doi.org/10.3390/pr11092789>

Academic Editor: Vladimir S. Arutyunov

Received: 13 August 2023

Revised: 10 September 2023

Accepted: 17 September 2023

Published: 19 September 2023



**Copyright:** © 2023 by the authors. Licensee MDPI, Basel, Switzerland. This article is an open access article distributed under the terms and conditions of the Creative Commons Attribution (CC BY) license (<https://creativecommons.org/licenses/by/4.0/>).

## 1. Introduction

Coalbed methane (CBM), a type of unconventional natural gas co-born with coal, has significant reserves in China and can reach up to  $36.81 \times 10^{12} \text{ m}^3$  at a shallow depth of 2000 m, with recoverable resources of  $10.87 \times 10^{12} \text{ m}^3$  (about 30%) and a large potential for development [1–3]. CBM is an efficient and clean energy source that brings considerable economic benefits, which is of great importance in alleviating the constricted natural gas supply [4]. However, the continuous development of deep CBM, the characteristics of high stress, and gas pressure are more likely to cause coal and gas outburst disasters. Wang et al. [5] developed a system for the in situ monitoring of spontaneous combustion gas emissions from fissure channels by considering spontaneous combustion gas, meteorological factors, and the thermal physical characteristics of fissures, and providing support for

taking corresponding fire extinguishing measures for the degree of coal fire re-ignition in coal fire areas. Bosikov et al. [6] developed a new modeling method for mine ventilation networks to reduce the cost of eliminating mine fires, in order to improve the reliability of mine gas mode control. Silva et al. [7] introduced the main technical differences of ICs in order to provide a type of guideline on the use of these reactive fire protections. This condition seriously limits the safe and efficient production of coal mines [8]. How to efficiently extract and utilize CBM is currently an urgent problem.

Pre-extraction through boreholes is a prominent technique for achieving efficient gas extraction from coal seams [9]. The deep coal seams in China are characterized by high geostress, high gas content, high gas stress, and low permeability, thus leading to a difficult extraction process, including borehole collapse, inadequate sealing of borehole plugging, and other phenomena [10,11]. Therefore, the selection of suitable grouting plugging materials is one of the key factors to improving gas extraction [12,13]. In this regard, related scholars have achieved many results in their research on the mechanism of grouting plugging. Wang et al. [14] studied the influence of sealing support force on the air leakage rate of boreholes, proposed the principle of active support grouting sealing, and analyzed the factors that affect the air leakage rate. Zhang et al. [15] systematically investigated the evolution law of permeability by establishing a two-media coupling model considering matrix shrinkage and effective stress. They found that the gas concentration increases with the increase in the seal length and pore diameter, and decreases with the increase in the negative pressure of pumping and coal permeability. Wang et al. [16] discussed the effects of extraction time, seal length, and air leakage rate on gas concentration by constructing a fluid–solid coupling model. Si et al. [17] developed a self-healing sealing material to reduce the impact of regenerated fractures on gas extraction efficiency, which can achieve self-healing of fractures. Xia et al. [18] systematically explored the effects of different seal lengths, leakage rates, and leakage crack widths on the concentration of gas discharged from the cracks by establishing a coupled model of coal seam deformation, coal seam gas flow and transport, and air flow in the coal seam. For cement additives, Chen et al. [19] synthesized a reactive halogen-free organic grouting reinforcement material with excellent thermal stability to address the problem of high halogen content in ordinary polyurethane grouting reinforcement materials, which causes catalyst poisoning and deactivation in coal chemical enterprises. Sun et al. [20] developed a new cement grouting materials and used scanning electron microscopy (SEM) to observe the product morphology under different sodium hydroxide dosages. Zhao et al. [21] analyzed the role of aluminate cement in the curing and expansion mechanism of the material by testing different aluminate cement dosages. Liu et al. [22] introduced 2-Acrylamido-2-methylpropanesulfonic acid combined with triethanolamine as an organic early strengthening component. They investigated the preparation and performance of the early strengthening agent through orthogonal tests and thermogravimetric analysis, X-ray diffraction analysis, and SEM. Qian et al. [23] conducted experiments on the water absorption performance of water absorbing resins in different slurry environments. They verified that using water-absorbing resins as the stopping grouting of boreholes grouting can significantly reduce the compressive strength of the cement in contact with it, and the influence range is about 100 mm. Guan et al. [24] developed an inorganic and organic composite grouting reinforcement material for deep soft rock based on prominent issues such as large deformation, crack closure, and permeability of surrounding rock in soft rock tunnels with a depth of one kilometer. The material exhibits “high early strength, high injectability, and high adhesion”.

For sealing the borehole using grouting, improving the performance of grouting materials is the key to improving the effectiveness of sealing. On the basis of previous research, this work formulates a water-rich grouting material (RW) with composite coagulants, analyzes the changes of setting time, water secretion rate, and compressive strength of RW by using the response surface method (RSM), and observes the microscopic microstructure characteristics of RW and Portland cement (PC). The microstructure of RW and injected coal is studied by using SEM, and the hydration process of slurry and hydration prod-

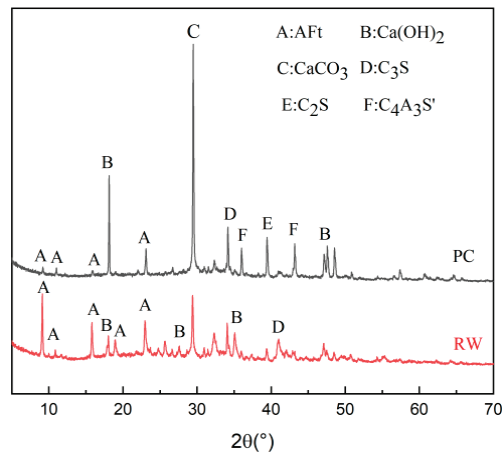
ucts is analyzed, thus providing a theoretical basis for improving the quality of grouting and sealing.

## 2. Materials Preparation and Test Methods

### 2.1. Raw Materials

RW is prepared by using ordinary PC as the base material, with compound component coagulant and a few additives. Its water–cement ratio can reach 1.0. The main mineral components of the base material are tricalcium silicate ( $C_3S$ ), dicalcium silicate ( $C_2S$ ), tricalcium chlorate ( $C_3A$ ), tetracalcium aluminoferrite ( $C_4AF$ ), and some free calcium oxide and magnesite. The mineral composition of coagulant A is mainly calcium sulfoaluminate ( $C_4A_3S$ ),  $C_2S$ , and so on. The main component of coagulant B is carbonate, and the main component of coagulant C is a complex of sulphate and calcium formate. The main component of the suspension is montmorillonite.

To understand the composition of hydration products in the preparation engineering of RW and PC materials, two sets of RW and PC materials were prepared. The phase differences between the two materials were compared through X-ray diffraction, in order to provide theoretical support for slurry improvement. The physical phase analysis of the mineral composition of RW and PC materials is shown in Figure 1. A certain amount of  $C_3S$ ,  $C_2S$ ,  $C_3A$ ,  $C_4AF$ , and  $C_4A_3S'$  are present in the mineral composition of cement.  $C_3S$  can hydrate with  $C_2S$  to form C-S-H gels,  $C_3A$  will hydrate with  $C_4AF$  to form CH gels, and  $C_4A_3S'$  hydration can react rapidly with gypsum to form smack ettringite (AFt) in the early stages of hydration. The hydration of the mineral components to form calcium aluminate crystals of different amounts and morphology will result in different grout properties, which will affect the grouting and sealing performance.



**Figure 1.** Physical composition analysis of basic materials.

### 2.2. Test Program

In the process of preparing grouting materials, a group of RW materials without the addition of coagulants was preferentially prepared and its slurry setting time was measured, which was found to be approximately 567 min, and the phenomenon of water secretion occurred. Therefore, a comparative experiment was carried out with the addition of three different coagulants to investigate the effect of the type and dosage of coagulants on the RW materials.

### 2.3. Test Methods

#### (1) Test for setting time

The time taken from the completion of the slurry preparation to the setting is known as the setting time. The slurry setting time was based on GB1346-89 “Test methods for water requirement of normal consistency, setting time and soundness of Portland cement”, which was applied using the ISO standard method of the Vickers apparatus [25].

#### (2) Test for water secretion rate

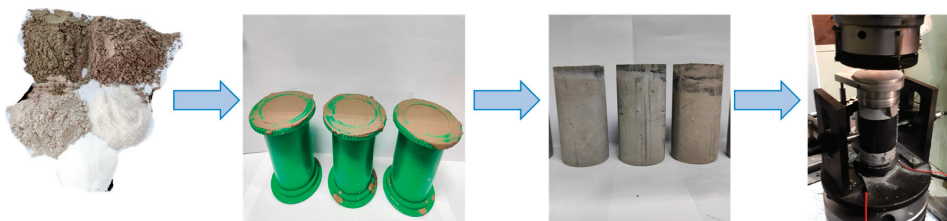
The water secretion rate was tested by first weighing the sample cylinder. Then, the mixed slurry was loaded into the sample cylinder and smoothed at the opening [26]. The outer surface and mouth of the specimen cylinder were wiped clean, and the total weight of the stirred slurry and the specimen cylinder were weighed. Afterward, the timer was started. Finally, the remaining weight of the slurry and sample cylinder was weighed at the end of water secretion. The rate of water secretion was calculated using Formula (1), and the water secretion rate is accurate to 0.01% [27].

$$c = \frac{a - b}{a} \times 100\% \quad (1)$$

where  $a$  is the full cylinder mass, g;  $b$  is the residual mass, g; and  $c$  is the water secretion rate, %.

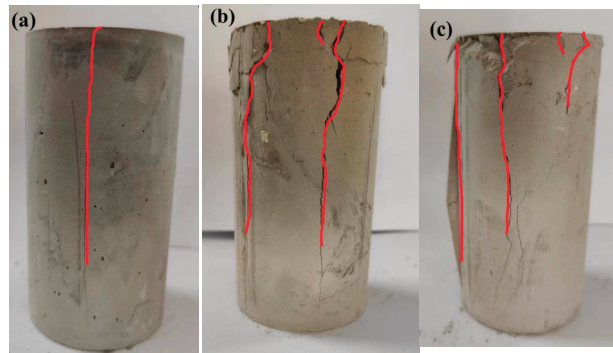
#### (3) Test for compressive strength

The uniaxial compression test was conducted on the prepared standard specimens under standard preservation conditions using the RMT-150 rock mechanics test system manufactured by the Wuhan Institute of Geotechnics, Chinese Academy of Sciences [28,29]. The experimental equipment and procedure are shown in Figure 2. The maximum horizontal load of the test system was up to 500 kN, the maximum axial load was up to 1000 kN, the maximum peripheral pressure was 50 MPa, the maximum axial travel was 50 mm, the displacement was 5 mm, and the transverse displacement was 2.5 mm. This test adopts the displacement loading method, and the loading rate was 0.12 mm/min. We mixed cement, admixtures, and water in a water–cement ratio of 0.8(A), 1.0(B), and 1.2(C) to produce three sets of slurry. Once the mixture was uniformly mixed, we poured it into a mold with a diameter of 61.8 mm and a height of 20 mm. We smoothed the surface and allowed it to cure at room temperature for 24 h before removing it from the mold. Afterward, we cured it in a standard curing room for 28 days to test its compressive strength. The process is outlined in Figure 2.



**Figure 2.** Flow chart of compressive strength experiment.

The compressive strength test results are shown in Figure 3, where A experiences shear failure. When the cylindrical specimen is subjected to pressure, shear failure may occur at the center of the specimen. This type of failure is more common when the material has high shear strength. B undergoes crush. When the pressure on the sample exceeds its compressive capacity, the sample may experience crush, which is more common when the compressive strength of the material is low. C exhibits delamination failure, and the surface of the sample exhibits layered delamination or cracks.



**Figure 3.** Compressive strength test results. (a) shear failure, (b) undergoes crush, (c) delamination failure.

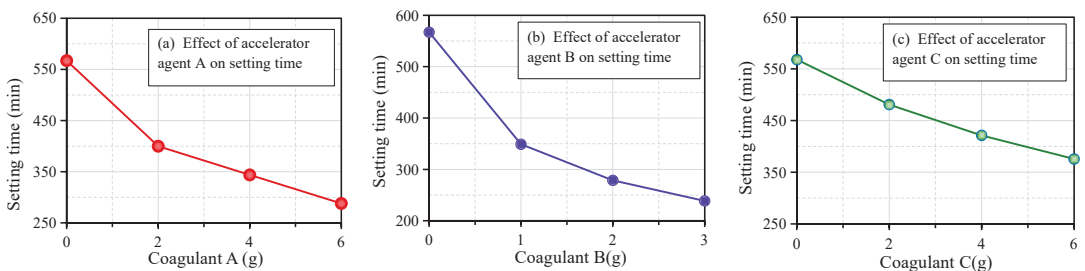
### 3. Response Surface Methodology Analysis

#### 3.1. Selection of Coagulants

The setting time of the RW material chosen for the experiment is 567 min. The long condensation time and the phenomenon of water secretion will lead to the formation of air leakage channels in the boreholes, which will cause the boreholes to not be sealed tightly and affect the overall pumping effect of the mine. Three kinds of coagulants were selected to study the effect of different kinds of coagulant and dosage on the setting time of the RW material. The experimental program is shown in Table 1. The experimental results are shown in Figure 4.

**Table 1.** Design of different kinds of coagulants dosage programs.

Coagulants Kinds	Dosage/g		
Coagulant A	2	4	6
Coagulant B	1	2	3
Coagulant C	2	4	6



**Figure 4.** Effect of type and dosage of coagulants on setting time of RW materials.

The experimental results show that the setting time of the RW material is 567 min without adding coagulants. From Figure 4a, the dosage of coagulant A is 2 g, and the setting time of the RW material is 400 min, which is 29.45% shorter than that without coagulants. In addition, the setting time of RW materials are shortened by 60.85% and 48.85% at the dosage of coagulant A are 4 g and 6 g, respectively, indicating that when 4 g of coagulant A is added, the setting time of the RW material achieves the maximum reduction.

In accordance with Figure 4b, the dosage of coagulant B is 1 g, the setting time of the RW material is reduced by 38.27% compared with that without coagulants. However, the setting time of the RW material is decreased by 50.62% when the dosage of coagulant B is 2 g. When the dosage of coagulant B is 3 g, the setting time of the RW material is reduced

by 57.67%. This shows that when the dosage of coagulant B is 3 g, the setting time of the RW material achieves maximum reduction.

As demonstrated in Figure 4c, when the dosage of coagulant C is 2 g, the setting time is shortened by 15.34%. The setting times of the RW materials are shortened by 25.93% and 33.86% when the dosage of coagulant C are 4 g and 6 g, respectively. Therefore, the shortening of the setting time of RW material is greatest when the dosage of coagulant C is 6 g.

As can be seen from Figure 4, the addition of coagulants is able to reduce the setting time of the RW material. Coagulants A and B show strong hydration promoting ability, which can greatly shorten the coagulation time of the RW material. Therefore, the combination of coagulants A and B, supplemented with a suspending agent, was selected for the study of accelerated coagulation modification of the RW material.

### 3.2. Experimental Response Surface Study

#### 3.2.1. Experimental Design and Results

RSM is a design methodology for establishing the accuracy of mathematical modeling to achieve optimum performance and economy [30,31]. This method is used to investigate the relationship between water–cement ratio ( $X_1$ ), coagulant A ( $X_2$ ), coagulant B ( $X_3$ ), and suspending agent dosage ( $X_4$ ) interactions with the response targets of setting time ( $Y_1$ ), water secretion rate ( $Y_2$ ), and compressive strength ( $Y_3$ ). The response model of the surfaces was designed using Design-Expert software. Central composite response surface analysis was applied to implement the program design, and a total of 29 groups were designed. The design of test factors and levels is shown in Table 2, and the detailed mix ratios and test results are shown in Table 3.

**Table 2.** Coding levels of factors in the text design.

Factors	Variables	Level		
		−1	0	1
Water–cement ratio	$X_1$	0.8	1.0	1.2
Coagulant A	$X_2$	2	4	6
Coagulant B	$X_3$	1	2	3
Suspending agent	$X_4$	5	10	15

**Table 3.** Detailed mix ratio and test results of RW.

Group	Level				Results		
	$X_1$	$X_2$	$X_3$	$X_4$	$Y_1/\text{min}$	$Y_2/\%$	$Y_3/\text{MPa}$
1	0	0	0	0	360	0.98	6.52
2	0	1	1	0	408	1.03	7.95
3	0	0	0	0	304	1.02	7.74
4	1	0	0	−1	240	0.61	11.41
5	0	1	0	1	300	1.06	8.56
6	1	1	0	0	276	0.89	7.3
7	−1	0	0	−1	516	2.35	5.45
8	−1	1	0	0	400	1.08	6.52
9	0	0	−1	−1	304	1.02	7.74
10	0	−1	1	0	272	0.93	8.37
11	1	0	−1	0	304	1.02	7.74
12	0	−1	0	−1	492	1.96	5.1
13	0	0	1	1	296	0.96	8.55
14	0	0	1	−1	480	1.77	5.91
15	0	0	0	0	240	0.61	11.41
16	1	−1	0	0	208	0.55	11.82
17	0	1	−1	0	420	1.13	7.92
18	−1	0	1	0	296	0.95	6.11
19	1	0	1	0	516	2.35	5.45
20	1	0	0	1	400	1.08	6.52
21	0	0	0	0	276	0.89	7.3
22	0	0	−1	1	280	0.99	7.25
23	0	0	0	0	304	1.02	7.74
24	0	1	0	−1	500	1.83	4.47
25	−1	0	0	1	404	1.07	8.96
26	−1	0	−1	0	176	0.44	11.15
27	0	−1	0	1	472	1.42	4.89
28	−1	−1	0	0	484	1.65	5.1
29	0	−1	−1	0	304	1.02	7.74

### 3.2.2. Analysis of Regression Model

The data in Table 3 were used to fit a polynomial model that represents  $Y_1$ ,  $Y_2$ , and  $Y_3$  as a function of  $X_1$ ,  $X_2$ ,  $X_3$ , and  $X_4$ . On the basis of the results of RSM, the response equation can be expressed as:

$$Y_1 = 304 + 130.67X_1 - 26.33X_2 - 58.33X_3 - 6.67X_4 + 8X_1X_2 + 11X_1X_3 + X_1X_4 + 9X_2X_4 + 2X_3X_4 + 34.17X_1^2 + 23.67X_2^2 + 24.67X_3^2 + 17.17X_4^2 \tag{2}$$

$$Y_2 = 1.02 + 0.64X_1 - 0.013X_2 - 0.144X_3 - 0.068X_4 - 0.01X_1X_2 - 0.17X_1X_3 - 0.05X_1X_4 - 0.003X_2X_3 + 0.02X_2X_4 + 0.09X_3X_4 + 0.18X_1^2 - 0.009X_2^2 - 0.007X_3^2 + 0.008X_4^2 \tag{3}$$

$$Y_3 = 7.74 - 3.1X_1 + 0.913X_2 - 0.313X_3 + 0.006X_4 + 0.07X_1X_4 - 0.025X_1X_3 + 0.058X_2X_3 - 0.003X_2X_4 + 0.005X_3X_4 + 0.589X_1^2 - 0.111X_2^2 - 0.047X_3^2 - 0.085X_4^2 \tag{4}$$

Analysis of variance (ANOVA) determined that the quadratic regression Equations (2)–(4) could explain the experimental data at a 95% confidence level [32]. The ANOVA of the quadratic model for setting time, water secretion rate, and compressive strength is shown in Table 4.  $P$  is the significance value, and  $F$  is the ratio of the mean squared error to its error, which is an important indicator of ANOVA.  $0.01 < P < 0.05$  indicates significant,  $P < 0.01$  indicates highly significant, and  $P > 0.05$  indicates not significant [33].  $R^2$  reflects the degree of difference between the response and actual value. A large  $R^2$  corresponds to better model correlation [34,35]. The  $R^2$  of the models  $Y_1$ ,  $Y_2$ , and  $Y_3$  were 97.77%, 97.39%, and 99.63%, respectively, with a CV < 10%, indicating that the experimental results had high credibility and accuracy. This model can be used to optimize the setting time, water secretion rate, and compressive strength of the RW material.

**Table 4.** Response surface ANOVA results.

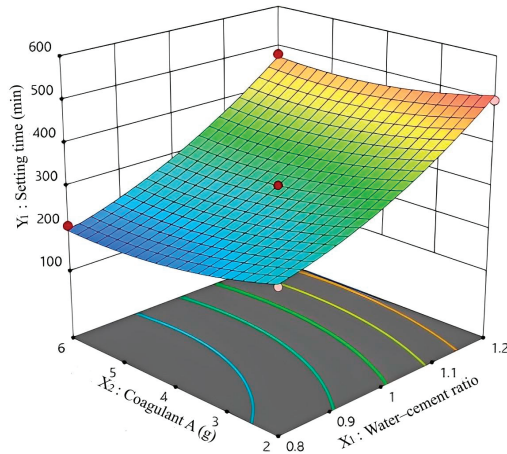
Data Sources	Degrees of Freedom	Setting Time		Water Secretion Rate		Compressive Strength	
		F	P	F	P	F	P
Model	14	30.8	<0.0001	37.27	<0.0001	268.78	<0.0001
X <sub>1</sub>	1	335.88	<0.0001	458.67	<0.0001	3353.07	<0.0001
X <sub>2</sub>	1	13.64	0.0006	0.2022	0.6598	292	<0.0001
X <sub>3</sub>	1	0.8743	<0.0001	5.18	0.0003	34.18	<0.0001
X <sub>4</sub>	1	66.94	0.2875	23.64	0.0390	0.0119	0.9146
X <sub>1</sub> X <sub>2</sub>	1	7.95	0.0155	0.0379	0.8484	15.72	0.0019
X <sub>1</sub> X <sub>3</sub>	1	5.44	0.0378	11.28	0.0047	13.31	0.0033
X <sub>1</sub> X <sub>4</sub>	1	0.0066	0.9366	6.05	0.0324	1.05	0.3254
X <sub>2</sub> X <sub>3</sub>	1	6.38	0.0281	1.47	0.2856	5.26	0.0407
X <sub>2</sub> X <sub>4</sub>	1	3.95	0.0755	0.0976	0.7593	1.12	0.3102
X <sub>3</sub> X <sub>4</sub>	1	0.0262	0.8737	8.93	0.0245	0.0029	0.9577
X <sub>1</sub> <sup>2</sup>	1	8.44	0.0115	19.55	0.0006	65.68	<0.0001
X <sub>2</sub> <sup>2</sup>	1	3.32	0.0899	0.0517	0.8235	2.32	0.1496
X <sub>3</sub> <sup>2</sup>	1	6.71	0.0448	0.0385	0.8472	1.35	0.2641
X <sub>4</sub> <sup>2</sup>	1	1.33	0.2688	0.0309	0.8631	0.4195	0.5277
Lack of Fit	10	1	0.5464	9.77	0.0732	11.04	0.0865
		$R^2 = 0.9777$		$R^2 = 0.9739$		$R^2 = 0.9963$	
		$R_{adj}^2 = 0.9533$		$R_{adj}^2 = 0.9477$		$R_{adj}^2 = 0.9926$	
		CV% = 6.05		CV% = 9.43		CV% = 2.35	

### 3.2.3. Analysis of Response Surface

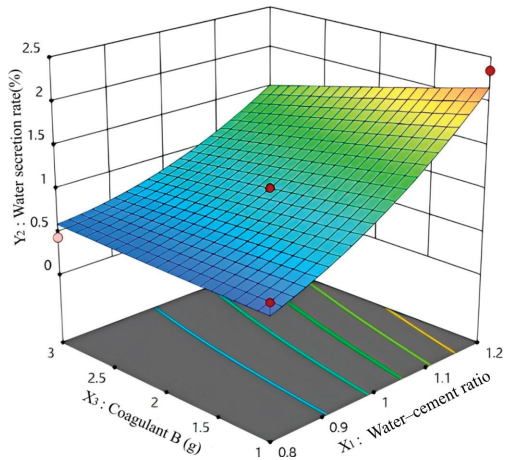
RSM is a statistical experimental design used to establish a continuous variable surface model, evaluate the influencing factors and their interactions of an indicator, determine the optimal level range, and require a relatively small number of experimental groups, which can save manpower and resources [36,37]. Therefore, this method has been successfully and widely applied. The significant terms ( $P < 0.05$ ) were used to propose models for each response, without damaging the model hierarchy. These models were then tested



for adequacy and fitness by analysis of variance (ANOVA). The response surface plots were generated to visualize the combined effect of two variables on a particular response. Three-dimensional diagrams based on two independent variables were constructed, as shown in Figures 5–7 to investigate the effects of the water–cement ratio, coagulant A, coagulant B, and suspending agent interaction on setting time, water secretion rate, and concretion compressive strength of the RW material.



**Figure 5.** Factor interactions on slurry setting time.

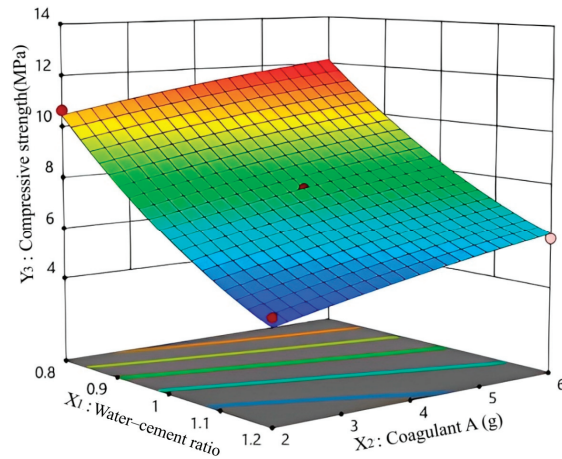


**Figure 6.** Factor interaction on slurry water secretion rate.

(1) Effect of interaction factors on setting time

The model ANOVA results in Table 4 show that the correlation coefficients  $R^2 = 0.9777$  and  $R_{adj}^2 = 0.9533$  are close to 1, indicating a strong correlation between actual and prediction. The coefficient of variation  $CV = 6.05\%$  ( $<10\%$ ) indicates that the model has a high level of confidence, explaining 97.77% of the variation in response values, and only 2.23% of the total variation could not be used in the model explanation, making the model an appropriate choice.  $X_1$  ( $P < 0.0001$ ),  $X_2$  ( $P = 0.0006$ ), and  $X_3$  ( $P < 0.0001$ ) are highly significant.  $X_1X_2$ ,  $X_1X_3$ ,  $X_2X_3$ ,  $X_1^2$ ,  $X_3^2$ , and  $X_4^2$  are significant. The degree of influence of the primary factors on the setting time ( $Y_1$ ) is  $X_1 > X_4 > X_2 > X_3$ , indicating that the water–cement ratio has the greatest influence on the setting time. The degree of influence

of interaction on the condensation time is  $X_1X_2 > X_2X_3 > X_1X_3 > X_2X_4 > X_3X_4 > X_1X_4$ , thus indicating that the interaction effect of the water–cement ratio and coagulant A on setting time is the most significant.



**Figure 7.** Factor interactions on compressive strength.

Figure 5 shows that the setting time of the RW material decreases with the increase in coagulant A when the water–cement ratio is a fixed value. When the amount of coagulant A is fixed, the setting time of the RW material is significantly prolonged with the increase in the water–cement ratio. Compared with changing coagulant A, increasing the water–cement ratio has a more significant effect on setting time. The main reason for this condition is that when the coagulant A is fixed, in the case of low water–cement ratio, the spacing of cement clinker particles in the slurry after mixing is smaller, and more cement clinker particles are present in the unit volume. Therefore, the hydration reaction of slurry per unit volume and unit time is slower, and the number of hydration products is less, thereby resulting in a longer time needed for the hydration products to lap and penetrate, and the slower formation of the skeleton structure, resulting in a longer setting time.

## (2) Effect of interacting factors on water secretion rate

The results of the response surface ANOVA in Table 4 ( $P < 0.0001$ ,  $F = 37.27$ ) show a significant relationship between  $Y_2$  and interacting factors. The lack of fit is not significant ( $F = 9.77$ ,  $P = 0.0732$ ), indicating that the regression model was a good fit. The coefficient of determination  $R^2 = 0.9739$  suggests a strong correlation between the actual and predicted values. Furthermore, the coefficient of variation  $CV = 9.43\%$  ( $< 10\%$ ) is reasonable and the model can explain 97.39% of the variation in response values, thereby implying that the model is chosen appropriately. The effect of  $X_1$  ( $P < 0.0001$ ),  $X_3$  ( $P = 0.0003$ ), and  $X_1X_3$  ( $P = 0.0047$ ) on  $Y_2$  is highly significant. The effect of  $X_4$ ,  $X_1X_4$ , and  $X_3X_4$  on water secretion rate is significant. The degree of influence of the primary term on the urinary rate is  $X_1 > X_4 > X_3 > X_2$ , indicating that the water–cement ratio has the greatest effect on the water secretion rate. The degree of influence of the secondary term on the water secretion rate is  $X_1X_3 > X_3X_4 > X_1X_4 > X_2X_3 > X_2X_4 > X_1X_2$ , indicating that the interaction of  $X_1$  and  $X_2$  had the greatest influence on the water secretion rate.

As can be seen from Figure 6, when the water–cement ratio is a fixed value, the water secretion rate with the increase in coagulant B is fixed. When the amount of coagulant B is fixed, the water secretion rate increases significantly with the increase in the water–cement ratio, especially in the case of coagulant dosage is 1 g, and the degree of increase in the water secretion rate is greater. This condition occurred mainly because coagulant B is unchanged and has a low water–cement ratio. Moreover, uniform slurry cement clinker particles in

the spacing are smaller, with more cement clinker particles per unit volume. In the unit time per unit volume of slurry hydration reaction is faster, hydration products between the rapid formation of a skeletal structure, locking the water to reduce the amount of free water, thus reducing the water secretion rate. Similarly, a large water–cement ratio corresponds to fewer cement clinker particles per unit volume. As a result, hydration products lap require a longer time, and the formation of the skeleton structure is slower. Moreover, a large volume of free water is present in the slurry system, leading to an increase in water secretion rate. Coagulant B has an inhibitory effect on the slurry water secretion rate by accelerating the formation of the skeleton structure, thereby shortening the slurry setting time, which, in turn, reduces the free water content in the slurry system to reduce the water secretion rate.

### (3) Effect of interaction factors on compressive strength

The ANOVA results in Table 4 show that the correlation coefficient  $R^2 = 0.9963$  and  $R_{adj}^2 = 0.9926$  are close to 1 in the response surface model, indicating that the designed model has rationality and consistency. Moreover,  $F = 268.71$ ,  $P < 0.0001$ , and the coefficient of variation  $CV = 2.35\%$  ( $<10\%$ ), indicating that this response surface model has a significant effect on the experimental results and can explain 99.63% of the variation in response values. Thus, the model is appropriately selected.  $X_1$ ,  $X_2$ ,  $X_3$ ,  $X_1X_2$ , and  $X_1X_3$  are highly significant for the compressive strength ( $Y_2$ ), and  $X_2X_3$  is significant for the compressive strength. The degree of influence of the primary term on the compressive strength is  $X_1 > X_2 > X_3 > X_4$ , indicating that the water–cement ratio has the greatest effect on the compressive strength. The degree of influence of the quadratic term on the compressive strength is  $X_1X_2 > X_1X_3 > X_2X_3 > X_2X_4 > X_1X_4 > X_3X_4$ , indicating that the interaction of the water–cement ratio and coagulant A has the greatest effect on the compressive strength.

Figure 7 shows that for a fixed water–cement ratio, the compressive strength increases with increasing coagulant A. For a constant volume of coagulants, the compressive strength decreases with the increase in water–cement ratio mainly because in slurries, the amount of water that can react chemically with the cement component is limited. When the water–cement ratio is high, the slurry has excess water, although the slurry can retain the excess water after setting to prevent water secretion. However, with the increase in time, the excess water will cause the solidified body microstructure to have more voids and be less dense, thus reducing compressive strength. The hydration products of coagulant A are mainly calcium sulfoaluminate hydrates, hydrated calcium silicate gel, calcium hydroxide crystals, and aluminum gel. Thus, the amount of AFt produced by the hydration reaction in the slurry is higher than that produced in the ordinary silicate slurry. As a result, the grouted consolidation is less porous and denser, thus having improved strength.

Table 4 and Figures 5–7 show that increasing the water–cement ratio can increase the setting time and the water secretion rate of the RW material, but weaken the compressive strength of the solids. The  $X_1X_2$  interaction has the greatest effect on the setting time and compressive strength of the RW material. The  $X_1X_3$  interaction has the greatest effect on the water secretion rate of the grouting material.

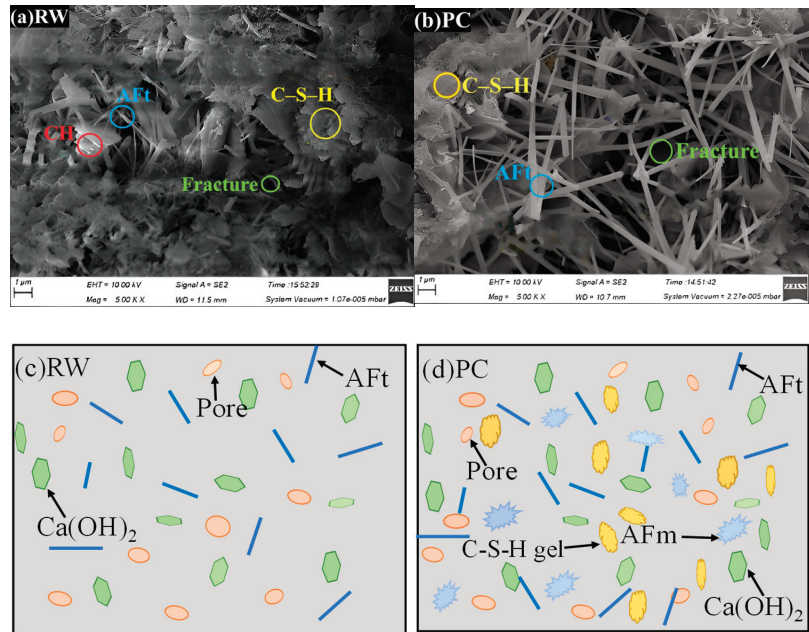
## 4. Microscopic Interface Analysis of Slurry–Coal Solids

### 4.1. Microscopic Morphology Analysis of Grouting Materials

SEM can visually and accurately predict the three-dimensional structure of the surface of the sample under test [38]. In the present research, the microstructural characteristics of the concretion after grouting of broken coal samples are investigated using SEM, as shown in Figure 8.

The figure depicts that the grouting materials contain needle-like AFt, six-sheeted CH crystals, and C-S-H gels, which are interweaved to form a spatial network-like structure. The density of the RW material is higher, as shown in Figure 8a, because the coagulant added to the RW material can increase the number of needle-like AFt in the hydration products and fill the pore structure of the cementitious material. The hydration products form a skeleton structure between them, and the generated hydrated C-S-H gel overlaps to form

a relatively dense network structure, thus causing the slurry to settle quickly, increasing the structural densification, and improving the strength of the solid. The microstructure in Figure 8b shows that the AFt crystals of PC material are loosely connected, and the resulting network structure has larger fractures, resulting in higher permeability compared with the RW.

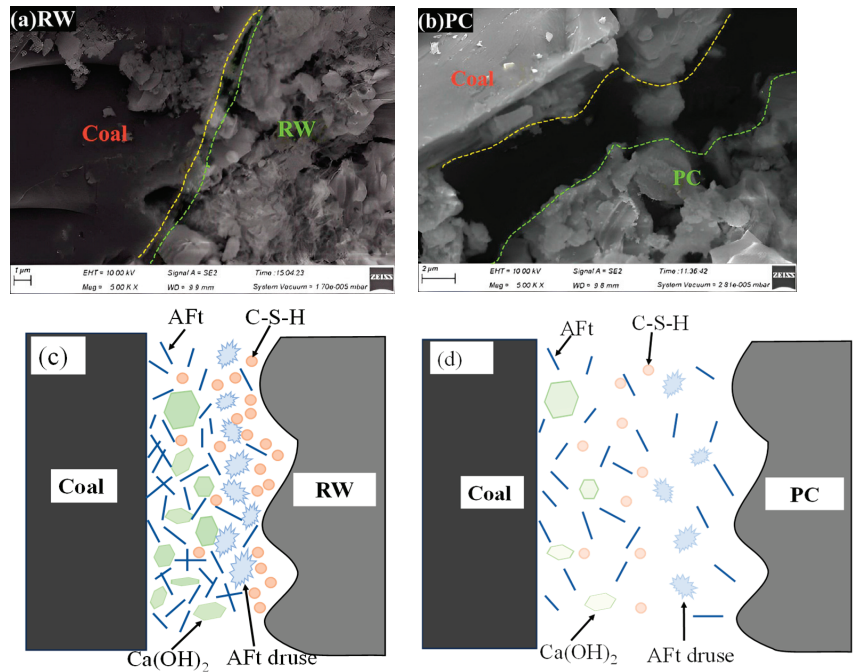


**Figure 8.** Hydration products of different grouting materials. (a) microstructure of RW material, (b) microstructure of PC material, (c) schematic diagram of the microscopic hydration process of RW material, (d) schematic diagram of the microscopic hydration process of PC material.

#### 4.2. Microscopic Morphology Analysis of Slurry–Coal Solids

The interfacial transition zone (ITZ) is an important component of the concretion, characterized by low strength and low modulus of elasticity, which affects compressive strength and permeability [39,40]. The transition zone at the grouting materials and injected coal interface exhibits differences because of the difference in the PC and RW grouting materials. In this study, we investigated the microscopic morphology of the slurry–coal transition zone in different concretes. The SEM results are presented in Figure 9.

As shown in Figure 9a,b, the fracture at the interface of the grouting materials and injected coal of the RW material is smaller than that of the PC material at 5000× magnification, indicating that the bonding between the RW material and the coal is better. This condition can be attributed to the presence of a high concentration of hydration products filled within the RW material and the coal. These products interweave to form a compact network structure that can endure some stress and absorb energy when subjected to an external load. As a result, the strength of the ITZ of the RW material is improved. In contrast, the ITZ of the PC has fewer hydration products, resulting in a looser skeletal structure and insufficient bonding strength, and is, thus, prone to misalignment and separation under external loading.



**Figure 9.** ITZ microstructure of different concrete samples. (a) microscopic morphology of the slurry—coal transition zone of RW material, (b) microscopic morphology of the slurry—coal transition zone of PC material, (c) schematic diagram of hydration process in slurry—coal transition zone of RW material, (d) schematic diagram of hydration process in slurry—coal transition zone of PC material.

Figure 9c,d present the microscopic cementation model of the RW and PC materials. Ordinary cement has a low hydration degree, which later leads to shrinkage boreholes. As a result, short columnar AFt and CH gel hydration products are formed. The  $C_4A_3S'$  minerals supplied by the coagulants experience additional hydration with the mineral particles in the cement, forming fine-needle AFt. The increased number of crystals results in the densification of pores within the pristine cement particles. The microscopic properties of the RW grouting materials have a significant effect on their macroscopic mechanical properties. This effect is due to the rapid early-stage hydration of the  $C_3A$ ,  $C_3S$ , and  $C_2S$  minerals in cement, forming the C-S-H gel and CH crystals, and the reaction of the  $C_4A_3S'$  minerals with calcium sulfate to form AFt and CH gels, accelerating the early hydration rate. The hydration products, AFt crystals, C-S-H gels, and lamellar CH crystals interact with each other. The particles depend on van der Waals forces and chemical bonding to provide cured paste properties, including microexpansion and mechanical strength.

## 5. Conclusions

(1) The effect of different coagulant additives on the RW material was investigated using one-factor analysis. The experimental results demonstrate that coagulants A and B exhibit strong hydration-promoting abilities, which significantly shorten the setting time of the RW material. When the coagulants A is 4 g and coagulants B is 2 g, the setting time of RW material reduced by 60.85% and 50.62%, respectively. Therefore, coagulants A and B were selected for the compounding process and, then, supplemented with suspending agents to study the coagulant modification of the RW material. The water–cement ratio and setting time should be strictly controlled when adding the coagulant additives to avoid affecting the engineering practice effect.

(2) The RSM was used to investigate the effect of each factor on the setting time, water secretion rate, and compressive strength of the RW material. A quadratic regression response model was fitted to indicate the influence of the interaction of each factor. The ANOVA results demonstrated that all models were statistically significant with  $P$  values less than 0.0001 and the model precision was high, effectively reflecting the degree of influence. All the correlation coefficients  $R^2$  of each response model were greater than 0.97 through variance analysis, indicating a high correlation between the actual and prediction results. The water–cement ratio had the most significant effect among all factors on setting time, water secretion rate, and compressive strength of the RW material. Coagulant B and water–cement ratio interaction had the second-greatest effect.

(3) The microstructure of the RW and PC materials was analyzed by SEM. The SEM microstructure of the coagulant-doped RW material showed an increase in the number of needle-like AFt crystals, which filled the internal pore structure of the material, and a cross-linked skeletal structure was formed between the hydration products, which was denser than the network structure of the PC material. The slurry–coal interface of the RW had no fractures, which showed that its sealing effect was superior to that of the PC grouting material.

**Author Contributions:** X.L.: conceptualization and investigation. G.H.: funding and software. Y.W.: investigation and writing—original draft. J.X.: conceptualization, methodology, and funding. J.D.: data curation and supervision. B.Y.: investigation and validation. M.Z.: investigation and methodology. T.L.: writing—review. B.L.: editing, funding and supervision. All authors have read and agreed to the published version of the manuscript.

**Funding:** The authors sincerely thank the following agents for their financial supports: the National Natural Science Foundation of China (grant no. 52274190), the Sponsored by Program for Science & Technology Innovation Talents in Universities of Henan Province (no. 23HASTIT008), and the Henan Provincial Science and Technology Research Project (no. 222102320086).

**Data Availability Statement:** The data applied to support the results in this study are available from the corresponding author upon request.

**Conflicts of Interest:** The authors declare no conflict of interest.

## References

- Asif, M.; Wang, L.; Wang, R.; Wang, H.; Hazlett, R. Mechanisms in CO<sub>2</sub>-enhanced coalbed methane recovery process. *Adv. Geo-Energy Res.* **2022**, *6*, 531–534. [CrossRef]
- Andrews-Speed, P.; Xu, X.; Jie, D.; Chen, S.; Zia, M. Deficiencies in China’s innovation systems for coal-bed methane development: Comparison with the USA. *J. Sci. Technol. Policy Manag.* **2023**, *14*, 511–528. [CrossRef]
- Wu, A.; Ruan, Z.; Raimund, B.; Yin, S.; Wang, J.; Wang, Y. Optimization of flocculation and settling parameters of tailings slurry by response surface methodology ology. *Miner. Eng.* **2020**, *156*, 106488. [CrossRef]
- Gao, Q.; Yang, X.; Wen, Z.; Chen, D.; He, J. Optimization of proportioning of mixed aggregate filling slurry based on BBD response surface methodology. *J. Hunan Univ. Nat. Sci.* **2019**, *46*, 6.
- Wang, H.; Fan, C.; Li, J.; Wu, Y.; Xing, S.; Wang, W. A Field Study of Coal Fire Areas Re-Burning Behavior Assessment and Related Carbon Emissions. *Fire* **2022**, *5*, 186. [CrossRef]
- Bosikov, I.; Martyushev, N.; Klyuev, R.; Savchenko, I.; Kukartsev, V.; Tynchenko, Y. Modeling and complex analysis of the topology parameters of ventilation networks when ensuring fire safety while developing coal and gas deposits. *Fire* **2023**, *6*, 95. [CrossRef]
- Silva, D.; Nuzzo, I.; Nigro, E.; Occhiuzzi, A. Intumescent coatings for fire resistance of steel structures: Current approaches for qualification and design. *Coatings* **2022**, *12*, 696. [CrossRef]
- Zhang, J.; Li, G.; Meng, Z.; Zhang, Y.; Liu, L.; Li, D.; Xu, Y. Key technology of surface extraction for coalbed methane wells crossing goaf. *J. China Coal Soc.* **2020**, *45*, 2552–2561.
- Joshi, D.; Prajapati, P.; Sharma, P.; Sharma, A. Past, present and future of coal bed methane (CBM): A review with special focus on the Indian scenario. *Int. J. Coal Prep. Util.* **2023**, *43*, 377–402. [CrossRef]
- Zhu, C.; Zhang, J.; Li, M.; He, Z.; Wang, Y.; Lan, Y. Effect mechanism of strata breakage evolution on stope deformation in extra-thick coal seams. *Alex. Eng. J.* **2022**, *61*, 6. [CrossRef]
- Kedzior, S.; Teper, L. Coal Properties and Coalbed Methane Potential in the Southern Part of the Upper Silesian Coal Basin, Poland. *Energies* **2023**, *16*, 3219. [CrossRef]
- Wang, H.; Li, B.; Wang, Y.; Li, S.; Zhang, G.; Yang, D. Key technology and bottlenecks of multi-energy complementary DC microgrid for residual coalbed methane in abandoned mine. *J. China Coal Soc.* **2023**, *48*, 1798–1813.

13. Jia, Q.; Liu, D.; Cai, Y. Research progress on wells interference in coalbed methane mining. *J. China Coal Soc.* **2020**, *45*, 882–893.
14. Wang, Z.; Zhou, Y.; Sun, Y.; Wang, Y. Novel gas extraction borehole grouting sealing method and sealing mechanism. *J. China Coal Soc.* **2015**, *40*, 588–595.
15. Zhang, J.; Liu, Y.; Ren, P. A fully multifield coupling model of gas extraction and air leakage for in-seam borehole. *Energy Rep.* **2021**, *7*, 1293–1305. [CrossRef]
16. Wang, H.; Wang, E.; Li, Z.; Wang, X.; Zhang, Q.; Li, B. Ali Muhammad. Study on sealing effect of pre-drainage gas borehole in coal seam based on air-gas mixed flow coupling model. *Process Saf. Environ. Prot.* **2020**, *136*, 15–27. [CrossRef]
17. Si, L.; Shi, W.; Wei, J.; Liui, Y.; Yao, B. Self-healing characteristics of fracture in sealing materials based on self-healing effect. *J. China Coal Soc.* **2023**, 1–14. [CrossRef]
18. Xia, T.; Zhou, F.; Liu, J.; Hu, S.; Liu, Y. A fully coupled coal deformation and compositional flow model for the control of the pre-mining coal seam gas extraction. *Int. J. Rock Mech. Min. Sci.* **2014**, *72*, 138–148. [CrossRef]
19. Chen, X.; Zhou, T.; Zhou, J.; Ma, L.; Liu, Q.; Xu, X. Study on the flame retardant property of reactive halogen-free organic grouting reinforcement materials for coal mines. *Min. Saf. Environ. Prot.* **2023**, *50*, 40–45.
20. Sun, W.; Guo, B.; Zhang, R. Effect of hydroxide properties of new material for sealing gas drainage boreholes. *China Saf. Sci. J.* **2016**, *26*, 98–102.
21. Zhao, Y.; Sun, Y.; Wang, Z. Mixed volume of aluminous cement affected to grouting material performances of borehole sealing for gas drainage. *Coal Sci. Technol.* **2018**, *46*, 146–152.
22. Liu, J.; Luo, Q.; Ji, X.; Wu, F.; Ma, M.; Zhang, C.; Wang, Q. Study on preparation and performance of an early strength grouting materials. *J. Saf. Sci. Technol.* **2018**, *14*, 95–99.
23. Qian, Z.; Han, B. Experimental study on water absorption performance of super absorbent resin in sealing and grouting process of gas drainage borehole. *Saf. Coal Mines* **2020**, *51*, 32–36.
24. Guan, X.; Li, X.; Zhang, H.; Yang, Z.; Li, H.; Di, H.; Zhang, L. Research and application of inorganic composite grouting reinforcement materials in deep weak rock. *Coal Sci. Technol.* **2023**, *51*, 1–11.
25. Liu, J.; Feng, H.; Zhang, Y.; Zheng, K. Performance Investigation of Geopolymer Grouting Material with Varied Mix Proportions. *Sustainability* **2022**, *14*, 13046. [CrossRef]
26. Zhang, J.; Wang, X.; Jin, B.; Zhang, X.; Li, Z.; Guan, X. Effect of superplasticizers on hydration kinetics of ultrafine sulfoaluminate cement-based grouting material. *Thermochim. Acta* **2021**, *703*, 178988. [CrossRef]
27. Ruan, W.; Zhang, Z.; Cai, M.; She, Y.; Liu, J.; Guo, W.; Ma, X.; Liao, J.; He, X. Comparative study of the effects of magnesium aluminum silicate and bentonite clay on the properties of magnesium phosphate cement-based grouting material. *Constr. Build. Mater.* **2023**, *401*, 132852. [CrossRef]
28. Choudhury, S.; Jena, T. Influence of surfactant on foam generation and stabilization in cement slurry. *Mater. Today Proc.* **2023**. [CrossRef]
29. Mahmood, W.; Mohammed, A.; Asteris, P.; Kurda, R.; Armaghani, D. Modeling flexural and compressive strengths behaviour of cement-grouted sands modified with water reducer polymer. *Appl. Sci.* **2022**, *12*, 1016. [CrossRef]
30. Pereira, L.; Milan, T.; Tapia-Blácido, D. Using Response Surface Methodology (RSM) to optimize 2G bioethanol production: A review. *Biomass Bioenergy* **2021**, *151*, 106166. [CrossRef]
31. Liu, Y.; Zhao, C.; Li, G.; Zhao, X.; Li, Z.; Zhang, X.; Li, Y.; Guo, J.; Guo, D. Optimized decision method of coordinated development mode of coal and coalbed methane in Jincheng mining area. *J. China Coal Soc.* **2020**, *45*, 2575–2589.
32. Liang, W.; Zhang, B.; He, W.; Yao, H. Experimental research on supercritical CO<sub>2</sub> enhanced coalbed methane recovery in different rank coals. *J. China Coal Soc.* **2020**, *45*, 197–203.
33. Zhang, J.; Liu, L.; Li, Q.; Peng, W.; Zhang, F.; Cao, J.; Wang, H. Development of cement-based self-stress composite grouting material for reinforcing rock mass and engineering application. *Constr. Build. Mater.* **2019**, *201*, 314–327. [CrossRef]
34. Zhang, Y.; Wang, Y.; Wu, Z.; Lu, Y.; Kang, A.; Xiao, P. Optimal design of geopolymer grouting material for semi-flexible pavement based on response surface methodology. *Constr. Build. Mater.* **2021**, *306*, 124779. [CrossRef]
35. Petruniak, M.; Rubel, V.; Chevhanova, V.; Kulakova, S. Application of grout slurries with the defecate addition for effective well cementing. *Min. Miner. Depos.* **2021**, *15*, 59–65. [CrossRef]
36. Liu, W.; Sun, Y.; Meng, X.; Qin, Y. Experimental analysis of Nano-SiO<sub>2</sub> modified waterborne epoxy resin on the properties and microstructure of cement-based grouting materials. *Energy* **2023**, *268*, 126669. [CrossRef]
37. Liu, J.; Li, X.; He, T. Application status and prospect of backfill mining in Chinese coal mines. *J. China Coal Soc.* **2020**, *45*, 141–150.
38. Behnia, B.; AaliAnvari, A.; Nazari, M. A study to examine the effect of grouting superfine cement slurry containing nano-silica additives by a simulator cylinder in environments with many joints and gaps. *Arab. J. Geosci.* **2021**, *14*, 1–15. [CrossRef]
39. Wei, Z.; Yang, K.; He, X.; Zhang, J.; Hu, G. Experimental study on the optimization of coal-based solid waste filling slurry ratio based on the response surface methodology. *Materials* **2022**, *15*, 5318. [CrossRef] [PubMed]
40. Basu, P.; Thomas, B.S.; Gupta, R.C.; Vinay, A. Properties of sustainable self-compacting concrete incorporating discarded sandstone slurry. *J. Clean. Prod.* **2021**, *281*, 125313. [CrossRef]

**Disclaimer/Publisher's Note:** The statements, opinions and data contained in all publications are solely those of the individual author(s) and contributor(s) and not of MDPI and/or the editor(s). MDPI and/or the editor(s) disclaim responsibility for any injury to people or property resulting from any ideas, methods, instructions or products referred to in the content.

## Article

# Research on the Positioning Accuracy of the Cutting Head of a Tunneling Machine Based on Ultra-Wideband Positioning Technology

Haiyan Ma <sup>\*</sup>, Hongkai Zhang, Kunlin Yang, Yingjie Hu, Zeyu Yang and Nianjie Ma

School of Energy and Mining Engineering, China University of Mining and Technology (Beijing), Beijing 100083, China

<sup>\*</sup> Correspondence: haiyanma232@163.com

**Abstract:** Directed at the problems of low positioning accuracy and irregular section forming of cutting heads of road header in coal mine production sites, a new cutting head positioning system based on ultra-wideband positioning technology is proposed based on the cutting head motion model and the working principle of ultra-wideband positioning technology, which verifies the anti-interference and the accuracy of its positioning. Combined with the simulation experiment under on-site working conditions, the influence degree of three typical influencing factors on positioning accuracy was obtained, and the accuracy optimization of the ultra-wideband positioning system was guided. Through the dynamic solution experiment, the positioning accuracy of the system is measured, and the results are verified based on the positioning system solution accuracy evaluation standard.

**Keywords:** ultra-wideband positioning; cutting head of roadheader; positioning accuracy; distance measurement

## 1. Introduction

The unmanned and intelligent coal production site is the main trend of the development of the current coal industry. In order to meet the needs of safe and efficient production on the coal mine site and improve the efficiency of mining replacement, the tunneling equipment is gradually transitioning to intelligence and automation [1–4]. At present, the cantilever roadheader has become the most widely used tunneling equipment in coal mines because of its strong universality, high tunneling efficiency, and advanced section control precision. Limited by the special working conditions of the coal mine site, the mining cantilever roadheader will be affected by factors such as occlusion, dust concentration, ranging spatial position, and so on when carrying out the cutting operation. Even most of the tunneling face needs manual observation and operation to complete the tunneling process, resulting in the decrease in the positioning accuracy of the cutting head, which directly affects the tunneling efficiency of the roadheader, and causes a series of problems, such as irregular formation of local roadway section [5–9].

With the actual production needs, domestic and foreign experts and scholars have conducted extensive research on the application of positioning technology of mining cantilever roadheader and adopted a variety of technical routes to achieve accurate positioning of the cutting head. Zhang M et al. [10] designed a positioning decision program by using a fuzzy decision controller, fuzzy logic controller, and dynamic error elimination controller. The mathematical model was established by the functional relationship between the pitch angle and the hydraulic cylinder. The experimental test of the decision program effectively improved the positioning accuracy. Cheluska P et al. [11] used visual ranging technology to realize the positioning of the cutting head, analyzed the positional relationship between the roadheader base and the cutting head, established the measurement model, and calculated the positional relationship between the base datum and the cutting head. Du et al. [12]

**Citation:** Ma, H.; Zhang, H.; Yang, K.; Hu, Y.; Yang, Z.; Ma, N. Research on the Positioning Accuracy of the Cutting Head of a Tunneling Machine Based on Ultra-Wideband Positioning Technology. *Processes* **2023**, *11*, 2534. <https://doi.org/10.3390/pr11092534>

Academic Editors: Feng Du, Aitao Zhou and Bo Li

Received: 25 July 2023

Revised: 14 August 2023

Accepted: 16 August 2023

Published: 24 August 2023



**Copyright:** © 2023 by the authors. Licensee MDPI, Basel, Switzerland. This article is an open access article distributed under the terms and conditions of the Creative Commons Attribution (CC BY) license (<https://creativecommons.org/licenses/by/4.0/>).



comprehensively analyzed various positioning methods and believed that machine vision technology is most suitable for the positioning of mine cantilever roadheader and designed a set of real-time monitoring system for the position and posture of the fuselage and the spatial position of the cutting head. Wu Miao et al. [13] proposed a walking trajectory and deviation perception method of cantilever roadheader based on a strapdown inertial navigation system, which can determine the azimuth deviation of roadheader fuselage in real-time and provide correction reference parameters for directional tunneling.

Many experts and scholars have carried out a lot of analysis and research from different angles on automation and intelligent research on the precise positioning of the cutting head of the mining cantilever roadheader, which provides a solid theoretical basis for the precise operation of the roadway excavation automation. However, the current mainstream roadheader positioning technology mainly obtains the pose information of the roadheader fuselage, and then indirectly determines the spatial coordinates of the cutting head through calculation. The indirect positioning method is affected by the roadheader fuselage's vibration and the moving joints' influence, and there is a certain accuracy error. On the other hand, the current cutting head positioning technology is numerous, but the applicability is limited, the underground working environment is relatively poor, and the positioning accuracy of many advanced electronic components on the ground is ideal, but the positioning accuracy in the underground is greatly reduced [14–17]. Through the multi-dimensional comparative analysis of wireless positioning technology, it is found that ultra-wideband positioning technology has outstanding advantages in positioning accuracy, positioning range and anti-interference ability. Based on the motion model of cutting head and the working principle of ultra-wideband positioning technology, this paper proposes a new cutting head positioning system based on ultra-wideband positioning technology, which can realize the direct positioning of cutting head and ensure good positioning accuracy.

## **2. Ultra-WideBand (UWB) Positioning Technology and Simplified Cutting Head Motion Model**

### *2.1. Ultra-WideBand (UWB) Positioning Technology*

Ultra-wideband positioning technology is a new positioning method, which in its early stage, was only used in the military field. Since the end of the last century, with the progressive maturity of its supporting equipment and cost reduction, it has gradually moved to the civilian field, and under the vision of intelligent coal mines, it has been recognized as the priority development and application direction of wireless positioning. Compared with many traditional narrowband communication technologies, UWB technology has many technical advantages, such as high positioning accuracy, strong penetration ability, simple structure, low power consumption, strong anti-interference ability, and low radiation. The characteristics of UWB technology make it suitable for high-resolution wireless positioning.

In this study, the ultra-wideband positioning base station, positioning tag, and its supporting debugging and monitoring software for coal mines provided by ANTEXIN (Beijing) Company were used to carry out related experiments. The integrated ultra-wideband ranging module of the internal circuit board of the equipment was built based on the DW1000 chip. The equipment has IIC intrinsically safe explosion-proof certification after packaging, which is specially designed and applied to coal mines, and is fully applicable to the environment of tunneling working face. The internal circuit board of the equipment integrates DW1000 ultra-wideband positioning chip, which can greatly reduce the application difficulty and cost. Accurate ranging is performed by signal time-of-flight ranging. The indoor positioning accuracy is high, and the dynamic tracking ability of positioning is strong. Strong anti-interference ability.

### *2.2. Simplified Cutting Head of Roadheader Motion Model*

The cutting part of the boom-type roadheader is composed of a cutting head, a cutting arm, multiple sets of hydraulic cylinders, and a cutting motor. In the cutting operation of



normal operation of the equipment. Three ultra-wideband positioning tags are arranged in this plane, and the positioning tags are fixed by the fixed bracket.

The comprehensive arrangement of the simulation experiment is shown in Figure 2.

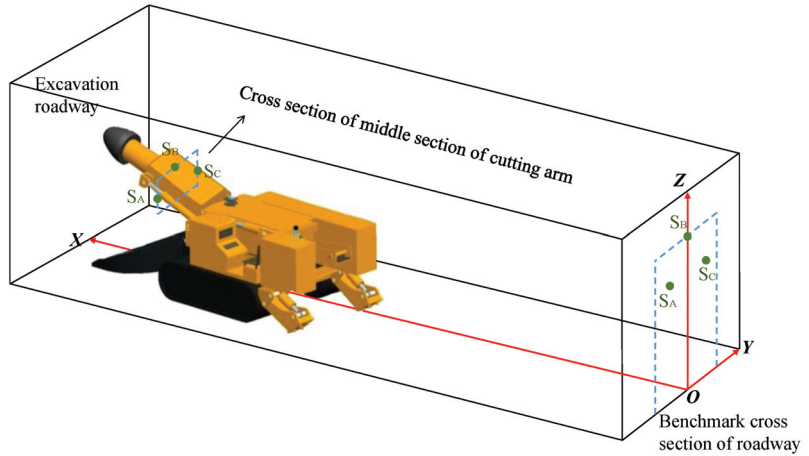


Figure 2. Schematic diagram of cutting head positioning scheme.

The ultra-wideband positioning system of the cutting head is based on sensor wireless ranging technology. By arranging the position-calibrated sensors  $S_A$ ,  $S_B$ , and  $S_C$  on the cross-section of the appropriate position in the middle and rear section of the cutting arm and arranging the position-calibrated sensors  $S_1$ ,  $S_2$ , and  $S_3$  on the cross-section of the roadway reference coordinate system behind the cantilever roadheader, the ranging parameters are obtained. Relying on the system logic solution, according to the distance measurement values of each sensor and sensors  $S_1$ ,  $S_2$ , and  $S_3$  on the middle section of the cutting arm and the spatial coordinates of sensors  $S_1$ ,  $S_2$ , and  $S_3$  in the roadway reference coordinate system, the spatial coordinates of sensors  $S_A$ ,  $S_B$ , and  $S_C$  are obtained, so as to determine the real-time pose of the cutting arm. According to the installation and calibration dimensions of  $S_A$ ,  $S_B$ , and  $S_C$ , the position of the cutting head in the standard coordinate system of the roadway can be solved. The operation process of the positioning system is shown in Figure 3.

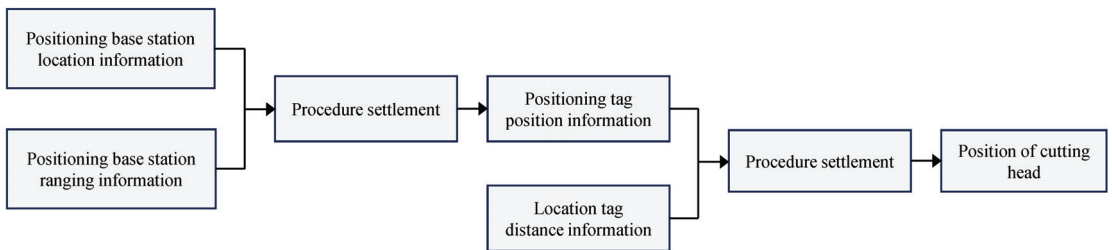


Figure 3. Flow chart of an ultra-wideband positioning system for cutting head.

### 3.2. Components of Positioning System

The simulation experiment platform of the ultra-wideband positioning system of the cutting head is composed of two parts: hardware and software. The hardware part of the platform includes an ultra-wideband positioning base station circuit board and supporting transceiver antenna 3 sets; antenna 3 sets; three ultra-wideband positioning tags; one gigabit five-port switch, one mine laser pointer, and one portable server; several groups of simulated brackets and fixed plates; several bundles of wire used to connect the

equipment; several sets of power supply and power lines for equipment power supply. The software part mainly includes wireless positioning base station configuration tool software, debugging tool software, and MATLAB cutting head 3D coordinate calculation program, which work together to achieve the data and experimental objectives required for the simulation experimental platform. The hardware components of the platform can meet the various needs of the simulation experiment and comply with the technical requirements and safety standards of the simulation experiment. The related experimental device is shown in Figure 4.

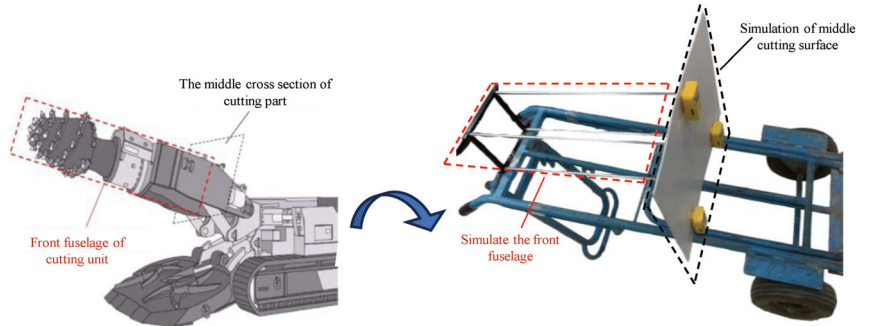


Figure 4. Schematic diagram of the overall experimental setup.

The ultra-wideband positioning base station is installed on the reference cross-section of the roadway behind the underground heading face, and the calibration laser pointer is also installed at this position. The base station is arranged in a triangular array, and the position and orientation of the phase center of the three transceivers are consistent and in the same plane. In the simulation experiment, the installation layout and size of the ultra-wideband positioning base station in the actual working condition are simulated on the reference plane of the simulated positioning base station, and the installation layout size is consistent with the actual situation. The layout size is shown in Figure 5.

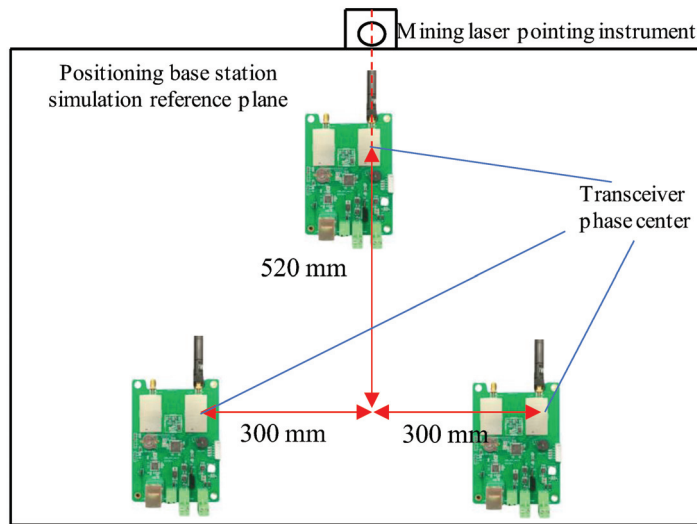
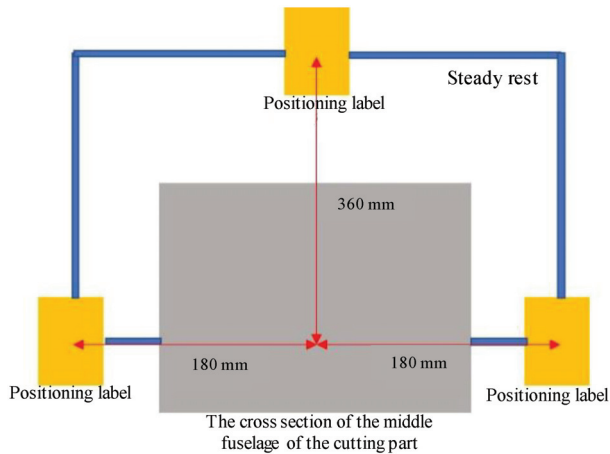


Figure 5. Layout dimension diagram of UWB positioning base stations.

The positioning label completes the position calibration through the fixed bracket according to the size of the cutting part in the actual working condition. In the simulation experiment, the fixed plate is used to complete the position calibration on the cross-section

of the middle section of the simulated cutting part. The accuracy of the positioning solution that needs to be analyzed in the follow-up simulation experiment, so in addition to the positioning base station, the layout and assembly size of each simulated structural component should be consistent with the actual working condition size, and the ratio of the simulated experimental layout size to the actual working condition layout size is set to 1:5. The layout size of the positioning label is shown in Figure 6.



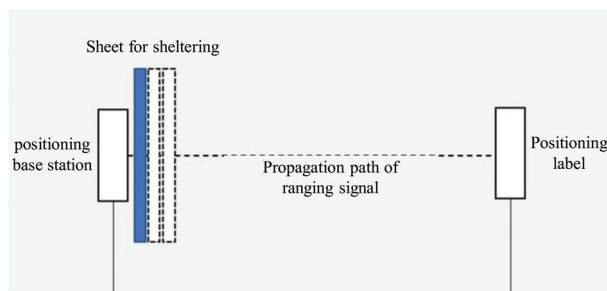
**Figure 6.** Layout dimension diagram of UWB positioning labels.

#### 4. Analysis of Interference Factors of System Positioning Accuracy

##### 4.1. Direct Occlusion Effects

The working environment of the heading face is relatively harsh. When the positioning system is put into field application, each precision component needs to be equipped with an explosion-proof and dust-proof shell, and at least two layers of material will be blocked on the linear propagation path of the ranging module signal. Therefore, based on the simulation experiment platform of the ultra-wideband positioning system of the cutting head, the direct occlusion effect experiment is carried out to analyze the interference of different material shells on the accuracy, and to determine the influence of physical properties such as material type, thickness, and wave transmission on the accuracy. Therefore, it is convenient to select materials with less precision interference to make the shell of the ultra-wideband positioning system equipment, so as to reduce the degree of positioning accuracy interference and ensure the accuracy of the positioning system.

In order to explore the influence of different material shells on the ranging accuracy of the ultra-wideband positioning system, the control variable comparison method was used for experiments. The experimental process is shown in Figure 7.



**Figure 7.** Schematic diagram of the experimental setup for the impact of obstructing objects.

A set of experimental positioning base stations and tags are selected as the experimental subjects. The fixed bracket is used to calibrate the attitude and relative position of the positioning base station and the positioning tag. Three acrylic plates, wood plates, and aluminum plates of similar thickness are prepared to ensure that their area can block the signal propagation path of the ranging module. The experimental plate is shown in Figure 8.

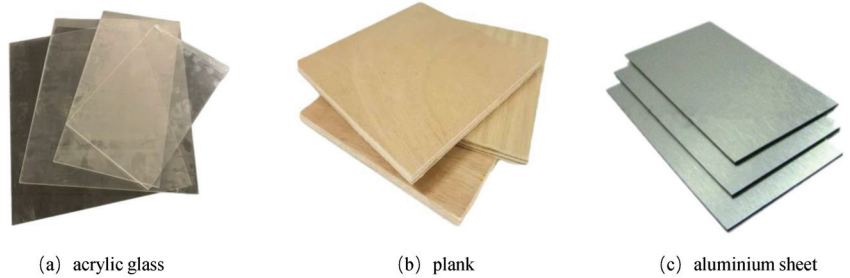


Figure 8. Experimental board.

The positioning base station and positioning tag are placed and fixed in the experimental space, and the posture and relative position of the equipment are calibrated to make the positioning base station and the positioning tag face-to-face. The ranging data are recorded, and the data are read within 30 s. The average value is taken as the ranging reference value, and the spatial position of the positioning base station and the positioning tag is kept unchanged. One to three layers of the same material plates are placed on the signal transmission path between the ranging base station and the ranging tag, and the three columns of ranging values are recorded by reading the reference value. By changing a material plate for three readings of the next set of experiments, a total of three sets of nine-column ranging values are obtained. Comparing the ranging value of each group with the ranging reference value, the trend of error value is shown in Figure 9.

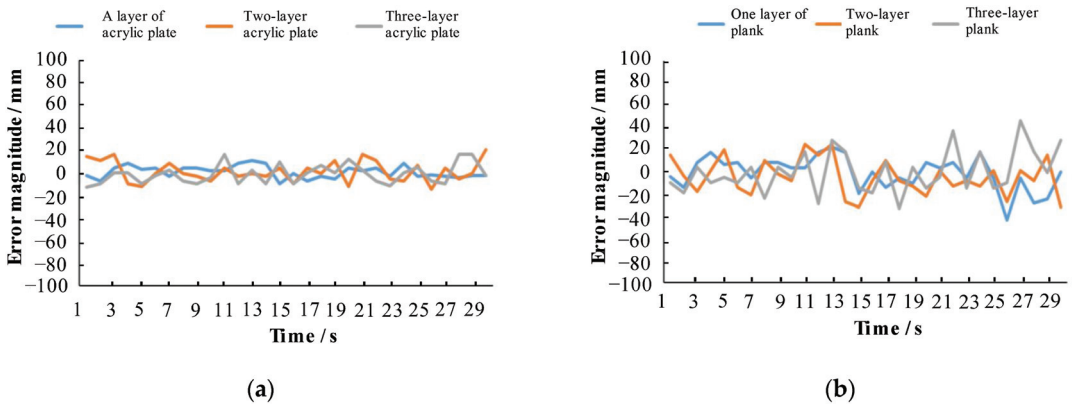


Figure 9. Error-values of obstructing object impact experiment. (a) Error values of acrylic board. (b) Error values of wooden board.

From the above experimental results, it can be seen that the error value of the three experiments of the acrylic plate group is very small, the error fluctuation level is very low, and the ranging error is within 20 mm. The three experimental error values of the board group are also small, the error fluctuation level is low, and the ranging error is always within 50 mm.

The dynamic reading of the aluminum plate experimental group is shown in Figure 10. It can be seen from the figure that when the aluminum plate is blocked in the ranging signal path, the module reading fluctuates dramatically. The ranging value of the aluminum plate group experiment is seriously distorted, and the error is extremely large, up to more than 1000 mm. We have been unable to analyze the error level, and the degree of interference is severe, which seriously affects the normal operation of the ranging module.

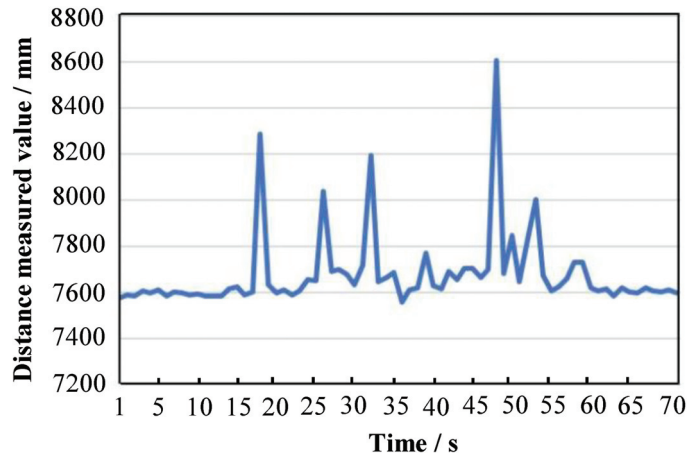


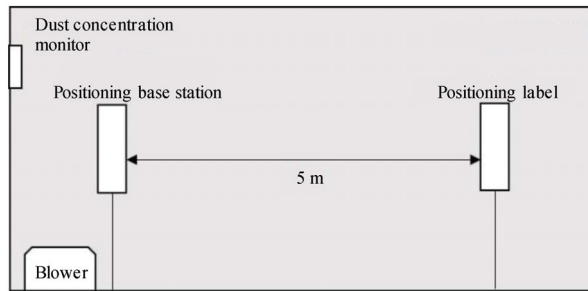
Figure 10. Measured distance values of aluminum plate obstruction experiment.

According to the analysis, the acrylic plate has little effect on the ultra-wideband signal propagation, the wood plate has little effect on the ultra-wideband signal propagation, and the aluminum plate has a serious effect on the ultra-wideband signal propagation. As a narrow pulse signal, the ultra-wideband itself has a strong ability to penetrate the medium. Both the acrylic plate and the wood plate have good wave permeability, and within the conventional thickness, they will not affect the accuracy level required by the system. The poor wave permeability of metal plates, such as aluminum plates, will seriously interfere with the ranging accuracy regardless of the thickness, thus affecting the positioning accuracy of the system. Therefore, plastic materials, such as acrylic, should be preferred for the packaging shell of the positioning system.

#### 4.2. Effect of Dust Concentration

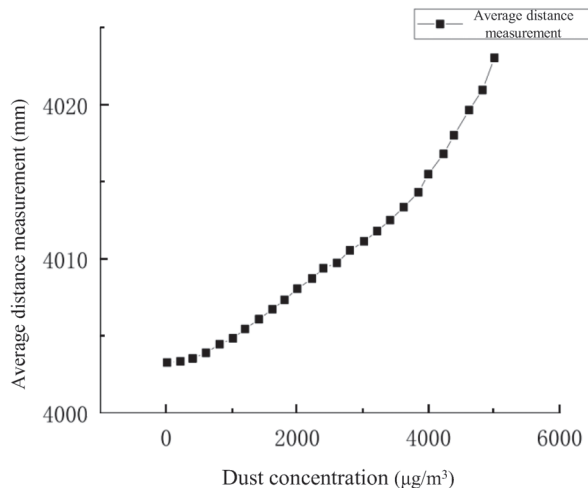
The dust produced in the operation project of coal mine heading face is mainly rock dust and coal dust. Due to the characteristics of the tunneling process, the process of coal rock crushing will produce a large amount of dust, accounting for about 80% [21] of the total number of dust, which is the main source of dust generation. In addition, there is dust generated by the process of coal rock crushing caused by factors such as collapse impact and transshipment friction, as well as secondary dust generated by ventilation operations [22]. The working environment of the positioning scheme designed in this paper is exposed to the influence of serious dust, and the dust concentration is an important factor affecting the accuracy of the system.

In order to explore the influence of dust concentration on the positioning accuracy of ultra-wideband positioning system, a regular cuboid confined space is set up to simulate the change of dust concentration in the local space of coal mine. The experimental environment is shown in Figure 11.



**Figure 11.** Schematic diagram of the experimental setup for the effect of dust concentration.

The allowable limit value of dust concentration in coal mine operations is  $5000 \mu\text{g}/\text{m}^3$ . Generally, the dust concentration is between  $1000 \mu\text{g}/\text{m}^3$  and  $3000 \mu\text{g}/\text{m}^3$ . Therefore, the reading gradient of dust concentration in the experiment is increased to  $5000 \mu\text{g}/\text{m}^3$ . To obtain this information one must keep the position of the positioning base station and the positioning label unchanged, control the dust concentration according to the experimental environment, blow into the experimental space with a blower, read and record the dust concentration detector after the indication is stable, read 10 times every 10 s, and take the average value and record. Finally, the change of location and ranging data with the increase in dust concentration is obtained, as shown in Figure 12.



**Figure 12.** System ranging error under different dust concentrations.

The data analysis shows that with the increase in dust concentration, the ranging error of ranging module increases, and the error growth rate increases with the increase in dust concentration. In the limited range of dust concentration in the coal mine excavation workplace, the influence of dust concentration on the ultra-wideband ranging module is small. The common dust concentration in the excavation face is not more than  $3000 \mu\text{g}/\text{m}^3$ . Under this condition, the positioning ranging error of 8 m is less than 11.28 mm. According to the principle of error accumulation of optical path influence, the positioning ranging error at 48 m is less than 67.68 mm, and the error level is low.

Therefore, as long as the dust concentration meets the requirements of safety regulations, the influence of dust concentration on the precision and accuracy of ultra-wideband positioning system can be effectively controlled. In the actual working process of the coal



mine tunneling face, the positioning system has good anti-dust interference performance and can effectively maintain good system positioning accuracy.

#### 4.3. Mutual Interference Effects of Ultra-Wideband Equipment

The ultra-wideband equipment itself has a strong anti-interference ability, and the equipment used in this system has an anti-interference optimization algorithm and a master-slave base station working mode switching function. However, the positioning scheme and positioning performance requirements of the system determine that the system equipment needs to be coordinated [23,24]. An operation is still needed to verify its anti-interference performance through control variable experiments.

Prepare three ultra-wideband positioning base stations and three positioning tags, select one of them, calibrate its relative position, turn it on, and start ranging reading; after 90 s, the remaining two base stations are opened and randomly placed around the calibration base station. After 90 s, the remaining two tags are opened and randomly placed around the calibration tags for ranging reading and storage. The experimental ranging values are shown in Figure 13.

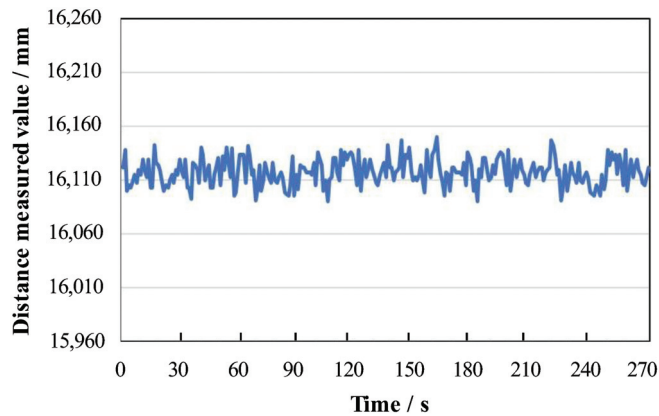


Figure 13. The equipment interference experiment changes the ranging value with time.

The analysis of the above figure shows that the error analysis values of the three groups of data in the three time periods are very different, and the data analysis values of different groups have no cross-order of magnitude difference. The data line chart is smooth, the dynamic characteristics are stable, and the data has no obvious accuracy and precision index difference, indicating that there is no obvious interaction between the system equipment.

## 5. Solution Experiment and Accuracy Evaluation

### 5.1. Positioning System Positioning Accuracy Evaluation Standard

The absolute error and the mean value of the absolute error in the X, Y, and Z axis directions are used as the standard to evaluate the positioning accuracy. The standard deviation of the solution in the X, Y, and Z axis is used as the standard for evaluating the positioning precision.

The calculation formula of the absolute error  $e_{Xai}$ ,  $e_{Yai}$ ,  $e_{Zai}$  is

$$e_{Xai} = |L_{xi} - L_{xt}|, \quad (1)$$

$$e_{Yai} = |L_{yi} - L_{yt}|, \quad (2)$$

$$e_{Zai} = |L_{zi} - L_{zt}|, \quad (3)$$

In the formula:

$(L_{xi}, L_{yi}, L_{zi})$  are the coordinates obtained by the  $i$ -th solution;

$(L_{xt}, L_{yt}, L_{zt})$  are the true coordinates of the point.

To solve the mean absolute error  $\bar{e}_{Xai}, \bar{e}_{Yai}, \bar{e}_{Zai}$ , the calculation formula is

$$\bar{e}_{Xai} = \frac{\sum_{i=1}^n e_{Xai}}{n}, \quad (4)$$

$$\bar{e}_{Yai} = \frac{\sum_{i=1}^n e_{Yai}}{n}, \quad (5)$$

$$\bar{e}_{Zai} = \frac{\sum_{i=1}^n e_{Zai}}{n}, \quad (6)$$

In the formula:

$n$  is the number of system solutions.

The  $SD_X, SD_Y,$  and  $SD_Z$  calculation formulas for the standard deviation of the X, Y, and Z axis are:

$$SD_X = \sqrt{\frac{\sum_{i=1}^n (L_{xi} - \hat{L}_x)^2}{n}}, \quad (7)$$

$$SD_Y = \sqrt{\frac{\sum_{i=1}^n (L_{yi} - \hat{L}_y)^2}{n}}, \quad (8)$$

$$SD_Z = \sqrt{\frac{\sum_{i=1}^n (L_{zi} - \hat{L}_z)^2}{n}}, \quad (9)$$

In the formula:

$(\hat{L}_x, \hat{L}_y, \hat{L}_z)$  is the reference value for the coordinate solution of the point, which is generally the arithmetic average of the solved coordinates for this group of experiments.

Combining the results of the above formulas, the value of the standard deviation of the solved 3D can be obtained:

$$SD_T = \sqrt{SD_X^2 + SD_Y^2 + SD_Z^2} \quad (10)$$

According to the performance requirements of the ultra-wideband positioning system of the cutting head, combined with the three-dimensional positioning principle of the ultra-wideband positioning technology, the system positioning solution deviation should not be greater than 200 mm, and the standard deviation of the settlement data should not be greater than 50 mm.

## 5.2. Dynamic Solution Experiment and Accuracy Evaluation Results

Based on the simulation experiment platform of ultra-wideband positioning system of cutting head, the dynamic positioning accuracy of ultra-wideband positioning system of cutting head is set up to analyze and evaluate the accuracy of positioning system. The experimental simulation experiment distance is set from 4 m to 32 m, each 4 m group, a total of eight groups. Three positioning base stations and their position fixing plates, three positioning tags and their position fixing plates, fuselage simulation brackets, and multi-motion joint trolleys were used to complete the dynamic experiment, and the experimental

scene was shown in Figure 4. In experiments at different distances, we kept the spatial position of the center point of the front end of the fuselage simulation bracket unmoving. That is, the solution calibration point is used as the anchor point, placing the anchor point at the distance reference position of each ranging group, within a period of 2 min, the stance of the bracket was changed at a speed not higher than that in the dynamic ranging experiment, the positioning position solution data was captured, and the scatter plot was drawn as shown in Figure 14.

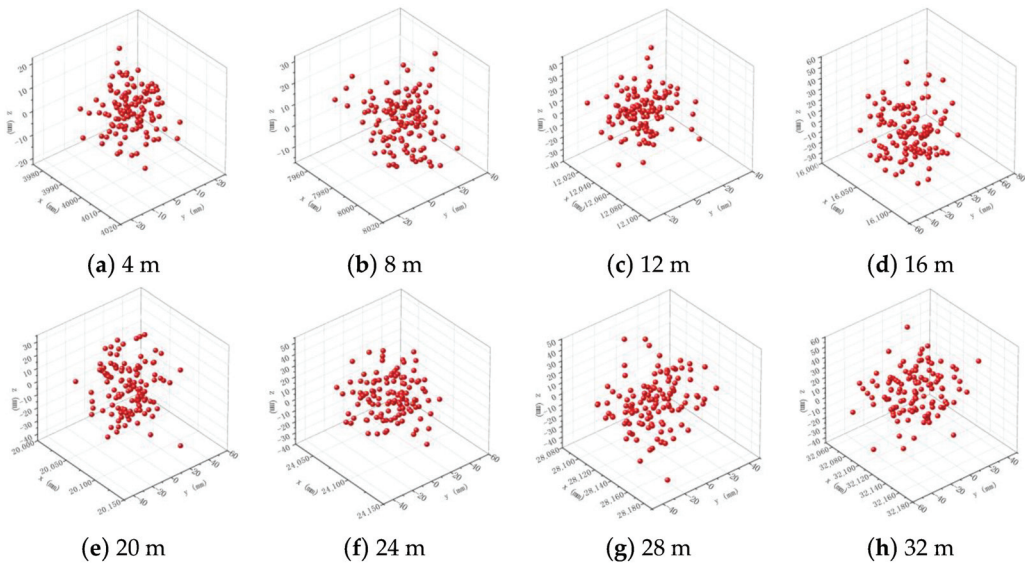


Figure 14. Scatter plot of positioning values.

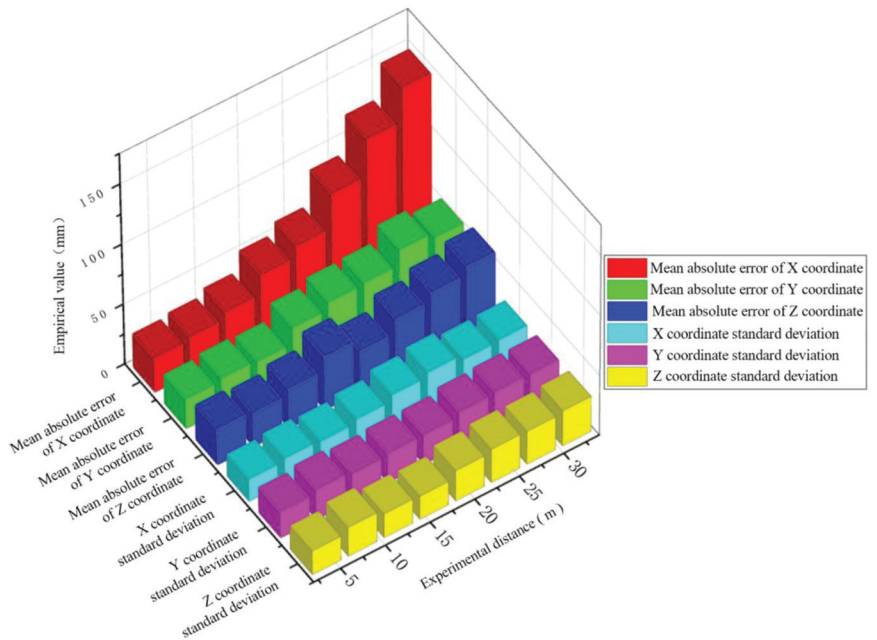
Observing the above three-dimensional scatter plot, it can be seen that the fluctuation range of the solution coordinates is better in the normal use range of the positioning system, the solution deviation belongs to the normal distribution category, the absolute error of the average value of the 3D coordinate data is small, and the precision and accuracy of the system positioning and solving data are high.

Based on the accuracy evaluation standard of the positioning system, the absolute error, the mean absolute error, and the standard deviation are obtained, and the specific evaluation results are shown in Table 1.

Table 1. Dynamic solution experiment precision evaluation table.

Experimental Distance (mm)	$\bar{e}_{Xai}$ (mm)	$\bar{e}_{Yai}$ (mm)	$\bar{e}_{Zai}$ (mm)	$SD_X$ (mm)	$SD_Y$ (mm)	$SD_Z$
4	28.32	24.65	29.65	18.62	21.54	20.04
8	30.65	26.93	27.84	20.65	24.66	24.25
12	36.21	25.63	32.79	19.45	22.63	20.06
16	52.31	38.62	40.63	22.78	24.23	19.47
20	61.36	44.57	34.23	27.86	24.54	25.45
24	89.62	45.69	45.32	31.42	28.31	28.00
28	120.34	48.32	42.32	27.12	29.62	27.61
32	147.95	49.52	49.34	28.01	29.46	29.56

In order to facilitate the intuitive analysis of the positioning accuracy and precision of the UWB positioning system, a three-dimensional histogram of the solution accuracy is drawn according to the accuracy evaluation results of the dynamic solution experiment, as shown in Figure 15.



**Figure 15.** Three-dimensional histogram of dynamic solution experimental accuracy.

From the absolute error and standard deviation level of the experimental results, it can be seen that the system dynamic positioning solution accuracy is good, the gain of the X-axis dynamic solution deviation increases with distance, and the error is less than 150 mm at 32 m. The gain of Y- and Z-axis dynamic solution deviation with increasing distance is not obvious, and the error is less than 50 mm at 32 m; The comprehensive 3D dynamic solution deviation is less than 170 mm, and the deviation is concentrated in the X-axis direction, which has little impact on the accuracy of the truncated section, the system meets the requirements of the system's dynamic positioning accuracy, and the standard deviation of the solution data is maintained within 30 mm, which meets the requirements of the system's dynamic positioning precision.

## 6. Conclusions

A new positioning system of cutting head based on ultra-wideband positioning technology is proposed, which abandons the complex solution logic of step-by-step fusion solution in different coordinate systems in two steps in traditional cutting head positioning technology. The cutting head is positioned directly through the roadway reference coordinate system, which can eliminate the system solution error caused through the transformation of different spatial coordinate systems.

Combined with the field working conditions, the simulation experiment is set up to analyze the anti-interference of positioning accuracy, and the influence degree of three typical influencing factors on the positioning accuracy is obtained. The results show that the wave transmission of the acrylic plate and the wood plate is good, and the ranging error is always maintained within 50 mm, which will not affect the normal accuracy level of the system. The ranging error of aluminum plate and other metal plates can reach up to 1000 mm, which has a great influence on the positioning accuracy. Plastic materials such as acrylic should be preferred for the packaging shell of positioning system. The normal dust concentration has no significant effect on the positioning accuracy. The ultra-wideband positioning system of the cutting head has good anti-interference performance

and can effectively maintain good system positioning accuracy when multiple devices work together.

The experimental results of the dynamic solution of the positioning accuracy of the ultra-wideband positioning system of the cutter head show that: The dynamic calculation accuracy of the ultra-wideband positioning system is high. The mean value of the three-dimensional absolute error is less than 170 mm, and the error is mainly located in the X-axis, which has little effect on the section forming accuracy. The mean value of the single-axis absolute error is less than 50 mm, and the standard deviation of the calculated data is less than 30 mm. The dynamic positioning accuracy and precision of the system meet the expected requirements.

**Author Contributions:** Conceptualization, H.M. and N.M.; methodology, H.M.; software, H.M. and Y.H.; validation, H.Z. and H.M.; formal analysis, H.M.; investigation, Z.Y.; data curation, H.Z. and Y.H.; writing—original draft preparation, H.M. and H.Z.; writing—review and editing, K.Y. and H.Z.; visualization, K.Y. and Y.H.; supervision, H.M. All authors have read and agreed to the published version of the manuscript.

**Funding:** This research received no external funding.

**Data Availability Statement:** The data can be provided if necessary.

**Conflicts of Interest:** The authors declare no conflict of interest.

## References

1. Wang, G.F.; Liu, F.; Meng, X.J.; Fan, J.; Wu, Q.; Ren, H.; Pang, Y.; Xu, Y.; Zhao, G.; Zhang, D.; et al. Research and practice on intelligent coal mine construction (primary stage). *Coal Sci. Technol.* **2019**, *47*, 1–36.
2. Wan, J.C.; Zhang, X.H.; Zhang, C.; Yang, W.; Lei, M.; Du, Y.; Dong, Z. Vision and Inertial Navigation Combined-Based Pose Measurement Method of Cantilever Roadheader. *Sustainability* **2023**, *15*, 4018. [CrossRef]
3. Yang, J.J.; Zhang, Q.; Wang, C.; Chang, B.; Wang, X.; Ge, S.; Wu, M. Status and development of robotization research on roadheader for coal mines. *J. China Coal Soc.* **2020**, *45*, 2995–3005.
4. Rycroft, M.J. Understanding GPS. Principles and applications. *J. Atmos. Sol. Terr. Phys.* **1997**, *59*, 598–599. [CrossRef]
5. Yang, W.; Zhang, X.; Ma, H.; Zhang, G. Laser Beams-Based Localization Methods for Boom-Type Roadheader Using Underground Camera Non-Uniform Blur Model. *IEEE Access* **2020**, *8*, 190327–190341. [CrossRef]
6. Adam, H.; Jaroslaw, J. Automatic control of roadheader cutting head speed and load torque. *IOP Conf. Ser. Earth Environ. Sci.* **2020**, *609*, 012081.
7. Bartoszek, S.; Stankiewicz, K.; Kost, G.; Ćwikła, G.; Dyczko, A. Research on Ultrasonic Transducers to Accurately Determine Distances in a Coal Mine Conditions. *Energies* **2021**, *14*, 2532. [CrossRef]
8. Want, R.; Hopper, A.; Falcão, V.; Gibbons, J. The active badge location system. *ACM Trans. Inf. Syst.* **1992**, *10*, 91–102. [CrossRef]
9. Zhao, J.X.; Yang, W.J.; Zhang, X.H.; Du, Y.Y.; Zhang, C. Study on accurate positioning method and its visual measurement technology of cantilever roadheader underground. *Coal Sci. Technol.* **2021**, *49*, 192–201.
10. Zhang, M.; Lyu, F.; Fu, S.; Cai, X.; Zong, K.; Wu, M. Study on the pitch angle control of a robotized hydraulic drive roadheader using different control methods. *J. Mech. Sci. Technol.* **2018**, *32*, 4893–4901. [CrossRef]
11. Cheluszka, P.; Jagiea-Zajc, A. Determining the position of pick holders on the side surface of the working unit of the cutting machine in the robotic technology of their assembly. *IOP Conf. Ser. Earth Environ. Sci.* **2019**, *261*, 012003. [CrossRef]
12. Du, Y.X. *Study on the Pose Perception and Positioning Mechanism of Boom-Type Roadheader in Mines*; China University of Mining and Technology: Xuzhou, China, 2019.
13. Wu, M.; Shen, Y.; Ji, X.D.; Wang, P.J.; Jiang, H.; Zheng, W.X.; Li, Y. Trajectory and deviation perception method of boom-type roadheader. *J. China Coal Soc.* **2021**, *46*, 2046–2056.
14. Wang, B.K. Current status and trend analysis of roadway driving technology and equipment in coal mine. *Coal Sci. Technol.* **2020**, *48*, 1–11.
15. Yang, W.J.; Zhang, X.H.; Ma, H.W.; Zhang, G.-M. Infrared LEDs-Based Pose Estimation with Underground Camera Model for Boom-Type Roadheader in Coal Mining. *IEEE Access* **2019**, *7*, 33698–33712. [CrossRef]
16. Olivart i Llop, J.M.; Moreno-Salinas, D.; Sánchez, J. Full Real-Time Positioning and Attitude System Based on GNSS-RTK Technology. *Sustainability* **2020**, *12*, 9796. [CrossRef]
17. Eric Calais, J. Bernard Minster, Michelle Hofton. Ionospheric signature of surface mine blasts from Global Positioning System measurements. *Geophys. J. Int.* **1998**, *132*.
18. Wang, S.Y.; Ma, D.C.; Ren, Z.; Wu, M. A multi-objective optimization method for cantilever roadheader section forming trajectory. *Chin. J. Sci. Instrum.* **2021**, *41*, 183–192.

19. Tian, Y.; Yang, X.; Yang, J.; Mao, K.K.; Yao, Y.J. Evolution dynamic of intelligent construction strategy of coal mine enterprises in China. *Heliyon* **2022**, *8*, e10933. [CrossRef]
20. Zang, X.H.; Yang, W.J.; Xue, X.S.; Zhang, C.; Wang, J.; Mao, Q.; Lei, M.; Du, Y.; Ma, H.; Zhao, Y. Challenges and developing of the intelligent remote control on roadheaders in coal mine. *J. China Coal Soc.* **2022**, *47*, 579–597.
21. Xu, M.G.; Liu, X.K.; Wen, X.Q. Full-mechanized excavation face efficient sprinkler & dust fall system. *J. Hunan Univ. Sci. Technol.* **2015**, *30*, 1–7.
22. Piotr, C. Optimization of the Cutting Process Parameters to Ensure High Efficiency of Drilling Tunnels and Use the Technical Potential of the Boom-Type Roadheader. *Energies* **2020**, *13*, 6597.
23. Yang, J.; Zhang, G.; Huang, Z.; Ye, Y.; Ma, B.; Wang, Y. Research on position and orientation measurement method for roadheader based on vision INS. In Proceedings of the International Conference on Optical Instruments and Technology 2017: Optoelectronic Measurement Technology and System, Beijing, China, 28–30 October 2017. Society of Photo-Optical Instrumentation Engineers Conference Series.
24. Orteu, J.; Catalina, J.; Devy, M. Perception for a roadheader in automatic selective cutting operation. In Proceedings of the IEEE International Conference on Robotics and Automation, Nice, France, 12–14 May 1992; Volume 5, pp. 626–632.

**Disclaimer/Publisher’s Note:** The statements, opinions and data contained in all publications are solely those of the individual author(s) and contributor(s) and not of MDPI and/or the editor(s). MDPI and/or the editor(s) disclaim responsibility for any injury to people or property resulting from any ideas, methods, instructions or products referred to in the content.

Article

# Carbon Dioxide Prevents Oxygen Adsorption at Low-Temperature Oxidation Stage of Low-Rank Coal: Laboratory Study and Molecular Simulation

Gang Cheng <sup>1,2,\*</sup>, Haiyan Wang <sup>3,\*</sup>, Bo Tan <sup>2</sup> and Shuhui Fu <sup>2</sup>

<sup>1</sup> School of Geology and Mining Engineering, Xinjiang University, Urumqi 830047, China

<sup>2</sup> School of Emergency Management and Safety Engineering, China University of Mining and Technology (Beijing), Beijing 100083, China; tanbo709@126.com (B.T.); wy19800302517@163.com (S.F.)

<sup>3</sup> School of Civil and Resource Engineering, University of Science and Technology Beijing, Beijing 100083, China

\* Correspondence: gang-ch@xju.edu.cn (G.C.); whycumb@163.com (H.W.)

**Abstract:** Carbon dioxide (CO<sub>2</sub>) is widely used in the prevention and control of spontaneous coal combustion. In this manuscript, three low-rank coals with different metamorphic degrees were selected as the research objects. The temperature-programmed experiments, in situ infrared cooling experiments, simulation of the competitive adsorption of CO<sub>2</sub> and oxygen (O<sub>2</sub>) in coal pores, and simulation study of the CO<sub>2</sub> inhibition of the coal oxygen composite reaction were used to obtain the role and effect of CO<sub>2</sub> in preventing oxygen adsorption in coal at the low-temperature oxidation stage. It was concluded that CO<sub>2</sub> can displace the O<sub>2</sub> near the pore wall to physically prevent the adsorption of O<sub>2</sub>. Through the changing law of heating rate and a kinetics analysis, it was found that CO<sub>2</sub> can increase its activation energy by 5.3–108.3% during the slow heating stage of coal and reduce its heat rate. At around 120 °C, coal loses the protective effect of CO<sub>2</sub>. From the changes in functional groups, it can be seen that when coal was cooled in the CO<sub>2</sub> atmosphere, mainly pyrolysis and condensation reactions occurred due to the lack of O<sub>2</sub>. In addition, CO<sub>2</sub> can also inhibit the chain reaction of the chemical adsorption of oxygen in coal. This work provides a theoretical basis for CO<sub>2</sub> prevention and the control of spontaneous coal combustion.

**Keywords:** carbon dioxide; prevent oxygen adsorption; fire prevention and extinguishing; activation energy; heat release; competitive adsorption

**Citation:** Cheng, G.; Wang, H.; Tan, B.; Fu, S. Carbon Dioxide Prevents Oxygen Adsorption at Low-Temperature Oxidation Stage of Low-Rank Coal: Laboratory Study and Molecular Simulation. *Processes* **2023**, *11*, 2504. <https://doi.org/10.3390/pr11082504>

Academic Editor: Jan Zawala

Received: 8 July 2023

Revised: 8 August 2023

Accepted: 17 August 2023

Published: 20 August 2023



**Copyright:** © 2023 by the authors. Licensee MDPI, Basel, Switzerland. This article is an open access article distributed under the terms and conditions of the Creative Commons Attribution (CC BY) license (<https://creativecommons.org/licenses/by/4.0/>).

## 1. Introduction

Spontaneous coal combustion is one of the five major disasters in coal mines [1–3], which restricts the safe and efficient exploitation and utilization of coal resources in our country [4–6]. With the continuous in-depth research on the mechanism of spontaneous coal combustion having been conducted for a long time, scholars have proposed various theories from different angles to explain the spontaneous coal combustion phenomenon, among which the coal–oxygen composite theory [7–11] has been widely recognized. At the microscopic level, coal is viewed as a porous media material. The coal–oxygen recombination reaction at the gas–solid interface inside the medium first requires the physical adsorption of oxygen by means of intermolecular forces (van der Waals forces). Based on this, the inert gas injection fire-fighting method, which can reduce the O<sub>2</sub> concentration in the goaf, has been widely used in the process of spontaneous coal combustion fire control [12,13].

Among them, nitrogen (N<sub>2</sub>) and CO<sub>2</sub> are widely used due to their advantages of inserting, cooling, explosion suppression, large diffusion range, no damage to instruments and equipment, and the ability to bypass obstacles [14]. At the same time, many scholars have conducted a lot of research on the effect of inert gas on preventing spontaneous combustion

of coal. Most of the research focuses on comparing the oxidation characteristics [15–20], ignition characteristics [21], combustion characteristics [22], changes in functional groups [23], and the generation of index gases [24] of coal samples in  $O_2/N_2$  and  $O_2/CO_2$  atmospheres. These results show that the presence of  $N_2$  and  $CO_2$  is helpful to prevent CSC, and the effect of  $CO_2$  injection is better than that of  $N_2$ . However, the timeliness of the  $CO_2$  protection of coal to prevent its spontaneous combustion is not described. Therefore, it is necessary to further clarify the mechanism of  $CO_2$  fire prevention in order to better prevent and control spontaneous coal combustion.

In explaining the mechanism of  $CO_2$  fire prevention, predecessors have mostly studied the adsorption and desorption mechanism of the gas. Many scholars have used the Grand Canonical Monte Carlo method to study the competitive adsorption mechanism of multiple gases using the coal unit cell model. Wu et al. [25] revealed the competitive adsorption mechanism of  $CO_2/O_2/N_2$  in coal through the Grand Canonical Monte Carlo method (GCMC) and molecular dynamics (MD) simulations, indicating that  $CO_2$  occupies a stronger adsorption site and has a stronger interaction energy with coal, so it is more easily adsorbed in coal. Zhang et al. [26] used the GCMC simulation method and concluded that the adsorption capacity of gas in lignite is greater than that of  $O_2$  for both single and binary components. Long et al. [27] studied the adsorption and diffusion characteristics of  $CO_2$  and  $N_2$  in the micropore and mesopore of coal by means of molecular dynamics. Dong et al. [28] used an adsorption simulation method to reveal the adsorption properties of two kinds of bituminous coals for  $CO$ ,  $CO_2$ , and  $O_2$  at different pressures and temperatures.  $CO_2$  is more easily adsorbed than  $O_2$ . Liu et al. [29] combined thermogravimetric analysis with the adsorption–desorption mechanism and confirmed that  $CO_2$  and  $H_2O$  chemisorption occurred using non-isothermal experiments. Liu et al. [30] simulated the gas transport law and explored the  $O_2$  distribution under the condition of inert gas injection into the goaf.

Coal is an extremely heterogeneous substance with abundant pores and a complex chemical structure [31,32]. The coal pore structure plays a crucial role in the process of gas adsorption, migration, and generation [33]. The above studies either did not consider the influence of pore structure, or they considered the pore structure but mostly used graphene slit pore and carbon nanotube models to simulate the nanopore structure of coal with different pore sizes. Although the above methods can effectively simplify the calculation, the coal surface has complex chemical heterogeneity and contains various functional groups, which cannot reflect the actual situation. Some scholars have confirmed that functional groups have an important influence on the adsorption of gases. Most of the above studies explain the mechanism of  $CO_2$  fire prevention and extinguishing from the perspective of gas competitive adsorption. In addition to the above physical effects,  $CO_2$  also has the effect of inhibiting the coal–oxygen composite chain reaction, and it is necessary to further reveal its inhibiting oxygen adsorption mechanism from a chemical point of view. The pore structure and surface chemical groups of porous materials, in particular, have a considerable impact on their adsorption and separation properties [34,35]. Moreover, the adsorption of  $CO_2$  by the porous materials could be significantly influenced by both heteroatom and microporous porosity [36].

We innovatively used the macromolecular model of low-rank coal to construct the pore structure of coal, revealing the microscopic mechanism of gas displacement more realistically. This manuscript also creatively simulates the effect of  $CO_2$  on the coal–oxygen complex chain reaction, and has experiments to verify it, as shown in Figure 1. This work explains both the physical and chemical effects of  $CO_2$  in preventing oxygen adsorption. The aging time and mechanism of preventing oxygen adsorption was clarified, and a model of  $CO_2$  preventing oxygen adsorption was constructed, which provided a theoretical basis for inert fire prevention and extinguishing.



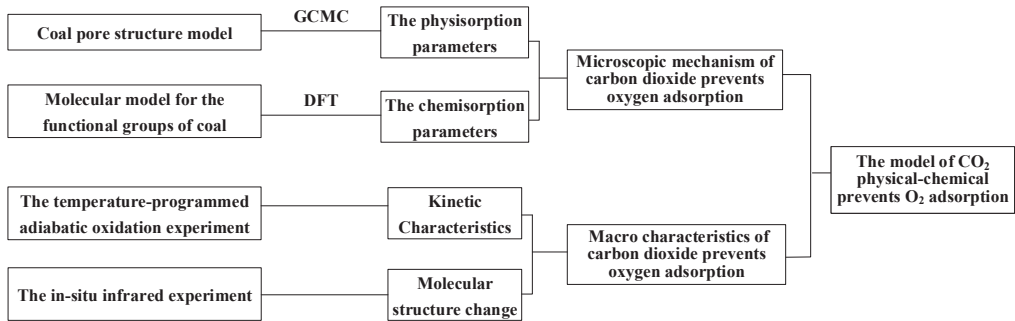


Figure 1. Molecular simulations and experimental structural diagram.

## 2. Coal Samples and Methods

### 2.1. Experimental

#### 2.1.1. Low-Rank Coal Sample Preparation

Low-rank coal has a high propensity for spontaneous combustion in goaf or coal seams, so it is the main research object of measures to prevent spontaneous coal combustion. Therefore, this manuscript selected lignite from the Huolinhe mining area, long-flame coal from the Yuheng mining area, and gas coal from the Aiweiergou mining area as the research objects, denoted as HL, YH, and AW, respectively [37]. The low-rank coal samples were crushed into 120-mesh-pulverized coal for industrial analysis, organic element (C, H, O, N) content determination, S element content determination, and vitrinite reflectance analysis. The analysis results are shown in Table 1.

Table 1. Each low-rank coal sample's analysis results.

Coal Sample	$M_{ad}$	$A_d$	$V_{daf}$	$FC_{ad}$	$C_{daf}$	$H_{daf}$	$N_{daf}$	$O_{daf}$	$S_{t,ad}$ /%	$R_{o,ran}$ /%
HL	14.35	6.92	42.46	36.27	73.29	5.16	1.06	19.22	1.27	0.35
YH	4.67	6.18	38.09	51.06	81.92	5.24	0.93	9.32	2.68	0.58
AW	0.82	8.73	35.82	54.63	86.25	5.91	1.13	6.37	0.34	0.78

Notes:  $M_{ad}$ —moisture;  $A_d$ —ash;  $V_{daf}$ —volatile;  $FC_{ad}$ —fixed carbon;  $C_{daf}$ —carbon content;  $H_{daf}$ —hydrogen content;  $N_{daf}$ —nitrogen content;  $O_{daf}$ —oxygen content;  $S_{t,ad}$ —sulfur content;  $R_{o,ran}$ —vitrinite reflectance.

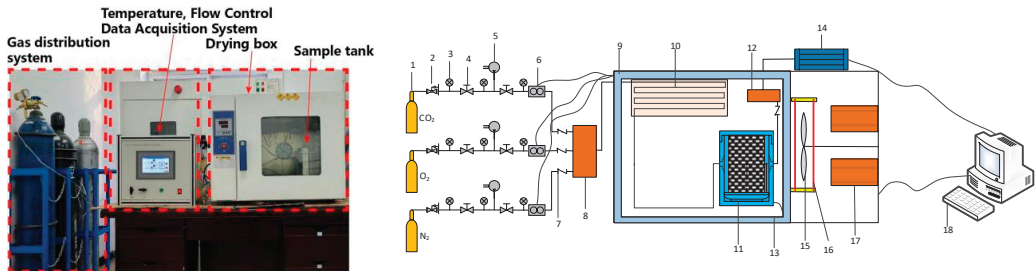
#### 2.1.2. Device and Process of Temperature-Programmed Adiabatic Oxidation Experiment

Under the same conditions as the coal type, particle size, air flow rate, heating rate, initial temperature, and final temperature, two spontaneous coal combustion adiabatic oxidation temperature programming tests were carried out for each coal sample, as shown in Figure 2. That is, under the condition of 30 °C, air or CO<sub>2</sub> was respectively introduced into the coal sample with a weight of 200 g and a diameter of about 1.5–2.4 mm, and the temperature-programmed adiabatic oxidation experiment was started after holding for 2 h. The temperature was raised to 200 °C with a heating rate of 1 K/min and then held at a constant temperature for 5 h.

#### 2.1.3. Device and Process of In Situ Infrared Cooling Experiment

The experimental test system was a TENSOR27 Fourier transform infrared spectrometer from BLUKE, Germany, which realized the testing of the changes in functional groups of coal at different temperatures through an in situ infrared reaction cell measurement. The in situ infrared reaction cell body was mainly made of 316 L stainless steel (high temperature resistance of 500 °C, pressure resistance of 3 MPa) and the reaction cell cavity cap had three windows (two infrared windows, one quartz window), providing three inlets/outlets for pumping out of the cell body and introducing gases. The general experimental program

was that coal samples (200 mesh) of about 5 g were selected each time and inserted in nitrogen for 6 h before being placed in the reaction cell. The coal samples were raised to 200 °C in an atmosphere of air (80% N<sub>2</sub> and 20% O<sub>2</sub>) and then cooled down by passing CO<sub>2</sub> and air, respectively. The atmosphere flow rate was 50 mL/min, the resolution of the infrared test program was 4 cm<sup>-1</sup>, the spectral scanning range was 800–4000 cm<sup>-1</sup>, data were collected every 30 s, and the collection time was 20 to 25 min.



**Figure 2.** Experimental setup for programmed thermal adiabatic oxidation. Legend: 1—gas cylinder; 2—pressure-reducing valve; 3—pressure gauge; 4—pressure regulator valve; 5—air compressor; 6—flow meter; 7—check valve; 8—intake mixing bin; 9—insulation layer; 10—gas-preheating copper pipe; 11—heat transfer coal sample tank; 12—outlet gas-mixing chamber; 13—program temperature control box; 14—cooler; 15—fan; 16—heater; 17—refrigerator; 18—PC.

## 2.2. Simulation Method

The simulation methods in this paper are categorized into physical and chemical adsorption. The physisorption was mainly simulated by material studio 8.0 software based on the GCMC for competitive physisorption. Chemisorption was mainly simulated thermodynamically and kinetically by Gaussian09 software, based on the density functional method (DFT).

### 2.2.1. Method of Physisorption Simulation

#### (1) GCMC physisorption method

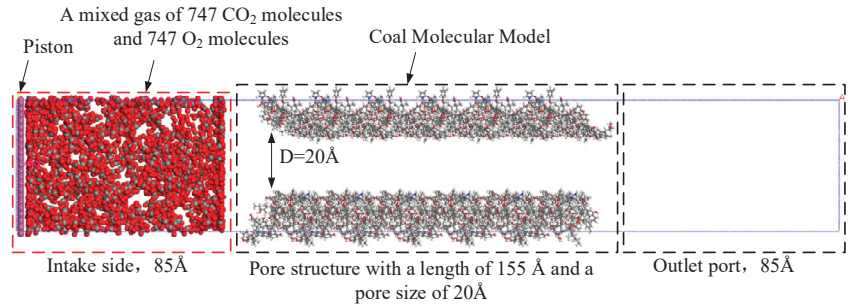
The physisorption simulations were carried out by the GCMC method, with the coal molecular unit cells as the adsorbent and oxygen molecules as the adsorbate [38], and the Metropolis algorithm was used to keep the chemical potential and volume stable during the simulations. The temperature was set to 298 K, the Ewald was used for the summation of electrostatic interactions and the Atom for van der Waals interactions, with the cut-off distance set to 15.5 Å.

The effect of carbon dioxide on oxygen adsorption in the coal pore structure was analyzed in the Forcite module of Materials Studio 8.0 software. The task was set to dynamics, the NVT ensemble was used, and based on the structural optimization of the initial configuration of the physisorption configurations, the molecular dynamics simulations were carried out at 298 K, a step size of 1 fs, a dynamics simulation time of 100 ps, and with the temperature control method set to Nose.

#### (2) Simulation of Competitive Adsorption of CO<sub>2</sub> and O<sub>2</sub> in Coal Surface Pores

The molecular structure of the HL coal sample selected for the physisorption simulation and the method of constructing the molecular pore structure of the HL coal sample can be referenced from the papers published by our group [37,39]. As shown in Figure 3, HL coal molecules were used as pore walls to construct pores with a diameter of 20 Å and a length of 155 Å. The left side of Figure 3 is the graphene structure “piston”. Under the conditions of 30 °C, 60 °C, 90 °C, and 120 °C, the “piston” moved 1 Å per 100 ps to push the mixture of CO<sub>2</sub> and O<sub>2</sub> to the intake side. The length of the intake side was set to 85 Å, and

the piston pushed forward a total of 75 Å. The mixed gas consisted of 747 CO<sub>2</sub> molecules and 747 O<sub>2</sub> molecules. The height and width of the entire model were 55 Å.



**Figure 3.** Gas adsorption model of coal surface pore.

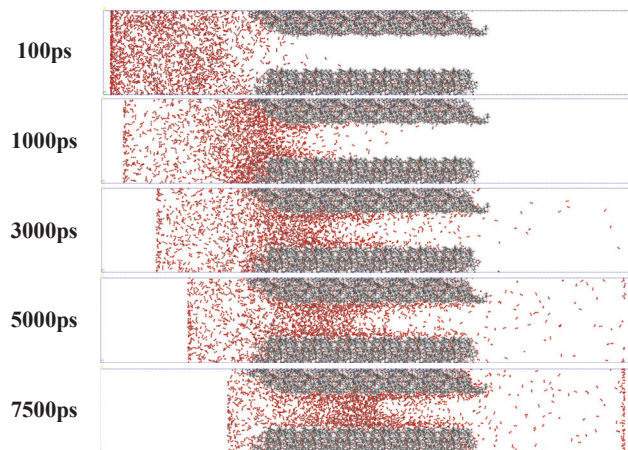
### 2.2.2. Method for Chemisorption Simulation

In this study, calculations were performed using density functional theory (DFT), the Gaussian09 package and the M06-2x/6-31G(d,p) [40] method. For the structure optimization and frequency calculation of the reactants, the TS (Beryny) method [41] was used to find the transition state, and the intrinsic reaction coordinate (IRC) method based on the LQA algorithm was used to analyze the reaction pathway. It should be noted that for groups (radicals and oxygen) with a spin multiplicity other than 1, calculations were performed in an open-shell environment.

## 3. Results and Analysis

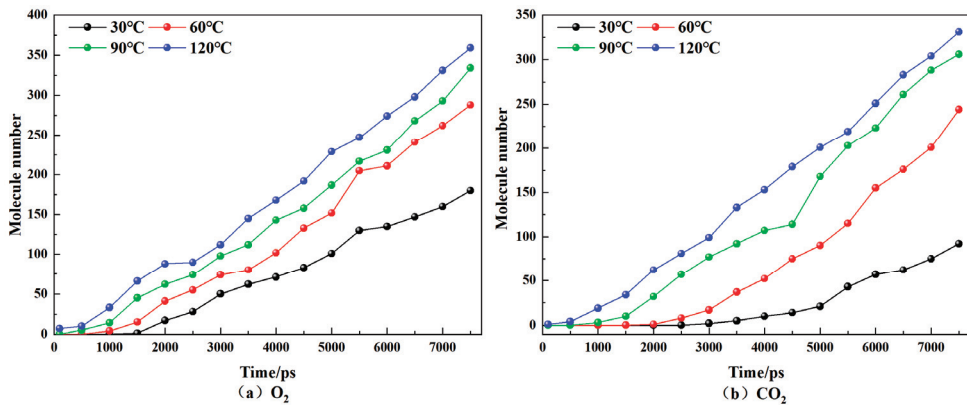
### 3.1. Analysis on the Physical Mechanism of CO<sub>2</sub> Preventing O<sub>2</sub> Adsorption

It can be seen from the author's previous work that the adsorption capacity of CO<sub>2</sub> in coal is stronger than that of O<sub>2</sub>, and CO<sub>2</sub> can displace O<sub>2</sub> in coal [38]. The mechanism of this macroscopic phenomenon is unknown, so this study used Materials Studio 8.0 software to simulate this phenomenon to explain its cause from a microscopic perspective. According to the simulation results in Materials Studio 8.0, the adsorption and diffusion of O<sub>2</sub> and CO<sub>2</sub> in the coal pore structure in each time period can be known, as shown in Figure 4.



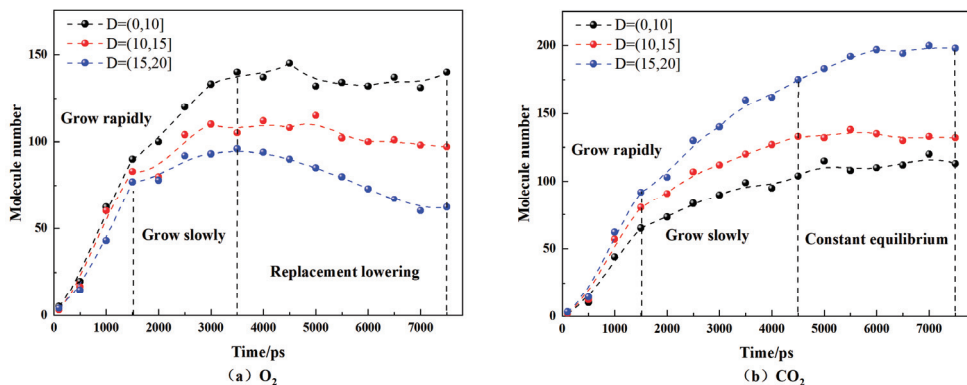
**Figure 4.** Adsorption and diffusion of O<sub>2</sub> and CO<sub>2</sub> in coal pore structure at 30 °C. The red dots are oxygen atomic, the black dots are carbon atomic.

Figure 5 shows the time-dependent changes in  $O_2$  and  $CO_2$  at the gas outlet port of the coal surface pore model at different temperatures. Under the same conditions, the amount of  $CO_2$  at the gas outlet port is always less than the amount of  $O_2$ . At 30 °C, 60 °C, 90 °C, and 120 °C,  $O_2$  appeared at the gas outlet port at 1500 ps, 1000 ps, 500 ps, and 100 ps, respectively, while  $CO_2$  appeared at 2500 ps, 1500 ps, 500 ps, and 100 ps, respectively. It can be seen that  $O_2$  can be desorbed from the coal pore structure earlier. This is consistent with the experimental results [30]. The diffusion rate of  $O_2$  was greater, that is,  $CO_2$  was more easily adsorbed in the coal. With the increase in temperature, the gas molecules at the gas outlet port continued to increase at the same time, indicating that the increase in temperature was conducive to the diffusion of gas in the coal pore structure. From the perspective of the proportion of gas at the outlet port of the pore model at 7500 ps at different temperatures, it can be seen that with the increase in temperature, the proportion of  $O_2$  continued to decrease, indicating that temperature had a greater impact on the adsorption of  $CO_2$  in coal pores.



**Figure 5.** Variations of  $O_2$  and  $CO_2$  with time at the gas outlet port of the coal surface pore model at different temperatures.

Based on gas density profile, the pore space was split into three zones. In order to observe the microscopic mechanism of  $CO_2$  replacing  $O_2$  in pores, taking the pore center of the coal as the center, the number of  $O_2$  and  $CO_2$  molecules in the range of 0~10 Å, 10~15 Å, and 15~20 Å from the center were calculated at a temperature of 30 °C, respectively. The results are shown in Figure 6.



**Figure 6.** Quantities of  $O_2$  and  $CO_2$  adsorbed in coal pores at 30 °C.

It can be seen that in the whole adsorption process, the number of CO<sub>2</sub> molecules in the pores increased for a longer time than that of O<sub>2</sub>. At the same time, the total number CO<sub>2</sub> molecules in the pores was greater, that is, the adsorption capacity of CO<sub>2</sub> was stronger. CO<sub>2</sub> molecules were mainly distributed in the range of 15~20 Å from the center of the pores, and its number in the pores increased rapidly before 1500 ps, then increased slowly from 1500 ps to 4500 ps. After 4500 ps, the numbers in the 0~10 Å and 10~15 Å spatial ranges remained unchanged, while the numbers in the 15~20 Å spatial range increased. O<sub>2</sub> molecules were mainly distributed in the range of 0~10 Å from the center in the coal pores. The O<sub>2</sub> molecules in the pores increased rapidly before 1500 ps, and the growth rate slowed down from 1500 ps to 3500 ps. After 3500 ps, the amount of O<sub>2</sub> in the range of 10~15 Å and 15~20 Å decreased slowly, while the number of CO<sub>2</sub> molecules in the same spatial range increased, indicating that CO<sub>2</sub> replaced O<sub>2</sub> molecules in this space. Additionally, this effect was stronger in the range of 15~20 Å. The number of O<sub>2</sub> and CO<sub>2</sub> molecules fluctuated in the range of 0~10 Å, that is, CO<sub>2</sub> had almost no replacement effect on them.

In a word, in the coal pores, CO<sub>2</sub> tended to be adsorbed more near the pore wall and O<sub>2</sub> tended to be adsorbed in the center of the pores, and the adsorption capacity of coal for CO<sub>2</sub> was stronger than that of O<sub>2</sub>. CO<sub>2</sub> could displace the O<sub>2</sub> adsorbed in coal, and this effect was stronger near the pore wall.

### 3.2. Analysis on the Chemical Mechanism of CO<sub>2</sub> Preventing O<sub>2</sub> Adsorption

#### 3.2.1. Influence of Pre-Injection of CO<sub>2</sub> into Coal on Its Heating Process

From the temperature-programmed experiment, the relationship between the heating rate and the temperature of each coal sample in the oxidation heating process between 30 and 200 °C can be obtained, as shown in Figure 7.

It can be seen from the experimental results that at 124 °C, 50 °C and 120 °C, the heating rates of the AW, YH, and HL coal samples pre-treated with CO<sub>2</sub> injection exceeded that of the coal without CO<sub>2</sub> injection. The above temperatures were in the initial adsorption stage and the fast reaction stage of coal. The turning points of the heating rate curve from rising to falling were all around the slow chemisorption temperature point. Overall, the heating rate of the coal samples injected with CO<sub>2</sub> was lower than that of the coal samples without CO<sub>2</sub> injection (except for YH coal) before the slow chemisorption temperature point. At 170 °C, 120 °C and 141 °C, the temperatures of the AW, YH, and HL coal samples injected with CO<sub>2</sub> exceeded that of the coal without CO<sub>2</sub> injection, and these temperatures were all in the fast reaction stage.

Before the rapid reaction stage, with the increase in coal temperature, the CO<sub>2</sub> adsorbed in the coal sample was gradually desorbed, and O<sub>2</sub> was adsorbed and participated in the reaction to release heat. The slower heating rate of the CO<sub>2</sub>-injected coal samples was because the desorbed CO<sub>2</sub> absorbed heat. Moreover, because more CO<sub>2</sub> in coal occupied the adsorption site of O<sub>2</sub>, less O<sub>2</sub> was adsorbed during the reaction, which slowed down the oxidation reaction process, so the heat release was slower. After reaching the slow chemisorption temperature point, the coal lost the protective effect of CO<sub>2</sub> due to a large amount of CO<sub>2</sub> extraction. In the early stage, due to the inserting effect of CO<sub>2</sub>, the consumption of active groups in the coal was slow. At this time, a large number of active groups combined with O<sub>2</sub> to react, releasing a lot of heat, so the heating rate was faster. The heating rate decreased when the number of active groups decreased. CO<sub>2</sub> was mainly adsorbed in the micropores of coal, and the gas in the micropores was not easily desorbed. The proportion of mesopores in YH coal was larger than that of micropores, while the opposite was true for the AW coal samples and HL coal samples. Therefore, the temperature at which the YH coal sample lost the protective effect of CO<sub>2</sub> was earlier.

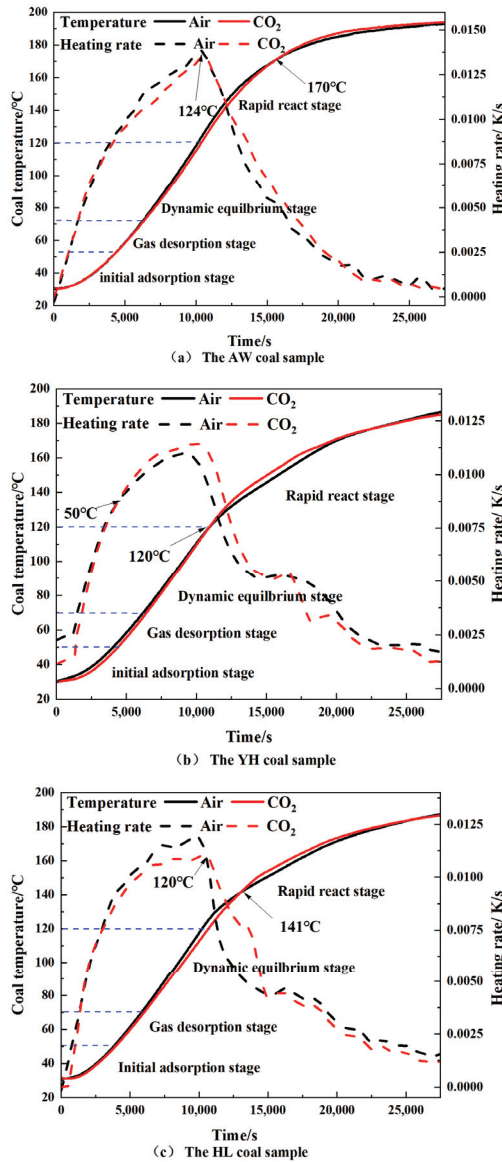


Figure 7. Variation of temperature and heating rate of each coal sample with time.

The Arrhenius formula is often introduced in the analysis of coal oxidation kinetics, and its expression is shown in Formula (1). The Arrhenius formula is based on the elementary reactions of substances and characterizes the relationship between the reaction rate constant and the apparent activation energy.

$$k = A \exp\left(-\frac{E}{RT}\right) \tag{1}$$

where  $k$  is the reaction rate constant (dimensionless);  $A$  is the exponent factor ( $s^{-1}$ );  $E$  is the activation energy (kJ/mol);  $R$  is the gas state constant.

Assuming that there is no heat convection, heat conduction, or moisture evaporation during the adiabatic oxidation process of the coal sample, Equation (1) can be transformed into:

$$\ln\left(\frac{dT}{dt}\right) = \ln\left(\frac{Q_c A}{C_c}\right) - \frac{E}{RT} \quad (2)$$

where  $dT/dt$  is the heating rate of the adiabatic oxidation of coal, and its value is approximately equal to  $(T_1 - T_2)/(t_1 - t_2)$ . Using this formula, the apparent activation energy of the experimental coal sample can be obtained.

The relationship between the heating rate of coal and the reciprocal temperature is obtained by Formula (2). It is divided into four stages according to the characteristics of the adsorption and consumption of oxygen, and the fitted straight line of each stage is obtained by linear fitting. The activation energy of coal in each stage of the low-temperature oxidation process is calculated as shown in Figures 8–10.

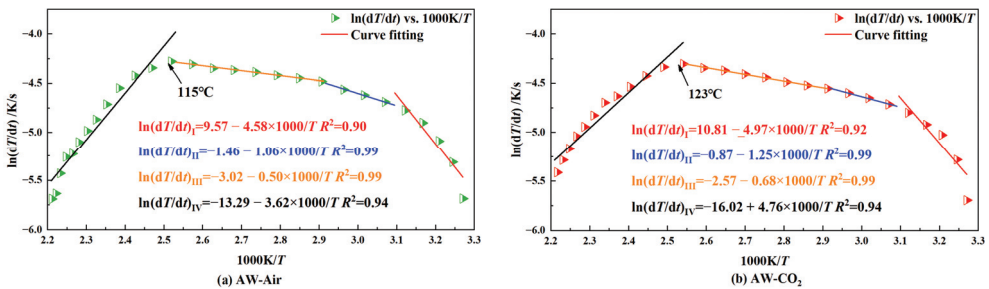


Figure 8. Diagram of the relationship between  $\ln(dT/dt)$  vs.  $1000/T$  for AW coal sample.

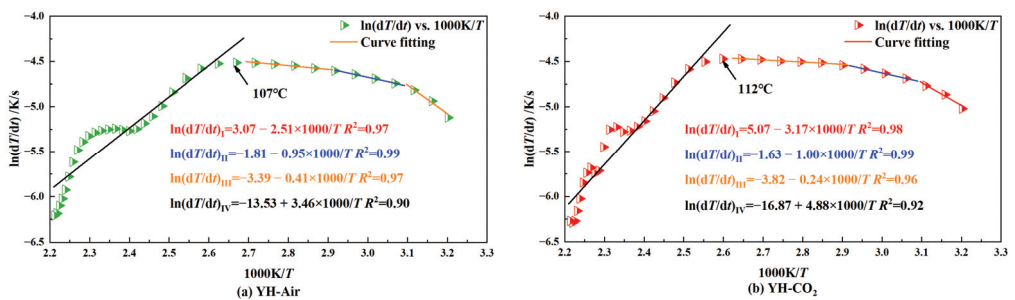


Figure 9. Diagram of the relationship between  $\ln(dT/dt)$  vs.  $1000/T$  for YH coal sample.

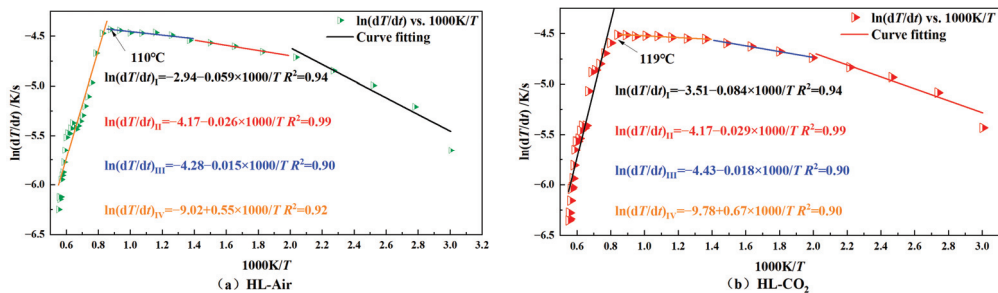


Figure 10. Diagram of the relationship between  $\ln(dT/dt)$  vs.  $1000/T$  for HL coal sample.

When the slope of the fitted line is negative, it indicates that the coal is in the slow heating stage in the early stage of low-temperature oxidation; when the slope is positive, it indicates that the coal has entered the stage of autothermal oxidation. The temperature corresponding to the turning point where the slope changes from negative to positive is the critical temperature of autoignition. It can be seen from the figure that the whole process of temperature programming can be divided into four stages. From stage I to stage III, the coal is mainly in the early and slow heating process, and stage IV is the autothermal oxidation stage. Table 2 shows the activation energy of each coal sample at each stage.

**Table 2.** Comparison of activation energy and critical temperature at each stage for the three coal samples with and without CO<sub>2</sub> injection.

Coal Sample	Oxidation Stage	Inject Air		Inject CO <sub>2</sub>	
		Activation Energy $E_a$ /kJ/mol	Critical Temperature of Spontaneous Combustion $T$ /°C	Activation Energy $E_a$ /kJ/mol	Critical Temperature of Spontaneous Combustion $T$ /°C
AW	I	38.08		41.32	
	II	8.81	115	10.39	123
	III	4.16		5.65	
	IV	−30.10		−39.58	
YH	I	20.87		26.36	
	II	7.90	107	8.32	112
	III	3.41		2.00	
	IV	−28.77		−40.57	
HL	I	33.67		47.72	
	II	6.90	110	7.40	119
	III	1.08		2.25	
	IV	−34.67		−43.90	

It can be seen from Table 2 that in both stage I and stage II, for the same coal type, the activation energy of the coal injected with CO<sub>2</sub> was higher than that of the coal without CO<sub>2</sub> injection. This shows that the injected CO<sub>2</sub> could hinder the coal's adsorption of O<sub>2</sub> in both stages. In stage III, the activation energy of the CO<sub>2</sub>-injected YH coal was lower than that of the non-injected coal, while the opposite was true for the other two coal samples. As already known, this was because the YH coal sample lost the CO<sub>2</sub> adsorption resistance to oxygen at 50 °C. In stage IV, the activation energy of the coal injected with CO<sub>2</sub> was lower than that of the coal not injected with CO<sub>2</sub>, indicating that CO<sub>2</sub> lost the effect of oxygen barrier adsorption at about 120 °C.

At about 120 °C, the oxidation process transitioned from stage III to stage IV, and each coal sample reached the critical temperature of spontaneous coal combustion. Additionally, for the same type of coal, the critical temperature of the spontaneous combustion of the coal injected with CO<sub>2</sub> was higher than that of the coal without CO<sub>2</sub> injection, which further showed that the adsorption of CO<sub>2</sub> in the coal had the added effect of preventing oxygen adsorption.

From the above analysis, it can be concluded that the injection of CO<sub>2</sub> into the coal can hinder the O<sub>2</sub> adsorption of its low-temperature oxidation process. Its hindering effect was mainly seen in stage I to stage III, which was manifested as increasing the activation energy of low-temperature coal oxidation and reducing the heating rate of coal. As the temperature increased, CO<sub>2</sub> was desorbed from the coal. Due to the adsorption of CO<sub>2</sub> in the early stage, the consumption of active groups was small. At this time, the active groups adsorbed O<sub>2</sub> in large quantities and reacted, resulting in the intensified low-temperature oxidation of coal. At the same time, the activation energy decreased and the heating rate increased. That is, at stage IV, the coal lost the protective effect of CO<sub>2</sub>.



### 3.2.2. Analysis of Functional Group Changes in CO<sub>2</sub> Injection during Coal Cooling

The in situ infrared experiments obtained the temperature change of the main functional groups of each coal sample under different atmospheric conditions, as shown in Figures 11–16.

#### (1) Peroxide (C–O–O·)

As shown in Figure 11, in the air atmosphere, the peroxides of the AW and HL coal samples showed a trend of first decreasing and then increasing, but the change range was different. The decrease in the AW coal samples was larger, while the increase in the HL coal samples was larger. The YH coal sample mainly exhibited an increasing trend. The main reason is that during the cooling process in the air atmosphere, the coal sample will chemically adsorb oxygen that is then autocatalyzed into peroxides, but when the temperature is further lowered, the chemical adsorption of oxygen will not be catalyzed into oxides, resulting in an increase in its content. The YH coal sample had a larger proportion of mesopores, so the O<sub>2</sub> adsorption was more rapid, and the peroxide content increased. This was consistent with the above result that the critical temperature of the spontaneous combustion of YH coal was the lowest.

In the CO<sub>2</sub> atmosphere, the absorbance of the peroxides of the AW and HL coal samples first decreased and then increased, and the change range was smaller than that in the air atmosphere. In the YH coal sample, there was a downward trend. This showed that the reaction and generation of peroxides did not change much under anoxic conditions, mainly relying on the partial autocatalytic reaction in the pyrolysis process.

#### (2) Free hydroxyl (HO·)

The change process of free hydroxyl (HO·) is shown in Figure 12. In the air atmosphere, for the AW coal sample, it first decreased and then tended to be smooth, and in the YH coal sample, it first increased and then tended to be smooth. However, in the HL coal samples, it first decreased and then increased. The free hydroxyl group is the product after peroxide autocatalysis, so it was found that the change trend of the absorbance of the free hydroxyl group and peroxide was similar in the air atmosphere. In the CO<sub>2</sub> atmosphere, the absorbance of free hydroxyl groups in each coal sample first increased and then tended to be smooth, which was similar to the change trend of the peroxide absorbance in the CO<sub>2</sub> atmosphere.

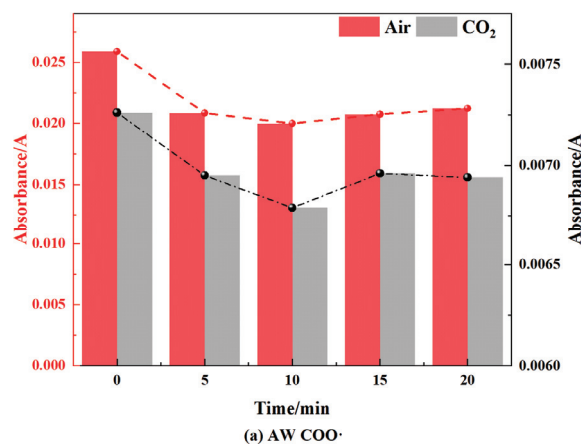
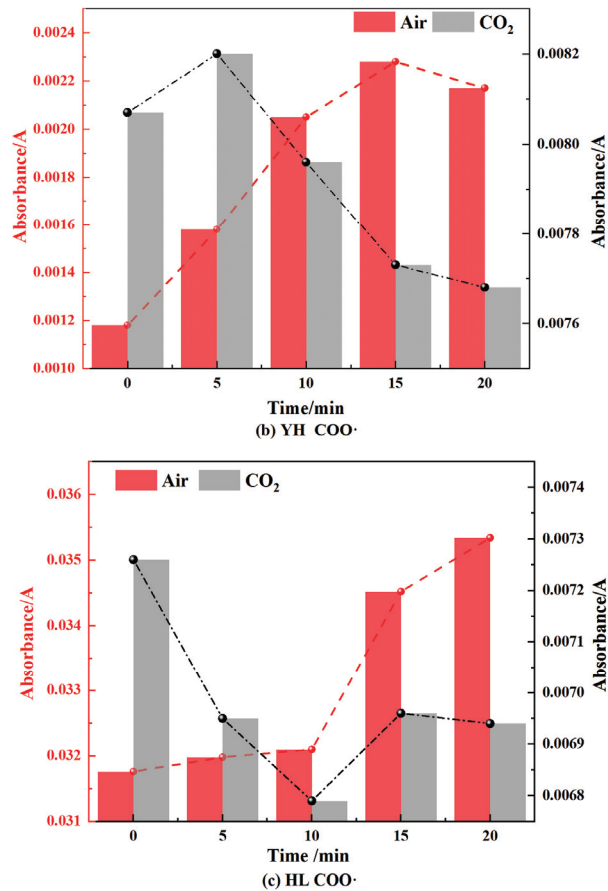


Figure 11. Cont.



**Figure 11.** Peroxide Changes in Coal during Cooling Process in Air and CO<sub>2</sub> Atmospheres.

### (3) Aldehyde group (-CH=O)

As shown in Figure 13, in the air atmosphere, the aldehyde groups in the AW and YH coal samples first increased and then tended to be smooth, and in the HL coal samples, they showed a trend of first decreasing and then increasing. The aldehyde group is an intermediate product of the coal chemisorption oxygen reaction, which is related to the difference in coal oxidation characteristics. Compared with the AW and YH coal samples, the HL coal samples had more aliphatic side chains, which easily reacted to generate CO or carboxyl groups. In the CO<sub>2</sub> atmosphere, the aldehyde group first increased and then decreased in the AW coal sample, gradually increased in the YH coal sample, and gradually decreased first and then increased in the HL coal sample, but the overall change range was not high. This indicated that a small number of aldehyde group generation and decomposition reactions occurred, and further indicated that the molecular structure of coal changed little during the cooling process under CO<sub>2</sub> atmosphere.

### (4) Carboxyl (-COOH)

As shown in Figure 14, in the air atmosphere, the carboxyl groups first decreased and then tended to be smooth in the AW coal sample, first smoothed and then increased in the YH coal sample, and showed an increasing trend in the HL coal sample. This showed that during the cooling process, the carboxyl group of the AW coal sample was generated and the decomposition reaction also occurred. When the temperature decreased,

the decomposition reaction weakened, while the YH coal samples and the HL coal samples were continuously oxidized to form carboxyl groups. In the CO<sub>2</sub> atmosphere, the carboxyl group first increased and then decreased in the AW coal sample, gradually increased in the YH coal sample, and gradually decreased first and then increased in the HL coal sample, but the overall change range was not high. This was the same as for carbonyl changes. It shows that in the CO<sub>2</sub> atmosphere, most carbonyl groups were converted into carboxyl groups, but due to the lack of O<sub>2</sub> in the environment, the main method of generating carboxyl groups was the combination of free hydroxyl groups and carbonyl radicals.

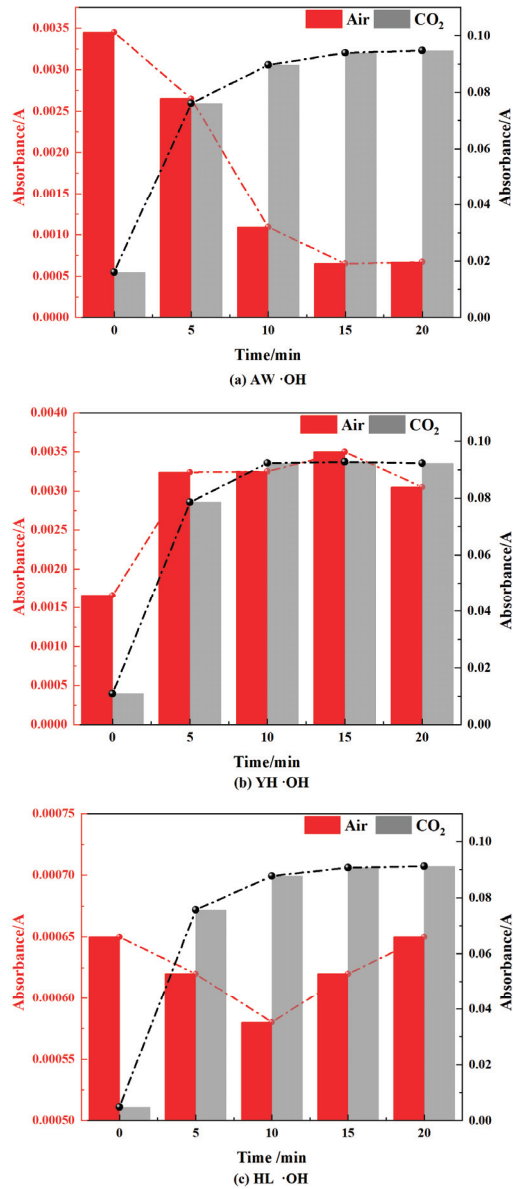
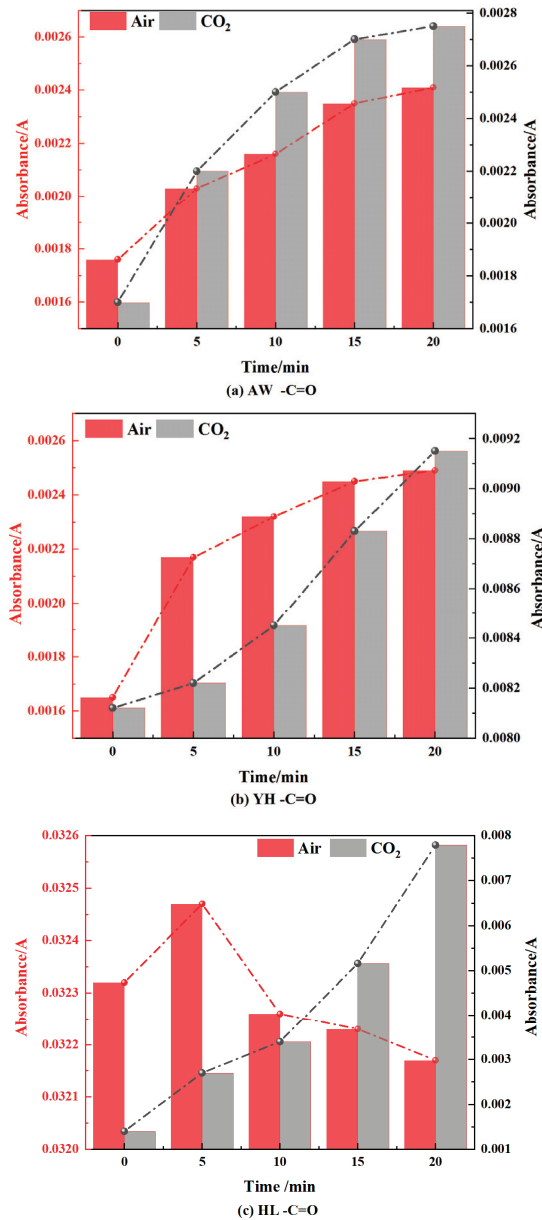


Figure 12. Free Hydroxyl Changes in Coal during Cooling Process in Air and CO<sub>2</sub> Atmospheres.



**Figure 13.** Carbonyl Changes in Coal during Cooling Process in Air and CO<sub>2</sub> Atmospheres.

(5) Methyl (-CH<sub>3</sub>) and methylene (-CH<sub>2</sub>-)

It can be seen from Figures 14 and 15 that in the air atmosphere, the methyl group and the methylene group showed a trend of increasing first and then decreasing. The main reason is that pyrolysis breaks aliphatic chains in coal to generate methyl and methylene groups. They then interact with oxygen for chemisorption reactions and low-temperature condensation.

In the CO<sub>2</sub> atmosphere, the absorbance of methyl and methylene increased first and then decreased, which was caused by the pyrolysis reaction and the condensation

of aliphatic chains. In an oxygen-deficient environment, the aliphatic chain of the coal molecule is broken to form methyl and methylene at high temperatures, which are condensed at low temperatures. However, the changes in methyl and methylene in the air atmosphere were not as large as those in the CO<sub>2</sub> atmosphere.

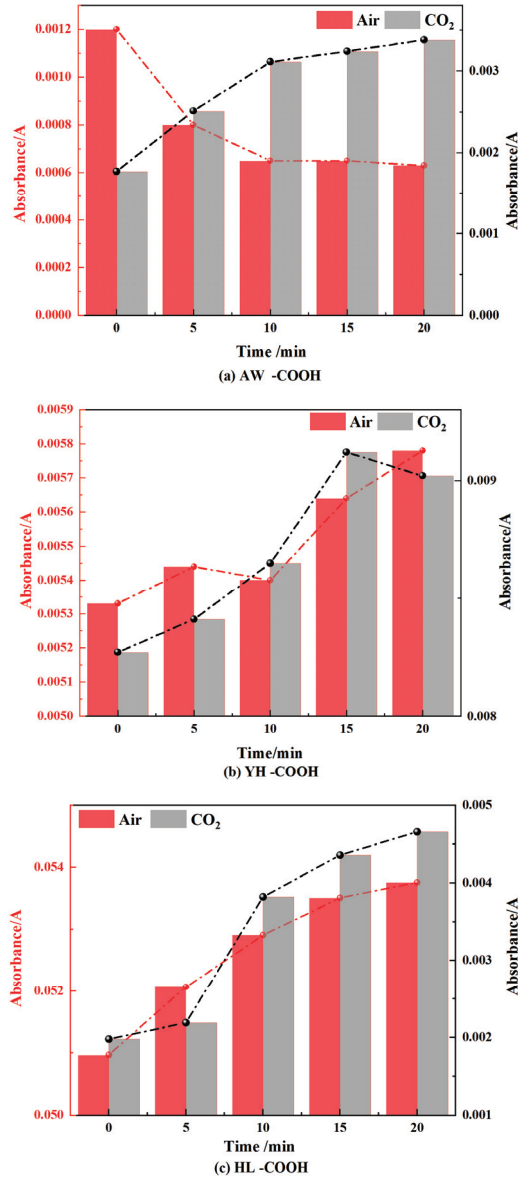


Figure 14. Carboxyl Changes in Coal during Cooling Process in Air and CO<sub>2</sub> Atmospheres.

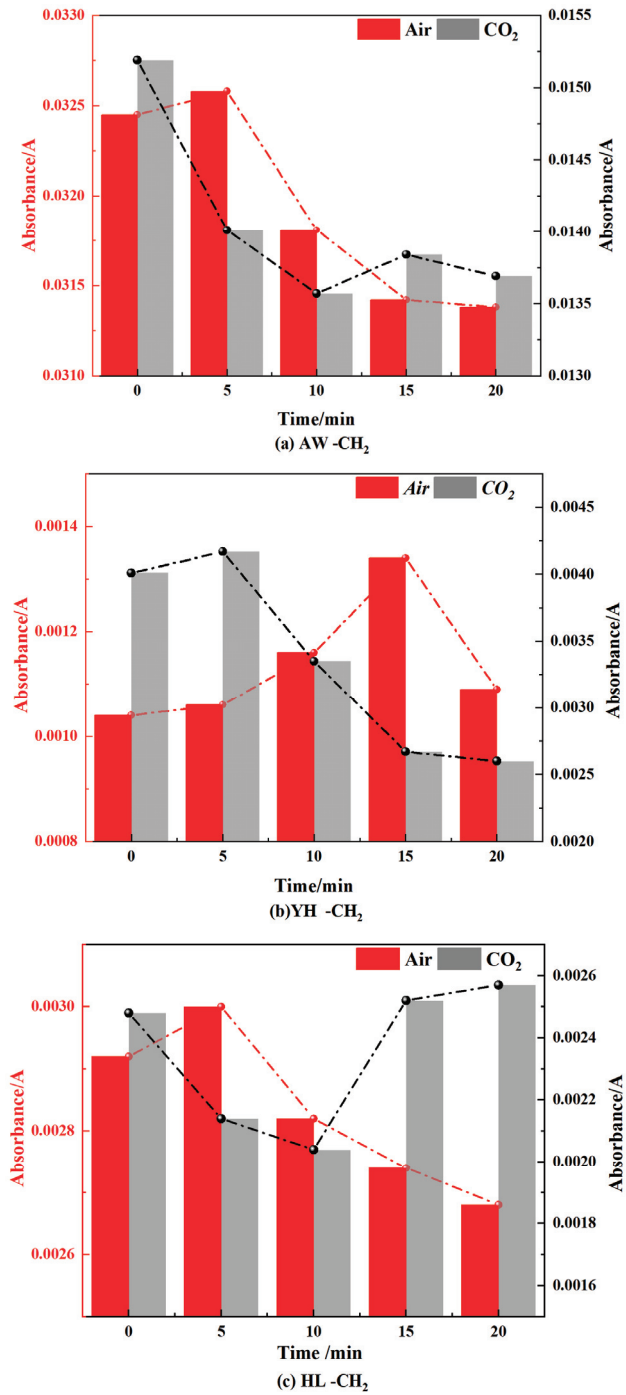


Figure 15. Methylene Changes in Coal during Cooling Process in Air and CO<sub>2</sub> Atmospheres.

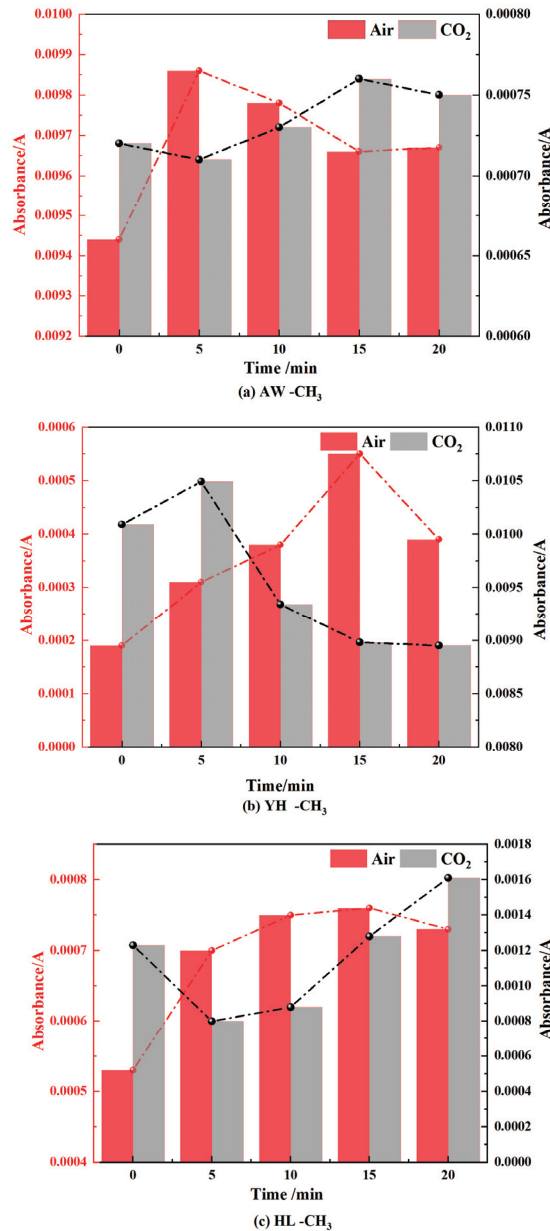
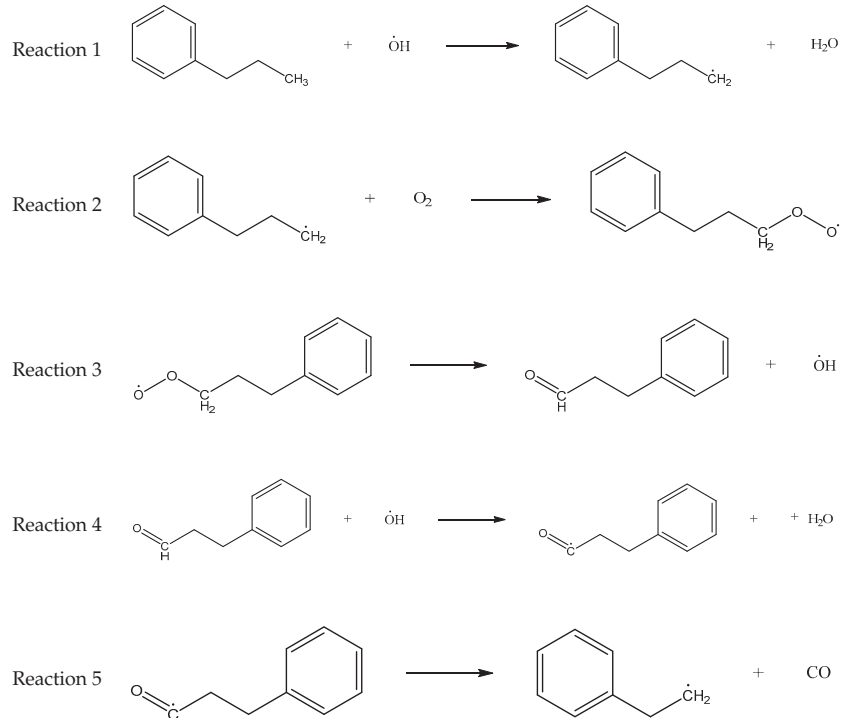


Figure 16. Methyl Changes in Coal during Cooling Process in Air and CO<sub>2</sub> Atmospheres.

Through the above analysis, it can be concluded that when the coal was cooled in the air atmosphere, the chemisorption products of coal oxide such as  $\cdot\text{OH}$  and  $\text{C-O-O}\cdot$ ,  $-\text{CH}=\text{O}$  and  $-\text{COOH}$  increased. When the coal was cooled in the CO<sub>2</sub> atmosphere, the main pyrolysis and condensation reactions occurred due to the lack of O<sub>2</sub>, and CO<sub>2</sub> hindered the decomposition of  $-\text{COOH}$ , etc., which eventually led to the increase in  $-\text{CH}=\text{O}$  and  $-\text{COOH}$  in the coal. Other structural changes were smaller.

### 3.2.3. Effect of CO<sub>2</sub> on the Reaction Process of Coal Chemical Adsorption of O<sub>2</sub>

While hindering the adsorption of O<sub>2</sub> by coal, CO<sub>2</sub> will have a weak interaction with coal molecules and O<sub>2</sub> molecules, which will affect the activation energy and exothermic conditions of the reaction process of the chemical adsorption of oxygen by coal, thereby affecting the reaction process. Taking methyl as an example, the chemical adsorption reaction process of coal was constructed as follows [28]:



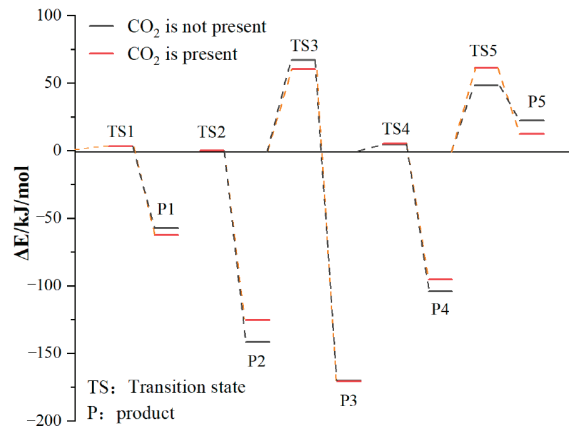
The above reactions were simulated with and without CO<sub>2</sub>, respectively. CO<sub>2</sub> had little effect on the activation energy of reaction 1, but had a significant effect on its heat release. When CO<sub>2</sub> was present, the heat release increased from 54.07 kJ/mol to 59.19 kJ/mol. Reaction 2 is the chemisorption of O<sub>2</sub>, which does not require activation energy, and its exothermic heat was reduced from 141.49 kJ/mol to 125.37 kJ/mol in the presence of CO<sub>2</sub>. Reaction 3 involves the active group in the chemisorbed state abstracting the surrounding hydrogen atoms. The presence of CO<sub>2</sub> reduced the activation energy of the reaction from 66.98 kJ/mol to 60.34 kJ/mol, and at the same time increased the heat release from 103.14 kJ/mol to 110.39 kJ/mol. The presence of CO<sub>2</sub> had little effect on the activation energy of reaction 4, but it could reduce the heat release from 99.73 kJ/mol to 90.22 kJ/mol. The effect of CO<sub>2</sub> on the activation energy and heat change of reaction 5 was more prominent: the activation energy increased from 48.55 kJ/mol to 61.49 kJ/mol and the heat absorption increased from 26.29 kJ/mol to 49.21 kJ/mol. The detailed heat change is shown in Figure 17.

To sum up, CO<sub>2</sub> had no significant effect on reaction 1 or reaction 4, it reduced the exothermic heat of reaction 2, thereby affecting the subsequent reaction process, and it promoted reaction 3 and hindered reaction 5.

It can be seen from the above that the injection of CO<sub>2</sub> will increase the carboxyl and aldehyde groups in the coal. According to the simulation results, this can be explained by CO<sub>2</sub> having a weak effect on the reaction of hydroxyl radicals and hindering the generation



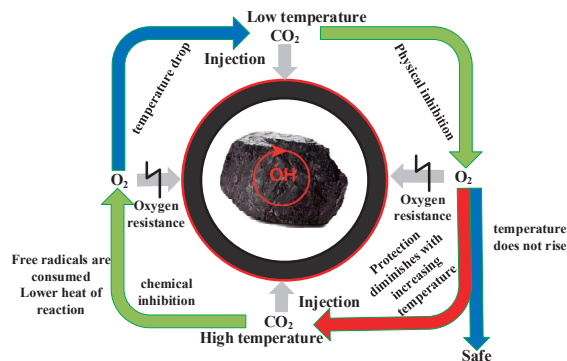
of CO, thus reducing the consumption of the above functional groups. CO<sub>2</sub> hinders the chemical adsorption reaction between O<sub>2</sub> and coal surface molecules, resulting in the inability of the continuous generation of hydroxyl radicals, thus playing a role in chemical inhibition. On the whole, CO<sub>2</sub> has an inhibitory effect on the reaction of coal chemical adsorption of O<sub>2</sub>.



**Figure 17.** Changes in reaction energy in the absence and presence of CO<sub>2</sub>.

### 3.3. Construction of the Model of CO<sub>2</sub> Prevents O<sub>2</sub> Adsorption

It can be seen from the above that CO<sub>2</sub> inhibited oxygen adsorption during the low-temperature oxidation of coal, and this effect included physical inhibition and chemical inhibition. Additionally, according to the experimental results and molecular simulation results, it was found that the effect of CO<sub>2</sub> on preventing O<sub>2</sub> adsorption was also different in the different stages of low-temperature coal oxidation. Therefore, the model of CO<sub>2</sub> physical–chemical inhibition of O<sub>2</sub> adsorption was established as shown in Figure 18.



**Figure 18.** The model of CO<sub>2</sub> physical–chemical prevention of O<sub>2</sub> adsorption.

At low temperatures, injecting CO<sub>2</sub> into the coal can form a protective layer on the surface of the coal, thereby blocking the contact between the coal and O<sub>2</sub>, and achieving the effect of inhibiting the low-temperature oxidation of the coal. At the same time, it can also replace the O<sub>2</sub> adsorbed on the coal surface, resulting in physical inhibition. However, it was found through experiments that when the temperature rose to the point of slow chemical adsorption, CO<sub>2</sub> lost its protective effect on the coal surface, and the coal and O<sub>2</sub> produced low-temperature oxidation after interacting again, resulting in an increase in the heating rate of coal. When coal temperature rises, a chemical adsorption chain reaction

is formed inside the coal. The injection of CO<sub>2</sub> at a high temperature will dilute the O<sub>2</sub> concentration in the coal, thereby reducing the chemical adsorption reaction between coal and O<sub>2</sub>, and at the same time increasing the activation energy and reducing the reaction heat. This creates a chemical inhibition. At the same time, due to the reduction of the coal chemical adsorption oxygen reaction, the free radicals cannot be generated and are continuously consumed, which slows down the low-temperature oxidation reaction process of coal and reduces the heat release. This achieves the effect of preventing the reaction from occurring.

#### 4. Conclusions

- (1) The adsorption capacity of coal pores for CO<sub>2</sub> is stronger than that of O<sub>2</sub>. CO<sub>2</sub> tends to be adsorbed near the pore wall and O<sub>2</sub> tends to be adsorbed in the center of the pores. Moreover, CO<sub>2</sub> can replace O<sub>2</sub> adsorbed in coal, and the replacement mostly occurs in the area near the pore wall.
- (2) The injection of CO<sub>2</sub> can block the adsorption of O<sub>2</sub> in the low-temperature oxidation process of coal, its hindering effect is mainly exerted in the slow heating stage, and at about 120 °C, the coal loses the protective effect of CO<sub>2</sub>.
- (3) When coal is cooled in a CO<sub>2</sub> atmosphere, the coal will mainly undergo pyrolysis and condensation reactions, which eventually leads to the increase in -CH=O and -COOH in the coal, and the changes in other structures are small.
- (4) In the chemisorption chain reaction of coal oxide, the effect of CO<sub>2</sub> on each step of the reaction chain is not the same, but in general, it increases the activation energy and reduces the heat release, which has the effect of inhibiting the chemical reaction.
- (5) In this paper, the model of carbon dioxide physical–chemical oxygen barrier adsorption is constructed based on experiments and simulations, which lacks field practice verification. However, the research in this paper can guide the work and improve the efficiency of underground fire prevention in coal mines and save labor, time, and material resources.

**Author Contributions:** G.C. writing original draft, experiments and simulation methods and data arrangement; H.W. provide coal sample and editing. B.T. writing review; S.F. simulating that the coal adsorbs oxygen. All authors have read and agreed to the published version of the manuscript.

**Funding:** This research was supported by the National Natural Science Foundation of China (52074156, 51804355, 51864045, 51774291), the Fundamental Research Funds for the Central Universities (2022YJSAQ13), Introduction Plan for “Tianchi Talent” in Xinjiang Uygur Autonomous Region.

**Institutional Review Board Statement:** Not applicable.

**Informed Consent Statement:** Not applicable.

**Data Availability Statement:** Not applicable.

**Conflicts of Interest:** The authors declare no conflict of interest.

#### References

1. Song, Z.; Kuenzer, C.; Zhu, H.; Zhang, Z.; Jia, Y.; Sun, Y.; Zhang, J. Analysis of coal fire dynamics in the Wuda syncline impacted by fire-fighting activities based on in-situ observations and Landsat-8 remote sensing data. *Int. J. Coal. Geol.* **2015**, *141–142*, 91–102. [CrossRef]
2. Liu, J.; Wang, Y.; Yan, S.; Zhao, F.; Li, Y.; Dang, L.; Liu, X.; Shao, Y.; Peng, B. Underground Coal Fire Detection and Monitoring Based on Landsat-8 and Sentinel-1 Data Sets in Miquan Fire Area, XinJiang. *Remote Sens.* **2021**, *13*, 1141. [CrossRef]
3. Tan, B.; Zhang, F.; Zhang, Q.; Wei, H.; Shao, Z. Firefighting of subsurface coal fires with comprehensive techniques for detection and control: A case study of the Fukang coal fire in the Xinjiang region of China. *Environ. Sci. Pollut. Res.* **2019**, *26*, 29570–29584. [CrossRef] [PubMed]
4. Wang, T.; Wang, Y.; Zhao, F.; Feng, H.; Liu, J.; Zhang, L.; Zhang, N.; Yuan, G.; Wang, D. A spatio-temporal temperature-based thresholding algorithm for underground coal fire detection with satellite thermal infrared and radar remote sensing. *Int. J. Appl. Earth Obs. Geoinf.* **2022**, *110*, 102805. [CrossRef]

5. Song, Z.; Kuenzer, C. Coal fires in China over the last decade: A comprehensive review. *Int. J. Coal. Geol.* **2014**, *133*, 72–99. [CrossRef]
6. Shao, Z.; Jia, X.; Zhong, X.; Wang, D.; Wei, J.; Wang, Y.; Chen, L. Detection, extinguishing, and monitoring of a coal fire in Xinjiang, China. *Environ. Sci. Pollut. Res.* **2018**, *25*, 26603–26616. [CrossRef] [PubMed]
7. Wang, Y.; Ge, S.; Guo, G. (Eds.) *Mining Science and Technology: Proceedings of the 5th International Symposium on Mining Science and Technology, Xuzhou, China, 20–22 October 2004*; CRC Press: Boca Raton, FL, USA, 2004.
8. Wang, H.; Dlugogorski, B.; Kennedy, E. Kinetic modeling of low-temperature oxidation of coal. *Combust. Flame* **2002**, *131*, 452–464. [CrossRef]
9. Tan, B.; Cheng, G.; Zhu, X.; Yang, X. Experimental Study on the Physisorption Characteristics of O<sub>2</sub> in Coal Powder are Effected by Coal Nanopore Structure. *Sci. Rep.* **2020**, *10*, 6946. [CrossRef]
10. Karsner, G.G.; Perlmutter, D.D. Model for coal oxidation kinetics. 1. Reaction under chemical control. *Fuel* **1982**, *61*, 29–34. [CrossRef]
11. Wang, H.; Dlugogorski, B.Z.; Kennedy, E.M. Coal oxidation at low temperatures: Oxygen consumption, oxidation products, reaction mechanism and kinetic modelling. *Prog. Energy Combust. Sci.* **2003**, *29*, 487–513. [CrossRef]
12. Xue, D.; Hu, X.; Cheng, W.; Wu, M.; Shao, Z.; Li, Y.; Zhao, Y.; Zhang, K. Carbon dioxide sealing-based inhibition of coal spontaneous combustion: A temperature-sensitive micro-encapsulated fire-retardant foamed gel. *Fuel* **2020**, *266*, 117036. [CrossRef]
13. Liu, Y.; Wen, H.; Guo, J.; Jin, Y.; Wei, G.; Yang, Z. Coal spontaneous combustion and N<sub>2</sub> suppression in triple goafs: A numerical simulation and experimental study. *Fuel* **2020**, *271*, 117625. [CrossRef]
14. Zhang, Y.; Xu, J.; Wang, D. Experimental Study on the Inhibition Effects of Nitrogen and Carbon Dioxide on Coal Spontaneous Combustion. *Energies* **2020**, *13*, 5256. [CrossRef]
15. Deng, J.; Ren, L.F.; Ma, L.; Qin, X.Y.; Wang, W.F.; Liu, C.C. Low-temperature oxidation and reactivity of coal in O<sub>2</sub>/N<sub>2</sub> and O<sub>2</sub>/CO<sub>2</sub> atmospheres, a case of carboniferous-permian coal in Shaanxi, China. *Environ. Earth Sci.* **2019**, *78*, 234. [CrossRef]
16. Khatami, R.; Stivers, C.; Levendis, Y.A. Ignition characteristics of single coal particles from three different ranks in O<sub>2</sub>/N<sub>2</sub> and O<sub>2</sub>/CO<sub>2</sub> atmospheres. *Combust. Flame* **2012**, *159*, 3554–3568. [CrossRef]
17. Wang, F.; Liu, H.W. Comparative experiment study on fire prevention and extinguishing in goaf by N<sub>2</sub>-water mist and CO<sub>2</sub>-water mist. *Arab. J. Geosci.* **2020**, *13*, 856. [CrossRef]
18. Liu, W.; Chu, X.; Xu, H.; Chen, W.; Ma, L.; Qin, Y.; Wei, J. Oxidation reaction constants for coal spontaneous combustion under inert gas environments: An experimental investigation. *Energy* **2022**, *247*, 123457. [CrossRef]
19. Su, H.; Kang, N.; Shi, B.; Ji, H.; Li, Y.; Shi, J. Simultaneous thermal analysis on the dynamical oxygen-lean combustion behaviors of coal in a O<sub>2</sub>/N<sub>2</sub>/CO<sub>2</sub> atmosphere. *J. Energy Inst.* **2021**, *96*, 128–139. [CrossRef]
20. Liu, H.W.; Wang, F. Thermal characteristics and kinetic analysis of coal-oxygen reaction under the condition of inert gas. *Int. J. Coal Prep. Util.* **2022**, *42*, 846–862. [CrossRef]
21. Wu, L.; Qiao, Y.; Yao, H. Experimental and numerical study of pulverized bituminous coal ignition characteristics in O<sub>2</sub>/N<sub>2</sub> and O<sub>2</sub>/CO<sub>2</sub> atmospheres. *Asia-Pac. J. Chem. Eng.* **2012**, *7*, S195–S200. [CrossRef]
22. Li, Q.; Zhao, C.; Chen, X.; Wu, W.; Lin, B. Properties of char particles obtained under O<sub>2</sub>/N<sub>2</sub> and O<sub>2</sub>/CO<sub>2</sub> combustion environments. *Chem. Eng. Process. Process Intensif.* **2010**, *49*, 449–459. [CrossRef]
23. Ma, L.; Yu, W.; Ren, L.; Qin, X.; Wang, Q. Micro-characteristics of low-temperature coal oxidation in CO<sub>2</sub>/O<sub>2</sub> and N<sub>2</sub>/O<sub>2</sub> atmospheres. *Fuel* **2019**, *246*, 259–267. [CrossRef]
24. Zhou, B.; Yang, S.; Yang, W.; Jiang, X.; Song, W.; Cai, J.; Xu, Q.; Tang, Z. Variation characteristics of active groups and macroscopic gas products during low-temperature oxidation of coal under the action of inert gases N<sub>2</sub> and CO<sub>2</sub>. *Fuel* **2022**, *307*, 121893. [CrossRef]
25. Wu, S.; Jin, Z.; Deng, C. Molecular simulation of coal-fired plant flue gas competitive adsorption and diffusion on coal. *Fuel* **2019**, *239*, 87–96. [CrossRef]
26. Zhang, J.; Wang, J.; Zhang, C.; Li, Z.; Zhu, J.; Lu, B. Molecular simulation of gases competitive adsorption in lignite and analysis of original CO desorption. *Sci. Rep.* **2021**, *11*, 11706. [CrossRef] [PubMed]
27. Long, H.; Lin, H.F.; Yan, M.; Bai, Y.; Tong, X.; Kong, X.G.; Li, S.G. Adsorption and diffusion characteristics of CH<sub>4</sub>, CO<sub>2</sub>, and N<sub>2</sub> in micropores and mesopores of bituminous coal: Molecular dynamics. *Fuel* **2021**, *292*, 120268. [CrossRef]
28. Dong, X.; Wang, F.; Guo, L.; Zhang, Y.; Dong, X. Investigation of Competitive Adsorption Properties of CO/CO<sub>2</sub>/O<sub>2</sub> onto the Kailuan Coals by Molecular Simulation. *ACS Omega* **2022**, *7*, 19305–19318. [CrossRef]
29. Liu, Y.; Fu, P.; Bie, K.; Gong, Y.; Xu, T. The intrinsic reactivity of coal char conversion compared under different conditions of O<sub>2</sub>/CO<sub>2</sub>, O<sub>2</sub>/H<sub>2</sub>O and air atmospheres. *J. Energy Inst.* **2020**, *93*, 1883–1891. [CrossRef]
30. Liu, M.-X.; Shi, G.-Q.; Guo, Z.; Wang, Y.-M.; Ma, L.-Y. 3-D simulation of gases transport under condition of inert gas injection into goaf. *Heat Mass Transf.* **2016**, *52*, 2723–2734. [CrossRef]
31. Yan, F.; Xu, J.; Peng, S.; Zou, Q.; Zhou, B.; Long, K.; Zhao, Z. Breakdown process and fragmentation characteristics of anthracite subjected to high-voltage electrical pulses treatment. *Fuel* **2020**, *275*, 117926. [CrossRef]
32. Yan, F.; Xu, J.; Lin, B.; Peng, S.; Zou, Q.; Zhang, X. Changes in pore structure and permeability of anthracite coal before and after high-voltage electrical pulses treatment. *Powder Technol.* **2019**, *343*, 560–567. [CrossRef]
33. Ren, J.; Song, Z.; Li, B.; Liu, J.; Lv, R.; Liu, G. Structure feature and evolution mechanism of pores in different metamorphism and deformation coals. *Fuel* **2021**, *283*, 119292. [CrossRef]

34. Kamran, U.; Rhee, K.Y.; Park, S.-J. Effect of Triblock Copolymer on Carbon-Based Boron Nitride Whiskers for Efficient CO<sub>2</sub> Adsorption. *Polymers* **2019**, *11*, 913. [CrossRef] [PubMed]
35. Kamran, U.; Rhee, K.Y.; Lee, S.Y.; Park, S.J. Solvent-free conversion of cucumber peels to N-doped microporous carbons for efficient CO<sub>2</sub> capture performance. *J. Clean. Prod.* **2022**, *369*, 133367. [CrossRef]
36. Kamran, U.; Park, S.J. Acetic acid-mediated cellulose-based carbons: Influence of activation conditions on textural features and carbon dioxide uptakes. *J. Colloid Interface Sci.* **2021**, *594*, 745–758. [CrossRef]
37. Fu, S.; Tan, B.; Cheng, G.; Wang, H.; Fang, X.; Shao, Z.; Li, Z. Study of Adsorption Characteristics of CO<sub>2</sub>, O<sub>2</sub>, and N<sub>2</sub> in Coal Micropores and Mesopores at Normal Pressure. *Ind. Eng. Chem. Res.* **2022**, *61*, 12845–12856. [CrossRef]
38. Bai, Y.; Lin, H.-F.; Li, S.-G.; Yan, M.; Long, H. Molecular simulation of N<sub>2</sub> and CO<sub>2</sub> injection into a coal model containing adsorbed methane at different temperatures. *Energy* **2021**, *219*, 119686. [CrossRef]
39. Cheng, G.; Tan, B.; Zhang, Z.; Fu, S.; Haiyan, W.; Wang, F. Characteristics of coal-oxygen chemisorption at the low-temperature oxidation stage: DFT and experimental study. *Fuel* **2022**, *315*, 123120. [CrossRef]
40. Zhu, H.; Huo, Y.; Wang, W.; He, X.; Fang, S.; Zhang, Y. Quantum chemical calculation of reaction characteristics of hydroxyl at different positions during coal spontaneous combustion. *Process Saf. Environ. Prot.* **2021**, *148*, 624–635. [CrossRef]
41. Chen, Q.; Zheng, J.; Xu, J.; Dang, Z.; Zhang, L. Insights into sulfamethazine adsorption interfacial interaction mechanism on mesoporous cellulose biochar: Coupling DFT/FOT simulations with experiments. *Chem. Eng. J.* **2019**, *356*, 341–349. [CrossRef]

**Disclaimer/Publisher’s Note:** The statements, opinions and data contained in all publications are solely those of the individual author(s) and contributor(s) and not of MDPI and/or the editor(s). MDPI and/or the editor(s) disclaim responsibility for any injury to people or property resulting from any ideas, methods, instructions or products referred to in the content.

## Article

# Research on the Evaluation of Emergency Management Synergy Capability of Coal Mines Based on the Entropy Weight Matter-Element Extension Model

Chaolun Sun <sup>1,2,3</sup>, Yu Hao <sup>1,3,\*</sup>, Jianping Wei <sup>2</sup> and Lijun Zhang <sup>1,3</sup>

<sup>1</sup> Emergency Management School, Henan Polytechnic University, Jiaozuo 454000, China; suncl@hpu.edu.cn (C.S.); zli13849117460@163.com (L.Z.)

<sup>2</sup> State Key Laboratory Cultivation Base for Gas Geology and Gas Control, Henan Polytechnic University, Jiaozuo 454000, China; weijianping@hpu.edu.cn

<sup>3</sup> Safety and Emergency Management Research Center, Henan Polytechnic University, Jiaozuo 454000, China

\* Correspondence: haoyu\_he@163.com

**Abstract:** Emergency management synergy capability is not only a “touchstone” to measure the operation effect of the emergency system of coal mine enterprises, it is an important symbol to reflect its level. In order to improve the level of emergency management in coal mines based on the PPRR theory of crisis management cycle, in this paper a hierarchical evaluation index system is constructed based on the emergency management process. A quantitative evaluation model of emergency synergy capacity is proposed based on the entropy-weighted elemental topology method to conduct evaluation and model validation for the case of J coal mine in Henan Province. The results show that the overall evaluation of the emergency management synergy capability of J Coal Mine is at a “good” level, with the emergency prevention synergy capability, emergency preparedness synergy capability, and recovery and reconstruction synergy capability at a “good” level and the emergency response synergy capability is at a “average” level. This indicates that the evaluation model is consistent with the current development of coal mining enterprises and has universal applicability. Therefore, this research can provide decision-making support for emergency management synergistic capacity building of coal mining enterprises to enhance the inherent driving force behind the early completion of the dual carbon task in the coal mining industry.

**Keywords:** coal mine accident; emergency coordination; the entropy weight matter-element extension model; level of emergency management; evaluation system

**Citation:** Sun, C.; Hao, Y.; Wei, J.; Zhang, L. Research on the Evaluation of Emergency Management Synergy Capability of Coal Mines Based on the Entropy Weight Matter-Element Extension Model. *Processes* **2023**, *11*, 2492. <https://doi.org/10.3390/pr11082492>

Academic Editor: Carlos Sierra Fernández

Received: 27 July 2023

Revised: 13 August 2023

Accepted: 16 August 2023

Published: 19 August 2023



**Copyright:** © 2023 by the authors. Licensee MDPI, Basel, Switzerland. This article is an open access article distributed under the terms and conditions of the Creative Commons Attribution (CC BY) license (<https://creativecommons.org/licenses/by/4.0/>).

## 1. Introduction

With carbon neutrality being one of the important topics of China’s Twentieth Congress, in-depth exploration of the emission reduction potential of coal mining enterprises will be an important contribution [1]. As an indispensable part of carbon reduction, the effective evaluation of the emergency synergistic capability of coal mining enterprises will greatly enhance the overall work efficiency of coal mining enterprises and enhance the coal mining industry’s early completion of the internal driving force behind the dual carbon task. Due to the complexity and variability of coal mining systems, emergency response capabilities are very important to coal mining enterprises. Effective accident prevention goes hand in hand with being able to handle crises, disasters, and post-disaster rehabilitation. Comprehensive assessment of the emergency response capability of coal mining enterprises is an effective way to ensure that coal mining enterprises have good emergency response capability.

With the continuous aging of coal mines and increasing mining depth, coal mines in China have to tackle a growing number of risk factors and a more severe emergency management situation in the production process [2]. In the face of unexpected disasters and accidents, a coal mine emergency management system is capable of minimizing property

losses and casualties only if it responds quickly and if all of its subsystem emergency synergy capabilities function correctly and in unison. Therefore, the construction and evaluation of an emergency management synergy (hereinafter referred to as EMS) system has become a core issue.

In recent years, emergency synergy has been highly valued by emergency management and has become a focus of emerging research on disaster risk management as a security discipline [3]. Compared with Chinese coal mines, foreign ones have a much lower accident rate due to their objective advantages in terms of mechanization level and coal seam conditions. As a result, emergency synergy capability has only been reported in few studies abroad, although research results have been yielded over a long span of time. In the early stage, Ikeda et al. employed advanced communication technology to support emergency rescue and proposed an emergency rescue model [4]. In recent years, wireless sensing communication technology has greatly improved the emergency management level of coal mine accidents [5]. In addition to improving the incidence of coal mine accidents at various technical levels [6,7], the organizational management factors of coal mine accidents are gradually being paid attention to. Yeo and Comfort believed that the emergency organization synergy network is highly fragmented and presents weak horizontal and vertical interconnections [8]. Schipper et al. studied the interaction in emergency response actions and the information communication between different subjects. In the hope of preventing and reducing the occurrence of coal mine accidents [9], Kinilakodi and Grayson strengthened emergency synergy capability by introducing the reliability method [10].

At present, emergency synergy capability of coal mines has not been extensively explored in China; the main representative studies are as follows. Hu studied the synergy between state-owned and local coal mines, emphasizing the necessity of signing synergy agreements between them [11]. Kong elaborated the necessity of strengthening the construction of disaster emergency rescue systems of coal mines in various regions [12]. Yang analyzed the current situation of coal mine disaster rescue and whether the establishment of mine rescue team cooperation is effective in solving coal mine emergency synergy capability [13]. Liang et al. used the AHP–fuzzy evaluation method to carry out grading evaluation of the coal mine emergency rescue capacity [14]. Qi et al. discussed the coal mine emergency synergy capability system and capability in China [15–17]. Wang et al. analyzed an evolutionary game among emergency synergy capability subjects according to evolutionary game theory and the numerical simulation method [18], while Shi et al. focused on an evolution game between coal mining enterprises and local governments [19]. Yang et al. divided the development and evolution process of coal mine emergency management capability into four stages, i.e., the initial stage, the growth stage, the maturity stage, and the stability stage; they then comprehensively analyzed and evaluated the emergency capability of a coal mining enterprise using the logistic curve [20]. Lan et al. evaluated the emergency rescue capability of coal mine emergencies according to the RS-IPA method; their results were consistent with the actual rescue level of the enterprises [21]. Cheng et al. established a calculation model for the maturity of coal mine emergency rescue capability and introduced the improved catastrophe progression method to calculate the maturity of coal mine emergency rescue capability [22]. Yang used Unity 3D to integrate the coal mine emergency and rescue drill systems in order to improve emergency rescue capability in coal mine emergency coordination [23].

In summary, emergency management synergy has become a hot spot and focus of current theoretical research. Many scholars have presented different research perspectives to study emergency collaboration [24–26]. However, current research concerning coal mine emergency-related aspects remains shallow, and there is a lack of perfect system models. In addition, evaluations of the emergency synergy capability of coal mine enterprises have mostly adopted qualitative methods and focused their analysis on the level, elements, and connotations of the emergency synergy capability system. Few scholars have quantitatively analyzed and measured the emergency synergy capability of coal mine enterprises on the ground of an emergency synergy capability system. Therefore, from the perspective of

synergy, in this study we built an index system and evaluation model of the emergency synergy capability of coal mine enterprises with reference to the matter-element extension theory. We selected a coal mine for use in an empirical case study. The results of our analysis lead to practical suggestions for rectification. These research results are expected to provide a relevant reference for improving the emergency synergy capability and level of coal mines. However, it is challenging to assess the emergency synergy capacity of coal mining businesses; several visits and professional guidance will be required in the future. In addition, the universality of the index system and the evaluation model obtained from the previous research results in the actual coal mine safety production has also met the challenge. Further improvements to the evaluation system are necessary in order to achieve the purpose applicable to the daily management decisions of all kinds of coal mining enterprises.

## 2. Evaluation Index System Construction and Classification of EMS Capability

### 2.1. Connotation of EMS Capability

The emergency synergy capability system, which is a collection of synergic relationships between the environment and the system, refers to various resources, organizations, processes, plans, personnel, and their interrelationships that are involved when coal mine enterprises respond to unexpected disasters and accidents. It is a multi-linked, nonlinear, and long-span system that runs through the four stages (i.e., preparation, prevention, response and recovery) of the emergency management life cycle. Specifically, the subsystem emergency synergy capabilities work independently and the synergy state is unordered in the production and management of coal mine companies in the absence of unanticipated disasters and accidents. The emergency synergy capability system's status changes instantly in the event of sudden disasters and accidents, and the supporting emergency synergy capability works properly and harmoniously to achieve synergistic management. Considering that the emergency synergy capability is both a "touchstone" to measure the operation effect of the emergency synergy capability system and an important symbol to reflect the emergency synergy capability and level, it was employed in this study to measure the synergic effect of the emergency synergy capability system of coal mine enterprises.

### 2.2. Construction of the Evaluation Index System of EMS Capability

Mining accidents are sudden, serious, and random, and may cause serious casualties and economic losses. Therefore, the focus of emergency management in mining enterprises is to prevent accidents and reduce economic losses. Referring to the theory of PPRR put forward by the U.S. Federal Safety Commission, the emergency management process is divided into four stages: emergency prevention, emergency preparedness, emergency response, and emergency recovery. These four stages together form the dynamic cycle of the emergency management process. Based on the PPRR theory, this paper establishes four main indexes: emergency prevention synergy, emergency preparedness synergy, emergency response synergy, and emergency recovery synergy. It is found that complete and mature basic information data management is the link of communication and cooperation between the subjects of emergency management [27]. It is a prerequisite to better play the preventive role of periodic safety inspection, identify risks in a timely manner, and implement monitoring and control [28,29]. At the same time, this emergency management work more needs supporting emergency management mechanisms along with emergency management laws and regulations, supports and guarantees [30]. On the basis of this, third-level evaluation indicators such as safety prevention inspection, identification of major hazard sources, monitoring and control of hazard sources, institution-building for emergency management, emergency management regulations, and operator safety education were compiled and screened from the literature (As shown in Table 1). Relevant experts in the field of emergency response in coal mines were consulted on the selection of indicators and the ranking of importance in the tables. This selection process was followed for all indicators in Table 1.

**Table 1.** Evaluation index system of EMS capability of coal mine enterprises.

Evaluation Objectives	First-Level Evaluation Index Factors	Second-Level Evaluation Index Factors
EMS capability of coal mine enterprises(C)	Emergency prevention capability (C <sub>1</sub> )	Completeness of basic data management C <sub>11</sub> ; Safety prevention inspection C <sub>12</sub> ; Identification of major hazard sources C <sub>13</sub> ; Hazard source monitoring and control C <sub>14</sub> ; Emergency management organization Construction C <sub>15</sub> ; Emergency management laws and regulations C <sub>16</sub> ; Safety education for operators C <sub>17</sub>
	Emergency preparation capability (C <sub>2</sub> )	Emergency rescue team construction C <sub>21</sub> ; Emergency rescue plan preparation C <sub>22</sub> ; Implementation of emergency drills C <sub>23</sub> ; Emergency supplies reserve C <sub>24</sub> ; Emergency aid equipment and technology C <sub>25</sub> ; Emergency rescue mutual aid agreement C <sub>26</sub>
	Emergency response capability (C <sub>3</sub> )	Emergency rescue response speed C <sub>31</sub> ; Emergency plan activation C <sub>32</sub> ; Emergency decision-making and command C <sub>33</sub> ; Emergency material allocation C <sub>34</sub> ; Synergy with government departments C <sub>35</sub> ; Synergy with relevant units C <sub>36</sub> ; Synergy with media C <sub>37</sub>
	Emergency recovery capability (C <sub>4</sub> )	Post analysis and summary C <sub>41</sub> ; Recovery and reconstruction C <sub>42</sub> ; Post emergency plan improvement C <sub>43</sub> ; Post emergency rescue system improvement C <sub>44</sub>

### 2.3. Classification of EMS Capability

In view of the connotations of the EMS capability of coal mine enterprises, in this paper we used [0, 1] as the value range of variables of the EMS capability level and divided the coal mine emergency (CME) capability into five levels in accordance with the standard of the five-level evaluation method and expert opinions (Table 2).

**Table 2.** Grading standard for the EMS capability of coal mine enterprises.

Evaluation Result	Level	Eigenvalue Interval
Excellent	I	(0.8, 1.0]
Good	II	(0.6, 0.8]
Average	III	(0.4, 0.6]
Poor	IV	(0.2, 0.4]
Bad	V	[0, 0.2]

## 3. Construction of the Entropy Weight Matter-Element Extension Model

### 3.1. Determination of Classical Field, Joint Domain and Matter-Element to Be Evaluated

The matter-element extension theory can integrate the information of various factors in the emergency synergy system, transform the indexes of the problem to be evaluated into a compatibility problem, and finally express the evaluation results in quantitative numerical values. In this way, the level of emergency synergy capability of coal mine enterprises can be evaluated completely and objectively. The specific process is introduced as follows.

#### 3.1.1. Determination of Classical Field

A matter element, also referred to as an ordered triple, generally includes matter, characteristics, and values [31]. The three elements are arranged in a fixed order and



expressed as  $H = (\text{matter } N, \text{characteristic } C, \text{value } V)$ . Therefore, the classical field can be expressed as follows:

$$H_j = (N_j, C_i, V_{ji}) = \begin{bmatrix} N_j & C_1 & V_{j1} \\ & C_2 & V_{j2} \\ \dots & \dots & \dots \\ & C_n & V_{jn} \end{bmatrix} = \begin{bmatrix} N_j & C_1 & (a_{j1}, b_{j1}) \\ & C_2 & (a_{j2}, b_{j2}) \\ \dots & \dots & \dots \\ & C_n & (a_{jn}, b_{jn}) \end{bmatrix} \quad (1)$$

In Formula (1),  $H_j$  is the classic domain, representing the value range of each evaluation index when the emergency synergies of coal mining enterprises are located at a certain level;  $N_j$  ( $j = 1, 2, 3 \dots m$ ) indicates the coal mining enterprises emergency synergy capacity of the  $J$  evaluation level, belongs to the evaluation level;  $C_i$  ( $i = 1, 2, 3 \dots n$ ) is different eigenvalues of  $N_j$ , which belongs to the evaluation index;  $V_{jn}$  indicates the range of values for the  $n$  feature indicator in the  $j$  rank; and  $(a_{ji}, b_{ji})$  is the range of values of classical matter-element parameters,  $a_{ji}$  being the minimum value and  $b_{ji}$  being the maximum value. Moreover,  $i$  is introduced to explain the different eigenvalues expressed by indicators  $C_i$ , which belong to the evaluation indicators;  $j$  indicates each evaluation level of the emergency synergistic capability of coal mining enterprises, such as the range of values of the  $n$  feature index in the  $j$  grade; and  $n$  represents a subsequent taking of the associated value.

### 3.1.2. Determination of Joint Domain

Assuming that the joint domain of emergency synergy capability is  $H_p$ , it can be expressed as

$$H_p = (N_p, C_i, V_{pi}) = \begin{bmatrix} N_p & C_1 & V_{p1} \\ & C_2 & V_{p2} \\ \dots & \dots & \dots \\ & C_i & V_{pi} \end{bmatrix} = \begin{bmatrix} N_p & C_1 & (a_{p1}, b_{p1}) \\ & C_2 & (a_{p2}, b_{p2}) \\ \dots & \dots & \dots \\ & C_i & (a_{pi}, b_{pi}) \end{bmatrix} \quad (2)$$

where  $H_p$  is the joint domain matter-element, representing the combination of the classical field and the overall range;  $N_p$  is all levels of the object to be evaluated;  $V_{pi}$  is the range of value of  $C_i$  corresponding to each level  $N_p$ ; and  $V_{ji} \subset V_{pi}$ ;  $i$  is the number of second-level indexes.

### 3.1.3. Determination of Matter-Element to Be Evaluated

$$H_0 = (N_0, C_i, V_i) = \begin{bmatrix} N_0 & C_1 & V_1 \\ & C_2 & V_2 \\ \dots & \dots & \dots \\ & C_n & V_n \end{bmatrix} \quad (3)$$

where  $H_0$  is the matter-element to be evaluated;  $N_0$  is the evaluation level;  $C_i$  is the index to be evaluated; and  $V_i$  is the measured value of the index to be evaluated.

## 3.2. Determination of Weights of Indexes

To enhance the accuracy and objectivity of index weight assignment, the entropy method is adopted to determine the weight of the index system. The calculation steps are as follows:

(1) Calculate the proportion of the  $i$ th object in the  $j$ th index:

$$\theta_{ji} = \frac{x_{ji}}{\sum_{i=1}^n x_{ji}} \quad (i = 1, 2, 3 \dots m, j = 1, 2, \dots n) \quad (4)$$

- (2) Calculate the entropy value of the  $j$ th index. Set  $e_j$  as the entropy value of the  $j$ th evaluation index; the calculation process is:

$$e_j = -\frac{1}{\ln m} \sum_{i=1}^m (\theta_{ji} x_{ji}), \quad e_j \in [0, 1] \quad (5)$$

- (3) Calculate the coefficient of variation:

$$g_j = 1 - e_j \quad (6)$$

- (4) Calculate the weight of the index  $j$ :

$$\theta_{ji} = \frac{g_j}{\sum_{j=1}^n g_j} \quad (7)$$

### 3.3. Determination of Correlation Degree and Evaluation Level

#### 3.3.1. Determination of Correlation Degree

The correlation degree refers to the degree of correlation between two things; a higher correlation degree means that the two things are correlated more closely. The correlation function is a functional relation expression used to represent the degree of correlation between the objective to be evaluated and a standard evaluation value. It is generally expressed by the correlation function value defined by the moment. The formulas for calculating the correlation degree of a single index are as follows:

$$K_j(V_i) = \begin{cases} \frac{-\rho(V_i, V_{ij})}{|V_{ij}|}, & V_i \in V_{ij} \\ \frac{\rho(V_i, V_{ij})}{\rho(V_i, V_{pi}) - \rho(V_i, V_{ji})}, & V_i \notin V_{ij} \end{cases} \quad (8)$$

$$\rho(v_i, V_{ji}) = \left| V_i - \frac{a_{ji} + b_{ji}}{2} \right| - \frac{b_{ji} - a_{ji}}{2} \quad (9)$$

$$\rho(v_i, V_{pi}) = \left| V_i - \frac{a_{pi} + b_{pi}}{2} \right| - \frac{b_{pi} - a_{pi}}{2} \quad (10)$$

In Equation (8),  $K_j(V_i)$  is the correlation degree of a single index;  $\rho(v_i, V_{ji})$  is the distance between the point  $v_i$  and the classical field of the evaluation index; and  $\rho(v_i, V_{pi})$  is the distance between the point  $v_i$  and the joint domain.

After the correlation functions for individual first- and second-level indexes are obtained, the comprehensive correlation degree can be calculated in a sequential and recursive manner based on the evaluation indexes in accordance with the hierarchical structure. The formula for calculating the comprehensive index correlation is

$$K_j(N) = \sum_{i=1}^n \omega_i K_j(V_i) \quad (11)$$

where  $K_j(N)$  is the correlation degree of the target to be evaluated with the  $j$ th level;  $K_j(V_i)$  is the correlation degree of the index  $C_i$  to be evaluated with the risk level  $j$ ; and  $\omega_i$  is the weight of the evaluation index  $C_i$ . According to the affiliation relationship, the comprehensive correlation degree is more accurate and objective because it takes into account the degrees of influence of all evaluation indexes on the overall evaluation results.

#### 3.3.2. Determination of Evaluation Levels

The specific evaluation level of the evaluation object can be determined according to the comprehensive correlation degree. Assuming that the level of the object  $N$  is evaluated as  $m$ , then:

$$\overline{K_j(N)} = \frac{K_j(N) - \min K_j(N)}{\max K_j(N) - \min K_j(N)} \quad (12)$$

$$j^* = \frac{\sum_{j=1}^m j \overline{K_j(N)}}{\sum_{j=1}^m \overline{K_j(N)}} \quad (13)$$

where  $j^*$  is the eigenvalue of the variable of the emergency synergy capability level, that is, the degree to which the emergency synergy capability falls into this level. The deviation degree between the target to be evaluated and its adjacent emergency synergy capability level can be judged by  $j^*$ .

#### 4. Empirical Case Analysis

In this section, an empirical evaluation was conducted on J Coal Mine in Henan Province, China using the evaluation index system and model of the emergency synergy capability of coal mine enterprises constructed in the above section. The evaluation results verify the rationality of the theoretical model, which boasts strong practical significance.

##### 4.1. Data Sources and Collection

The research data came from relevant staff from various departments of J Coal Mine, including the safety and environmental protection supervision and management department, the production technology department, the ventilation management department, and the mechanical and electrical management department. A total of 185 questionnaires were issued, of which 180 were recovered. After eight invalid questionnaires were removed, the effective return rate was 92.97%.

##### 4.2. Determination of Evaluation Index Weight

Twenty experts in the fields of safe coal production and emergency management, including university researchers, leaders of government emergency management departments, and managers of coal mine enterprises, were invited to score the index weights using a Likert scale. The second-level evaluation index weights obtained after normalization are listed in Table 3.

**Table 3.** Evaluation index weights of emergency coordination capacity of coal mines.

Level 1 Indicator	Weighting of First-Level Indicators	Level 2 Indicator	Scores	Secondary Indicator Entropy Value	Secondary Indicator Weights
Emergency prevention synergy capability ( $C_1$ )	0.168	Completeness of basic data management $C_{11}$	88	0.0439	0.0286
		Safety prevention inspection $C_{12}$	86	0.1032	0.0223
		Identification of major hazard Sources $C_{13}$	72	0.0824	0.0256
		Hazard source monitoring and control $C_{14}$	89	0.0891	0.0236
		Emergency management organization Construction $C_{15}$	87	0.1552	0.0223
		laws and regulations $C_{16}$	85	0.1817	0.0237
		Safety education for operators $C_{17}$	77	0.1322	0.0219
Emergency preparation synergy capability ( $C_2$ )	0.335	Emergency rescue team construction $C_{21}$	75	0.0504	0.0491
		Emergency rescue plan preparation $C_{22}$	70	0.1276	0.0471
		Implementation of emergency drills $C_{23}$	68	0.0975	0.0494
		Emergency supplies reserve $C_{24}$	75	0.1228	0.0573
		Emergency aid equipment and technology $C_{25}$	75	0.0506	0.0852
		Emergency rescue mutual aid agreement $C_{26}$	64	0.1272	0.0469

Table 3. Cont.

Level 1 Indicator	Weighting of First-Level Indicators	Level 2 Indicator	Scores	Secondary Indicator Entropy Value	Secondary Indicator Weights
Emergency response synergy capability (C <sub>3</sub> )	0.338	Emergency rescue response speed C <sub>31</sub>	70	0.1082	0.0693
		Emergency plan activation C <sub>32</sub>	75	0.1325	0.0389
		Emergency decision-making and command C <sub>33</sub>	80	0.1789	0.0598
		Emergency material allocation C <sub>34</sub>	75	0.1278	0.0472
		Synergy with government departments C <sub>35</sub>	65	0.0976	0.0478
		Synergy with relevant units C <sub>36</sub>	68	0.1621	0.0381
		Synergy with media C <sub>37</sub>	65	0.1026	0.0369
Emergency recovery synergy capability (C <sub>4</sub> )	0.159	Post analysis and summary C <sub>41</sub>	85	0.1078	0.0375
		Recovery and reconstruction C <sub>42</sub>	75	0.1857	0.0482
		Post emergency plan improvement C <sub>43</sub>	70	0.1582	0.0365
		Post emergency rescue system improvement C <sub>44</sub>	80	0.1451	0.0368

4.3. Determination of Classical Field, Joint Domain, and Matter-Element to Be Evaluated

4.3.1. Determination of Classical Field

According to the five levels of emergency synergy capability established above, the classic field is determined as follows:

$$H_1(B_1) = (N_1, B_1, V_{1j}) = \begin{bmatrix} N_1 & B_{11} & [85, 100] \\ & B_{12} & [70, 85] \\ & B_{13} & [55, 70] \\ & B_{14} & [40, 55] \\ & B_{15} & [0, 40] \end{bmatrix}$$

The classical field matter-elements of other second-level indexes  $B_2$  and  $B_3 \dots B_7$  under the first-level index are determined in the same way; thus, their determination is not elaborated here.

4.3.2. Determination of Joint Domain

The joint domain is determined in a similar way as the classical field. With the above index as an example, if the union of score ranges of all five levels of the index  $B_1$  is  $[0, 100]$ , the joint domain can be obtained according to the definition of the joint domain:

$$H_p(B_1) = (N_p, B_1, V_{1p}) = \begin{bmatrix} N_p & B_{11} & [0, 100] \\ & B_{12} & [0, 100] \\ & \dots & \dots \\ & B_{15} & [0, 100] \end{bmatrix}$$

4.3.3. Determination of Matter-Element to Be Evaluated

According to the scores of various indexes of J Coal Mine in the questionnaire survey, it is confirmed that the matter-element to be evaluated is

$$H_1(B_1) = (N_1, B_1, V_{1j}) = \begin{bmatrix} N_1 & B_{11} & 88 \\ & B_{12} & 72 \\ & B_{13} & 63 \\ & B_{14} & 54 \\ & B_{15} & 39 \end{bmatrix}$$

4.4. Calculation of Correlation Degree

According to Equations (8)–(10), the correlation degrees of individual evaluation indexes at the two levels are calculated by Matlab 7.0 software. Subsequently, the com-

prehensive correlation degree is calculated. Taking the second-level index “completeness of basic data management” under the first-level evaluation index “emergency prevention capability” as an example, the correlation degrees of the indexes is calculated as follows:

$$\rho(v_1, V_{11}) = \left| 88 - \frac{85 + 100}{2} \right| - \frac{100 - 85}{2} = -3$$

$$\rho(v_1, V_{12}) = \left| 88 - \frac{70 + 85}{2} \right| - \frac{85 - 70}{2} = 3$$

$$\rho(v_1, V_{13}) = \left| 88 - \frac{55 + 70}{2} \right| - \frac{70 - 55}{2} = 18$$

$$\rho(v_1, V_{14}) = \left| 88 - \frac{40 + 55}{2} \right| - \frac{55 - 40}{2} = 33$$

$$\rho(v_1, V_{15}) = \left| 88 - \frac{0 + 40}{2} \right| - \frac{40 - 0}{2} = 48$$

$$\rho(v_1, V_{1p}) = \left| 88 - \frac{0 + 100}{2} \right| - \frac{100 - 0}{2} = -12$$

It can be calculated by Equations (8)–(10) that = 0.74610; = -0.74512; = -0.8284; = -0.4026; and = -0.5270.

The correlation degrees of all second-level indexes can be obtained by repeating the above steps. Afterwards, the comprehensive correlation degrees of the first-level indexes can be calculated by Equation (7); the results are shown in Tables 4 and 5.

**Table 4.** Correlation values of secondary indicators of emergency synergy capacity of coal mines.

Level 1 Indicators	Level 2 Indicators	Relevance				
		j = 1	j = 2	j = 3	j = 4	j = 5
Emergency prevention synergy capability (C <sub>1</sub> )	c <sub>11</sub>	0.746	0.745	0.828	0.403	0.527
	c <sub>12</sub>	0.356	0.059	0.452	0.307	0.472
	c <sub>13</sub>	0.253	0.452	0.268	0.504	0.638
	c <sub>14</sub>	0.300	0.290	0.472	0.512	0.560
	c <sub>15</sub>	0.322	0.210	0.360	0.482	0.243
	c <sub>16</sub>	0.737	0.650	0.547	0.052	0.045
	c <sub>17</sub>	0.086	0.027	0.813	0.750	0.625
Emergency preparation synergy capability (C <sub>2</sub> )	c <sub>21</sub>	0.255	0.061	0.925	0.910	0.850
	c <sub>22</sub>	0.079	0.016	0.776	0.100	0.312
	c <sub>21</sub>	0.025	0.185	0.093	0.916	0.045
	c <sub>22</sub>	0.038	0.230	0.712	0.617	0.415
	c <sub>23</sub>	0.119	0.153	0.812	0.750	0.625
	c <sub>24</sub>	0.096	0.936	0.915	0.900	0.750
	c <sub>25</sub>	0.875	0.833	0.750	0.500	0.167
c <sub>26</sub>	0.688	0.582	0.375	0.250	0.167	
Emergency response synergy capability (C <sub>3</sub> )	c <sub>31</sub>	0.186	0.260	0.585	0.866	0.128
	c <sub>32</sub>	0.495	0.625	0.390	0.278	0.095
	c <sub>33</sub>	0.712	0.592	0.308	0.820	0.918
	c <sub>34</sub>	0.038	0.626	0.538	0.732	0.829
	c <sub>35</sub>	0.498	0.600	0.308	0.762	0.810
	c <sub>36</sub>	0.766	0.029	0.198	0.646	0.828
	c <sub>37</sub>	0.351	0.782	0.324	0.566	0.914
	c <sub>38</sub>	0.403	0.780	0.306	0.642	0.788

Table 4. Cont.

Level 1 Indicators	Level 2 Indicators	Relevance				
		j = 1	j = 2	j = 3	j = 4	j = 5
Emergency recovery synergy capability (C <sub>4</sub> )	C <sub>41</sub>	0.875	0.832	0.753	0.500	0.489
	C <sub>42</sub>	0.625	0.612	0.258	0.480	0.250
	C <sub>43</sub>	0.870	0.833	0.750	0.500	0.500
	C <sub>44</sub>	0.682	0.583	0.376	0.248	0.178

Table 5. Correlation of primary indicators of emergency management capacity of coal mining enterprises.

Projects		j = 1	j = 2	j = 3	j = 4	j = 5	Eigen-Value j*	Level
Level 1 Indicators	Emergency prevention synergy capability	0.412	0.705	0.456	−0.46	−0.62	0.76	Good
	Emergency preparation capability	−0.02	0.09	−0.42	−0.63	−0.70	0.68	Good
	Emergency response synergy capability	−0.01	0.09	−0.42	−0.61	−0.65	0.53	Average
	Emergency recovery synergy capability	−0.06	0.09	−0.38	−0.57	−0.68	0.72	Good

According to the correlation degrees of first-level indexes and the determined weights in Table 4, the eigenvalue  $j^*$  of variables of the emergency synergy capability level can be calculated. According to the eigenvalue, the overall emergency synergy capability level is evaluated as “good”, that is, the emergency synergy capability of J Coal Mine is generally good though it can be improved. The evaluation result agrees with the actual production and operation situation of the mine.

#### 4.5. Analysis of Evaluation Results

With the aid of the matter-element extension comprehensive evaluation model, the evaluation results of various evaluation indexes of the emergency synergy capability of J Coal Mine can be obtained (Table 6).

According to the evaluation results in Table 6, the comprehensive evaluation level of the emergency synergy capability of J Coal Mine is “good”. To be more specific, the first-level index emergency prevention synergy capability is “good”. All its second-level indexes are “good” or “excellent” except for emergency management laws and regulations, which is “average”. The first-level index emergency preparation synergy capability is “good”; among the second-level indexes, the implementation of emergency drills, emergency aid equipment and technology, and emergency rescue mutual aid agreement are “average” and the others are “good” or above. The first-level index emergency response synergy capability is “average”; among the second-level indexes, emergency material allocation, synergy with government departments, and synergy with relevant units are “average”, while the others are “good”. The first-level index recovery and reconstruction capability is “good”; all the second-level indexes are “good” except for post-emergency plan improvement, which is “average”.

**Table 6.** Evaluation results of emergency management capacity of coal mining enterprises can be improved.

Evaluation Object	Ability Level	Level 1 Indicators	Evaluation Level	Level 2 Indicators	Evaluation Level	
Coal Mine Emergency Management Capability	Good	Emergency prevention synergy capability (C <sub>1</sub> )	Good	Completeness of basic data management C <sub>11</sub>	Good	
				Safety prevention inspection C <sub>12</sub>	Good	
				Identification of major hazard sources C <sub>13</sub>	Good	
				Hazard source monitoring and control C <sub>14</sub>	Good	
				Emergency management organization Construction C <sub>15</sub>	Good	
				Emergency management laws and regulations C <sub>16</sub>	Average	
				Safety education for operations C <sub>17</sub>	Good	
		Emergency preparation synergy capability (C <sub>2</sub> )	Good	Good	Emergency rescue team construction C <sub>21</sub>	Excellent
					Emergency rescue plan preparation C <sub>22</sub>	Good
					Implementation of emergency drills C <sub>23</sub>	Average
					Emergency supplies reserve C <sub>24</sub>	Good
					Emergency aid equipment and technology C <sub>25</sub>	Average
					Emergency rescue mutual aid agreement C <sub>26</sub>	Average
		Emergency response synergy capability (C <sub>3</sub> )	Average	Average	Emergency rescue response speed C <sub>31</sub>	Good
					Emergency plan activation C <sub>32</sub>	Good
					Emergency decision-making and command C <sub>33</sub>	Good
Emergency material allocation C <sub>34</sub>	Average					
Synergy with government departments C <sub>35</sub>	Average					
Synergy with relevant units C <sub>36</sub>	Average					
Synergy with media C <sub>37</sub>	Good					
Emergency recovery synergy capability (C <sub>4</sub> )	Good	Good	Post analysis and summary C <sub>41</sub>	Good		
			Recovery and reconstruction C <sub>42</sub>	Good		
			Post emergency plan improvement C <sub>43</sub>	Average		
			Post emergency rescue system improvement C <sub>44</sub>	Good		

#### 4.6. Rectification Suggestions

Our comprehensive evaluation of the emergency synergy capability of J Coal Mine aimed to find any deficiencies in its emergency management and take corresponding rectification measures to improve its overall emergency capability. According to the evaluation results, the following rectification suggestions are proposed:

- (1) In terms of emergency prevention, J Coal Mine should vigorously promote the construction of a dual prevention system for safety production risk and hidden danger, improve the prediction and early warning technology for coal mine accidents, continuously and effectively promote preventive safety inspections, and strengthen the source control of coal mine safety. A sound emergency plan should be formulated to ensure coordination with relevant plans of local government departments to form a joint force with local government and relevant departments.
- (2) With respect to emergency preparedness, it is suggested to intensely enhance the intelligent construction of coal mines and governance according to law, strengthen the education of coal mine employees by means of safety training, and promote the overall improvement of the emergency response capability of employees. Meanwhile, it is necessary to increase investment and research and development of emergency rescue equipment, strengthen the signing of emergency rescue agreements with surrounding coal mines, and boost rescue cooperation.
- (3) With regard to emergency response, importance should be attached to building an emergency rescue team, enhancing the emergency synergy capability, raising the level of the emergency communication guarantee system, and strengthening the synergistic interaction between “Internet plus” and coal mine emergency management. In addition, collaboration between the government and other units should be stressed for achieving on-site emergency linkage synergy and multiparty emergency synergy capability within the region.
- (4) For emergency recovery, the post-emergency recovery and reconstruction plan should be further improved and production recovery should be accelerated through scientific

and comprehensive formulation of the accident recovery plan, to ensure minimal loss due to unexpected disasters while ensuring safety.

## 5. Conclusions

- (1) Based on engineering practice and experts' experience, from the perspective of synergy and considering factors affecting the coal mine emergency response synergy ability in various aspects, the evaluation index system of coal emergency prevention synergy capability, emergency preparedness synergy capability, emergency response synergy capability, and recovery synergy capability was constructed, and 24 factors such as hazard source monitoring and control, emergency rescue plan preparation, emergency decision-making and command, and post-emergency plan improvement were used as indexes. The evaluation index system of coal mine emergency response synergistic capability is scientific, reasonable, and comprehensive. Moreover, the index system is scientific, reasonable, comprehensive, and in line with the engineering reality.
- (2) An empirical evaluation of the emergency synergy capability capacity of J coal mine in Henan Province was carried out as an example. According to the evaluation results, the overall evaluation of the emergency synergy capability of J Coal Mine was "good". Among the four first-level evaluation indexes, the levels of emergency prevention synergy capability, emergency preparedness synergy capability and recovery and reconstruction synergy capability were "good", while the emergency response synergy capability was "average", which is in line with the actual situation. These results indicate that the evaluation model constructed in this paper has good practical significance and can scientifically and effectively evaluate emergency synergy. The successful practice of the J Coal Mine demonstrates the feasibility of popularizing this method of evaluation of emergency synergistic capability in China and even other mining enterprises around the world.
- (3) Emergency management is an important means of effectively reducing accident losses by taking scientific precautionary measures according to the idea of system theory, organically combining micro- and macro-level factors inducing accidents while taking into full consideration the inducing effect, linkage effect, and superposition effect of each factor. The improvement of the emergency response synergy of coal mining enterprises is due to the influence of many factors, and requires the people, machines, environment, and management of the whole emergency management system of coal mining enterprises to cooperate with each other and respond synergistically to ensure the sustainable operations on the scale of individual coal mines.

**Author Contributions:** Conceptualization, Y.H.; methodology, Y.H.; validation, Y.H.; resources, L.Z.; data curation, C.S.; writing—original draft preparation, Y.H.; writing—review and editing, J.W.; supervision, C.S. and J.W. All authors have read and agreed to the published version of the manuscript.

**Funding:** This research was funded by the Soft Science Research Programme of Henan Province (232400410197), the State Key Laboratory Cultivation Base for Gas Geology and Gas Control (Henan Polytechnic University) (WS2021B12), the Strategic Research and Consulting Project of the Chinese Academy of Sciences (2023HENZDB05), the Young Key Teachers in Henan Polytechnic University (2018XQG-21), the PhD Foundation of Henan Polytechnic University (B2019-10 and B2022-57-10), and the Major Project "Emergency Management System Construction Research" of Henan Polytechnic University (SKYJ2021-01).

**Data Availability Statement:** The data used to support the findings of this study are available from the first author or corresponding author upon request.

**Conflicts of Interest:** The authors declare that they have no conflict of interest with respect to the research, authorship, and/or publication of this article.



## References

1. Zhang, S.; Ma, M.; Xiang, X.; Cai, W.; Feng, W.; Ma, Z. Potential to decarbonize the commercial building operation of the top two emitters by 2060. *Resour. Conserv. Recycl.* **2022**, *185*, 106481. [CrossRef]
2. Cheng, J.; Zhao, G.; Feng, G.; Li, S. Characterizing strata deformation over coal pillar system in longwall panels by using subsurface subsidence prediction model. *Eur. J. Environ. Civ. Eng.* **2020**, *24*, 650–669. [CrossRef]
3. Zheng, X.R.; Cheng, J.W.; Zhang, J.F. An overview of hotspots research in the field of safety science from 2016 to 2021 based on VOS viewer. *J. Xi'an Uni. Archit. Technol.* **2022**, *42*, 674–688. [CrossRef]
4. Ikeda, Y.; Beroggi, G.E.; Wallace, W.A. Supporting multi-group emergency management with multimedia. *Saf. Sci.* **1998**, *30*, 223–234. [CrossRef]
5. Xu, Y.; Xue, Y.; Hua, G.; Cheng, J. An adaptive distributed compressed video sensing algorithm based on normalized Bhat-tacharyya coefficient for coal mine monitoring video. *IEEE Access* **2020**, *8*, 158369–158379. [CrossRef]
6. Huang, L.; Li, B.; Wang, B.; Zhang, J. Study on mechanical properties and energy evolution of coal under liquid nitrogen freezing. *Eng. Fract. Mech.* **2023**, *282*, 109158. [CrossRef]
7. Huang, L.; Li, B.; Wang, B.; Zhang, J. Effects of coal bedding dip angle on hydraulic fracturing crack propagation. *Geomech. Geophys. Geo-Energy Geo-Resour.* **2023**, *9*, 30. [CrossRef]
8. Yeo, J.; Comfort, L.K. An expected event, but unprecedented damage: Structure and gaps of large-scale response coordination of the 2011 Thailand floods. *Disaster Prev. Manag.* **2017**, *43*, 305–312. [CrossRef]
9. Schipper, D.; Gerrits, L.; Koppenjan, J.F. A dynamic network analysis of the information flows during the management of a railway disruption. *Eur. J. Transp. Infrastruct. Res.* **2015**, *12*, 255–263.
10. Kinilakodi, H.; Grayson, R.L. Citation-related reliability analysis for a pilot sample of underground coal mines. *Accid. Anal. Prev.* **2011**, *43*, 1015–1021. [CrossRef]
11. Hu, S. Exploring the joint transformation of local coal mines by large state-owned coal enterprises. *China Coal* **2008**, *34*, 18–20. [CrossRef]
12. Kong, L. Research on the Construction of National and Regional Mine Emergency Rescue Team System. Master's Thesis, Liaoning University of Engineering and Technology, Fuxin, China, 2012.
13. Yang, H.Y. Exploration on setting up mine rescue team and fire station in mine merger. *Coal Engine* **2012**, *S1*, 106–108.
14. Liang, Y.; Chen, H.; Wei, C.Y.; Zhang, Y.L. Level-by-level Evaluation of Coal Mine Emergency Rescue Coordination Capability Based on AHP-Fuzzy Comprehensive Evaluation Method. *J. Ins. Disaster Prev.* **2022**, *24*, 54–59.
15. Qi, H.L.; Ning, Y.C. Study on the synergistic mechanism and capability of coal mine safety emergency management. *Coal Technol.* **2014**, *33*, 182–184. [CrossRef]
16. Zhu, Y.Q. Exploration on the synergistic mechanism and capacity of coal mine safety emergency management. *Inn. Mong. Coal Econ.* **2016**, *34*, 44–45. [CrossRef]
17. Wang, H.Q.; Zhao, J.; Qi, H.L. Research on regional coal mine emergency management system based on collaboration. *Coal Econ. Res.* **2016**, *36*, 66–69. [CrossRef]
18. Wang, J.F.; Chang, H.Y.; Zhai, X.; Feng, L. Evolutionary game and simulation analysis of emergency cooperation of coal mines. *Min. Saf. Environ. Prot.* **2017**, *44*, 110–114.
19. Shi, P.; Hao, Y.; Sun, C.; Zhang, L. Evolutionary game and simulation analysis on management synergy in China's coal emergency coordination. *Front. Environ. Sci.* **2023**, *11*, 171. [CrossRef]
20. Yang, F.F.; Zhang, J.F.; Zheng, C.; Tai, X.U.; Jiao, Y.F. Research on emergency response capacity of coal mines based on logistic curve and fuzzy hierarchical analysis. *Coal Engine* **2019**, *51*, 154–157.
21. Lan, G.H.; Chen, Y.S.; Xun, S.K. Evaluation of emergency rescue capability of coal mine emergencies based on RS-IPA. *China J. Saf. Sci.* **2020**, *30*, 169–176. [CrossRef]
22. Cheng, L.H.; Zhou, R.X.; Yan, J.; Guo, H.M. Construction and application of maturity evaluation model of coal mine emergency rescue capability. *China J. Saf. Sci.* **2021**, *31*, 180–186. [CrossRef]
23. Yang, D.S. Design of collaborative emergency drill system for coal mine emergencies based on Unity 3D. *China Energy Environ. Prot.* **2022**, *44*, 263–268. [CrossRef]
24. Li, Q.; Zhao, D.; Yin, J.; Zhou, X.; Li, Y.; Chi, P.; Han, Y.; Ansari, U.; Cheng, Y. Sediment Instability Caused by Gas Production from Hydrate-bearing Sediment in Northern South China Sea by Horizontal Wellbore: Evolution and Mechanism. *Nat. Resour. Res.* **2023**, *32*, 1595–1620. [CrossRef]
25. Wang, F.L.; Liu, X.; Jiang, B.H.; Zhou, H.; Chen, W.; Chen, Y.; Li, X. Low-loading Pt nanoparticles combined with the atomically dispersed FeN4 sites supported by FeSA-N-C for improved activity and stability towards oxygen reduction reaction/hydrogen evolution reaction in acid and alkaline media. *J. Colloid Interface Sci.* **2023**, *635*, 514–523. [CrossRef] [PubMed]
26. Li, Q.; Zhang, C.; Yang, Y.D.; Ansari, U.; Han, Y.; Li, X.; Cheng, Y. Preliminary experimental investigation on long-term fracture conductivity for evaluating the feasibility and efficiency of fracturing operation in offshore hydrate-bearing sediments. *Ocean Eng.* **2023**, *281*, 114949. [CrossRef]
27. Zhang, G.R.; Lei, Y.; Feng, W. Research on Emergency Information Collaboration Mechanism Driven by Big Data. *J. Intell.* **2022**, *41*, 181–185.
28. Ning, J.; Nie, F. Evolutionary game research on employee disengagement and coal enterprise security inspection. *China Mineral. Mag.* **2019**, *28*, 158–162.

29. Chen, Z.L.; Shi, J.W.; Ye, Y.Q.; Wang, Y.; Wang, H. Research on risk management and prevention and control system of major disasters in coal mine based on fish-bone diagram and STAMP/STPA model. *Int. J. Front. Eng. Technol.* **2022**, *4*, 86–95. [CrossRef]
30. Shang, G.Y.; Li, J.P.; Zhang, L.H. Thoughts on Emergency Management of Large Coal Mining Enterprises. *China Saf. Sci. J.* **2022**, *32*, 225–230. [CrossRef]
31. Li, S.; Kuang, Z.; Xiao, Y.; Qiao, Z.; Yang, W. Rockburst tendency prediction based on an integrating method of combination weighting and matter-element extension theory: A case study in the Bayu Tunnel of the Sichuan-Tibet Railway. *Eng. Geol.* **2022**, *308*, 106796. [CrossRef]

**Disclaimer/Publisher’s Note:** The statements, opinions and data contained in all publications are solely those of the individual author(s) and contributor(s) and not of MDPI and/or the editor(s). MDPI and/or the editor(s) disclaim responsibility for any injury to people or property resulting from any ideas, methods, instructions or products referred to in the content.

## Article

# Analysis of the Current Status and Hot Technologies of Coal Spontaneous Combustion Warning

Feiran Wang <sup>1</sup>, Zhansuo Ji <sup>2</sup>, Haiyan Wang <sup>3,\*</sup>, Yue Chen <sup>1</sup>, Tao Wang <sup>3</sup>, Ruoyi Tao <sup>1</sup>, Chang Su <sup>1</sup> and Guchen Niu <sup>1</sup>

<sup>1</sup> School of Emergency Management and Safety Engineering, China University of Mining and Technology (Beijing), Beijing 100083, China; wangfeiran2003@163.com (F.W.); 18883163779@163.com (Y.C.); taoruoyi011115@126.com (R.T.); suchang3203@163.com (C.S.); nnniu188@163.com (G.N.)

<sup>2</sup> Kailuan (Group) Company Limited Qianjiaying Mining Branch Company, Tangshan 063000, China; jizhansuo@kailuan.com.cn

<sup>3</sup> School of Civil and Resources Engineering, University of Science and Technology Beijing, Beijing 100083, China; m202120089@xs.ustb.edu.cn

\* Correspondence: whycumtb@163.com

**Abstract:** Coal spontaneous combustion disasters are one of the most serious types of mine disasters in China at present, posing a huge threat to underground personal safety and coal production operations. In order to prevent and control coal spontaneous combustion hazards and construct an efficient early warning system, this paper presents a review of coal spontaneous combustion early warning based on the Web of Science database search of 583 papers related to coal spontaneous combustion early warning collected from 2002 to 2021, using VOSviewer visualization software. The number of publications and partnerships at the author, institution and country levels are obtained, and the research hotspots in the field of coal spontaneous combustion warning are obtained based on keyword co-occurrence and clustering. The results show that the research results of scholars with a high publication volume have significant influence in the field of coal spontaneous combustion warning and prevention and control, and a more mature camp has been formed among the research authors; a more stable core group of institutions has been formed in the field of coal spontaneous combustion warning; most of the national publications are concentrated in mineral resource-mining countries; the analysis of hot keywords shows that “sign gas warning” and “warning models and technologies” are the key contents of this field. The analysis of hot keywords shows that “sign gas early warning” and “early warning model and technology” are the key contents of this field. The research content of this paper is helpful for researchers to find the latest information on the current research and trends in the field of spontaneous combustion prevention and coal seam monitoring.

**Keywords:** coal spontaneous combustion warning; marker gas; warning model; VOSviewer

**Citation:** Wang, F.; Ji, Z.; Wang, H.; Chen, Y.; Wang, T.; Tao, R.; Su, C.; Niu, G. Analysis of the Current Status and Hot Technologies of Coal Spontaneous Combustion Warning. *Processes* **2023**, *11*, 2480. <https://doi.org/10.3390/pr11082480>

Academic Editors: Feng Du, Aitao Zhou and Bo Li

Received: 29 July 2023

Revised: 12 August 2023

Accepted: 16 August 2023

Published: 18 August 2023



**Copyright:** © 2023 by the authors. Licensee MDPI, Basel, Switzerland. This article is an open access article distributed under the terms and conditions of the Creative Commons Attribution (CC BY) license (<https://creativecommons.org/licenses/by/4.0/>).

## 1. Introduction

### 1.1. Coal Spontaneous Combustion Hazards and the Need for Early Warning

Energy is an important part of the national economy, which is related to the development of the national economy. China is rich in coal resource reserves and ranks first in the world in coal resource reserves; behind the high reserves, China is also a country with a high incidence of major coal mine accidents. In recent years, with the development of scientific and technological progress and disaster warning systems, the number and severity of coal mine disasters have been decreasing, but coal spontaneous combustion is still a serious threat to the safe mining of coal. The spontaneous combustion of coal is one of the five major disasters in mines. The spontaneous combustion of coal not only generates toxic and harmful gases and easily causes gas, coal dust and other explosive accidents, but also seriously threatens the safe mining of mines, causing serious casualties and significant economic losses. According to statistics, there are 4108 coal mines in China, with a production capacity of  $4303 \times 10^9$  Mg, of which 852 coal mines are mining coal

seams prone to spontaneous combustion, with a production capacity of  $1631 \times 10^9$  Mg; and 1540 coal mines are mining spontaneous combustion seams, with a production capacity of  $1542 \times 10^9$  Mg. The proportion of coal mines mining easy spontaneous combustion and spontaneous combustion seams is 58.2% and the production capacity is 73.7% [1], which shows that the problem of spontaneous combustion of coal seriously affects the safety of coal mining. In recent years, coal spontaneous combustion accidents have occurred frequently. On 7 December 2018, the spontaneous combustion pyrolysis gas explosion of coal left in the mining area of Tang Yang coal mine of Shandong Yulong Mining Group killed three people and injured three others [2]; on 16 December 2015, the spontaneous combustion of coal in the coal mine of Xiangyang District, Hegang City, Heilongjiang province caused a gas explosion that killed 19 people [3]. This series of catastrophic events shows that the situation of coal spontaneous combustion disaster prevention and control is still serious. And in recent years, as China's shallow coal resources tend to be mined out, coal mining is gradually developing in the direction of deep mining, thus leading to the increasing complexity of coal spontaneous combustion disaster management; therefore, the construction of an efficient coal spontaneous combustion warning system has been the key to preventing and controlling coal spontaneous combustion in mines.

Experts and scholars have made great contributions to the study of the coal spontaneous combustion early warning system and provided abundant guiding theories for the establishment of the system. Guo et al. [4] combined experimental data and numerical simulation to reconstruct the data curve and established an early warning model for coal spontaneous combustion. Yue et al. [5] used the self-designed coal spontaneous combustion experimental platform to simulate the self-heating and oxidation heating of processed raw coal, and finally established a six-level warning system of "gray, blue, yellow, orange, red, and black" to quantitatively classify the risk of coal spontaneous combustion and effectively prevent and control underground coal fire disasters. Shu et al. [6] established a coal spontaneous combustion grading warning prediction prevention and control system, which realized the dynamic grading identification of coal fire disaster. Xie et al. [7] established a mine fire accident early warning prediction system based on the comprehensive consideration of various functions such as monitoring, alarm, feedback, and linkage. Lei [8] made targeted improvements to the shortcomings of the currently adopted early warning system and proposed a new fire warning scheme, which realized accurate and timely monitoring of underground fires and provided a guarantee for rapid elimination of fire hazards. Tan [9] et al. obtained the relationship between temperature and maker gas during coal warming based on the programmed warming method, and used it as an early warning reference for coal spontaneous combustion fires. Zhong [10] et al. reviewed the principle of coal spontaneous combustion monitoring and early warning technology and the current status of research and application from two aspects of coal spontaneous combustion precursor information monitoring technology and prediction forecasting methods. Ren et al. [11] established a novel early warning indicator for the marker gas produced during coal spontaneous combustion. Wen H. et al. [12] used the gas index to judge the development trend and initial characteristic temperature point of coal spontaneous combustion, and put forward a multi-index comprehensive early warning method based on the comprehensive index of Graham (G), carbon monoxide/carbon dioxide and  $100 \times$  (ethylene/carbon monoxide). Graham (G) is mostly calculated by the increase in carbon monoxide concentration and the decrease in oxygen concentration in the process of coal oxidation. Under normal circumstances, its value is less than 0.5%. If the value continues to rise and exceeds 0.5%, it indicates that self-heating occurs in the mine, and active measures should be taken to prevent disasters. When it exceeds 1%, it indicates that the spontaneous combustion of coal has occurred in the coal mine, and measures should be taken to prevent the expansion of disasters. Wang K. et al. [13] divided the coal oxidation process into a slow oxidation stage, rapid oxidation stage, and accelerated oxidation stage by critical temperature and dry cracking temperature. A three-level early warning index for quantitative prediction of coal spontaneous combustion is proposed. Zhou et al. [14] obtained the change curve of the

volume fraction of the index gas of low, medium and high metamorphic degree through the temperature programmed control experiment, and then used the Logistic function to fit the volume fraction of the index gas with the temperature to obtain the mathematical model of the index gas and temperature of different metamorphic degree, determined the inflection point temperature, and finally combined with the initial temperature of the index gas to divide the risk level of coal spontaneous combustion. According to the experimental data of low-temperature oxidation, Guo et al. [15] established a mathematical model between coal temperature and carbon monoxide concentration. Taking oxygen, carbon dioxide and ethanol as independent variables, the carbon monoxide concentration was calculated by the GA-SVR model, and a set of prediction model of coal body temperature was established. Wu et al. [16] established a mathematical prediction model of carbon monoxide concentration in a return air corner of a working face under normal operating conditions. Then, based on the carbon monoxide formation rate of coal oxidation at room temperature and critical temperature, the carbon monoxide safety prediction and spontaneous combustion warning concentration were calculated, and a new index of coal spontaneous combustion warning was established.

### 1.2. Knowledge Graph Development

At present, coal spontaneous combustion early warning has become a popular research topic; the research content of coal spontaneous combustion early warning is extensive and diverse, and the research hotspots are in continuous evolution; the research network of domestic and foreign scholars in the direction of coal spontaneous combustion early warning is concentrated, and there are few frontier branches; the research results lack systematic correlation and integration; the coal spontaneous combustion early warning methods still need to be improved; and there is a lack of comprehensive research on the application of coal spontaneous combustion early warning. The rise of knowledge graph visualization technology provides a new direction to better understand the research hotspots and research frontiers in the field of coal spontaneous combustion early warning. Shao et al. [17] used CiteSpace and VOSviewer for coal hole visualization. Hong et al. [18] demonstrated the origin and knowledge base and basic and frontier disciplines of international coal safety management research through knowledge mapping visualization. Hong et al. [19] used CiteSpace to demonstrate the current status of research in the field of coal and gas protrusion and predicted the future development trend. Liu et al. [20] reviewed and analyzed the research progress of spontaneous combustion hazard using CiteSpace and VOSviewer. Wang et al. [21] conducted a research hotspot of mine fires based on CiteSpace and development trends were analyzed and studied. Jamroz D [22] applied visualization technology to identify coal types and determine the possibility of significant differences among different coal types. Yang et al. [23] used Citespace to conduct a bibliometric analysis of coal spontaneous combustion scientific publications worldwide, showing the characteristics and research trends of coal spontaneous combustion databases.

Through the above analysis, a large number of scholars have conducted theoretical analysis, numerical simulations and field experimental research on coal spontaneous combustion early warning. However, due to the diversity of research contents, the research results and research directions in this field still cannot be accurately controlled. In this paper, we use the Web of Science core database as the data source to conduct statistical analysis and data mining of coal spontaneous combustion early warning research literature from 2002 to 2021; track the distribution characteristics of the literature volume, research subjects and hot fronts; and draw a knowledge map to reveal the trajectory, characteristics and laws of coal spontaneous combustion early warning research in order to provide reference and information on the knowledge framework, dynamic changes and development trends in the field of coal spontaneous combustion early warning.

## 2. Data Sources and Research Methods

### 2.1. Data Sources

In this paper, Web of Science (core collection) is selected as the data source, which has been accepted by many scholars as the world's largest comprehensive digital literature resource database covering the largest number of disciplines [24] and contains more than 12,000 authoritative and high-impact academic journals in various research fields such as natural sciences, engineering and technology [25,26], and is considered the most suitable database for bibliometric analysis. In this paper, we use the search engine of WoS with the search formula TS = (coal spontaneous combustion warning) OR TS = (coal spontaneous combustion prediction) OR TS = (coal spontaneous combustion iconic gas) OR TS = (coal spontaneous combustion index) AND PY = (2002–2021). A total of 583 papers were searched.

### 2.2. Research Methodology

VOSviewer is a mainstream visual analytics tool for knowledge graphs, a visual analytics software developed by Dr. NeesJan van Eck and Prof. Ludo Waltman at the Center for Science and Technology (CWTS) of Leiden University [27,28], which uses a probabilistic approach to data normalization to provide easy and graphically beautiful production of web knowledge graphs. In this paper, 583 valid documents in the field of coal spontaneous combustion early warning research were retrieved and exported in tab-delimited file format (the records contain full records and references), and VOSviewer (version 1.16) was used to analyze the distribution characteristics of the literature carriers and research subjects as well as hot fronts through cooperative network topology and keyword co-occurrence analysis, and present them in a visual form. It is intended to help researchers accurately grasp the main lines of research, recognize the knowledge structure and distribution characteristics, and gain insight into research hotspots.

## 3. Analysis of Collaboration Characteristics

### 3.1. Author Co-Authorship Analysis

An analysis of the literature authors in the field of coal spontaneous combustion warning reveals the representative scholars and core authors in the field. According to Price, a leading American scientometrician [29], half of the papers on the same research topic are authored by a group of highly productive authors who are numerically equal to the square root of the total number of authors (Equation (1)).

$$\sum_{m+1}^I n(x) = \sqrt{N} \quad (1)$$

where  $n(x)$  denotes the number of authors who have authored a paper,  $I = n_{max}$  denotes the number of papers by the most productive authors in the field, and  $N$  is the total number of authors.

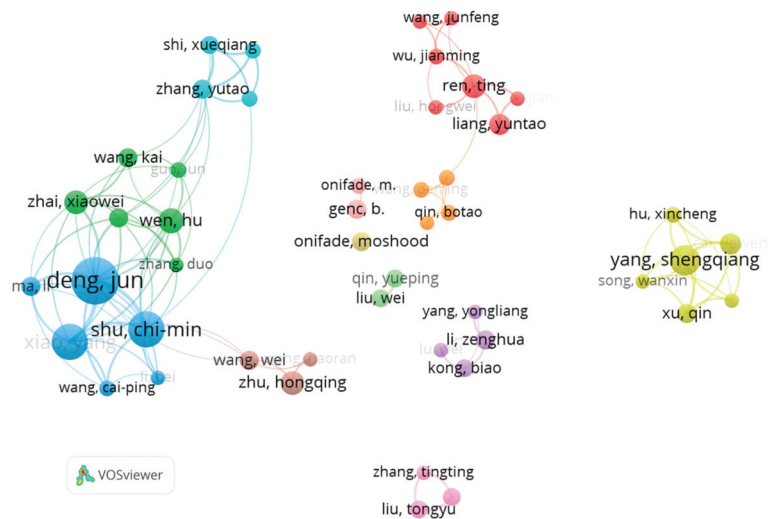
The VOSviewer statistics show that  $n_{max} = 32$ ,  $N = 1802$ . The minimum number of core author publications  $m$  in the field of coal spontaneous combustion warning is represented by Equation (2).

$$m = 0.749 \times \sqrt{n_{max}} = 0.749 \times \sqrt{32} = 4.24 \quad (2)$$

Therefore, the authors with more than 5 publications (including 5) were positioned as the core authors in this field, and the core authors were counted as 53, with a total of 421 publications, accounting for 72.2% of the total publications, which exceeded the threshold of 50% proposed by price, and therefore, the core author group in the field of coal spontaneous combustion early warning research was considered to have emerged.

The core group of authors in the field of coal spontaneous combustion early warning is shown in Figure 1. As shown in Figure 1, the size of the node represents the amount of the author's posting, the color of the node represents different cooperative groups, and the

thickness of the connection between the nodes represents the strength of the cooperative relationship. Throughout the cooperation group, there was a red camp represented by Liang Y.T., Liu H.W., Ren T., Wang J.F., Wu J.M., Zhang J. and Zhang Y.L.; a green camp represented by Guo J., Wang K., Wang W.F., Wen H., Zhai X.W. and Zhang D.; a blue camp represented by Deng J., Li B., Ma L., Shu Chi-Min, Wang C.P. and Xiao Y.; a red camp represented by Cai J.W., Hu X.C., Song W.X., Xu Q., Yang S.Q., Cai J.W., Hu X.C., Song W.X., Yu Q. and Zhang Y.L.; and a yellow camp represented by Xu Q., Yang S.Q. and Zhou B.Z. On the whole, international collaborative relationships in the field of coal spontaneous combustion warning are fragmented, the connectivity of the collaborative network is not high and the characteristics of small-scale collaboration among authors are more obvious. Specifically, the collaboration among emerging and highly productive authors is obvious and closer, concentrated among Deng J., Wen H. and Zhang Y., with a high degree of collaboration and close cooperative relationships. In contrast, several other subnetworks have smaller authors and limited mutual collaborative relationships among authors. In addition, the subnetworks are less connected and more independent from each other.



**Figure 1.** Collaborative group of core authors in the field of coal spontaneous combustion warning.

The top 10 most prolific authors with more than 5 publications in this field are shown in Table 1. Analyzed in terms of publication volume, the top three authors are Deng J., Xiao Y. and Xu Q.M. (Taiwanese name: Shu Chi-Min), with publication volumes of 32, 21 and 21, respectively. Deng J. and Xiao Y. work at Xian Univ. Sci. & Technol. in Taiwan, and Xu Q.M. works at Yunlin Univ. Sci. & Technol. in Taiwan, and the three scholars have had several collaborative experiences. From the analysis of their published papers, the three scholars are more concerned with the research and application of coal fire disaster prevention and control theories and technologies, such as the analysis of coal gangue spontaneous combustion characteristics by thermogravimetric-Fourier infrared spectroscopy, the study of oxidation thermodynamic parameters of poor coal, and the discussion of the mechanism of coal spontaneous combustion resistance and its application technology [30–32]. At the same time, from the level of authors, the Citations index of these three authors is basically consistent with the ranking of the number of articles. It can be seen that both the number and the level of academic output are in the forefront. They were followed by Prof. Yang S.Q. from China Univ. Min. & Technol. and Wen H. from Xian Univ. Sci. & Technol. with 16 and 12 publications, respectively. These two scholars have paid more attention to the disaster-causing mechanism of coal spontaneous combustion and prediction and

prevention and control technology, such as exploring the disaster-causing mechanism of gas and spontaneous combustion composite in high gas-prone coal seams [33], the graded warning method of coal natural fire and studying the preferred index for early prediction of spontaneous combustion in high gas coal seams [34–36]. All of the above scholars have been cited more than 13 times/article, indicating that the research results of these scholars have significant influence in the field of coal spontaneous combustion warning and prevention and control.

**Table 1.** Information statistics of the top 10 most prolific authors.

Rank	Author	Documents	Citations	Avg. Citations	Total Link Strength
1	J. Deng	32	527	16.47	72
2	Chi-Min Shu	21	347	16.52	50
3	Y. Xiao	21	417	19.86	53
4	S.Q. Yang	16	280	17.50	33
5	H. Wen	12	167	13.92	27
6	T. Ren	11	220	20.00	18
7	X.W. Zhai	11	92	8.36	21
8	H.Q. Zhu	11	137	12.45	9
9	J.W. Cai	9	139	15.44	28
10	Y.T. Lian	9	245	27.22	8

### 3.2. Analysis of Institutional Cooperation

The analysis of the collaborating organizations in coal spontaneous combustion early warning research makes it possible to clarify information about the most productive organizations in the field and how they cooperate with each other. Globally, there are 464 institutions involved in coal spontaneous combustion early warning research and published papers, among which, there are 36 institutions with more than five publications, and the top 10 research institutions with the greatest number of papers published in this field shown in Table 2. In Table 2, 90% of the organizations are from China, which is mainly due to the fact that China is one of the world's leading countries in mining mineral resources. In order to meet the national requirements of building intelligent fire monitoring systems for coal mines and to guarantee the safe mining of coal mines and the effective implementation of coal spontaneous combustion prevention, the organizations are conducting more in-depth research on coal spontaneous combustion warning. Three institutions, China Univ. Min. & Technol., Xian Univ. Sci. & Technol. and China Univ. Min. & Technol. Beijing, ranked as the top three in terms of number of publications, with 128, 71 and 29, respectively. In terms of average citations per article, China Univ. Min. & Technol. topped the list with 19.05 citations per article, while Natl. Yunlin Univ. Sci. & Technol., Univ. Witwatersrand and Shaanxi Key Lab Prevent & Control Coal Fire ranked 2nd to 4th with 18.52 citations per article, 18.39 citations per article and 18.25 citations per article, respectively. Natl. Yunlin Univ. Sci. & Technol., Univ. Witwatersrand and Shaanxi Key Lab Prevent & Control Coal Fire were ranked 2nd to 4th with 18.52, 18.39 and 18.25 times/article, respectively. China Univ. Min. & Technol., Xian Univ. Sci. & Technol., China Univ. Min. & Technol. (Beijing) are both domestic public comprehensive universities. Natl Yunlin Univ. Sci. & Technol. is a national university of science and technology established by the Taiwan government. Univ. Witwatersrand is a comprehensive public university, formerly known as the South African Mining School, which was founded in 1896 and is a famous century-old school in South Africa. It ranks fourth in the domestic university rankings in South Africa and is also a world-class top university. It is a world-class university enjoying an international reputation, with advanced teaching facilities, high-level teachers and high-tech scientific research results. Shaanxi Provincial Key Laboratory of Coal Fire Disaster Prevention and Control was approved by Shaanxi Provincial Science and Technology Department in October 2016. Facing the major needs of fire prevention and control in coal resources and their exploitation and utilization process, the key laboratory mainly carries out research work in the following three directions, with the

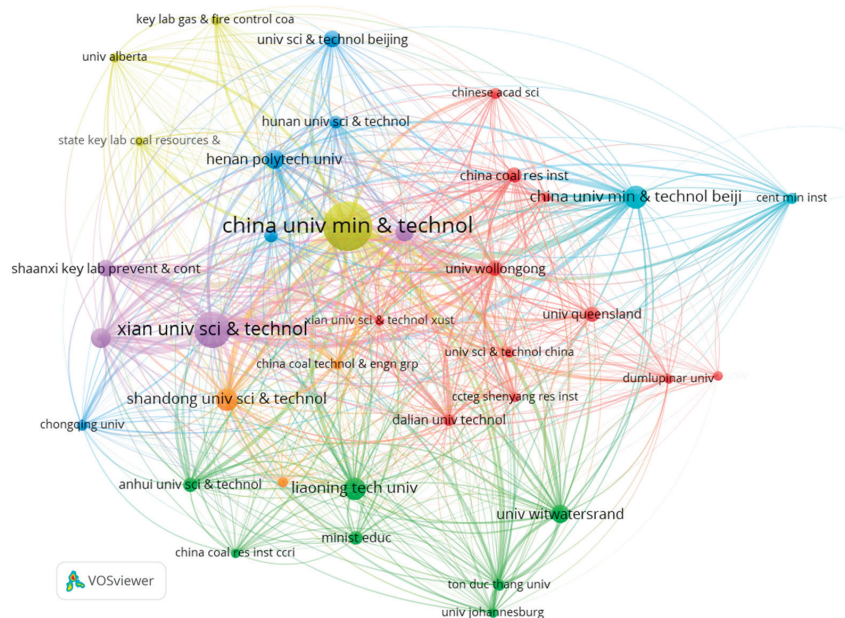


goal of solving the formation mechanism of coal fire and its induced disasters, identification and early warning, prevention and control, and other key issues: (1) the dynamic basis of coal fire disaster formation; (2) identification and early warning of coal fire hazards; (3) coal fire disaster prevention and control theory and technology.

**Table 2.** Information statistics of the top 10 high-productivity institutions.

Rank	Organization	Country	Documents	Citations	Total Link Strength
1	China Univ. Min. & Technol.	China	128	2439	66
2	Xian Univ. Sci. & Technol.	China	71	929	49
3	China Univ. Min. & Technol. Beijing	China	29	244	15
4	Shandong Univ. Sci. & Technol.	China	27	409	17
5	Liaoning Tech. Univ.	China	26	215	10
6	Natl. Yunlin Univ. Sci. & Technol.	China	21	389	30
7	Henan Polytech. Univ.	China	20	316	24
8	Taiyuan Univ. Technol.	China	18	183	10
9	Univ. Witwatersrand	South Africa	18	331	11
10	Shaanxi Key Lab Prevent & Control Coal Fire	China	16	292	26

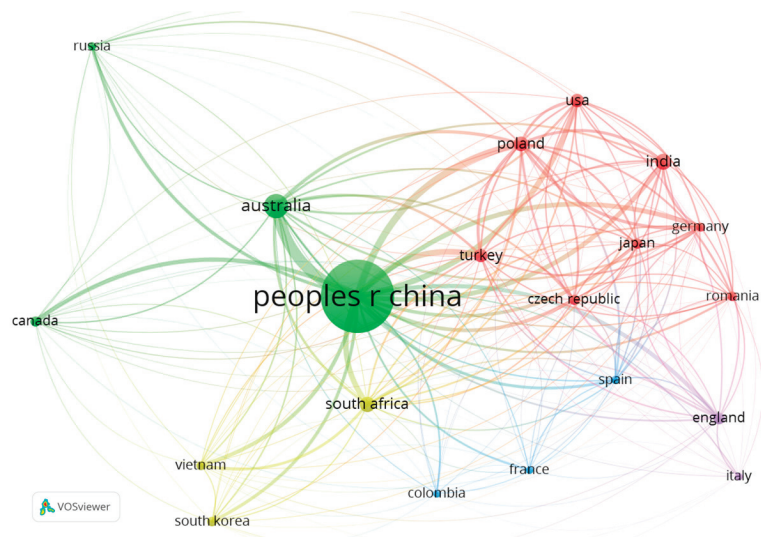
Cooperation among countries is shown in Figure 2. In terms of linkage, China Univ. Min. & Technol. and Chinese Acad. Sci., Key Lab Gas & Fire Control Coal Mines, State Key Lab Coal Resources and Tsinghua Univ., Univ. Alberta form the yellow camp; China Coal Res. Inst., Chongqing Univ., Henan Polytech Univ., Hunan Univ. Sci. & Technol., North China Inst. Sci. & Technol., Univ. Queensland and Univ. Sci. & Technol. Beijing are in the blue camp; Ccteg Shenyang Res. Inst., Dalian Univ. Technol., Taiyuan Univ. Technol., Univ. Sci. & Technol. China, Univ. Wollongong and Xian Univ. Sci. & Technol. Xust form the red camp. In general, a more stable and mature core group of institutions has been formed in the field of coal spontaneous combustion warning, and the limited cooperation is often due to various factors such as research area, research direction, working mode and geographical location.



**Figure 2.** Collaborative clusters of core institutions in the field of coal spontaneous combustion warning.

### 3.3. Country Cooperation Analysis

Close cooperation between countries is an important factor driving the development of coal spontaneous combustion early warning research, using VOSviewer to map the knowledge of cooperation between cooperating countries. As shown in Figure 3, the size of the node represents the number of documents issued by the country, the color of the node represents different clusters and the thickness of the connection between the nodes indicates the strength of the cooperative relationship between the countries. As many as 45 countries in the world are engaged in coal spontaneous combustion early warning research, and the top 20 high-productivity countries are collated in Figure 4. Overall, studies on coal spontaneous combustion warning are mainly concentrated in mineral resource-producing countries such as China, Australia and India, with China topping the list with 425 articles. These mineral resources mining countries are the core force of the current international research in the field of coal spontaneous combustion warning, to ensure that the safe and stable supply of coal plays a vital role in the economic development of these countries; this is because of the huge demand of coal for the development of the country, and thus promotes the development of the field of coal spontaneous combustion warning. Specifically, three distinct regional cooperation camps have formed from the geographical span: the green camp, with China as the core, such as Australia, Canada, Russia, etc.; the yellow camp, represented by South Africa, South Korea and Vietnam; and the red camp, represented by the USA, Poland, Turkey India, Germany and Japan. In terms of coal reserves, it is in line with the distribution of coal reserves in the Asia-Pacific market and the Europe and America Atlantic market: the coal-exporting countries and regions in the Asia-Pacific coal market mainly include Australia, Indonesia, China, Russia, Vietnam, North Korea, etc.; the coal exporting countries and regions in the Europe and America coal market mainly include Australia, South Africa, Russia, Poland, USA, Canada, Colombia, etc.



**Figure 3.** Core national cooperation groups in the field of coal spontaneous combustion early warning. Note: The size of nodes indicates the number of publications, the color of nodes indicates different cooperation groups, and the connecting lines between nodes indicate the cooperation relationship.

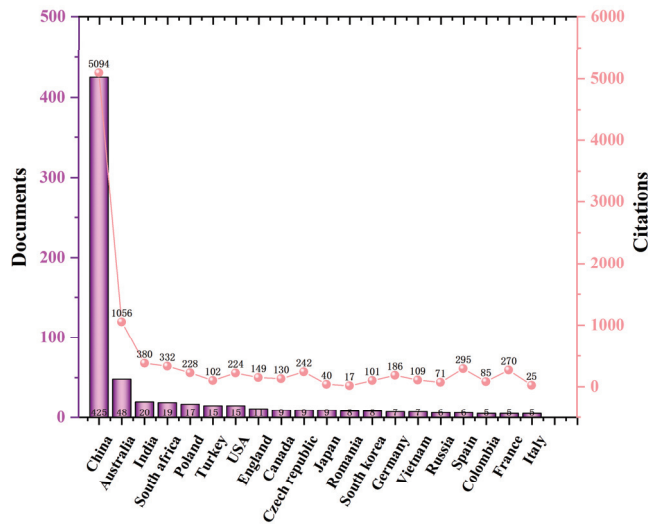


Figure 4. Information on the top 20 high-yielding countries.

#### 4. Analysis of Research Hotspots

The key words in the literature are extracted, and the key words are co-occurred to analyze the hot areas of coal natural warning research. The keywords of the literature reflect the research subject and core of the paper, which is a high summary of the topic of the article, so the keywords can be used to explore the hot topics and cutting-edge trends in the research field. VOSviewer was used to statistically analyze the selected collection of papers, with a total of 2168 keywords, 152 keywords with a co-occurrence frequency greater than 5 and 41 keywords with a co-occurrence frequency greater than 15. Figure 5 shows the co-occurrence network diagram of keywords for coal spontaneous combustion early warning research. It can be seen that the key words “Coal Spontaneous Combustion, Index Gas, Oxygen-Consumption, Goaf, Numerical Simulation” are representative terms in the field of coal spontaneous combustion warning, and they together constitute the cornerstone of the research in the field of coal natural warning. In terms of network layout, these keywords are also key nodes in the field of coal spontaneous combustion warning research, and the nodes around them together form high-impact research themes and hot research directions in the field of coal spontaneous combustion warning. The keyword information of the research in the field of coal spontaneous combustion warning was ranked and analyzed according to the co-occurrence frequency (those with more than five co-occurrence frequencies), and 30 high-frequency important keywords were obtained, as shown in Table 3. The top 10 keywords are coal spontaneous combustion, index gas, oxygen-consumption, goaf, numerical simulation, coal oxidation, ftir, self-ignition characteristics, 3-phase foam, model predictions. The whole process of coal spontaneous combustion and oxidation is accompanied by the consumption and generation of gas. In recent years, with the development of technology, the detection threshold of sensors has been gradually reduced and the sensitivity of detection has been gradually improved, which provides strong technical support towards determining the signs and status of coal spontaneous combustion by detecting the gas released by partial coal spontaneous combustion. According to Figure 5, “sign gas early warning” and “early warning model and technology” can be summarized as the core hot topics in this field.



#### 4.1. Marker Gas Early Warning Study

In the process of coal oxidation, a series of marker gases such as carbon oxides, alkanes, olefins and alkynes are produced along with the consumption of oxygen. With the increase in temperature, the above-mentioned marker gases will show regular changes consistent with the change in temperature. Therefore, to a certain extent, the use of marker gases can reflect the spontaneous combustion of coal and the state of ignition. Some of these gases, such as CO, are always present throughout the process of self-heating and the heating of coal, and the lowest temperature that can be monitored is only 50 °C with high concentration; organic gases such as olefins and alkynes will only appear at higher coal temperatures, so they are usually used as a sign that the coal has entered the high-temperature stage of spontaneous combustion. In actual production, some gases that are selected as indicators to monitor coal spontaneous combustion can reliably determine the signs and status of natural ignition. Scholars at home and abroad have explored various aspects of the generation patterns and characteristics of the marker gases.

Chen et al. [37] simulated the simulation experiment of self-heating oxidation and the heating of coal samples using a self-developed experimental platform, and provided a basis for the establishment of an early indicator system for spontaneous combustion warning in the goaf. Wen et al. [38] used the traditional programmed warming test method to study the whole process of spontaneous combustion of coal at five kinds of oxygen concentrations: 21%, 17%, 9%, 5% and 3%. Experimental results show that the variation in the marked gas precipitation of the spontaneous combustion process of coal under the concentration of lean oxygen is very complicated. Therefore, in the field application, the impact of the dynamic change of the lean oxygen concentration on the spontaneous combustion process of coal can be combined into the production conditions, which will greatly help fire prevention. Coal spontaneous combustion disasters mainly occur in the oxygen-poor environment under coal mines. The formation law of hydrocarbon gases can accurately reflect the degree of spontaneous combustion of coal. Guo et al. [39] studied the influence of the degree of hypoxia on the formation of hydrocarbon gases by heating experiments of coal spontaneous combustion program under different anoxic environments. Studying the characterization temperature is of great significance for predicting and preventing spontaneous combustion of coal. Deng et al. [40] on the basis of the programmed heating experimental system and the analysis of the original marked gas, established the gas growth rate analysis, and tested the characteristic temperature of the marked gases such as CO and C<sub>2</sub>H<sub>4</sub>, CO/CO<sub>2</sub> and alkane ratios, in order to determine the characteristic temperature of coal with different degrees of metamorphism and compare it with the gas index analysis. The results show that the temperature corresponding to the extreme value of the heating rate is the characteristic temperature point of spontaneous combustion of coal, and different metamorphic coal has different extreme values. What's more, the growth rate analysis is more concise, effectively identifying key temperature points and reducing uncertainty.

The coal spontaneous combustion process of coal with different metamorphic degrees is quite different, and there is a possible relationship between the parameters of coal spontaneous combustion characteristics and metamorphic degrees. Therefore, the degree of metamorphism during low-temperature oxidation becomes a factor that cannot be ignored. Deng et al. [41] studied the influence of coal metamorphism on gas precipitation and characteristic temperature point variation in the low-temperature oxidation stage by using thermogravimetric programmed temperature system. The results show that the release amount and heat release intensity of CO and CO<sub>2</sub> released from coal by self-thermal oxidation at low temperature increase with the increase in temperature, and the oxygen consumption rate accelerates and increases exponentially. With the deepening of the metamorphic degree of coal samples, the difference among all the above parameters is small and does not change much. Wang et al. [42] studied the characteristic gas release law in the low-temperature oxidation process of long-flame coal for a specific coal seam. The experimental results show that the precipitation amount of CO, C<sub>2</sub>H<sub>4</sub> and C<sub>2</sub>H<sub>6</sub> gas produced by self-thermal oxidation of coal in specific coal seam increases with the increase

in temperature. The trend is exponential growth first. Particle size, as an important factor on the amount of gas precipitation, has an important role. The production rate is negatively correlated with the particle size, and the yield is positively correlated with the temperature. CO and C<sub>2</sub>H<sub>4</sub> can be used as important index gases for the prediction of coal spontaneous combustion. The critical temperature of coal spontaneous combustion is judged by the initial appearance temperature of various index gases and the correlation change rate between index gases and oxygen consumption of coal samples. The critical temperature is determined to be 60–80 °C. Deng et al. [43] used a self-built large-scale experimental platform for the large-scale simulation of coal spontaneous combustion. In the experiment, the changes in temperature, gas ratio, oxygen consumption and thermal strength in the whole process of coal rising from room temperature to 452.7 °C and then falling to room temperature were simulated. The ratios of CO<sub>2</sub>/CO, CH<sub>4</sub>/C<sub>2</sub>H<sub>6</sub>, C<sub>2</sub>H<sub>4</sub>/C<sub>2</sub>H<sub>6</sub> and C<sub>3</sub>H<sub>8</sub>/C<sub>2</sub>H<sub>6</sub> were analyzed. The results showed that the spontaneous combustion temperature of coal below 70 °C increased slowly with time, and the oxygen consumption and thermal strength increased slowly with temperature and accelerated when the temperature exceeded 100 °C. In anaerobic cooling, the cooling rate decreases with decreasing temperature. The temperature characteristics of coal spontaneous combustion can be better reflected by using a variety of gas ratios. Liang et al. [44] used the commonly used beam tube system, gas chromatography, infrared spectroscopy and other gas detection methods to monitor most of the gas compounds in the process of coal spontaneous combustion, and analyzed the generation order of these gas products. The results show that carbon oxides, hydrogen, methylene and other hydrocarbon gases are produced in the initial self-heating stage of coal spontaneous combustion. Based on the above conclusions, it is a more accurate method to determine the process of coal spontaneous combustion by using different gas ratios.

Among the various characteristic gases of spontaneous combustion of coal, the production of hydrocarbon gases is an important marker, and the production mechanism of hydrocarbons is not the same, but its production and consumption are mostly related to the types of microscopic functional groups. Since the production of hydrocarbons mostly occurs in the high-temperature stage, the monitoring of hydrocarbon marks that the risk of spontaneous combustion of coal has entered a serious harm stage. For example, the production of aromatic hydrocarbons shows a tendency to increase and then decrease [45,46] and release a variety of polycyclic aromatic hydrocarbons at high temperatures. The polycyclic aromatic hydrocarbons produced in raw coal are highly toxic, so monitoring them can reduce personnel hazards. Methane is another common hydrocarbon in the spontaneous combustion of coal, and it is very easy to cause spontaneous combustion. The presence of methane causes significant changes in the spontaneous combustion process of coal, which are often reflected in the content of functional groups. Cai [47] and Zhao [48] analyzed the changes in functional groups in coal under methane action using Fourier transform infrared spectroscopy (FTIR), thereby analyzing the formation of methane and the process changes of spontaneous combustion of coal under a methane atmosphere. Yang et al. [49] studied the role of ethylene and propylene in gas products, and found that small particles of coal can delay the time of coal adsorption to reach the saturation state in the process of adsorption by using two gases, and ethylene exhibits stronger activity in the adsorption process, so the detection of the content of hydrocarbons in the air can effectively warn the early stage of the coal spontaneous combustion process.

#### 4.2. Research on Early Warning Model and Technology

In order to achieve the fine classification of the coal spontaneous combustion process and the accurate early warning of the hidden dangers of spontaneous combustion and to ensure the effective development of the prevention and control of spontaneous combustion of underground coal and the safe mining of coal resources, Guo et al. [4] reconstructed the data curve by combining experimental data and numerical simulations, and established an early warning model of spontaneous combustion of coal. Yue et al. [5] treated the fresh raw

coal mined from the working surface and conducted a large-scale experiment of kilogram size in the laboratory, and used the self-designed coal spontaneous combustion experimental platform to simulate the self-heating oxidation and heating up. In the experiment, the gas and temperature indicators are collected and the curve fits of the stages of spontaneous combustion of coal are divided, and the characteristics of each stage are analyzed. After screening, CO, O<sub>2</sub>, C<sub>2</sub>H<sub>4</sub> and C<sub>2</sub>H<sub>6</sub> are selected as the main application indicators, supplemented by  $\varphi(\text{CO})/\varphi(\text{O}_2)$  and  $\varphi(\text{C}_2\text{H}_4)/\varphi(\text{C}_2\text{H}_6)$  as auxiliary analysis standards. According to the size of each index, the spontaneous combustion of coal is predicted, and a six-level early warning system of “gray, blue, yellow, orange, red and black” is established to quantitatively divide the risk of spontaneous combustion of coal, and effectively prevent and control underground coal fire disasters. Shu et al. [6] monitored the characteristics of the spontaneous combustion stage of coal through laboratory coal spontaneous combustion and ignition tests for coal samples from the western region. The characteristic gas reference standards with CO, O<sub>2</sub>,  $\Delta\varphi(\text{CO})/\Delta\varphi(\text{O}_2)$ , C<sub>2</sub>H<sub>4</sub> and C<sub>2</sub>H<sub>6</sub> as the indicators were determined, and a coal spontaneous combustion grading early warning prediction and prevention and control system was established. Among the five indicators, CO, O<sub>2</sub> and  $\Delta\varphi(\text{CO})/\Delta\varphi(\text{O}_2)$  have a good effect on the prediction of coal spontaneous combustion hazards, thus realizing the dynamic classification identification of coal fire disasters.

In addition, many scholars have established a series of fire hazard assessment methods based on the temperature characteristics and gas characteristics of the coal spontaneous combustion process, mainly including the fire coefficient R-2 [50], electromagnetic radiation (EMR) [51], PSO-SVR model [52], RF model [53], R/S analysis [54], and carbon monoxide generation rate (SCOGR) [55]. These methods were analyzed for a large number of data in the process of spontaneous combustion and heating of coal, extracted the temperature change law, used big data calculation methods or fitted the heating curve, or captured the physical parameters with landmark changes, and finally obtained an accurate, reliable and stable coal spontaneous combustion risk assessment method.

In addition, scholars [56–59] analyzed the movement law of gas in the goaf, predicted the spontaneous combustion of coal combined with the change of underground gas flow, and established a related model. The prediction of coal spontaneous combustion from the perspective of gas release mainly relies on the change in the stress of the underground coal seam, leading to the change in the pore structure, leading to an increase in air leakage; the channel of coal–oxygen binding is expanded, and oxygen is more likely to enter the depth of the coal body through these gaps, so the coal–oxygen composite reaction occurs internally. So far, a variety of means to predict the spontaneous combustion of underground coal have made great development and progress in both the theoretical stage and the application stage. Generally, in the field application, the characteristic gas early warning is the mainstay, and the temperature change of the coal body is assisted by other monitoring signals for real-time monitoring, which greatly reduces the disaster hazard of spontaneous combustion of coal, improves the safety and quality of underground operators and greatly reduces the economic losses in the mining process.

In the field of coal seam monitoring, Martirosyan, A.V. [60], in response to the high implementation cost of coal mine monitoring systems, proposed to consider the prototype of a real-time monitoring system for toxic and combustible gas concentrations that has been developed, triggering a response mechanism when concentrations exceed prescribed limits. Kazanin O. I. [61] analyzed the methane emission process of long wall panels through numerical simulation and proposed to adjust the degassing parameters and change the distance between ventilation crosscuts to improve the methane control of long wall panels. Sidorenko A.A. [62] made a proposal to achieve the highest possible level of coal production.

## 5. Conclusions

In this paper, 583 valid documents collected by Web of Science (core collection) are selected, and VOSviewer (version 1.16) is used to analyze the distribution characteristics of literature carriers, research subjects and hot spot frontiers through cooperative network

topology and keyword co-occurrence analysis, and systematically and comprehensively analyze the evolution process of coal spontaneous combustion early warning research, and draw the following conclusions:

- (1) The research authors have formed a fixed research cluster, and the degree of cooperation between the clusters is high and the relationship is close, but the connection and cooperation between the clusters is not high, and the international cooperation is relatively lacking. Research institutions have formed the main research force of scientific research institutions such as China Univ. Min. & Technol., Xian Univ. Sci. & Technol., and China Univ. Min. & Technol. Beijing, and have formed a relatively mature core community in the field of coal spontaneous combustion early warning. The number of research results in the field of spontaneous combustion of coal between countries is consistent with the distribution trend of geographical reserves of coal resources, and articles in this field are mostly found in large coal resource-producing countries, and the number of articles published has obvious geographical distribution characteristics.
- (2) The research on spontaneous combustion of coal is of great significance to the safe mining of underground mines, and the hot topics of research in this field can be summarized as “flag gas early warning” and “early warning model and technology”. In the research field of marker gases, it is often used to detect landmark gases such as carbon monoxide produced during the spontaneous combustion of coal as the judgment criteria for the signs and status of spontaneous combustion of coal, and this method has achieved remarkable results in practical application. Early warning model and technology research is guaranteed research that serves the safe production of underground coal mines, and this research field focuses on the precise early warning of the fine classification and spontaneous combustion hazards of the spontaneous combustion process of coal. The future development of early warning model and technology research will be based on big data, supported by intelligence and informatization, to achieve real-time monitoring of coal body status, early perception of dangerous situations, and timely early warning to ensure production safety. In the future, in the field of coal spontaneous combustion early warning, we should also strengthen information exchange and data exchange between authors, institutions and countries, rely on big data, artificial intelligence, digital twins and other technologies to achieve interdisciplinary integration and development in multiple fields, and further promote the research in the field of coal spontaneous combustion to be precise and intelligent.
- (3) The paper provides valuable information to experts involved in the prevention of spontaneous combustion of coal. On the one hand, it helps researchers to reduce the time spent in developing research questions for empirical articles, conducting bibliometric analysis or conducting content analysis for systematic literature reviews. On the other hand, it helps them to seek the latest information on the existing research and trends in the field of coal spontaneous combustion prevention, such as internal coal fire, coal chemical composition, coal pollution scale and type, coal crushing degree, moisture and ash content and coal seam monitoring.

**Author Contributions:** F.W.: formal analysis, writing—original draft, visualization. Z.J.: methodology, conceptualization, writing—review and editing. H.W.: methodology, conceptualization, writing—review and editing. Y.C.: writing—original draft, visualization. T.W.: formal analysis, visualization. R.T.: investigation. C.S.: investigation. G.N.: investigation. All authors have read and agreed to the published version of the manuscript.

**Funding:** This work was financially sponsored by the National Natural Science Foundation of China (52074156).

**Data Availability Statement:** The data are available from the corresponding author on reasonable request.



**Conflicts of Interest:** The authors declare that they have no known competing financial interests or personal relationships that could have appeared to influence the work reported in this paper.

## References

- Meng, Y.; Xie, D.H.; Su, B.; Gu, A.X. Statistics and Analysis of Coal Mine Production Safety Accidents in China from 2010 to 2019. *Miner. Eng. Res.* **2020**, *35*, 27–33.
- Investigation Report of “12.7” Spontaneous Combustion Pyrolysis Gas Explosion in Tang Yang Coal Mine. Available online: <https://www.mkaq.org/html/2019/08/25/493922.shtml> (accessed on 1 January 2022).
- Hegang Xiangyang Coal Mine Accident Was Initially Identified as a Major Fire Caused by a Gas Explosion. Available online: <https://heilongjiang.dbw.cn/system/2015/12/18/056997574.shtml> (accessed on 1 January 2022).
- Guo, J.; Jin, Y.; Wang, F.; Yang, P.P.; Sun, M.F. Research on multi-level warning method of coal spontaneous combustion based on Logistic regression analysis. *J. Saf. Sci. Technol.* **2022**, *18*, 88–93.
- Yue, N.F.; Jin, Y.; Sun, M.F.; Yang, C.F.; Ran, X.C.; Cheng, M. Multi-staged warning system for controlling the coal spontaneous combustion based on the various index gases. *J. Saf. Environ.* **2022**, *18*, 88–93.
- Shu, Y.G.; Zhao, Q.W.; Yu, Y.N. Research on prediction and forecast indicators system of easy spontaneous combustion coal seam. *Coal Sci. Technol.* **2019**, *47*, 229–234.
- Xie, X.C.; Liang, Y.Q.; Lin, C.; Li, L.L. Early warning system for mine fire accidents. *Saf. Coal Mines* **2019**, *47*, 229–234.
- Lei, Z.Q. Study on mine fire warning technology. *Coal Chem. Ind.* **2015**, *38*, 148–149.
- Tan, B.; Shao, Z.Z.; Guo, Y.; Zhao, T.; Zhu, H.Q.; Li, C.X. Research on grading and early warning of coal spontaneous combustion based on correlation analysis of index gas. *China Saf. Sci. J.* **2021**, *31*, 33–39.
- Zhong, X.X.; Wang, J.T.; Zhou, K. Monitoring and early warning technology of coal spontaneous combustion in coal mines: Research status and intelligent development trends. *Ind. Mine Autom.* **2021**, *47*, 7–17.
- Ren, W.X.; Guo, Q.; Shi, J.T.; Lu, W.; Sun, Y. Construction of early warning indicators for coal spontaneous combustion based on statistical characteristics of index gases. *J. China Coal Soc.* **2021**, *46*, 1747–1758.
- Wen, H.; Liu, Y.; Guo, J.; Jin, Y.F.; Zheng, X.Z. A multi-index-classified early warning method for spontaneous combustion of coal under air leakage blocking. *Int. J. Oil Gas Coal Technol.* **2021**, *27*, 208–226. [CrossRef]
- Wang, K.; Wang, Z.; Zhai, X.; Jiang, H. An experimental investigation of early warning index for coal spontaneous combustion with consideration of particle size: A case study. *Int. J. Coal Prep. Util.* **2022**, *43*, 233–247. [CrossRef]
- Zhou, X.X.; Zhang, X.F.; Qing, G. Classification of Spontaneous Combustion Hazard Levels of Coal with Different Metamorphism Degrees. *Combust. Sci. Technol.* **2022**, 1–4.
- Guo, Q.; Ren, W.; Lu, W. A Method for Predicting Coal Temperature Using CO with GA-SVR Model for Early Warning of the Spontaneous Combustion of Coal. *Combust. Sci. Technol.* **2022**, *194*, 523–538. [CrossRef]
- Wu, Y.; Zhang, Y.; Zhou, C.; Wang, J.; Wu, J.; Ren, T. Study of CO Sources and Early-warning Concentration of Spontaneous Combustion at Air Return Corner in Fully Mechanized Mining Faces. *Combust. Sci. Technol.* **2021**, *193*, 1587–1604. [CrossRef]
- Shao, Z.; Tan, B.; Guo, Y.; Li, T.; Li, X.; Fang, X.; Wang, F.; Zhang, Q.; Wang, H. Visualization and analysis of mapping knowledge domains for coal pores studies. *Fuel* **2022**, *320*, 123761. [CrossRef]
- Hong, X.L.; Long, Z.Z. Coal mine safety management researching situation analysis based on knowledge map. *Adv. Mater. Res.* **2014**, *3246*, 962–965.
- Xie, H.; Dai, W. Research status analysis of coal and gas outburst based on journal database. *J. North China Inst. Sci. Technol.* **2020**, *17*, 22–28.
- Liu, H.; Hong, R.; Xiang, C.; Lv, C.; Li, H. Visualization and analysis of mapping knowledge domains for spontaneous combustion studies. *Fuel* **2020**, *262*, 116598. [CrossRef]
- Wang, F.; Tan, B.; Chen, Y.; Fang, X.; Jia, G.; Wang, H.; Cheng, G.; Shao, Z. A visual knowledge map analysis of mine fire research based on CiteSpace. *Environ. Sci. Pollut. Res.* **2022**, *29*, 77609–77624. [CrossRef]
- Jamroz, D.; Niedoba, T. Application of multidimensional data visualization by means of self-organizing Kohonen maps to evaluate classification possibilities of various coal types. *Arch. Min. Sci.* **2015**, *60*, 39–50.
- Yang, F.; Qiu, D. Exploring coal spontaneous combustion by bibliometric analysis. *Process Saf. Environ. Prot.* **2019**, *132*, 1–10. [CrossRef]
- Ding, X.; Yang, Z. Knowledge mapping of platform research: A visual analysis using VOSviewer and CiteSpace. *Electron. Commer. Res.* **2022**, *22*, 787–809. [CrossRef]
- Thelwall, M. Bibliometrics to webometrics. *J. Inf. Sci.* **2008**, *34*, 605–621. [CrossRef]
- Zeng, L.; Li, R.Y.M. Construction safety and health hazard awareness in Web of Science and Weibo between 1991 and 2021. *Saf. Sci.* **2022**, *152*, 105790. [CrossRef]
- Pan, X.; Yan, E.; Cui, M.; Hua, W. Examining the usage, citation, and diffusion patterns of bibliometric mapping software: A comparative study of three tools. *J. Inf.* **2018**, *12*, 481–493. [CrossRef]
- van Eck, N.J.; Waltman, L. VOS: A New Method for Visualizing Similarities Between Objects. In Proceedings of the 30th Annual Conference of the Gesellschaft für Klassifikation eV, Freie Universität Berlin, Berlin, Germany, 8–10 March 2006; Studies in Classification, Data Analysis, and Knowledge Organization. Springer: Berlin/Heidelberg, Germany, 2007; pp. 299–306.

29. Shao, X.H.; Zhang, X.R.; Wang, W.C. Comparison of density functional theory and molecular simulation methods for pore size distribution of mesoporous materials. *Acta Physicochim. Sin.* **2003**, *19*, 538–542.
30. Deng, J.; Bai, Z.J.; Xiao, Y.; Song, Z. Present situation and challenge of coal spontaneous combustion disasters prevention and control technology. *Saf. Coal Mines* **2020**, *51*, 118–125.
31. Wang, W.F.; Deng, J.; Hou, Y.B. Design and application of high density network monitoring and warning system in coal spontaneous combustion hazardous area. *Coal Technol.* **2018**, *37*, 218–220.
32. Deng, J.; Xiao, Y.; Chen, X.K.; Cheng, F.M.; Wang, W.F. Study on early warning method of multi-source information fusion for coal mine fire. *J. Min. Saf. Eng.* **2011**, *28*, 638–643.
33. Yang, S.Q.; Qin, Y.; Sun, J.W.; Jiang, C.L.; Lun, J.L. Research on coupling hazard mechanism of mine gas and coal fire for a gassy and high spontaneous combustion propensity coal seam. *J. China Coal Soc.* **2014**, *39*, 1094–1101.
34. Wen, H.; Zhao, X.T.; Wang, W.F.; Wang, L.B.; Tian, Q.; He, J. Analysis on characteristics of indicator gases of spontaneous combustion of different coals. *Coal Convers.* **2020**, *43*, 16–25.
35. Wen, H.; Guo, X.M.; Zhang, D.; Cheng, X.J.; Wei, G.M.; Tang, R. Optimization of early prediction index for spontaneous combustion of gassy coal seam in Jianbei Coal Mine. *Min. Saf. Environ. Prot.* **2022**, *49*, 1–8.
36. Wen, H.; Lai, J.; Guo, X.M.; Zhang, D.; Dai, A.P.; Tong, P.; Li, P.; Wang, Y.; Chen, J. Research on classification and warning methods of coal spontaneous combustion in Gubei Coal Mine. *Coal Technol.* **2022**, *41*, 82–85.
37. Chen, X.X.; Bi, R.Q.; Huang, J.J.; Shan, W.X.; Xiao, J.; Wang, D.Y. Experimental study on early prediction index gas for spontaneous combustion. *Energy Sources Part A Recovery Util. Environ. Eff.* **2020**, 1–15. [CrossRef]
38. Wen, H.; Guo, J.; Jin, Y.F.; Wang, K.; Zhang, Y.T.; Zheng, X.Z. Experimental study on the influence of different oxygen concentrations on coal spontaneous combustion characteristic parameters. *Int. J. Oil Gas Coal Technol.* **2017**, *16*, 187–202. [CrossRef]
39. Guo, X.; Deng, C.; Zhang, X.; Wang, Y. Formation law of hydrocarbon index gases during coal spontaneous combustion in an oxygen-poor environment. *Energy Sources Part A Recovery Util. Environ. Eff.* **2019**, *41*, 626–635. [CrossRef]
40. Deng, J.; Zhao, J.Y.; Zhang, Y.N.; Geng, R.L. Study on coal spontaneous combustion characteristic temperature of growth rate analysis. *Procedia Eng.* **2014**, *84*, 796–805.
41. Deng, J.; Zhang, M.; Lei, C.K.; Wang, C.P.; Bai, Z.J.; Zhao, X.Y. Kinetic analysis of the low temperature spontaneous oxidation combustion of the coal seams due to the different metamorphism extents. *J. Saf. Environ.* **2021**, *21*, 94–100.
42. Wang, H.T.; Liu, L.Y.; Fan, B.; Fan, C.H.; Zhang, J.L. Analysis on Index Gas Characteristics of Long-flame Coal Spontaneous Combustion. *Coal Technol.* **2021**, *40*, 167–170.
43. Deng, J.; Xiao, Y.; Li, Q.; Lu, J.; Wen, H. Experimental studies of spontaneous combustion and anaerobic cooling of coal. *Fuel* **2015**, *157*, 261–269. [CrossRef]
44. Liang, Y.; Zhang, J.; Wang, L.; Luo, H.; Ren, T. Forecasting spontaneous combustion of coal in underground coal mines by index gases: A review. *J. Loss Prev. Process Ind.* **2019**, *57*, 208–222. [CrossRef]
45. Wang, H.; Cheng, C.; Chen, C. Characteristics of polycyclic aromatic hydrocarbon release during spontaneous combustion of coal and gangue in the same coal seam. *J. Loss Prev. Process Ind.* **2018**, *55*, 392–399. [CrossRef]
46. Altarawneh, M.; Oluwoye, I.; Dlugogorski, B.Z. Singlet-diradical character in large PAHs triggers spontaneous-ignition of coal. *Combust. Flame* **2020**, *212*, 279–281. [CrossRef]
47. Cai, J.; Yang, S.; Hu, X.; Xu, Q.; Zhou, B.; Zhang, Z. The Relationship between Functional Groups and Gaseous Productions and Micropore Structures Development of Coal Oxidized at Low Temperature under Methane-Diluted Atmospheres. *Combust. Sci. Technol.* **2019**, *191*, 1337–1353. [CrossRef]
48. Zhao, J.; Wang, T.; Deng, J.; Shu, C.-M.; Zeng, Q.; Guo, T.; Zhang, Y. Microcharacteristic analysis of CH<sub>4</sub> emissions under different conditions during coal spontaneous combustion with high-temperature oxidation and in situ FTIR. *Energy* **2020**, *209*, 118494. [CrossRef]
49. Yang, S.; Dai, G.L.; Tang, M.Y. Experiment Study on Mark Gas of Coal Spontaneous Combustion Based on Programmed Temperature Program. *Saf. Coal Mines* **2018**, *49*, 24–27.
50. Guo, J.; Wen, H.; Zheng, X.; Liu, Y.; Cheng, X. A method for evaluating the spontaneous combustion of coal by monitoring various gases. *Process Saf. Environ. Prot.* **2019**, *126*, 223–231. [CrossRef]
51. Kong, B.; Li, Z.; Wang, E.; Lu, W.; Chen, L.; Qi, G. An experimental study for characterization the process of coal oxidation and spontaneous combustion by electromagnetic radiation technique. *Process Saf. Environ. Prot.* **2018**, *119*, 285–294. [CrossRef]
52. Deng, J.; Lei, C.; Xiao, Y.; Cao, K.; Ma, L.; Wang, W.; Laiwang, B. Determination and prediction on “three zones” of coal spontaneous combustion in a gob of fully mechanized caving face. *Fuel* **2018**, *211*, 458–470. [CrossRef]
53. Lei, C.; Deng, J.; Cao, K.; Ma, L.; Xiao, Y.; Ren, L. A random forest approach for predicting coal spontaneous combustion. *Fuel* **2018**, *223*, 63–73. [CrossRef]
54. Hu, X.; Yang, S.; Zhou, X.; Yu, Z.; Hu, C. Coal spontaneous combustion prediction in gob using chaos analysis on gas indicators from upper tunnel. *J. Nat. Gas Sci. Eng.* **2015**, *26*, 461–469. [CrossRef]
55. Liu, W.; Qin, Y. A quantitative approach to evaluate risks of spontaneous combustion in longwall gobs based on CO emissions at upper corner. *Fuel* **2017**, *210*, 359–370. [CrossRef]
56. Liu, W.; Qin, Y. Multi-physics coupling model of coal spontaneous combustion in longwall gob area based on moving coordinates. *Fuel* **2017**, *188*, 553–566. [CrossRef]

57. Hu, Z.; Xia, Q. An integrated methodology for monitoring spontaneous combustion of coal waste dumps based on surface temperature detection. *Appl. Therm. Eng.* **2017**, *122*, 27–38. [CrossRef]
58. Su, H.; Sun, S.; Zhou, F.; Song, X.; Shi, B. Risk analysis of coal self ignition in long wall gob: A modeling study on three dimensional hazard zones. *Fire Saf. J.* **2016**, *83*, 54–65.
59. Lyu, P.; Chen, N.; Mao, S.; Li, M. LSTM based encoder-decoder for short-term predictions of gas concentration using multi-sensor fusion. *Process Saf. Environ. Prot.* **2020**, *137*, 93–105. [CrossRef]
60. Martirosyan, A.V.; Ilyushin, Y.V. The Development of the Toxic and Flammable Gases Concentration Monitoring System for Coalmines. *Energies* **2022**, *15*, 8917. [CrossRef]
61. Sidorenko, A.A.; Dmitriev, P.N.; Alekseev, V.Y.; Sidorenko, S.A. Improvement of techno-logical schemes of mining of coal seams prone to spontaneous combustion and rockbumps. *J. Min. Inst.* **2023**, 1–13. [CrossRef]
62. Kazanin, O.I.; Sidorenko, A.A.; Sidorenko, S.A.; Ivanov, V.V.; Mischo, H. High productive longwall mining of multiple gassy seams: Best practice and recommendations. *Acta Montan. Slovaca* **2022**, *27*, 152–162. [CrossRef]

**Disclaimer/Publisher’s Note:** The statements, opinions and data contained in all publications are solely those of the individual author(s) and contributor(s) and not of MDPI and/or the editor(s). MDPI and/or the editor(s) disclaim responsibility for any injury to people or property resulting from any ideas, methods, instructions or products referred to in the content.

## Article

# Preliminary Exploration of the Technology of Coal Reshaping and Replacement Mining of Abandoned Coal in Goafs

Li Li <sup>1,2,3,\*</sup>, Xiao Zhang <sup>1,2,3</sup>, Bin Hu <sup>1</sup> and Shun Lei <sup>1,2,3</sup>

<sup>1</sup> CCTEG Coal Mining Research Institute, Beijing 100083, China; zhangxiao@tdkcsj.com (X.Z.); yixintiankong@163.com (B.H.); cumt\_leishun@163.com (S.L.)

<sup>2</sup> Tiandi (Yulin) Mining Engineering & Technology Co., Ltd., Yulin 719000, China

<sup>3</sup> Tiandi Science and Technology Co., Ltd., Beijing 100013, China

\* Correspondence: lilizmk@163.com

**Abstract:** Recycling of coal resources left behind in goafs and the treatment and utilization of solid waste from mines are topical issues faced by the global coal mining industry at present. With the annual reduction of recoverable reserves of coal resources and the dependence on coal resources that are difficult to replace, the problems have become increasingly prominent, seriously limiting the development of coal resources and the implementation of environmental protection work. The mutual influence between the strength of filling materials and the size of loose coal in the CRRM process through numerical simulation experiments, laboratory rock mechanics experiments, and on-site large-scale similar simulation material experiments is explored. It is ultimately believed that selecting a filling material with a 20 cm particle size of loose coal and a 90% proportion of loose coal for 7 days can meet the requirements of the CRRM process, and this conclusion has been verified through on-site engineering scale experiments. The scientific problems faced by various links in the process of filling and replacing abandoned coal in goafs were analyzed, and improvement methods were further proposed; the technical system of filling and replacing abandoned coal was improved, and new directions for the efficient and safe recovery of abandoned coal resources worldwide in the future were developed.

**Citation:** Li, L.; Zhang, X.; Hu, B.; Lei, S. Preliminary Exploration of the Technology of Coal Reshaping and Replacement Mining of Abandoned Coal in Goafs. *Processes* **2023**, *11*, 2474. <https://doi.org/10.3390/pr11082474>

Academic Editors: Carlos Sierra Fernández, Feng Du, Aitao Zhou and Bo Li

Received: 18 July 2023  
Revised: 8 August 2023  
Accepted: 16 August 2023  
Published: 17 August 2023



**Copyright:** © 2023 by the authors. Licensee MDPI, Basel, Switzerland. This article is an open access article distributed under the terms and conditions of the Creative Commons Attribution (CC BY) license (<https://creativecommons.org/licenses/by/4.0/>).

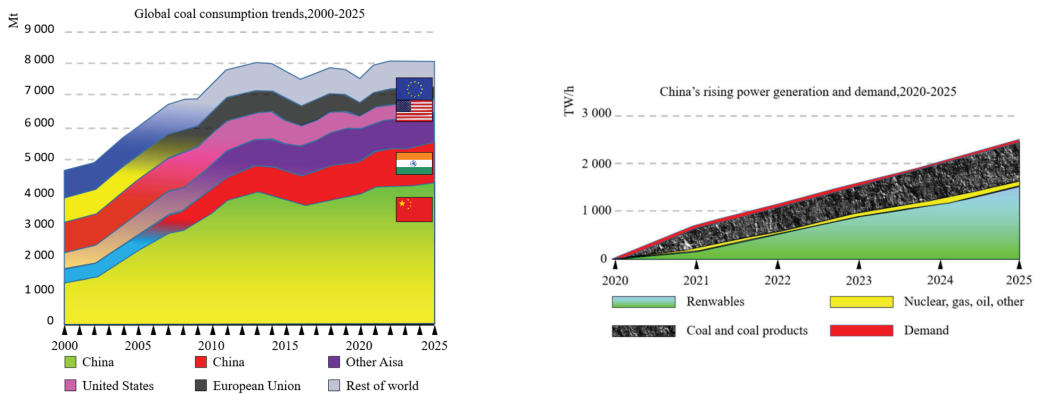
**Keywords:** coal recycling; replacement mining; filling material

## 1. Introduction

Coal has long been one of the most abundant and widely distributed pillar energy sources on Earth, with the most convenient ease of use and downstream products [1]. By the end of 2022, the world's proven coal resources reserve was 1.07 trillion tons, of which the United States accounts for 23.2% [2], reaching 248.941 billion tons, and China accounts for 13.3% [3], reaching 207.886 billion tons [4]. Although major energy production and consumption entities around the world are constantly and vigorously adjusting their energy structure, the dependence of various countries on coal resources will be difficult to change for a considerable period in the future. Moreover, in the early stages of mining technology development, China, the United States, and European countries generally have mining processes such as room pillars and knife pillars that support the roof and overlying rock through leftover coal bodies [5]. Many high-quality coal resources still need secondary development [6].

The United States Geological Survey (USGS), together with the U.S. Bureau of Mines and the Energy Information Administration (EIA), jointly found that the mining output of coal only accounts for 50~60% of the proven reserves, while the average recovery rate of coal mines in China is 30~35% [7], the recoverable reserves of coal reserves in China reach 40 billion tons [8,9], and the burial depth is generally shallow. Current coal resource mining has entered the deep stage and is facing many complex environmental stress problems.

The secondary development of high-quality coal resources left behind in shallow buried areas is even more urgent, as shown in Figure 1.



**Figure 1.** Global coal consumption trends (2000–2025) and China’s energy supply and demand relationship (2020–2025). [Coal medium-term market report—Details—Trove].

In recent years, experts and scholars around the world have also conducted a large amount of targeted research on the mining pressure theory and the technology of residual coal mining.

Stefaniak S and Twardowska I et al. [10] studied the range of rock disturbance during the process of residual coal remining and the reuse of secondary coal resources. They also studied the impact of acid (ARD) and neutral rock drainage (NRD) on the environment from two physical and chemical perspectives on the mining waste generated during coal mining.

Shimada H [11] et al. analysed and discussed the applicability of longwall mining faces in the large-scale recovery of residual coal and their industrial design methods through numerical simulation, focusing on the stability of coal walls and the improvement of the recovery rate during the stage of residual coal remining. They conducted in-depth research on the slope and mining boundary stability issues that occurred during the recovery of residual coal resources and comprehensively considered the coal resource recovery rate. Reasonable support design parameters were provided under safe and environmental conditions.

Scientific research on the theory of residual coal resource extraction by Chinese experts and scholar teams has also made significant progress.

Feng, GR, Zhang, RJ [12,13] et al. carried out an analysis on the structural stability of the surrounding rock of the stope when the full seam residual coal is mined by longwall working face filling or full caving method by means of numerical simulation, field measurement and physical similar simulation experiments and put forwards the idea and technology of constructing a “filling body direct roof” structure through gangue filling to control the movement of rock strata and protect the longwall working face of residual coal recovery.

Xv, JC et al. [14] proposed a calculation method for the limit parameters of coal spontaneous combustion in residual coal mining areas based on heat generation intensity, oxygen consumption rate, and energy conservation principle of loose coal determined by coal spontaneous combustion experiments. This provides an effective theoretical basis for the prevention and control of concealed dangers of spontaneous coal combustion during the residual coal remining stage.

Cheng, WM et al. [15] studied the coupling mechanism of gas and residual coal spontaneous combustion in the goaf of a fully mechanized top coal caving face and further derived the multiparameter influence evolution law of residual coal spontaneous combustion and gas coupling disaster in the goaf through a multifield coupling 3D reconstruction method.

They improved the high-level drilling gas drainage and the injection of fireproof material technology in the goaf of residual coal, ensuring the gas limit requirements of the working face during the process of residual coal remining.

Regarding the application of rock pressure theory and filling materials in the filling mining process, Zhou, HQ et al. [16] proposed five paste material filling mining methods and verified their feasibility.

Zhang JX et al. [17] systematically studied the characteristics of mining pressure, key rock strata movement, and surface deformation in the application process of the gangue direct filling comprehensive mining method through experimental analysis and numerical simulation.

Bai, JB et al. [18] started from two main lines, stress control and surrounding rock reinforcement, and analysed the impact of advanced mining on the working face during high water material filling mining, the stability of the retained roadway surrounding rock, and the stress and deformation characteristics of the adjacent working face during the mining stage. They proposed a design method for key parameters of surrounding rock control in high-water material filling mining.

Feng and GM [19] proposed through a large number of laboratory experiments that A and B mixed ultrahigh water filling materials, with a 95% water volume ratio as the boundary between high and ultrahigh water materials. They successfully used ultrahigh water materials in coal mining sites to extract coal seams under buildings.

To fill and remine the remaining coal resources in the goaf, the mechanical support parameters of the filling material on the goaf roof were studied. For the preparation of inorganic high water materials using fly ash (CFA) and residual slag as raw materials, second-order and pseudo-first-order dynamic models were fitted to reduce the maintenance synthesis time [20–22].

For the process of recycling and utilizing residual coal resources, Wang, F., and Zhang, C team [23] used the Mark Bieniawski formula and numerical simulation to calculate the reasonable width of coal pillars and intelligent slope mining in the longwall working face. They analysed the stress state of the surrounding rock in the goaf of residual coal resources, achieving safe, efficient, and high recovery rates in the longwall working face mining of the goaf.

During the secondary mining process, under the action of mining stress, the continuous fracture and instability of the roof in the roof caving area (RCZ), as well as the evolution process of the safety and efficiency of mining residual coal resources [24], were simulated physically and analysed on-site. It was found that the rotation of the basic roof fracture towards the goaf in the RCZ area significantly increases the support pressure of the hydraulic support in the working face, and the sudden instability of the coal pillar also weakens its support effect on the basic roof. A mechanical model was established for the interaction between the surrounding rock and support in the goaf of residual coal remining, and the pregroting solidification repair technology in the RCZ was studied to improve the bearing capacity of the coal pillar.

For mining areas after noncomplete caving mining activities, Prakash A et al. [25] systematically studied the effects of rainfall, secondary mining disturbances, and other behaviours on the surface subsidence effect of working faces. Mine entries close to residual bearing coal pillars (RBCPs) will suffer large deformation that may cause rock burst. To better understand the deformation mechanism and develop safe and practical guidelines for entry design, most studies focus on the absolute size of the stress field in and around the pillar. Kang J's team [26] proposed a formula for deriving the support pressure of residual coal pillar surrounding rock using the stress concentration coefficient (SCC), stress gradient (SG), and lateral pressure coefficient (CLP), which can serve as a guide for designing mining in similar geological and mining environments.

The working condition matching between the key equipment and the caving zone (RCZ) in the secondary mining of leftover coal, as well as the structural mode of roof fracture, have been studied through similar simulation experiments and finite element

numerical simulation experiments [27,28]. It is believed that the main reason for the sudden increase in working resistance of the support in the mining area is that long key blocks cross the RCZ zone.

Hao H [29] conducted in-depth research on the evolution law of gas oxygen nitrogen adsorption coupling under goaf conditions based on Monte Carlo simulation and believed that the free state gas analysed in the goaf would affect the interaction between coal and air, thereby hindering the spontaneous combustion of residual coal.

For the phenomenon of roadway surrounding rock fragmentation and difficulty in supporting during the secondary development of residual coal resources, Chen Y and Shimada H team et al. [30–32] found that retaining roadway coal pillars with a width-to-height ratio of 1 or more is a key measure in maintaining the stability of roadway surrounding rock during the re-mining process of goaf residual coal.

In addition, Xca B., Sza B et al. [33–35] established a reasonable calculation model for residual coal and natural gas resources in abandoned mine goafs and conducted in-depth research on the impact mechanism of CH<sub>4</sub> storage and collection in the secondary development process of residual coal in goafs.

For the current situation of the recovery of coal resources left behind in the existing room pillar type goaf, high water material filling or flexible membrane pier pillar support is usually used to support the roof of the goaf. The high water material filling cost is high, and it is often difficult to adapt economically to the profit cost brought by residual coal mining. In addition, during the mining process, the shearer is difficult to cut high water materials with a hardness far higher than the coal seam. The method of flexible membrane pier column support also has limitations, such as high cost and limited support area. Therefore, the CRRM method is used to reshape the entire floor of the room column-type goaf to form a new long wall-type goaf, which has great potential for application and theoretical research in the local area [36].

The method of using inorganic high-water materials to fill the goaf and control the movement of overlying strata has been relatively mature in the first mining face. The strength, stability, and economy of the materials are suitable for mines that require filling mining methods [37]. However, it is still urgent to study and explore the complex roof and floor integrity conditions and the performance of mixing loose solid waste or loose coal during the operation of residual coal mining. This article focuses on the preliminary exploration of the method of using inorganic high-water materials to cement and fill loose coal and gangue into a pillar-type goaf to reshape the remaining coal in the goaf into a whole coal seam. It provides a theoretical basis for the ratio parameters of inorganic high-water materials, the control requirement parameters of roof rock layers, and the difficulties in construction technology.

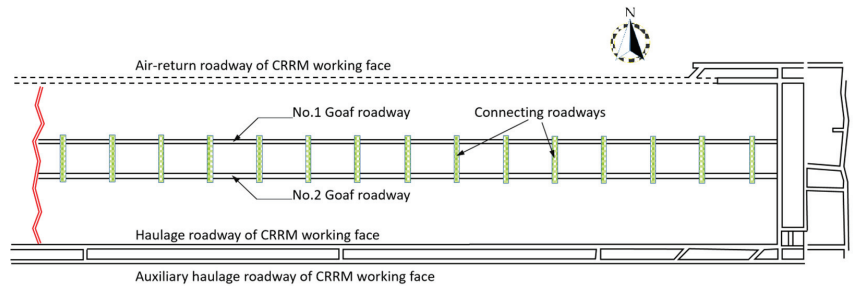
## 2. Coal Remoulding and Replacement Mining Technology (CRRM)

### 2.1. Engineering Application Background of CRRM

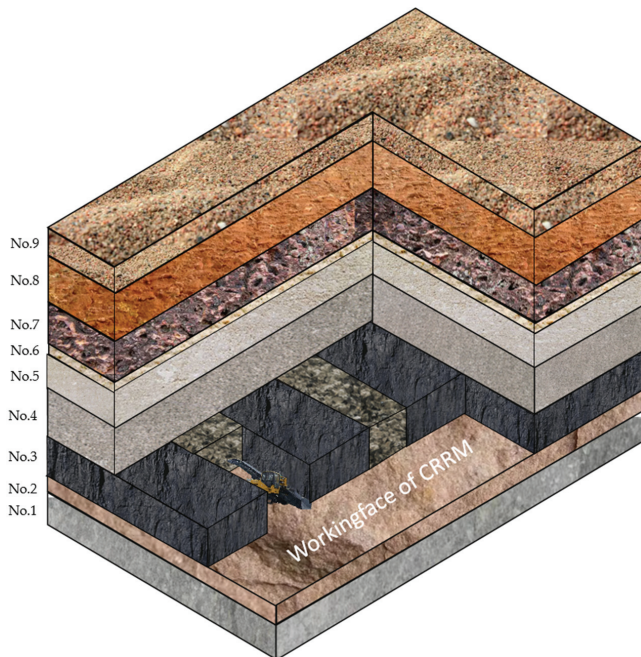
To solve the contradiction between the recovery of coal resources left behind in a pillar-type goaf and the difficult matching of time and space between water sand filling and pipeline paste filling coal mining methods, as well as the poor economic efficiency, the author's team proposes the concept of "coal seam reshaping and replacement filling" in a pillar-type goaf, which means that the coal or gangue produced by the excavation face or other mining faces is filled into the goaf through a dumping machine and initially compacted. The use of inorganic high-water materials to cement and form loose coal (gangue) bodies achieves the goal of filling the free space of the old goaf again to form a hole, reshaping the complete coal seam, and effectively controlling the roof rock layer of the old goaf. It has the economic advantages of a fast construction period, no impact on the quality of the recovered coal, safety and reliability and is difficult to compare with other methods [38–40].

The engineering background shown in Figure 2 is a pillar-type goaf residual coal mining face arranged in the #5 coal seam of a coal mine in Shenmu City, Shaanxi Province.

The working face has a length of 1529.4 m, a width of 193.5 m, and an area of  $2.96 \times 10^5 \text{ m}^2$ , with an average coal thickness of 5.4 m. The coal seam has a low coefficient of variation and is a horizontal coal seam. The average width of the two empty alleys in the middle is 6.12 m, and there is a total of 21 connecting alleys, with an average width of 6.12 m. After deducting the total amount of coal extracted from the goaf, the remaining minable coal in the working face is approximately  $1.68 \times 10^6$  tons, and the coal quality is ultralow ash, ultralow sulfur, ultralow chlorine, high calorific value, high volatility, medium fixed carbon, high quality and easy to select nonstick coal. The burial depth of Coal Seam #5 is 140 m, and the characteristics of the roof and floor of Coal Seam #5 are shown in Table 1. The direct roof of Coal Seam #5 is medium hard and dense 5.2 m fine sandstone, the basic roof is 18.7 m medium hard and stable fine sandstone, and the floor is siltstone and fine sandstone, as shown in Figure 3. According to the preliminary analysis, the direct roof is hard and easily falls with mining. The basic roof is thick and hard and can form a good protective structure for the stope under the condition of crustal stress with a buried depth of 140 m.



**Figure 2.** Mining layout scheme of CRRM working face.



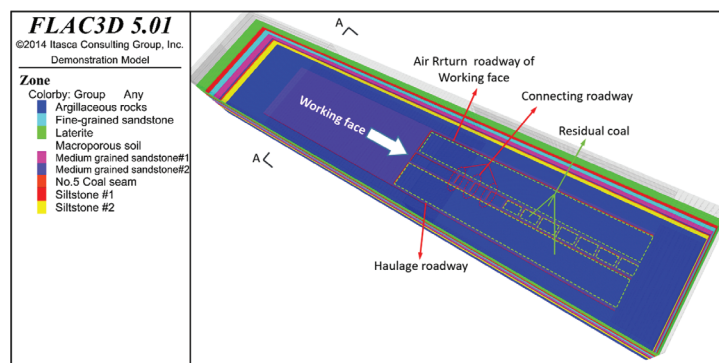
**Figure 3.** Spatial comprehensive geological histogram of CRRM working face in the engineering field.

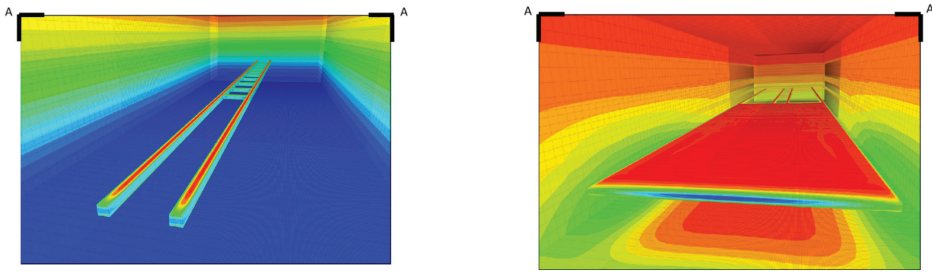


**Table 1.** Rock layer name, annotation to Figure 3.

Stratum Name & Hermeneutics	Lithology	Thickness (m)	Feature Description
	Macroporous soil	50.0	Sediments mainly composed of silt and containing a certain proportion of fine sand, extremely fine sand, and clay particles
	Laterite	35.0	Reddish brown with high water content, low density, and high strength
9	Siltstone #1	15.0	Contains more quartz, followed by feldspar and rock debris, with a hard texture and low density
8	Fine-grained sandstone	18.7	It is generally light grey, containing feldspar and a small amount of rock debris
7. Main roof	Medium grained sandstone #1	21.3	Mainly fine sandstone, grey, dark grey with thin layer of siltstone
6. Immediate roof	Medium grained sandstone #2	5.2	Fine-grained sandstone is mainly grey and light grey, with medium sorting, containing muscovite flakes and dark minerals intercalated with thin layers of siltstone, in an interlayered and wavy bedding.
5. Coal seam	Coal	5.4	Proctor hardness reaches 2.38, thickness is stable
4. Immediate floor	Siltstone #2	20.0	Light grey, intercalated with thin layers of fine-grained sandstone, interbedded, containing fragments of plant fossils.
3. Main floor	Argillaceous rocks	30.0	Grey, light grey, well sorted, locally calcareous cementation, containing a small amount of plant fossils, wavy bedding.
2. Refilling bearing structure	Inorganic high water filling material + scattered coal/Gangue	5.4	Refill the roadway space via two methods: accumulation compaction grouting or mixing water spray cementation
1	Crawler gangue filling machine		Suitable for all-around filling of coal mine roadways, with the function of ejection compaction, high filling density, and good roof connection effect

As shown in Figure 4, the spatial relationship between the CRRM process working face of Coal Seam #5 and the eastern old goaf is modelled. After forming longwall mining conditions in the working face, there are two reshaped coal tunnels formed by the reinforcement of loose coal in the near central position. After applying ground stress in the finite element numerical simulation model, it was found that the peak stress values of the roof of the two empty tunnels are relatively large, and the relative displacement of the two sides is also relatively large.

**Figure 4.** Cont.



**Figure 4.** 3D schematic diagram of excavation space and mining sequence in the mining area. (A—A represents the profile).

### 2.2. Analysis of the Mechanical State of the Surrounding Rock in the Closed Goaf

The eastern goaf of the #5 coal seam working face is a typical pillar-type goaf formed before 2009. The No. 1 goaf extends from west to east with a length of 937 m and a width of 6.12 m. The No. 2 goaf is arranged parallel to the No. 1 goaf, with a length of approximately 945 m. There are 21 connecting roadways and 22 interval coal pillars between the two goafs, with an average width of 6.12 m. The average recovery rate in this area is less than 23%, and nearly 70% of the coal resources urgently need to be recycled and utilized. Due to the burial depth of coal seam #5 being approximately 140 m, the internal stress of the surrounding rock and connecting roadway pillars in the eastern goaf is relatively small, and the mechanical properties of the coal in this area are good, belonging to the medium hard coal seam. Through borehole television observation, it was found that after nearly 14 years of stress release and full displacement of the surrounding rock towards the free space, the retaining state of the goaf surrounding rock is good, and there is no significant difference in the amount of roof subsidence and the relative movement of the two sides of the connecting roadway compared to before the goaf closed.

However, considering the secondary disturbance caused by the roadway excavation in the working face and the stress redistribution impact caused by the third disturbance caused by mining on the eastern goaf, in combination with local coal mining safety policies, laws and regulations and according to the latest version of coal mine safety regulations on goaf management and the relevant regulations of the Shaanxi Provincial Emergency Department on goaf management, it is necessary to strictly detect and explore the internal roof situation of the goaf. The content of toxic and harmful gases, as well as the water damage situation of the surrounding rock layer in the goaf, must be strictly verified and approved before the goaf can be disturbed again, and goaf operations are strictly prohibited. Therefore, before designing the parameters related to the CRRM process, it is necessary to estimate and evaluate the impact of mining disturbance on the surrounding rock of the #5 coal seam goaf and the CRRM working face when passing through the goaf through measurement and numerical simulation experiments. The numerical simulation experimental model is shown in Figure 2. Considering the excavation length of the stope roadway and the provisions in the Adhémar Jean Claude Barré de Saint-Venant Principle [22], the external boundary size of the model is 1500 m × 500 m × 200 m long × wide × high), and the model height ranges from the basic floor to the macroporous soil layer on the surface. After excavation, the natural gravity of each part of the rock layer is shared and transmitted to the surrounding rock of the mining site, with fixed horizontal boundary constraints. Based on the actual mining geological conditions, two empty tunnels and 21 connecting tunnels in the east were first extracted, and the built-in Fish language [23] was used to fully consider the full impact of a 14-year time step on the stress redistribution and displacement of the surrounding rock in the goaf. After excavation balance, the calculation results showed that the top view slice of the goaf location roof is shown in Figure 3.

In Figure 5, it can be seen that the distance between two adjacent alleys is 50 m, and the leading peak stress of the alleys reaches about 4.28 MPa, with an impact range of about

2.2 m. The top view of the eastern goaf (a) and the cross-sectional map of the surrounding rock state of the goaf are comprehensively analysed. The colour cloud map in the figure represents the variation law of the vertical stress field, and the contour line represents the displacement; (b), (d) and (f) are the stress displacement states of the surrounding rock in the middle of the left coal pillar at 1235 m, 1285 m, and 1335 m, respectively; (c), (e) and (g) are 1260 m, respectively. The stress displacement state of the surrounding rock near the free surface of the excavation of the connecting roadway near the coal pillars at 1310 m and 1360 m positions.

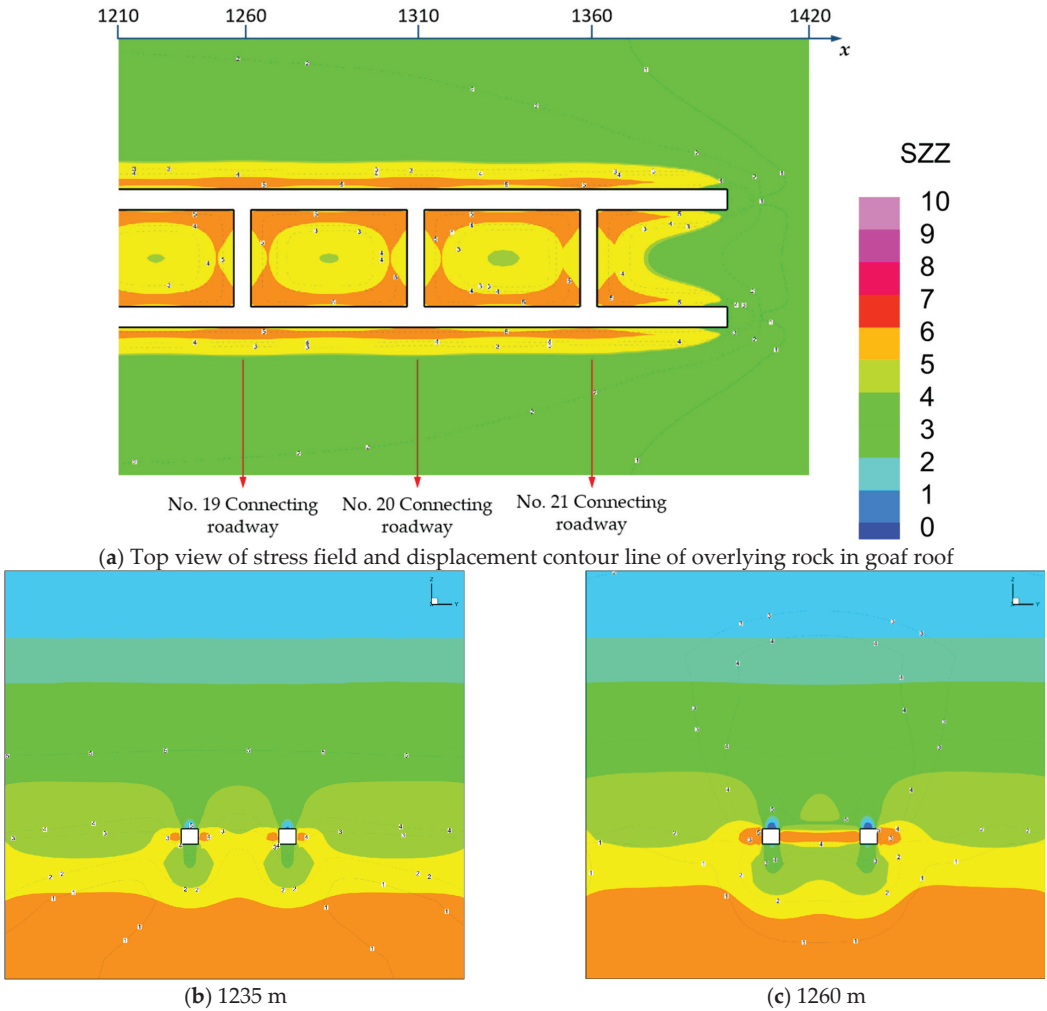
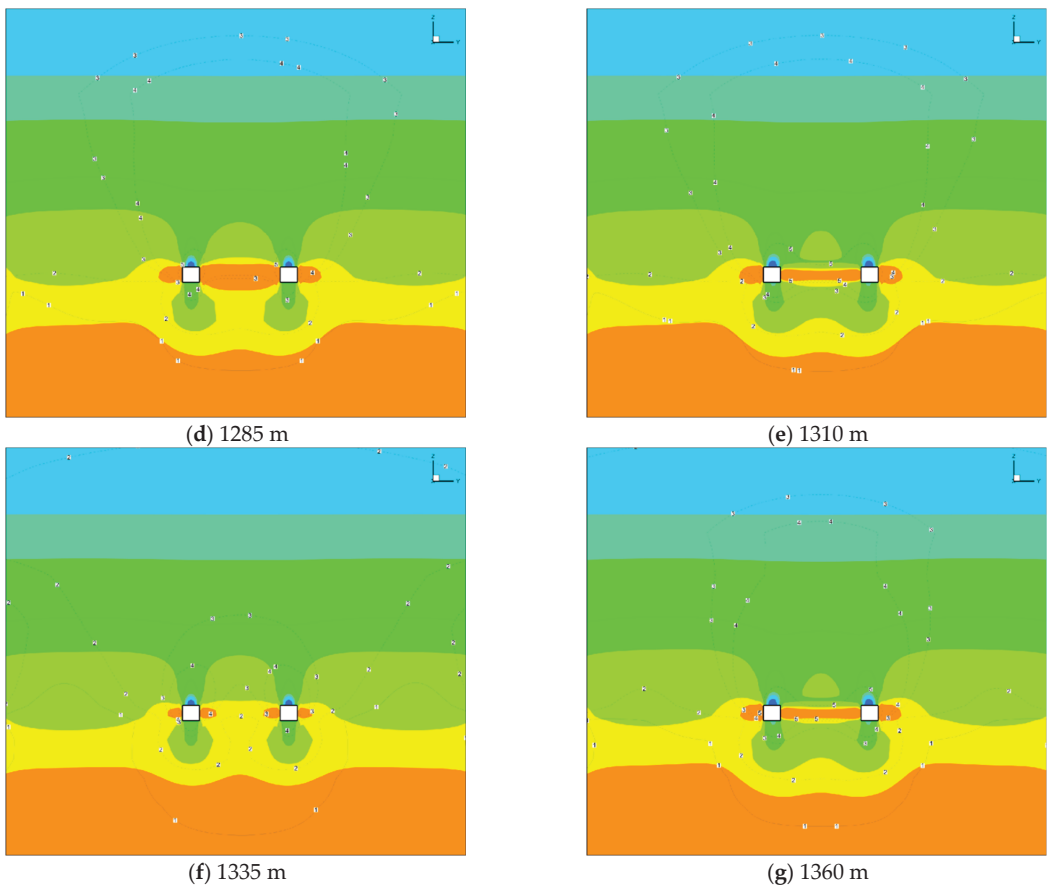


Figure 5. Cont.



**Figure 5.** Surrounding rock in the middle of the empty roadway (b,d,f) and state of the connecting roadway surrounding rock.

Through an analysis of the evolution law of the vertical stress displacement field, as the section position of the tunnel extends from west to east ( $x: 1235 \text{ m} \rightarrow 1285 \text{ m} \rightarrow 1335 \text{ m}$ ), it is not difficult to see that the stress concentration range on both sides of the tunnel first increases and then decreases, and the peak stress value reaches approximately 5.32 MPa. The maximum displacement occurs at the top of the roadway, with a peak displacement of approximately 0.5 m, and the mining disturbance, with a displacement of 0.2–0.4 m in the surrounding rock of the roadway, also shows a trend of first increasing and then decreasing in the range of influence on the top and bottom of the roadway. Analysis of the stress-strain displacement variation law of the surrounding rock of the two roadways extending from west to east indicates that the stress and displacement peaks in the central area of the roadway are greater than those at the cut and stop line positions. The characteristics exhibited are significantly different from the stress state changes of the surrounding rock of the roadway exhibited by traditional longwall mining techniques. Therefore, it is of great significance to simulate the surrounding rock state of the pillar goaf before remining.

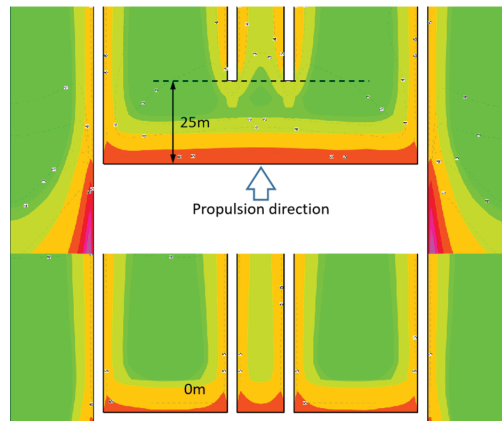
As the profile position of the remaining coal pillar extends from west to east ( $x: 1260 \text{ m} \rightarrow 1310 \text{ m} \rightarrow 1360 \text{ m}$ ), the peak stress of the coal pillar near the connecting roadway reaches approximately 4.27 MPa, and the influence range of the peak stress also shows a pattern of first increasing and then decreasing. The development range of the 0.2–0.4 m displacement contour line first increases and then decreases, and the development height affects the basic

top #1 medium-grained sandstone, and the surrounding rock displacement reaches 0.5 m, penetrating the coal pillar between the connecting roadways. The average stress value of the residual coal pillar near the connecting roadway is smaller than that of the surrounding rock in the middle of the empty roadway, while the displacement is greater than that in the middle of the empty roadway. Therefore, the control effect of the filling body in the connecting roadway on the top, bottom, and two sides of the surrounding rock, as well as the support strength and deformation capacity, is crucial. It directly affects the safety of the mining site, the operational efficiency of the coal mining machine, and the pushing efficiency of the hydraulic support when CRRM is used to reshape the coal seam.

Furthermore, it is necessary to study the influence of advanced support stress during secondary mining on the surrounding rock state of the goaf. The goaf is selected as an unsupported and unfilled bare goaf state for simulation to obtain the effect of secondary mining disturbance under adverse conditions and obtain suitable guidance for the strength parameters of the filling material.

### 2.3. Selection of the Simulation Method

Figure 6 shows that as the secondary mining face approaches the eastern goaf from the 25 m position, the goaf roadway is affected by advanced stress within a range of approximately 27 m, with a maximum peak value of 5.72 MPa at a distance of 2.4 m from the coal wall of the working face. Moreover, as the working face continues to advance to the front of the goaf, the maximum displacement of the coal pillars between the goafs increases from 0.407 m to 0.54 m, which indicates that the advanced stress superposition disturbance caused by secondary mining will further have a relatively small adverse impact on the stability of the goaf coal pillars.



**Figure 6.** Evolution of surrounding rock mechanical state when the CRRM working face gradually advances towards goaf position.

### 2.4. Preliminary Determination of the Overall Strength of the Required Filling Materials

The migration of roof rock layers and redistribution of stress caused by secondary mining require that the materials filled in the goaf not only timely limit the displacement of the roof and two sides but also bear the high roof force caused by the disturbance of the advanced support pressure during remining [26].

It is also necessary to consider that after the coal seam is reshaped into a long wall working face, when the shearer cuts, the cohesive force and stiffness of the filling material should not bring excessive working strength to the cutting teeth of the coal mining machine. Furthermore, considering the chemical pollution caused by coal washing to the environment, the filling material is more suitable for selecting a certain proportion of loose coal and inorganic high-water cementitious materials to mix and form a whole.

In consideration of the above aspects, the optimal scheme is when the overall mechanical properties of the bulk coal mixed material are similar to those of the original coal seam. Then, the rock mechanics parameters of middling coal under the geological conditions in this paper are calibrated in the laboratory, and the target properties of the bulk coal mixed filling material that needs to be achieved are as follows. 1. The uniaxial compressive strength (UCS) reaches 1.5 MPa. 2. The cohesion  $C$  reaches 1.3 MPa. 3. The proportion of loose coal quality should exceed 80%. 4. The damage time shall not be less than 500 s.

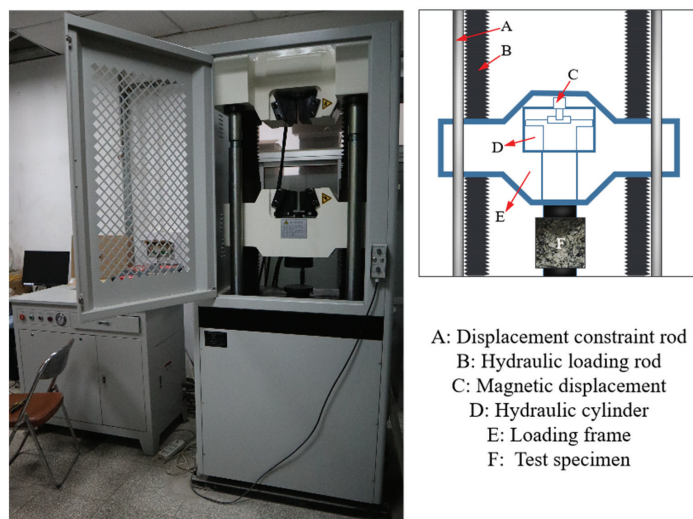
### 3. Maintenance Mechanics of Bulk Coal Cementitious Materials in the Laboratory

There are usually two ways to add cementitious materials to the bulk coal pile for reinforcement during on-site construction. 1. Premix solid powder inorganic high-water cementitious materials with water and inject them into the bulk coal pile through short pipe grouting. 2. Mix solid powdery inorganic high-water cementitious material with loose coal and lay it layer by layer into the goaf connecting the roadway and the interior of the roadway, and spray with water to form cementitious material until it reaches the top. It is difficult to control the grouting radius and cementation range when loose coal blocks are used.

To truly replicate the cementitious process of loose coal in the laboratory, inorganic high-water cementitious materials in the form of solid powder were mixed with loose coal and placed layer by layer in a 10 cm × 10 cm × 10 cm specimen curing box and soaked with water in layers. After seven days of curing, uniaxial loading mechanical experiments were conducted to investigate the influence of different factors (bulk coal particle size, proportion of inorganic high water cementitious materials) on whether the overall mechanical properties of bulk coal cementitious materials can reach the target reference value.

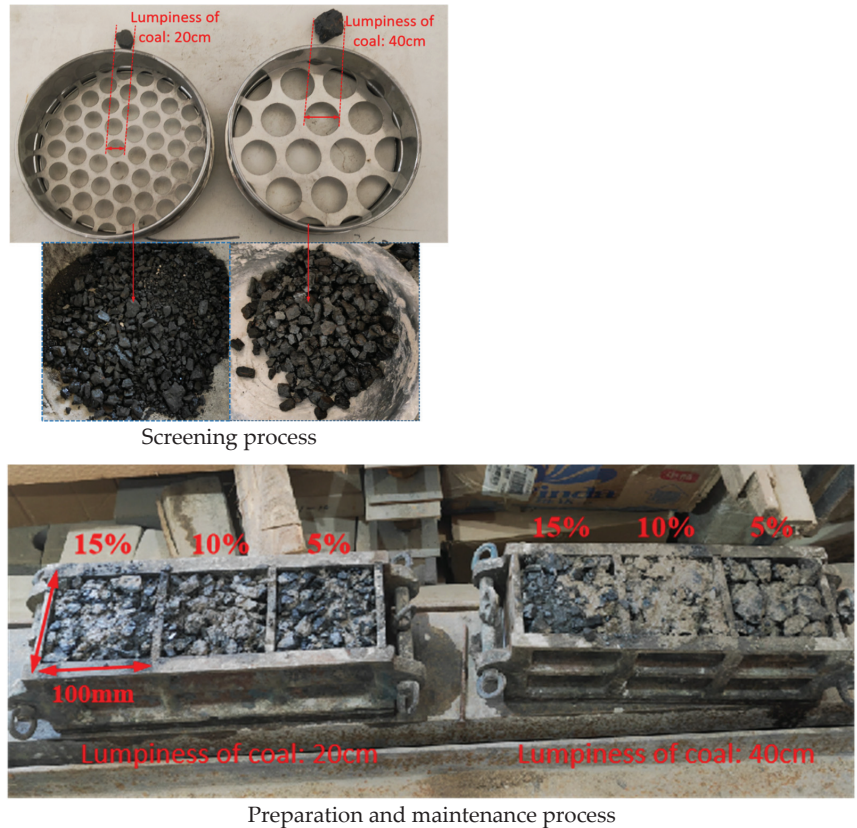
#### 3.1. Specimen Preparation and Apparatus for Tests

For the prepared and cured specimens of different schemes, in the uniaxial compressive rock mechanics experimental device shown in Figure 7, after the CRRM filling material is filled into the gob roadway and cross roadway in the simulated engineering practice, when the CRRM forms the whole layer of mining of the working face, under the disturbance of the advance abutment pressure, the stress of the surrounding rock of the gob roadway and cross roadway is redistributed again, and the roof and floor are relatively moved in.



**Figure 7.** CRRM material specimen strength testing device.

When using uniform, similar simulations as in the previous numerical simulation, the relative moving speed of the roadway roof and floor is 0.2 m/year, the relative moving speed of two trays under the action of the oil pump of the single axle hydraulic press is set to 0.05 mm/min, and the size of the test piece is set to a  $100 \times 100 \times 100$  mm standard specimen, as specified by the International Rock Mechanics Association, as shown in Figure 8.



**Figure 8.** Four processes of screening, mixing, curing, and demoulding for CRRM specimen preparation.

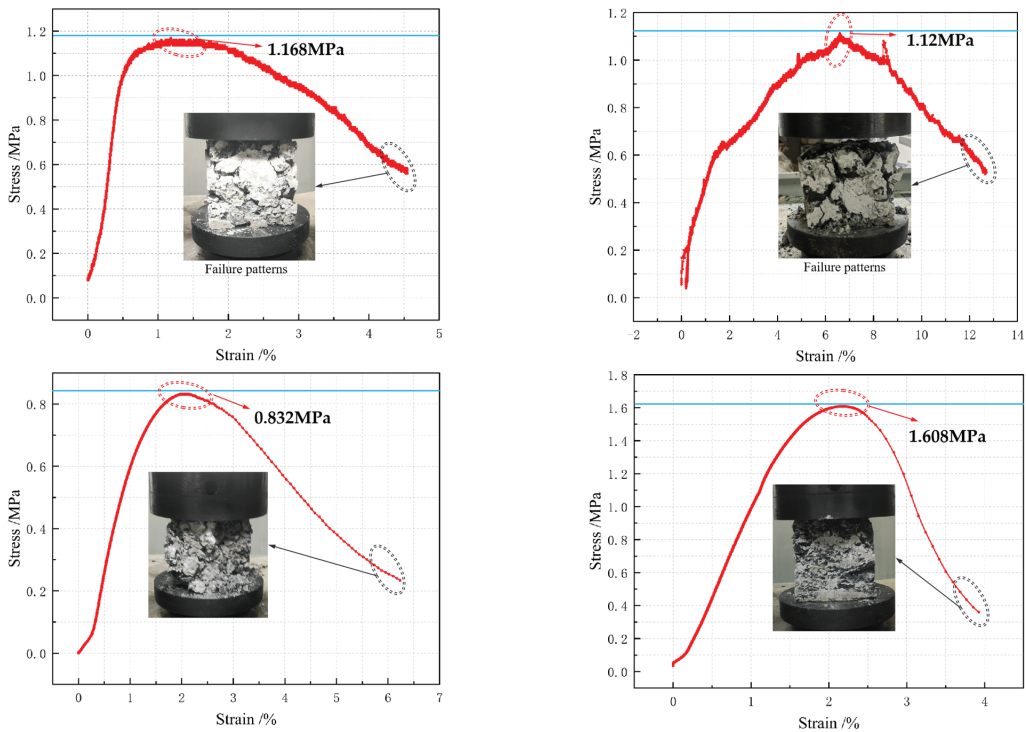
The experimental middling coal sample is taken from the coal bunker of a coal mine located in Shenmu City, Shaanxi Province, where the CRRM process will be applied in this engineering background. Sieves with particle sizes of 2 cm and 4 cm are used to separate the raw coal and specimen preparation and orthogonal experiments are conducted based on the size of the loose coal, the proportion of loose coal (coal to inorganic cementitious materials and water), and the curing time (Figure 6). The specimen preparation parameters are recorded in Table 2.

**Table 2.** Orthogonal experimental plan data record table.

Specimen Number	Lumpiness of Coal	Proportion of Coal Quality	Curing Duration	Compressive Strength
1	2 cm-100%	95%	3 d	
2	2 cm-50% and 4 cm-50%	90%	7 d	
3	4 cm-100%	80%	14 d	
...				

### 3.2. Analysis of CRRM Material Strength Experimental Results

After conducting a total of 27 orthogonal experiments with three factors and three parameters, four sets of specimens with a dynamic failure time exceeding 500 s and a hardness close to 1 MPa were obtained. Among them, the failure time of sample 1 (loose coal block size 2 cm 100%—loose coal proportion 80%—curing 14 d) was 527 s, that of sample 2 (loose coal block size 2 cm 100%—loose coal proportion 90%—curing 14 d) was 818 s, and that of sample 3 (loose coal block size 2 cm 50%—loose coal proportion 90%—curing 7 d) was 1289 s. The failure time of sample 4 (with a particle size of 2 cm 100%—a proportion of 95%—a curing time of 7 d) was 617 s. The entire process curve of uniaxial compressive strength testing is shown in Figure 9.



**Figure 9.** The stress-strain curve characteristics of four sets of specimens that met the dynamic response characteristics (specimen #s 1, 2, 3 and 4).

It can be seen that among the four samples that met the dynamic failure duration requirement, the strength of sample #1, sample #2, and sample #4 all exceeded 1 MPa, and the strength of sample #4 reached 1.6 MPa. The strength of sample #4 also exceeded 1 MPa during a considerable post-peak strain process. Further analysis was conducted on all samples, and the experimental data of 27 samples were divided into three groups based on the differences in coal block size, coal content proportion, and curing time to calculate the average value. The evolution and influence of three influencing factors on the strength of CRRM specimens can be preliminarily obtained, as shown in Figure 10.



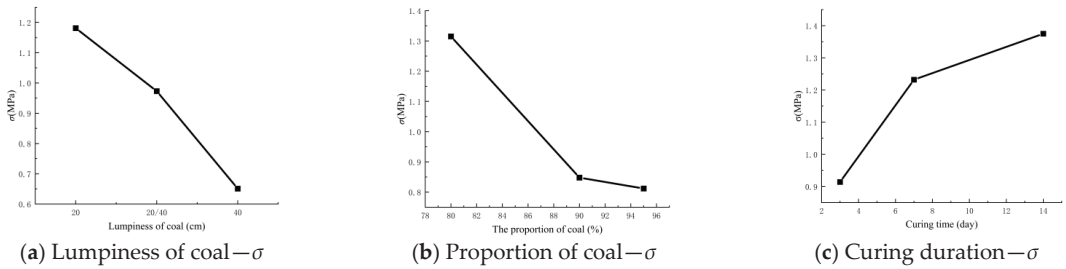


Figure 10. The influence of three main influencing factors on the strength of CRRM materials.

As the particle size of loose coal increases from 2 cm in size to 50% of 4 cm in size, the average strength monotonically decreases. The average strength of the two stages decreases by 17.6% and 33.1%, respectively. As the proportion of coal content increases from 80% to 90% and eventually reaches 95%, the average strength of the two stages decreases by 35.5% and 4.2%, respectively. During the process of extending the maintenance period from 3 days to 7 days and finally to 14 days, the average strength of the two stages increased by 34.8% and 11.6%, respectively.

Based on comprehensive analysis, it was found that under the environmental protection policy requirements for coal impurity separation in the washing process, it is appropriate to choose a ratio scheme with a coal quality ratio of 90% or more. This requires minimizing the coal particle size and increasing the curing time to 7 days, which serves as a theoretical guide for conducting on-site large-scale CRRM practical engineering material solidification and reinforcement experiments.

#### 4. Ultra-Large Size Similarity Simulation Experiment of CRRM Materials

To promote the above CRRM coal seam reshaping and remining technology to the engineering application stage, on-site experiments were conducted on the cementitious strength of oversized CRRM remining filling materials. To avoid interference from unpredictable factors such as wind direction and temperature during the experiment, two blocks with a  $2.2 \times 2.2 \times 2.2$  m displacement limited boundary mould (as shown in Figure 11) are used, and sieves with the same particle size of 20 cm are mixed and placed in layers into the mould. After 7 days of standing and curing indoors in adjacent positions, samples are taken for strength testing after demoulding.

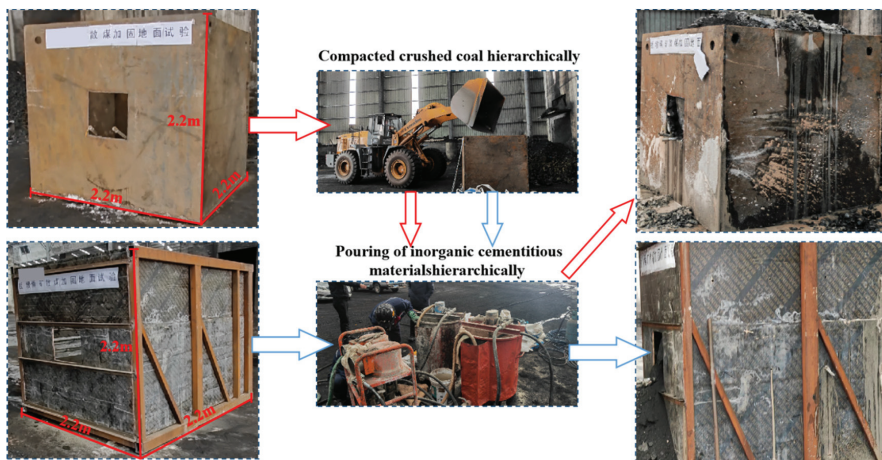


Figure 11. Experimental process scheme for the strength test of cured ultra-large CRRM materials.

#### 4.1. Development of On-Site Experimental Ideas and Construction Techniques in Engineering Practice

1. During the on-site construction process, the raw coal blocks collected from the #5 coal seam in the coal bunker were first screened (the 2 cm particle size in the laboratory ratio was enlarged to the actual 20 cm particle size), and the screened coal blocks were filled layer by layer into the oversized mould.
2. The cementitious material with strong fluidity was mixed at a 1:2 ratio with water and evenly poured onto the surface of the coal block layer that was filled into the mould.
3. Within 2 min of the rapid solidification effect of the cementitious material, the second layer of coal blocks was quickly filled into the upper surface of the first layer of the coal block cementitious material mixture layer and preliminarily compacted it.
4. After filling the mould with cementitious coal blocks in layers according to steps 1–3, following the characteristics of the relative movement of the top and bottom of the tunnel, the upper free boundary was compacted twice and cured at a constant temperature and wind speed indoor environment for 7 days.

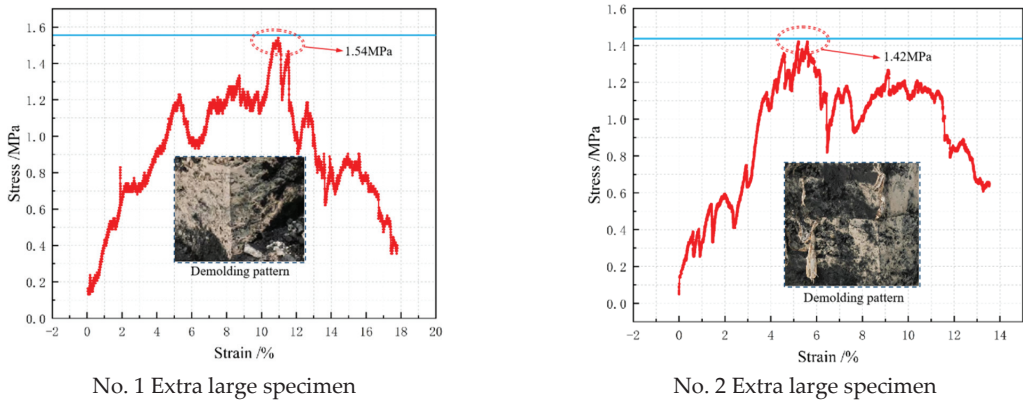
As shown in Figure 11, a method to obtain ultra-large CRRM simulation test blocks was achieved. During the test block preparation process, it was found that to ensure that the slurry of the cementitious material did not run along the weak surface of the coal block during the strong fluidity stage, a plastic film needs to be laid inside the mould, which also provides empirical guidance for on-site construction.

#### 4.2. Analysis of the Strength of the Results of the Ultra-Large-Scale Similarity Simulation Experiment Demoulding Sampling Experiment

After 7 days of curing, it was found that the overall moulding effect of CRRM loose coal cementitious material was good, and no collapse or other damage occurred after removing the fixed boundary limit. The model was broken using a pneumatic drill, and the middle position with lower strength was selected as the strength analysis sample. Two oversized specimens, No. 1 and No. 2, were each trimmed to form a  $20 \times 20 \times 20$  cm CRRM material test block for the laboratory rock mechanics strength test.

Analysis of the stress-strain curves of the two test blocks from No. 1 and No. 2 revealed that the overall uniaxial compressive strength reached 1.54 MPa and 1.42 MPa, respectively (Figure 12, The red dotted line represents the uniaxial pressure test data, and the blue line represents the peak intensity position marking line), which can meet the support strength requirements for the surrounding rock of the tunnel obtained from previous research. Moreover, the true characteristics reflected by its ultra-large size show that the strong heterogeneity of small laboratory specimens causes them to be difficult to model, and the stress-strain curve oscillates significantly during the loading process. Both the prepeak and postpeak stages exhibit strong oscillation characteristics, and the residual strength stage still exhibits good load-bearing characteristics, which is a positive attribute for the on-site application of the CRRM process.

When the CRRM material plays a supporting role on the top and bottom of the goaf under working conditions, it works in conjunction with the newly added anchor rods, anchor cables, anchor mesh, and spraying materials inside the goaf. The CRRM material mainly plays a role in limiting displacement on the top and bottom of the goaf and reshaping the front coal wall that is scattered throughout the goaf during the mining process, forming an overall coal seam for the formation of a long wall working face for bidirectional coal cutting by the coal machine during mining. Therefore, based on the comprehensive analysis of the strength results of laboratory experiments and on-site large-scale similar simulation experiments, it can be concluded that the CRRM material can meet the filling strength requirements of the coal seam reshaping resource replacement mining process by selecting an inorganic high water cementitious material with a particle size of 20 cm and a mass of 10% by weight of mixed coal blocks and maintaining it for 7 days.



**Figure 12.** Stress-strain curve of the ultra-large CRRM specimen.

## 5. Conclusions

Coal seam reshaping replacement type abandoned coal mining technology (CRRM) was proposed, and finite element simulation experiments on the overall surrounding rock state of the mining site and strength experiments on CRRM loose coal cementitious filling materials were carried out based on the actual engineering background on site. The aforementioned stages were used as theoretical parameters to guide on-site maintenance experiments on oversized CRRM materials. The main conclusions of this study are as follows:

(1) When designing the CRRM process plan, it is necessary to determine the stress and displacement status of the surrounding rock of the old goaf and the connecting roadway through a numerical simulation. In shallow coal seams, the stress of the surrounding rock of the goaf roadway is generally not high, and the peak stress concentration coefficient is approximately 1.08. Therefore, the CRRM material mainly plays a role in limiting displacement in supporting the top and bottom of the goaf. When combined with anchor rod anchor cable mesh support, the strength requirement should meet 1.5 MPa.

(2) As the particle size of coal increases, the strength of the CRRM material decreases accordingly. The strength of the CRRM material decreases with an increasing proportion of the bulk coal mass. The increase in curing time will lead to an increase in the overall strength of the CRRM materials.

(3) The maintenance experiment of oversized CRRM material shows that the on-site large-sized filling block is different from the 10 cm. The size effect of the 10 cm specimen brings significant strength differences, and the characteristics of the prepeak and postpeak curves are different from those obtained in laboratory experiments. In the next step of the experiment, microscopic research will be conducted to explore the refinement differences in oversized and small-sized CRRM specimens under an electron microscope, which can improve the strength properties of the specimen and make it suitable for mines containing residual coal resources with more complex geological conditions.

**Author Contributions:** L.L. and X.Z. wrote the main manuscript text and dealt with all figures, B.H. prepared Figures 5 and 6, and S.L. conducted a preliminary translation of the manuscript. All authors have read and agreed to the published version of the manuscript.

**Funding:** This research received funding from the National Natural Science Foundation of China project "Research on the Time Effect Mechanism and Dynamic Response of Overburden goaf Coal Pillar Synergistic Action and Residual Coal Re mining", 52074291, the National Natural Science Foundation of Surface Project of China, 51774289 and the National Natural Science Foundation of the Youth Science Foundation of China, 51404270.

**Data Availability Statement:** The results/data/figures in this manuscript have not been published elsewhere, nor are they under consideration by another publisher.

**Conflicts of Interest:** The authors declare that there are no conflict of interest regarding the publication of this paper.

## References

- Jiang, Z.M. Reflections on China's energy issues. *J. Shanghai Jiao Tong Univ.* **2008**, *3*, 345–359. [CrossRef]
- Hao, Y.; Zhang, Z.Y.; Liao, H.; Wei, Y.-M. China's farewell to coal: A forecast of coal consumption through 2020. *Energy Policy* **2015**, *86*, 444–455. [CrossRef]
- Tarascon, J.M.; Armand, M. Issues and challenges facing rechargeable lithium batteries. *Nature* **2001**, *414*, 359–367. [CrossRef]
- Xie, H.P.; Wu, L.X.; Zheng, D.Z. Prediction of China's Energy Consumption and Coal Demand in 2025. *J. Coal Sci.* **2019**, *44*, 1949–1960. [CrossRef]
- Agency, I.E. *Medium-Term Coal Market Report, Medium-Term Coal Market Report 2011: Market Trends and Projections to 2016*; OECD Publishing: Paris, France, 2014.
- Wang, Q.; He, M.C.; Yang, J.; Gao, H.K.; Jiang, B.; Yu, H.C. Study of a no-pillar mining technique with automatically formed gob-side entry retaining for longwall mining in coal mines. *Int. J. Rock Mech. Min. Sci.* **2018**, *110*, 1–8. [CrossRef]
- He, Y.G.; Ye, X.D.; Wang, Z. Thoughts on the “13th Five Year Plan” of coal industry. *Coal Econ. Res.* **2015**, *35*, 6–8+21.
- Qian, M.G. Scientific Mining of Coal. *J. Coal Sci.* **2010**, *35*, 529–534. [CrossRef]
- Brown, M.T.; Protano, G.; Ulgiati, S. Assessing geobiosphere work of generating global reserves of coal, crude oil, and natural gas. *Ecol. Model.* **2011**, *222*, 879–887. [CrossRef]
- Stefaniak, S.; Twardowska, I. Impact of engineering constructions made of carboniferous waste rock on groundwater deterioration. In Proceedings of the International Mine Water Association Symposium 2010, Sydney, NS, Canada, 5–9 September 2010.
- Shimada, H.; Chen, Y.; Hamanaka, A.; Sasaoka, T.; Shimada, H.; Matsui, K. Application of Highwall Mining System to Recover Residual Coal in End-walls. *Procedia Earth Planet. Sci.* **2013**, *6*, 311–318. [CrossRef]
- Feng, G.R.; Zhang, Y.J.; Qi, T.Y.; Kang, L.X. The current situation and research progress of residual coal mining in China. *J. Coal Sci.* **2020**, *45*, 151–159. [CrossRef]
- Feng, G.; Li, J.; Qi, T.; Zhang, Y.; Du, X.; Bai, J. Research progress on the mining methods and pressure control of residual coal in China. *Shanxi Coal* **2022**, *42*, 1–8.
- Xu, J.C.; Wen, H.; Zhang, X.H.; Deng, J.; Xu, M.G. Research on the method for determining the risk zone of coal spontaneous combustion in goaf of fully mechanized top coal caving face. *J. China Univ. Sci. Technol.* **2002**, *6*, 39–44.
- Cheng, W.M.; Zhang, X.Q.; Wang, G.; Yang, X.X.; Xin, L. Reconstruction Technology for Coupled Hazards of Gas and Residual Coal Spontaneous Combustion in Fully Mechanized Caving Gob. *J. Coal Ind.* **2016**, *41*, 662–671. [CrossRef]
- Zhou, H.; Hou, C.; Sun, X. Solid waste paste filling for none-village-relocation coal mining. *J. China Univ. Min. Technol.* **2004**, *33*, 154–158.
- Zhang, J.X. Research on Rock Movement Control and Its Application in Fully Mechanized Mining with Direct Filling of Gangue. Ph.D. Thesis, China University of Mining and Technology, Beijing, China, 2008.
- Bai, J.B.; Zhang, Z.Z.; Wang, X.Y.; Xu, Y.; Yan, S.; Xu, J. Stress control and surrounding rock strengthening mechanism and application of high water material filling along goaf retaining roadway. *Coal Sci. Technol.* **2022**, *50*, 16–28. [CrossRef]
- Feng, G.M. Research and Application of Ultra High Water Filling Materials and Filling Mining Technology. Ph.D. Thesis, China University of Mining and Technology, Beijing, China, 2009.
- Kang, H.P.; Xu, G.; Wang, B.M.; Wu, Y.Z.; Jiang, P.F.; Pan, J.F.; Ren, H.W.; Zhang, Y.J.; Pang, Y.H. China's Coal Mining and Strata Control Technology Development for 40 Years and Prospects. *J. Min. Strat. Control. Eng.* **2019**, *1*, 7–39. [CrossRef]
- Hui, K.S.; Chao, C.Y.H.; Kot, S.C. Removal of mixed heavy metal ions in wastewater by zeolite 4a and residual products from recycled coal fly ash. *J. Hazard. Mater.* **2005**, *127*, 89–101. [CrossRef] [PubMed]
- Zhang, Y.; Feng, G.; Zhang, M.; Ren, H.; Bai, J.; Guo, Y.; Jiang, H.; Kang, L. Residual coal exploitation and its impact on sustainable development of the coal industry in china. *Energy Policy* **2016**, *96*, 534–541. [CrossRef]
- Wang, F.; Zhang, C. Reasonable coal pillar design and remote control mining technology for highwall residual coal resources. *R. Soc. Open Sci.* **2019**, *6*, 181817. [CrossRef]
- Zhao, T.; Liu, C. Roof instability characteristics and pre-grouting of the roof caving zone in residual coal mining. *J. Geophys. Eng.* **2017**, *14*, 1463–1474. [CrossRef]
- Prakash, A.; Lokhande, R.D.; Singh, K.B. Impact of rainfall on residual subsidence in old coal mine workings. *J. Environ. Sci. Eng.* **2010**, *52*, 75–80. [PubMed]
- Kang, J.; Shen, W.; Bai, J.; Yan, S.; Wang, X.; Li, W.; Wang, R. Influence of abnormal stress under a residual bearing coal pillar on the stability of a mine entry. *Int. J. Min. Sci. Technol.* **2017**, *27*, 945–954. [CrossRef]
- Li, N.; Li, X.; Shu, C.; Shen, W.; He, M.; Meng, J. Study of the influence of the characteristics of loose residual coal on the spontaneous combustion of coal gob. *Energy Sci. Eng.* **2020**, *8*, 689–701. [CrossRef]
- Zhao, T.; Liu, C.; Yetilmeszooy, K.; Gong, P.; Li, J. Realization and engineering application of hydraulic support optimization in residual coal remining. *J. Intell. Fuzzy Syst. Appl. Eng. Technol.* **2017**, *32*, 2207–2219. [CrossRef]

29. Hao, H. Multi-component gases competitive adsorption on residual coal under goaf conditions based on monte carlo simulation. *Chem. Phys. Lett.* **2021**, *771*, 138557. [CrossRef]
30. Chen, Y.; Shimada, H.; Sasaoka, T.; Hamanaka, A.; Matsui, K. Research on exploiting residual coal around final end-walls by highwall mining system in china. *Int. J. Surf. Min. Reclam. Environ.* **2013**, *27*, 166–179. [CrossRef]
31. Zhao, T.; Lu, Y.; Liu, C. Comprehensive optimization and engineering applications of thick residual coal re-mining methodology. *J. Intell. Fuzzy Syst. Appl. Eng. Technol.* **2017**, *32*, 2111–2122. [CrossRef]
32. Qiu, P.; Wang, J.; Ning, J.; Liu, X.; Hu, S.; Gu, Q. Rock burst criteria of deep residual coal pillars in an underground coal mine: A case study. *Nat. Rev. Cancer* **2019**, *19*, 499.
33. Xca, B.; Sza, B.; Lla, C.; Xia, D.; Nk, A. Effect of ambient pressure on gas adsorption characteristics of residual coal in abandoned underground coal mines. *J. Nat. Gas Sci. Eng.* **2021**, *90*, 103900.
34. Wodarski, K.; Bijańska, J.; Gumiński, A. The method of validity evaluation of hard coal excavation in residual seam parts. *Arch. Min. Sci.* **2017**, *62*, 675–687. [CrossRef]
35. Huang, W.G.; Zhang, S.W.; Lu, X.; Wu, S.L.; Huang, J. Residual coal distribution in china and adaptability evaluation of its resource conditions to underground coal gasification. *Sustain. Energy Technol. Assess.* **2022**, *49*, 101654. [CrossRef]
36. Jia, L.; Cheng, P.; Yu, Y.; Chen, S.-H.; Wang, C.-X.; He, L.; Nie, H.-T.; Wang, J.-C.; Zhang, J.-C.; Fan, B.-G.; et al. Regeneration mechanism of a novel high-performance biochar mercury adsorbent directionally modified by multimetal multilayer loading. *J. Environ. Manag.* **2023**, *326 Pt B*, 116790. [CrossRef]
37. Toupin, R.A. Saint-Venant's Principle. *Arch. Rational Mech. Anal.* **1965**, *18*, 83–96. [CrossRef]
38. Xie, H.P.; Zhou, H.W.; Wang, J.A.; Li, L.; Kwasniewski, M.A. Application and comparative analysis of FLAC in prediction of coal mining subsidence. *J. Rock Mech. Eng.* **1999**, *4*, 29–33.
39. Feng, G.R.; Hao, C.L.; Wang, P.F.; Guo, J.; Qian, R.; Wen, X.; Liu, J. Asymmetric deformation mechanism and control measures of mining tunnels under close range goaf. *J. China Univ. Min. Technol.* **2022**, *51*, 617–631. [CrossRef]
40. Homer, A.W. Coal Mine Safety Regulation in China and the USA. *J. Contemp. Asia* **2009**, *39*, 424–439. [CrossRef]

**Disclaimer/Publisher's Note:** The statements, opinions and data contained in all publications are solely those of the individual author(s) and contributor(s) and not of MDPI and/or the editor(s). MDPI and/or the editor(s) disclaim responsibility for any injury to people or property resulting from any ideas, methods, instructions or products referred to in the content.

## Article

# Study on the Influence Mechanism of Air Leakage on Gas Extraction Effect—A Numerical Case Study of the Coal Mine Site in Anhui

Han Gao <sup>1,2</sup>, Feng Du <sup>2,\*</sup>, Xiaoyu Cheng <sup>1</sup>, Jinjie Zhang <sup>3</sup> and Aitao Zhou <sup>2</sup>

<sup>1</sup> China Coal Energy Research Institute Co., Ltd., Xi'an 710054, China; gaohan1986@126.com (H.G.); chengxiaoyu89@126.com (X.C.)

<sup>2</sup> School of Emergency Management and Safety Engineering, China University of Mining and Technology (Beijing), Beijing 100083, China; cumtbzat@126.com

<sup>3</sup> China Coal Xinji Liuzhuang Mining Co., Ltd., Fuyang 236200, China; 18755435573@163.com

\* Correspondence: fdu@cumtb.edu.cn

**Abstract:** Air leakage in mine gas drainage drilling is a critical factor that affects gas extraction efficiency. It leads to a rapid decline in gas concentration, resulting in lower extraction efficiency and potential secondary disasters. To address this issue, a fully coupled gas–air mixed flow model is established in this study. The model examines the effects of extraction time, different negative pressures, and gas leakage on gas concentration. Additionally, it reveals the mechanism of air leakage around gas drainage boreholes. The simulation data are then compared with field gas drainage monitoring data to verify the reliability of the model. This verification serves as a basis for extraction regulation and control. The results demonstrate that during the later stages of extraction, the negative pressure decreases, causing a decline in gas concentration. Moreover, higher negative pressure leads to increased air inflow into the borehole, thereby reducing gas concentration. Consequently, selecting an appropriate negative pressure is crucial to improve pumping efficiency. The research findings hold significant guidance in achieving efficient gas mining.

**Keywords:** gas extraction; air leakage; permeability; diffusion-seepage

**Citation:** Gao, H.; Du, F.; Cheng, X.; Zhang, J.; Zhou, A. Study on the Influence Mechanism of Air Leakage on Gas Extraction Effect—A Numerical Case Study of the Coal Mine Site in Anhui. *Processes* **2023**, *11*, 2161. <https://doi.org/10.3390/pr11072161>

Academic Editor: Guining Lu

Received: 15 June 2023

Revised: 17 July 2023

Accepted: 18 July 2023

Published: 19 July 2023



**Copyright:** © 2023 by the authors. Licensee MDPI, Basel, Switzerland. This article is an open access article distributed under the terms and conditions of the Creative Commons Attribution (CC BY) license (<https://creativecommons.org/licenses/by/4.0/>).

## 1. Introduction

In recent years, new energy sources have experienced rapid development. However, coal is expected to remain the primary energy source in China for the foreseeable future. In order to ensure resource utilization and minimize secondary disasters, the co-mining of coal and gas has gained significance [1–4]. First and foremost, it is crucial to prioritize the safety of coal mining operations. The mining process is prone to various dynamic disasters, with gas-related incidents being particularly common. The quantity and efficiency of gas extraction from coal seams directly impact the safety of coal mines. One major challenge in mine gas drainage is the rapid attenuation of gas concentration. This hampers effective gas utilization, leading to environmental pollution and the risk of gas explosions and other hazards [5–8]. Therefore, implementing effective gas pre-drainage measures holds immense importance in ensuring coal mine safety and optimizing gas resource utilization.

The coal seam gas drainage boreholes are typically categorized into main pipes and branch pipes. Multiple boreholes are interconnected and eventually merged into the main extraction pipeline [9,10]. Currently, it is a common practice to arrange these pipes from the surface to the underground coal seam for gas pre-drainage [11–13]. However, the majority of coal seams in our country have low permeability, resulting in poor gas drainage effectiveness. Additionally, there is a significant issue of gas leakage due to limitations in sealing technology. Although sealing technology has witnessed advancements in recent years, these challenges have not been fundamentally resolved. As extraction progresses

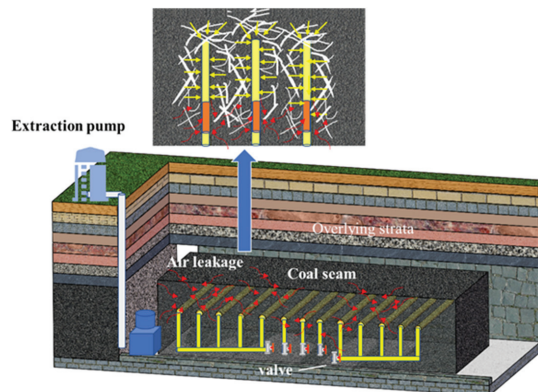
into the middle and later stages, there is a noticeable decline in gas concentration, which attenuates rapidly [14]. This is attributed to the development of coal and rock mass cracks caused by mining disturbances. Furthermore, the overall gas concentration is further reduced due to the decrease in the total gas volume. If the gas concentration in the drainage pipeline falls within the explosion limit, it poses a threat to the safe production of the coal mine. Simultaneously, the discharge of gas with lower concentrations into the atmosphere can have adverse environmental impacts.

Coal is considered a dual-porosity medium [15], where gas exists both in the fractures of coal in a free state and in the matrix pores in an adsorbed state, with a significant proportion being adsorbed gas. During the process of gas extraction from coal seams, the gas typically undergoes three processes: desorption, diffusion, and seepage [16]. To understand the cross-coupling mechanism of various physical fields during coalbed methane drainage, extensive research has been conducted by scholars. Liu et al. [17] conducted a comprehensive analysis of the research progress on multiphysics coupling processes in coalbed methane mining. They concluded that the complex interaction between stress, chemical fields, mining processes, and geological fluid injection significantly impacts the geomechanical characteristics of coal. Liang et al. [18] constructed a multi-field coupling model incorporating stress–diffusion–seepage to investigate the gas flow behavior around drilled holes during coal seam extraction, focusing on the optimal spacing of boreholes for gas drainage. Wu et al. [19] developed a multi-field coupling model considering coal deformation, gas adsorption, diffusion, seepage, and humidity effects to study the evolution of flow fields and competitive gas adsorption behavior during CO<sub>2</sub> geological storage and enhanced coalbed methane mining. Zhai et al. [20] integrated coal gas permeability with mechanical properties and gas adsorption/desorption, establishing a mathematical model to analyze transient stresses and dynamic leakage flow fields around extraction boreholes. Cheng et al. [21] established a gas–solid coupling model considering fracture gas seepage, permeability evolution, and coal deformation to analyze the influence of diffusion and seepage on gas transport and investigate the mechanism of negative pressure in the gas extraction process. Hao et al. [22] developed a fluid–structure interaction model that accounted for coal creep effects to determine the effective radius of boreholes at different burial depths. Wang et al. [23] established a dynamic permeability change model of coal seams considering effective stress, gas desorption, and coal matrix shrinkage effects, simulating the penetration changes based on different coal seam gas pressures. Wang et al. [24] derived a formula representing the gas flow resistance of coal seams using the matchstick model combined with Darcy’s law and the Hagen–Poiseuille equation, illustrating the influence of fracture curvature, gas pressure, and effective stress on gas flow resistance. Zang et al. [25] derived an orthotropic permeability evolution equation considering effective stress and expansion stress based on coal body mechanical properties and initial porosity anisotropy. Liu et al. [26] simulated gas pressure distribution under different adsorption times and investigated the influence of the Klinkenberg effect on gas extraction. Liu et al. [27] applied a diffusion–seepage gas migration model to simulate the change in matrix pore and fracture gas pressure over time under dynamic changes in the diffusion coefficient. Zhang et al. [28] studied the influence mechanism of negative pressure on drainage effectiveness, simulated the change in gas concentration under different negative pressures and sealing parameters, and provided guidance for improving gas drainage drilling hole sealing technology. Liu et al. [29] conducted a systematic analysis of the multi-field coupling process and various factors affecting gas drainage in deep mines, offering guidance for enhancing gas drainage efficiency. Although extensive studies have been conducted on the multi-field coupling of coal–gas systems, research on underground gas extraction processes in coal mines has primarily focused on single-component gas flow, with limited exploration of multi-field coupling in air–gas binary gas systems involving borehole air leakage processes. The lack of systematic research and a comprehensive theoretical basis presents certain challenges.

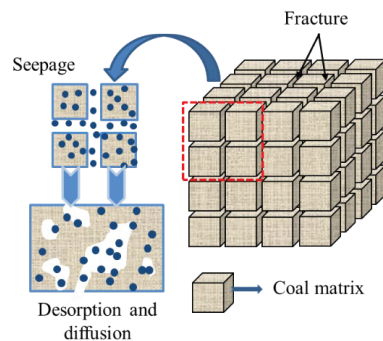
In order to tackle these challenges, this paper introduces a multi-field coupling model that focuses on the “air–gas” binary gas flow during borehole gas extraction. The model takes into account various factors, including coal matrix deformation, pore gas diffusion, fracture gas seepage, and the coupling effect of air leakage. By considering these interconnected aspects, the model provides a comprehensive understanding of the gas extraction process. The research findings from this multi-field coupling model hold great significance in terms of improving the efficiency of gas utilization and preventing and mitigating disasters. This approach allows for a better optimization of gas extraction processes and enhances the overall safety of mining operations.

## 2. Theoretical Model Construction

During the gas pre-drainage process from boreholes in this coal seam, it is commonly observed that there is initially a high gas concentration and flow rate. However, as the extraction time progresses, there is a varying degree of decrease in gas concentration and flow. This decline can be attributed to changes in the number, spacing, and aperture of cracks influenced by mining-induced stress and gas pressure, indicating the dynamic development of the fracture state. Figure 1 illustrates the pathways created by the development and penetration of the fracture network, allowing ventilation air from the roadway to enter the extraction hole. The pore structure of the coal is depicted in Figure 2. Identifying the precise locations of high permeability areas for air leakage around the borehole is crucial for effective sealing and plugging of fracture channels. To accomplish this, a double-hole-mixed gas seepage coupling model was established to study the permeability evolution in different coal areas surrounding gas drainage boreholes and identify the areas with high permeability for air leakage.



**Figure 1.** Schematic diagram of the on-site drilling layout.



**Figure 2.** Schematic diagram of ideal coal body composed of coal matrix and cracks.



This model makes the following assumptions:

- (1) The pressure generated by air in the fractures is considerably lower than the gas pressure within the pores of the coal matrix. Hence, the adsorption and migration of air within the coal matrix are not considered. Air is assumed to flow solely within the coal fissures.
- (2) Gas behavior follows the principles of Fick's diffusion and Darcy's seepage during its flow.
- (3) The migration of gas and air within the coal is assumed to be isothermal, neglecting any heat exchange.
- (4) The seepage of gas and air within the fracture space is treated as independent processes. The deformation and permeability evolution of coal are mainly influenced by the superposition of gas pressure and air pressure.

### 2.1. Mechanical Constitutive Relation of Coal

Under the action of free gas and adsorbed gas, the deformation and mechanical properties of gas-bearing coal change, which makes the stress field change accordingly.

Coal is a double-pore structure; the relationship between surface stress and bulk stress can be expressed as outlined in reference [30]:

$$\sigma_{ij,j} + F_i = 0, \quad (1)$$

where  $\sigma_{ij,j}$  is the stress tensor along  $j$  direction, MPa; and  $F_i$  is the volume force in the direction of  $i$ , MPa.

The coal cracks considering air leakage contain gas–air two-component gas. Therefore, the gas pressure in coal fissures and the gas pressure in coal matrix pores can be expressed as follows:

$$p_f = p_{fa} + p_{fg}, \quad (2)$$

where  $p_f$  is the total gas pressure in coal fissures, MPa;  $p_{fa}$  is the air pressure in coal fissures, MPa; and  $p_{fg}$  is the gas pressure in coal fissures, MPa.

$$p_m = p_{mg}, \quad (3)$$

where  $p_m$  is the total pressure of gas in coal matrix, MPa; and  $p_{mg}$  is the gas pressure in coal matrix, MPa.

According to the effective stress principle put forward by Terzaghi, combined with the continuous modification of the effectiveness of rock mass media, the effective stress of coal is expressed by Formula (4):

$$\begin{cases} \sigma_{ij} = \sigma_{ij}^e - \left[ \alpha_f (p_{fa} + p_{fg}) + \alpha_m p_{mg} \right] \delta_{ij} \\ \alpha_f = 1 - \frac{K}{K_m} \\ \alpha_m = \frac{K}{K_m} - \frac{K}{K_s} \\ K_m = \frac{E_m}{3(1-2\nu)} \\ K_s = \frac{E_m}{3(1-2\nu) - 9\phi_m(1-\nu)/2} \end{cases}, \quad (4)$$

where  $\sigma_{ij}$  is the normal stress acting on coal, MPa;  $\sigma_{ij}^e$  is the effective stress on coal, MPa;  $\alpha_f$  is the effective stress coefficient of coal body crack;  $\alpha_m$  is the effective stress coefficient of coal matrix;  $\delta_{ij}$  is the Kronecker function;  $K$  is the coal bulk modulus, MPa;  $K_m$  is the coal matrix bulk modulus, MPa;  $K_s$  is the coal solid skeleton bulk modulus, MPa;  $E$  is the young's modulus of coal, MPa;  $E_m$  is the young's modulus of coal matrix, MPa;  $\phi_m$  is the porosity of coal matrix; and  $\nu$  is the Poisson's ratio of coal.

The constitutive relation of stress and strain of gas-bearing coal is expressed as follows [31]:

$$\sigma_{ij}^e = 2G\varepsilon_{ij} + \frac{2G}{1-\nu}\varepsilon_v\delta_{ij} - K\varepsilon_b^s\delta_{ij}, \quad (5)$$

where  $G$  is the shear modulus of coal, MPa,  $G = \frac{E}{2(1+\nu)}$ ;  $\varepsilon_{ij}$  is the strain tensor of coal mass;  $\varepsilon_v$  is the volumetric strain of coal; and  $\varepsilon_b^s$  is the volumetric strain caused by coal adsorption.

Among them is the following:

$$\varepsilon_b^s = \frac{\varepsilon_{b\max}^s p_m}{p_m + p_L}, \quad (6)$$

where  $\varepsilon_{b\max}^s$  is the maximum strain produced by adsorbing gas; and  $p_L$  is the type Langmuir adsorption strain pressure.

Displacement and strain can be expressed by Equation (7):

$$\varepsilon_{ij} = \frac{1}{2}(u_{i,j} + u_{j,i}), \quad (7)$$

where  $\varepsilon_{ij}$  is the strain component; and  $u_{i,j}$ ,  $u_{j,i}$  are the displacement component.

The following Equation (8) is obtained:

$$Gu_{i,ij} + \frac{G}{1-2\nu}u_{j,ji} - \alpha_f(p_{fg,i} + p_{fa,i}) - \alpha_m p_{m,i} - K\varepsilon_{b,i}^s\delta_{ij} + F_i = 0. \quad (8)$$

The failure behavior of coal can be expressed by formula [32]:

$$F = \frac{\sin \varphi}{\sqrt{3}\sqrt{3 + \sin^2 \varphi}} I_1 + \frac{3C \cos \varphi}{\sqrt{3}\sqrt{3 + \sin^2 \varphi}} - \sqrt{J_2}, \quad (9)$$

where  $I_1$  is the first invariant of the stress tensor,  $I_1 = \sigma_1 + \sigma_2 + \sigma_3$ ;  $I_2$  is the second invariant of the stress tensor,  $I_2 = \sigma_1\sigma_2 + \sigma_2\sigma_3 + \sigma_3\sigma_1$ ;  $J_2$  is the second invariant of stress deviation,  $J_2 = \frac{1}{3}I_1^2 - I_2$ ;  $\varphi$  is the internal friction angle; and  $C$  is the cohesive force.

## 2.2. Gas Migration Model

Considering air leakage, a diffusion-seepage model is established.

### 2.2.1. Subsubsection

In a coal body structure with a double pore system, the gas components in the coal matrix primarily consist of adsorbed gas within the matrix and free gas within the matrix pores. Therefore, the total gas quantity per unit volume of the coal matrix can be expressed as stated in reference [33]:

$$m_m = \frac{V_L p_m}{p_m + P_L} \cdot \frac{\rho_c M_C}{V_m} + \frac{\phi_m p_m M_g}{RT}, \quad (10)$$

where  $m_m$  is the total amount of gas per unit volume of coal matrix,  $\text{kg}/\text{m}^3$ ;  $p_m$  is the total pressure of gas in coal matrix, Mpa;  $V_m$  is the coal matrix volume,  $\text{cm}^3$ ;  $M_c$  is the molar mass of methane under the standard condition,  $\text{g}/\text{mol}$ ;  $V_L$  is the Langmuir volume,  $\text{m}^3/\text{kg}$ ;  $P_L$  is the Langmuir pressure, MPa;  $\phi_m$  is the Coal matrix porosity;  $\rho_c$  is the coal density,  $\text{kg}/\text{m}^3$ ;  $R$  is the gas constant;  $T$  is the gas temperature, K;  $M_g$  is the molar mass of gas, the equivalent of gas in this paper is methane, its value is 16  $\text{g}/\text{mol}$ .

In the absence of mining disturbances, the gas pressure within the original coal seam remains constant. However, the gas balance state within the coal matrix and fracture system undergoes changes due to gas drainage. During the operation of the extraction system, the gas flow velocity differs between the coal matrix and fracture system. The gas pressure within the fractures is relatively lower compared to the matrix. As a result, gas in the

fractures is replenished by the gas present in the coal matrix. This replenishment is driven by the difference in gas concentration. Therefore, the diffusion equation can be expressed as follows [34]:

$$Q_m = D\chi_s V_m (c_m - c_{fg}), \quad (11)$$

where  $Q_m$  is the diffusion source,  $\text{kg}/(\text{m}^3 \cdot \text{s})$ ;  $D$  is the diffusivity,  $\text{m}^2/\text{s}$ ;  $\chi_s$  is the matrix shape factor,  $\text{m}^{-2}$ ,  $\chi_s = \frac{3\pi^2}{L^2}$ ;  $V_m$  is the coal matrix volume,  $\text{cm}^3$ ;  $c_m$  is the gas concentration in coal matrix,  $\text{kg}/\text{m}^3$ ,  $c_m = \frac{M_g}{Z_m RT} p_m$ ;  $c_{fg}$  is the gas concentration in coal fissures,  $\text{kg}/\text{m}^3$ ,  $c_{fg} = \frac{M_g}{Z_{fg} RT} p_{fg}$ ; and  $L$  is the pore spacing,  $\text{m}$ .

Due to the shape factor being related to the adsorption time, the adsorption time  $\tau$  is introduced as a parameter to characterize the diffusion behavior. It is numerically equal to the time it takes for the gas content in the coal matrix to be desorbed to 62.3% of the total. The matrix shape factor can be specifically expressed as follows [35]:

$$\tau = \frac{1}{D\chi_s}. \quad (12)$$

It can be expressed by mass conservation equation in the process of gas diffusion:

$$Q_m = -\frac{\partial m_m}{\partial t}. \quad (13)$$

By bringing Formulae (10) and (11) into Formula (13), you can obtain the following:

$$\frac{\partial p_m}{\partial t} = -\frac{V_m}{\tau \rho_c RT} \cdot \frac{(p_m - p_{fg})}{\left(\frac{V_L p_L}{(p_m + p_L)^2} + \frac{\phi_m}{\rho_c p_0}\right)}. \quad (14)$$

### 2.2.2. Seepage Control Equation of Gas–Air Two-Component Gas in Fissures

The amount of gas in coal fissures per unit mass can be expressed as follows:

$$m_{fg} = \frac{\phi_f p_{fg} M_g}{RT} \quad (15)$$

$$m_{fa} = \frac{\phi_f p_{fa} M_a}{RT}, \quad (16)$$

where  $m_{fg}$  is the gas content in coal fissures per unit mass,  $\text{m}^3/\text{kg}$ ;  $m_{fa}$  is the air content in coal fissures per unit mass,  $\text{m}^3/\text{kg}$ ; and  $M_a$  is the molar mass of air,  $\text{g}/\text{mol}$ .

In the fracture system, the gas–air two-component gas flows under the action of the driving force caused by the gas concentration difference. There are as follows:

$$V_f = -\frac{k_f}{\mu} \nabla (p_{fg} + p_{fa}) \quad (17)$$

$$\mu = \frac{\mu_g}{1 + \frac{x_a}{x_g} \sqrt{\frac{M_a}{M_g}}} + \frac{\mu_a}{1 + \frac{x_g}{x_a} \sqrt{\frac{M_g}{M_a}}}, \quad (18)$$

where  $V_{fg}$  is the gas seepage rate in coal fissures,  $\text{m}/\text{s}$ ;  $V_{fa}$  is the air seepage rate in coal fissures,  $\text{m}^3/\text{kg}$ ;  $\mu$  is the average dynamic viscosity of gas mixture in coal fissures,  $\text{Pa}\cdot\text{s}$ ;  $\mu_g$  is the dynamic viscosity of gas,  $\text{Pa}\cdot\text{s}$ ;  $\mu_a$  is the dynamic viscosity of air,  $\text{Pa}\cdot\text{s}$ ;  $x_g$  is the mole fraction of gas; and  $x_a$  is the mole fraction of air.

Combined with the ideal state gas equation, the mole fraction of each component can be expressed as follows:

$$\begin{cases} x_g = \frac{n_g}{n_g+n_a} = \frac{p_{fg}}{p_{fg}+p_{fa}} \\ x_a = \frac{n_a}{n_a+n_g} = \frac{p_{fa}}{p_{fg}+p_{fa}} \end{cases} \quad (19)$$

There are

$$\mu = \frac{\mu_g}{1 + \frac{p_{fa}}{p_{fg}} \sqrt{\frac{M_a}{M_g}}} + \frac{\mu_a}{1 + \frac{p_{fg}}{p_{fa}} \sqrt{\frac{M_g}{M_a}}} \quad (20)$$

The gas flow equation of each component can be expressed as follows:

$$\begin{cases} \frac{\partial m_{fg}}{\partial t} = -\nabla(\rho_{fg} V_f) + (1-\phi_f) Q_m \\ \frac{\partial m_{fa}}{\partial t} = -\nabla(\rho_{fa} V_f) \end{cases} \quad (21)$$

The Formulae (15)–(17) are brought into the Formula (18), respectively, and the gas flow equation of each component in the crack is obtained.

$$\phi_f \frac{\partial p_{fg}}{\partial t} + p_{fg} \frac{\partial \phi_f}{\partial t} + \nabla \left( \frac{k_f}{\mu} p_{fg} \nabla (p_{fg} + p_{fa}) \right) = \frac{V_m}{\tau \rho_c RT} \cdot \frac{(1-\phi_f)(p_m - p_{fg})}{\left( \frac{V_L p_L}{(p_m + p_L)^2} + \frac{\phi_m}{\rho_c p_0} \right)} \quad (22)$$

$$\phi_f \frac{\partial p_{fa}}{\partial t} + p_{fa} \frac{\partial \phi_f}{\partial t} + \nabla \left( \frac{k_f}{\mu} p_{fa} \nabla (p_{fg} + p_{fa}) \right) = 0 \quad (23)$$

### 2.2.3. Evolution Law of Fracture Porosity and Permeability

According to the definition and geometric model, the porosity of the fracture system can be expressed as presented in reference [36].

$$\phi_f = \frac{(L_f + L_m)^3 - L_m^3}{(L_f + L_m)^3} \cong \frac{3L_f}{L_m} \quad (24)$$

Assuming that the deformation of coal body is elastic, and the deformation of coal matrix is much less than that of coal fracture system, which can be ignored, there are the following:

$$\frac{\phi_f}{\phi_{f0}} = \frac{L_f}{L_{f0}} \cdot \frac{L_{m0}}{L_m} \cong 1 + \frac{\Delta L_f}{L_{f0}} = 1 + \Delta \varepsilon_f, \quad (25)$$

where  $\phi_f$  is the porosity of coal fracture system;  $L_m$  is the length of coal matrix;  $L_f$  is the crack width;  $L_{m0}$  is the initial length of coal matrix;  $L_{f0}$  is the crack width; and  $\Delta \varepsilon_f$  is the volume strain of the fracture system.

Considering the movement of air components, the effective stress change in the cracks of the coal can be expressed as follows, based on the mechanical analysis of the coal:

$$\Delta \sigma^e = \sigma - \sigma_0 - \left[ \alpha_f (p_{fa} - p_{fa0} + p_{fg} - p_{fg0}) + \alpha_m (p_{mg} - p_{mg0}) \right], \quad (26)$$

where  $\Delta \sigma^e$  is the variation of effective stress in coal;  $\sigma$  is the stress acting on coal; and  $\sigma_0$  is the initial stress acting on coal.

The volumetric strain of the coal fracture system can be expressed as the sum of the strain resulting from matrix adsorption and the strain induced by effective stress in the fracture system, as follows:

$$\varepsilon_f = \varepsilon_s - \frac{\Delta \sigma^e}{K_f} = -\varepsilon_L \left( \frac{p_m}{p_L + p_m} - \frac{p_{m0}}{p_L + p_{m0}} \right) - \frac{1}{K_f} \left\{ (\sigma - \sigma_0) - \left[ \alpha_f (p_{fa} - p_{fa0} + p_{fg} - p_{fg0}) + \alpha_m (p_{mg} - p_{mg0}) \right] \right\} \quad (27)$$

$$K_f = L_f K_n. \tag{28}$$

The stress changes of the fracture system are as follows:

$$\Delta\sigma_f = -K_f \varepsilon_L \left( \frac{p_m}{p_L + p_m} - \frac{p_{m0}}{p_L + p_{m0}} \right) - \left\{ (\sigma - \sigma_0) - \left[ \alpha_f (p_{fa} - p_{fa0} + p_{fg} - p_{fg0}) + \alpha_m (p_{mg} - p_{mg0}) \right] \right\}, \tag{29}$$

where  $\varepsilon_f$  is the strain of coal mass fracture system;  $\Delta\sigma_f$  is the stress variation of coal fracture system;  $\varepsilon_s$  is the adsorption strain caused by coal matrix;  $K_f$  is the equivalent bulk modulus of fracture; and  $K_n$  is the fracture stiffness.

The Formula (24) can be obtained in the substitution (22):

$$\frac{\phi_f}{\phi_{f0}} = 1 + \Delta\varepsilon_f = 1 - \varepsilon_L \left( \frac{p_m}{p_L + p_m} - \frac{p_{m0}}{p_L + p_{m0}} \right) - \frac{1}{K_f} \left\{ (\sigma - \sigma_0) - \left[ \alpha_f (p_{fa} - p_{fa0} + p_{fg} - p_{fg0}) + \alpha_m (p_{mg} - p_{mg0}) \right] \right\}. \tag{30}$$

Previous research has demonstrated a cubic relationship between coal permeability and coal porosity.

$$\frac{k_f}{k_{f0}} = \left( \frac{\phi_f}{\phi_{f0}} \right)^3 = \left\{ 1 - \varepsilon_L \left( \frac{p_m}{p_L + p_m} - \frac{p_{m0}}{p_L + p_{m0}} \right) - \frac{1}{K_f} \left\{ (\sigma - \sigma_0) - \left[ \alpha_f (p_{fa} - p_{fa0} + p_{fg} - p_{fg0}) + \alpha_m (p_{mg} - p_{mg0}) \right] \right\} \right\}^3 \tag{31}$$

Figure 3 illustrates the governing equations and cross-coupling relationships of each physical field.

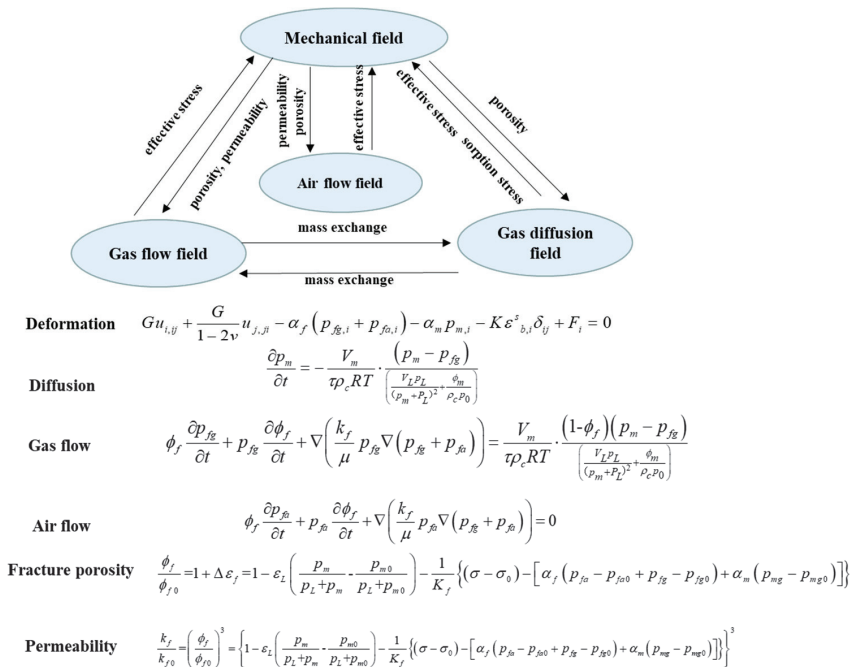


Figure 3. Governing equations and cross-coupling relations of each physical field.

### 3. Physical Model Establishment and Simulation Analysis

Using the constructed gas–air mixed flow model, numerical simulations were conducted to analyze the impact of extraction time, various negative pressures, and air leakage on gas concentration. The simulations also provided insights into the air leakage mechanism around the gas extraction borehole.

### 3.1. General Situation of Mine

Liuzhuang Coal Mine is situated in the western part of the Huainan coalfield and falls within the administrative jurisdiction of Yingshang County, Anhui Province. The mine's geographical coordinates range from approximately  $116^{\circ}07'30''$  to  $116^{\circ}20'40''$  east longitude and  $32^{\circ}45'00''$  to  $32^{\circ}51'15''$  north latitude. The mine field extends longitudinally for about 16 km from east to west and has a north–south width ranging from 3.5 to 8 km. The total area of the mine is approximately 82.2114 square kilometers, and the mining depth reaches  $-350$  million meters. Within the Liuzhuang Coal Mine, several coal seams are identified as primary minable coal seams, namely, 13-1, 11-2, 8, 5, and 1. These seams have an average total thickness of 18.51 m. Additionally, there are several local minable coal seams, namely, 17-1, 16-1, 11-1, 9, 7-2, 6-1, 5-1, and 4, with a combined average total thickness of 9.07 m.

### 3.2. Physical Model

In this study, the numerical solution for the multi-field coupled seepage model is implemented using Comsol Multiphysics numerical simulation software 5.6, utilizing its built-in PDE module. The software employs a custom ultra-fine meshing method, resulting in a total of 6804 grids.

A gas drainage model is established for underground drilling at Liuzhuang Coal Mine, taking into account the geological, gas, and site conditions (as shown in Figure 4). The model has dimensions of 50 m (length)  $\times$  11 m (width), with a coal seam thickness of 3.10 m and an extraction hole diameter of 94 mm. It incorporates both mechanical and flow field boundaries. Regarding the mechanical boundary, the top of the model experiences a load boundary, representing an overlying strata pressure of 16 MPa, corresponding to a burial depth of 620 m. The left and right sides of the model have roller support boundaries with constrained normal displacement, while the bottom is fixed. As for the flow field boundary, which includes the matrix diffusion field and fracture seepage field, the initial gas pressure of the coal seam is set at 0.42 MPa. The boundary surrounding the coal seam and the sealing section of the borehole (16 m in length) are set with zero flow conditions. The effective drainage section of the borehole (20 m in length) is set to a negative pressure of 0.080 MPa (equivalent to a negative pressure of 15 kPa). Coal seam gas is naturally discharged from the coal wall of the roadway, with the boundary set at atmospheric pressure of 0.1 MPa. Table 1 provides the key parameters used as input for the model.

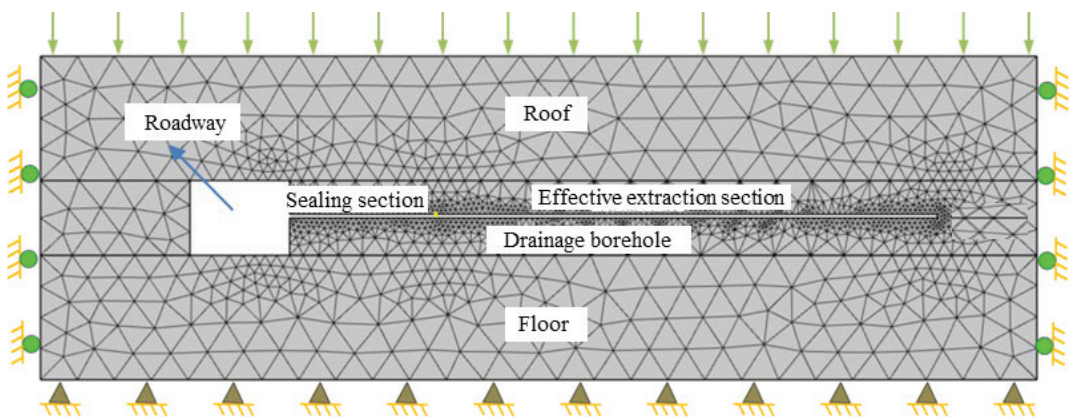


Figure 4. Gas drainage model by borehole.

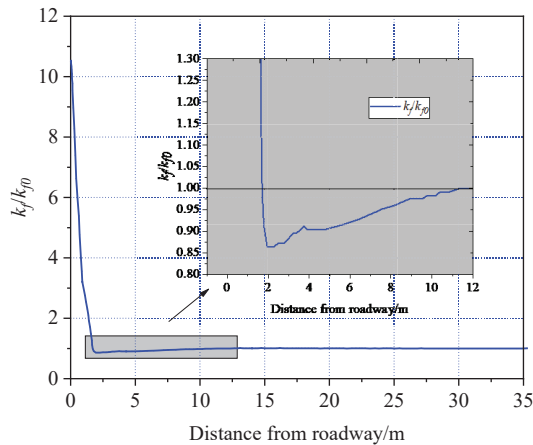
**Table 1.** Parameters of multi-field coupling model.

Parameter	Value	Parameter	Value
Langmuir pressure constant ( $p_L$ )	6.019 (MPa)	Poisson's ratio of coal ( $\nu_b$ )	0.3369
Molar volume ( $V_m$ )	16(m <sup>3</sup> /mol)	Young's modulus of coal ( $E_b$ )	2843 (MPa)
Langmuir volume constant ( $V_L$ )	0.024 (m <sup>3</sup> /kg)	Young's modulus of the coal grains ( $E_m$ )	8139 (MPa)
Langmuir volumetric strain constant ( $\epsilon_L$ )	0.1726 (%)	Gas dynamic viscosity ( $\mu$ )	$1.08 \times 10^{-5}$ (Pa·s)
Internal swelling ratio ( $F$ )	0.2	Density of coal ( $\rho_c$ )	1390 (kg/m <sup>3</sup> )
Initial cohesion of coal ( $c$ )	1.6 (MPa)	Internal friction angle of coal ( $\varphi$ )	22 (°)
Coal temperature ( $T$ )	303.15 (K)	Molar gas constant( $R$ )	8.314 (J/(mol·k))
Initial porosity of the matrix ( $\phi_{m0}$ )	0.06	Molar mass of gas ( $M_c$ )	0.016 (kg/mol)
Coal matrix adsorption time ( $\tau$ )	13.66 (d)	Initial residual plastic strain ( $\gamma^{p*}$ )	0.3326 (%)
Initial permeability of the matrix $k_{f0}$	0.05 (mD)	Initial fracture rate of coal ( $\phi_{f0}$ )	0.012

### 3.3. Permeability Distribution Law

Parallel to 1 m above the borehole, the distribution of coal seam permeability is as follows.

Figure 5 illustrates the distinctive characteristics of coal seam permeability along the depth of the borehole, dividing it into three zones: the pressure relief area, stress concentration area, and original stress area. When the borehole is in close proximity to the coal wall, the stress exerted on the coal body exceeds its yield limit, leading to the formation of fractures and a significant increase in permeability. This increased permeability creates pathways for air leakage, resulting in a decrease in gas concentration in this region. Without proper sealing measures, the gas concentration will continue to decrease. As the distance from the borehole increases, stress concentration occurs. In the stress concentration area, the permeability of the coal decreases, which leads to reduced gas fluidity and a decrease in the volume of gas extraction. When the coal body is located at a distance from the roadway and remains unaffected by driving and mining activities, its permeability maintains its original state. In this original stress area, the gas extraction volume stabilizes at a certain value.

**Figure 5.** The change law of permeability along the depth of boreholes.

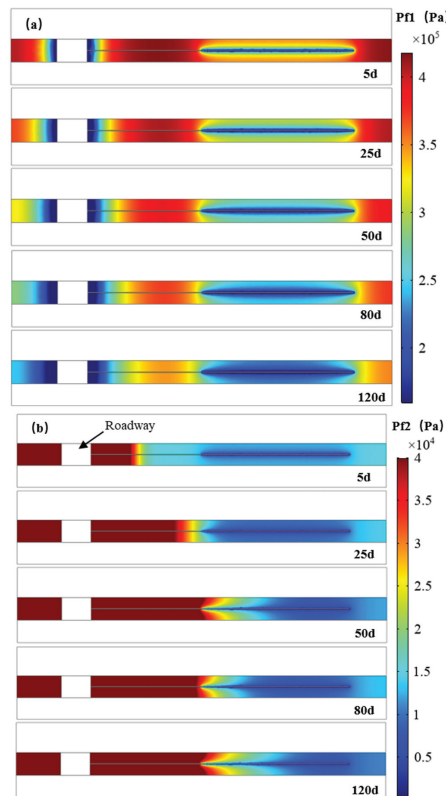
### 3.4. Analysis of the Influence of Negative Pressure on Gas Drainage

The application of negative pressure in gas drainage is aimed at facilitating the flow of free gas from fractures into boreholes. Once the fracture gas is expelled, a pressure difference is created between the gas in the matrix and the gas in the fractures. This pressure difference enables effective gas drainage. Theoretical Equations (19) and (20) suggest that in theory, increasing the negative pressure in drainage should weaken the flow of gas by reducing the pressure gradient of the fracture gas. In this study, a control variable

approach is utilized to simulate the occurrence of coal seam gas and borehole drainage under different negative pressure conditions while keeping other parameters constant. The simulation includes borehole gas flow, air leakage, and gas concentration. By analyzing the results, the relationship between borehole negative pressure and gas drainage is revealed. This research provides a theoretical basis for intelligently controlling the negative pressure in boreholes during the later stages of gas drainage.

### 3.4.1. Analysis of Gas Occurrence Law in Coal Seam under Different Negative Pressure

The simulation results demonstrate that the distribution of gas migration around the borehole follows a consistent trend across different borehole negative pressures (13 kPa, 15 kPa, 17 kPa, and 20 kPa). Therefore, Figure 6 displays the gas–air migration distribution specifically under a negative pressure of 15 kPa.



**Figure 6.** Gas distribution and migration in coal seam fissures around boreholes under the condition of 15 kPa negative pressure: (a) gas migration; (b) air migration.

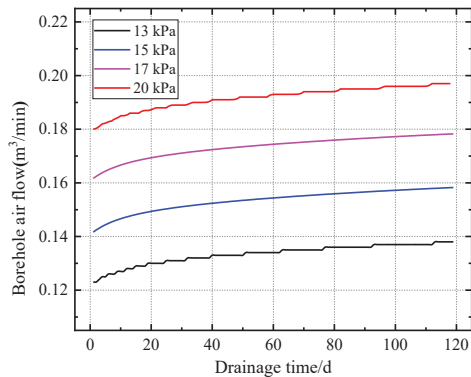
In Figure 6, it is observed that the coal wall adjacent to the roadway, affected by mining disturbances, exhibits lower gas pressure compared to the extension of the boreholes where the gas pressure increases. This pressure difference drives the gas to flow into the boreholes and roadways under negative drainage pressure. Simultaneously, air in the roadway is pushed through mining-induced fracture channels towards the coal seam and boreholes by pressure gradients. During the initial stage of borehole gas drainage, the coal seam fissures have a high gas content and pressure gradient. As a result, a substantial amount of gas rushes into the boreholes under the influence of negative pressure drainage. Consequently, during this period, the gas concentration in the extraction borehole is relatively high, and the flow rate is considerable. However, as the drainage time progresses, the gas content



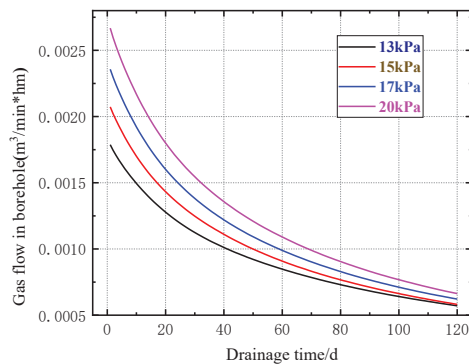
and pressure gradient in the coal surrounding the borehole gradually decrease. Conversely, the air content and pressure gradient in the coal around the borehole increase, leading to a continuous influx of air into the borehole. As a result, the flow rate of pure gas decreases while the gas concentration in the extraction borehole continues to decrease.

### 3.4.2. Gas Extraction from Boreholes under Different Negative Pressure

Different negative pressures of extraction have an impact on the air leakage in the cracks surrounding the borehole. Figure 7 illustrates the borehole drainage, including borehole gas flow, air leakage, and gas concentration, under different borehole negative pressures (13 kPa, 15 kPa, 17 kPa, and 20 kPa). According to Figure 7a,b, increasing the negative pressure of the borehole leads to an increase in gas flow and its attenuation rate within the borehole, along with an increase in air leakage. This can be attributed to several factors. Firstly, as the extraction time progresses, the effectiveness of negative pressure gradually weakens. Larger negative pressures contribute less to gas extraction. Instead, the larger negative pressure is primarily utilized to extract the air rushing into the borehole from the cracks surrounding it, resulting in a gradual increase in air leakage. Secondly, due to the dynamic pressure disturbance from the extraction borehole and the coal matrix shrinkage, the cracks surrounding the borehole gradually develop, resulting in a decrease in air leakage resistance and an increase in air leakage. Therefore, increasing the negative pressure of the boreholes reduces the gas concentration within the boreholes. Consequently, selecting an appropriate negative pressure is crucial for ensuring the economic cost and effectiveness of the project. It involves finding a balance between gas extraction efficiency, air leakage control, and overall project feasibility.

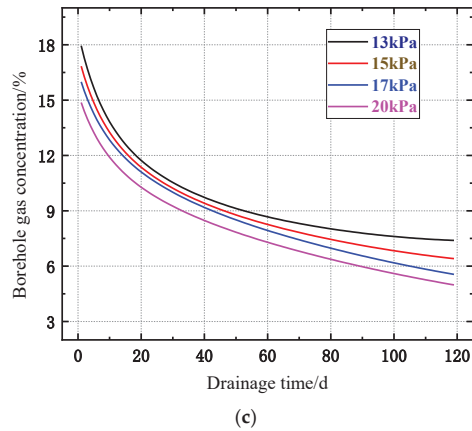


(a)



(b)

Figure 7. Cont.

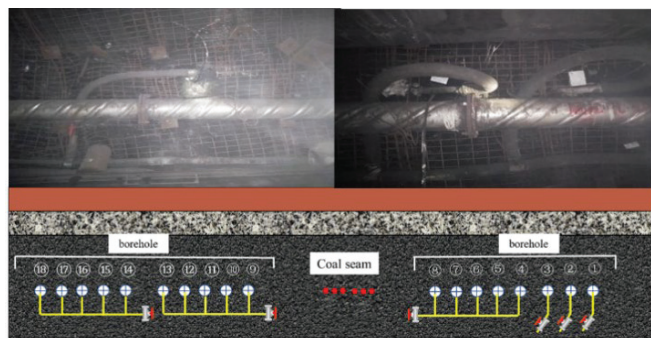


**Figure 7.** Gas drainage from boreholes with different negative pressure orders: (a) borehole air flow; (b) borehole gas flow; (c) gas concentration in boreholes.

### 3.4.3. Field Verification

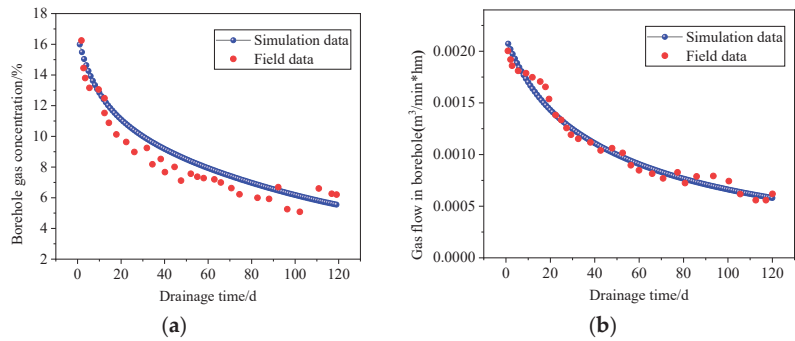
According to the simulation results, the field test of 150804 is carried out to verify the accuracy of the model and provide the basis for regulation and control. The test scheme is as follows.

Figure 8 displays the specific drilling hole numbers along the groove, corresponding to the actual situation of the 150804 tape. The changes in flow rate and concentration negative pressure over time are investigated under different negative pressure conditions, namely, 13 kPa (No. 1), 15 kPa (No. 2), and 20 kPa (No. 3). The single holes are identified as No. 1–3 boreholes, while the group boreholes are labeled as No. 4–18. The group holes are further divided into three groups: 13 kPa (No. 4–8), 15 kPa (No. 9–13), and 20 kPa (No. 14–18). The specific connection mode among these boreholes is illustrated in Figure 8.



**Figure 8.** 150804 Test drilling scheme diagram.

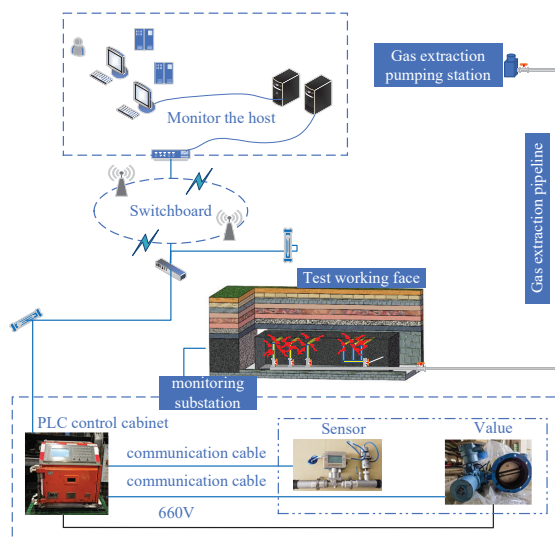
Figure 9 illustrates a comparison between the field-measured concentration and flow data of hole 2 (15 kPa) and the corresponding simulated data. The results show that as the pumping time increases, the extraction concentration and flow rate of the test borehole exhibit a decreasing trend. Specifically, the extraction concentration decreases from 16% to approximately 5%, while the flow rate decreases from 0.002 m<sup>3</sup>/min to 0.0005 m<sup>3</sup>/min. Importantly, the field-measured data demonstrate a good agreement with the simulated data, with concentration and flow rate errors of less than 10%. This confirms the validity of the model and provides a solid basis for the regulation and control of gas drainage boreholes.



**Figure 9.** Comparison between field data and simulation data: (a) drill gas concentration decay curve over time; (b) drill flow decay curve over time.

### 3.4.4. Negative Pressure Control System

Figure 10 illustrates the architecture of the gas extraction control system, which consists of three main components: an intelligent integrated management and control platform, an underground monitoring and control substation, and a system communication transmission. The intelligent terminal includes a laser methane multi-parameter analyzer installed on the gas pumping pipelines at the test face, as well as an electric device for mine flame-proof valves. These terminals are responsible for monitoring the extraction state parameters such as gas concentration, extraction negative pressure, flow rate, CO concentration, and temperature. They also adjust the valve opening state accordingly. The underground monitoring and control substation performs essential functions such as data storage, data transit, and direct control of terminal equipment. These functions are realized through the substation’s PLC control cabinet. The communication transmission part facilitates the underground data upload, transit, and ground command issuance. The logic of this component is as follows: the underground monitoring and control substation accesses the mining industrial ring network through optical fiber; the relevant information is then transmitted back to the ground intelligent integrated management and control platform via a switch. Valve regulation can be effectively carried out on the ground platform.



**Figure 10.** Gas negative pressure regulation system architecture.

In order to further validate the effectiveness of negative pressure control, a solenoid valve is installed for the purpose of opening, closing, and adjusting, as shown in Figure 11. Based on the research conclusions regarding the influence of negative pressure on gas extraction effectiveness, a negative pressure adjustment test was conducted on the extraction at the 150804 face of Liuzhuang Coal Mine. The results indicate that after pumping the test single hole, the initial gas concentration is approximately 40%. However, the gas concentration decreases rapidly over time. After implementing control measures, the concentration in the drilling hole increased by around 10%, representing a relative increase ratio of more than 40%. The higher concentration extraction was maintained for nearly 3 to 4 weeks, significantly improving the extraction effectiveness (Figure 12). Considering the fast attenuation rate of gas concentration in the working face and the short duration of high concentration extraction, the simulation results mentioned above suggest that the borehole gas concentration in the control group during the later stages of extraction is lower than that in the test hole. This discrepancy could be attributed to the increased air leakage resulting from the mining side's negative pressure setting being too high.



Figure 11. Installation drawing of solenoid valve.

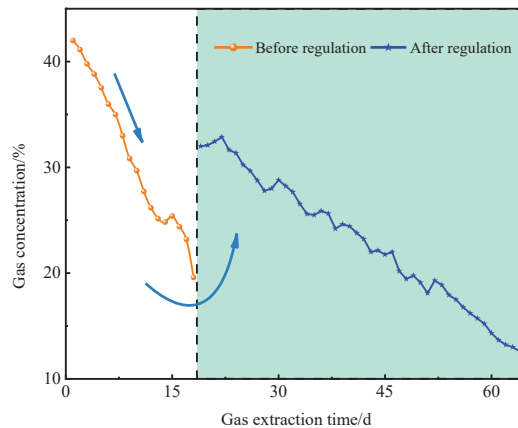
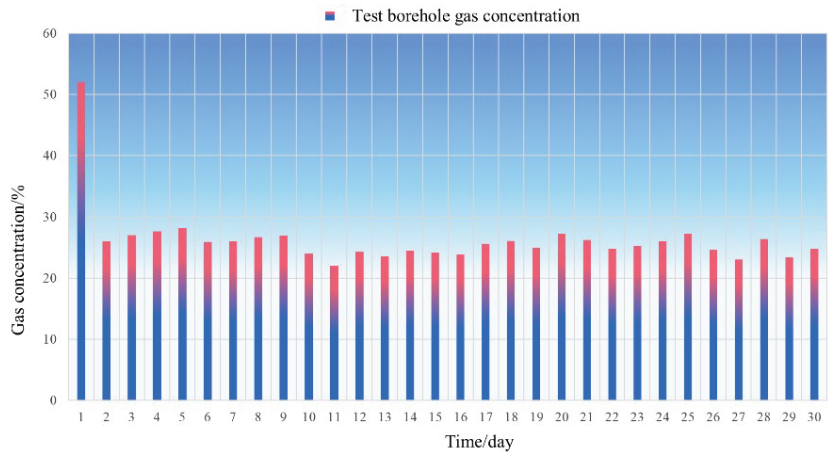


Figure 12. Drill control effect diagram.

Manual regulation of the negative pressure is carried out to assess its impact on gas drainage. By carefully regulating and controlling the negative pressure, the gas concentration in an individual borehole is maintained at a stable level exceeding 25%. Figure 13 illustrates this data, highlighting the improved extraction capacity of the mine and ensuring the safe production of the coal mine.



**Figure 13.** Gas concentration diagram of test borehole.

#### 4. Conclusions

In this paper, we have successfully established an air leakage model for boreholes in coal mining. We have investigated the gas–air migration law and air leakage mechanism during gas drainage using this model and verified its accuracy. The main findings of our study are summarized as follows:

- (1) In this study, we have incorporated the elastic–plastic mechanics theory of coal, Fick’s law, and Darcy’s law to derive the governing equation for coal deformation and the dynamic change equation for permeability. Building upon the double porosity medium model, we have developed a comprehensive coupling model for the “coal seam gas–air” binary mixed gas. This model takes into account crucial factors such as coal matrix deformation, pore gas diffusion, fracture gas seepage, and gas leakage. By considering these elements, our model provides a solid theoretical foundation for analyzing the impact of negative pressure on gas drainage effectiveness.
- (2) In our research, we have conducted simulations to study the variations of gas flow and gas concentration over time under different negative pressure conditions. By comparing the simulation results with the field test data, we have found that our model exhibits good agreement with the actual measurements. This validation of our model provides a solid basis for regulating negative pressure in gas drainage operations.
- (3) During the gas drainage process, the application of negative pressure plays a crucial role in facilitating the flow of free gas into the borehole. This creates a pressure difference between the matrix and the fractured gas, allowing for the effective drainage of gas. However, as the extraction time increases, the diminishing effect of negative pressure reduces its contribution to gas flow, leading to more significant air leakage. To address this issue, it is important to reduce the negative pressure during the later stages of gas extraction. By doing so, we can minimize air leakage, improve gas concentration, and enhance the utilization of resources.
- (4) The collected data clearly indicate that the implementation of negative pressure control in gas drilling at the test face has resulted in a significant improvement in the gas concentration of the borehole. The gas concentration of the drainage gas is consistently maintained at levels exceeding 25%. This enhancement in gas concentration has led to a significant improvement in the extraction capacity, which effectively ensures the safety of mine production.

**Author Contributions:** Conceptualization, H.G. and F.D.; methodology, X.C.; software, H.G.; validation, J.Z., X.C. and A.Z.; formal analysis, H.G.; investigation, F.D.; resources, H.G.; data curation, F.D.; writing—original draft preparation, H.G.; writing—review and editing, H.G.; project administration, J.Z.; funding acquisition, F.D. All authors have read and agreed to the published version of the manuscript.

**Funding:** This research was funded by National Natural Science Foundation of China (No. 52130409, No. 52121003).

**Data Availability Statement:** The data are available from the corresponding author on reasonable request.

**Acknowledgments:** We would like to thank the anonymous reviewers for their valuable comments and suggestions that lead to a substantially improved manuscript.

**Conflicts of Interest:** The authors declare no conflict of interest.

## References

1. Cai, Y.; Liu, D.; Pan, Z.; Yao, Y.; Li, J.; Qiu, Y. Pore structure and its impact on CH<sub>4</sub> adsorption capacity and flow capability of bituminous and subbituminous coals from Northeast China. *Fuel* **2013**, *103*, 258–268. [CrossRef]
2. Hao, Y.; Zhang, Z.; Liao, H.; Wei, Y. China's farewell to coal: A forecast of coal consumption through 2020. *Energy Pol.* **2015**, *86*, 444–455. [CrossRef]
3. Tang, X.; Wang, Z.; Ripepi, N.; Kang, B.; Yue, G. Adsorption affinity of different types of coal: Mean isosteric heat of adsorption. *Energy Fuels* **2015**, *29*, 3609–3615. [CrossRef]
4. Sun, L.; Wang, H.; Zhang, C.; Zhang, S.; Liu, N.; He, Z. Evolution of methane ad-/desorption and diffusion in coal under in the presence of oxygen and nitrogen after heat treatment. *J. Nat. Gas Sci. Eng.* **2021**, *95*, 104196. [CrossRef]
5. Aguado, M.; Nicieza, C. Control and prevention of gas outbursts in coal mines, Riosa–Olloniego coalfield, Spain. *Int. J. Coal Geol.* **2007**, *69*, 253–266. [CrossRef]
6. Beamish, B.; Crosdale, P. Instantaneous outbursts in underground coal mines: An overview and association with coal type. *Int. J. Coal Geol.* **1998**, *35*, 27–55. [CrossRef]
7. Black, D.J. Review of coal and gas outburst in Australian underground coal mines. *Int. J. Min. Sci. Technol.* **2019**, *29*, 815–824. [CrossRef]
8. Zhao, W.; Wang, K.; Cheng, Y. Evolution of gas transport pattern with the variation of coal particle size: Kinetic model and experiments. *Powder Technol.* **2020**, *367*, 336–346. [CrossRef]
9. Yuan, L. Theory of pressure-relieved gas extraction and technique system of integrated coal production and gas extraction. *J. China Coal Soc.* **2009**, *34*, 1–8.
10. Cheng, Y.; Fu, J.; Yu, Q. Development of Gas Extraction Technology in Coal Mines of China. *J. Min. Saf. Eng.* **2009**, *26*, 127–139.
11. Frank, H.; Ting, R.; Naj, A. Evolution and application of in-seam drilling for gas drainage. *Int. J. Min. Sci. Technol.* **2013**, *23*, 543–553. [CrossRef]
12. Hungerford, F.; Ren, T. Directional drilling in unstable environments. *Int. J. Min. Sci. Technol.* **2014**, *24*, 397–402. [CrossRef]
13. Aminossadati, S.; Amanzadeh, M.; Prochon, E. Step change approaches in coal technology and fugitive emissions research. *Int. J. Min. Sci. Technol.* **2014**, *24*, 363–367. [CrossRef]
14. Zhou, F.; Sun, Y.; Li, H.; Yu, G. Research on the theoretical model and engineering technology of the coal seam gas drainage hole sealing. *J. China Univ. Min. Technol.* **2016**, *45*, 433–439.
15. Wang, G.; Wang, K.; Jiang, Y. Reservoir Permeability Evolution during the Process of CO<sub>2</sub>-Enhanced Coalbed Methane Recovery. *Energies* **2018**, *11*, 2996. [CrossRef]
16. Liu, T.; Lin, B.; Yang, W. Dynamic diffusion-based multifield coupling model for gas drainage. *J. Nat. Gas Sci. Eng.* **2017**, *44*, 233–249. [CrossRef]
17. Liu, J.; Chen, Z.; Elsworth, D. Interactions of multiple processes during CBM extraction: A critical review. *Int. J. Coal Geol.* **2011**, *87*, 175–189. [CrossRef]
18. Liang, B.; Yuan, X.; Sun, W. Seepage coupling model of in-seam gas extraction and its applications. *J. China Univ. Min. Technol.* **2014**, *2*, 208–213.
19. Wu, Y. Dual poroelastic response of coal to CO<sub>2</sub> sequestration. *J. China Coal Soc.* **2011**, *36*, 889–890.
20. Zhai, C.; Chen, Z.; Kizil, M. Characterisation of mechanics and flow fields around in-seam methane gas drainage borehole for preventing ventilation air leakage: A case study. *Int. J. Coal Geol.* **2016**, *162*, 123–138.
21. Cheng, Y.; Dong, J.; Li, W.; Chen, M.; Liu, K. Effect of negative pressure on coalbed methane extraction and application in the utilization of methane resource. *J. China Coal Soc.* **2017**, *42*, 1466–1473.
22. Hao, F.; Liu, Y.; Long, W.; Zuo, W. Effective gas extraction radius of different burial depths under creep-seepage coupling. *J. China Coal Soc.* **2017**, *42*, 130–136.
23. Wang, D.; Peng, M.; Fu, Q.; Qin, H.; Xia, Y. Evolution and numerical simulation of coal permeability during gas drainage in coal seams. *Chin. J. Rock Mech. Eng.* **2016**, *35*, 704–712.

24. Wang, K.; Liu, A.; Zhou, A. Theoretical analysis of influencing factors on resistance in the process of gas migration in coal seams. *Int. J. Min. Sci. Technol.* **2017**, *27*, 315–319. [CrossRef]
25. Zang, J.; Wang, K.; Liu, A.; Zhang, X.; Yan, Z. An orthotropic coal permeability model. *J. China Univ. Min. Technol.* **2019**, *4*, 36–45.
26. Liu, Q.; Cheng, Y.; Zhou, H. A mathematical model of coupled gas flow and coal deformation with gas diffusion and Klinkenberg effects. *Rock Mech. Rock Eng.* **2015**, *48*, 1163–1180. [CrossRef]
27. Liu, T.; Lin, B.; Yang, W. Impact of matrix–fracture interactions on coal permeability: Model development and analysis. *Fuel* **2017**, *207*, 522–532. [CrossRef]
28. Zhang, X.; Gao, J.; Jia, G.; Zhang, J. Study on the influence mechanism of air leakage on gas extraction in extraction boreholes. *Energy Explor. Exploit.* **2022**, *40*, 1344–1359. [CrossRef]
29. Liu, T.; Zhao, Y.; Kong, X.; Lin, B.; Zou, Q. Dynamics of coalbed methane emission from coal cores under various stress paths and its application in gas extraction in mining-disturbed coal seam. *J. Nat. Gas Sci. Eng.* **2022**, *104*, 104677. [CrossRef]
30. Zhang, N.; Li, X.; Cheng, H. A coupled damage-hydro-mechanical model for gas drainage in low-permeability coalbeds. *J. Nat. Gas Sci. Eng.* **2016**, *35*, 1032–1043. [CrossRef]
31. Guan, C.; Liu, S.; Li, C.; Wang, Y.; Zhao, Y. The temperature effect on the methane and CO<sub>2</sub> adsorption capacities of Illinois coal. *Fuel* **2018**, *211*, 241–250. [CrossRef]
32. Liu, T.; Lin, B.; Fu, X. Modeling air leakage around gas extraction boreholes in mining-disturbed coal seams. *Process Saf. Environ. Prot.* **2020**, *141*, 202–214. [CrossRef]
33. Wang, H.; Wang, E.; Li, Z. Study on sealing effect of pre-drainage gas borehole in coal seam based on air-gas mixed flow coupling model. *Process Saf. Environ. Prot.* **2020**, *136*, 15–27. [CrossRef]
34. Chen, M.; Cheng, Y.; Li, H.; Wang, L.; Jin, K.; Dong, J. Impact of inherent moisture on the methane adsorption characteristics of coals with various degrees of metamorphism. *J. Nat. Gas Sci. Eng.* **2018**, *55*, 312–320. [CrossRef]
35. Ji, H.; Li, Z.; Yang, Y.; Hu, S.; Peng, Y. Effects of organic micro molecules in coal on its pore structure and gas diffusion characteristics. *Transp. Porous Media* **2015**, *107*, 419–433. [CrossRef]
36. Liu, T.; Lin, B.; Fu, X. Modeling coupled gas flow and geomechanics process in stimulated coal seam by hydraulic flushing. *Int. J. Rock Mech. Min. Sci.* **2021**, *142*, 104769. [CrossRef]

**Disclaimer/Publisher’s Note:** The statements, opinions and data contained in all publications are solely those of the individual author(s) and contributor(s) and not of MDPI and/or the editor(s). MDPI and/or the editor(s) disclaim responsibility for any injury to people or property resulting from any ideas, methods, instructions or products referred to in the content.

## Article

# The Influence of High-Pressure Water Jet Cutting Parameters on the Relief of Pressure around the Coal Slot

Zuo Sun <sup>1</sup>, Yingjie Liu <sup>1</sup>, Qingjie Qi <sup>1</sup>, Jiamei Chai <sup>1,\*</sup> and Beifang Gu <sup>2</sup>

<sup>1</sup> Emergency Science Research Institute, Chinese Institute of Coal Science, Beijing 100013, China; sunzuo@mail.ccri.ccteg.cn (Z.S.); liuyingjie@mail.ccri.ccteg.cn (Y.L.); qiqingjie@mail.ccri.ccteg.cn (Q.Q.)

<sup>2</sup> School of Environmental and Municipal Engineering, North China University of Water Resources and Electric Power, Zhengzhou 450045, China; gubeifang@ncwu.edu.cn

\* Correspondence: chajjiami@mail.ccri.ccteg.cn

**Abstract:** This research aims to investigate the impact of high-pressure water jet cutting parameters on pressure alleviation around the coal slot. A numerical model of high-pressure water jet cutting coal was developed using FLAC<sup>3D</sup> software, allowing for a detailed study of how each cutting parameter affects the pressure relief effect of the slot. The key findings are as follows: as the water jet pressure increases, the plastic area of the coal body around the kerf expands, although the rate of increase diminishes, with the optimal water jet pressure being 30 Mpa. The results suggest that hydraulic slotting measures are particularly beneficial for outburst prevention in high in situ stress coal seams. The pressure relief range exponentially grows with an increase in the kerf depth, signifying that enhancing the kerf depth has a notable effect on improving the hydraulic kerf pressure relief. As the slit width increases, the volume of the slit enlarges, leading to a significant rise in the pressure relief range of the surrounding coal body. Given that an increase in the slit width necessitates an increase in the nozzle outlet diameter and slotting time, the optimal slit width is determined to be 0.2 m. The research concludes that the optimal hydraulic slit spacing is 3 m. This study offers valuable theoretical guidance for high-pressure water jet slotting.

**Keywords:** high-pressure water jet; pressure relief; FLAC<sup>3D</sup>; slot parameters; in situ stress

**Citation:** Sun, Z.; Liu, Y.; Qi, Q.; Chai, J.; Gu, B. The Influence of High-Pressure Water Jet Cutting Parameters on the Relief of Pressure around the Coal Slot. *Processes* **2023**, *11*, 2071. <https://doi.org/10.3390/pr11072071>

Academic Editors: Feng Du, Aitao Zhou and Bo Li

Received: 24 May 2023

Revised: 4 July 2023

Accepted: 7 July 2023

Published: 11 July 2023



**Copyright:** © 2023 by the authors. Licensee MDPI, Basel, Switzerland. This article is an open access article distributed under the terms and conditions of the Creative Commons Attribution (CC BY) license (<https://creativecommons.org/licenses/by/4.0/>).

## 1. Introduction

Coal is the main energy source in China. In recent years, with the increase in mining depth, the gas content in low-permeability coal seams has gradually increased, resulting in low gas drainage efficiency and poor effects [1,2]. Various measures can enhance coal seam permeability to address mining challenges technically. Improving the coal seam's permeability enhances gas circulation, thus boosting the coal seam's gas drainage effect to prevent outbursts [3,4]. For coal exhibiting poor gas permeability, an array of effective technical methods can be employed to augment coal's gas permeability [5–7]. Various efficacious strategies and methods can be distilled from domestic and international practice, such as mining protective layers and implementing various hydraulic measures, among others [8–14].

The hydraulic slotting technology uses high-pressure jet water as the medium to cut coal in a borehole to form a new slot, so as to increase the permeability of the coal seam and reduce the stress of the original rock coal seam, so as to form pressure relief and permeability enhancement effects on the surrounding coal and improve the gas drainage efficiency. Therefore, the application effect of hydraulic slotting for harder coal is significant, and hydraulic slotting is an effective outburst prevention measure [15].

Ye et al. investigated the mechanism of high-pressure abrasive hydraulic kerf anti-outburst technology, analyzed its technological process, and verified its beneficial application effect through experiments [16]. Kou et al. conducted a comparable simulation experiment to determine the nozzle rotation parameters when hydraulic kerf was utilized



for pressure relief and permeability enhancement in the coal seam [17]. Chen examined the anti-outburst mechanism and corresponding supportive equipment of the integrated construction of drilling and hydraulic slotting technology, applying it on-site [18]. Liu et al. evaluated the effects of different slotting techniques, analyzed the impact of progressive and regressive hydraulic slotting on the pressure relief and permeability enhancement of coal seams, and proposed slotting techniques suitable for different mining conditions [19]. Yi et al. studied the pressure relief effect of a high-pressure water jet fracturing coal through a theoretical analysis, analogous experiments, and numerical simulation, and analyzed the pressure relief law with various cutting parameters [20]. Zhang et al. acquired a theoretical model of the annular kerf depth of the high-pressure water jet through theoretical modeling and field test validation [21]. Zhang et al. concluded, through theoretical analysis, numerical simulation, and field tests, that high-pressure water jets can cut annular slots in the coal seam to lessen the coal body's stress, thereby enhancing the coal seam's permeability and improving gas drainage [22]. Liu et al. designed a high-pressure rotary sealing device, demonstrating that a water jet can effectively reduce dust concentration when cutting rocks [23]. Xiao et al. examined the distribution of particle size, morphology, and fractal characteristics during coal crushing under high-pressure water jet cutting [24]. Zhou et al. established an elastoplastic damage numerical model based on the material point method, and simulated the effect of hydraulic slotting on pressure relief desorption and permeability enhancement of linking deep CBM [25]. Deng et al. used COMSOL Multiphysics multi field coupling software to carry out numerical simulation, and selected slotting radius, drainage time, gas pressure and permeability as the main influencing factors, analyzed the variation law of gas drainage radius under different influencing factors, and carried out field test [26].

Scholars have carried out a lot of research on the optimization measures and effects of hydraulic slotting but, due to the complexity of the coal mass's failure process, current research on the pressure relief failure effect on the surrounding coal mass, based on hydraulic kerf parameters, is inadequate. Taking Tanjiachong No.6 Coal Seam as an example, this study uses the method of numerical simulation and field engineering verification to analyze the influence of slotting parameters on the distribution of stress-strain and plastic regions of coal around the slot, obtain reasonable hydraulic slotting parameters, and determine the optimal spacing of hydraulic slotting in the working face. This study has important theoretical and engineering significance for improving the efficiency of hydraulic slotting and the effect of coal and rock pressure relief.

## 2. Numerical Model Construction

FLAC<sup>3D</sup> was developed by ITASA in the United States, and is widely used for simulating the three-dimensional structural stress characteristics and plastic flow analysis of rocks and soil. FLAC<sup>3D</sup> is solved by a three-dimensional fast Lagrange algorithm, including five kinds of solution models, which are the static model, dynamic model, creep model, seepage model and temperature model. Because mesh generation affects the simulation results, FLAC<sup>3D</sup> has built-in automatic 3D mesh generator.

The FLAC<sup>3D</sup> numerical model parameters were established according to the geological data of the Tanjiachong No.6 coal seam. The model, a cuboid, has dimensions of 17 m along the strike (X-axis), 10 m along the dip (Y-axis), and 17 m vertically (Z-axis). The model's grid sizes are 1 m, 1 m, and 0.05 m in the X, Z, and Y-axis directions, respectively. The drilling grid is cylindrical, with a set kerf depth of 1 m. The numerical calculation model is divided into 53,600 units. According to the site conditions, the working face direction in the model is set as the x-axis direction, and the working face inclination is set as the y-axis direction. In order to facilitate the observation of the slotted model, the slotted model is locally enlarged, as shown in Figure 1. The numerical model's material parameters are shown in Table 1.

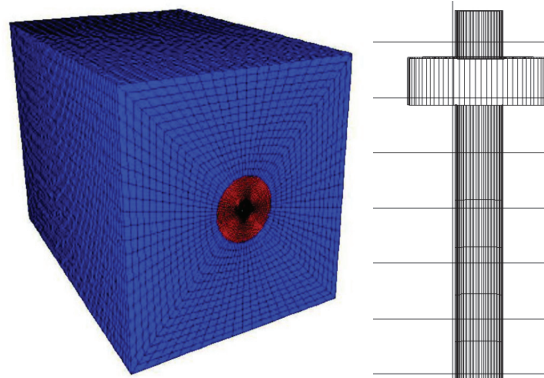


Figure 1. Numerical simulation model and hydraulic cutting model.

Table 1. The mechanical parameters in numerical simulation.

Shear Modulus <i>S</i>	Internal Friction Angle <i>F</i>	Bulk Modulus <i>B</i>	Density <i>D</i>	Tensile Strength <i>T</i>	Cohesion <i>C</i>
(Pa)	(°)	(Pa)	(kg/m <sup>3</sup> )	(Pa)	(Pa)
$0.19 \times 10^9$	20	$0.36 \times 10^9$	1400	$0.03 \times 10^6$	$1 \times 10^6$

FLAC<sup>3D</sup> has a variety of initial in situ stress field methods. According to the numerical simulation, in order to be simple and fast, the elastic solution method is selected. The specific steps of the elastic solution method are: first, set the model material as the elastic model, then set the shear modulus and volume modulus in the material parameters to the maximum value, which can prevent the plastic failure of the model during stress initialization, and finally apply the initial in situ stress field to the model.

The numerical simulation employs the Mohr–Coulomb constitutive model, with the calculation accuracy set to  $10^{-5}$ . Maximum values are assigned to the shear modulus and bulk modulus in the material parameters, which prevent the model from initializing the stress. The stress nephogram following in situ stress initialization is presented in Figure 2.

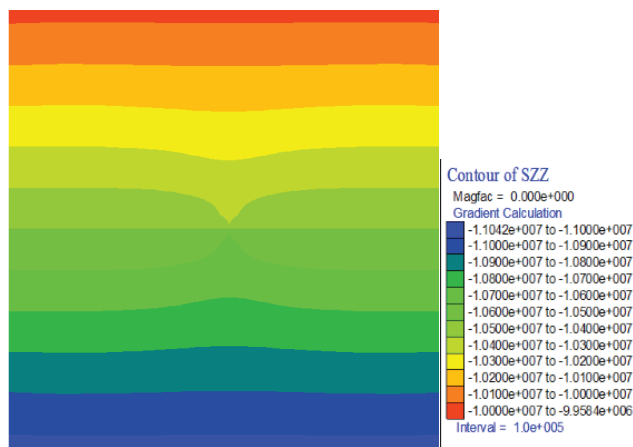


Figure 2. Initial stress field vertical stress state.

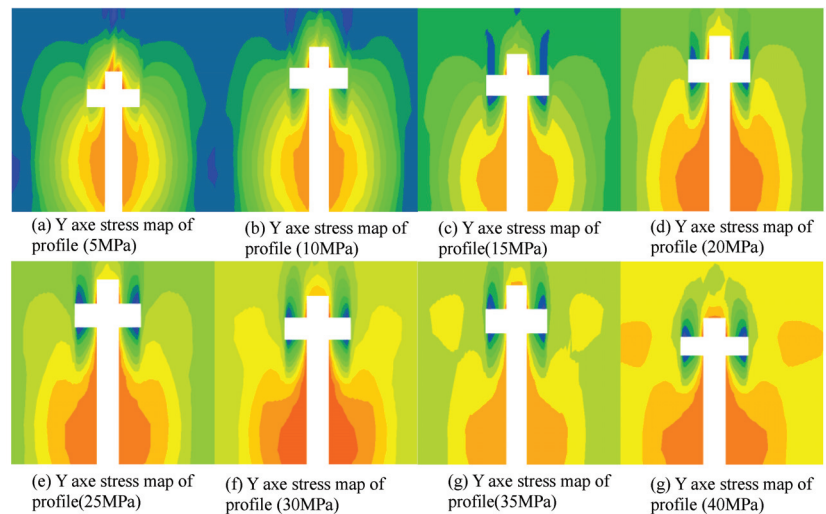
### 3. Simulation Results of Different Kerf Parameters

Various slotting parameters were selected for numerical simulation research. The chosen parameters include: nozzle outlet pressure  $P$ , in situ stress  $F$ , slit depth  $r$ , slit width  $d$  and slit spacing  $L$ . After the completion of numerical simulation, the deformation and plastic distribution nephogram under various working conditions is derived. The stress–strain and plastic region changes of coal around the slit are recorded through the nephogram, and the influence of different parameters on coal pressure relief is analyzed.

#### 3.1. Simulation Analysis of Nozzle Outlet Pressure

Focusing on the water jet pressure's influence, the slit width was set to 0.2 m, the slit depth to 1 m, and pressure value gradients were chosen as 5 MPa, 10 MPa, 15 MPa, 20 MPa, 25 MPa, 30 MPa, 35 MPa, and 40 MPa, respectively, to examine coal stress–strain and plastic failure states.

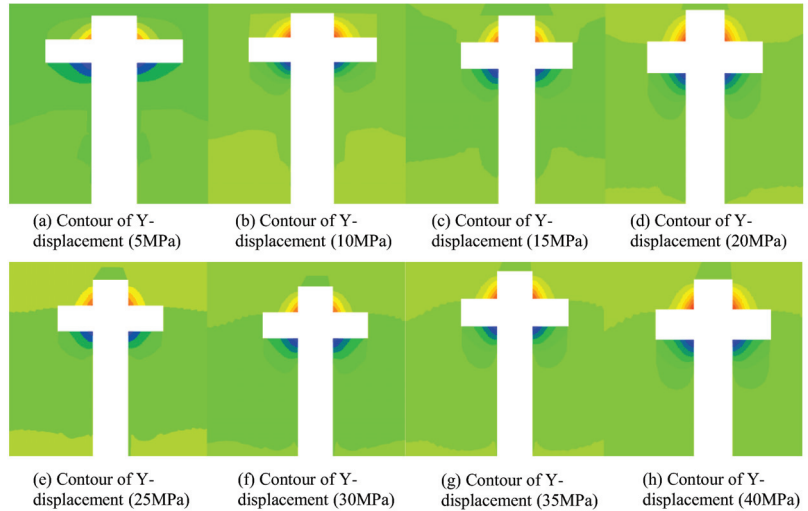
Figure 3 displays the stress cloud diagram of the coal body surrounding the slit in the Y direction under varying water jet pressures. The area far from the slit maintains its original stress state. In the numerical model, as the impact force of the water jet applied by the nozzle on the bottom of the slot gradually increases, the stress unloading of the coal body around the slot likewise increases in all directions. Under various pressure gradients, stress unloading in the Y direction is greater than in the other two directions, and is proportional to the pressure gradient. As the water jet pressure increases, the high-stress area in the coal body gradually shifts towards the deeper part, thereby achieving pressure relief. This indicates that increasing the water jet pressure is an effective method to augment the pressure relief range of the slot.



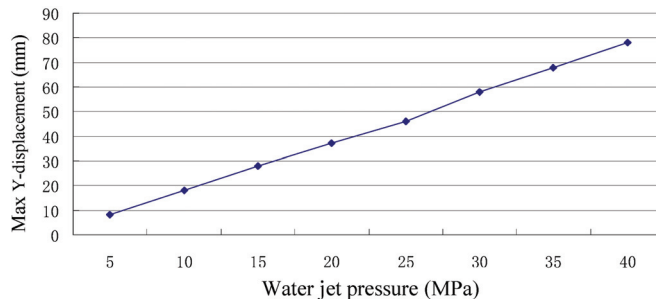
**Figure 3.** Y axis stress map of profile.

As depicted in Figure 4, the displacement cloud map of the coal mass surrounding the slit in the Y direction under varying pressure gradients at the water jet nozzle outlet was analyzed. As discerned from the figure, deformation towards the kerf is observed on either side following hydraulic slotting, and the nodes' displacement on both kerf sides incrementally increases with rising water jet pressure. The displacement contrasts on either kerf side are approximately symmetrical, but in opposing directions. With a nozzle outlet pressure of 5 MPa, the coal body's maximum displacement in the Y direction is 8.5 mm, and this maximum displacement increases as the nozzle outlet pressure gradient rises. By tracking the maximum displacement change, a curve portraying the maximum displacement of the coal mass around the seam versus the nozzle outlet pressure gradient

is plotted in Figure 5. As can be inferred from the figure, the relationship between the two is nearly proportional, indicating that the pressure relief effect of hydraulic cutting can be notably improved by increasing the water jet pressure.

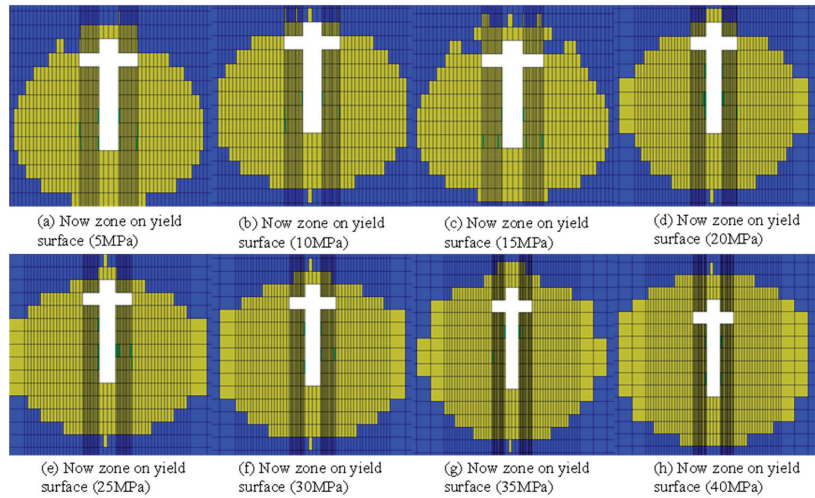


**Figure 4.** Contour of Y-displacement.



**Figure 5.** Contour of max Y-displacement with different water jet pressure.

Figure 6 illustrates the area where the coal mass around the slit reaches the current yield surface under different water jet pressures. It is evident from the figure that, as water jet pressure persistently increases from 5 MPa to 40 MPa, the plastic region of the coal mass around the cut enlarges, and the pressure gradient between the coal mass around the cut and the nozzle outlet water pressure does not follow a simple linear relationship. As shown in Figure 6, it can be observed that, when the nozzle outlet pressure escalates from 5 MPa to 30 MPa, the coal mass area surrounding the slit in the current plastic region increases rapidly, whereas it increases more slowly from 30 MPa to 40 MPa. Given the complications related to safety and maintenance when hydraulic slotting equipment operates at excessively high water jet pressures, it is recommended that the water jet pressure be set to around 30 MPa to ensure an extensive influence range and economical operation. Consequently, the hydraulic slit's water jet pressure is set to approximately 30 MPa.



**Figure 6.** Now zone on yield surface.

### 3.2. Simulation Analysis of Ground Stress

Numerical simulation was conducted to assess the impact of ground stress,  $F$  represented by the depth of the coal seam. In situ stress comprises vertical stress  $\sigma_v$  and horizontal stress  $\sigma_h$ . Typically, the vertical stress  $\sigma_v$  is equivalent to the overlying coal strata's weight, represented as  $\sigma_v = rH$ . Horizontal stress encompasses two components: the maximum horizontal principal stress  $\sigma_{h,max}$  and the minimum principal stress  $\sigma_{h,min}$ , with the approximate relationship between the two and burial depth given shown in Equation (1) [27]:

$$\begin{cases} \sigma_{h,max} = 0.03H + 4.4 \\ \sigma_{h,min} = 0.02H + 2.1 \end{cases} \quad (1)$$

In accordance with the site's actual conditions, the horizontal stress  $\sigma_h$  is chosen as the average value of the maximum horizontal principal stress  $\sigma_{h,max}$  and the minimum principal stress  $\sigma_{h,min}$ , denoted as  $\sigma_h = \frac{\sigma_{h,max} + \sigma_{h,min}}{2}$ . Taking into account the actual situation, and calculation convenience, five burial depth gradients were established at 200 m, 400 m, 600 m, 800 m, and 1000 m, respectively. Other parameters were set as follows: kerf depth at 1 m, and kerf width at 0.2 m. Using Equation (1), the in situ stress values under different burial depths can be calculated, and are presented in Table 2.

**Table 2.** The mechanical parameters in numerical simulation.

Coal Seam Depth (m)	Vertical Stress $\sigma_v$ (MPa)	Horizontal Stress $\sigma_h$ (MPa)
200	5.2	8.0
400	10.5	13.0
600	15.7	17.9
800	20.9	22.7
1000	26.2	27.6

Figure 7 delineates the relationship between in situ stress (burial depth) and the maximum values of the plastic region and the maximum stress unloading in the X, Y and Z axes of the model. As the burial depth increases, as observed from the figure, the pressure relief range of the coal mass surrounding the kerf across the three coordinate axes also expands. The maximum value of stress unloading in all directions exceeds that of the plastic region, suggesting that, despite the absence of coal mass damage in these regions, stress reduction still occurs.

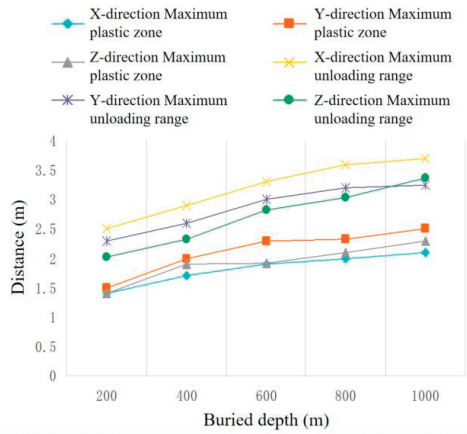


Figure 7. Relationship between buried depth and maximum unloading range.

The numerical simulation yields the stress unloading volume of the coal mass around the slot in all directions, and the correlation between the pressure unloading volume in each direction and the coal seam’s burial depth is depicted in Figure 8. The figure reveals a similar trend in the stress unloading volume change of the coal mass around the slit in all directions, indicating an increase in the pressure unloading degree of the coal mass in the three axes with the rise in the coal seam depth. The stress unloading volume in the X direction is most affected by the buried depth of coal seam, followed by the Z direction, and finally the Y direction, but only the Z direction is not linear. This suggests that a deeper coal seam burial corresponds to higher in situ stress and a greater degree of pressure relief for the coal mass around the slot. This implies that in situ stress contributes to the pressure relief of the coal mass, and that the impact of hydraulic slotting measures is more pronounced in areas with high in situ stress.

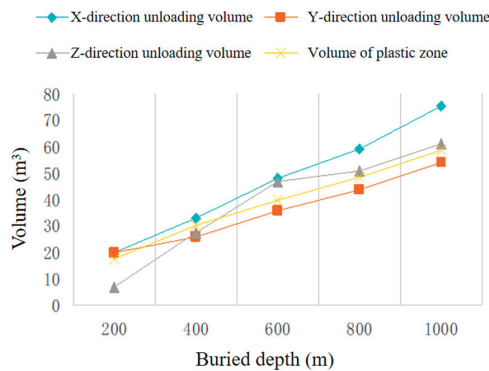
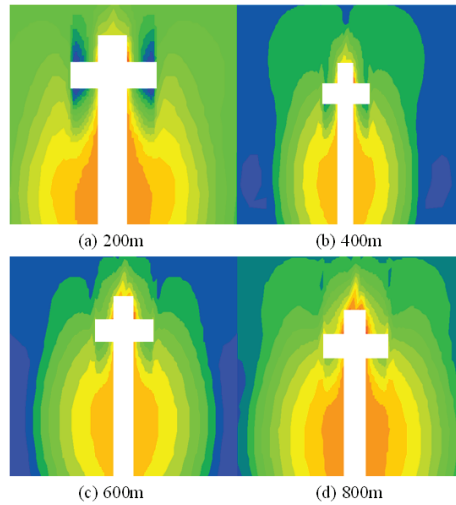


Figure 8. Relationship between buried depth and unloading volume of all directions.

Figure 9 presents the stress cloud diagram of the coal mass near the kerf in the Y direction under varying in situ stresses. As the in situ stress rises, the stress reduction area enlarges, and the pressure relief effect becomes more noticeable. This demonstrates that the increase in in situ stress widens the difference between the coal mass stress and the stress around the slot post-slotting. Additionally, when a new stress equilibrium is formed, the stress relief range also expands. Based on the above analysis, the greater the in situ stress, the more effective hydraulic cutting proves to be, indicating that hydraulic cutting technology is more suitable for outburst coal seams under large burial depth conditions.

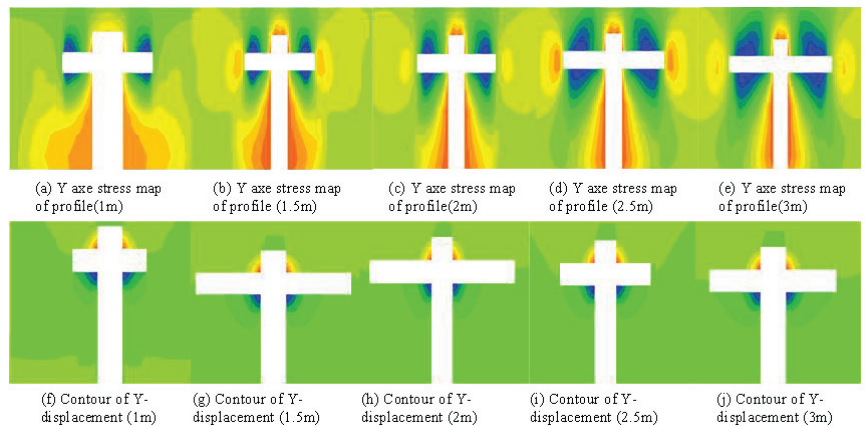


**Figure 9.** Contour of Y-stress at different ground stress.

### 3.3. Simulation Analysis of Kerf Depth

Kerf depths were set at 1 m, 1.5 m, 2 m, 2.5 m, and 3 m, respectively. Other parameters included a kerf width of 0.2 m, a water jet pressure of 30 MPa, and a coal seam burial depth of 400 m.

Figure 10a–e depicts the stress change cloud map of the coal mass around the slot in the Y direction under different slot depths. The region farther from the slot retains its original stress state. As kerf depth increases, the stress reduction area expands, and the magnitude of the stress reduction on either kerf side is essentially identical, but in opposite directions. For the kerf depth parameter, being significantly larger than the kerf width results in a greater degree of pressure relief in the Y direction than in other axes. Also, as the cutting depth increases, the coal area controlled by the hydraulic cutting measures expands, and the influence radius enlarges.



**Figure 10.** Y axis stress map of profile and contour of Y-displacement.

Figure 10f–j presents the displacement change diagram of the coal mass in the Y direction. Following hydraulic slotting, deformation towards the kerf is observed on both kerf sides, and as kerf depth increases, the nodes' displacement on either kerf side also

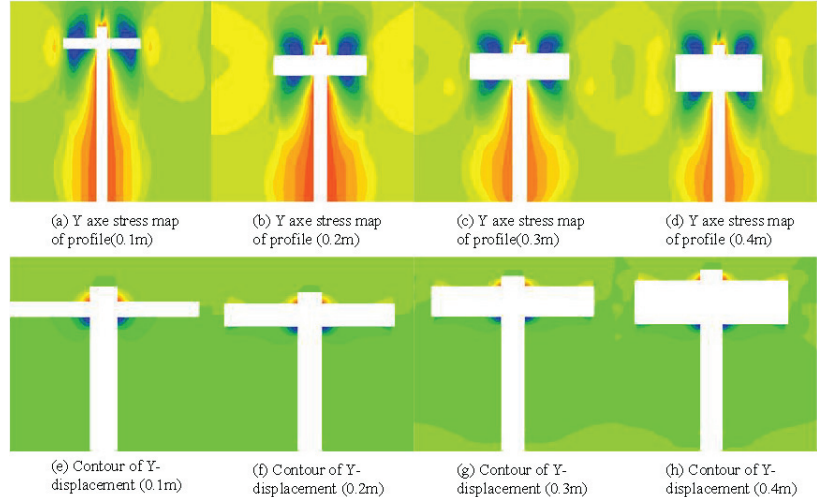
gradually rises. The displacement contrasts on either kerf side are roughly equal, but in opposite directions. This suggests that enhancing the kerf depth can improve the pressure relief effect of the hydraulic kerf.

Taking into account the practical circumstances on site, increasing the kerf depth necessitates a higher water pressure which, in turn, imposes more stringent equipment requirements. These conditions prove challenging to meet on site, and will result in a proportionate increase in kerf time. Therefore, the kerf depth cannot be infinitely increased; it must be determined in conjunction with field equipment conditions and field test data.

### 3.4. Simulation Analysis of Kerf Width

The kerf width was set in increments of 0.1 m, 0.2 m, 0.3 m, and 0.4 m. Other parameters include a kerf depth of 1 m, water jet pressure of 30 MPa, and a coal seam burial depth of 400 m. The stress–strain behavior of the coal mass around the slot and the failure state of the plastic region were investigated.

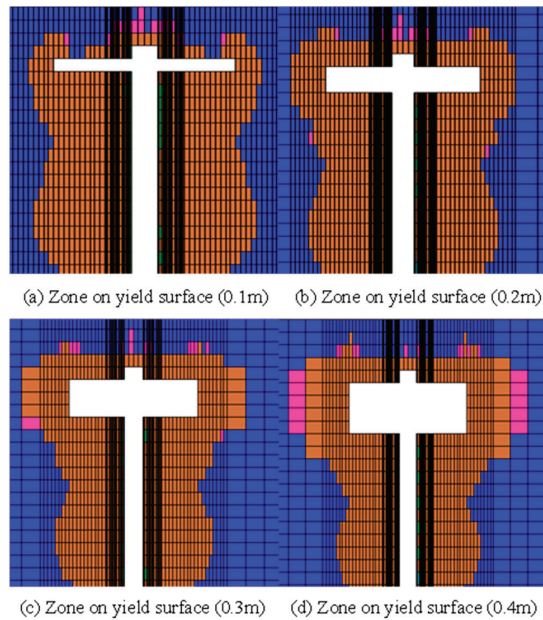
Figure 11 illustrates the stress change cloud map and displacement change cloud map of the coal mass around the slot in the Y direction under different slit widths. The slit width significantly influences the coal body's pressure relief. As the slot width increases, the degree of pressure relief for the coal mass around the slot is enhanced, and the stress unloading range of the coal mass widens. As more coal is removed, the slot's volume increases, thereby increasing the coal body's movement towards the slot and expanding the deformation and damage range of the coal body. This can effectively increase the contact area for gas migration, thereby enhancing the gas drainage effect. However, increasing the slit width requires a larger water jet nozzle outlet diameter and additional slotting time, which demands more advanced equipment, thus limiting the extent to which the slit width can be increased.



**Figure 11.** Y axis stress map of profile and contour of Y-displacement.

Figure 12 presents the extent of the plastic region of the coal mass around the kerf under different kerf widths. As the kerf width increases, the plastic region rapidly expands. When the kerf width is set to 0.1 m, the corresponding plastic failure area is 0.9 m. When the kerf width is set to 0.4 m, the plastic region expands to 3.4 m, exhibiting exponential growth. This suggests that increasing the slit width has a significant pressure relief effect on the surrounding coal body.





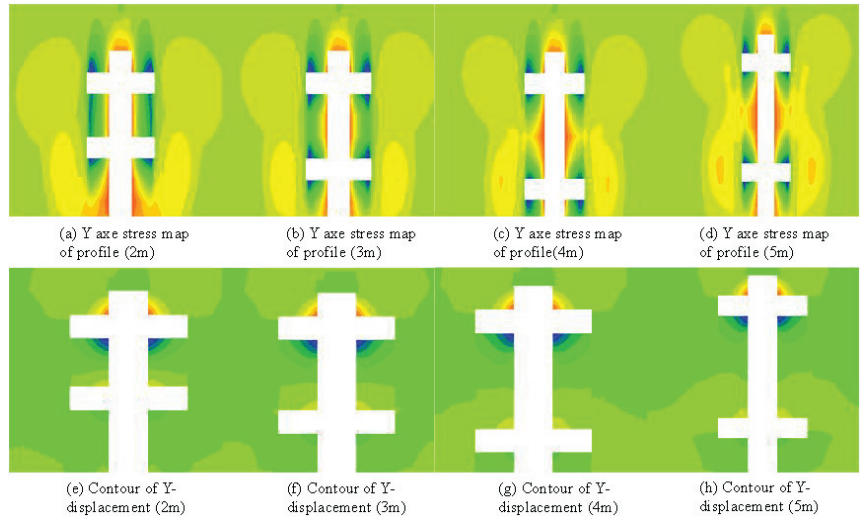
**Figure 12.** Zone on yield surface.

### 3.5. Simulation Analysis of Slot Spacing

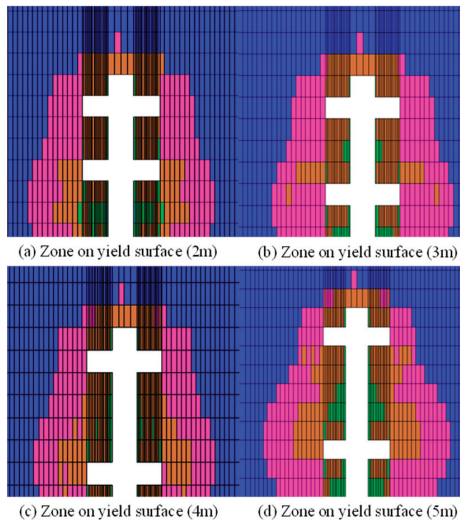
The slot spacings were set at 2 m, 3 m, 4 m, and 5 m, respectively, with other parameters set as: a kerf depth of 1 m, a water jet pressure of 30 MPa, and a kerf width of 0.2 m. The assessment criteria were the stress–strain and plastic deformation regions between the two slots.

Figure 13 displays the stress change cloud map and displacement change cloud map of the coal body around the slot in the Y direction under different slot spacings. When the gap between the slots is relatively small, the coal mass between the slots undergoes repeated depressurization, and coal mass fissures are fully penetrated. As the slot spacing increases, the pressure relief overlap area between the slots gradually diminishes. When the gap between the slots widens to 4 m, an area in the middle of the two slots no longer undergoes repeated depressurization, and as the gap continues to expand, this area becomes more prominent. Moreover, the cloud map of the coal mass displacement between the slots reveals that as the spacing between the slots increases, the area with large displacement between the slots gradually shrinks until 5 m, at which point the coal mass in the middle of the slots is no longer affected by the slots on either side, leading to a suboptimal pressure relief effect in the coal seam.

The slot spacing significantly impacts the plastic deformation area of the coal mass between the slots. Figure 14, obtained by slicing the model, demonstrates the range of the plastic deformation area of the coal mass between slots under varying slot spacings. After the borehole is established, the surrounding coal mass undergoes plastic deformation. Following the construction of the water jet slit, this segment of the coal mass deforms again, resulting in a more pronounced pressure relief effect. There exists a recurring damage area in the coal mass between the slots. When the spacing between the slots extends to 4 m, a non-recurring damage area emerges between the slots, which adversely affects the pressure relief effect.



**Figure 13.** Y axis stress map of profile and contour of Y-displacement.



**Figure 14.** Zone on yield surface.

Based on these conclusions, it can be inferred that excessively close slot spacing impairs the stress unloading effect, leading to project inefficiencies. Therefore, in light of these research findings, it is proposed that the field application gap between the kerfs be set at 3 m, which satisfies the requirements for outburst prevention and project efficiency.

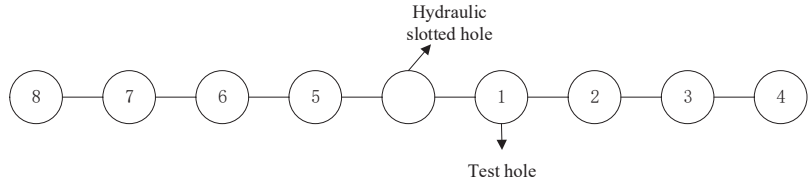
#### 4. Field Validate

In order to verify the effectiveness of numerical simulation results, on-site experiments were conducted in the No.6 coal seam of Tanjiachong Coal Mine to determine the optimal spacing of hydraulic cutting seams.

##### 4.1. Test Method

- (1) Firstly, 8 investigation boreholes with a diameter of 75 mm are constructed. All the investigation boreholes are required to be parallel to each other, and the spacing of

boreholes is 1 m. The drilling arrangement is shown in Figure 15. For the extraction drilling with the same construction parameters, the hole shall be sealed immediately after the completion of construction, and the pressure gauge shall be connected to observe the pressure change;

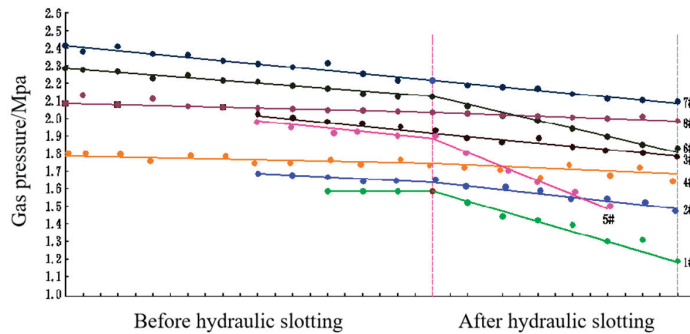


**Figure 15.** Sketch map of borehole.

- (2) After the construction of all test holes is completed and the pressure gauge is stable, the hydraulic slotting drilling shall be constructed. After the completion of drilling construction, connect the hydraulic slotting drilling hole to the gas drainage system immediately, and regularly observe each test hole until the pressure is stable;
- (3) After the gas pressure is stable, the hydraulic slotting operation shall be implemented. In order to solve the problem of borehole collapse and deformation, the casing hole is first carried out, and then the hydraulic cutting construction is carried out. After the construction is completed, the hole shall be sealed and the drainage shall be continued until the gas pressure in the test hole is stable. The basis for determining that the test hole is within the influence range of hydraulic cutting is that the gas pressure in the test hole is reduced by more than 10% compared with that before pre-drainage.

#### 4.2. Test Results

The gas pressure changes of test holes 1–8 before and after the implementation of hydraulic slotting measures are counted, as shown in Figure 16.



**Figure 16.** Gas pressure change of test boreholes.

As shown in Figure 16, there was a significant change in gas pressure during the construction of the hydraulic cutting measures for holes 1 and 5, resulting in a 35% decrease in gas pressure. The number of holes 2 and 6 decreased by 25%, while the number of holes 3 and 7 decreased slightly, but still reached 15%. According to the judgment basis, these test holes are all within the influence range of hydraulic cutting. The decrease in gas pressure in holes 4 and 8 is relatively small, about 5% and less than 10%, respectively.

Therefore, the optimal spacing of hydraulic slits determined in this experiment is between 3 m and 4 m. Considering redundancy, the optimal spacing of hydraulic slits is set at 3 m, which is consistent with the numerical simulation results.

## 5. Conclusions

A numerical model of a high-pressure water jet slotted coal mass was developed using FLAC<sup>3D</sup>, and the impact of each slotting parameter on the slot's pressure relief effect was examined. The primary conclusions are as follows:

- (1) With the steady rise in water jet pressure, the plastic area of the coal mass around the cut progressively enlarges. When the nozzle's water outlet pressure increases from 5 MPa to 30 MPa, the area of the coal mass around the cut within the plastic region rapidly expands, and the water outlet from the nozzle increases. When the pressure escalates from 30 MPa to 40 MPa, the plastic region's extent grows more slowly. Taking all factors into consideration, the optimal water jet pressure is 30 MPa;
- (2) As vertical stress increases, the pressure relief range and damage range of the coal mass around the slot progressively enlarge, indicating that hydraulic slotting measures are particularly suitable for outburst elimination in coal seams with high in situ stress;
- (3) As the kerf depth increases, the pressure relief range progressively expands, leading to an increased influence radius of the hydraulic kerf. The pressure relief range grows exponentially with the kerf depth, implying that increasing the kerf depth notably enhances the hydraulic kerf pressure relief effect;
- (4) As the slit width increases, the volume of the slit enlarges, leading to a significant increase in the pressure relief range of the surrounding coal mass. However, considering that widening the slit requires increasing the nozzle outlet diameter and slotting time, the optimal slit width is determined to be 0.2 m;
- (5) If the gap between the slits is too close, it affects the stress unloading effect and results in wasted resources. If the gap between the kerfs is too wide, a stress unloading blind spot emerges, which impairs the pressure unloading of the coal seam. When considering all factors, the optimal spacing for hydraulic slits and grooves is determined to be 3 m;
- (6) Through field engineering tests, the optimal spacing of hydraulic cutting is determined to be 3 m, which verifies the results of numerical simulation.

**Author Contributions:** Methodology, investigation, writing—original draft, Z.S. and B.G.; formal analysis, conceptualization, writing—review and editing, Y.L. and Q.Q.; writing—review and editing, J.C. All authors have read and agreed to the published version of the manuscript.

**Funding:** The authors gratefully acknowledge the support provided by the National Natural Science Foundation of China (52204220, 52174188), and the China Coal Technology & Engineering Group Co., Ltd. (2022-QN001, 2023-TD-MS009).

**Institutional Review Board Statement:** Not applicable.

**Informed Consent Statement:** Not applicable.

**Data Availability Statement:** Not applicable.

**Conflicts of Interest:** The authors declare no conflict of interest.

## References

1. Sun, Z.; Liu, Y.; Qi, Q.; Liu, W.; Li, D.; Chai, J. Risk Assessment of Coal Mine Flood Disasters Based on Projection Pursuit Clustering Model. *Sustainability* **2022**, *14*, 11131. [CrossRef]
2. Tang, Y.; Li, P.; Zhu, G. Application of ultra-high pressure hydraulic slotting technology in medium hardness and low permeability coal seam. *Coal Sci. Technol.* **2022**, *50*, 43–49.
3. Jiang, G.; Sun, M.; Fu, J. Research and application of complete set of technology for directional fracturing to increase coal seam permeability and eliminate coal/gas outbursts in underground coal mines. *China Coal* **2009**, *11*, 10–14.
4. Ma, X.; Li, Z.; Tu, H. Technology of deep-hole blasting for magnifying permeability in coal seam with high methane-content and low permeability. *Coalmining Technol.* **2010**, *1*, 92–93.
5. Duan, K.; Feng, Z.; Zhao, Y. Testing study of methane drainage by bore and hydraulic-cutting seam from low permeability coal seam. *J. China Coal Soc.* **2002**, *1*, 50–53.
6. Dong, G.; Lin, F. Experiment of high-pressure water jet reaming to improve pre-pumping effect of through-layer drilling. *Min. Saf. Environ. Prot.* **2001**, *3*, 17–18.

7. Gong, M.; Liu, W.; Wang, D.; Wu, H.; Qiu, D. Controlled blasting technique to improve gas pre-drainage effect in a coal mine. *J. Univ. Sci. Technol. Beijing* **2006**, *3*, 223–226.
8. Zhang, C.; Liu, Z.; Wang, B.; Li, L.; Zhu, X. Numerical simulation and test study on mechanical properties evolution of high-pressure water injection coal seam. *Chin. J. Rock Mech. Eng.* **2009**, *28*, 3371–3375.
9. Yu, B. *Technical Manual for Gas Disaster Prevention and Utilization*; China Coal Industry Publishing House: Beijing, China, 2005.
10. Guo, H. Theory and Technology of Underground Coal Mine Gas Drainage Based on Hydraulic Fracturing. Ph.D. Thesis, Henan Polytechnic University, Jiaozuo, China, 2010.
11. Zhang, G. Numerical Simulation of Hydraulic Fracturing in Horizontal Wells. Ph.D. Thesis, University of Science and Technology of China, Hefei, China, 2010.
12. Zarrouk, S.J.; Moore, T.A. Preliminary reservoir model of enhanced coalbed methane (ECBM) in a subbituminous coal seam, Huntly Coalfield, New Zealand. *Int. J. Coal Geol.* **2009**, *77*, 153–161. [CrossRef]
13. Liu, J.; Wang, H.; Yuan, Z.; Fan, X. Experimental Study of Pre-splitting Blasting Enhancing Pre-drainage Rate of Low Permeability Heading Face. *Procedia Eng.* **2011**, *26*, 818–823.
14. Tan, B.; He, J.; Pan, F. Application and analysis of deep hole pre-split blasting in low permeability and high outburst coal seam. *China Saf. Sci. J.* **2011**, *11*, 72–78.
15. Zhou, L.; Li, L.; Xia, B.; Yu, B. Study of fracture pattern and influencing factors of guided hydraulic fracturing with radial slot and well borehole. *J. China Coal Soc.* **2022**, *47*, 1559–1570.
16. Ye, Q.; Li, B.; Lin, B. Technology of high-pressure abrasive hydraulic cutting seam. *Saf. Coal Mines* **2005**, *12*, 13–16.
17. Kou, J.; Zhou, Z. Research on the influence of coal seam hydraulic slitting speed on the slit radius. *Coal Sci. Technol.* **2014**, *2*, 74–76.
18. Chen, L. Integrated technology of dual-power synergistic drilling and cutting coal and rock pressure relief, penetration enhancement and slitting. *Saf. Coal Mines* **2011**, *9*, 30–32.
19. Liu, F.; Huang, Y.; Xu, Q. Influence of advance and retreat high-pressure water jet slits on the effect of pressure relief and permeability enhancement in coal seam. *Saf. Coal Mines* **2014**, *9*, 165–168.
20. Yi, E.; Zhang, Y. Composite hazards prevention with breaking coal seam and roof by super high pressure water jet. *J. China Coal Soc.* **2021**, *46*, 1271–1279.
21. Zhang, Y.; Guo, S. Theoretical model of annular slotting depth for high pressure water jet and its application. *J. China Coal Soc.* **2019**, *44*, 126–132.
22. Zhang, Y.; Huang, Z.; Li, C. Investigation and application of high pressure water jet annularity slotting self pressure release mechanism. *J. China Coal Soc.* **2018**, *43*, 3016–3022.
23. Liu, S.; Ji, H.; Han, D.; Guo, C. Experimental investigation and application on the cutting performance of cutting head for rock cutting assisted with multi-water jets. *Int. J. Adv. Manuf. Technol.* **2018**, *94*, 2715–2728. [CrossRef]
24. Xiao, S.; Ge, Z.; Lu, Y.; Zhou, Z.; Li, Q. Investigation on Coal Fragmentation by High-Velocity Water Jet in Drilling: Size Distributions and Fractal Characteristics. *Appl. Sci.* **2018**, *8*, 1988. [CrossRef]
25. Zhou, L.; Peng, Y.; Lu, Y.; Xia, B. Numerical simulation of deep CBM hydraulic slotting pressure relief and desorption and permeability enhancement based on the MPM. *J. China Coal Soc.* **2022**, *47*, 3298–3309.
26. Deng, G.; Liu, W.; Li, G. Influence radius of hydraulic slotted hole drainage in low permeability coal seam. *J. Xi'an Univ. Sci. Technol.* **2022**, *42*, 619–628.
27. Jing, F.; Sheng, Q.; Yu, M. The change rule of the geostress and the elastic modulus of rock with depth and their mutual impact. In Proceedings of the 11th China Rock mechanics and Engineering Academic Conference, Wuhan, China; 2010; pp. 69–74.

**Disclaimer/Publisher's Note:** The statements, opinions and data contained in all publications are solely those of the individual author(s) and contributor(s) and not of MDPI and/or the editor(s). MDPI and/or the editor(s) disclaim responsibility for any injury to people or property resulting from any ideas, methods, instructions or products referred to in the content.

## Article

# Research on Hydraulic Thruster-Enhanced Permeability Technology of Soft Coal Drilling through Strata Based on Packer Sealing Method

Zhuangzhuang Yao <sup>1,2,3,\*</sup>, Zhigang Zhang <sup>1,2,3,\*</sup> and Linchao Dai <sup>2,3</sup><sup>1</sup> CCTEG Chinese Institute of Coal Science, Beijing 100013, China<sup>2</sup> State Key Laboratory of the Gas Disaster Detecting, Preventing and Emergency Controlling, Chongqing 400037, China; 20212001047g@ccqu.edu.cn<sup>3</sup> CCTEG Chongqing Research Institute, Chongqing 400037, China

\* Correspondence: 17300238664@163.com (Z.Y.); zzg-2@163.com (Z.Z.); Tel.: +86-02365239102 (Z.Y.)

**Abstract:** According to the characteristics of “Three Soft” outburst coal seams in the Henan area with large gas content, poor air permeability, and extremely difficult extraction, the hydraulic fracturing and punching technology of soft coal with packer tool string sealing method was studied. Xinzheng Coal Electric Power Company is a coal and gas outburst mine, and the second coal seam is a typical soft outburst coal seam. In 14201, upper bottom drainage roadway, which has a broken top plate, a test of penetration hydraulic pressure thrust-enhanced permeability technology based on packer sealing mode was carried out. The average concentration in the press-punching area was 4.8 times that in the non-press-punching area (to be tested), and the average pure volume of 100 holes in the test area was 42 times that in the untested area. During hydraulic pressure punching in the test area, affected by fracturing disturbance, the concentration and purity of the test area and the adjacent test area significantly increased. The test verifies that the large range of fracturing communication cracks at the same time through the interception hole punching plays a synergic permeability and pressure relief effect, providing a new idea and technical support for the hydraulic permeability increase technology in this area.

**Keywords:** “Three Soft” coal seam; cross-bed drilling; hydraulic fracturing; hydraulic punching; straddle double packer; anti-reflection effect

**Citation:** Yao, Z.; Zhang, Z.; Dai, L. Research on Hydraulic Thruster-Enhanced Permeability Technology of Soft Coal Drilling through Strata Based on Packer Sealing Method. *Processes* **2023**, *11*, 1959. <https://doi.org/10.3390/pr11071959>

Academic Editors: Feng Du, Aitao Zhou and Bo Li

Received: 31 May 2023

Revised: 24 June 2023

Accepted: 26 June 2023

Published: 28 June 2023



**Copyright:** © 2023 by the authors. Licensee MDPI, Basel, Switzerland. This article is an open access article distributed under the terms and conditions of the Creative Commons Attribution (CC BY) license (<https://creativecommons.org/licenses/by/4.0/>).

## 1. Introduction

In recent years, with the increase of coal mining depth and strength, the coal seam gas content and control difficulty has increased, the coal and gas outburst problem has become more prominent [1,2]. Among these, soft coal seam gas control is particularly difficult due to the low permeability of soft coal seam, poor damage resistance, and other factors, which has been a bottleneck problem restricting the safe and green mining of coal mines. Therefore, it is of great significance to carry out research on soft coal gas control issues for the safe and efficient development of coal mines.

Scholars have carried out extensive research on the gas control of soft and outburst coal seam. The primary structural coal and broken coal, which are less affected by geological processes, are called hard coal, while the crushed coal and mylonitic coal, which are strongly affected by geological processes, are called soft coal [3]. Lei et al. carried out a triaxial seepage test and conducted a triaxial compression seepage test on hard and soft coal samples to compare the gas flow characteristics of hard and soft coal at different stress stages [4]. Xu et al. proposed that the instability of soft coal drilling is mainly affected by the basic mechanical properties of coal; carried out the research on the mechanism and law of the instability of soft coal drilling; analyzed the influence of factors such as the stress environment around drilling, pore pressure, and drilling method; and pointed out

that increasing the mechanical strength of surrounding rock and reducing the scope of plastic zone and the radial displacement of drilling are the key to improve the stability and porosity of drilling [5]. Zhao et al. tested and analyzed the mechanical properties of different coal rock types and found that soft coal and hard coal not only have significant differences in strength, but also have very different stress–strain curves [6].

Aiming at the problem of gas control in soft coal seams, scholars at home and abroad have carried out a lot of research, and a series of anti-reflection enhanced gas extraction technology of coal seams has been formed, mainly hydraulic fracturing and hydraulic punching. In the research of anti-reflection increasing permeability of coal seams technology of hydraulic fracturing, Lv et al. introduced a new method of soft coal gas drainage to improve the effect of soft coal gas drainage, according to the occurrence characteristics of coal seams, calculated the starting pressure required for fracking of coal seams, and optimized fracking parameters. Using the method of field test, the gas drainage enhancement test of fracturing permeability was carried out, and the gas extraction effect and migration mechanism were analyzed and studied [7,8]. Sun et al. carried out field tests on the anti-permeability technology of hydraulic fracturing in the low-permeability outburst coal seam and found that the gas flow rate of the borehole increased by more than 127.6 times before and after fracturing [9]. Ma et al. established an artificial fracture network in coal seam based on hydraulic fracturing technology and proposed a new method of gas extraction in soft coal seam to increase production [10]. Based on common hydraulic fracturing, Zhai et al. proposed the pressure relief and permeability improvement technology of pulsating hydraulic fracturing, which improved the concentration and flow of borehole gas extraction in low permeability coal seam [11]. Combined with the existing hydraulic reflection improvement technology, Li et al. put forward a new method of soft coal mining along the soft sub-layer by using directional drilling rig and hydraulic jet, effectively reducing the risk of coal and gas outburst [12]. Based on the theory of gas flow and coal body deformation, Zhang et al. found that the gas pressure in cracks of soft coal seam decreases under high pressure abrasive water jet reflection improvement, and the extraction volume is three times higher than that of conventional drilling [13]. The key to the success of hydraulic fracturing lies in the accuracy and reliability of sealing holes. Traditional downhole hydraulic fracturing is mostly cement mortar sealing; cement mortar grouting hole sealing mainly has the following problems: first, it is difficult to control the water cement ratio of cement mortar grouting, if the cement precipitation is large, it is difficult to ensure that the sealing layer reaches the preset position requirements, the hole sealing is not in place, resulting in ineffective fracturing. Second, it is difficult to master the viscosity of cement mortar. If it is too thick when the slurry is regrouting from the fracturing screen, it is easy to cause fracturing pipe plugging and make water injection not smooth. Ge et al. developed a new type of hydraulic fracturing sealing material composed of cement, early strength water reducer, polypropylene fiber, etc., aiming at the problems of easy shrinkage, poor sealing effect, and high cost of sealing material for hydraulic fracturing drilling in coal mines. Through laboratory experiments, the ratio of sealing materials and the sealing parameters of fracturing boreholes were optimized when the shrinkage and compressive strength were optimal. The calculation relationship between the bearing capacity of new materials and the sealing length was established and verified on site [14].

In view of the existing problems of the sealing method, scholars studied the sealing method based on the packer sealing method. Wen et al. carried out the design and test of coalbed methane near-horizontal hole bottom hydraulic packer [15]. Qu et al. used a self-inflatable packer to seal holes in coalbed methane wells in Australia, and verified the reliability of packer sealing holes [16]. Zhang et al. improved the packer support method and carried out field tests in Songzao and Yanjing No.1 Mine. The results show that the encapsulation packer is suitable for the sealing of hydraulic fracture holes in an underground coal mine. The sealing quality is reliable, the effect is good, and the recycling can meet the requirements of hydraulic fracturing [17]. It can be seen that the

sealing method of the packer can effectively solve the sealing problem in the anti-reflection technology of coal seam.

In terms of the research on anti-penetration technology of hydraulic punching, Liu et al. studied the anti-outburst mechanism of hydraulic punching technology and found that hydraulic punching technology can effectively eliminate the outburst stress and increase the amount of gas release in coal seam [18]. Chen et al. carried out a directional hydraulic punching test of structural soft coal seam and found that when the diameter of punching coal was 3–4 m, the vertical stress of the main coal seam was relieved to the maximum, and the gas extraction efficiency was significantly improved [19]. Ren et al. studied the influence of hydraulic punching coal rate on pressure relief and permeability improvement and gas extraction efficiency of low permeability coal seam and found that the coal punching rate was positively correlated with the gas pre-extraction effect of coal seam [20]. In order to study the morphological characteristics of hydraulic punching holes in soft coal, Ma et al. established gravity and friction force of granular coal rock in accordance with hydraulic punching by referring to the Bergmark–Roos equation in ore drawing theory, and deduced the characteristic equation of hydraulic punching holes [21]. Feng et al. studied the hydraulic punching pressure relief and permeability improvement mechanism of three soft single coal seams and carried out field tests [22]. Zhang et al. proposed a new type of non-continuous hydraulic punching technology for bedding drilling and applied it to coal mines containing soft coal seams, and found that the new fissure caused by hydraulic punching can increase the permeability of coal by 2–3 orders of magnitude [23]. Based on the stress-unloading and anti-permeability principle, Zhang et al. proposed cavity building as the key technology of hydraulic punching, studied the highly integrated hydraulic punching roadway forming equipment, and carried out cavity building application in a coal seam with soft and low permeability structure [24]. It can be found that hydraulic fracturing and hydraulic punching coal seam pressure relief and permeability improvement technology can effectively improve gas extraction efficiency, and are widely used in coal mines with high gas and low permeability conditions. However, there are still some deficiencies in the above two coal seam permeability improvement measures. Among them, the hydraulic fracturing technology has different degrees of closure after fracturing; especially in the low permeability coal seam, it is difficult to achieve the ideal water pressure for effectiveness. The holes formed by hydraulic punching technology are not controllable, and there are problems, such as large coal output, uneven pressure relief, stress concentration, gas accumulation, and so on [25–28]. The research shows that the single anti-reflection technology is limited by its own test conditions, so it is difficult to completely eliminate the coal and gas outburst problem and it cannot meet the safety production requirements of coal mine [29–31].

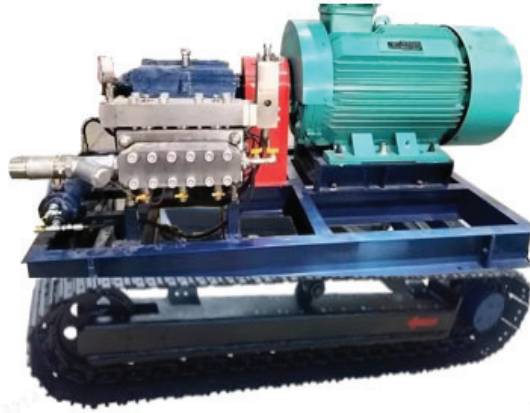
According to the research status of hydraulic fracturing and hydraulic punching, seepage, and pressure relief technology for soft coal seam carried out by domestic and foreign scholars, the organic combination of the two technologies is rarely reported. Therefore, it is urgent to explore a collaborative anti-reflection gas extraction technology that organically combines a variety of adaptive technologies for coal seams with complex conditions of high gas and low permeability. Therefore, through the research of soft coal hydraulic fracturing and hydraulic punching collaborative anti-reflection pressure relief technology, the authors put forward a soft coal hydraulic fracturing–punching permeability increase technology based on packer sealing mode. The pumping system injects high pressure water into the coal seam to carry out fracturing and anti-reflection communication. After the crack reaches the surrounding pressure relief intercepting hole, with the continuous pressure of high-pressure water, it enters the hydraulic pressure punching stage, and the high-pressure water carries the coal slime out from the surrounding intercepting hole to realize further pressure relief, capacity, and anti-reflection effect. This study has a practical demonstration and guiding significance for efficient gas management under similar conditions.



## 2. Permeability Improvement Equipment for Hydraulic Fracturing and Punching

### 2.1. Layer Penetration Hydraulic Measures Power Pump Group

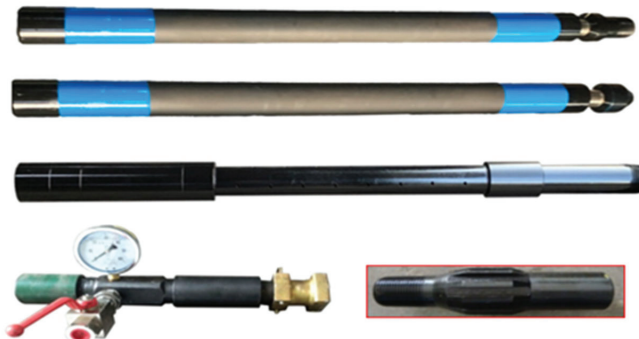
The underground hydraulic fracturing equipment along the coal seam mainly includes fracturing pump set, fracturing packer hole sealing tool string, monitoring and security system, etc. The hydraulic measure power source pump group is shown in Figure 1.



**Figure 1.** Hydraulic measure power pump group.

### 2.2. Research on Packer Tool String Sealing Technology

The composition of fracturing hole sealing tool string, including lead shoe, packer, screen, sealing drill pipe, centralizer, and hole pressure retaining device, is shown in Figure 2. The packer can withstand a high pressure of 70 MPa, and has the characteristics of large expansion coefficient, reliable sealing, and reusable.



**Figure 2.** The actual picture of the expansion stage fracturing tool string.

A simulation study was carried out on the length of the packer rubber bucket, and the force on the rubber bucket was calculated when the rubber bucket was 600 mm, 700 mm, 800 mm, and 900 mm. It was found that the maximum force was on the shoulder of the rubber bucket, and the shear resistance of the packer rubber bucket was the strongest when the size of the rubber bucket was 800 mm. See Figures 3–6 for the optimal design length.

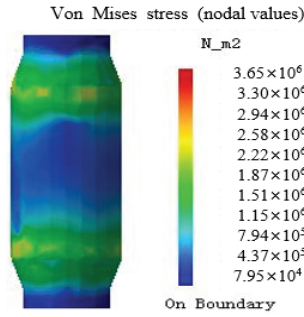


Figure 3. Stress cloud diagram of 600 mm rubber barrel.

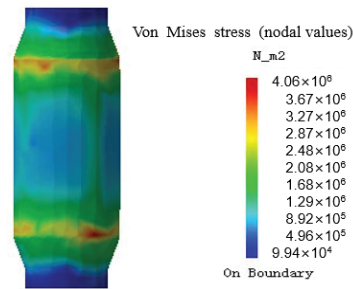


Figure 4. Stress cloud diagram of 700 mm rubber barrel.

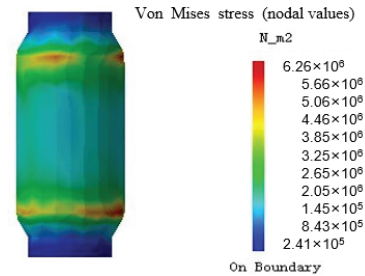


Figure 5. Stress cloud diagram of 800 mm rubber barrel.

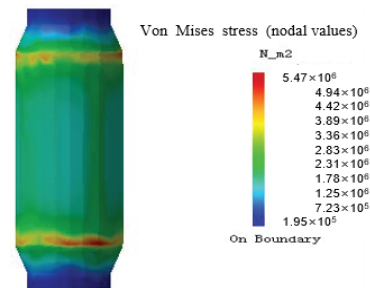


Figure 6. Stress cloud diagram of 900 mm rubber barrel.

The packer hole sealing reliability experiment was carried out. The double packers were put into the sleeve and pressed between the two packers. When the pressure was 30 MPa and 60 MPa, respectively, the packer moved 2 cm and 5 cm (marked by red and

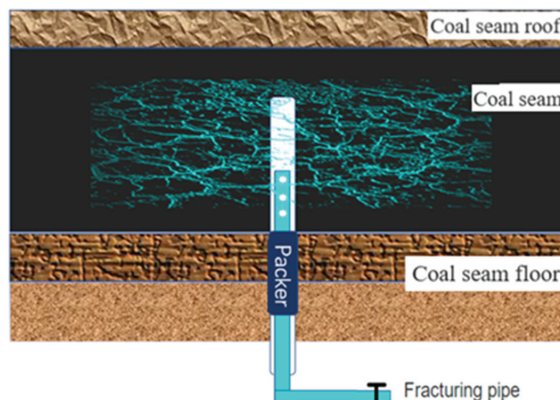
blue chalk in the lower left figure), which verified the reliability of the packer setting. After being pressed, the shoulder wear of the packer was observed to be large. The numerical simulation results are in line with those shown in Figure 7.



**Figure 7.** Reliability test of inflatable fracturing packer.

### 2.3. Sealing Process of Hydraulic Fracturing Packer through Zone Drilling

(1) A single packer was used to lower the packer to the coal–rock interface, and the packer was inflated and set by high pressure water. The high-pressure water entered the borehole cavity through the screen tube to fracturing the coal seam. This process has the characteristics of short depth under packer and high construction efficiency. The disadvantage is that the sealing in soft coal is not reliable, the high-pressure water forms one-way thrust on the packer, and the tool string is easily affected by high-pressure water extrusion and external impact. See Figure 8 for the schematic diagram of the process.



**Figure 8.** Schematic diagram of sealing process of inflatable packer through zone drilling.

(2) In view of coal and rock geological conditions such as broken roof, fault distribution and soft structure, the fracturing technology of penetrating double packer is developed, as shown in Figure 9. The cross-type double packer cross-type fracturing tool string is developed to convert the one-way pressure of high-pressure water on the packer in the fractured interval into the internal tension of the packer. While meeting the requirements

of perforating hydraulic fracturing, it also solves the problems of poor packer sealing effect and backwash of packer tool string in the hole.

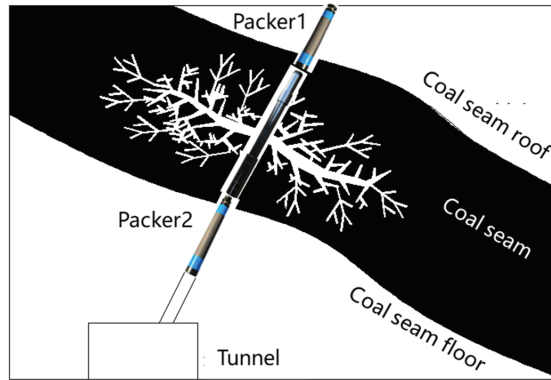


Figure 9. Schematic diagram of double packer sealing process in perforating zone drilling.

During the fault, the thickness of the coal seam on the weak surface of coal rock changes greatly, the fracture direction is uncontrollable in areas such as igneous rock intrusion, and the fracturing fluid leaks easily, the double packer sealing process can realize the advantages of avoiding structure and precise fracturing.

The coal seam with fault structure can be hydraulically fractured with double packers. There is a frac zone between the two packers. The length of the frac zone can be adjusted by the number of pipe seals between the two packers. The frac tool string is shown in Figure 10. According to the drilling data, the structure position can be predicted, and the tool string of the double packer can be lowered to the preset position at the bottom of the hole to fracturing stage by stage from the inside out. Field tests have verified that the process of lowering, setting, unsealing, and driving the packer tool string is stable and reliable. See Figure 11.



Figure 10. Physical connection diagram of double packer fracturing tool string.

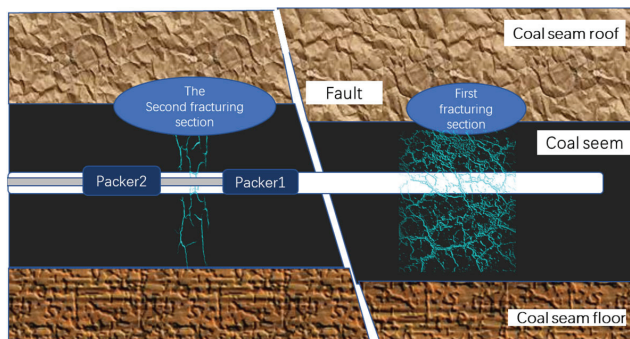


Figure 11. Dual packer to avoid the structural stage fracturing.

### 3. Field Test of Fracturing Punching in Bottom Pumping Lane 14201

#### 3.1. Site Selection of Hydraulic Pressure and Flushing Combined Permeability Test

- (a) In Henan province, gas extraction by floor roadway has been adopted as a regional measure, and hydraulic fracturing by drilling through floor roadway or hydraulic punching has been adopted to increase permeability and relieve pressure [32–36]. Yuan et al. aimed at the gas treatment problem in the strip pre-pumping area of low permeability and high permeability coal seam, applied the theory of elasticity, and combined with the characteristics of high-pressure hydrodynamics, proposed the anti-outburst technology of strip hydraulic fracturing of coal seam drilling through the layer, established the calculation model of target coal seam cracking pressure, and integrated supporting complete sets of downhole fracturing equipment [37]. Yu et al. carried out a study on the application of enhanced gas extraction and anti-outburst technology through strata drilling hydraulic fracturing [38]. Zhang et al. aimed at the anti-outburst technology of pre-pumping coal roadway gas strip area in single coal seam floor roadway through drilling [39].
- (b) At present, hydraulic fracturing is widely used in coal mines in the floor roadway penetration drilling; in penetration drilling fracturing for low permeability prominent coal seam, the anti-outburst effect is obvious, there is flexible drilling hole distribution, convenient drilling rig construction, and other advantages. However, there are also drawbacks such as large drilling quantities, intensive construction, and long pumping cycle. Therefore, it is of great practical significance to use hydraulic measures to strengthen gas extraction and realize permeability improvement of coal reservoir.
- (c) In this paper, with the use of fracturing and punching collaboratively, the pumping system will be high-pressure water into the coal seam to carry out fracturing anti-reflection communication coal seam, crack to the surrounding pressure relief intercepting hole, with the continuous pressure water into the hydraulic pressure punching stage, high-pressure water carrying coal slime from the surrounding intercepting hole discharge, to achieve further pressure relief and increase the permeability effect.
- (d) The Xinzheng Coal and Electricity Company is a coal and gas outburst mine, which is located in Xinzheng, Henan Province. The second coal seam is an outburst coal seam. The occurrence of gas in the second coal seam is high in the west and low in the east. With the increase of mining depth and the replacement of 14 mining areas, gas pressure and gas content increase, making it difficult to control gas during mining.
- (e) The Xinzheng Coal and Electricity Company is a coal and gas outburst mine, and the gas occurrence in the second coal seam of the mine field is high in the west and low in the east, which has the characteristics of soft top, soft bottom, and soft coal seam. The maximum gas pressure of coal seam is 0.45 MPa, the maximum gas content is 18.11 m<sup>3</sup>/t (located in the 14 mining area), the permeability coefficient of coal seam is 0.00092–0.178 m<sup>2</sup>/(MPa<sup>2</sup>·d). The firmness coefficient *f* of coal tested in the laboratory is 0.09–0.28, and the initial gas release velocity Δ*P* is 15.7–22.
- (f) The author selected the bottom pumping roadway on the 14201 working surface of Xinzheng Coal and Electricity as the test site, and used the bottom roadway to drill through the layer and rationally arranged the spacing of pressure crack hole and pressure relief intercepting hole to realize the combination of fracturing and punching two hydraulic measures to increase permeability and strengthen gas extraction. This demonstration project has an important reference significance for the permeability improvement of coal reservoir under similar coal seam conditions.

#### 3.2. Implementation Plan of Perforating Hydraulic Fracturing and Punching

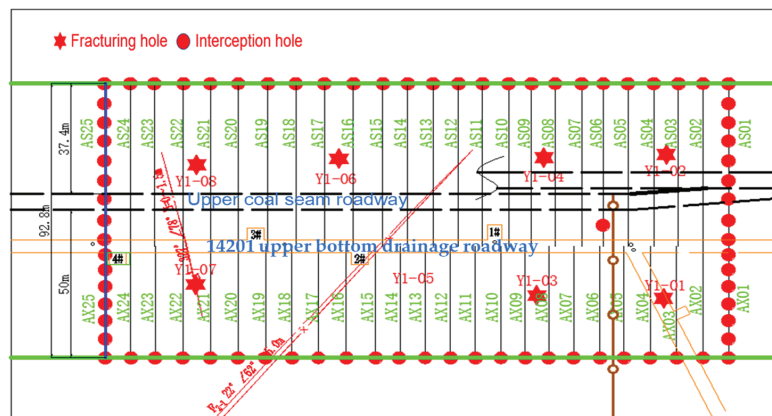
##### 3.2.1. Fracturing and Interception Hole Layout in the Test Area

In the sequence of drilling layout, pressure relief and interception drilling holes should be arranged at the boundary of the control area before the construction of pressure crack holes, so as to control the control range of hydraulic fracturing and effectively prevent

the late gas backflow caused by fracturing displacement. In the fracturing process, when the high-pressure water reaches the initiation pressure of coal seam, the fracture network begins to extend. With the fracture extension and gas driven away, the stress balance state of the original coal body and surrounding rock in the water injection area is broken, the stress is redistributed, and the stress concentration appears in a certain range of the coal body after fracturing. By optimizing the drilling layout and fracturing construction sequence, the effective penetration of the fracture network in the fracturing area and the control of the pressure relief space can be realized, so as to avoid the influence of stress concentration in the process of fracturing coal seam on the late mining work.

Intercepting boreholes are arranged at the strike and dip boundary of the control area of the test area, and the spacing between the intercepting boreholes and the adjacent fracturing holes is 20–30 m. The spacing of intercepting boreholes is 8–16 m. There are 78 intercepting boreholes designed and constructed 189 m in front of 14201 working surface upper and lower roadway pumping strip area.

One group of fracturing boreholes shall be arranged every 40–60 m along the strike of the coal roadway strip area of the upper roadway, and two fracturing boreholes shall be arranged at a distance of 20–30 m from both sides of the strip and a hole spacing of about 40 m. Eight fracturing boreholes are arranged in the upper roadway strip test area. The design of fracturing and intercepting boreholes in the test area is shown in Figure 12.



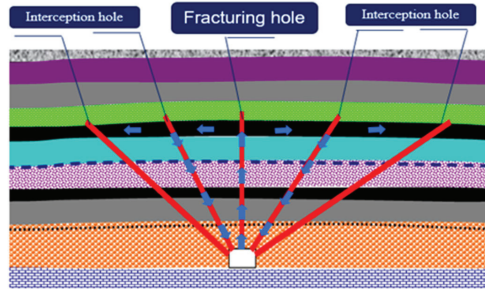
**Figure 12.** Fracturing drilling design plan of 14201 working surface strip upper roadway test area.

### 3.2.2. Through Fracturing–Punching Enhanced Permeability Technology in the Test Area

Hydraulic fracturing destroys coal body by water pressure and forms a fissure network. It is widely used in increasing the permeability of coal seam, but the fracturing effect is also different. Especially in soft coal, to carry out fracturing, due to low firmness coefficient, plastic characteristics, and low strength, permeability is lower than hard coal, as well as crack development and connectivity; these characteristics determine that soft coal in hydraulic fracturing increases permeability. It is difficult to form a high permeability of the main crack, based on the elastic characteristics of the coal reservoir applied to hard coal seam which has good applicability. Soft coal is mainly characterized by plastic deformation, and its crack initiation and permeability increase rules have obvious differences, so it is difficult to guarantee the effect of hydraulic fracturing solely for soft coal conditions.

In this test, the coal seam is injected with water through the fracturing hole, and the fracturing is carried out in the area between the fracturing hole and the coal unloading hole. When the fracture penetrates to the coal unloading hole, the coal and gas will be emitted from the coal unloading hole and enter the tee of the coal unloading hole, the gas will be pumped into the low negative pressure drainage system, and the coal slime is stored in the coal storage tank, thus forming a “U”-shaped channel between the fracturing hole and

the coal unloading hole. The flushing coal unloading at the coal unloading hole is realized by injecting water into the fracturing hole. When the designed coal unloading volume is reached, the gate valve at the coal unloading hole orifice is closed. After the pressure is suppressed, the high-pressure water is driven to other coal unloading holes. After the connection, the flushing coal unloading is continued until the coal unloading holes near the fracturing hole are completed. The soft coal layer multi drill hole through fracturing flushing method can effectively achieve both large-scale permeability increase through fracturing and linkage permeability increase and pressure relief through flushing of coal unloading hole. The process diagram is shown in Figure 13.

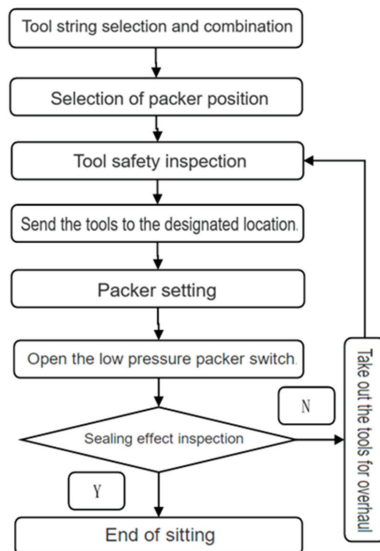


**Figure 13.** Schematic diagram of fracturing flushing permeability enhancement of fracturing holes and intercepting holes.

### 3.2.3. Hole Sealing Scheme of Crack Pressure and Interception Hole in the Test Area

#### (1) Pressure hole sealing process scheme

Packer down: This time, the packer quick hole sealing tool string was used to seal the fracture stage with double packers. The simple tool combination is conducive to reducing the hole accidents. The packer is dilated using high-pressure water to drive the packer to swell and seal the capsule in full contact with the hole wall. The packer is suitable for open hole setting and is relieved using pressure relief. The specific process of tool string lowering is shown in Figure 14.



**Figure 14.** Packer running and setting hole sealing flow chart.

## (2) Interception hole sealing process plan

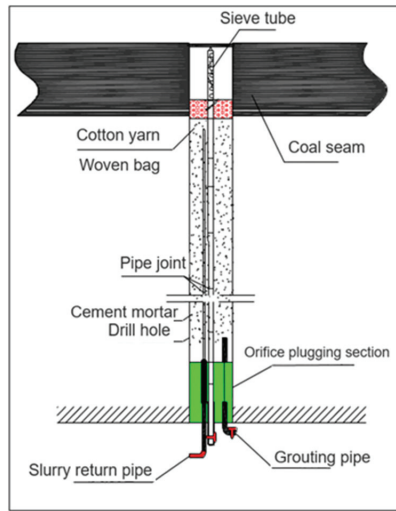
Intercepting drilling adopts the “one block and two injection flexible sealing” mode in the whole rock hole section. The coal seam section is drilled with screen pipe, and the remaining part is sealed with solid pipe. A seamless steel pipe with a wall thickness of 4 mm is adopted.

The specific hole sealing process is as follows:

- (a) Lower the screen pipe and water injection steel pipe. The screen with the plug is placed in front of the fracturing steel pipe and lowered more than 2/3 of the depth of the coal hole. Ensure a high-pressure seal between the fractured pipe and between the screens.
- (b) Fix the cotton yarn and woven bag on the fractured steel pipe at the lower end of the screen tube (specification: 45# steel, 25 mm) for flexible sealing. The cotton yarn and woven bag are lowered to 1–2 m above the coal–rock junction of the coal seam floor, and the bunched regrouting pipe is lowered at the same time. The regrouting pipe (4 decimeter tube) exceeds the coal seam floor by 0.5–1 m, and a 6 m long grouting pipe (4 decimeter tube) is lowered to the orifice. After the pipe is placed, the sealing bag at the external hole is placed at 0.5 m away from the hole.
- (c) Grouting hole sealing. The hole sealing material shall be the hole sealing cement with the mark of 425 or above and the “U”-type expansion agent, which shall be proportioned as 1:1 (or the finished grouting material that has been proportioned) and mixed evenly. After the pipeline is placed, the slurry pump is used to continuously inject the cement slurry into the borehole through the grouting pipe at one time, and the orifice valve of the slurry return pipe is opened. When it is estimated that the injected cement slurry will soon reach the position of the sieve tube, technicians or senior skilled workers should observe and measure whether there is cement slurry reflux at the mouth of the slurry return tube. If the slurry return is successful, immediately turn off the power supply of the grouting pump, and the grouting of this hole is completed. After that, immediately close the ball valve of the grouting pipe, dismantle the high-pressure grouting pipe, connect the rubber pipe used for grouting to the return pipe, open the orifice valve of the return pipe, flush the cement slurry in the return pipe and the fracturing steel pipe with clean water, stop the pump after cleaning for 5–10 min, dismantle the rubber pipe used for grouting, and keep the orifice valve of the return pipe open. After the cement slurry is solidified for 16 h, inject the cement slurry into the fracturing hole through the slurry return pipe. After the slurry return of the seamless steel pipe, stop injecting the cement slurry, close the orifice valve of the slurry return pipe, and complete the interception and borehole sealing. After the completion of borehole sealing, observe whether there is gas at the orifice of the fracturing pipe to judge and ensure that the intercepting hole is unobstructed. See Figure 15 for the schematic diagram of hole sealing.

The effective range of fracturing and the end of fracturing are determined by examining the water discharge of the fracturing hole on both sides of the fracturing hole. In order to ensure fracturing safety, the spacing between pressure holes in the test area should be designed at the maximum 20 m, and water from the holes on both sides of the pressure hole should be investigated to ensure that the effective fracturing radius reaches 10 m. Drag-type subsection fracturing to each drag to a fracturing drilling section must ensure that the water is out of the inspection hole, to ensure the effectiveness of fracturing in different drilling sections.





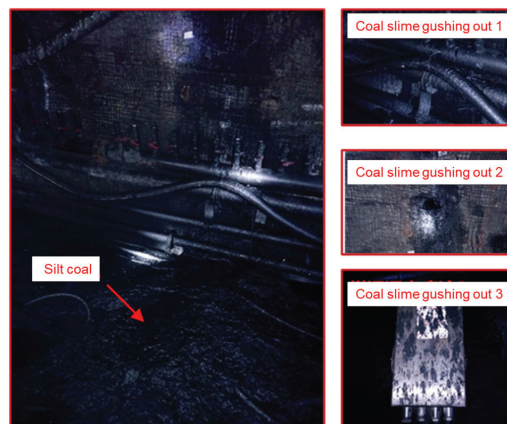
**Figure 15.** Intercepting hole block two injection flexible sealing process diagram.

#### 4. Analysis of Fracturing Effect

##### 4.1. Fracturing Test Results

The preparation for fracturing equipment commissioning in the upper roadway test area of 14201 working face was completed on 15 September 2021. The fracturing start time was 8:00 on 17 September, and the fracturing end time was 8:00 on 30 September. The construction period was 12 days. Before each fracturing, it was checked whether the fracturing hole and the interceptor hole were abnormal. The camera was aimed at the fracturing hole and the nearest interceptor hole, and fracturing started after warning and inspection.

The video monitor verifies that a large amount of slime is ejected from the intercepting hole, indicating that the hydraulic fracture extends from the fracturing hole to the pressure relief intercepting hole. After the black water and slime are discharged from the intercepting hole near the fracturing hole, the orifice valve of the intercepting hole was closed, so that the high-pressure water-induced crack continued to expand in the direction of other intercepting holes. See Figure 16 for the coal slurry emission from the intercepting hole.



**Figure 16.** Site picture of coal slime gushing from interception hole punching.

The total injection water of the eight pressure holes is up to 1037 m<sup>3</sup>. The arrow points to the position of coal water from the interception hole punching, and the oval marks represent the measured orifice gas concentration after fracturing, as shown in Figure 17.

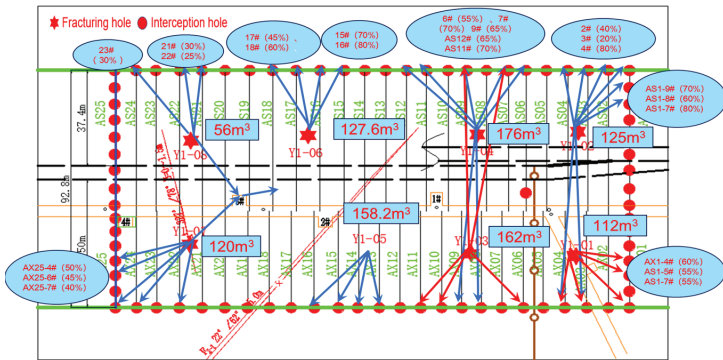


Figure 17. Water discharge from interceptor holes and gas concentration at orifice.

#### 4.2. Comparison of Extraction Effect between Test Area and Non-Test Area

After fracturing and punching measures were carried out in the test area, extraction holes were constructed, and single-hole extraction data (measured by YZC5 of Chongqing Institute) of three groups (6 groups, 9 groups, 13 groups) were analyzed. Group 6: the average single hole concentration was 23.3%, and the daily net volume of single hole pumping was 38.5 m<sup>3</sup>; Group 9: the average single hole concentration was 33.7%, and the daily net volume of single hole pumping was 41.9 m<sup>3</sup>; Group 13: the average single hole concentration was 14.6%, and the daily net volume of single hole pumping was 20.6 m<sup>3</sup>. From the analysis of the relative position with the pressure hole, the gas concentration and daily extraction volume of the single hole in Group 9 were obviously higher near the 3# and 4# pressure hole, and it was preliminary judged that the closer the gas concentration is to the pressure hole, the better the permeability enhancement effect is. The position of Group 6 was between the Group 1–2 pressure hole and the Group 3–4 pressure hole, and the permeability enhancement effect was worse than that in Group 9, and the gas content in the extraction hole area of Group 13 was smaller than that in the outer section. Moreover, it had structural influence, and the drainage effect was not as good as that of Group 6 and Group 9, as shown in Figure 18.

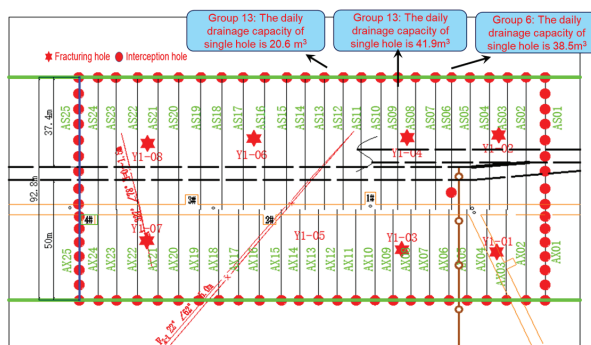
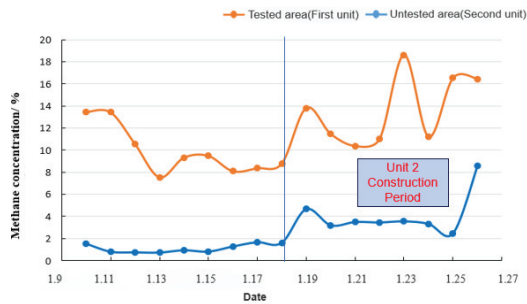


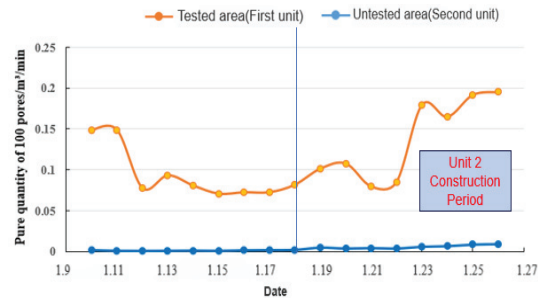
Figure 18. Relative positions of the three groups of extraction holes in the test area.

The test area was the first extraction unit, with the maximum gas content of 8.89 m<sup>3</sup>/t, which was fractured and punched. The second extraction unit was the area to be fractured.

The strike and dip boundaries of the strip control area were equipped with intercepting boreholes, and the spacing between the intercepting boreholes and the adjacent pressure holes was 20–30 m. The interception hole spacing was 8–16 m, and the maximum gas content was  $8.09 \text{ m}^3/\text{t}$ . The data of orifice pumping in the two units from 10 January to 26 January 2022 were calculated. The average concentration of boreholes in the first extraction unit was 4.8 times that of the second extraction unit, as shown in Figure 19. The average 100-hole pure volume in the fractured area was 42 times that in the unfractured area. See Figure 20. The fracturing of the second unit started on 17 January 2022. As can be seen from Figures 19 and 20, the concentration and purity of the two extraction units increased significantly during the second unit fracturing due to fracturing disturbances.



**Figure 19.** Concentration comparison curve between fracturing flushing area and untested area.



**Figure 20.** The 100-hole purity comparison curve between fractured area and unfractured area.

## 5. Conclusions

(1) Research was carried out on the perforating drilling hydraulic fracturing packer sealing process. The reliability of packer sealing was verified through ground experiments and numerical analog verification. After pressurization, the shoulder wear of the packer was relatively large, which is consistent with the results of numerical simulation. On this basis, the formation penetrating single packer integral fracturing and straddle dual packer integral fracturing and hole sealing processes were adopted, and the lowering, setting, unsealing, dragging, and recovery were smooth, realizing rapid plugging, effectively avoiding faults, and meeting the requirements of precise fracturing.

(2) The research on soft coal hydraulic fracturing flushing and permeability enhancement technology by packer tool string sealing was carried out. The high-pressure water trigger made the straddle front and rear double packers expand and set, sealed the fractured coal seam section, and then carried out fracturing and permeability enhancement. After communicating with the surrounding pressure relief interceptor holes, with the continuous pressure of high-pressure water, it entered the hydraulic pressure flushing stage, and the high-pressure water carried the coal slime discharged from the surrounding interceptor holes to realize further pressure relief, capacity, and permeability enhancement.

The combined high-pressure fracking and punching technology will achieve the dual effect of pressure relief and permeability enhancement within the influence range of the extracted coal seam, thus greatly improving the permeability coefficient of the original coal seam, thereby significantly improving the efficiency of gas extraction, and greatly shortening the time for gas extraction to meet the standard.

(3) The hydraulic pressure flushing test was carried out in the upper and bottom drainage roadway of 14201 working face in Xinzheng Coal and Electricity Company, and the reliability of the process was verified. Compared with the gas drainage effect in the pressure flushing area and the non-pressure flushing area, the average concentration in the test area was 4.8 times that in the test area (without fracturing), and the average 100-hole purity test area was 42 times that in the non-test area. During the hydraulic flushing period in the test area, the pressure crack disturbance has an obvious impact on the concentration and purity of the test area and adjacent test areas. This test verifies that the fracturing plays a synergistic role in increasing permeability and pressure relief by flushing the interceptor hole while connecting the fractures in a large range.

**Author Contributions:** Conceptualization, Z.Y.; methodology, Z.Y., Z.Z. and L.D.; validation, Z.Y., Z.Z. and L.D.; formal analysis, Z.Y.; investigation, L.D.; resources, Z.Y.; data curation, Z.Y. and L.D.; writing—original draft preparation, Z.Y., Z.Z. and L.D.; writing—review and editing, Z.Y., Z.Z. and L.D.; visualization, Z.Y. and L.D.; supervision, Z.Z. and L.D.; project administration, Z.Y., Z.Z. and L.D.; funding acquisition, Z.Y. and L.D. All authors have read and agreed to the published version of the manuscript.

**Funding:** This research was funded by Technological Innovation and Entrepreneurship Fund Special Project of Tiandi Technology Co., Ltd. (No. 2022-2-TD-ZD008), National Natural Science Foundation of China (No. 51874348), Natural Science Foundation of Chongqing (No. CSTB2022NSCQ-MSX1080).

**Institutional Review Board Statement:** The study did not require ethical approval.

**Informed Consent Statement:** Informed consent was obtained from all subjects involved in the study.

**Data Availability Statement:** All data and/or models used in the study appear in the submitted article.

**Conflicts of Interest:** The authors declare no conflict of interest.

## References

1. Wang, C.H.; Cheng, Y.P. Role of coal deformation energy in coal and gas outburst: A review. *Fuel* **2023**, *332*, 126019. [CrossRef]
2. Dai, L.C.; Liu, Y.B.; Cao, J. A study on the energy condition and quantitative analysis of the occurrence of a coal and gas outburst. *Shock. Vib.* **2019**, *2019*, 8651353. [CrossRef]
3. Hou, J.X.; Zhang, Y.G.; Zhang, J.C. Multiple statistical comparison of the micropore structures between the tectonically deformed and undeformed coal particles and cause analysis of the difference. *J. Saf. Environ.* **2018**, *18*, 139–146.
4. Lei, W.J.; Liu, X.F. Gas flowing features of hard and soft coal seams under the 3D compression stress. *J. Saf. Environ.* **2018**, *18*, 156–160.
5. Xu, C.P.; Li, H.; Lu, Y. Research status of borehole instability characteristics and control technology for gas extraction in soft coal seam. *Min. Saf. Environ. Prot.* **2022**, *49*, 131–135.
6. Zhao, Z.G.; Li, C.S.; Ying, C.J. Mechanical characteristics of soft coal, hard coal, mudstone gangue and their significance in gas geology. *Mine Constr. Technol.* **2016**, *37*, 1–4.
7. Lv, Y.C. Application the hydraulic fracturing technology in the high pressure and low permeability mine. *J. Chongqing Univ.* **2010**, *33*, 102–108.
8. Li, B.; Song, Z.M.; Ren, J.G. Gas migration mechanism of hydraulic fracturing on soft coal roof. *J. Liaoning Tech. Univ. Nat. Sci.* **2014**, *33*, 317–320.
9. Sun, B.X.; Wang, Z.F.; Wu, H.R. Hydraulic pressurized cracking and permeability improvement technology applied to gas drainage. *Coal Sci. Technol.* **2010**, *38*, 78–80+119.
10. Ma, Y.K.; Mao, X.Y.; Yang, K.; Liu, J.; Zhao, A.H. Improvement on gas drainage of soft gassy coal seam with underground hydraulic flushing and fracturing: A case study in Huainan. *Arab. J. Geosci.* **2020**, *13*, 178. [CrossRef]
11. Zhai, C.; Li, X.Z.; Li, Q.G. Research and application of coal seam pulse hydraulic fracturing technology. *J. China Coal Soc.* **2011**, *36*, 1996–2001.

12. Li, D.Q.; Chen, Y.B.; Zhang, J.B.; Wang, M.Z. Research and application of pressure relief and permeability improvement in high gas outburst mines by directional drilling and hydraulic jet. *Front. Earth Sci.* **2023**, *10*, 1029429. [CrossRef]
13. Zhang, X.Z.; Wisniewski, P.; Dykas, S.; Zhang, G.J. Permeability enhancement properties of high-pressure abrasive water jet flushing and its application in a soft coal seam. *Front. Energy Res.* **2021**, *9*, 679623. [CrossRef]
14. Ge, Z.L.; Mei, X.D.; Lu, Y.Y.; Cheng, L.; Xia, B.W.; Chen, J.F. Drilling sealed parameters and optimization of a new type sealing material for hydraulic fracturing in underground coalmines. *J. Basic Sci. Eng.* **2014**, *22*, 1128–1139.
15. Wen, G.J.; Wu, X.M.; Wang, S.W.; Liu, Y.L.; Niu, H.L.; Liu, J.; Shao, M.L. Design and experiment of downhole hydraulic packer for coalbed methane subhorizontal drilling. *Coal Geol. Explor.* **2008**, *36*, 73–77.
16. Qu, C.F.; Zhang, Y.Q.; Wang, Z.H. Application of swelling packer in coalbed methane wells in Australia. *Oil Drill. Prod. Technol.* **2014**, *36*, 119–121.
17. Zhang, F.W.; Guo, C.Y.; Zhuo, Z.Q. Research on capsule packer plugging technology of coal mine downhole pressure hole. *Min. Saf. Environ. Prot.* **2012**, *39*, 9–12.
18. Liu, M.J.; Kong, L.A.; Hao, F.C. Application of hydraulic punching technology in severely protruding coal seam. *J. China Coal Soc.* **2005**, *04*, 451–454.
19. Chen, Y.; Li, D.; Wang, S. Study on Mechanism of Pressure Relief and Permeability Enhancement in Soft-hard Composite Coal Seam by Directional Hydraulic Flushing Technology. *Acta Montan. Slovaca* **2022**, *27*, 522–536.
20. Ren, P.L.; Liu, Y.W.; Han, H.K. Study on influence laws of coal flushing rate on coal seam stress relief and gas extraction. *Coal Sci. Technol.* **2022**, *50*, 102–109.
21. Ma, G.; Liu, X.; Li, F. Study on morphology features of hydraulic flushing hole based on ore drawing theory. *Coal Sci. Technol.* **2016**, *44*, 73–77.
22. Feng, W.J.; Su, X.B.; Wang, J.W. The mechanism and field test of permeability improvement by hydraulic flushing in three-soft and single coal seam. *Coal Geol. Explor.* **2015**, *43*, 100–103.
23. Zhang, H.; Cheng, Y.; Deng, C. A novel in-seam borehole discontinuous hydraulic flushing technology in the driving face of soft coal seams: Enhanced gas extraction mechanism and field application. *Rock Mech. Rock Eng.* **2022**, *55*, 885–907. [CrossRef]
24. Zhang, R.; Hao, C. Research on the development of hydraulic flushing caverning technology and equipment for gas extraction in soft and low permeability tectonic coal seams in China. *ACS Omega* **2022**, *7*, 21615–21623. [CrossRef] [PubMed]
25. Liu, X.; Li, Y.; Xuan, D.Q. Numerical simulation and test of Layered water jet gas extraction in soft coal sandwich with pressure relief and permeability improvement. *Coal Geol. Explor.* **2021**, *49*, 54–61.
26. Tang, Y.Z.; Li, P.; Zhu, G.W. Application of ultra-high pressure hydraulic slotting technology in medium hardness and low permeability coal seam. *Coal Sci. Technol.* **2022**, *50*, 43–49.
27. Lin, B.Q.; Li, Z.W.; Zhai, C. Pressure relief and permeability-increasing technology based on high pressure pulsating hydraulic fracturing and its application. *J. Min. Saf. Eng.* **2011**, *28*, 452–455.
28. He, Q.Y.; Zhu, L.; Li, Y.C.; Li, D.Q.; Zhang, B.Y. Simulating hydraulic fracture re-orientation in heterogeneous rocks with an improved discrete element method. *Rock Mech. Rock Eng.* **2021**, *54*, 2859–2879. [CrossRef]
29. Su, X.B.; Song, J.X.; Guo, H.Y. Increasing production mechanism and key technology of gas extraction in coal mines. *Coal Sci. Technol.* **2020**, *48*, 1–30.
30. Qin, J.T.; Chen, Y.T. Research and application of combined antireflection technology of high pressure hydraulic fracturing and punching in low permeability coal seam. *Min. Saf. Environ. Prot.* **2021**, *48*, 53–57.
31. Xu, T.; Feng, W.J.; Su, X.B. Experimental research on enhanced gas extraction application with hydraulic fracturing and flushing. *J. Xi'an Univ. Sci. Technol.* **2015**, *35*, 303–306+312.
32. Jiang, J.H. New method of improving gas releasing rate from weak seepage seam. *Coal* **2000**, *2*, 9–12.
33. Zhang, G.H.; Wei, G.P. Theory of start-split affusion stress and start-split location about through coal delaminations' bore of hydraulic fracture. *J. China Coal Soc.* **2007**, *32*, 52–55.
34. Xu, R. Research and application of hydraulic fracturing technology for strip gas treatment in comb borehole in inclined and soft coal seam. *Coal Technol.* **2021**, *40*, 106–109.
35. Xiao, C.H.; Wang, C.G. Numerical simulation of pressure relief and reflection improvement effect of hydraulic punching in protruding coal seam. *Coal Technol.* **2015**, *34*, 147–149.
36. Hao, F.C.; Sun, L.J.; Liu, M.J. Research on boreholes space optimization of hydraulic flushing considering press relief and gas drainage effect. *J. Min. Saf. Eng.* **2014**, *31*, 756–763.
37. Yuan, Z.G.; Ren, M.Q.; Shen, Y.H. Anti-surge technology and application of hydraulic fracturing in coal roadway with perforated borehole. *J. Chongqing Univ.* **2016**, *39*, 72–78.
38. Yu, T.; Lu, M.; Zhu, G.W. Study on enhanced gas drainage by hydraulic fracture in cross-measure boreholes. *J. Saf. Environ.* **2010**, *10*, 172–175.
39. Zhang, M.J.; Hua, J.J.; Hua, J.T. Outburst prevention technology in gas strip area of single coal seam floor roadway through layer drilling and pre-extraction coal roadway. *Saf. Coal Mines* **2011**, *42*, 30–32.

**Disclaimer/Publisher's Note:** The statements, opinions and data contained in all publications are solely those of the individual author(s) and contributor(s) and not of MDPI and/or the editor(s). MDPI and/or the editor(s) disclaim responsibility for any injury to people or property resulting from any ideas, methods, instructions or products referred to in the content.

Review

# Exploration and Frontier of Coal Spontaneous Combustion Fire Prevention Materials

Dandan Han <sup>1,2</sup>, Guchen Niu <sup>1,\*</sup>, Hongqing Zhu <sup>1</sup>, Tianyao Chang <sup>1</sup>, Bing Liu <sup>1</sup>, Yongbo Ren <sup>1</sup>, Yu Wang <sup>1</sup> and Baolin Song <sup>1</sup>

- <sup>1</sup> School of Emergency Management and Safety Engineering, China University of Mining and Technology (Beijing), Beijing 100083, China; handd.2006@tsinghua.org.cn (D.H.); zhq@cumbt.edu.cn (H.Z.); tzctyzkd@163.com (T.C.); bingliu2024@163.com (B.L.); ryb1092499545@163.com (Y.R.); 18654315930@163.com (Y.W.); sb1922922@163.com (B.S.)
- <sup>2</sup> International Exchange and Cooperation Center, Ministry of Emergency Management, Beijing 100012, China
- \* Correspondence: nnniu188@163.com

**Abstract:** Mine fires have always been one of the disasters that restrict coal mining in China and endanger the life safety of underground workers. The research and development of new fire prevention materials are undoubtedly important to ensure the safe and efficient production of modern mines. At present, the main inhibiting materials used are grout material, inert gas, retarding agent, foam, gel, and so on. In order to explore the current situation of coal spontaneous combustion (CSC) fire prevention, the existing fire prevention materials were reviewed and prospected from three aspects: physical, chemical, and physicochemical inhibition. The results show that, at present, most of the methods of physicochemical inhibition are used to inhibit CSC. Antioxidants have become popular chemical inhibitors in recent years. In terms of physical inhibition, emerging biomass-based green materials, including foams, gels, and gel foams, are used to inhibit CSC. In addition, CSC fire-fighting materials also have shortcomings, including incomplete research on the mechanism of material action, poor stability of inhibitory properties, low efficiency, and economic and environmental protection to be improved. The future research direction of fire-fighting materials will be based on theoretical experiments and numerical simulation to study the mechanism and characteristics of CSC and develop new directional suppression materials with physicochemical synergies. These findings have extremely important implications for improving materials designed to prevent CSC.

**Keywords:** fire-fighting materials; coal spontaneous combustion; synergistic inhibition; research status; visualization

**Citation:** Han, D.; Niu, G.; Zhu, H.; Chang, T.; Liu, B.; Ren, Y.; Wang, Y.; Song, B. Exploration and Frontier of Coal Spontaneous Combustion Fire Prevention Materials. *Processes* **2024**, *12*, 1155. <https://doi.org/10.3390/pr12061155>

Academic Editor: Raymond Cecil Everson

Received: 9 May 2024

Revised: 27 May 2024

Accepted: 31 May 2024

Published: 3 June 2024



**Copyright:** © 2024 by the authors. Licensee MDPI, Basel, Switzerland. This article is an open access article distributed under the terms and conditions of the Creative Commons Attribution (CC BY) license (<https://creativecommons.org/licenses/by/4.0/>).

## 1. Introduction

China's energy structure is characterized by abundant coal resources, which have become the pillar of national economic growth and cannot be ignored to promote rapid economic development [1–3]. However, with the diversity of coal reserves and the complexity of geological structure, coal spontaneous combustion (CSC) is representative of the frequent occurrence of coal mine disasters, which is a serious challenge facing the mining industry [4–6]. Mine fires not only pose direct threats to production safety but also represent one of the primary types of coal mine disasters that lead to substantial economic losses and casualties [7–9]. In recent years, the Chinese government has significantly strengthened its supervision over coal mine safety production and implemented a series of robust measures for comprehensive treatment, resulting in a marked reduction in both frequency and fatality rates associated with such accidents [10]. However, in the face of huge coal production, widely distributed mine networks, coal seams with different mining conditions, and uneven application of safety technology and management effectiveness among regions, CSC still faces serious challenges [11].

Faced with the serious safety hazard of coal mine fire, researchers at home and abroad have made unremitting exploration and successfully developed diversified fire prevention and extinguishing products, including slurry, foam, inert gas, colloid, and chemical retardant [12–15]. These materials are essential in preventing CSC and are integral to ensuring the safety of coal mines. However, despite their significant practical efficacy, certain limitations and deficiencies still persist. In view of this, this paper aims to systematically summarize and deeply evaluate the existing research status of CSC prevention materials, clarify the fire suppression mechanism and inhibition effect of various types of materials, and reveal the problems faced by existing fire prevention materials. This study aims to lay a scientific foundation for the future practice of CSC prevention and control and make targeted recommendations for improvement, with the aim of guiding and optimizing practical operations in this field.

## 2. Visual Analytics

In order to comprehensively review and summarize the research achievements and development trends in the field of CSC prevention and control materials, we used the core database of Web of Science to conduct an in-depth literature search by keywords “mine fire materials” and “coal spontaneous combustion materials”, and collected a total of 867 relevant research literature. This number indicates that a relatively comprehensive and influential academic system has been established in this field. In order to further analyze the internal correlation and evolutionary trajectory among research hotspots within this domain, we utilized CiteSpace, a professional literature knowledge mapping tool, for visualization purposes (refer to Figure 1).

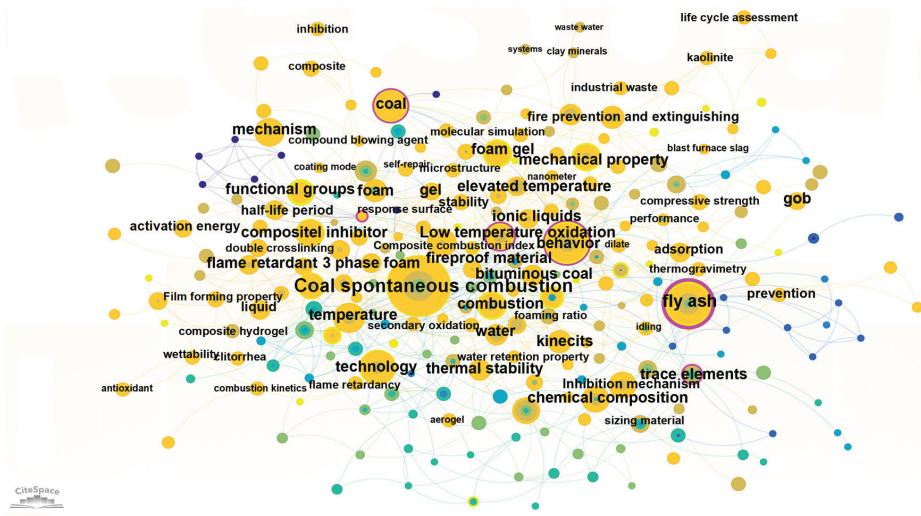


Figure 1. Keyword co-occurrence map.

In this graph, each node represents an individual keyword. The size of the nodes is precisely quantified based on scientometric principles, encompassing occurrence frequency, citation frequency, influence index, and other key indicators for the specified time period or literature collection. Consequently, substantial disparities in node size intuitively disclose the significance and attention attributed to each research topic within the broader academic landscape: larger nodes indicate heightened activity levels, greater influence, or wider scholarly discourse within contemporary research domains. These are considered as focal points of investigation. The color of the node represents the time when the keyword appears, and the darker the color, the earlier the keyword appears.

Figure 1 illustrates a range of prevalent strategies employed for the prevention of CSC. From the color of the keyword nodes, it can be seen that the development of CSC fire-fighting materials has gone through multiple stages, such as grouting, inert gas injection, colloid, inhibitor, foam, and gel foam. In addition, nowadays, researchers mostly use composite materials to synergistically inhibit CSC. When addressing the intricate issue of CSC, researchers tend to employ advanced and efficient fire-prevention measures like colloids, gel foams, and compound retardant agents. As a potential fire prevention medium, it is very important to investigate the basic properties of colloids. Through laboratory testing, scholars have conducted detailed investigations into the fundamental parameters of colloids, such as gelation kinetics, water retention capacity, plugging efficiency, and rheological behavior. These parameters are utilized to evaluate the colloid's ability to infiltrate coal formations, retain moisture content, and seal void spaces. For the inhibition of colloids in the CSC process, thermochemical techniques, including thermogravimetric analysis and temperature programming experiments, will be employed to quantitatively assess the inhibition efficiency of colloids at different temperatures and elucidate their mechanism in suppressing coal oxidation. Foam technology has attracted extensive attention in the field of CSC prevention and control because of its special film-forming properties and excellent durability. It focuses on key indicators, such as the strength and durability of foam film formation (e.g., half-life), with the aim of ensuring that the foam can effectively establish a stable and long-lasting isolation layer on the coal seam surface. This layer serves as a barrier to oxygen diffusion and inhibits coal oxidation and exothermic reactions, thereby enhancing its stability. An ideal foam product should possess outstanding adhesion, expansibility, and anti-evaporation ability while maintaining a long-lasting flame-retardant barrier within complex underground environments. The compound inhibitor synergistically combines diverse components to enhance inhibition efficiency and prolong the duration of inhibitory effects. The purpose of these preparations is to conduct a comprehensive analysis of their chemical inhibition, including determining the effective inhibition time, determining the active site of chemical inhibition, and elucidating the interaction mechanism between chemical inhibitors and coal molecules. It is crucial to elucidate how composite chemical inhibitors can disrupt the oxidation chain process of coal through specific chemical reactions or modify the surface properties of coal to mitigate its oxidation activity. These contents play a decisive role in optimizing formulation design and field application. At present, the research frontier has shifted to the molecular level. For instance, molecular simulation techniques can be employed to elucidate the microscopic interaction mechanism between chemical inhibitors and coal macromolecules and to elucidate how chemical inhibition agents accurately interfere with the thermochemical path of CSC. This theoretical analysis is not only helpful in guiding the design and synthesis of high-performance inhibitors but is also expected to promote the coal spontaneous combustion prevention technology to achieve a new leap of precision and intelligence.

Based on the above overview of the relevant keywords of coal spontaneous combustion anti-fire materials and the elaboration of their respective research focuses, the following will further launch a detailed review of various types of anti-fire materials, in-depth analysis of their working principles, performance characteristics, and practical application effects, in order to fully demonstrate the technical progress and future development direction in this field.

### **3. Current Situation of Fire Prevention Materials**

#### *3.1. Physically Inhibited Material*

##### *3.1.1. Grouting Material*

The grouting method, commonly employed for the prevention of CSC, entails the blending of clay, crushed gangue, fly ash, and other materials with water to generate a highly mobile slurry. This slurry is then injected into the coal seam through dedicated pipes to effectively wrap the outside of the seam and strengthen the integrity of the coal rock by



plugging existing cracks. Because the grouting technology is simple, safe, and reliable, it is widely used in underground coal mining [16,17].

Wang Deming et al. [18] added the thickening additive KDC (a polysaccharide polymer extracted from natural plants, whose molecular structure is mannuronic acid and guluronic acid) to the mortar to form a loose three-dimensional network structure in water. At a low shear rate, the viscosity was 0.33~2.94 Pa·s. The surface viscosity is less than 0.28 Pa·s at high shear rate. At 0.4% aqueous solution concentration, the viscosity is more than 1500 times that of water. The material has a strong suspension capacity and reduces the flow resistance of the material in the pipeline. Wang [19] utilized fly ash as a substitute for loess and mixed it with water to prepare a fly ash grouting material. Considering economic factors, an optimal formulation consisting of 71 g coal ash, 14 g curing activator, 5–6 g hardening accelerator, and 50–55 g water was determined. This material not only retains the advantages of low cost and convenient production associated with traditional grouting materials but also effectively addresses key issues such as poor controllability and stacking difficulties, demonstrating significant improvement and advantages. Xiao Yang [20], combined with the actual situation of coal mines, proposed to use fly ash instead of loess as mine grouting materials and researched a new type of grouting and injection fire prevention materials (thickening suspending agent JXF1930 and gelling agent FCJ12) to realize the in situ resource utilization of fly ash in pithead power stations, and the performance of the materials is shown in Table 1.

**Table 1.** Properties of new materials and applicable conditions [20].

Category	Highly Effective Suspension JXF1930	Compound Colloidal Additives FCJ12
Performance	It is added into the slurry to form a thickening colloid so that the fly ash in the slurry is suspended, and the problem of pipeline blockage in the long-distance transportation of high-concentration slurry is solved	It is added to the slurry to form a complex colloid so that the slurry gels in a certain time and then loses its fluidity
Main role	The slurry containing the JXF1930 suspension agent exhibits excellent water retention, permeability, suspension, and compactness properties. It can be effectively encapsulated within coal for prolonged periods without separation during transportation due to its superior fluidity	The slurry, supplemented with FCJ12 gelling agent, can undergo solidification at the designated location to effectively seal the voids within coal deposits and encapsulate high-temperature coal. Allow its accumulated heat to be fully released to prevent the extinguished fire area from reigniting
Use scales	0.10%	0.06%
Usage	Sprinkle evenly into the slurry in the ground grouting pool according to the proportion used	The ZM-5/1.8G coal mine grouting machine proportionally injects it into the grouting pipeline in the vicinity of the underground grouting site
Applicable place	End mining line, eye cutting, gob area, coal field outcrop, surface coal yard, and other large areas of grouting glue to prevent fire	

However, the grouting fire prevention technology also exhibits certain limitations. Firstly, due to the substantial weight of the slurry itself, it is susceptible to gravitational effects, resulting in instances of slurry flow and bursting that restrict its coverage over the coal seam. Secondly, traditional grouting materials possess inadequate water retention capabilities. After the evaporation of water, the grout on the surface of the coal easily dries and cracks, which may produce new air leakage channels, thus affecting the fire prevention and control effect. Additionally, during water evaporation, the exothermic reaction generated by the coal body may pose a risk of water gas explosion under high-temperature conditions. Lastly, although low-concentration slurries exhibit good fluidity characteristics, their treatment area is limited due to sedimentation caused by high solid material density [21].

### 3.1.2. Gas Material

Inert gas fire prevention technology, as a scientific and effective means of CSC prevention and control, its core principle is to systematically inject inert gases, such as nitrogen and carbon dioxide, which do not easily react with other substances, into those mine areas where there are hidden dangers of spontaneous combustion or signs of spontaneous

combustion have occurred in the early stage [22,23]. The large input of these gases can dilute the oxygen content of the internal environment, effectively reducing the oxygen concentration to a level insufficient to support the continuous oxidation of the coal. In this way, the necessary conditions for maintaining the oxidation reaction chain between coal and oxygen are fundamentally broken, and the potential oxidative heat release process inside coal is inhibited, thus effectively preventing or slowing down the further development of CSC. This technology exhibits exceptional diffusibility, covering the entire fire area rapidly. Moreover, it is non-toxic and non-corrosive, so it plays an important role in the prevention and control of CSC. Since the 1980s, our country initiated the theoretical investigation and practical implementation of N<sub>2</sub> fire prevention and control [24].

Some scholars have conducted numerous theoretical and practical research studies on the suppression of CSC by inert gas. Tang et al. [22] conducted a field test on the compound inert gas of carbon dioxide and N<sub>2</sub> injected into the goaf of a certain working face. The results showed that merely 9 days subsequent to the administration of a composite inert gas, the CO concentration of return air flow decreased significantly from 14.9 ppm to 0.1 ppm, and the CO concentration at the corner of the return air also rapidly decreased from 4821 ppm to 21 ppm. It can significantly reduce the risk of mine fires without endangering the safety of underground workers. Ding [25] conducted an in-depth study on dry air, CO<sub>2</sub>, and N<sub>2</sub> to investigate how the inert gases inhibit the mechanism of CSC. The results showed that the ability of coal to absorb oxygen was drastically weakened by the inert gas injection method, thus greatly hindering the coal–oxygen combination reaction and successfully guarding against the phenomenon of CSC. In controlled experiments, we found that the diffusion activity of oxygen was enhanced by 5.89% when carbon dioxide (CO<sub>2</sub>) was used as an injection gas relative to nitrogen (N<sub>2</sub>), as shown in Figure 2. Therefore, CO<sub>2</sub> was more effective than N<sub>2</sub> in inhibiting CSC. Lei et al. [26] investigated the inhibitory influence of N<sub>2</sub> and CO<sub>2</sub> on CSC under varying flow rates, revealing that both gases effectively suppress CSC; however, CO<sub>2</sub> exhibits superior efficiency due to its ability to not only dilute oxygen but also impede the positive progression of chain reactions, thereby facilitating faster fire control.

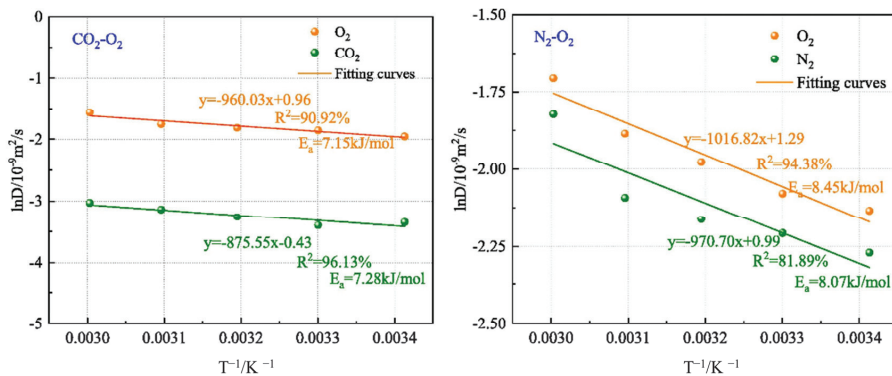


Figure 2. Diffusion activation energy of O<sub>2</sub> in different systems [25].

### 3.1.3. Colloid Material

In colloidal fire-fighting materials, with the help of drilling technology, the colloidal transport to the designated position after gelling, the surface of the coal is covered by colloidal, plays a role in oxygen blocking and cooling [7,27,28]. Colloidal materials used to inhibit coal spontaneous combustion include gels, corrosion retarding gels, aggregate suspension colloids, and inorganic mineral colloids [29].

Domestic and foreign scholars have widely used a variety of characterization methods to achieve the performance evaluation of gel-based fire-proofing materials, including programmed warming, FTIR infrared spectroscopy, TG-DSC simultaneous thermal analysis,

and SEM. The inhibitory effect of gels on CSC was primarily assessed through the analysis of gas yield, characteristic temperature, heat release, and microstructural changes in untreated and gel-treated coal samples [30,31]. The results are shown in Table 2, and the inhibition of CSC is positively influenced by the gel material.

**Table 2.** Inhibition effect of different gels on spontaneous combustion of coal.

Author	Gel System	Effect
Huang et al. [32]	Sodium silicate, sodium bicarbonate, and sodium polyacrylate	The optimal ratio of 4%, 5%, and 0.75% can increase the oxidation temperature rising zone by 8 m, shorten the length by 20 m, and increase the blocking zone by 28 m
Zhao [33]	The swelling gel was prepared with chitosan, sodium carboxymethyl cellulose (CMC), guar gum, and sodium bicarbonate	The optimal formulations were 0.75 wt%, 2.5 wt%, 0.15 wt%, 0.4 wt% and 0.5 wt% acetic acid. The gel viscosity was 5852 mPa·s, the expansion factor was 0.846, and the strength was 319.925 N/m <sup>2</sup> after 6 h of storage. The permeability of loose coal was 93.52%. At 200 °C, the CO <sub>2</sub> content of coal samples with 1 g of gel is 12,829 ppm, and that of coal samples with 5 g of gel is 23,239 ppm, which is 59.15% and 188.29% higher than that of raw coal, respectively
Zhou et al. [34]	CMC, cross-linking agent aluminum citrate (AlCit), and pH regulator δ-gluconate lactone (GDL)	Compared with the raw coal sample, the cross point temperature is increased by 13.9 °C, the activation energy is increased by 16.34%, and the amount of CO gas produced is reduced by 34.5%
Dong et al. [35]	CMC, Zirconium Citrate (ZrCit) and GDL	When the ratio is 2.5 wt%, 20 wt%, 2 wt%, the gel can effectively inhibit the spontaneous combustion of floating coal. When the ratio is 3 wt%, 20 wt%, 2 wt%, the gel is suitable for sealing and extinguishing fire sources
Wei et al. [36]	Polyvinyl alcohol (PVA), Xanthan gum (XG), and acrylic acid (AA)	Solve the problem of poor mechanical properties of gel materials. The contents of PVA, XG, and AA were 1.5 g, 0.1 g, and 6 g, respectively, and the optimum reaction temperature was 55 °C. Under the optimum conditions, the viscosity was 45 mPa·s, and the surface tension was 30 mN/m

### 3.1.4. Foam Material

Foam fire prevention technology, an innovative coal fire prevention and control strategy, has demonstrated excellent effectiveness in preventing and controlling CSC [37–39]. The technology is based on a unique foam generation system that produces large volumes of inert foam with high stability through a precise mix of water, foam agents, and, in some cases, inert gas, which is quickly mixed in a specific facility and treated by a foaming unit. These foams not only have excellent flow and spreading properties, which can quickly cover the coal surface and all corners of the mine, but also their internal structure is rich in tiny gas vesicles, which not only insulate oxygen but also form a thermal barrier. It has the characteristics of high viscosity, large acting area, low density, excellent stacking, and flow performance, and is economical and practical. In practice, inert, three-phase, and gel foams are three common types, which show superior fire prevention and extinguishing effects through different modification methods.

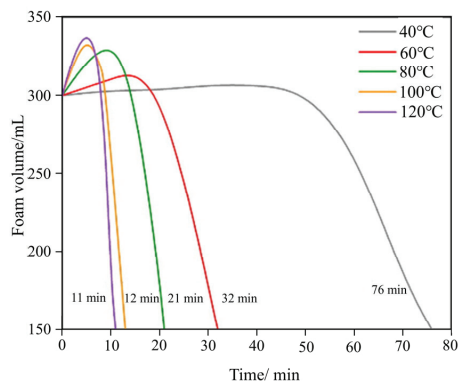
#### Two-Phase Foam

Based on the synergistic mechanism, Li [40] investigated the compound foaming agents ACFA ( $\alpha$ -alkene sulfonate sodium: AOS; fatty alcohol polyoxyethylene ether sulfate: AES; hexadecanoate propyl trimethylammonium chloride: YN2031; xanthan gum: XG) and AFA (AOS, XG), and employed the Foamscan system to quantify foam properties. The results demonstrate that ACFA exhibits a faster foam generation rate at lower concentrations with a decay rate of 66.5%. The CO concentration of raw coal at 100 °C is 2287.9 ppm, which decreases to 974 ppm and 726 ppm after treatment with ACFA and AFA, respectively. A new type of foam was proposed by Tang et al. [41], which has high expansibility and good stability. The optimal proportions of sodium dodecyl benzene sulfonate (SDBS), MgCl<sub>2</sub>, and guar gum were 2%, 1%, and 0.5%, respectively. In evaluating flame retardant performance, an in-depth analysis is conducted from three key dimensions: functionality, free radical control, and fire protection characteristics. This two-phase system offers advantages such as large foam volume and good fluidity when injected with inert gas for diluting gas concentration and reducing goaf heat in underground mines. However, a two-phase bubble also has some disadvantages, such as fast water erosion and bubble liquid membrane

stability and inert gas, which is vulnerable, especially when addressing hidden dangers related to spontaneous combustion in high areas or deep goaves where its efficacy is limited.

### Three-Phase Foam

The concept was first introduced by China University of Mining and Technology [42]. Based on the concept of two-phase foam, solid substances such as fly ash or yellow mud are added to form a solid–liquid–gas three-phase system [43]. The three-phase foam exhibits the characteristics of encapsulation, heat absorption, and dissipation, as well as oxygen isolation, thereby enhancing its effectiveness in suppressing mine fires [44,45]. Zhu et al. [46] selected two anionic foaming agents: sodium dodecyl sulfate (SDS) and SDBS; one cationic foaming agent: cetyltrimethylammonium bromide (CTAB); and two non-ionic foaming agents: lauryl glucoside (APG1214) and coconut oil glucoside (APG0814) to carry out the compounding of the three types of foaming agents. The experimental results show that the foaming properties of anionic, cationic, and non-ionic foaming agents can be optimized when the three foaming agents are formulated according to a specific ratio of 2:1:1. The optimal combination of compound foaming agents was SDBS, CTAB, and APG0814 with a maximum foaming volume reaching 2700 mL. This value was 3.8% higher than the SDBS, CTAB, and APG1214 combination and 10.2% higher than SDS, CTAB, and APG0814 combination; moreover, it exceeded SDS, CTAB, and APG1214 by 12.5%. Wang [47] employed sodium soil as a dispersing agent, whereby the mass fraction of AOS was 0.5%. Sodium soil accounted for 33.3% of the solid particle mass, while the mass fraction of solid particles was 5.0%. A foaming volume of 275 mL and an analyte half-life of 72 min indicate that the three-phase foam under these conditions exhibits excellent foaming and stability. Through an in-depth investigation into its stability mechanism, it was discovered that the addition of sodium soil effectively enhanced particle suspension dispersion and prevented aggregation and sedimentation. Furthermore, incorporating solid particles augmented foam viscoelasticity. The synergistic effect of these two results in a significant increase in stability. Zhang [48] designed a new fire-extinguishing material (SMTP-20) by combining sea mud particles containing inert substances with three-phase foam. SMTP-20, characterized as a thin and tough foam, effectively seals cracks in coal to prevent oxygen ingress, exhibiting 2.19 times higher stability compared to traditional three-phase foams (Figure 3). When conducting dimensional experiments, it was observed that the internal temperature of the coal dropped sharply, reaching a rate of 117 °C/min and rapidly dropping below 100 °C, which demonstrated excellent fire prevention and cooling efficiency. However, it is worth noting that in three-phase foam, a large number of gathered solid particles produce a large extrusion stress on the foam liquid film when flowing, which not only affects the structural stability of the foam but also weakens its ability to seal cracks and prevent air infiltration [49].



**Figure 3.** Volume trend of SMTP-20 at different temperatures [48].

### Gel Foam

Gel foam technology cleverly combines the lightweight, porous nature of the foam with the highly absorbent expansion capacity of the gel. That is, in the process of forming the foam, the cross-linking agent is cross-linked with the polymer to form a colloid and is adsorbed in the liquid film of the foam to form a dispersion system [50,51]. The key indicators to measure the performance of the gel foam include its foaming ratio, the time required to form the gel, and its own water retention. The inhibitory effects of various systems on CSC are presented in Table 3. Thanks to the distinctive properties of colloids, gel foam exhibits exceptional stability and water retention capabilities, effectively reducing coal temperature while obstructing cracks and pores within the coal matrix to impede oxygen contact. Nevertheless, it is worth noting that the production process of gel foam is relatively intricate and costly, necessitating further attention and resolution.

**Table 3.** Inhibition of spontaneous coal combustion by different gel foam systems.

Authors	Gel Foam System	Effect
Han et al. [52]	SA (sodium alginate), CL (L-calcium lactate), CFA (tea saponin, alkyl glycoside), and TA (tannic acid)	Compared to the TA-free foam, the half-life was extended from 0.4 to 30 days, and the strength exhibited a remarkable increase of 72.9%. The concentration of CO decreased significantly from 7556.8 ppm to undetectable levels (0 ppm). SA-CA2+@TA-GF elevated the coal temperature by 60 °C during the rapid oxidation stage, achieving an impressive inhibition rate of 79.6% at 200 °C.
Wu et al. [53]	Sodium silicate, polyacrylamide, and film-forming agent	The strength and stability of the sodium silicate gel foam were enhanced. With the optimized formulation, the foaming ratio increased to 3–3.5 times, while the gelation time extended to 480 s. Moreover, the half-life of the gel foam was prolonged to 7 days, and its resistivity reached a remarkable value of 78.35% at 100 °C and 79.6% at 200 °C.
Wu et al. [54]	CMC cellulose, compound foaming agent ( $\alpha$ -alkenyl sulfonate sodium; fatty alcohol polyoxyethylene ether sodium sulfate), cross-linking agent	The optimized formulations were 0.7 wt%, 0.7 wt%, and 1.1 wt%, exhibiting a foaming time ranging from 4 to 7 min and a gel time spanning from 3 to 10 min. Low-temperature oxygen consumption of the coal sample decreased by 9.74%.
Qiao et al. [55]	Superhydrophobic nanoparticles, PVA, sodium bicarbonate, and sodium tetraborate	The gel foam (PGF) without the addition of a foaming agent was prepared with a foaming multiple of 3.29 times, exhibiting a half-life exceeding 13 h and water retention for over 15 h at 100 °C. Furthermore, its inhibitory ability remained effective even under high temperatures up to 400 °C.
Xi et al. [56]	Polymer complex (PC) microbial polysaccharide and galactomannan biopolymer, organic boron complex (OBC), homemade anionic surfactant, and non-ionic surfactant foaming agent	The cross-linking time is more than 30 min, and the foam water content is more than 60% after 120 h. The temperature of the burned coal is reduced from about 700 °C to 34.7 °C within 30 min.

### 3.1.5. Physical Inhibitors

Physical inhibitors are preferred due to their excellent heat dissipation, low preparation complexity, and economic advantages. Common physical resistance agents include  $\text{CaCl}_2$ ,  $\text{MgCl}_2$ ,  $\text{NaCl}$ ,  $\text{NH}_4\text{Cl}$ ,  $\text{NH}_4\text{HCO}_3$ ,  $\text{NH}_4\text{H}_2\text{PO}_4$ , among others. Physical retardant agents inhibit CSC through two primary mechanisms: firstly, they exhibit strong water absorption properties that ensure prolonged wetness of the coal. At high temperatures, a portion of the absorbed water vaporizes and absorbs heat while the remainder forms a liquid film on the coal surface, effectively isolating it from oxygen contact. Secondly, certain inhibitors generate  $\text{CO}_2$  during pyrolysis, which not only dilutes oxygen concentration but also absorbs heat generated during the CSC process, thereby inhibiting or retarding coal oxidation [57,58].

Wei [59] successfully prepared a sodium salt microcapsule inhibitor by using the melt dispersion condensation method, using polyethylene glycol 20,000 as the outer wall of the microcapsule and coating the sodium salt inhibitor in the microcapsule. Microcapsule coating technology was employed to reduce the moisture absorption rate of the sodium salt inhibitor at room temperature. If the quality of the core wall ratio is optimized to 1:2, the moisture absorption rate significantly decreases by 67.3%. The initial decomposition temperatures for the sodium salt inhibitor and its corresponding microcapsule form were

measured as 753.1 °C and 384.5 °C, respectively, indicating reduced thermal stability for the microencapsulated sodium salt inhibitor. The inhibition effect of microencapsulated inhibitors at different concentrations is presented in Table 4. Li et al. [60] proposed that the deterioration degree of coal can affect the inhibition effect of halogenated salts. By comparing the characteristic temperature and activation energy of raw coal samples with those with retarding agent added, halogen salt, as a kind of efficient retarding agent, has shown a more significant inhibitory effect on inhibiting the spontaneous combustion of bituminous coal compared with its application on lignite and anthracite. In addition, some scholars [61,62] have studied the inhibition performance of inhibitors based on the solution temperature, action time, injection pressure, and coal temperature changes and found that the traditional salt inhibitors can hardly meet the safety requirements for the prevention of CSC and that the coal itself and the characteristics of the inhibitor, as well as the external environmental conditions, should be considered comprehensively, and the applicable fire prevention materials should be selected according to the target.

**Table 4.** Average inhibition rate of different concentrations of inhibitors [59].

Inhibitors	Average Inhibition Rate	Inhibitors	Average Inhibition Rate
5% sodium salt inhibitor	24.5	5% sodium salt microcapsule inhibitor	41.5
10% sodium salt inhibitor	36.7	10% sodium salt microcapsule inhibitor	52.8
15% sodium salt inhibitor	46.5	15% sodium salt microcapsule inhibitor	66.6
20% sodium salt inhibitor	57.7	20% sodium salt microcapsule inhibitor	60.8

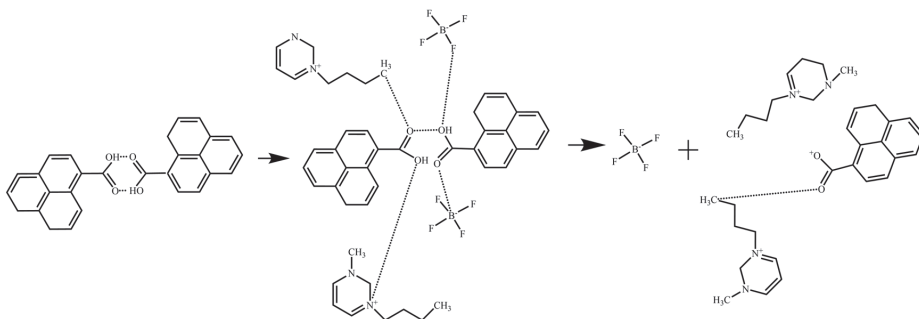
### 3.2. Chemical Inhibited Material

#### 3.2.1. Chemical Inhibitors

The mechanism of action of chemical inhibitors is that they can penetrate into the molecular structure of coal, closely bind with the active functional groups inside coal, and restrict and passivate these active sites that are easy to trigger chain oxidation reactions by generating more stable ring or cross-linked structures. This process effectively hinders the formation and propagation of free radicals in coal molecules, which are usually the key media to accelerate the coal oxidation process. Through this interventional effect, chemical inhibitors can significantly inhibit the direct contact and reaction between coal and atmospheric oxygen, thus greatly reducing the speed of coal oxidation, effectively controlling and even preventing the occurrence of the CSC phenomenon. The ionic liquid inhibitor, classified as a chemical inhibitor, is primarily employed to prevent CSC through chemical inhibition. Imidazoles represent the most extensively utilized type of ionic liquid inhibitors in this regard. Comprising an imidazole ring group and an anion that replaces the branched hydrogen, these inhibitors exhibit exceptional solubility and inertness [63–66]. The blocking mechanisms of [BMIM][BF<sub>4</sub>], [P4,4,4,2]Br, and TEMPO are shown in Figures 4–6. The inhibition effect of each chemical inhibitor is shown in Table 5. Ionic liquids, as a new type of green material to inhibit the spontaneous combustion of coal, can change the microstructure of the coal body, destroying or reducing the active functional groups to reduce the propensity of spontaneous combustion of coal. Additionally, ionic liquids can be easily separated from mixtures and recycled [67]. However, due to its high cost, complex production process, and limited thermal stability, widespread application of ionic liquid in mine fire prevention is currently hindered.

Table 5. Inhibition effect of chemical inhibitor.

Author	Materials	Effect
Li Yiheng [68]	Rare earth hydroxalicates	The -OH group in the inhibitor can react with the oxygen-containing functional groups such as -COO- in the coal, effectively preventing the active -COO- functional groups in the coal from continuing to participate in the oxidation process at low temperatures, reducing the possibility of coal oxidation.
Zhang Yutao [69]	Zn <sub>1</sub> Mg <sub>2</sub> Al <sub>1</sub> -CO <sub>3</sub> -LDHs	The starting exothermic temperature of the coal sample was delayed by 30–60 °C; when the addition amount reached 25%, the heat absorbed in the dehydration and desorption stage was three times that of the original coal sample, and the exothermic amount in the oxidation and combustion process was reduced by 5510 J, and the maximum heat-releasing power was also reduced from 32.96 to 23.5 mW/mg. The inhibition rate increased linearly with the addition of 1% Zn <sub>1</sub> Mg <sub>2</sub> Al <sub>1</sub> -CO <sub>3</sub> -LDHs, and the inhibition rate increased by 1.6%.
Deng et al. [70]	Ionic liquid	The ionic liquid with the greatest effect on independent hydrogen bonding, methylene, and carbonyl groups is [Bmim][BF <sub>4</sub> ], and the ionic liquid with the greatest effect on conjugated hydrogen bonding, methyl, and carboxyl groups is [Bmim][I]. Based on the inhibitory effects, the four ionic liquids were ranked in the following order: [Bmim][I] < [Emim][BF <sub>4</sub> ] < [Bmim][NO <sub>3</sub> ] < [Bmim][BF <sub>4</sub> ].
Li et al. [71]	2,2,6,6-Tetramethyl-1-piperidinoyloxy (TEMPO)	The exothermic peak of the raw coal sample appeared at 383 °C, the exothermic peak of the MgCl <sub>2</sub> -treated sample was delayed to 396 °C, and the exothermic peaks of CaCl <sub>2</sub> and TEMPO were delayed to 438 and 452 °C, respectively, and the inhibition of the reactive functional groups such as C-O, C-H, C=O, and O-H in the coal by TEMPO was more significant, which reduced the concentration of the reactive free radicals.
Lv et al. [72]	[BMIM][BF <sub>4</sub> ]	The high content of ionic liquids can induce exothermic reactions, thus reducing their inhibitory effect; with the decrease in O <sub>2</sub> concentration, the inhibitory effect of ionic liquids is enhanced, and the inhibitory effect of ionic liquids is significantly elevated when the O <sub>2</sub> volume fraction is lower than 10 percent
Sandeep Kumar et al. [73]	NaCl, CaCO <sub>3</sub> , KI, NaNO <sub>3</sub> , KCl	According to the results of the flammability temperature (FT) test, crossing point temperature (CPT) test, and differential thermal analysis (DTA), KCl and CaCO <sub>3</sub> are the most effective inhibitors. At 15% weight ratio of CaCO <sub>3</sub> , CPT is 35 °C higher than that of raw coal, and at 20% weight ratio of KCl, CPT is 29 °C higher than that of raw coal. At a 20% weight ratio, FT of KCl and CaCO <sub>3</sub> increased by 15 °C and 40 °C, and DTA increased by 32.01 °C and 31.96 °C compared with raw coal.

Figure 4. [BMIM][BF<sub>4</sub>] inhibition mechanism [74].

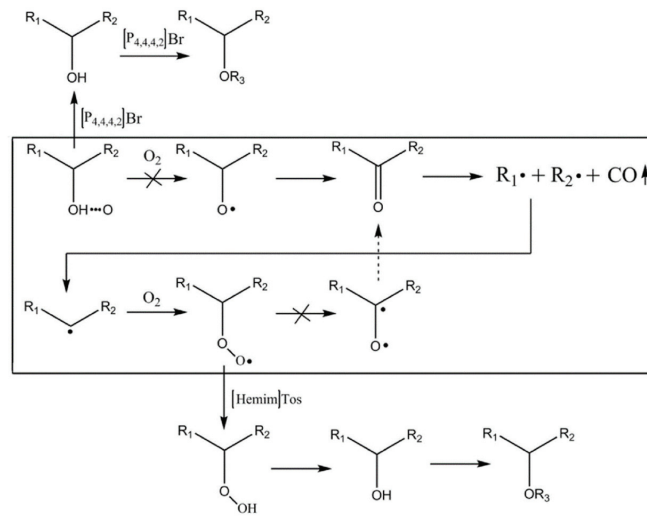


Figure 5. [P4,4,4,2]Br inhibition mechanism [75].

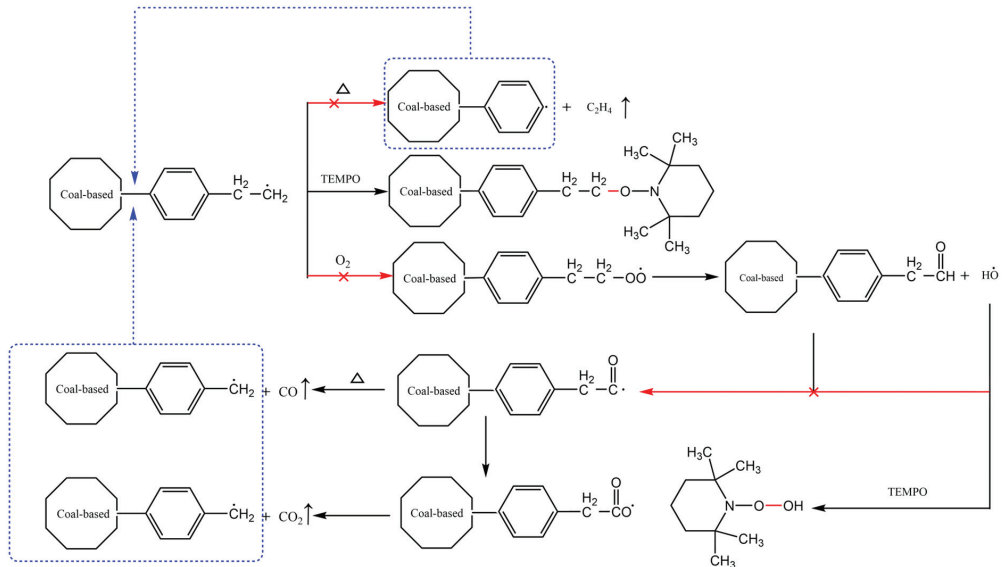


Figure 6. TEMPO inhibition mechanism [71].

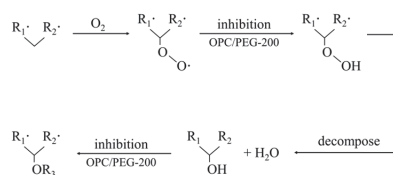
### 3.2.2. Antioxidant Inhibitor

Antioxidants are mainly used to prevent the formation of groups in coal, consume the active chemical groups that easily trigger reactions, and weaken the ability of coal's own oxidation reaction to effectively prevent the occurrence of the CSC phenomenon [76,77]. The antioxidants that inhibit CSC can be classified into inorganic and organic categories. Organic antioxidants include citric acid, polyethylene glycol (PEG), L-ascorbic acid (VC), malic acid, etc., and inorganic antioxidants include urea, chloride, sulfate, and acetate.

Dou et al. [78] conducted a study on the impact of acidic substances. Following the addition of citric acid to three coal samples, the crossing point temperature exhibited an increase of 8–12 °C, accompanied by a corresponding delay in time of 30–40 min. Lu



et al. [79] adopted DL-malic acid as an inhibitor in the study of how to reduce the production of active free radicals during coal oxidation. The experimental results show that compared with untreated raw coal, the cross-point temperature of lignite increases by 15.13 °C, and this temperature of bituminous coal also increases by 13.19 °C. In addition, when the coal samples were treated with 5% and 10% concentration solution, the free radicals in lignite decreased significantly by 57.35%, and the free radicals in bituminous coal also decreased by 53.94%. With the different impregnation times of the inhibitor, the content of aliphatic functional groups in the coal samples can be reduced by up to 41.30%. This change is directly related to the enhanced low-temperature stability of the coal, which means that the treated coal has achieved a significant improvement in thermal stability, confirming that malic acid has a high protective effect on wet coal. In addition, malic acid has a better protective effect on lignite with low metamorphism, especially at low-concentration treatment, and the inhibition efficiency is particularly excellent, which provides a new perspective for optimizing the use of inhibitors according to different coal characteristics. Wang Feng [80] enzymatically treated grape seed meal and combined it with metal ions to form chelates, and the optimal chelation ratio was 1:3. The clearance rates of hydroxyl free radicals and peroxides were significantly increased by 54% and 46%, respectively, compared with those before chelation, 75% and 70%, respectively, compared with that of grape seed meal before enzymolization, and more than 60% and 25%, respectively, compared with a single conventional chemical inhibitor. After treating coal with a gel foam containing a composite inhibitor, oxygen consumption is reduced by 60% compared with raw coal, and the coal crossover temperature is significantly increased by 23 °C. This treatment greatly inhibits the production of CO and C<sub>2</sub>H<sub>4</sub> during coal oxidation. Huang [81] combined PEG and proanthocyanidin (OPC) with environmentally friendly characteristics, as shown in Figure 7. The intersection temperature of OPC and PEG increased by 14.3 °C and 17.6 °C, respectively, and the stability of the ether bond increased by 18.41% and 42.71%, respectively. The free radical concentration decreased to 0.1178 Ng/1017 g<sup>-1</sup> and 0.1512 Ng/1017 g<sup>-1</sup>, and the associated and free hydroxyl groups decreased by 24.37% and 59.72%, respectively, indicating that the two inhibitors had significant inhibitory effects. When the samples were treated with OPC and PEG, and the two were mixed at a ratio of 1:2, the crossing temperature increased significantly by 25 °C, showing that there was a highly efficient synergistic effect between OPC and PEG, which greatly improved the oxidation resistance. Qin et al. [82] conducted a thermal analysis experiment aimed at evaluating the efficacy of VC as a flame retardant. The experimental results reveal that VC shows a better inhibition effect than water when coal undergoes a low-temperature oxidation process, which significantly improves the antioxidant performance of coal at this stage. However, due to the decomposition of VC at about 200 degrees Celsius, this property limits its practical application potential in the field of preventing CSC. Figure 8 illustrates the inhibition mechanism of VC and tea polyphenols (TP), highlighting their synergistic effect surpassing the individual inhibitory effects. Li et al. [83] selected six different antioxidants: VC, butylhydroxytoluene (BHT), triphenyl phosphite (TPPI), TEMPO, phytic acid (PA), and ethylenediamine tetraacetic acid (EDTA), to compare the inhibition properties of these inhibitors. The results show that TEMPO exhibits the strongest flame-retardant effect with a high retarding efficiency of 73.08%. In order of inhibition efficiency from high to low, the order is TEMPO, BHT, EDTA, TPPI, and PA.



**Figure 7.** Complex inhibition mechanism of polyethylene glycol and procyanidin [81].



**Figure 8.** Synergistic inhibition of CSC by VC and TP [84].

Taraba et al. [85] studied the inhibition rate of 14 inorganic antioxidants, such as chloride, urea, and phosphate. The results revealed that urea exhibited a high inhibition rate against CSC, while a 10% uric acid solution demonstrated a low-temperature oxygen inhibition rate of 70%. The effects of inorganic antioxidants at different temperatures vary. Slovak and Taraba [86] mentioned in their study that  $\text{CaCl}_2$  can effectively slow down the oxidation activity of coal under the temperature of 300 °C. When urea is below 200 °C, it is very effective in inhibiting coal oxidation, but when the ambient temperature exceeds 200 °C, urea instead begins to promote the oxidation process of coal.

### 3.2.3. Microbial Inhibition

Microbiological technology is gradually showing its application value and spreading in the field of CSC. Li et al. [87,88] conducted a bacterial-coal matching degradation experiment on Zhaotong lignite from Yunnan Province, which was subjected to oxidation by five strains of actinomycetes and nitric acid. Through screening, they identified *Streptomyces chlorophylla* as the dominant degradation bacterium. The degradation of Shengli lignite in Inner Mongolia was performed using *Pingeria xanthosporium*. Kang and Mishra [89,90] found that microorganisms can consume free radicals in coal and decompose sulfides and macromolecular organic substances in coal. Microorganisms consume oxygen through their growth metabolism and proliferation activities, and this natural process helps to slow down the coal oxidation rate and effectively curb the occurrence of the CSC phenomenon.

### 3.3. Physicochemical Synergistic Inhibition Material

The existing single physical or chemical fire prevention materials have certain shortcomings in solving coal fire disaster problems due to their own shortcomings. At present, scholars at home and abroad have carried out research on new anti-fire materials, and their inhibition mechanism has gradually shifted from single inhibition to compound and collaborative inhibition, combining physical and chemical ways to jointly inhibit the CSC process so as to realize the control of the whole process of CSC.

#### 3.3.1. Composite Foam

Zhang et al. [91] addressed the limitations of limited temporal efficacy and suboptimal efficiency in the early release of retarding agents for preventing CSC by developing a temperature-controlled self-reactive retarding foam using hollow balls as solution carriers. The foam can be generated and released at temperatures ranging from 59 °C to 61 °C, covered by the inhibitor solution, which is approximately 12.9 to 13.9 times smaller than the total area affected. After the foam release, the oxidation heating rate of coal has been significantly controlled, and the inhibition effect reaches 78.7% to 91.6%, which delays the oxidation process of coal by 22 to 35 °C. Through combined foam suppression and inerting effects, the inhibition efficiency against coal oxidation reaches 88.51–97.06% at a temperature of 160 °C. Lu et al. [92] developed a high-performance antioxidant gel material by adding OPC into a gel containing sodium silicate, bentonite, and coagulant. In particular, under the formulation of coagulant and sodium silicate concentrations of 2.5% and 5%, respectively, the prepared gel showed excellent flame-retardant properties. In addition, when the mass ratio of surfactant SDS to SAS was optimized to 1:1, the foaming capacity was dramatically increased to 482 mL, and the stability of the composite foaming agent was significantly enhanced. The inhibition effect of this method on CO was also very significant, and the inhibition efficiency reached 68.7%. In the dimensional experiment, the rapid drop from 727 °C to the ambient temperature was achieved within 1850 s. By utilizing foam as a carrier for chemical retarder transportation, the composite foam takes advantage of its large flow capacity, wide diffusion range, and excellent stacking properties to effectively

cover the area prone to CSC and ensure full contact between the chemical retarder and coal body, thereby maximizing their synergistic effect.

### 3.3.2. Composite Gel

Wang [93] selected a highly absorbent resin polymer (SP) in combination with ascorbic acid (A) to create a cage-type composite inhibitor material with dual physical and chemical effects. Experimental data revealed that the inhibition system demonstrated the best inhibition efficacy when the mass ratio of SP to A reached an optimal 1:5 and the mass percentage of the composite inhibitor in the whole was 10%. Moreover, this compound inhibitor exhibited remarkable capability in reducing the presence of methyl, methylene, aromatic hydrocarbons, and hydroxyl groups, thereby inerting its oxidation activity. Xue et al. [94] prepared a novel composite corrosion inhibitor by grafting oligo-PC radicals onto a sodium acrylate and acrylic acid copolymer, followed by combining it with polyphosphoric acid (APP). The concentration of free radicals decreased by 6.00%, the heat release of coal decreased significantly by 62.83%, and the activation energy increased by 13.93%. These data strongly prove the excellent results of the gel in enhancing the chemical stability of coal and effectively delaying the corrosion process. Huang et al. [95] prepared a modified antioxidant-based hydrogel with sodium acrylate, tert-butyl hydroquinone (TBHQ), and montmorillonite, and TBHQ significantly reduced  $-CH_3$ ,  $-CH_2-$ ,  $-OH$ , and  $-COOH$  while increasing the number of ether bonds. The thermal mass loss rate decreased by 0.84%/min and the dry cracking temperature increased by 52.8 °C. The results show that the thermal stability of the coal sample is significantly improved, and the oxidation loss is reduced.

### 3.3.3. Compound Inhibitor

The composite inhibitor can play a synergistic role through the combination of various inhibitor components and significantly improve the inhibition effect. Table 6 shows the inhibition effect of various compound chemical retardants on CSC.

**Table 6.** Inhibition effect of composite inhibitors.

Authors	Composite Inhibitors	Effect
Wang et al. [96]	MgCl <sub>2</sub> , CaCl <sub>2</sub> , N, N-dibenzylhydroxylamine (DBHA), BHT	The release of CO decreased by 88.7% at 128 °C. The inhibition rate reached 82.5% at 100 °C. Reducing hydroxyl, methyl, and methylene groups and carbonyl-containing active components in coal. The relative content of aromatic ketones decreased significantly. The oxygen adsorption process of the coal body is shortened, and the adsorption capacity is reduced. The activation energy was increased by 53.2% during oxygen inhalation
Jiao [97]	Oxidant microcapsule compound inhibitor, tea polyphenol, polyethylene glycol 20,000, Pentaerythrityl tetrastearate	When the mass ratio of polyethylene glycol 20,000 and pentaerythritol stearate is 1:1, 1:2, and 1:3, the microcapsule wall material obtained by the combination of polyethylene glycol 20,000 and pentaerythritol stearate has better hydrophobicity. When the wall-material ratio was 1:1 and the core-wall ratio was 1:1, the coating rate of microcapsule material was the highest. When the wall-material ratio was 1:1 and the core-wall ratio was 1:1, the inhibition rate reached 76.8%, which was 11.4% higher than that of single tea polyphenol. The cross point temperature was increased by 43 °C compared with the raw coal
Huo [98]	MgCl <sub>2</sub> , BHT, TPPI, and polyethylene glycol 400	The optimal quality fractions were 10.26%, 3.15%, 2.09%, and 0.58%, respectively. The optimal quality fraction of P&C was 12% of coal. The cross point temperature of the coal sample was increased to 155.08 °C, 22.48 °C higher than that of the raw coal sample
Xue [99]	Melatonin, polyacrylate-alginate sodium	When 6 wt% melatonin was added to the coal, the inhibition effect was the best. When the optimal mass ratio of melatonin and polyacrylic acid-sodium alginate was 1:4, it could effectively inhibit the generation of CO, increase the crossing point temperature of coal oxidation, reduce the oxygen consumption rate at 70 °C, and significantly reduce the risk of CSC

Table 6. Cont.

Authors	Composite Inhibitors	Effect
Huang et al. [100]	Tea polyphenols, halloysite nanotubes	The maximum heat absorption was 67.15 J/mg, the shortest heat release interval was 120.22 °C to 572.22 °C, and the minimum total heat release was 2536.73 J/mg. Lower the hydroxyl content and reduce the number of aliphatic functional groups converted to carbonyl and carboxyl groups
Xi et al. [101]	Compound antioxidant containing superoxide dismutase (SOD)	The results showed that the energy barrier of SOD for eliminating peroxy radicals was 31.3 kJ/mol, and SOD could automatically eliminate peroxy radicals at room temperature.
Zhang et al. [102]	Rare earth hydrotalcite, halogen salt	The activity of acid functional groups such as -COOH in coal is weakened due to weak hydrogen bonds between -OH and acid functional groups such as -COOH in rare-earth hydrotalc laminates. Mg <sup>2+</sup> is complexed with -COO- in coal molecules to form -COOMg-, resulting in reduced C=O activity in -COO-. Compared with the raw coal, the peak temperature of the coal is shifted back by 50–60 °C, the T <sub>1</sub> temperature is shifted back by 90–100 °C, and the total heat release is reduced by 19–27 kJ·g <sup>-1</sup> .
Zhang [103]	Polyethylene glycol 6000, LDHs	Increase the inhibition time. The best effect was obtained when the core wall ratio was 1:5. The critical temperature and maximum weight loss temperature were increased by 8.8 °C and 33.6 °C, respectively. The apparent activation energy of water evaporation and gas desorption stage was increased by 13.42 kJ/mol. The thermal decomposition stage and combustion stage increased by 88.64 kJ/mol
Pan et al. [104]	Sodium dodecyl sulfate, sodium laurylsulfonate, flame-retardant compound (CaCl <sub>2</sub> , MgCl <sub>2</sub> , NaHCO <sub>3</sub> , (NH <sub>4</sub> ) <sub>2</sub> HPO <sub>4</sub> , CO(NH <sub>2</sub> ) <sub>2</sub> ), XG	The higher the concentration of compound inhibitor, the better the effect; the 20% inhibitor solution has the most significant effect. The inhibition rate is 85.92%, and the average inhibition rate is 15 times that of water. The oxidation inhibition effect of coal samples after water treatment can be observed only at 140 °C, and the oxidation rate increases with the increase in temperature. Chloride ions and phosphate elements break down into ions and small molecules, forming stable substances with free radicals, reducing the number of free radicals, and preventing spontaneous combustion.

#### 4. Conclusions

Based on the in-depth analysis of CSC fire-prevention materials, a series of quantitative and network analyses is carried out by using visualization software CiteSpace, revealing the frontier trend, cooperation network, and key nodes of mine fire prevention materials research. The fire-fighting mechanism and inhibition effect of existing fire-fighting materials are summarized and sorted out, and the conclusions are as follows:

- (1) The keyword co-occurrence map of CSC fire-fighting materials was obtained through CiteSpace visual analysis. Through the Atlas network, it is concluded that the development of CSC fire-fighting materials has experienced several stages, such as grouting, inert gas, colloid, retarder, foam, and gel foam. The characterization methods of CSC prevention and control by each inhibitory material were analyzed. Through the keyword network, it is concluded that the current research frontier focuses on the verification of the inhibition mechanism of different inhibition materials by molecular simulation.
- (2) The existing CSC fire-fighting materials can be divided into physical inhibition, chemical inhibition, and physicochemical coordination inhibition according to the form of action. These materials reduce the oxidation rate of coal and inhibit CSC by diluting oxygen, isolating oxygen, and hindering chain reaction.
- (3) In terms of application, composite inhibitors, environmentally friendly foams, gels, gel foams, etc., not only improve flame retardant efficiency but also show great potential in environmental protection and durability. In addition, the synergistic mechanism of compound antioxidants enhances the flame-retardant effect, reveals the microscopic mechanism of chemical inhibitors, and provides theoretical guidance for the design of high-performance inhibitors. In the future, the use of microbial inhibition of CSC will show environmental friendliness and long-term action, which is a frontier direction worthy of attention, and its management strategy and potential application deserve further exploration.

## 5. Existing Problems and Development Trends

Well-known scholars at home and abroad have conducted extensive research on various kinds of suppression materials to prevent CSC disasters. Currently, a relatively comprehensive system has been established. However, the situation regarding the prevention and control of CSC disasters within our country remains severe, requiring further enhancement of the research system for preventing and controlling mine fires.

- (1) Affected by factors such as the increasing depth of mining and the complex and dynamic mining environment, CSC prevention and control pose significant challenges. The existing fire prevention materials still fail to fully meet the requirements for effective fire prevention and control. Therefore, developing novel fire prevention materials with prolonged resistance life, enhanced fire prevention efficiency, and simplified manufacturing processes is a pressing issue that needs to be addressed.
- (2) The retarding effect of the same coal varies when subjected to the same fire-proof material. Therefore, it is imperative to analyze the alterations in key functional groups, free radicals, reaction pathways, and other factors during the retarding process while comprehensively elucidating the mechanism underlying CSC.
- (3) Some materials may decompose into toxic and harmful substances when exposed to heat, which can potentially exert significant ramifications on human health and the ecological environment. Additionally, fire-fighting materials may adhere to coal surfaces and form complex solid impurities, potentially leading to soil and water pollution as well as increased secondary treatment costs. Further research is needed to investigate these potential effects.
- (4) Through continuous exploration and innovation, the use of refractory materials with strong popularity and excellent fire protection effect can implement accurate and efficient flame-retardant strategies for different types of coal, greatly enhancing the overall effectiveness of fire prevention measures.

As a valuable fossil fuel, coal is expected to undergo advancements in cleanliness, efficiency, and refinement in the future. Additionally, re-mining or reuse of coal reserves within closed mining areas will emerge as a prominent development trend. Therefore, the prevention and control of re-mining fires in closed mining areas should also be considered in planning. In addition, firefighting materials in other fields need to be actively explored and evaluated for their usefulness and effectiveness in CSC prevention and control applications. Given that coal serves as the predominant energy source in our nation, ensuring effective prevention and management of CSC holds significant long-term implications. Consequently, enhancing fire prevention systems within coal mines becomes imperative.

**Author Contributions:** Conceptualization, D.H., G.N. and H.Z.; Investigation, B.L., Y.R., and Y.W.; Writing—original draft, D.H., G.N., and T.C.; Writing—review & editing, G.N., T.C., B.L., Y.R., Y.W., and B.S. All authors have read and agreed to the published version of the manuscript.

**Funding:** This research received no funding.

**Data Availability Statement:** Data are contained within the article.

**Conflicts of Interest:** The authors declare no conflicts of interest.

## References

1. Xu, L.; Tan, J. Financial Development, Industrial Structure and Natural Resource Utilization Efficiency in China. *Resour. Policy* **2020**, *66*, 101642. [CrossRef]
2. Dong, F.; Li, J.; Wang, Y.; Zhang, X.; Zhang, S.; Zhang, S. Drivers of the Decoupling Indicator between the Economic Growth and Energy-Related CO<sub>2</sub> in China: A Revisit from the Perspectives of Decomposition and Spatiotemporal Heterogeneity. *Sci. Total Environ.* **2019**, *685*, 631–658. [CrossRef]
3. Li, H.; Long, R.; Chen, H. Economic Transition Policies in Chinese Resource-Based Cities: An Overview of Government Efforts. *Energy Policy* **2013**, *55*, 251–260. [CrossRef]

4. Laryea, A.E.N.; Ren, W.; Guo, Q.; Kang, Z. Spontaneous Coal Combustion, Direct and Indirect Impact on Mining in China: A Prospective Review and Proposal of a Five-Level Comprehensive Mine Safety Management Structure (5L-CMSMS) Coupled with Hazard Zoning and Barrier Systems. *Combust. Sci. Technol.* **2024**. [CrossRef]
5. Qiao, M.; Ren, T.; Roberts, J.; Yang, X.; Li, Z.; Wu, J. New Insight into Proactive Goaf Inertisation for Spontaneous Combustion Management and Control. *Process Saf. Environ. Prot.* **2022**, *161*, 739–757. [CrossRef]
6. Chu, C.; Muradian, N. Safety and Environmental Implications of Coal Mining. *Int. J. Environ. Pollut.* **2016**, *59*, 250–268. [CrossRef]
7. Kong, B.; Li, Z.; Yang, Y.; Liu, Z.; Yan, D. A Review on the Mechanism, Risk Evaluation, and Prevention of Coal Spontaneous Combustion in China. *Environ. Sci. Pollut. Res.* **2017**, *24*, 23453–23470. [CrossRef]
8. Zhang, J.; Fu, J.; Hao, H.; Fu, G.; Nie, F.; Zhang, W. Root Causes of Coal Mine Accidents: Characteristics of Safety Culture Deficiencies Based on Accident Statistics. *Process Saf. Environ. Prot.* **2020**, *136*, 78–91. [CrossRef]
9. Mahdevari, S.; Shahriar, K.; Esfahanipour, A. Human Health and Safety Risks Management in Underground Coal Mines Using Fuzzy TOPSIS. *Sci. Total Environ.* **2014**, *488*, 85–99. [CrossRef]
10. Eliopoulou, E.; Alissafaki, A.; Papanikolaou, A. Statistical Analysis of Accidents and Review of Safety Level of Passenger Ships. *J. Mar. Sci. Eng.* **2023**, *11*, 410. [CrossRef]
11. Zhang, J.; Xu, K.; Reniers, G.; You, G. Statistical Analysis of Extraordinarily Severe Coal Mine Accidents (ESCMAs) in China from 1950 to 2018. *Process Saf. Environ. Prot.* **2020**, *133*, 332–340. [CrossRef]
12. Zhang, L.; Bian, Y.; Kuai, D. Preparation and Flame Retardant Property of Nano-Aluminum Hydroxide Foam for Preventing Spontaneous Coal Combustion. *Fuel* **2021**, *304*, 121494. [CrossRef]
13. Qin, B.; Jia, Y.; Lu, Y.; Li, Y.; Wang, D.; Chen, C. Micro Fly-Ash Particles Stabilized Pickering Foams and Its Combustion-Retardant Characteristics. *Fuel* **2015**, *154*, 174–180. [CrossRef]
14. Hunter, T.N.; Pugh, R.J.; Franks, G.V.; Jameson, G.J. The Role of Particles in Stabilising Foams and Emulsions. *Adv. Colloid Interface Sci.* **2008**, *137*, 57–81. [CrossRef]
15. Xue, D.; Hu, X.; Cheng, W.; Wu, M.; Shao, Z.; Li, Y.; Zhao, Y.; Zhang, K. Carbon Dioxide Sealing-Based Inhibition of Coal Spontaneous Combustion: A Temperature-Sensitive Micro-Encapsulated Fire-Retardant Foamed Gel. *Fuel* **2020**, *266*, 117036. [CrossRef]
16. Yuan, S.; Sun, B.; Han, G.; Duan, W.; Wang, Z. Application and Prospect of Curtain Grouting Technology in Mine Water Safety Management in China: A Review. *Water* **2022**, *14*, 4093. [CrossRef]
17. Yang, S.; Li, M.; Song, G.; Yang, Y.; Xie, F. Optimization of Face Flexible Bolting and Grouting Technology for Longwall Face Support under Difficult Geological Conditions. *Energy Sci. Eng.* **2020**, *8*, 1260–1270. [CrossRef]
18. Wang, D.; Li, Z.; Qin, B.; Liang, X.; Chen, J. Development of a new green material for preventing mine fires. *J. China Univ. Min. Technol.* **2004**, *33*, 81–84.
19. Wang, Z.P.; Song, X.M.; Xiao, Y.; Wang, H.Q. Research and application of coal bed fire prevention technology based on fly ash resource utilization. *China Coal* **2010**, *36*, 99–102.
20. Xiao, Y.; Ma, T.; Deng, J.; Wang, Z.P.; Song, X.M. Fire suppression technology for coal ash utilization in mines. *Min. Saf. Environ. Prot.* **2010**, *37*, 29–31.
21. Jian, S. Research on the Preparation and Performance of Fire Suppression Materials for Coal Mining. Master's Thesis, Beijing Institute of Technology, Beijing, China, 2017.
22. Tang, L.; Qi, Y.; Li, X.; Wang, J. Coal Fire Prevention in Large Areas over Long Term with a Composite Inert Gas—a Case Study in Tangkou Coal Mine, China. *Energy Sources Part A-Recovery Util. Environ. Eff.* **2019**. [CrossRef]
23. Si, J.; Li, L.; Cheng, G.; Shao, H.; Wang, Y.; Li, Z. Characteristics and Safety of CO<sub>2</sub> for the Fire Prevention Technology with Gob-Side Entry Retaining in Goaf. *ACS Omega* **2021**, *6*, 18518–18526. [CrossRef]
24. Ray, S.K.; Singh, R.P. Recent Developments and Practices to Control Fire in Underground Coal Mines. *Fire Technol.* **2007**, *43*, 285–300. [CrossRef]
25. Ding, C.; Li, Z.; Wang, J.; Lu, B.; Gao, D. Effects of Inert Gas CO<sub>2</sub>/N<sub>2</sub> Injection on Coal Low-Temperature Oxidation Characteristic: Experiments and Simulations. *Arab. J. Chem.* **2023**, *16*, 104510. [CrossRef]
26. Lei, B.; He, B.; Xiao, B.; Du, P.; Wu, B. Comparative Study of Single Inert Gas in Confined Space Inhibiting Open Flame Coal Combustion. *Fuel* **2020**, *265*, 116976. [CrossRef]
27. Cao, N.-F.; Liang, Y.-T. Research on the Control Process of Mining and Combustion Disturbance Zone Based on the Three-Dimensional Dynamic Distribution Model of Void Fraction. *Combust. Sci. Technol.* **2022**. [CrossRef]
28. Lu, Y.; Yan, Z.; Shi, S.; Wang, G.; Li, H.; Niu, H.; Guo, Z.; Wang, P. Delineation and Prevention of the Spontaneous Combustion Dangerous Area of Coal in a Regenerated Roof: A Case Study in the Zhoujing Coal Mine, China. *Energy Fuels* **2020**, *34*, 6401–6413. [CrossRef]
29. Niu, H.; Sun, Q.; Bu, Y.; Yang, Y.; Sun, S.; Li, S.; Tao, M.; Mao, Z. Review and Prospects of Research on Materials to Prevent and Extinguish Mine Fires. *Fire Mater.* **2023**, *47*, 739–757. [CrossRef]
30. Ren, X.; Hu, X.; Xue, D.; Li, Y.; Shao, Z.; Dong, H.; Cheng, W.; Zhao, Y.; Xin, L.; Lu, W. Novel Sodium Silicate/Polymer Composite Gels for the Prevention of Spontaneous Combustion of Coal. *J. Hazard. Mater.* **2019**, *371*, 643–654. [CrossRef]
31. Cheng, W.; Hu, X.; Xie, J.; Zhao, Y. An Intelligent Gel Designed to Control the Spontaneous Combustion of Coal: Fire Prevention and Extinguishing Properties. *Fuel* **2017**, *210*, 826–835. [CrossRef]

32. Huang, Z.; Sun, C.; Gao, Y.; Ji, Y.; Wang, H.; Zhang, Y.; Yang, R. R&D of Colloid Components of Composite Material for Fire Prevention and Extinguishing and an Investigation of Its Performance. *Process Saf. Environ. Prot.* **2018**, *113*, 357–368.
33. Zhao, Z. Research on Temperature Sensitive Expanded Gel Material for Mining and Its Fire Fighting Characteristics. Master's Thesis, China University of Mining and Technology, Beijing, China, 2023.
34. Zhou, C.; Tang, Y. A Novel Sodium Carboxymethyl Ellulose/Aluminium Citrate Gel for Extinguishing Spontaneous Fire in Coal Mines. *Fire Mater.* **2018**, *42*, 760–769. [CrossRef]
35. Dong, K.; Wang, J.; Zhang, Y.; Liang, Z.; Shi, Q. Performance of Fire Extinguishing Gel with Strong Stability for Coal Mine. *Combust. Sci. Technol.* **2022**, *194*, 1661–1677. [CrossRef]
36. Wei, J.; Zhao, Y.; Yu, S.; Du, J.; Hu, X.; Bai, G.; Wang, Z. Environment-Friendly Dual-Network Hydrogel Dust Suppressant Based on Xanthan Gum, Polyvinyl Alcohol and Acrylic Acid. *J. Environ. Manag.* **2021**, *295*, 113139. [CrossRef]
37. Yan, Q.; Lu, Y.; Wang, Q.; Gu, W.; Wu, F. Research Progress and Development Trend of Coal Spontaneous Combustion Prevention Technology. *Combust. Sci. Technol.* **2024**. [CrossRef]
38. Yu, M.; Yang, N.; Liu, Z.; Li, H.; Wang, L.; Wu, M.; Li, J.; Yu, Y. Experimental Preparation and Mechanism Analysis of a Neotype Composite Gel for Coal Spontaneous Combustion Prevention and Coal-Fire Extinguishment. *Fuel* **2023**, *339*, 127448. [CrossRef]
39. Kong, B.; Li, J.; Lu, W.; Fu, W.; Song, H.; Liu, J. Research on a Spontaneous Combustion Prevention System in Deep Mine: A Case Study of Dongtan Coal Mine. *Combust. Sci. Technol.* **2022**. [CrossRef]
40. Li, M.; Wang, D.; He, S.; Shao, Z.; Shen, Y. Experimental Study on Foaming Properties of Anion-Cation Compound Foaming Agent to Prevent Coal Spontaneous Combustion. *Colloids Surf. A-Physicochem. Eng. Asp.* **2019**, *581*, 123847. [CrossRef]
41. Tang, Z.; Xu, G.; Yang, S.; Deng, J.; Xu, Q.; Chang, P. Fire-Retardant Foam Designed to Control the Spontaneous Combustion and the Fire of Coal: Flame Retardant and Extinguishing Properties. *Powder Technol.* **2021**, *384*, 258–266. [CrossRef]
42. Xie, H.; Ju, Y.; Ren, S.; Gao, F.; Liu, J.; Zhu, Y. Theoretical and Technological Exploration of Deep in Situ Fluidized Coal Mining. *Front. Energy* **2019**, *13*, 603–611. [CrossRef]
43. Wang, H.; Du, Y.; Wang, D.; Qin, B. Recent Progress in Polymer-Containing Soft Matters for Safe Mining of Coal. *Polymers* **2019**, *11*, 1706. [CrossRef]
44. Shao, Z.; Wang, D.; Wang, Y.; Zhong, X.; Tang, X.; Hu, X. Controlling Coal Fires Using the Three-Phase Foam and Water Mist Techniques in the Anjialing Open Pit Mine, China. *Nat. Hazards* **2015**, *75*, 1833–1852. [CrossRef]
45. Zhang, Y.; Sun, Y.; Du, W.; Dong, H.; Wang, B.; Wang, Y.; Cao, X. Preparation and Characteristic Study of the Hydrogel of Coal Spontaneous Combustion Environmental Protection. *Fuel* **2024**, *360*, 130505. [CrossRef]
46. Zhu, H.; Hu, C.; Guo, J.; Wang, X.; Wu, B. Experimental study on optimization of three-phase foam blowing agent for fire prevention. *Coal Technol.* **2019**, *38*, 45–48.
47. Wang, Z.; Qi, X.; He, S.; Yu, T.; Fan, H.; Sun, L.; Yang, Y. Preparation of three-phase foam from fly ash and its stabilization mechanism. *J. China Univ. Pet. (Nat. Sci. Ed.)* **2020**, *44*, 166–176.
48. Zhang, B.; Qin, Y.; Shen, H.; Meng, H.; Cui, J.; Pan, R. Constructing Fibrous-like Skeleton by Simulated Sea Mud to Improve Three-Phase Foam for Stability and Fire-Extinguishing Performance. *J. Dispers. Sci. Technol.* **2023**, *44*, 2311–2321. [CrossRef]
49. Wang, L.; Liu, Z.; Yang, H.; Li, H.; Yu, M.; He, T.; Luo, Z.; Liu, F. A Novel Biomass Thermoresponsive Konjac Glucomannan Composite Gel Developed to Control the Coal Spontaneous Combustion: Fire Prevention and Extinguishing Properties. *Fuel* **2021**, *306*, 121757. [CrossRef]
50. Dickinson, E. Biopolymer-Based Particles as Stabilizing Agents for Emulsions and Foams. *Food Hydrocoll.* **2017**, *68*, 219–231. [CrossRef]
51. Xiong, J.; Zhao, Z.; Sun, W.; Liu, W. Foam Stabilization Mechanism of a Novel Non-Cross-Linked Foam Fracturing Fluid. *ACS Omega* **2021**, *6*, 32863–32868. [CrossRef]
52. Han, C.; Nie, S.; Liu, Z.; Liu, S.; Zhang, H.; Li, J.; Zhang, H.; Wang, Z. A Novel Biomass Sodium Alginate Gel Foam to Inhibit the Spontaneous Combustion of Coal. *Fuel* **2022**, *314*, 122779. [CrossRef]
53. Wu, X.; Nie, S.; Han, C.; Dai, G.; Yang, W.; Fang, C. Preparation of Gel Foam Material for Coal Mine Fire Prevention and Its Performance. *China Prod. Saf. Sci. Technol.* **2022**, *18*, 78–84.
54. Wu, M.; Liang, Y.; Zhao, Y.; Wang, W.; Hu, X.; Tian, F.; He, Z.; Li, Y.; Liu, T. Preparation of New Gel Foam and Evaluation of Its Fire Extinguishing Performance. *Colloids Surf. A-Physicochem. Eng. Asp.* **2021**, *629*, 127443. [CrossRef]
55. Qiao, J.; Hu, X.-M.; Liang, Y.-T.; Zhang, Q.; Wang, W.; Zhao, Y.-Y.; Ju, S.; Tian, F.-C. Preparation and Characterization of PVA-H18 Gel Foam for Preventing Spontaneous Combustion of Coal Based on Interfacial Self-Assembly. *Fuel* **2022**, *327*, 125081. [CrossRef]
56. Xi, X.; Shi, Q. Study of the Preparation and Extinguishment Characteristic of the Novel High-Water-Retaining Foam for Controlling Spontaneous Combustion of Coal. *Fuel* **2021**, *288*, 119354. [CrossRef]
57. He, Y.; Deng, J.; Yi, X.; Xiao, Y.; Deng, Y.; Chen, W. Effect of Rare-Earth-Containing Inhibitors on the Low-Temperature Oxidation Characteristics and Thermodynamic Properties of Coal. *Energy* **2023**, *281*, 128316. [CrossRef]
58. Shu, P.; Zhang, Y.; Deng, J.; Duan, Z.; Zhai, F. Characteristics and Mechanism of Modified Hydrotalcite for Coal Spontaneous Combustion Preventing. *Energy* **2023**, *265*, 126353. [CrossRef]
59. Wei, Z. Experimental Study on the Inhibition of Coal Spontaneous Combustion by Sodium Salt Microencapsulated Retardants. Master's Thesis, Xi'an University of Science and Technology, Xi'an, China, 2022.
60. Li, X.; Chen, Y.; Zhang, J.; Wang, R. Study on the effect of chlorine salt composite inhibitor on the spontaneous combustion inhibition of different coal samples. *Coal Engineering* **2020**, *52*, 106–110.

61. Guo, Q.; Ren, W.; Zhu, J.; Shi, J. Study on the Composition and Structure of Foamed Gel for Fire Prevention and Extinguishing in Coal Mines. *Process Saf. Environ. Prot.* **2019**, *128*, 176–183. [CrossRef]
62. Lu, W.; Guo, B.; Qi, G.; Cheng, W.; Yang, W. Experimental Study on the Effect of Preinhibition Temperature on the Spontaneous Combustion of Coal Based on an  $MgCl_2$  Solution. *Fuel* **2020**, *265*, 117032. [CrossRef]
63. Cummings, J.; Shah, K.; Atkin, R.; Moghtaderi, B. Physicochemical Interactions of Ionic Liquids with Coal; the Viability of Ionic Liquids for Pre-Treatments in Coal Liquefaction. *Fuel* **2015**, *143*, 244–252. [CrossRef]
64. Raj, J.J.; Magaret, S.; Pranesh, M.; Lethesh, K.C.; Devi, W.C.; Mutalib, M.I.A. Dual Functionalized Imidazolium Ionic Liquids as a Green Solvent for Extractive Desulfurization of Fuel Oil: Toxicology and Mechanistic Studies. *J. Clean. Prod.* **2019**, *213*, 989–998. [CrossRef]
65. Cummings, J.; Tremain, P.; Shah, K.; Heldt, E.; Moghtaderi, B.; Atkin, R.; Kundu, S.; Vuthaluru, H. Modification of Lignites via Low Temperature Ionic Liquid Treatment. *Fuel Process. Technol.* **2017**, *155*, 51–58. [CrossRef]
66. To, T.Q.; Shah, K.; Tremain, P.; Simmons, B.A.; Moghtaderi, B.; Atkin, R. Treatment of Lignite and Thermal Coal with Low Cost Amino Acid Based Ionic Liquid-Water Mixtures. *Fuel* **2017**, *202*, 296–306. [CrossRef]
67. Li, Q.-W.; Xiao, Y.; Zhong, K.-Q.; Shu, C.-M.; Lü, H.-F.; Deng, J.; Wu, S. Overview of Commonly Used Materials for Coal Spontaneous Combustion Prevention. *Fuel* **2020**, *275*, 117981. [CrossRef]
68. Li, Y.-H. Research on the Mechanism of Coal Spontaneous Combustion Retardation by Rare Earth-like Hydrotalcite. Master's Thesis, Xi'an University of Science and Technology, Xi'an, China, 2018.
69. Zhang, Y.; Shi, X.; Li, Y.; Wen, H.; Huang, Y.; Li, S.; Liu, Y. Zinc-magnesium-aluminum layered double hydroxide inhibition properties on spontaneous coal combustion. *J. Coal* **2017**, *42*, 2892–2899.
70. Deng, J.; Bai, Z.-J.; Xiao, Y.; Shu, C.-M.; Laiwang, B. Effects of Imidazole Ionic Liquid on Macroparameters and Microstructure of Bituminous Coal during Low-Temperature Oxidation. *Fuel* **2019**, *246*, 160–168. [CrossRef]
71. Li, J.; Li, Z.; Yang, Y.; Kong, B.; Wang, C. Laboratory Study on the Inhibitory Effect of Free Radical Scavenger on Coal Spontaneous Combustion. *Fuel Process. Technol.* **2018**, *171*, 350–360. [CrossRef]
72. Lü, H.-F.; Xiao, Y.; Deng, J.; Li, D.; Yin, L.; Shu, C.-M. Inhibiting Effects of 1-Butyl-3-Methyl Imidazole Tetrafluoroborate on Coal Spontaneous Combustion under Different Oxygen Concentrations. *Energy* **2019**, *186*, 115907. [CrossRef]
73. Asarapalli, S.K.; Pal, B.K.; Bisoyi, S.K. Assessment of the Role of Chemical Retardants on the Spontaneous Heating Liability of Coal. *Min. Metall. Explor.* **2024**, *41*, 287–295. [CrossRef]
74. Xiao, Y.; Lv, H.; Ren, S.; Deng, J.; Wang, C. Study on the spontaneous combustion inhibition characteristics of coal by imidazolium ionic liquids. *J. China Univ. Min. Technol.* **2019**, *48*, 175–181.
75. Ma, L.; Wang, D.; Kang, W.; Xin, H.; Dou, G. Comparison of the Staged Inhibitory Effects of Two Ionic Liquids on Spontaneous Combustion of Coal Based on in Situ FTIR and Micro-Calorimetric Kinetic Analyses. *Process Saf. Environ. Prot.* **2019**, *121*, 326–337. [CrossRef]
76. Gao, M.; Li, X.; Ren, C.; Wang, Z.; Pan, Y.; Guo, L. Construction of a Multicomponent Molecular Model of Fugu Coal for ReaxFF-MD Pyrolysis Simulation. *Energy Fuel* **2019**, *33*, 2848–2858. [CrossRef]
77. Qu, Z.; Sun, F.; Gao, J.; Pei, T.; Qie, Z.; Wang, L.; Pi, X.; Zhao, G.; Wu, S. A New Insight into the Role of Coal Adsorbed Water in Low-Temperature Oxidation: Enhanced-OH Radical Generation. *Combust. Flame* **2019**, *208*, 27–36. [CrossRef]
78. Dou, G.; Jiang, Z. Sodium Humate as an Effective Inhibitor of Low-Temperature Coal Oxidation. *Thermochim. Acta* **2019**, *673*, 53–59. [CrossRef]
79. Lu, W.; Sun, X.; Gao, L.; Hu, X.; Song, H.; Kong, B. Study on the Characteristics and Mechanism of DL-Malic Acid in Inhibiting Spontaneous Combustion of Lignite and Bituminous Coal. *Fuel* **2022**, *308*, 122012. [CrossRef]
80. Feng, W. Experimental Study on Green Composite Retardant to Inhibit Spontaneous Combustion of Coal. Master's Thesis, China University of Mining and Technology, Beijing, China, 2019.
81. Huang, Z.; Liu, X.; Gao, Y.; Zhang, Y.; Li, Z.; Wang, H.; Shi, X. Experimental Study on the Compound System of Proanthocyanidin and Polyethylene Glycol to Prevent Coal Spontaneous Combustion. *Fuel* **2019**, *254*, 115610. [CrossRef]
82. Qin, B.; Dou, G.; Wang, D. Thermal Analysis of Vitamin C Affecting Low-Temperature Oxidation of Coal. *J. Wuhan Univ. Technol.-Mat. Sci. Ed.* **2016**, *31*, 519–522. [CrossRef]
83. Li, J.; Li, Z.; Yang, Y.; Zhang, X.; Yan, D.; Liu, L. Inhibitive Effects of Antioxidants on Coal Spontaneous Combustion. *Energy Fuels* **2017**, *31*, 14180–14190. [CrossRef]
84. Guo, S.; Yan, Z.; Yuan, S.; Geng, W. Inhibitory Effect and Mechanism of L-Ascorbic Acid Combined with Tea Polyphenols on Coal Spontaneous Combustion. *Energy* **2021**, *229*, 120651. [CrossRef]
85. Taraba, B.; Peter, R.; Slovák, V. Calorimetric Investigation of Chemical Additives Affecting Oxidation of Coal at Low Temperatures. *Fuel Process. Technol.* **2011**, *92*, 712–715. [CrossRef]
86. Slovak, V.; Taraba, B. Urea and  $CaCl_2$  as Inhibitors of Coal Low-Temperature Oxidation. *J. Therm. Anal. Calorim.* **2012**, *110*, 363–367. [CrossRef]
87. Li, J.; Liu, X.; Pi, S.; Yue, Z.; Jia, J. Optimization of Process Conditions for Degradation of Yunnan Zhaotong Lignite by Actinobacteria. *Appl. Chem. Eng.* **2017**, *46*, 1683–1687+1691.
88. Li, J.; Liu, X.; Huang, L.; Yang, X.; Li, T. Optimization of microbial degradation process conditions for lignite from Shengli, Inner Mongolia. *Coal Technol.* **2017**, *36*, 266–268.



89. Kang, H.; Liu, X.; Zhao, S.; Yang, Z.; Yang, Z. Experimental study on the degradation of lignite by four bacteria in Chifeng, Inner Mongolia. *Coal Technol.* **2019**, *38*, 130–133.
90. Mishra, S.; Akcil, A.; Panda, S.; Erust, C. Biodesulphurization of Turkish Lignite by *Leptospirillum Ferriphilum*: Effect of Ferrous Iron, Span-80 and Ultrasonication. *Hydrometallurgy* **2018**, *176*, 166–175. [CrossRef]
91. Zhang, X.; Yang, J.; Xie, P.; Liu, H.; Deng, Q.; Dai, F. Experimental Study on Controlled-Release Inhibitor Foam for Restraining Spontaneous Combustion of Coal. *Energy Explor. Exploit.* **2020**, *38*, 1159–1177. [CrossRef]
92. Lu, W.; Zhang, X.; Yuan, Y.; Qi, G.; Hu, X.; Li, J.; Liang, Y.; Guo, B. Study on the Characteristics and Mechanism of a New Type of Antioxidant Gel Foam for Coal Spontaneous Combustion Prevention. *Colloids Surf. A-Physicochem. Eng. Asp.* **2021**, *628*, 127254. [CrossRef]
93. Yang, W. Research on the Effect of Physical-Chemical Cage Composite Retardant on Coal Spontaneous Combustion. Master's Thesis, China University of Mining and Technology, Beijing, China, 2017.
94. Xue, D.; Hu, X.; Cheng, W.; Yu, X.; Wu, M.; Zhao, Y.; Lu, Y.; Pan, R.; Niu, H.; Hu, S. Development of a Novel Composite Inhibitor Modified with Proanthocyanidins and Mixed with Ammonium Polyphosphate. *Energy* **2020**, *213*, 118901. [CrossRef]
95. Huang, Z.; Song, D.; Hu, X.; Zhang, Y.; Gao, Y.; Quan, S.; Yin, Y.; Yang, Y.; Luo, H.; Ji, Y. A Novel Nano-Modified Inhibitor of Tert-Butyl Hydroquinone/Sodium Polyacrylate for Inhibiting Coal Spontaneous Combustion. *Energy* **2022**, *256*, 124439. [CrossRef]
96. Wang, J.; Zhang, Y.; Wang, J.; Wu, Y.; Zhou, C.; Zhang, Z. Synergistic inhibition of coal spontaneous combustion by inorganic salt-based inhibitors and free radical trappers. *J. Coal Sci.* **2020**, *45*, 4132–4143.
97. Jiao, G. Research on Antioxidant Microencapsulated Retardant for Preventing Coal Spontaneous Combustion. Master's Thesis, China University of Mining and Technology, Beijing, China, 2021.
98. Huo, Y.; Huo, Y. Efficient Physicochemical Coupling Inhibitor Compounding Method for Low-Temperature Oxidation of Coal and Its Mechanism of Action. Ph.D. Thesis, China University of Mining and Technology, Beijing, China, 2023.
99. Xue, H. Research on Antioxidant-Based Composite Retardant to Inhibit Key Active Groups of Coal Spontaneous Combustion Process. Master's Thesis, China University of Mining and Technology, Beijing, China, 2019.
100. Huang, Z.; Yan, L.; Zhang, Y.; Gao, Y.; Liu, X.; Liu, Y.; Li, Z. Research on a New Composite Hydrogel Inhibitor of Tea Polyphenols Modified with Polypropylene and Mixed with Halloysite Nanotubes. *Fuel* **2019**, *253*, 527–539. [CrossRef]
101. Xi, Z.; Jin, B.; Shan, Z. Reaction Mechanisms Involving Peroxy Radical in the Low-Temperature Oxidation of Coal. *Fuel* **2021**, *300*, 120943. [CrossRef]
102. Zhang, Y.; Hou, Y.; Liu, B.; Deng, J.; Liu, C.; Yang, J.; Wen, X. Mechanism and performance of halite carrier inorganic salts for retardation of coal spontaneous combustion. *J. Eng. Sci.* **2021**, *43*, 1295–1303.
103. Zhang, Y.; Shu, P.; Zhai, F.; Chen, S.; Wang, K.; Deng, J.; Kang, F.; Li, L. Preparation and Properties of Hydrotalcite Microcapsules for Coal Spontaneous Combustion Prevention. *Process. Saf. Environ. Prot.* **2021**, *152*, 536–548. [CrossRef]
104. Pan, R.; Ma, J.; Fu, D.; Li, C.; Jia, H.; Zheng, L. Experimental Study on the New Environmental Protection Chemical Composite Inhibitor for the Inhibition of Coal Spontaneous Combustion. *J. Therm. Anal. Calorim.* **2020**, *139*, 37–45. [CrossRef]

**Disclaimer/Publisher's Note:** The statements, opinions and data contained in all publications are solely those of the individual author(s) and contributor(s) and not of MDPI and/or the editor(s). MDPI and/or the editor(s) disclaim responsibility for any injury to people or property resulting from any ideas, methods, instructions or products referred to in the content.

MDPI AG  
Grosspeteranlage 5  
4052 Basel  
Switzerland  
Tel.: +41 61 683 77 34

*Processes* Editorial Office  
E-mail: [processes@mdpi.com](mailto:processes@mdpi.com)  
[www.mdpi.com/journal/processes](http://www.mdpi.com/journal/processes)



Disclaimer/Publisher's Note: The title and front matter of this reprint are at the discretion of the Guest Editors. The publisher is not responsible for their content or any associated concerns. The statements, opinions and data contained in all individual articles are solely those of the individual Editors and contributors and not of MDPI. MDPI disclaims responsibility for any injury to people or property resulting from any ideas, methods, instructions or products referred to in the content.





Academic Open  
Access Publishing

[mdpi.com](http://mdpi.com)

ISBN 978-3-7258-3136-4